MICROFLUIDIC ORGAN-ON-A-CHIP: REVOLUTIONARY PLATFORMS FOR DISEASE COMPREHENSION AND TREATMENT

EDITED BY: Shi-Cong Tao, Shang-Chun Guo, Wei Seong Toh, Nuno M. Neves and Owen Gareth Davies

PUBLISHED IN: Frontiers in Bioengineering and Biotechnology and Frontiers in Molecular Bioscience

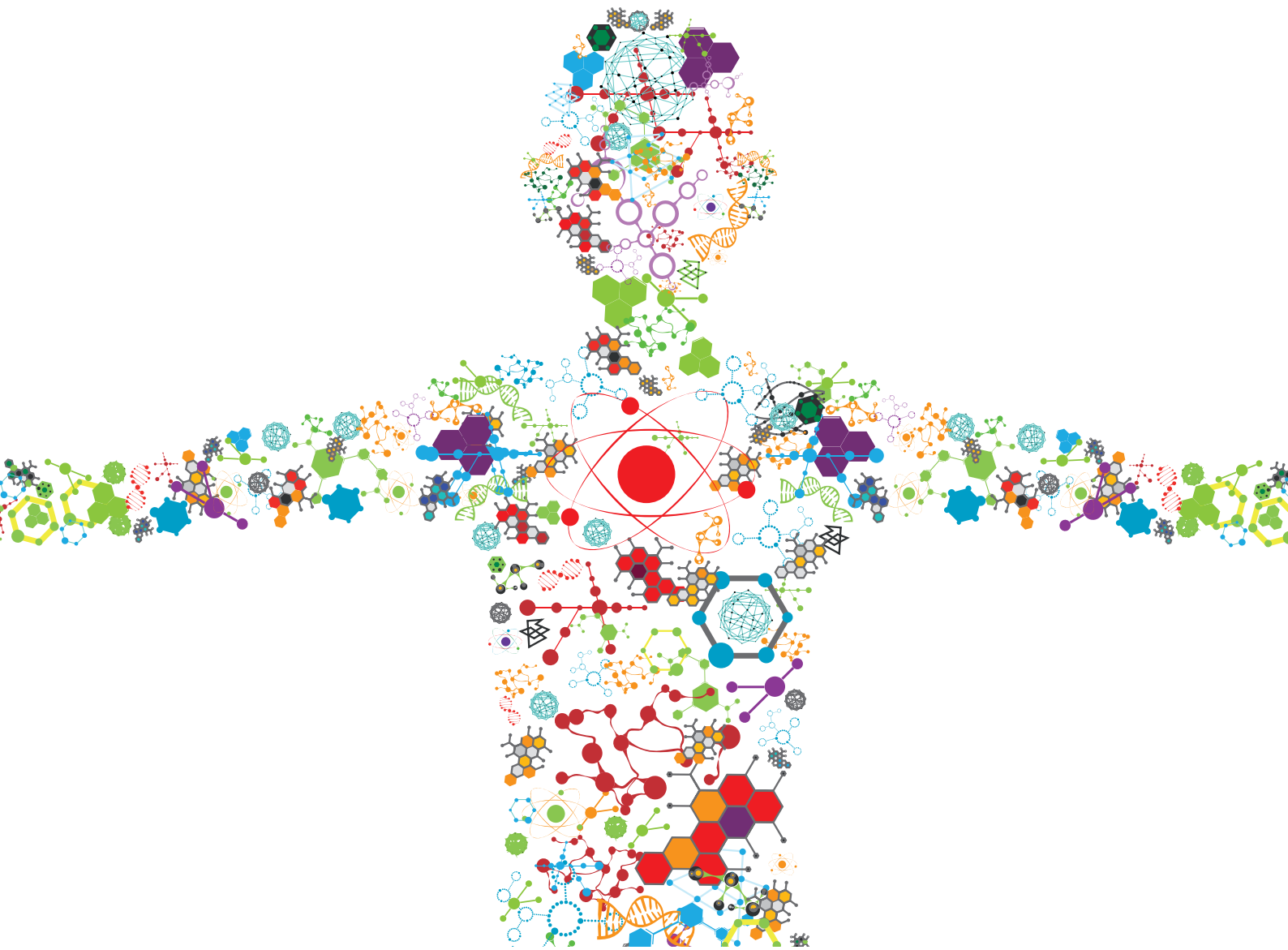

frontiers Research Topics

frontiers

ISSN 1664-8714
ISBN 978-2-88974-028-4
DOI 10.3389/978-2-88974-028-4

About Frontiers

Frontiers is more than just an open-access publisher of scholarly articles: it is a pioneering approach to the world of academia, radically improving the way scholarly research is managed. The grand vision of Frontiers is a world where all people have an equal opportunity to seek, share and generate knowledge. Frontiers provides immediate and permanent online open access to all its publications, but this alone is not enough to realize our grand goals.

Frontiers Journal Series

The Frontiers Journal Series is a multi-tier and interdisciplinary set of open-access, online journals, promising a paradigm shift from the current review, selection and dissemination processes in academic publishing. All Frontiers journals are driven by researchers for researchers; therefore, they constitute a service to the scholarly community. At the same time, the Frontiers Journal Series operates on a revolutionary invention, the tiered publishing system, initially addressing specific communities of scholars, and gradually climbing up to broader public understanding, thus serving the interests of the lay society, too.

Dedication to Quality

Each Frontiers article is a landmark of the highest quality, thanks to genuinely collaborative interactions between authors and review editors, who include some of the world's best academicians. Research must be certified by peers before entering a stream of knowledge that may eventually reach the public - and shape society; therefore, Frontiers only applies the most rigorous and unbiased reviews.
Frontiers revolutionizes research publishing by freely delivering the most outstanding research, evaluated with no bias from both the academic and social point of view. By applying the most advanced information technologies, Frontiers is catapulting scholarly publishing into a new generation.

What are Frontiers Research Topics?

Frontiers Research Topics are very popular trademarks of the Frontiers Journals Series: they are collections of at least ten articles, all centered on a particular subject. With their unique mix of varied contributions from Original Research to Review Articles, Frontiers Research Topics unify the most influential researchers, the latest key findings and historical advances in a hot research area! Find out more on how to host your own Frontiers Research Topic or contribute to one as an author by contacting the Frontiers Editorial Office: frontiersin.org/about/contact

MICROFLUIDIC ORGAN-ON-A-CHIP: REVOLUTIONARY PLATFORMS FOR DISEASE COMPREHENSION AND TREATMENT

Topic Editors:
Shi-Cong Tao, Shanghai Jiao Tong University, China
Shang-Chun Guo, Shanghai Jiao Tong University, China
Wei Seong Toh, National University of Singapore, Singapore
Nuno M. Neves, University of Minho, Portugal
Owen Gareth Davies, Loughborough University, United Kingdom

Existing culture systems have a limited ability to reproduce the complicated and dynamic microenvironment of a functioning organ. To solve the issues of conventional culture techniques, multidisciplinary researchers, involving medical doctors, stem cell and developmental biology experts, engineers and physical scientists, have emerged to innovate methods and devices.

A microfluidic organ-on-a-chip (μOOC) is a cell culture device, based on microfluidic technology, which contains continuously perfused chambers with cells to simulate organ-level physiology/pathology. The μOOC is not to build a whole living organ, but rather to synthesize minimal functional units that recapitulate organ-/tissue-level functions. The μOOC can be applied to study not only the convention stimulation on cells by molecular/drugs, but also physical forces (fluid shear stress, cyclic strain and mechanical compression), organ-specific cell-cell intercommunication, and organ-organ coupling responses.

There is an emerging need for innovative approaches for the production, control, analysis, and utilization of the μOOC, and even the multiple interconnected μOOC (Human-on-a-Chip). Although the μOOC has attracted much attention and is continuous being studied, there are still many difficult problems to be solved. Some of the most mentioned challenges include microenvironmental (biochemical, biophysical, biomechanical, nutrient, etc.) control, modeling tissue–tissue and multi-organ interactions, and reducing variability (automated control, high-throughput manipulation/analysis, integration of biosensing and etc.).

Citation: Tao, S.-C., Guo, S.-C., Toh, W. S., Neves, N. M., Davies, O. G., eds. (2021). Microfluidic Organ-on-a-Chip: Revolutionary Platforms for Disease Comprehension and Treatments. Lausanne: Frontiers Media SA.
doi: 10.3389/978-2-88974-028-4

Table of Contents

frontiers in Bioengineering and Biotechnology

ORIGINAL RESEARCH
published: 24 July 2020
doi: 10.3389/fbioe.2020.00763

A Theoretical and Experimental Study to Optimize Cell Differentiation in a Novel Intestinal Chip

Nicky Langerak[1†], Haysam M. M. Ahmed[2†], Yang Li[3], Igor R. Middel[2], Hossein Eslami Amirabadi[2,4], Jos Malda[3], Rosalinde Masereeuw[2‡] and René van Roij[1‡]*

[1] Institute for Theoretical Physics, Utrecht University, Utrecht, Netherlands, [2] Division of Pharmacology, Institute for Pharmaceutical Sciences, Utrecht University, Utrecht, Netherlands, [3] Utrecht Biofabrication Facility, University Medical Center Utrecht, Utrecht, Netherlands, [4] Human Cell Biology Group, Division of Metabolic Health Research, TNO, Zeist, Netherlands

Microphysiological systems have potential as test systems in studying the intestinal barrier, in which shear stress is critical for the differentiation of Caco-2 cells into enterocytes. The most commonly used *in vitro* gut model for intestinal barrier studies is based on trans-well cultures. Albeit useful, these culture systems lack physiological shear stress which is believed to be critical for the differentiation of Caco-2 cells into enterocytes and to form tight monolayers. Conversely, organ-on-chip models have presented themselves as a promising alternative since it provides cells with the required shear stress. To this end, a novel biocompatible 3D-printed microfluidic device was developed. In this device, Caco-2 cells were seeded under physiologically-relevant unidirectional shear stress and compared to cells cultured under gravity-driven flow. Using numerical studies, the flow rate that corresponds to the required shear stress was calculated. Experimental tests were conducted to verify the effect of this on cell differentiation. The experiments clearly showed an enhancement of cell differentiation potential in a unidirectional physiologically-relevant pump-driven flow system (PDFS) as opposed to the simpler bidirectional gravity-driven flow system (GDFS). Additionally, computational modeling of an adapted design confirmed its ability to supply all cells with a more homogeneous shear stress, potentially further enhancing their differentiation. The shear stress in the adapted design can be well-approximated with analytic methods, thus allowing for efficient predictions for all parameter values in the system. The developed novel microfluidic device led to the formation of a tighter monolayer and enhanced functional properties of the differentiated Caco-2 cells, which presents a promising tool for preclinical *in vitro* testing of drugs in an animal-free platform.

Keywords: gut-on-chip, shear stress, cell differentiation, 3D printing, numerical computation

OPEN ACCESS

Edited by:
Shang-Chun Guo, Shanghai Jiao Tong University, China

Reviewed by:
Yves-Jacques Schneider, Catholic University of Louvain, Belgium
George Alexander Truskey, Duke University, United States

***Correspondence:**
Rosalinde Masereeuw
r.masereeuw@uu.nl

[†] These authors have contributed equally to this work

[‡] These authors share senior authorship

Specialty section:
This article was submitted to Nanobiotechnology, a section of the journal Frontiers in Bioengineering and Biotechnology

Received: *15 March 2020*
Accepted: *16 June 2020*
Published: *24 July 2020*

Citation:
Langerak N, Ahmed HMM, Li Y, Middel IR, Eslami Amirabadi H, Malda J, Masereeuw R and van Roij R (2020) A Theoretical and Experimental Study to Optimize Cell Differentiation in a Novel Intestinal Chip. Front. Bioeng. Biotechnol. 8:763. doi: 10.3389/fbioe.2020.00763

1. INTRODUCTION

The small intestine plays a key role in the selective absorption of nutrients and drugs, and forms the first line of defense via its epithelial barrier. Three-dimensional (3D) experimental set-ups that can mimic human intestinal micro-environments may be instrumental in studying absorption processes and intestinal barrier integrity, which is now widely addressed by the so-called organ-on-a-chip technology. These chips aim to mimic the human organ physiology by replicating functional parts of organs in a controlled laboratory environment.

Microphysiological systems with biomimicry micro-architectures are usually fabricated from an optically clear plastic, such as polydimethylsiloxane (PDMS) and contain perfused hollow microchannels inhabited by living human cells as described by Bhatia and Ingber (2014). As a result of this structure, they allow for high-resolution, real-time imaging of biochemical activities in living human cells in a functional, yet controlled, organ context as described by Sontheimer-Phelps et al. (2019).

Various microphysiological systems have been developed that mimic mechanical, structural, and functional properties of the human small intestine (see e.g., Kim and Ingber, 2013; Trietsch et al., 2017; Kasendra et al., 2018; Jochems et al., 2019). These devices have already displayed the capability to reproduce organ-level responses and may be transferred to pharmaceutical industries to be implemented in preclinical research and have potential to replace animal studies for e.g., drug screening.

As carefully reviewed by Sontheimer-Phelps et al. (2019), however, microphysiological systems still have their limitations. One of these is the materials used to fabricate the device; PDMS is for instance known to non-specifically absorb small molecules, including certain drugs (Li et al., 2009; Su et al., 2011). In this work, we present a newly designed microfluidic device to study drug transport and metabolic functions of initially the intestine, with the potential to study other organs at a later stage. The experimental setup is constructed using an inert biocompatible polylactic acid (PLA) instead of the common microfabrication with PDMS to minimize solute absorption. In a comparison study, PDMS majorly absorbed hydrophobic small molecules, while PLA absorbed neither hydrophobic nor hydrophilic small molecules (Ongaro et al., 2020). Furthermore, we used a hollow fiber membrane set-up as in Jochems et al. (2019) to make the system compatible with transepithelial transport studies. The design of the microfluidic chip was meant to optimize cell differentiation toward a tight monolayer of functional organ cells. To enhance cell differentiation, we aim for a tuneable, time oscillating and homogeneous shear stress on the cells in the physiologically relevant regime of $0.002 - 0.8\text{dyne/cm}^2$ for intestinal cells (Olesen et al., 1988; Lentle and Janssen, 2008; Ishikawa et al., 2011). As a secondary optimization condition, we aim to achieve this shear stress at a low flow rate to allow for solute diffusion and drug transport in our experiments.

In **Figure 1A**, we show an overview of the experimental setup. The fluid flow in the setup is driven by a peristaltic pump, with an approximate harmonic pressure gradient as a result. This aims to mimic the time-dependent nature of fluid flow in human organs. The pump uses two reservoirs to independently perfuse two types of medium through side and top pathways, representing the intra- and extraluminal fluids, respectively. An off-scale cross-section of the system is shown in **Figure 1B**, which indicates that a perfusable hollow fiber is inserted into the flow channel. Cells were seeded on the outside of this fiber and shear stress, induced by the flow, will lead to the cell differentiation into a tight and, functional monolayer. A more detailed schematic with the system size and flow around the cells and fiber is shown in **Figure 1C**. Note that a fluid flow through the fiber was implemented as well to ensure a small pressure difference between the in- and outside of the fiber walls.

To find an optimal design in terms of cell differentiation, our methods can be divided in three steps. To give the reader a clear overview, we briefly discuss these steps before we go into detail on the methodology. First, numeric calculations on the flow velocity and shear stress were performed in potential devices, to find a simple design that gave shear stresses in the physiological relevant regime. Second, experiments were performed in the resulting experimental design (**Figure 1**) to quantitatively verify the calculations and measure the cell differentiation. Finally, as the third step, we investigated further optimization options in the design using both numerical and analytic calculations.

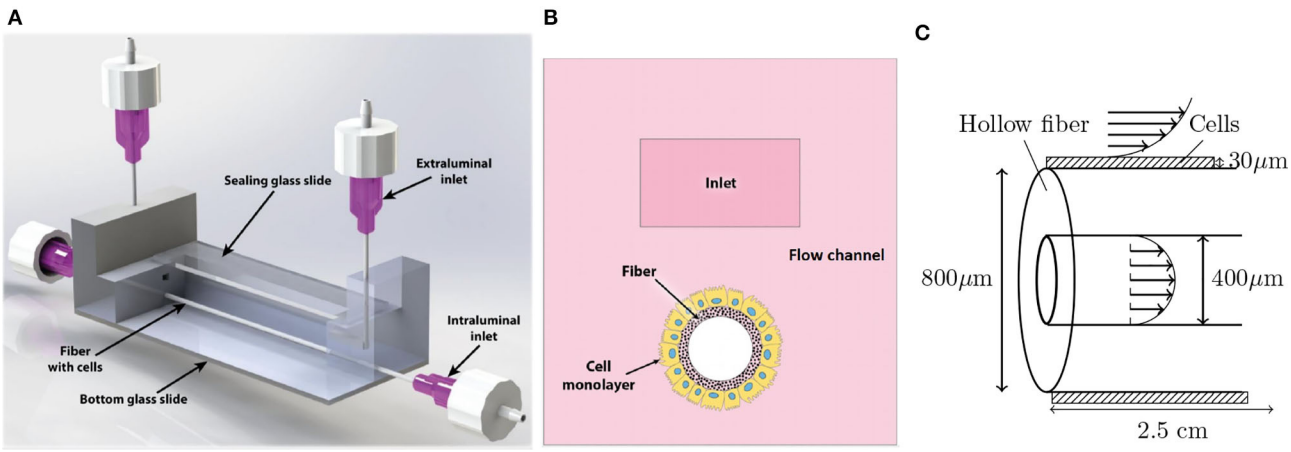

FIGURE 1 | Overview of the experimental setup. **(A)** The microfluidic chip with the in- and outlets as well as the fiber and transparent glass top and bottom. Fluid flow is driven by a peristaltic pump that is separately connected to the intra- and extraluminal inlets and outlets. **(B)** Cross section of the microfluidic chip. **(C)** Detailed view of the fiber and cells. The patterned domain indicates the cell layer, on which the fluid exerts a shear stress. The fluid velocity is indicated with the arrows inside and around the fiber. The steady flow rates in this device will be of order $Q_0 = 125\mu\text{L/min}$. Note that the figures are not to scale.

2. MATERIALS AND METHODS

2.1. Chamber Fabrication

The device is constructed through Fused Deposition Modeling (FDM) 3D printing with Ultimaker 3 (Ultimaker B.V.), which extrudes and selectively deposits thermoplastic (Polylactic acid, PLA) filament in the pre-determined position in a layer-by-layer manner. This fabrication process allows for efficient reflection of theoretical studies into prototypes. The 3-dimensional printable file was first designed in SolidWorks 2018 (Solidworks Corp.) and exported to G-code file via Ultimaker Cura (Ultimaker B.V.). The layerwise G-code file was thus read by the 3D printer and printed through a 0.4 mm nozzle in a layer-by-layer manner at a layer resolution of 60 microns. For the convenience of imaging, the top and bottom surfaces of the printed devices were partially open and sealed with cover slips, respectively.

In a typical chamber with the dimension of 75 mm (length) by 12.5 mm (width) by 3.65 mm (height), a open inner liquid reservoir of 25.1 mm (length) by 3 mm (width) sits in the very center of the chamber. Two flow pathways (as in **Figure 1B**), i.e., tubular channel (1.47 mm diameter) and cuboid channel (1.3 by 0.7 mm), are separated by 0.4 mm along the thickness direction of the chamber.

2.2. Chamber Assembly

SENUOfil type H-MF-0.2 hollow fiber capillary membranes (SENUOFIL, Tianjin, China) were fitted into the 3D-printed chambers and fixed in place with a high-viscosity dental glue "GI-MASK" (Coltene, Altstätten, Switzerland). Glass cover slips were used to seal the top and bottom of the chamber and fixed in place using medical-grade epoxy glue "Loctite Hysol M-31CL" (Henkel adhesives, Bopfingen, Germany). 18g syringe needles were used for intraluminal compartment.

2.3. Hollow Fiber Membrane Coating and Seeding

All chemicals were purchased from Sigma-Aldrich (Zwijndrecht, The Netherlands) unless stated otherwise. Following the assembly, the chambers were decontaminated in 70% (v/v) EtOH for 30 min. Next, chambers were washed with phosphate-buffered saline (PBS) twice and the hollow fiber membranes (HFM) were coated with filter-sterilized L-3,4-di-hydroxy-phenylalanine (L-Dopa, 2 mg/mL in 10 mM Tris buffer, pH 8.5). L-Dopa has been widely used in tissue engineering, and is known to be enriched in mussel-like adhesive proteins (Lee et al., 2009) and can adhere to a wide range of surfaces. L-Dopa self-polymerizes and exploits the reactivity of the film to covalently bind the biomolecule Coll I on the membrane surface to form an extracellular matrix (Oo et al., 2011). The fibers were then incubated at 37°C for 4 h to allow full polymerization of L-Dopa. After drying at 37°C for 5 min, HFM were washed with PBS and put in human collagen I solution (25 μg/mL in PBS) for another incubation at 37°C for 2 h. HFM were dried for 5 min at 37°C and unbound human collagen I was washed off with PBS. Finally, HFM were washed and stored in PBS awaiting cell seeding for a maximum of 4 days. Caco-2 cells (ATCC, Wesel, Germany) passages between 70 and 80 were washed, trypsinized and resuspended in culture medium [high glucose Fluorobrite medium (Gibco) with fetal calf serum (10% v/v), Glutamax (1%v/v), MEM Non-Essential Amino Acids (1%v/v), and penicillin/streptomycin (1% v/v)] at a concentration of 10^6 cells/ml; hereafter referred to as cell suspension. For cell seeding, 0.25 mL cell suspension was added per channel and incubated at 37°C, 5% CO_2 for 4 h in static conditions to allow cell adherence.

2.4. Flow Experiments

Following initial seeding, chambers were either exposed to passive gravity-driven flow for a period of 21 days or active pump-driven flow for 10 days. In the gravity-driven flow system (GDFS), flow was achieved by means of a 2-dimensional rocking platform (VWR, Breda, The Netherlands) with a speed rate of six rotations per minute at an angle of 10°, as described previously by Jochems et al. (2019). As for the pump-driven flow system (PDFS), flow rates of 30, 60, 90, and 125 μL/min were tested. Medium was refreshed every 2–3 days.

2.5. Cell Counting

Cell counting for normalization of activity per cell number was carried out utilizing the Cell Counting Kit (CCK-8) according to the manufacturer's protocol. Briefly, cell suspensions were seeded in 12-well plates and incubated at 37°C, 5% CO_2 for 24 h. Subsequently, the medium was removed and replaced with the CCK-8 reagent diluted 1:10 in culture medium. The plate was incubated for 4 h at 37°C, 5% CO_2, after which absorbance was measured at 450 nm with iMARK™microplate absorbance reader (Biorad, Veenendaal, Netherlands). Cell number was calculated using a standard curve prepared using a serial dilution of Caco-2 cells.

2.6. p-Cresol Metabolism

To assess the metabolic capacity of the differentiated Caco-2 cells, p-cresol was used as a model compound. After culturing the Caco-2 cells for 3 weeks in the GDFS, p-cresol was added either at a concentration of 50 μM for 3 and 6 h, or 100 μM for 12 and 24 h. The effect of p-cresol and its metabolites on the monolayer tightness was assessed using FITC-inulin leakage as described later. Based on the results of the initial experiment, exposure to p-cresol at a concentration of 50 μM for 3 h was used for all subsequent experiments.

To investigate the effect of 1,25-dihydroxyvitamin D3 (Vit D3) on the cell membrane integrity and the metabolic function of Caco-2 cells upon p-cresol treatment, cells in the GDFS were pre-treated with 100 nM Vit D3 for 24 h after 21 days in culture. 50 μM p-Cresol was then added for 3 h. Samples were then collected and analyzed using an ultra-high performance liquid chromatography mass-spectrometry (UHPLC-MS) method, as described by Mutsaers et al. (2011) to determine the concentration of the p-cresol metabolites p-cresol sulfate and p-cresol glucuronide.

To assess the effect of physiologically-relevant flow in the PDFS on p-cresol metabolism, both GDFS and PDFS were treated with 100 nM Vit D3 for 24 h after 21 and 10 days in culture, respectively. After which they were exposed to 50 μM p-cresol for 3 h. Samples were then collected and analyzed.

2.7. Immunofluorescent Staining

To investigate epithelial-layer integrity, phenotypical and morphological characteristics, immunostainings were performed. Cells were fixed using 2% paraformaldehyde for 15 min and then permeabilized using 0.3% (v/v) Triton X-100 in HBSS for 5 min. To prevent non-specific binding of antibodies, blocking was performed using 2% (w/v) bovine serum albumin (BSA) fraction V and 0.1% (v/v) Tween-20 in HBSS for 1 h. Fixed cells were incubated with primary antibodies, diluted in block solution, used were tight junction protein, zonula occludens-1 (ZO-1, 1:400) (Thermo Fisher Scientific, Bleiswijk, The Netherlands), enterocyte marker, Villin (1:400) (SCBT, Texas, USA) for 4 h. This was followed by incubation with goat-anti-mouse Alexafluor 488 (1:1,000; Thermo Fisher Scientific) or goat-anti-rabbit CF640R (1:1,000) as secondary antibodies. Finally, HFM were mounted using Prolong gold containing DAPI (Cell signaling technology, Leiden, The Netherlands) for nuclei staining. Images were acquired using the Leica TCS SP8 X (Leica Biosystems, Amsterdam, The Netherlands).

2.8. Leakage Assay

To assess monolayer integrity, an inulin-FITC (0.1 mg/ml in PBS) leakage assay was performed, as described in Jochems et al. (2019). The intraluminal inlet of the chamber was connected to warm inulin-FITC reservoir via a peristaltic pump (Ismatec Reglo, Cole parmer, Wertheim, Germany). The HFM was then perfused with inulin-FITC with a molecular weight of 3–6 kDa at a flow rate of 0.1 mL/min for 10 min. Samples were taken from the apical compartment. Fluorescence of the samples was measured at excitation wavelength of 492 nm and emission wavelength of 518 nm using Tecan infinite M200PRO plate reader (Tecan Austria GmbH).

The values of the apparent permeability P_{app} (in cm/s), which indicate the leakage of inulin-FITC, were calculated according to:

$$P_{app} = \frac{\frac{\mathrm{d}Q}{\mathrm{d}t}}{AC_0} \tag{1}$$

where $\mathrm{d}Q/\mathrm{d}t$ indicates the appearance rate of inulin-FITC over time (relative fluorescence unit/s), A is the surface area of the exposure area and C_0 is the initial concentration of the warm inulin-FITC reservoir. As a control, coated-fibers without cells were used to determine leakage through the fiber which was then set to 100% leakage for further calculations.

2.9. Alkaline Phosphatase Activity

Alkaline phosphatase (ALP) activity was measured as enterocyte differentiation marker, using Amplite™Colorimetric Alkaline Phosphatase assay kit (AAT Bioquest, Sunnyvale, USA). The assay was performed according to the manufacturer protocol. Briefly, HFM were incubated with the pNPP substrate solution (diluted 1:1 in culture medium) for 15 min at 37°C; thereafter, absorbance was measured at 400 nm with iMARK™microplate absorbance reader (Biorad, Veenendaal, the Netherlands).

2.10. Statistical Significance

Every experiment was at least performed in triplicate, results are depicted as mean ± standard error of the mean. Statistical analysis was performed in Graphpad version 7 using either one-way ANOVA followed by a Dunnett's test, Student's T-test or Unpaired T-test (where applicable). A P-value of $p < 0.05$ was considered significantly different.

2.11. Governing Equations

We determined the flow around the cells theoretically with the standard Stokes equations, by solving

$$\rho\frac{\partial \mathbf{u}}{\partial t} = -\nabla p + \eta\nabla^2\mathbf{u}, \quad \nabla\cdot\mathbf{u} = 0 \tag{2}$$

for the velocity profile $\mathbf{u}(\mathbf{r}, t)$ and the pressure $p(\mathbf{r}, t)$ at position $\mathbf{r}$ and time t. In Equation (2), $\rho = 997.8\mathrm{kg/m}^3$ and $\eta = 0.78\mathrm{mPa\,s}$ are the mass density and dynamic (shear) viscosity of the fluid, respectively. Note that $\rho(\mathbf{r}, t) = \rho$ is a spatial and temporal constant, since we assume an isotropic and incompressible medium. Furthermore, we have no external forces on our fluid and we restricted attention to the low-Reynolds number regime, where the flow is laminar without any turbulence.

We have determined the flow in three different geometries. In order of increasing stress homogeneity (and thus potentially a more homogeneous monolayer of differentiated cells) they are: the experimental geometry from **Figure 1**, the optimal geometry from **Figure 2A** and concentric cylinders as in **Figure 2C**. Without any practical constraints, we could achieve a purely homogeneous shear stress upon embedding the fiber in an infinitely long concentric cylinder. The suggested optimal design, identified in **Figure 2A**, approaches this theoretical optimum as well as possible, with the practical constraints taken into account. Note that the dimensions of the optimal design are decreased compared to that of the experimental design, to allow for relevant shear stresses at a lower flow rate.

2.12. Analytic Methods

For the analytic calculations of axial flow between two concentric cylinders as in **Figure 2C**, we consider a purely pressure driven flow in the longitudinal z-direction. Based on the peristaltic pump, we assume the pressure gradient G to be varying harmonically with steady offset G_0 and amplitude $G_1 = \epsilon G_0$, thus we have

$$-\frac{\partial p}{\partial z} \equiv G(t) = G_0(1 + \epsilon\sin(\omega t)), \tag{3}$$

where ω is the (angular) driving frequency. We used symmetry arguments and the pressure gradient from Equation (3), to simplify the Stokes equations. Pulsatile flow in a simple tube is well-studied in Leal (2007) and we followed similar (but not identical) calculation steps to find the flow profile between concentric cylinders (see **Supplementary Material** for detailed calculations). The governing equations were written in adimensional form, to reveal that the functional form of the velocity profile in this system depends on only three dimensionless parameters: the ratio of the cylinders radii R_2/R_1, the relative amplitude ϵ and the Strouhal number $R_\omega = \frac{\omega R_1^2}{\nu}$,

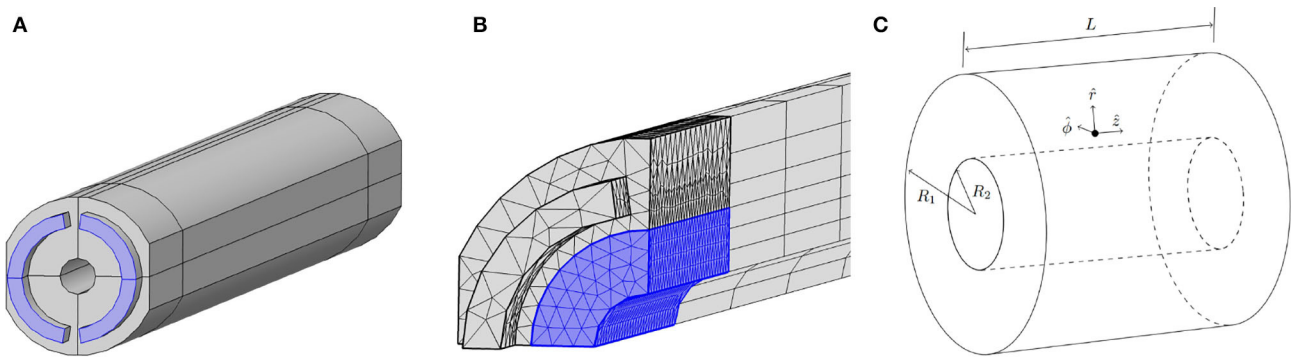

FIGURE 2 | (A) Optimal design of the flow channel for the PDFS. The blue semi-annulus shaped regions represent the inflow tubes and the hollow cylinder in the center represents the outside of the fiber. The lines that partition the channel in quarters indicate the symmetry planes of the geometry and show that the channel can be partitioned into four equal parts. The development length that is considered for mesh refinement is indicated with the lines around the outside of the flow channel. Compared to the existing experimental design, shown in **Figures 1A,C**, all dimensions are decreased: the fiber radius here is 0.25mm, the flow channel radius is 1.1mm, the length of the device is still 2.5cm and the fiber is placed concentrically in the flow channel. Detailed dimensions can be found in the **Supplementary Material**. **(B)** The mesh that is used to compute the velocity profile numerically in the optimal geometry. Only the first 8mm of the region near the inlet is shown here; the mesh is similar near the outlet. The blue region indicates the domain near the fiber where the mesh is refined. Note that to speed up computation only a quarter of the device is meshed, exploiting the symmetries in the system. To retrieve the full velocity profile in the PDFS, we could then mirror our solution. **(C)** Concentric cylinders with inner radius R_2, outer radius R_1, and length L. The unit vectors $(\hat{z}, \hat{r}, \hat{\phi})$ in cylindrical coordinates are depicted at a point between the cylinders, where the fluid will flow in the $\hat{z}$ direction. The inner cylinder represents the outside of the cell layer. This geometry is used to approximate the PDFS; a comparison in terms of shear stress between the two geometries is described in section 3.4.

which can be viewed as a dimensionless frequency. Here, $\nu = \eta/\rho = 7.8 \cdot 10^{-7}\text{m}^2/\text{s}$ is the kinematic viscosity.

2.13. Numerical Methods

Numerical studies were performed in the experimental and optimal geometry using the software COMSOL Multiphysics® V5.2. We used a 3D model with the creeping-flow module from the single-phase flow package. We used no-slip boundary conditions (BC) on all the walls and on the outside of the fiber, with an incoming Poiseuille mass flux BC at the inlet and a normal-stress-free BC at the outlet. For steady-state computation of the flow in the experimental geometry, a standard tetrahedral mesh was used with a refinement around the fiber for higher accuracy in the shear stress. The element size was determined empirically until a stable solution was found. To speed up time-dependent computations in the optimal geometry, the computational domain was divided into three parts, (i) the vicinity of the fiber, with a fine mesh of tetrahedral basis elements, (ii) the bulk of the device with a swept mesh of hexahedrons as basis elements, and (iii) the vicinity of the inlet and outlet with tetrahedral basis elements. The extent of the domains are determined using the boundary layer of the flow from time-dependent analytical approximations similar to those in Leal (2007) and an analytic result for the development length as described by Durst et al. (2005). We used about 2.5 times the development length to determine the length L_m of region (iii) in the mesh. This resulted in $L_m \approx 2.5 l_d \approx 1.5 D_H$, with l_d the development length and D_H the hydraulic diameter as written by Langerak (2019). In the optimal geometry, this resulted in $L_m = 0.6\text{mm}$ for the in- and outlets and $L_m = 3.3\text{mm}$ for the flow channel. We used $\delta = \sqrt{\frac{\nu}{\omega}}$ for the thickness of the boundary layer (Langerak, 2019), and we refined the mesh over a thickness of $3 \cdot \delta$. This resulted in a refined mesh around the fiber with a thickness of 0.33mm. The resulting mesh in the optimal geometry, illustrated in **Figure 2B**, consists of 34,788 elements. The numerical time-dependent studies were performed for a real time flow of five oscillations and it was confirmed both theoretically (Langerak, 2019) and numerically that this was sufficient for the transient regime to die off.

2.14. Parameters for Design Comparison

To compare the numerical calculations in the optimal design (**Figure 2A**) with the analytic calculations between concentric cylinders (**Figure 2C**), we used one characteristic set of parameters. For the inner cylinder radius, we have the fiber radius and the cell height (from Hidalgo et al., 1989), which gives $R_2 = 250\mu\text{m} + 30\mu\text{m} = 0.28\text{mm}$. The outer radius is minimized, given practical constraints for device strength, and yields $R_1 = 1.1\text{mm}$. This gives a radii ratio of $R_2/R_1 \approx 0.2545$. We choose experimentally realistic flow rates of $Q_0 = 125\mu\text{L/min}$ for the average flow and $Q_1 = Q_0/2$ for the amplitude of the oscillatory flow. With a cylinder length of $L = 2.5\text{cm}$, this yielded pressure gradients of $G_0 = 7.9\text{Pa/m}$ and $G_1 = 22.1\text{Pa/m}$ over the concentric cylinder flow channel (see **Supplementary Material** for this calculation). Thus, we have $\epsilon = G_1/G_0 = 2.8$, and the pressure differences over the flow channel are $\Delta p_0 = LG_0 = 0.20\text{Pa}$ and $\Delta p_1 = LG_1 = 0.55\text{Pa}$. With the chosen peristaltic pump, the average flow rate of $Q_0 = 125\mu\text{L/min}$ can be achieved with a pump setting of about 50 rotations per minute. Given that the pump has 12 rollers, we approximated the oscillation frequency of the pressure gradient as $\frac{\omega}{2\pi} = f = 12 \cdot 50\text{RPM} = 10\text{Hz}$. This yielded for the Strouhal number $R_\omega = \omega R_1^2/\nu \approx 97.3 \gg 1$, which indicates that the time-dependent nature of the

solution cannot at all be neglected for the final results; we can not approximate our solution with a quasi steady-state.

3. RESULTS AND DISCUSSION

3.1. Characterization of the Flow Around the Hollow Fiber Membrane in the Pump-Driven Flow System

A numerical evaluation of the steady state flow in the experimental geometry from **Figure 1** is performed using COMSOL and depicted in **Figure 3A**. In the bulk of the channel, we verified that we have (essentially) parallel streamlines, indicating a unidirectional flow; thus the only significant contribution to the flow in the centre of the device is in the longitudinal direction. We confirmed that the in- and outlet effects occur over a length scale of only a few a millimeter, which is negligible for the experiment.

Given the laminar velocity profile $u_z(r,\phi)$ in the bulk of the device, we can evaluate the shear stress $\tau_{zr}(r,\phi) = \eta\frac{\partial u_z(r,\phi)}{\partial r}$ numerically. Here, r is still the radial distance from the center of the fiber and ϕ is the azimuthal angle, defined with $\phi = 0$ on the top of the fiber. Note that we are most interested in the shear stress on the cells, given by

$$\tau_{zr,cells}(\phi) = \eta \left.\frac{\partial u_z(r,\phi)}{\partial r}\right|_{r=R_2}. \quad (4)$$

The numerical evaluation of the shear stress on the cells around the fiber is depicted in **Figure 3B**. With a steady flow rate of $Q_0 = 125\mu$L/min, we observed a heterogeneous shear stress on the cells around the fiber with a maximum of about $11.5\cdot10^{-3}$dyne/cm^2 at the top of the fiber and a minimum of about $7.4\cdot10^{-3}$dyne/cm^2 at the bottom. Thus, a relative deviation from the average of 22%. Despite the stress heterogeneity, we did observe that our inflow of $Q_0 = 125\mu$L/min gives a shear stress that is of the order of magnitude of the required physiological shear stress for the intestinal cells to differentiate (as determined by Olesen et al., 1988; Lentle and Janssen, 2008; Ishikawa et al., 2011). Our measurements on cell differentiation were performed in this device for flow rates around this value. A more detailed analysis of a more homogeneous shear stress on the cells in the optimal geometry is described after the experimental results.

3.2. Experimental Results

An overarching goal of this work was to develop a gut-on-a-chip model that can be combined with other organs, primarily kidney, to study the effect of uremic toxins in chronic kidney disease

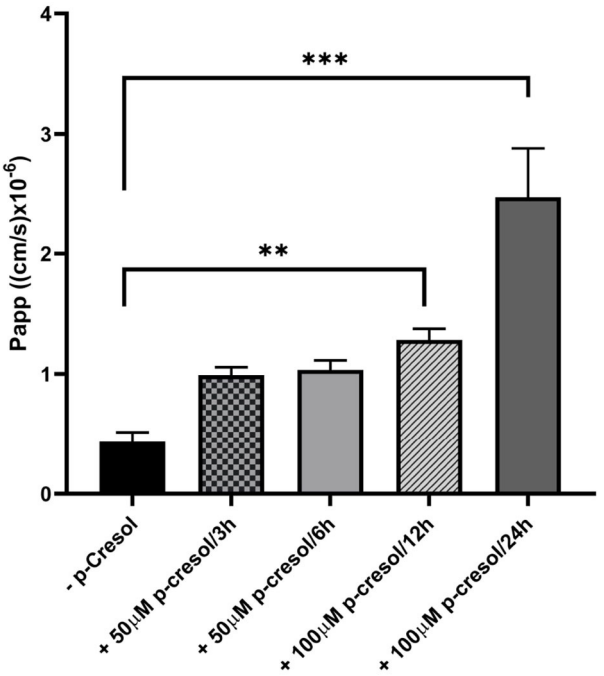

FIGURE 4 | Monolayer integrity of Caco-2 cells in GDFS cultures when treated with or without p-cresol at 50 or 100 μM for 3, 6, 12, or 24 h. Data are shown as mean ± SD, $n = 4$. $^{**}p < 0.01$; $^{***}p < 0.001$.

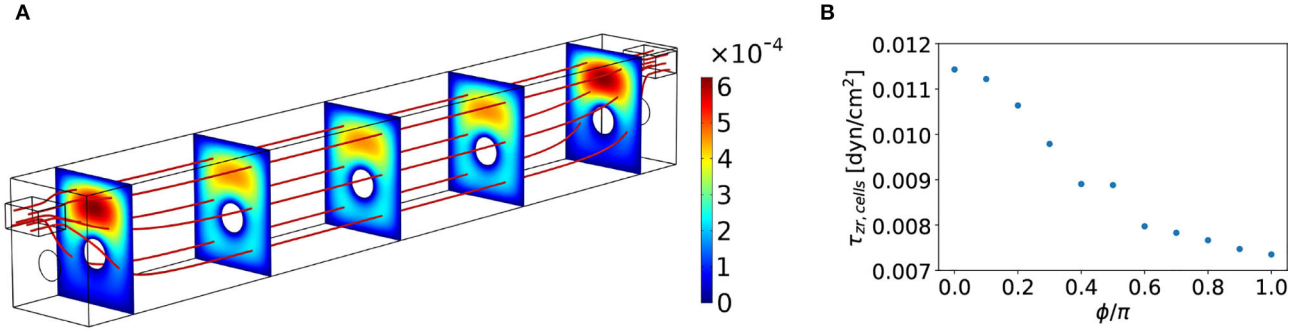

FIGURE 3 | (A) Steady-state velocity field $u_z(\mathbf{r})$ in the experimental flow channel, the magnitude is indicated with the colorbar in (m/s). The red lines indicate streamlines and the cut planes show the velocity magnitude. The dimensions are as indicated in **Figure 1C** and the channel has a total width of 3 mm and height of 3.65 mm. An aqueous fluid with viscosity $\eta = 0.78$mPa s and density $\rho = 997.8$ kg/m^3 flows through the device at a steady flow rate of $Q_0 = 125$ μL/min. **(B)** Shear stress on the cells $\tau_{zr,cells}$ in the center of the microfluidic device as a function of the azimuthal angle ϕ around the fiber. Here, $\phi = 0$ corresponds to the top of the fiber.

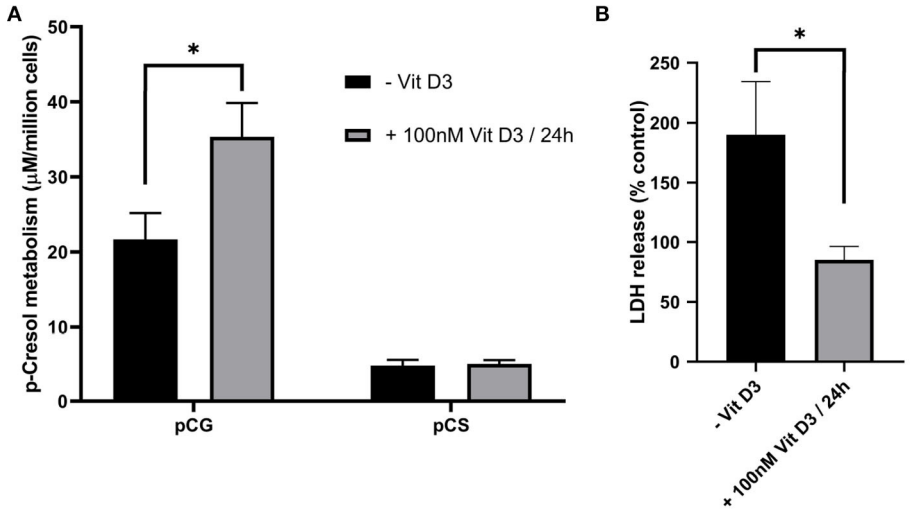

FIGURE 5 | The effect of vitamin D3 pre-treatment on Caco-2 metabolic capacity **(A)** and membrane integrity **(B)** upon subsequent treatment with 50 μM p-cresol for 3 h. Data are shown as mean ± SD, $n = 4$. *$p < 0.05$.

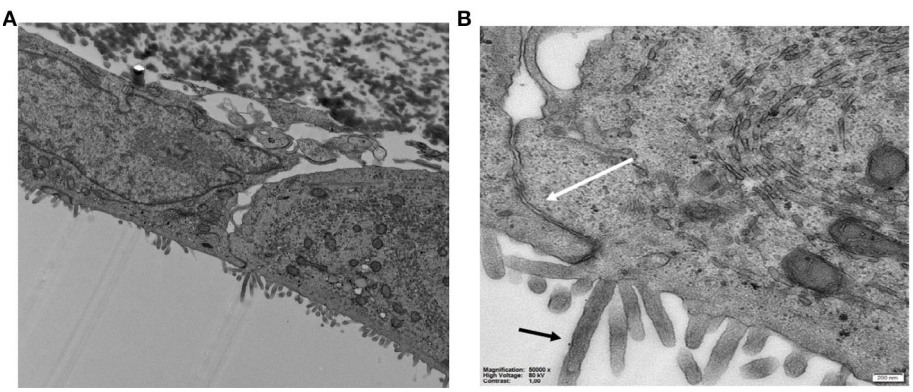

FIGURE 6 | (A,B) TEM images of Caco-2 cells on HFM in the GDFS cultures showing **(B)** the tight junctions (white arrow) and microvilli (black arrow).

on the gut. For that purpose, p-cresol was chosen as a model compound for uremic toxins.

To determine the optimal conditions and establish a baseline, Caco-2 cells were cultured on collagen-coated hollow fibers in the gravity-driven flow system (GDFS) for 3 weeks. L-Dopa/collagen-coated hollow fibers have been previously shown by Chevtchik et al. (2016) not to present any significant mass transfer limitations.

p-Cresol was subsequently added to investigate its effect on monolayer integrity and cell viability, as determined by apparent paracellular permeability (P_{app}) and LDH release, respectively. Exposure to p-cresol resulted in strongly compromised barrier function (**Figure 4**), due to the toxic nature of this compound and its metabolites on the cells (Vaziri et al., 2015; Gryp et al., 2017).

Vitamin D3 has been shown to improve CYP3A4 induction in Caco-2 cells by Kasendra et al. (2020) and improve tight junction conductance (Chirayath et al., 1998) possibly through the interaction with Claudin-2 gene as shown by Zhang et al. (2015). We found that vitamin D3 treatment prior to p-cresol exposure improved membrane integrity, while enhancing p-cresol metabolism (**Figure 5**).

To verify the differentiation and polarization, cells were examined with TEM and the images obtained (**Figure 6**) clearly shows the formation of microvilli on the apical membrane and tight-junctions at the lateral side.

Next, the optimization for the pump-driven flow system (PDFS) was performed. We carried out computations to determine the range of flow rates that would result in physiologically relevant shear stresses for gut tubules. Our fluid dynamics' simulation showed a fairly uniform shear stress along almost the whole length of the fiber with the top surface being exposed to the maximal stress (**Figure 3**). Flow rates of 30, 60, 90, and 125 μL/min, corresponding to maximum shear stresses of 0.003, 0.005, 0.008 and 0.011 dyne/cm^2, were chosen in the physiologically relevant range.

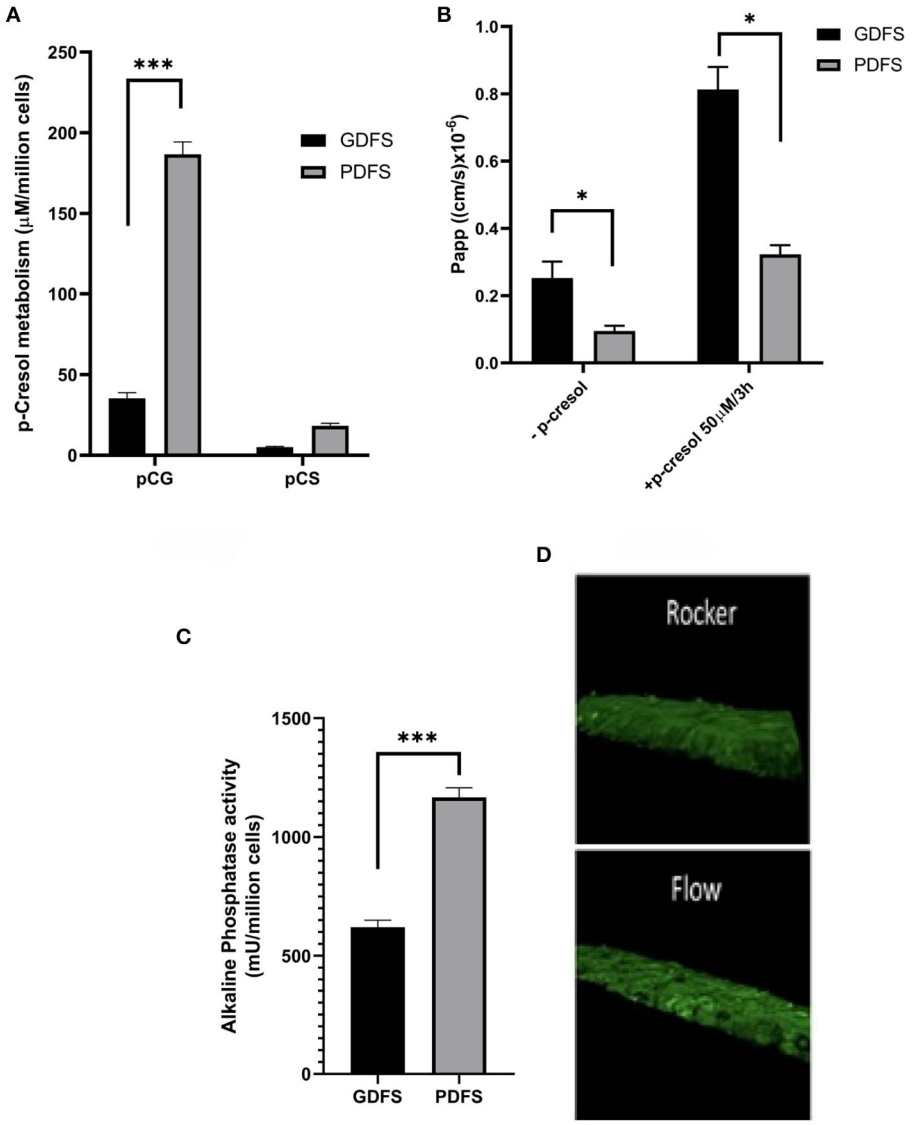

FIGURE 7 | Functional analysis of Caco-2 cells in GDFS vs. PDFS. PDFS exhibited higher p-cresol metabolic capacity into p-cresol glucuronide (pCG) and p-cresol sulfate (pCS) **(A)**, tighter monolayer formation **(B)**, improved brush border activity **(C)** and better differentiation in terms of villi formation **(D)**. Data are shown as mean ± SD, $n = 2$–4. $^{*}p < 0.05$; $^{***}p < 0.001$.

GDFS has been shown to improve Caco-2 differentiation and functionality compared to static cultures (Jochems et al., 2019). Similarly, shear stress has been shown to improve Caco-2 differentiation compared to static cultures (Kim and Ingber, 2013; Shim et al., 2017). Additionally, a time-course experiment investigating the effect of shear stress on P_{app} has been recently reported by Kasendra et al. (2020). In this work, P_{app} of Duodenum-on-a-chip was shown to decrease over time for cells cultured under shear stress.

In our work, Caco-2 cells cultured in a GDFS for 21 days were compared to ones cultured in a PDFS for 10 days. We have shown that uni-directional flow achieved by the PDFS was crucial for the formation of a tight monolayer as evident by the apparent permeability (P_{app}) (**Figure 7B**) when compared to the bi-directional flow of the GDFS.

Moreover, Caco-2 cells in the PDFS formed villi and crypts reminiscent of intestinal villi (**Figure 7D**). The protective and metabolism-inducing effect of Vit. D3 on Caco-2 cells was augmented in the PDFS as compared to the GDFS (**Figures 7A,B**). Additionally, the brush-border activity expressed in terms of alkaline phosphatase activity was significantly improved under uni-directional flow in the PDFS compared to the bi-directional flow of the GDFS (**Figure 7C**).

Fibers were subjected to these flows for 10 days and analyzed by confocal imaging, showing the formation of tight-junctions

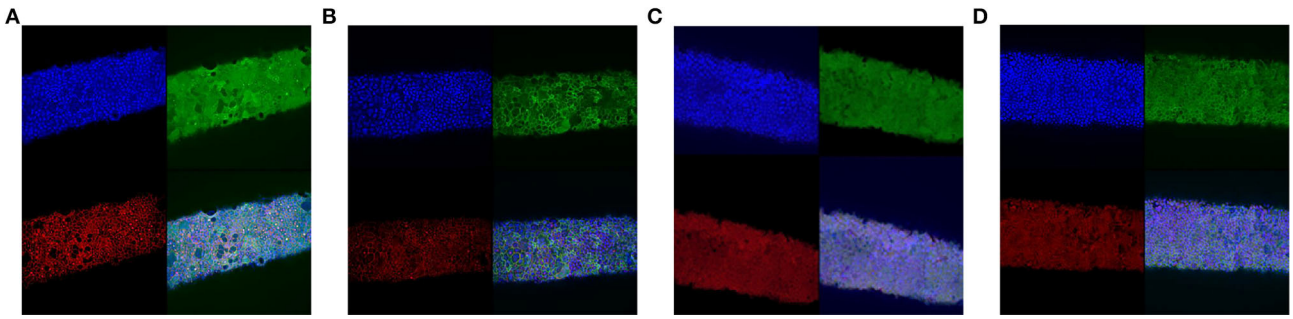

FIGURE 8 | Confocal microscope images of Caco-2 cells in PDFS after 10 days under 30 **(A)**, 60 **(B)**, 90 **(C)**, and 125 **(D)** μL/min. Images show staining for tight-junctions (ZO-1, red), villi (villin, green), and nuclei (DAPI, blue).

without considerable interruptions at 90 and 125 μL/min (**Figure 8**).

3.3. Axial Flow Between Concentric Cylinders

Recall that the flow in our experiment was driven by a peristaltic pump to mimic the time oscillating nature of fluid flow in human organs. In the experimental geometry, we have only determined the steady state flow rate, since the design results in a computationally heavy numerical evaluation. We have determined the full time-harmonic flow rate between concentric cylinders to have a more complete prediction of the shear stress on the cells in our (optimal) experiment.

Solving Equation (2) for axial flow between concentric cylinders and using the spatial derivative from Equation (4), resulted in an explicit expression for the shear stress on the cells of the form (see **Supplementary Material** for details on the calculation):

$$\tau_{\mathrm{zr,cells}} = G_0 R_1 \left(\frac{-R_2}{2R_1} + \frac{\frac{R_1}{R_2} - \frac{R_2}{R_1}}{4 \ln\left(\frac{R_1}{R_2}\right)} \right) \left[1 + \epsilon A_\tau \sin\left(\omega t + \phi_\tau\right) \right]. \tag{5}$$

Equation (5) reveals not only a phase shift, ϕ_τ, between the applied pressure and experienced stress – which is not so relevant given the long duration of exposure to stress – but also a reduction factor $A_\tau(R_\omega, R_2/R_1)$ of the time-dependent stress amplitude compared to the stationary stress. Explicit expressions of A_τ and ϕ_τ in terms of R_ω and R_2/R_1 are given in the **Supplementary Material**. Thus, with Equation (5), we have an explicit evaluation of the shear stress on the cells for all system parameters, which allows for efficient prediction of the shear under any conditions. In **Figure 9**, we plot A_τ as a function of R_ω for a few cylinder geometries R_2/R_1.

In **Figure 9** we observe that, in the static limit ($R_\omega \to 0$), there is no reduction of the shear stress, i.e., $A_\tau \to 1$ for each radii ratio. We also confirmed in Langerak (2019) that $\phi_\tau \to 0$ in the same $R_\omega \to 0$ limit, such that the shear stress (Equation 4) reduces to a stationary shear stress in the static limit, as predicted. Furthermore, in **Figure 9** we see that A_τ goes to zero algebraically for high frequencies as $R_\omega^{-\alpha}$ with a non-universal (radii ratio dependent) exponent $\alpha > 0$ that we do not study in any detail here. Thus, qualitatively, **Figure 9** shows that there is a reduction factor $A_\tau \leq 1$ of the time-dependent stress compared to the stationary stress, that decreases for increasing driving frequency.

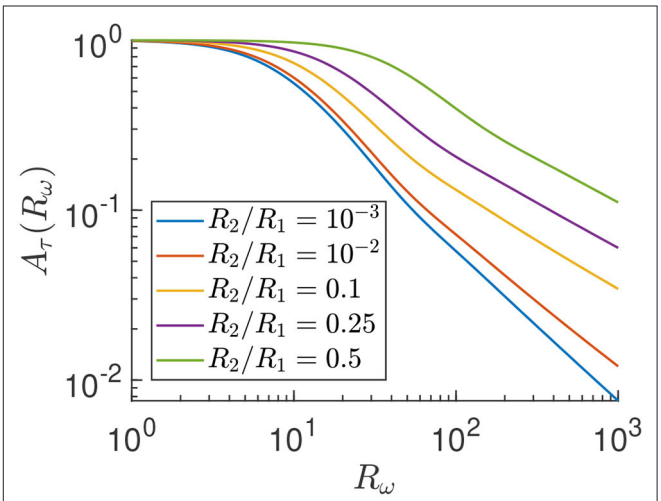

FIGURE 9 | Reduction factor A_τ of the time-dependent shear stress amplitude compared to the stationary stress as in Equation (5) on log-log scale.

Note that for our parameters, $R_\omega \approx 100$ and $R_2/R_1 \approx 0.25$, we have a reduction factor of $A_\tau \approx 0.2$. This indicates that the time oscillating behavior of the system is non-negligible in terms of the effect on the shear stress and we indeed need the full time-dependent calculations instead of a much easier quasi steady-state approach.

3.4. Asymmetry in Optimal Geometry

To use our analytic results for efficient predictions in the optimal geometry, we analyzed the difference in shear stress on the cells in the optimal geometry (**Figure 2A**) and the concentric cylinder geometry **Figure 2C** for one set of parameter values as described in the section 2. The analysis is performed for both the steady state and time-oscillating solution, where we used data of the shear stress on points of the fiber for fixed angles $\phi/\pi = 0, 1/8, 1/4, 3/8, 1/2$ in the center of the device. The resulting

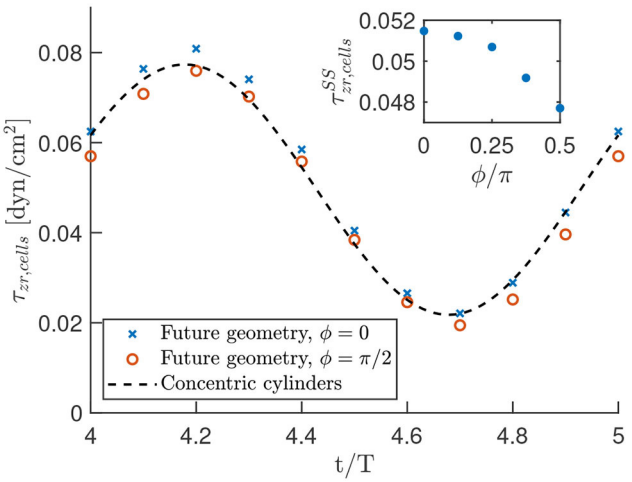

FIGURE 10 | Oscillating shear stress on the cells in the optimal geometry as a function of time. The data points result from the numerical calculations in COMSOL, while the black dashed line is the analytic prediction in a concentric cylinder geometry. These results are obtained with the parameter settings as described in the section 2 and oscillation period $T = 0.1$s. The shown shear stress is the sum of a steady and a time-harmonic contribution. The inset highlights the steady state shear stress on the cells for various values of ϕ/π to indicate the homogeneity of the shear stress.

shear stress on the cells, as well as the analytic prediction is shown in **Figure 10**.

First, **Figure 10**, suggests that there is only a small error when we approximate the optimal geometry with concentric cylinders. An analysis of the results yielded a maximum deviation of about 10% in the shear stress between the two geometries. The minimum error was achieved using our analytic results with an outer cylinder of 98.6% of the radius we used to construct the optimal geometry. This suggests that we can use our analytic results as a reasonable approximation of the shear stress in the experiment.

Although the time dependent oscillatory stress is only shown for $\phi/\pi = 0, 1/2$ in the main graph of **Figure 10**, we verified that the shear stress is in between these values for other azimuthal angles. Furthermore, we see in the inset of **Figure 10** that we have a very homogeneous steady-state shear stress in the optimal geometry, with a relative deviation from the average of only 4%. Thus, we observed a nearly homogeneous shear stress on the cells in the optimal geometry, which is well-approximated by our analytic calculations.

4. CONCLUSIONS

A new intestinal chip was designed using numerical computation of the fluid flow and the result is shown in **Figure 1**. This three dimensional setup is constructed using an inert biocompatible polylactic acid instead of the common microfabrication with PDMS to minimize solute absorption. The setup does still allow for high-resolution, real-time imaging of biochemical activities. Furthermore, cells are seeded on a hollow fiber, which adds curvature to the cell structure and does not hinder transport of physiological solutes.

With our design, we aimed to optimize cell differentiation toward a tight mono-layer of functional organ cells. With numerical and analytic calculations, we found a design that result in a tuneable, time oscillating and (nearly) homogeneous shear stress on the cells in the physiologically relevant regime.

The cells in our flow setup exhibited a higher p-cresol metabolic capacity, tighter monolayer formation, improved brush border activity (alkaline phosphatase) and better differentiation in terms of villi formation (**Figure 7**) compared to previous studies like Jochems et al. (2019). Thus, this novel microphysiological system is already a promising tool for studies of the metabolic functions of the intestine.

Furthermore, we have shown that we can improve the homogeneity of the shear stress even further with a design similar to concentric cylinders (**Figure 2A**). Using analytic calculations, we can fully predict and tune the time-dependent shear stress on the cells with an error of order 10%. We predicted a nearly homogeneous shear stress on the cells with a relative deviation of 4% around the fiber, compared to a 22% deviation in the experimental geometry. Since the shear stress is determined as a function of all free system parameters, in future studies, these analytic results can be used to efficiently predict the stress for all pressure gradient ratios ϵ and driving frequencies ω.

In addition to design optimization to ensure homogenous shear stress, future work will also focus on optimization of the biological component through using organoids instead of Caco-2 cells; thereby recapitulating the complexity of the intestinal tissue. Furthermore, the use of Caco-2 is not ideal since the use of organoids or iPSC-derived cells will better recapitulate the complexity of the *in vivo* intestinal tissue (Dutton et al., 2019). However, this was a first step to establish a novel gut-on-a-chip and in the future more experiments optimizing such a chip both in terms of fluid dynamics and biological relevance to the intestine will be carried out.

In conclusion, we have shown that our new intestinal chip gives an improved functional mono-layer of cells. Finally, it has the potential to study other organs (in a modular way) at a later stage, since the shear stress is fully tuneable.

DATA AVAILABILITY STATEMENT

Numerical datasets generated for this study are included in the article/**Supplementary Material**. All experimental data are available on request.

AUTHOR CONTRIBUTIONS

NL performed the numerical and analytic calculations under supervision of RR. HA performed the experiments in collaboration with IM and HE under supervision of RM. YL constructed the 3D microfluidic device under supervision of JM. NL, HA, and RM drafted this manuscript. All authors

provided critical feedback and helped shape the results analysis and manuscript.

FUNDING

This work was part of the D-ITP consortium, a program of the Netherlands Organisation for Scientific Research (NWO) that was funded by the Dutch Ministry of Education, Culture and Science (OCW). This work was further supported by the Dutch Kidney Foundation (DKF, 17OI13).

ACKNOWLEDGMENTS

The authors thank Prof. Dr. Judith Klumperman and Dr. Nalan Liv for their help in electron microscopy.

SUPPLEMENTARY MATERIAL

The Supplementary Material for this article can be found online at: https://www.frontiersin.org/articles/10.3389/fbioe.2020.00763/full#supplementary-material

REFERENCES

Bhatia, S. N., and Ingber, D. E. (2014). Microfluidic organs-on-chips. *Nat. Biotechnol.* 32:760. doi: 10.1038/nbt.2989

Chevtchik, N. V., Fedecostante, M., Jansen, J., Mihajlovic, M., Wilmer, M., Rüth, M., et al. (2016). Upscaling of a living membrane for bioartificial kidney device. *Eur. J. Pharmacol.* 790, 28–35. doi: 10.1016/j.ejphar.2016.07.009

Chirayath, M. V., Gajdzik, L., Hulla, W., Graf, J., Cross, H. S., and Peterlik, M. (1998). Vitamin d increases tight-junction conductance and paracellular Ca2+ transport in Caco-2 cell cultures. *Am. J. Physiol. Gastroint. Liver Physiol.* 274, G389–G396. doi: 10.1152/ajpgi.1998.274.2.G389

Durst, F., Ray, S., Ünsal, B., and Bayoumi, O. (2005). The development lengths of laminar pipe and channel flows. *J. Fluids Eng.* 127, 1154–1160. doi: 10.1115/1.2063088

Dutton, J. S., Hinman, S. S., Kim, R., Wang, Y., and Allbritton, N. L. (2019). Primary cell-derived intestinal models: recapitulating physiology. *Trends Biotechnol.* 37, 744–760. doi: 10.1016/j.tibtech.2018.12.001

Gryp, T., Vanholder, R., Vaneechoutte, M., and Glorieux, G. (2017). p-Cresyl sulfate. *Toxins* 9:52. doi: 10.3390/toxins9020052

Hidalgo, I. J., Raub, T. J., and Borchardt, R. T. (1989). Characterization of the human colon carcinoma cell line (Caco-2) as a model system for intestinal epithelial permeability. *Gastroenterology* 96, 736–749. doi: 10.1016/S0016-5085(89)80072-1

Ishikawa, T., Sato, T., Mohit, G., Imai, Y., and Yamaguchi, T. (2011). Transport phenomena of microbial flora in the small intestine with peristalsis. *J. Theor. Biol.* 279, 63–73. doi: 10.1016/j.jtbi.2011.03.026

Jochems, P. G., van Bergenhenegouwen, J., van Genderen, A. M., Eis, S. T., Versprille, L. J. W., Wichers, H. J., et al. (2019). Development and validation of bioengineered intestinal tubules for translational research aimed at safety and efficacy testing of drugs and nutrients. *Toxicol. In Vitro* 60, 1–11. doi: 10.1016/j.tiv.2019.04.019

Kasendra, M., Luc, R., Yin, J., Manatakis, D. V., Kulkarni, G., Lucchesi, C., et al. (2020). Duodenum intestine-chip for preclinical drug assessment in a human relevant model. *eLife* 9:e50135. doi: 10.7554/eLife.50135

Kasendra, M., Tovaglieri, A., Sontheimer-Phelps, A., Jalili-Firoozinezhad, S., Bein, A., Chalkiadaki, A., et al. (2018). Development of a primary human small intestine-on-a-chip using biopsy-derived organoids. *Sci. Rep.* 8:2871. doi: 10.1038/s41598-018-21201-7

Kim, H. J., and Ingber, D. E. (2013). Gut-on-a-chip microenvironment induces human intestinal cells to undergo villus differentiation. *Integr. Biol.* 5, 1130–1140. doi: 10.1039/c3ib40126j

Langerak, N. (2019). *Optimization of fluid flow in a novel organ chip* (Master's thesis), Utrecht University, Utrecht, Netherlands.

Leal, L. G. (2007). *Advanced Transport Phenomena: Fluid Mechanics and Convective Transport Processes*, Vol. 7. Cambridge: Cambridge University Press.

Lee, H., Rho, J., and Messersmith, P. B. (2009). Facile conjugation of biomolecules onto surfaces via mussel adhesive protein inspired coatings. *Adv. Mater.* 21, 431–434. doi: 10.1002/adma.200801222

Lentle, R., and Janssen, P. (2008). Physical characteristics of digesta and their influence on flow and mixing in the mammalian intestine: a review. *J. Compar. Physiol. B* 178, 673–690. doi: 10.1007/s00360-008-0264-x

Li, N., Schwartz, M., and Ionescu-Zanetti, C. (2009). PDMS compound adsorption in context. *J. Biomol. Screen.* 14, 194–202. doi: 10.1177/1087057108327326

Mutsaers, H. A., Van Den Heuvel, L. P., Ringens, L. H., Dankers, A. C., Russel, F. G., Wetzels, J. F., et al. (2011). Uremic toxins inhibit transport by breast cancer resistance protein and multidrug resistance protein 4 at clinically relevant concentrations. *PLoS ONE* 6:e18438. doi: 10.1371/journal.pone.0018438

Olesen, S.-P., Claphamt, D., and Davies, P. (1988). Haemodynamic shear stress activates a K^+ current in vascular endothelial cells. *Nature* 331:168. doi: 10.1038/331168a0

Ongaro, A. E., Di Giuseppe, D., Kermanizadeh, A., Miguelez Crespo, A., Mencattini, A., Ghibelli, L., et al. (2020). Polylactic is a sustainable, low absorption, low autofluorescence alternative to other plastics for microfluidic and organ-on-chip applications. *Anal. Chem.* 92, 6693–6701. doi: 10.1021/acs.analchem.0c00651

Oo, Z. Y., Deng, R., Hu, M., Ni, M., Kandasamy, K., Bin Ibrahim, M. S., et al. (2011). The performance of primary human renal cells in hollow fiber bioreactors for bioartificial kidneys. *Biomaterials* 32, 8806–8815. doi: 10.1016/j.biomaterials.2011.08.030

Shim, K.-Y., Lee, D., Han, J., Nguyen, N.-T., Park, S., and Sung, J. H. (2017). Microfluidic gut-on-a-chip with three-dimensional villi structure. *Biomed. Microdev.* 19:37. doi: 10.1007/s10544-017-0179-y

Sontheimer-Phelps, A., Hassell, B. A., and Ingber, D. E. (2019). Modelling cancer in microfluidic human organs-on-chips. *Nat. Rev. Cancer* 19:65–81. doi: 10.1038/s41568-018-0104-6

Su, X., Young, E. W., Underkofler, H. A., Kamp, T. J., January, C. T., and Beebe, D. J. (2011). Microfluidic cell culture and its application in high-throughput drug screening: cardiotoxicity assay for herg channels. *J. Biomol. Screen.* 16, 101–111. doi: 10.1177/1087057110386218

Trietsch, S. J., Naumovska, E., Kurek, D., Setyawati, M. C., Vormann, M. K., Wilschut, K. J., et al. (2017). Membrane-free culture and real-time barrier integrity assessment of perfused intestinal epithelium tubes. *Nat. Commun.* 8:262. doi: 10.1038/s41467-017-00259-3

Vaziri, N. D., Zhao, Y.-Y., and Pahl, M. V. (2015). Altered intestinal microbial flora and impaired epithelial barrier structure and function in ckd: the nature, mechanisms, consequences and potential treatment. *Nephrol. Dialys. Transplant.* 31, 737–746. doi: 10.1093/ndt/gfv095

Zhang, Y., Wu, S., Lu, R., Zhou, D., Zhou, J., Carmeliet, G., et al. (2015). Tight junction CLDN2 gene is a direct target of the vitamin D receptor. *Sci. Rep.* 5:10642. doi: 10.1038/srep10642

Conflict of Interest: The authors declare that the research was conducted in the absence of any commercial or financial relationships that could be construed as a potential conflict of interest.

frontiers in Bioengineering and Biotechnology

ORIGINAL RESEARCH
published: 18 August 2020
doi: 10.3389/fbioe.2020.00931

A Modular Microscale Granuloma Model for Immune-Microenvironment Signaling Studies *in vitro*

*Samuel B. Berry[1], Maia S. Gower[1], Xiaojing Su[1], Chetan Seshadri[2] and Ashleigh B. Theberge[1,3]**

[1] Department of Chemistry, University of Washington, Seattle, WA, United States, [2] Department of Medicine, University of Washington, Seattle, WA, United States, [3] Department of Urology, University of Washington, Seattle, WA, United States

Tuberculosis (TB) is one of the most potent infectious diseases in the world, causing more deaths than any other single infectious agent. TB infection is caused by inhalation of *Mycobacterium tuberculosis* (Mtb) and subsequent phagocytosis and migration into the lung tissue by innate immune cells (e.g., alveolar macrophages, neutrophils, and dendritic cells), resulting in the formation of a fused mass of immune cells known as the granuloma. Considered the pathological hallmark of TB, the granuloma is a complex microenvironment that is crucial for pathogen containment as well as pathogen survival. Disruption of the delicate granuloma microenvironment *via* numerous stimuli, such as variations in cytokine secretions, nutrient availability, and the makeup of immune cell population, can lead to an active infection. Herein, we present a novel *in vitro* model to examine the soluble factor signaling between a mycobacterial infection and its surrounding environment. Adapting a newly developed suspended microfluidic platform, known as Stacks, we established a modular microscale infection model containing human immune cells and a model mycobacterial strain that can easily integrate with different microenvironmental cues through simple spatial and temporal "stacking" of each module of the platform. We validate the establishment of suspended microscale (4 μL) infection cultures that secrete increased levels of proinflammatory factors IL-6, VEGF, and TNFα upon infection and form 3D aggregates (granuloma model) encapsulating the mycobacteria. As a proof of concept to demonstrate the capability of our platform to examine soluble factor signaling, we cocultured an *in vitro* angiogenesis model with the granuloma model and quantified morphology changes in endothelial structures as a result of culture conditions ($P < 0.05$ when comparing infected vs. uninfected coculture systems). We envision our modular *in vitro* granuloma model can be further expanded and adapted for studies focusing on the complex interplay between granulomatous structures and their surrounding microenvironment, as well as a complementary tool to augment *in vivo* signaling and mechanistic studies.

Keywords: *in vitro* granuloma model, open microfluidics, immune signaling, paracrine signaling, microenvironment, modular

OPEN ACCESS

Edited by:
Nuno M. Neves, University of Minho, Portugal

Reviewed by:
Fransisca Leonard, Houston Methodist Research Institute, United States
Luciana Dini, Sapienza University of Rome, Italy

***Correspondence:**
Ashleigh B. Theberge
Abt1@uw.edu

Specialty section:
This article was submitted to Nanobiotechnology, a section of the journal Frontiers in Bioengineering and Biotechnology

Received: *14 April 2020*
Accepted: *20 July 2020*
Published: *18 August 2020*

Citation:
Berry SB, Gower MS, Su X, Seshadri C and Theberge AB (2020) A Modular Microscale Granuloma Model for Immune-Microenvironment Signaling Studies in vitro. Front. Bioeng. Biotechnol. 8:931. doi: 10.3389/fbioe.2020.00931

INTRODUCTION

Tuberculosis (TB) is one of the most potent infectious diseases in the world, causing more deaths than any other single infectious agent (World Health Organization, 2019). TB infection is caused by inhalation of *Mycobacterium tuberculosis* (Mtb) and subsequent phagocytosis and migration into underlying lung tissue and the lymph system by responding immune cells (e.g., alveolar macrophages and dendritic cells) (Kaufmann, 2004; Saunders and Britton, 2007). Due to the inability of these innate immune cells to clear Mtb, persistent Mtb induce an adaptive immune response, leading to the formulation of a fused mass of immune cells around Mtb known as a granuloma (Saunders and Britton, 2007). Within the granuloma, Mtb typically enter a latent phase characterized by a non-proliferative phenotype and lipid uptake (Peyron et al., 2008; Deb et al., 2009; Russell et al., 2009), leading to a latent infection that is effectively contained (World Health Organization, 2019). However, disruption of the delicate equilibrium between proinflammatory factors [e.g., tumor necrosis factor-α (TNFα), interferon-γ (IFNγ)], microenvironment conditions (e.g., hypoxia and pH), and immune cell populations (e.g., macrophages and T cells) can lead to reactivation of latent Mtb and deterioration of the granuloma, initiating an active TB infection and dissemination of infectious mycobacteria (Russell et al., 2009; Ramakrishnan, 2012).

Deciphering the impact of microenvironment variations around the granuloma remains a significant challenge, and researchers often rely on *in vivo* animal models or biological samples (e.g., blood and tissue biopsy), considered the gold standard for studying TB, to reconstruct this complex environment. These methods have laid the foundation for understanding the pathogenesis and immunology behind TB, yet many existing *in vivo* models do not accurately recapitulate Mtb infection as seen in humans (although recent advances in mouse models and the established zebrafish/*M. marinum* model are closing this gap) (Cronan and Tobin, 2014; Myllymäki et al., 2016; Gern et al., 2017; Zhan et al., 2017; Cronan et al., 2018; Yong et al., 2018). Additionally, despite recreating the complexity of an *in vivo* environment, spatial manipulation and probing of the granuloma microenvironment through introduction or removal of immune and tissue components is difficult in most animal models (Scanga and Flynn, 2014; Foreman et al., 2017; Zhan et al., 2017). Further, human-derived biological samples provide detailed cellular information regarding the granuloma, the immune response, and disease status (Guyot-Revol et al., 2006; Berry et al., 2010; Darboe et al., 2019; Ogongo et al., 2020), but are inherently limited as they only reflect a singular point in time, rather than the dynamic interactions that occur during the early stages of infection or disease progression.

Alternatively, researchers have utilized *in vitro* models to examine specific processes and immune phenomena associated with TB infection and granuloma formation, augmenting the valuable information elucidated from *in vivo* models (Birkness et al., 2007; Peyron et al., 2008; Deb et al., 2009; Kapoor et al., 2013; Elkington et al., 2019). These models, which often rely on infection of patient-derived peripheral blood mononuclear cells (PBMCs) with mycobacterial strains, have successfully mimicked granuloma formation and behavior through soluble factor signaling between immune cells (Puissegur et al., 2004; Birkness et al., 2007; Crouser et al., 2017), Mtb reactivation (Kapoor et al., 2013), and PBMC differentiation (Peyron et al., 2008). However, many of these *in vitro* models consist of granulomas grown inside of well plates (Puissegur et al., 2004; Birkness et al., 2007; Peyron et al., 2008; Kapoor et al., 2013; Crouser et al., 2017), limiting the ability of the researchers to easily manipulate the microenvironment of the granulomas and increase the complexity of their granuloma models through multiculture and introduction of key components of the microenvironment on demand. Recently, more complex, biomimetic models have been developed that have successfully recapitulated important biological phenomena (Parasa et al., 2014, 2017) and examined novel therapeutic approaches to combat TB infection (Bielecka et al., 2017; Tezera et al., 2017), while simultaneously demonstrating innovative and tractable platforms. However, these models face limitations in studies where users wish to subject granulomas to various microenvironmental cues over time, or in enabling the addition of tissue components after the model is established.

Building upon the foundation created by previous *in vitro* models, we present the creation of a novel microscale *in vitro* granuloma model that can be adapted to study the soluble factor signaling between granulomas and their surrounding microenvironment immediately following infection. Using a recently developed modular microfluidic coculture platform, known as "Stacks"(Yu et al., 2019), we demonstrate a multi-layered coculture that can be spatially and temporally manipulated to mimic different microenvironments and timepoints. The Stacks platform utilizes suspended cultures, wherein a droplet is contained in a well consisting of walls but lacking a ceiling or floor (Casavant et al., 2013; Humayun et al., 2018; Berthier et al., 2019), thereby enabling users to vertically stack layers containing different cell types and place them in signaling contact (Yu et al., 2019). The modular component of the Stacks, as well as of other microfluidic platforms, offers a notable advantage as users can optimize model conditions individually and connect each component to create different complex systems (Ong et al., 2019; Yu et al., 2019). As a proof of concept, we use a model mycobacterial strain known to induce granuloma formation *in vitro* (Seitzer and Gerdes, 2003; Puissegur et al., 2004), *Mycobacterium bovis* Bacillus Calmette- Guérin (BCG), with human blood-derived immune cells and validate its ability to form an *in vitro* granuloma model on the microscale (4 μL culture volume) in a layer of the Stacks platform. Further, to demonstrate the ability of our stackable microscale infection model to signal with its surrounding microenvironment in a proof-of-concept system, we miniaturize an existing *in vitro* angiogenesis model (containing primary human endothelial cells) within a separate stackable layer (Koh et al., 2008; Lonza, 2018; Yu et al., 2019). Here, we validate the development of our microscale *in vitro* granuloma model and demonstrate the capability of the system to support soluble factor signaling between the granuloma model and a separate stackable endothelial culture. We envision our modular *in vitro* granuloma model can be further developed to

include additional layers of immune cells, tissue models, and pathogens for studies examining the complex interplay between granulomatous structures and their surrounding environment, as well as a complementary tool to augment *in vivo* signaling and mechanistic studies.

RESULTS AND DISCUSSION

Microscale Granuloma Model Design and Overview

We present a modular *in vitro* platform that we adapted to enable the ability to add, modify, and manipulate the granuloma microenvironment for studying the effects of cellular signaling on granuloma formation and development. To create this *in vitro* model, we adapted a previously described open microfluidic platform ["Stacks"(Yu et al., 2019; **Figure 1**)] that relies on key fluidic principles, namely capillary pinning, to enable vertical stacking and removal of discrete cell culture wells without leakage or horizontal flow between stacked layers. The pinning of fluids within this platform is vital to contain cultures within the open wells and allows for the connection and separation of the wells without bonding or disruption of the cultures, respectively. Additionally, the Stacks platform provides numerous advantages such as pipette accessibility (due to its open culture wells), bio- and imaging compatibility (due to its fabrication from polystyrene or polypropylene), and microscale culture wells. Further, the Stacks device relies on surface tension and capillary forces for functionality, removing the need for external pumps commonly associated with microfluidic chips (i.e., syringe pumps) and allowing it to fit within common cell culture materials (e.g., OmniTray^{TM}, petri dish) and incubators. For our *in vitro* model system, we created an independent layer that can be clicked together with other layers containing culture models to initiate paracrine signaling or separated for independent analysis, thereby allowing us to temporally introduce different signaling microenvironments to our *in vitro* granuloma model (**Figure 1**; Yu et al., 2019). This Stacks layer, herein called the granuloma layer, consists of an infection model of human monocyte-derived macrophages (MDMs) and a model mycobacterium strain, *Mycobacterium bovis* Bacillus Calmette-Guérin (BCG), suspended in a 3D extracellular matrix (ECM) plug to mimic some aspects of *in vivo* granuloma behavior (e.g., pathogen encapsulation, soluble factor secretion, aggregate formation) previously observed in other *in vitro* granuloma models (Birkness et al., 2007; Kapoor et al., 2013; Crouser et al., 2017).

Previous *in vitro* granuloma models successfully recapitulated important components of granulomatous infections including leukocyte recruitment and signaling, establishment of dormancy and resuscitation, and genetic diversity at scales ranging from 12 well plates to 96 well plates (Birkness et al., 2007; Kapoor et al., 2013; Crouser et al., 2017). Our model adds to these existing techniques through miniaturization and introduction of modularity to enable examination of the signaling phenomena between a mycobacterial infection and its surrounding microenvironment. We reduce the volume of our cultures (4 μL/well) more than 10-fold from previous examples (50–500 μL/well) to decrease cell and reagent usage in our model; further, we mix BCG and MDMs together in a 3D extracellular matrix (ECM), without pre-infecting the MDMs, to establish the infection in our granuloma layer after a minimum of 24 h (**Figure 1**). However, due to the scale of the model (4 μL/well), the media buffering capacity, nutrient availability, waste accumulation, and multiplicity of infection (MOI) all needed to be optimized to permit successful formation of the granuloma layer (**Supplementary Information 2**). This is consistent with prior investigations on the effects of miniaturization on mammalian cell cultures (Su et al., 2013).

Validation of Granuloma Model in Stacks Platform

To validate the successful establishment of a microscale *in vitro* granuloma model within our platform, we used three separate previously reported readouts: (1) aggregate formation, (2) encapsulation of the mycobacterium within host immune cells, and (3) soluble factor analysis (Birkness et al., 2007; Kapoor et al., 2013; Crouser et al., 2017; Tezera et al., 2017). After initiating infection by mixing MDMs and BCG into the ECM (collagen I) and seeding it into the wells, we consistently observed aggregate formation in the granuloma layer containing BCG when wells were fixed and imaged on Day 4 post infection (p.i.) (**Figure 2**, **Supplementary Figure 3**, and **Supplementary Table 1**). Using mCherry-expressing BCG, we observed aggregation of CellTracker Green-stained MDMs around the BCG in infection wells, whereas little to no aggregate formation was observed in the uninfected control wells (**Figure 2**); the 3D structure of the aggregates containing MDMs and BCG was confirmed through confocal imaging of the granuloma layers on Day 4 p.i. (**Figure 2**). We observed complete encapsulation of BCG within the multi-cellular aggregate, oftentimes noting the presence of multiple spatially distinct BCG within one aggregate and little to no extracellular BCG (**Figure 2**). An advantage of mixing the BCG and MDMs without direct pre-infection of the MDMs is that MDMs must sample and migrate through the 3D collagen matrix in order to initiate the infection and respond to other infected MDMs, a process which is further supported by the microscale culture wells and an optimized MOI of 0.05. Further, CellTracker Green staining of the MDMs enables live cell imaging of these multicellular aggregates (no fixation and additional preparation steps required), as the dye stains live cells and is retained intracellularly (**Supplementary Figure 3**).

To illustrate the capability of our model to be used for soluble factor signaling studies, we analyzed the secretion profile of three granuloma-associated proinflammatory factors: interleukin-6 (IL-6), tumor necrosis factor α (TNFα), and vascular endothelial growth factor (VEGF) (**Figure 3**) from the model granuloma layer (in monoculture) (Lin et al., 2007; Martinez et al., 2013; Singh and Goyal, 2013; Polena et al., 2016). In accordance with previous models and studies (Birkness et al., 2007; Lin et al., 2007; Martinez et al., 2013; Singh and Goyal, 2013; Polena et al., 2016) we observed significantly greater secretion of IL-6 (P = 0.005) and VEGF (P = 0.039) in our infected granuloma layers (+BCG) when compared to

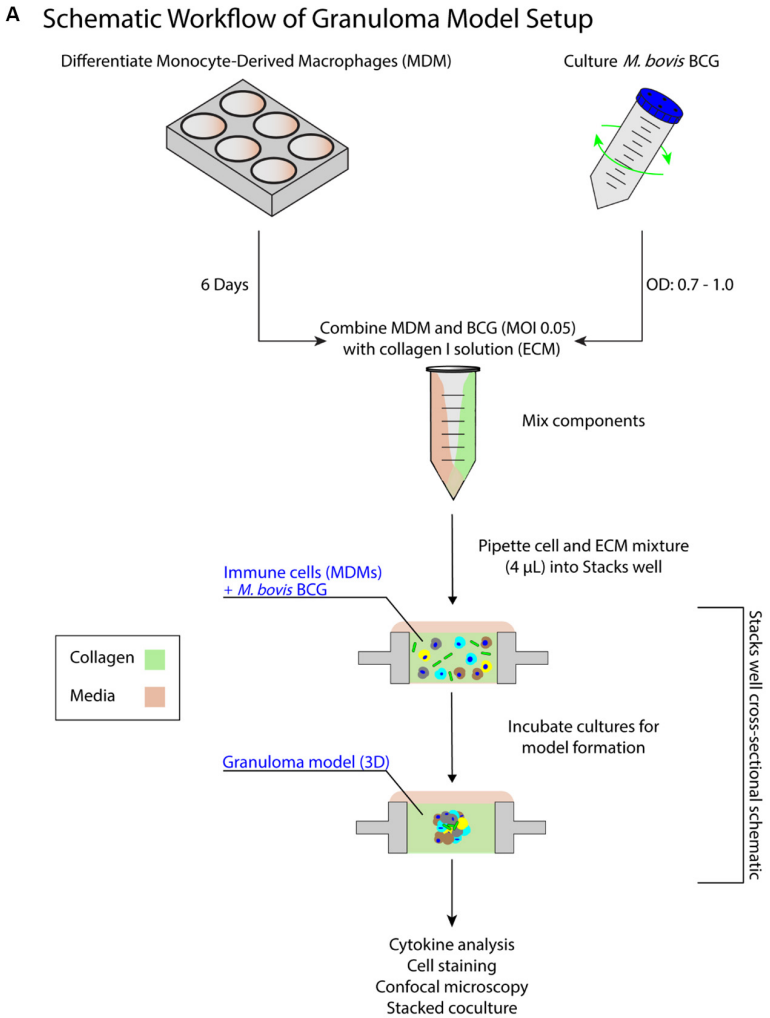

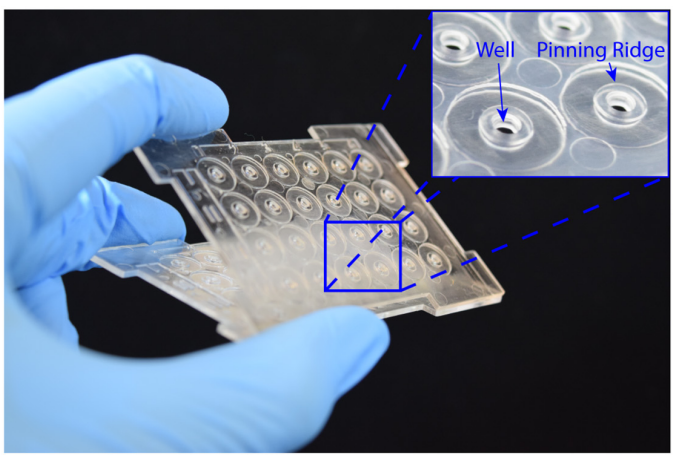

FIGURE 1 | Suspended open microfluidic platform enables creation of a modular *in vitro* granuloma model. **(A)** Schematic workflow showing setup and establishment of the model granuloma layer in the Stacks platform. Once established, the model granuloma layer can be stacked with other layers to initiate coculture paracrine signaling. **(B)** The "Stacks" platform (Yu et al., 2019) contains an array of 24 individual suspended wells to facilitate the exchange of signals through the top and bottom of the well to neighboring layers and can be easily combined and removed. The inset illustrates the open suspended wells (2 mm diameter) and pinning ridges required to prevent leakage within the platform.

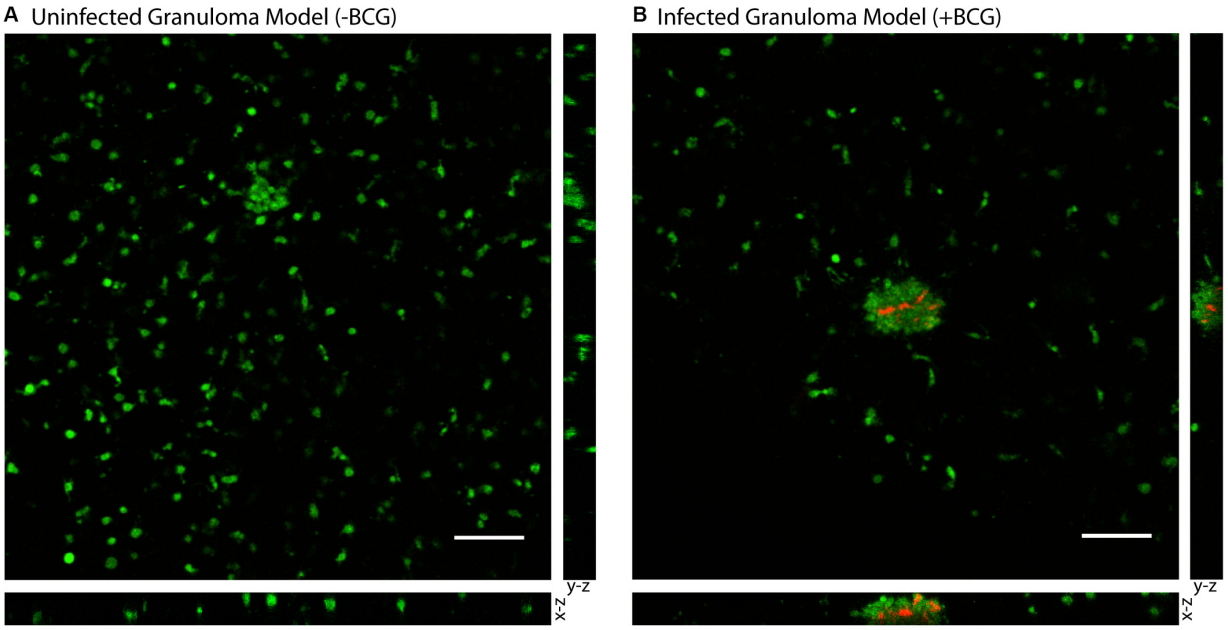

FIGURE 2 | Aggregation of *M. bovis* BCG and MDMs in 3D collagen plugs within a layer of the Stacks microscale culture system. **(A)** CellTracker Green-stained MDMs remain dispersed in a 3D collagen plug in the absence of coincubation with BCG. **(B)** MDMs encapsulate mCherry-expressing BCG in the granuloma layer and form large multicellular aggregates that surround the BCG-infected MDMs and contain the mycobacterium within the aggregate. Confocal microscopy shows the structure of the aggregated MDMs with BCG and illustrates containment of the BCG within the aggregate of MDMs in the suspended 3D collagen plug. Representative images obtained on Day 4 p.i. MOI: 0.05. Scale bar: 100 μm. Bottom image depicts *x-z* plane (66.5 μm thickness) and right image depicts *y-z* plane (66.5 μm thickness).

our control layers containing uninfected MDMs in monoculture (−BCG); further, we observed a 5–17-fold increase in TNFα secretion in 3 out of 4 independent experiments under the same conditions and a strong trend toward greater TNFα secretion (**Figure 3** and **Supplementary Figure 4**). We also observed decreasing secretion of IL-6, TNFα, and VEGF over 5 days, with the greatest concentrations observed for IL-6 and TNFα on Day 1 and for VEGF on Day 2 (**Figure 3** and **Supplementary Figure 4**). These results indicate that our platform is able to exhibit infection-dependent increases in soluble factor secretion, wherein there is a large burst of proinflammatory factors immediately following infection, that then decreases and stabilizes over time as we begin to observe aggregate formation in the granuloma layers. Additionally, while we observe the anticipated increases in the secretion of these factors, we would expect a more robust response if more virulent strains than BCG were used, as increased secretion of factors has been observed with infection by more virulent mycobacterial strains (Engele et al., 2002; Polena et al., 2016). In this work, we selected IL-6, VEGF, and TNFα as well-established cytokines to validate the secretion profile of our model (Birkness et al., 2007; Kapoor et al., 2013; Domingo-Gonzalez et al., 2016; Polena et al., 2016; Crouser et al., 2017); in particular, we included factors relevant for angiogenesis (i.e., VEGF) to validate its use in vasculature coculture models. Importantly, many other customizable combinations of signaling molecules can be analyzed depending on the biological question of interest, further supporting the use of this model granuloma layer for different biological assays. Thus, these results support the use of our microscale granuloma model for studies of soluble factor signaling involving the granuloma layer, and its broader use for mycobacterial infection cytokine studies (Domingo-Gonzalez et al., 2016).

BCG Granulomas Modulate Endothelial Structure Morphology *in vitro*

As a proof of concept to demonstrate the use of our microscale granuloma model in the Stacks platform, we developed a coculture system containing an established angiogenesis model (Koh et al., 2008; Sarkanen et al., 2011; Theberge et al., 2015; Lonza, 2018; Yu et al., 2019) that can be used to probe granuloma-associated angiogenesis (Datta et al., 2015; Oehlers et al., 2015; Osherov and Ben-Ami, 2016; Polena et al., 2016). Mycobacterium-mediated angiogenic processes and granuloma vascularization result from the secretion of proangiogenic factors by the infected immune cells that compose the granuloma and play a complex and evolving role during the course of infection (Oehlers et al., 2015, 2017; Polena et al., 2016; Torraca et al., 2017). Extensive work has been conducted on understanding the role of angiogenesis in granuloma outcome, finding that inhibition of VEGF and other signaling pathways reduces pathogenicity and dissemination of infectious mycobacteria (Oehlers et al., 2015; Polena et al., 2016; Harding et al., 2019) while normalizing surrounding vasculature, improving small molecule delivery, and decreasing hypoxia within the granuloma

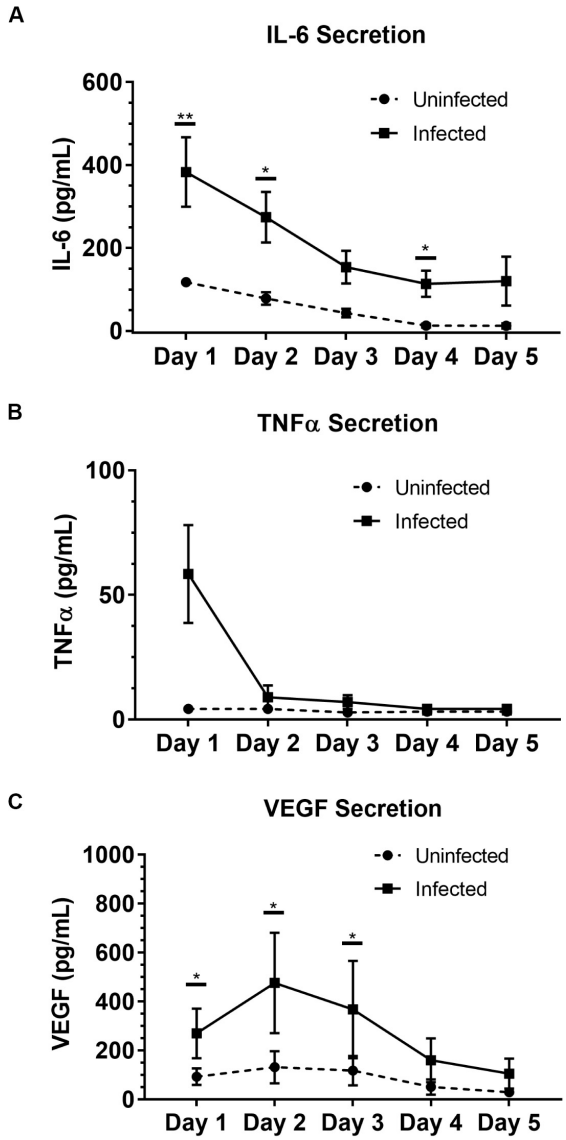

FIGURE 3 | Soluble factor analysis of granuloma layer supernatants illustrates proinflammatory profile of infection model. Infection with BCG causes significant increases in secretion of **(A)** IL-6 and **(C)** VEGF in the Stacks platform, and shows an increasing trend in **(B)** TNFα secretion Day 1 p.i. Secretion of IL-6, TNFα, and VEGF decreases over time in infected granuloma layers following infection, corresponding with the formation of aggregates starting around Day 3 p.i. For Day 1–5 p.i., media was replaced daily and supernatant collected from each day was analyzed. Each point represents pooled supernatant samples from 24 technical replicates from $n = 4$ independent experiments. Error bars: SEM. $^{*}P < 0.05$; $^{**}P < 0.01$; Ratio paired *t*-test. Results from each independent experiment on each day are provided in **Supplementary Figure 4** for reference.

(Datta et al., 2015). Similarly, we observed increased secretion of VEGF from infected cells within our microscale granuloma model (**Figure 3C**), and therefore sought to illustrate one potential use of our platform as a complimentary tool for studies examining this infection-mediated process.

To establish this granuloma-vasculature model coculture system, we created a second Stacks layer containing a floor, enabling culture of human endothelial cells on a hydrogel plug (Matrigel) while retaining the ability to be placed in soluble factor signaling contact with the granuloma layer. We selected an *in vitro* model of angiogenesis that has been extensively used to screen angiogenic stimulants and inhibitors, wherein human endothelial cells cultured in well plates self-assemble into tubule-like networks and demonstrate cell sprouting and branching (Bishop et al., 1999; Koh et al., 2008; Sarkanen et al., 2011; Lonza, 2018). To adapt this *in vitro* angiogenesis model into a Stacks layer (herein called the endothelial layer) for use, we miniaturized the established *in vitro* angiogenesis assay (Koh et al., 2008; Lonza, 2018) and seeded it into a separate Stacks layer that could then be subsequently clicked together with the granuloma layer to initiate soluble factor signaling between the two layers (**Figure 4** and **Supplementary Information 3**).

By placing the primary human endothelial cells on a separate Stacks layer, we demonstrate one potential use of our model to examine the induction of angiogenic processes around the granuloma layer and how those angiogenic processes are affected by the soluble factor signaling profile of the granuloma layer in a proof of concept system. In order to examine the influence of the soluble factor profile from the granuloma layer on the endothelial layer, we independently established the granuloma layer and the endothelial layer under their optimized culture conditions (**Figure 4**); the modularity of the Stacks platform enables both layers to be cultured in their optimal conditions (and in separate incubators) without risk of cross contamination prior to joining the layers. The granuloma layers were infected and incubated 24 h prior to clicking with the endothelial layer, and the endothelial layers were seeded 2 h prior to allow the cells to self-assemble into a tubule-like network (Sarkanen et al., 2011; Lonza, 2018). Within this experimental timeframe, we note the absence of large multicellular aggregates within the granuloma layer like those observed on Day 4 p.i., and this is in accordance with our temporal observations (**Supplementary Table 1**). Separate layers were then stacked together and connected by a bridge of shared media to allow passage of factors between the two layers (**Figure 4**). After 16 h of signaling, we separated the layers and fixed, stained, and imaged the vasculature to analyze its morphology as a result of coculture with the granuloma layer (**Figure 5**). We found that after 16 h of coculture, endothelial cells in contact with infected granuloma layers (+BCG) formed thinner, centralized structures with diffuse cell sprouts extending from the center, whereas endothelial cells in contact with uninfected control layers (−BCG) formed wider and larger structures that retained some interconnected networks (**Figure 5**). We quantified these morphological differences through measurement of their tubule index, a metric that measures the ratio of the endothelial structure perimeter to the endothelial structure area and can be used to discern between endothelial structure morphologies (e.g., tubule network, single tubule, and islands/clusters) (Theberge et al., 2015), and found significant morphological differences between endothelial layers cocultured with infected granuloma layers (+BCG) when compared with uninfected granuloma layers (−BCG) (**Figure 5**).

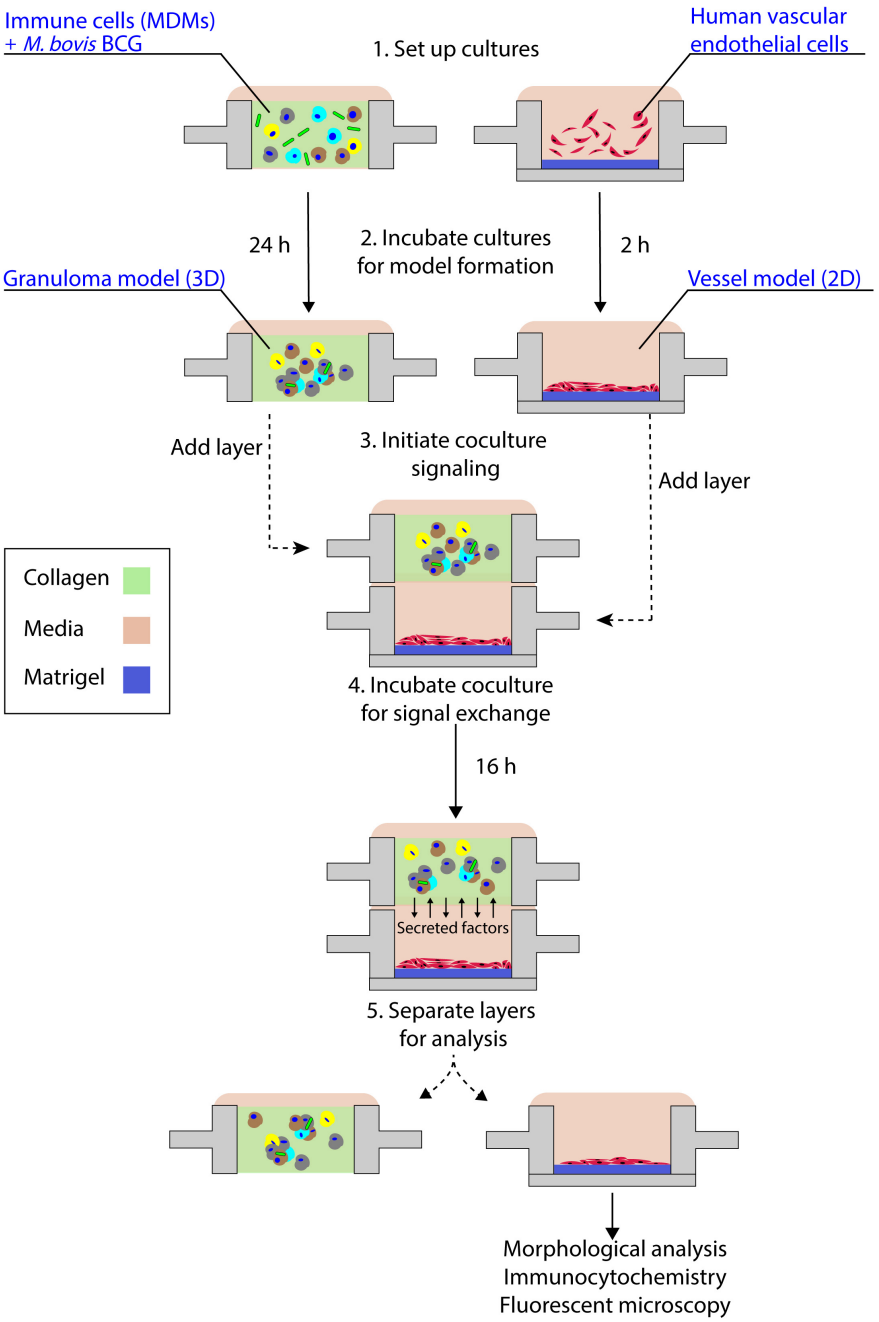

FIGURE 4 | Schematic representation of granuloma layer-endothelial layer coculture workflow. The granuloma model layer and the endothelial layer (representing a model microenvironment system) are independently cultured in optimized conditions prior to stacking the layers to initiate soluble factor signaling; after coculture, layers are separated and the morphology of the multicellular endothelial structures is analyzed. For the experimental time points used in this coculture system, we note the absence of large multicellular aggregates within the granuloma model layer, in accordance with our temporal observations (**Supplementary Table 1**).

The morphological change is likely the result of the increased secretion of factors from BCG-infected MDMs, such as VEGF (**Figure 3C**); however, it is possible that additional factors we did not quantify are also contributing to the differences in endothelial morphology. Ultimately, the induction of morphology changes in the endothelial layer as a result of coculture with different model granuloma layers illustrates the ability of the granuloma layer to signal with a neighboring layer representing microenvironmental components.

As we chose to connect the layers at Day 1 p.i. to correlate with increased levels of VEGF and cytokine secretion (**Figure 3**), we expect our model and results would mimic an earlier time point in infection, when the mycobacteria-infected cells are still secreting proinflammatory factors to recruit other immune cells

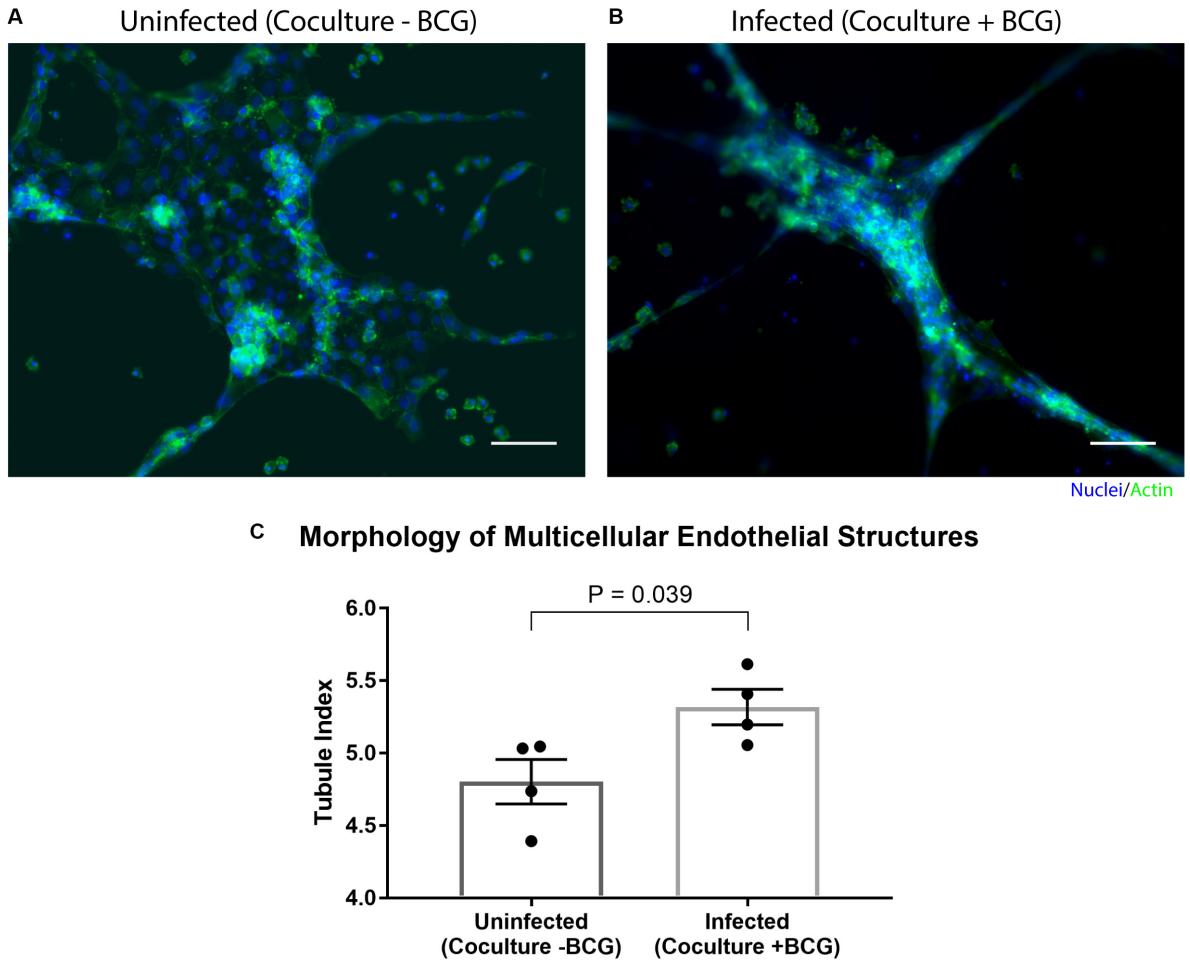

FIGURE 5 | Coculture of endothelial layer with granuloma layer impacts morphology of multicellular endothelial structures. Representative images of an endothelial layer cocultured with an uninfected (-BCG) layer **(A)** or infected (+BCG) layer **(B)** for 16 h, illustrating the difference in endothelial morphology as a result of coculture. **(C)** The tubule index (perimeter/area ratio) was used to quantify the morphology of endothelial structures and shows a significant difference between coculture conditions, demonstrating the ability of the model granuloma layer to signal with the endothelial layer. Scale bar: 100 μm. Error bars: SEM. $P < 0.05$, unpaired *t*-test. Each point represents the average ratio of an independent experiment ($n = 4$ independent experiments are plotted).

and the vasculature. Depending on user queries, these layers can also be stacked at more advanced time points (such as from Day 2 p.i. to Day 3 p.i., Day 4 p.i. to Day 5 p.i., and so forth) to study the effect of a later soluble factor profile on the surrounding vasculature, illustrating a key advantage of the modularity of the Stacks system and the flexibility in timing to combine the layers (**Figure 4**). Further, the ability of the model granuloma layer to communicate with the vasculature and modulate the endothelial morphology demonstrates the usage of this platform for signaling studies between our infected granuloma layers and microenvironment components. It is important to note that in our platform, the granuloma layer is not vascularized directly, as is observed *in vivo* (Datta et al., 2015), and that in our system, our endothelial layer is more akin to modeling the surrounding vasculature that is manipulated during early TB infection (Oehlers et al., 2015; Polena et al., 2016). The ability to create two independent layers that are in soluble factor signaling contact enables users to isolate the effects of the soluble factors from the granuloma layer on its surrounding microenvironment without interference from juxtacrine signaling or physical interactions.

CONCLUSION

Microenvironmental effects, such as soluble factor signaling, play a vital role in granuloma outcome, as the immune system attempts to contain and impede pathogenic mycobacterium from manipulating its environment in favor of its survival (Ramakrishnan, 2012). For example, induction of angiogenic processes by Mtb in the microenvironment surrounding a granuloma have been linked to pro-pathogen outcomes (Oehlers et al., 2015; Osherov and Ben-Ami, 2016), while treatment with anti-angiogenic factors can be a potential treatment option to improve the effects of existing drug regiments (Datta et al., 2015). To further understand the signaling environment and timeline of these phenomena, we created a novel *in vitro* granuloma

model that can be used to study soluble factor signaling between the granuloma and its surrounding microenvironment. As a proof of concept model, we created a two-layered modular microfluidic system containing a mycobacterial infection and an endothelial vasculature model that can be used to compliment *in vivo* granuloma and angiogenesis models (Datta et al., 2015; Oehlers et al., 2015, 2017; Polena et al., 2016). We demonstrate creation of a viable mycobacterial infection using human blood-derived immune cells and BCG within a 4 μL suspended collagen plug, and validate the secretion of proinflammatory cytokines associated with mycobacterial infection. Further, we provide a model coculture system that can be used to probe granuloma-associated angiogenic processes *in vitro*. The modularity and microscale size of our model enables users to add or remove additional cell types at various time points, and to utilize limited cell populations, such as patient cells or rare immune cells, and valuable reagents, such as antibodies or expensive drugs. In this work, we demonstrate the use of the Stacks platform within a system containing predetermined analytical endpoints; however, the modularity of the platform allows users to conduct exploratory studies to examine the effect of the duration or configuration of the Stacked coculture on various biological outputs without predefined time points. Additionally, the design of the platform and fabrication method supports the creation of arrays to test various culture conditions/treatments and customizability to introduce additional functionality (e.g., flow), as well as easy integration with BSL3 laboratory workflows as the device is disposable and fits inside common cell culture materials (e.g., petri dish, OmniTray^{TM}, etc.). Further development of our system includes the addition of adaptive immune cells (e.g., T cells) and introduction of parenchymal and stromal cells (e.g., epithelial cells, fibroblasts) to model signaling interactions in the pulmonary environment, probing the soluble factor profile of varied mycobacterial infection signaling phenomena (i.e., expanding the cytokines measured), as well as the use of virulent *M. tuberculosis* to induce more *in vivo*-like responses. Ultimately, we created a tractable and customizable mycobacterial infection model that can be utilized by other researchers to examine the various signaling components of a complex tuberculosis infection.

MATERIALS AND METHODS

Stacks Device Fabrication

Stacks devices (Yu et al., 2019) were fabricated from either polypropylene (PP) (granuloma layer) or polystyrene (PS) (endothelial layer) (**Supplementary Figure 1** and **Supplementary Table 1**). PP devices were injection molded (ProtoLabs, Maple Plain, MN, United States) and were flattened using a bench top manual heated press (#4386, Carver Inc., Wabash, IN, United States) for 1 h at 110°C (protocol in **Supplementary Information 1**). After flattening, devices were cleaned with isopropanol (IPA) sonication for 1 h to remove any fabrication residue or contaminants, and then rinsed twice with fresh IPA before drying with compressed air. Prior to use, devices were UV-sterilized for 30 min in a biosafety cabinet. PS devices containing a floor were designed using Fusion360 CAD software (Autodesk, San Rafael, CA, United States) and milled using a Datron Neo CNC mill (Datron Dynamics Inc., Livermore, CA, United States). PS devices and bottoms (floors, 53 mm × 53 mm) were milled from 1.2 mm thick PS sheets (Goodfellow Corp., Coraopolis, PA, United States). To attach the floor to the PS Stacks layer, floors were solvent bonded to the bottom of the Stacks layer using acetonitrile at 75°C for 10 min, followed by 15 min at 75°C to allow excess acetonitrile to evaporate. Solvent-bonded devices were then sonicated in IPA for 80 min and 70% ethanol for 15 min. Devices were then soaked in sterile deionized water for a minimum of 3 h, dried with compressed air, and UV-sterilized for 30 min prior to use. Device holders were designed on Solidworks CAD software (Solidworks Corp., Waltham, MA, United States), converted into G-code using SprutCAM CAM software (SprutCAM, Naberezhnye Chelny, Russia), and milled using a Tormach PCNC Micromill (Tormach Inc., Waunakee, WI, United States). Device holders were fabricated from 4 mm thick PS and were sonicated in IPA for 1 h and UV-sterilized for 30 min prior to use. All device and device holder design files are included in the **Supplementary Table 1**.

To prevent evaporation of microliter volumes of samples, culture platforms were placed in a Nunc Omnitray^{TM} (Thermo Fisher Scientific) which was then placed in a bioassay dish (#240835, Thermo Fisher Scientific) for secondary containment; both the Omnitray and bioassay dish were filled with sacrificial water droplets (1 mL and 5 mL, respectively) to create a humidified environment around the platform, and all cultures were then placed into a water-jacketed incubator.

Cell Culture

Human peripheral blood mononuclear cells (PBMCs) were isolated from patient whole blood samples (Bloodworks NorthWest, Seattle, WA, United States) using the Ficoll-Paque PLUS media density separation protocol (Thermo Fisher Scientific, Waltham, MA, United States). Briefly, blood samples were diluted with PBS (Thermo Fisher Scientific) and layered atop the Ficoll-Paque. Tubes were then centrifuged for 20 min at 1900 RPM without brakes, and afterward white blood cells at the plasma-Ficoll-Paque interface were collected and resuspended in PBS + 2% fetal bovine serum (FBS, Thermo Fisher Scientific) + 1 mM ethylenediaminetetraacetic acid (EDTA, Gibco, Thermo Fisher Scientific). Cells were then rinsed with subsequent centrifugation (10 min, 500 × *g*) and resuspension until the supernatant was clear. Isolated PBMCs were then cryopreserved in solution containing 90% heat-inactivated FBS (HI-FBS) (Thermo Fisher Scientific) and 10% dimethyl sulfoxide (DMSO) (Sigma-Aldrich, St. Louis, MO, United States) and stored in liquid nitrogen until use. To differentiate the PBMCs into monocyte-derived macrophages (MDMs), PBMCs were thawed and resuspended in serum free RPMI 1640 media (Gibco, Thermo Fisher Scientific); following resuspension, PBMCs were seeded into a 6 well plate (#3516, Corning Inc., Corning, NY, United States) and allowed to incubate for 3 h at 37°C and 5% CO_2 for monocyte adhesion. After 3 h, suspended cells were removed, adherent cells were

washed once with 1X phosphate-buffered saline (PBS, Fisher Scientific), and then RPMI 1640 containing 10% HI-FBS, 2 mM L-glutamine, 25 mM HEPES, and 50 ng/mL macrophage colony-stimulating factor (M-CSF) (R&D Systems, Minneapolis, MN, United States) was added to each well. Media was changed on Day 3 and Day 6 post-seeding, and MDMs were used after Day 6. For specific experiments or assays where users require a high purity of cells, we suggest the use of alternative methods, such as light-based or magnetic-activated cell sorting (MACS), to the methods we present here.

mCherry-expressing *M. bovis* Bacillus Calmette-Guérin (BCG) (graciously provided by the Urdahl Lab, Seattle Children's Research Institute, Seattle, WA, United States) was cultured in Middlebrook 7H9 broth (Thermo Fisher Scientific) containing 10% Middlebrook ADC enrichment supplement (Thermo Fisher Scientific), 0.003% Tween-80 (Fisher Scientific), and 50 μg/mL hygromycin B (Sigma-Aldrich). A lower Tween-80 concentration had to be used to ensure that the surfactant did not interfere with the microfluidic media pinning in the Stacks device (**Supplementary Information 2**). BCG was cultured at 37°C and 170 RPM to an OD of 0.7–1.0 for use, passed through a 27G needle to break up aggregates, and diluted to a working concentration for the experiment. BCG was used for all experiments as it can be used within a BSL2 facility, and we did not have access to virulent mycobacterium strains nor a BSL3 facility to perform these experiments.

Human umbilical vein endothelial cells (HUVECs) (Lonza, Basel, Switzerland) were cultured in completed EGM-2 media and maintained at 37°C and 5% CO_2 until 80–90% confluence. Passage 5–7 cells were used.

3D Granuloma Assay

Monocyte-derived macrophages were differentiated for a minimum of 6 days prior to use, and BCG was grown to an OD of 0.7–1.0 for use. MDMs were rinsed once with 1X PBS and detached with enzyme-free Cell Dissociation Buffer (#13151014, Life Technologies, Thermo Fisher Scientific) at 37°C for 5 min and vigorous pipetting. Detached cells were neutralized with complete RPMI 1640 media, counted, and resuspended at a density of 4×10^7 cell/mL. BCG was vortexed for 30 s, vigorously mixed via pipetting, and then diluted into 4 mL of complete RPMI 1640 media for a final concentration of 2×10^6 BCG/mL. An extracellular matrix (ECM) mix containing 80 μL 3 mg/mL type I bovine collagen (Advanced Biomatrix Inc., Carlsbad, CA, United States), 10 μL 10X HEPES buffer, 7 μL deionized H_2O, 3 μL 0.5N NaOH, and 2.25 μL 1 mg/mL human fibronectin (Sigma-Aldrich) was mixed and stored on ice until use. To prepare the suspended cell-laden collagen plugs, 25 μL of MDMs (at 4×10^7 cells/mL) and 25 μL of BCG (at 2×10^6 BCG/mL) or 25 μL of complete RPMI 1640 was added to the ECM mix for a final volume of 152.25 μL and an MOI of 0.05. After mixing, 4 μL of the cell-laden ECM mix was added to each well in a PP device and allowed to gel at 37°C and 5% CO_2 for 2 h. After gelation, 8 μL of RPMI 1640 containing 15% HI-FBS and 25 mM HEPES was added atop each well and returned to the incubator. Media was changed daily for the entirety of the experiments. For all monoculture infection experiments (**Figures 2**, **3**), MDMs were stained with CellTracker Green CMFDA dye (Thermo Fisher Scientific) according to manufacturer's protocols. Briefly, MDMs were rinsed with 1X PBS, and 10 μM CellTracker Green in serum-free media was added for 30 min at 37°C, washed once with 1X PBS, and then incubated with complete media for 10 min prior to further processing or use. It is important to note that CellTracker Green CMFDA dye only stains live cells.

2D Angiogenesis Assay

Prior to seeding, PS Stacks devices containing a floor were chilled for 5 min at −80°C and then kept on ice for Matrigel seeding. 3 μL of Matrigel (8.6 mg/mL) was added to each well and devices rested on ice 30 min. The Matrigel was then polymerized for 30 min at 37°C. After polymerization, 3 μL of HUVECs were added atop the Matrigel for a final concentration of 1,650 cells per well (5.5×10^5 cells/mL). Cells were allowed to adhere and self-assemble for 2 h at 37°C and 5% CO_2. Media was then aspirated and replaced with 2 μL of EGM-2 + 10% FBS coculture media.

To stack the layers, media was first removed from the model granuloma layers. Model granuloma layers were then placed atop the endothelial layers (containing 3 μL of media) and 7 μL of coculture media was placed atop each well of the stacked granuloma layers, to allow for feeding of both layers. Layers were separated by a thin layer of tape along the sides of the devices to ensure reproducible separation. Stacked devices were then placed in the incubator at 37°C and 5% CO_2. After 16 h, devices were inverted and separated, fixed with 4% paraformaldehyde for 30 min at 25°C, and stained as specified under Imaging. It is important to note that the self-assembled tubule network disassembles after 18–24 h of culture, therefore limiting the duration of the coculture experiment to within 2–18 h of seeding (Lonza, 2018); however, the modularity of this system enables users to combine layers at different time points (i.e., Day 2 p.i. to Day 3 p.i., etc.) to examine various temporal signaling profiles.

Imaging

To validate granuloma layer formation within our platform, MDMs were prestained with CellTracker Green CMFDA dye prior to infection and seeding into the Stacks. For imaging, the Stacks platform was placed on a 50 mm x 75 mm glass coverslip (#260462, Ted Pella Inc., Redding, CA, United States) and placed into an OmniTray™ with a 45 mm x 70 mm rectangle cut out of the bottom. Fluorescent images were obtained on a Zeiss Axiovert 200 coupled with an Axiocam 503 mono camera (Carl Zeiss AG, Oberkochen, Germany). For confocal imaging, all wells were fixed with 4% paraformaldehyde for 1 h at 25°C and then covered with PBS; the same imaging protocol was then followed as above. Fluorescent confocal images were obtained on a Leica TCS SP5 II Laser Scanning Confocal Microscope (Leica Camera AG, Wetzlar, Germany), with a z-depth of 66.47 μm and step size of 1.01 μm. Images obtained with the Zeiss Axiovert 200 were analyzed with Fiji (ImageJ), and images obtained with the Leica TCS SP5 II were analyzed with Leica LAS X software (Leica).

For vasculature layer imaging, cells were permeabilized with 0.5% Triton-X 100 for 30 min and then stained with Phalloidin 488 (1:50) (Molecular Probe A12379) and Hoechst nuclear stain

(1:1000) (Molecular Probe H1399) overnight. After overnight incubation, cells were rinsed thrice with 0.2% Triton-X 100 for 10 min each and then covered with PBS for imaging. Devices were placed on a 75 mm × 50 mm glass coverslip (#260462, Ted Pella Inc., Redding, CA, United States) and placed in an Omnitray™ with a 45 mm × 70 mm rectangle cut out of the bottom. Fluorescent images were obtained on a Zeiss Axiovert 200 coupled with an Axiocam 503 mono camera (Carl Zeiss AG, Oberkochen, Germany). Images obtained were analyzed with Fiji (ImageJ).

Angiogenesis Morphological Analysis

To analyze differences in morphology in the endothelial layer we used default functions of Image J (Fiji) to quantify the tubule index (perimeter/area ratio) (Theberge et al., 2015). The image analysis procedure is described in the methods and SI of Theberge et al. (2015), a summary is included here. For quantification, the 8-bit image containing the phalloidin channel (488) was selected and a threshold (Huang Dark) was applied to get the outline of the endothelial culture and saved (Image 1). The "Fill Holes" function was applied and saved (Image 2), and then Image 2 was subtracted from Image 1 to generate an image containing the holes/gaps in the endothelial morphology (Image 3). The total area of the phalloidin stain was then calculated by subtracting the area of Image 3 (holes) from Image 2 (fill holes), and the perimeter of the stain was calculated by adding the perimeter of Image 2 and Image 3. The area and perimeter were measured using the function "Analyze Particles," with the following parameters: size: 25-infinity (include pixel units), circularity: 0.00–1.00. The ImageJ macro for this process is included in the **Supplementary Material** and is based off the macro used in Yu et al. (2019).

Exclusion criteria for experimental artifacts that interfered with the imaging technique was developed to exclude wells unable to be analyzed with this technique. For example, if a collagen plug from the model granuloma layer detached and fell into a endothelial layer well during separation of the layers, the endothelial morphology was obscured by signal from the MDMs in the collagen plug and therefore unable to be accurately measured. All images were assigned a randomized code and individuals not involved in the project determined which images to exclude base on established criteria. Images were then analyzed according to the measurement protocol above.

Cytokine Analysis

Cytokine analyses were performed with a custom Luminex ProcartaPlex multiplex assay for IL-6, TNFα, and VEGF (Thermo Fisher Scientific). Supernatant samples were collected and pooled from a single device (n = 24 wells, 8 μL/well) during daily media changes and stored at −80°C until use. Samples were collected from the same device over a 5-day period, such that each sample contains cytokines secreted within 24 h of collection (i.e., Day 2 p.i. cytokine levels indicate what was secreted between Day 1 and Day 2 p.i., etc.). In order to ensure sufficient volume of supernatant for analysis with the Luminex multiplex assay (50 μL), samples were pooled across individual wells; while this volumetric limitation is linked to the specific readout we selected, alternative analyses such as mRNA analysis (Yu et al., 2019) or intracellular cytokine staining can be applied to the cells within a single well. For analysis, samples were thawed on ice and analyzed according to the manufacturer's protocols for Luminex multiplex assays. Samples were analyzed on a Luminex 100/200 System instrument with xPONENT software (Fred Hutchinson Cancer Center Core Facility). All results were analyzed and visualized using Prism 7 software (GraphPad Software, San Diego, CA, United States).

DATA AVAILABILITY STATEMENT

The raw data supporting the conclusions of this article will be made available by the authors, without undue reservation.

AUTHOR CONTRIBUTIONS

SB and AT conceived of the project. SB and MG performed all experiments and data analysis and wrote the manuscript. XS, CS, and AT advised the project and edited, revised, and provided feedback on the manuscript. All authors reviewed and approved the final manuscript.

FUNDING

We acknowledge the support of the Biochemical Diagnostics Foundry for Translational Research supported by the M. J. Murdock Charitable Trust. This work was supported by NIH R35GM128648, the University of Washington, the Mary Gates Endowment, and by the National Science Foundation Graduate Research Fellowship Program under Grant No. DGE-1256082 (SB). Any opinions, findings, and conclusions or recommendations expressed in this material are those of the author(s) and do not necessarily reflect the views of the National Science Foundation.

ACKNOWLEDGMENTS

We would like to thank Dr. Shahin Shafiani (Urdahl Lab) for providing the mCherry *Mycobacterium bovis* BCG strain, Dr. Jason Yu for providing help on the Stacks platform, Tammi van Neel and Tianzi Zhang for image review, Ashley Dostie for obtaining the Stacks image, and Erik Layton (Seshadri Lab) for PBMC isolation training.

SUPPLEMENTARY MATERIAL

The Supplementary Material for this article can be found online at: https://www.frontiersin.org/articles/10.3389/fbioe.2020.00931/full#supplementary-material

REFERENCES

Berry, M. P. R., Graham, C. M., McNab, F. W., Xu, Z., Bloch, S. A. A., Oni, T., et al. (2010). An interferon-inducible neutrophil-driven blood transcriptional signature in human tuberculosis. *Nature* 466, 973–977. doi: 10.1038/nature09247

Berthier, E., Dostie, A. M., Lee, U. N., Berthier, J., and Theberge, A. B. (2019). Open microfluidic capillary systems. *Anal. Chem.* 91, 8739–8750. doi: 10.1021/acs.analchem.9b01429

Bielecka, M. K., Tezera, L. B., Zmijan, R., Drobniewski, F., Zhang, X., Jayasinghe, S., et al. (2017). A bioengineered three-dimensional cell culture platform integrated with microfluidics to address antimicrobial resistance in tuberculosis. *mBio* 8:e02073-16. doi: 10.1128/mBio.02073-16

Birkness, K. A., Guarner, J., Sable, S. B., Tripp, R. A., Kellar, K. L., Bartlett, J., et al. (2007). An in vitro model of the leukocyte interactions associated with granuloma formation in *Mycobacterium tuberculosis* infection. *Immunol. Cell Biol.* 85, 160–168. doi: 10.1038/sj.icb.7100019

Bishop, E. T., Bell, G. T., Bloor, S., Broom, I. J., Hendry, N. F. K., and Wheatley, D. N. (1999). An in vitro model of angiogenesis: basic features. *Angiogenesis* 3, 335–344. doi: 10.1023/A:1026546219962

Casavant, B. P., Berthier, E., Theberge, A. B., Berthier, J., Montanez-Sauri, S. I., Bischel, L. L., et al. (2013). Suspended microfluidics. *PNAS* 110, 10111–10116. doi: 10.1073/pnas.1302566110

Cronan, M. R., Matty, M. A., Rosenberg, A. F., Blanc, L., Pyle, C. J., Espenschied, S. T., et al. (2018). An explant technique for high-resolution imaging and manipulation of mycobacterial granulomas. *Na. Methods* 15, 1098–1107. doi: 10.1038/s41592-018-0215-8

Cronan, M. R., and Tobin, D. M. (2014). Fit for consumption: zebrafish as a model for tuberculosis. *DMM Dis. Models Mech.* 7, 777–784. doi: 10.1242/dmm.016089

Crouser, E. D., White, P., Caceres, E. G., Julian, M. W., Papp, A. C., Locke, L. W., et al. (2017). A novel in vitro human granuloma model of sarcoidosis and latent tuberculosis infection. *Am. J. Respir. Cell Mol. Biol.* 57, 487–498. doi: 10.1165/rcmb.2016-0321OC

Darboe, F., Mbandi, S. K., Naidoo, K., Yende-Zuma, N., Lewis, L., Thompson, E. G., et al. (2019). Detection of tuberculosis recurrence, diagnosis and treatment response by a blood transcriptomic risk signature in HIV-infected persons on antiretroviral therapy. *Front. Microbiol.* 10:1441. doi: 10.3389/fmicb.2019.01441

Datta, M., Via, L. E., Kamoun, W. S., Liu, C., Chen, W., Seano, G., et al. (2015). Anti-vascular endothelial growth factor treatment normalizes tuberculosis granuloma vasculature and improves small molecule delivery. *Proc. Natl. Acad. Sci. U.S.A.* 112, 1827–1832. doi: 10.1073/pnas.1424563112

Deb, C., Lee, C. M., Dubey, V. S., Daniel, J., Abomoelak, B., Sirakova, T. D., et al. (2009). A novel in vitro multiple-stress dormancy model for *Mycobacterium tuberculosis* generates a lipid-loaded, drug-tolerant, dormant pathogen. *PLoS One* 4:6077. doi: 10.1371/journal.pone.0006077

Domingo-Gonzalez, R., Prince, O., Cooper, A., and Khader, S. A. (2016). Cytokines and chemokines in *Mycobacterium tuberculosis* infection. *Microbiol. Spectr.* 4, 1–37. doi: 10.1128/microbiolspec.tbtb2-0018-2016

Elkington, P., Lerm, M., Kapoor, N., Mahon, R., Pienaar, E., Huh, D., et al. (2019). In vitro granuloma models of tuberculosis: potential and challenges. *J. Infect. Dis.* 219, 1858–1866. doi: 10.1093/infdis/jiz020

Engele, M., Stößel, E., Castiglione, K., Schwerdtner, N., Wagner, M., Bölcskei, P., et al. (2002). Induction of TNF in human alveolar macrophages as a potential evasion mechanism of virulent *Mycobacterium tuberculosis*. *J. Immunol.* 168, 1328–1337. doi: 10.4049/jimmunol.168.3.1328

Foreman, T. W., Mehra, S., Lackner, A. A., and Kaushal, D. (2017). Translational research in the nonhuman primate model of tuberculosis. *ILAR J.* 58, 151–159. doi: 10.1093/ilar/ilx015

Gern, B., Plumlee, C., Gerner, M., and Urdahl, K. (2017). Investigating immune correlates of protection to tuberculosis using an ultra-low dose infection in a mouse model. *OFID* 4(Suppl. 1), 47–48.

Guyot-Revol, V., Innes, J. A., Hackforth, S., Hinks, T., and Lalvani, A. (2006). Regulatory T cells are expanded in blood and disease sites in patients with tuberculosis. *Am. J. Respir. Crit. Care Med.* 173, 803–810. doi: 10.1164/rccm.200508-1294OC

Harding, J. S., Herbath, M., Chen, Y., Rayasam, A., Ritter, A., Csoka, B., et al. (2019). VEGF-A from granuloma macrophages regulates granulomatous inflammation by a non-angiogenic pathway during mycobacterial infection. *Cell Rep.* 27, 2119.e6–2131.e6. doi: 10.1016/j.celrep.2019.04.072

Humayun, M., Chow, C. W., and Young, E. W. K. (2018). Microfluidic lung airway-on-a-chip with arrayable suspended gels for studying epithelial and smooth muscle cell interactions. *Lab Chip* 18, 1298–1309. doi: 10.1039/c7lc01357d

Kapoor, N., Pawar, S., Sirakova, T. D., Deb, C., Warren, W. L., and Kolattukudy, P. E. (2013). Human granuloma in vitro model, for TB dormancy and resuscitation. *PLoS One* 8:e0053657. doi: 10.1371/journal.pone.0053657

Kaufmann, S. H. E. (2004). New issues in tuberculosis. *Ann. Rheumat. Dis.* 63(Suppl. 2), 50–56. doi: 10.1136/ard.2004.028258

Koh, W., Stratman, A. N., Sacharidou, A., and Davis, G. E. (2008). Chapter 5 in vitro three dimensional collagen matrix models of endothelial lumen formation during vasculogenesis and angiogenesis. *Methods Enzymol.* 443, 83–101. doi: 10.1016/S0076-6879(08)02005-3

Lin, P. L., Plessner, H. L., Voitenok, N. N., and Flynn, J. A. L. (2007). Tumor necrosis factor and tuberculosis. *J. Investigat. Dermatol. Sympos. Proc.* 12, 22–25. doi: 10.1038/sj.jidsymp.5650027

Lonza (2018). *Clonetics Endothelial Cell System Technical Information & Instructions*. 1–15. Avaliable online at: https://bioscience.lonza.com/lonza_bs/US/en/download/product/asset/29423 (accessed April 12, 2020).

Martinez, A. N., Mehra, S., and Kaushal, D. (2013). Role of interleukin 6 in innate immunity to *Mycobacterium tuberculosis* infection. *J. Infect. Dis.* 207, 1253–1261. doi: 10.1093/infdis/jit037

Myllymäki, H., Bäuerlein, C. A., and Rämet, M. (2016). The zebrafish breathes new life into the study of tuberculosis. *Front. Immunol.* 7:196. doi: 10.3389/fimmu.2016.00196

Oehlers, S. H., Cronan, M. R., Beerman, R. W., Johnson, M. G., Huang, J., Kontos, C. D., et al. (2017). Infection-induced vascular permeability aids mycobacterial growth. *J. Infect. Dis.* 215, 813–817. doi: 10.1093/infdis/jiw355

Oehlers, S. H., Cronan, M. R., Scott, N. R., Thomas, M. I., Okuda, K. S., Walton, E. M., et al. (2015). Interception of host angiogenic signalling limits mycobacterial growth. *Nature* 517, 612–615. doi: 10.1038/nature13967

Ogongo, P., Steyn, A. J. C., Karim, F., Dullabh, K. J., Awala, I., Madansein, R., et al. (2020). Differential skewing of donor-unrestricted and γδ T cell repertoires in tuberculosis-infected human lungs. *J. Clin. Investigat.* 130, 214–230. doi: 10.1172/JCI130711

Ong, L. J. Y., Ching, T., Chong, L. H., Arora, S., Li, H., Hashimoto, M., et al. (2019). Self-aligning Tetris-Like (TILE) modular microfluidic platform for mimicking multi-organ interactions. *Lab Chip* 19, 2178–2191. doi: 10.1039/c9lc00160c

Osherov, N., and Ben-Ami, R. (2016). Modulation of host angiogenesis as a microbial survival strategy and therapeutic target. *PLoS Pathog.* 12:e1005479. doi: 10.1371/journal.ppat.1005479

Parasa, V. R., Muvva, J. R., Rose, J. F., Braian, C., Brighenti, S., and Lerm, M. (2017). Inhibition of tissue matrix metalloproteinases interferes with *Mycobacterium tuberculosis*-induced granuloma formation and reduces bacterial load in a human lung tissue model. *Front. Microbiol.* 8:2370. doi: 10.3389/fmicb.2017.02370

Parasa, V. R., Rahman, M. J., Hoang, A. T. N., Svensson, M., Brighenti, S., and Lerm, M. (2014). Modeling *Mycobacterium tuberculosis* early granuloma formation in experimental human lung tissue. *DMM Dis. Models Mech.* 7, 281–288. doi: 10.1242/dmm.013854

Peyron, P., Vaubourgeix, J., Poquet, Y., Levillain, F., Botanch, C., Bardou, F., et al. (2008). Foamy macrophages from tuberculous patients' granulomas constitute a nutrient-rich reservoir for *M. tuberculosis* persistence. *PLoS Pathog.* 4:e1000204. doi: 10.1371/journal.ppat.1000204

Polena, H., Boudou, F., Tilleul, S., Dubois-Colas, N., Lecointe, C., Rakotosamimanana, N., et al. (2016). *Mycobacterium tuberculosis* exploits the formation of new blood vessels for its dissemination. *Sci. Rep.* 6:33162. doi: 10.1038/srep33162

Puissegur, M. P., Botanch, C., Duteyrat, J. L., Delsol, G., Caratero, C., and Altare, F. (2004). An in vitro dual model of mycobacterial granulomas to investigate the molecular interactions between mycobacteria and human host cells. *Cell. Microbiol.* 6, 423–433. doi: 10.1111/j.1462-5822.2004.00371.x

Ramakrishnan, L. (2012). Revisiting the role of the granuloma in tuberculosis. *Nat. Rev. Immunol.* 12, 352–366. doi: 10.1038/nri3211

Russell, D. G., Cardona, P. J., Kim, M. J., Allain, S., and Altare, F. (2009). Foamy macrophages and the progression of the human tuberculosis granuloma. *Nat. Immunol.* 10, 943–948. doi: 10.1038/ni.1781

Sarkanen, J. R., Mannerström, M., Vuorenpää, H., Uotila, J., Ylikomi, T., and Heinonen, T. (2011). Intra-laboratory pre-validation of a human cell based in vitro angiogenesis assay for testing angiogenesis modulators. *Front. Pharmacol.* 1:147. doi: 10.3389/fphar.2010.00147

Saunders, B. M., and Britton, W. J. (2007). Life and death in the granuloma: immunopathology of tuberculosis. *Immunol. Cell Biol.* 85, 103–111. doi: 10.1038/sj.icb.7100027

Scanga, C. A., and Flynn, J. L. (2014). Modeling tuberculosis in nonhuman primates. *Cold Spring Harbor Perspect. Med.* 4:a018564. doi: 10.1101/cshperspect.a018564

Seitzer, U., and Gerdes, J. (2003). Generation and characterization of multicellular heterospheroids formed by human peripheral blood mononuclear cells. *Cells Tissues Organs* 174, 110–116. doi: 10.1159/000071151

Singh, P. P., and Goyal, A. (2013). Interleukin-6: a potent biomarker of mycobacterial infection. *SpringerPlus* 2, 2–9. doi: 10.1186/2193-1801-2-686

Su, X., Theberge, A. B., January, C. T., and Beebe, D. J. (2013). Effect of microculture on cell metabolism and biochemistry: do cells get stressed in microchannels? *Anal. Chem.* 85, 1562–1570. doi: 10.1021/ac3027228

Tezera, L. B., Bielecka, M. K., Chancellor, A., Reichmann, M. T., Shammari, B., Al Brace, P., et al. (2017). Dissection of the host-pathogen interaction in human tuberculosis using a bioengineered 3-dimensional model. *eLife* 6:e2128. doi: 10.7554/eLife.21283

Theberge, A. B., Yu, J., Young, E. W. K., Ricke, W. A., Bushman, W., and Beebe, D. J. (2015). Microfluidic multiculture assay to analyze biomolecular signaling in angiogenesis. *Anal. Chem.* 87, 3239–3246. doi: 10.1021/ac503700f

Torraca, V., Tulotta, C., Ewa Snaar-Jagalska, B., and Meijer, A. H. (2017). The chemokine receptor CXCR4 promotes granuloma formation by sustaining a mycobacteria-induced angiogenesis programme. *Sci. Rep.* 7, 18–20. doi: 10.1038/srep45061

World Health Organization (2019). *Global Tuberculosis Report*. Geneva: WHO.

Yong, K. S. M., Her, Z., and Chen, Q. (2018). Humanized Mice as Unique Tools for Human-Specific Studies. *Arch. Immunol. Ther. Exp.* 66, 245–266. doi: 10.1007/s00005-018-0506-x

Yu, J., Berthier, E., Craig, A., de Groot, T. E., Sparks, S., Ingram, P. N., et al. (2019). Reconfigurable open microfluidics for studying the spatiotemporal dynamics of paracrine signalling. *Nat. Biomed. Eng.* 3, 830–841. doi: 10.1038/s41551-019-0421-4

Zhan, L., Tang, J., Sun, M., and Qin, C. (2017). Animal models for tuberculosis in translational and precision medicine. *Front. Microbiol.* 8:717. doi: 10.3389/fmicb.2017.00717

Conflict of Interest: The authors acknowledge the following potential conflicts of interest in companies pursuing open microfluidic technologies: AT: Stacks to the Future, LLC.

frontiers in Bioengineering and Biotechnology

BRIEF RESEARCH REPORT
published: 08 September 2020
doi: 10.3389/fbioe.2020.568092

Recapitulation of Human Embryonic Heartbeat to Promote Differentiation of Hepatic Endoderm to Hepatoblasts

*Koki Yoshimoto[1,2,3], Nicolas Minier[1], Jiandong Yang[4], Satoshi Imamura[1], Kaylene Stocking[1,5], Janmesh Patel[1,6], Shiho Terada[1], Yoshikazu Hirai[4] and Ken-ichiro Kamei[1,7,8]**

[1] Institute for Integrated Cell-Material Sciences, Kyoto University, Kyoto, Japan, [2] Department of Biosystems Science, Institute for Frontier Life and Medical Sciences, Kyoto University, Kyoto, Japan, [3] Laboratory of Cellular and Molecular Biomechanics, Graduate School of Biostudies, Kyoto University, Kyoto, Japan, [4] Department of Micro Engineering, Kyoto University, Kyoto, Japan, [5] Department of Bioengineering, University of Pittsburgh, Pittsburgh, PA, United States, [6] Department of Biomedical Engineering, University of Wisconsin–Madison, Madison, WI, United States, [7] Wuya College of Innovation, Shenyang Pharmaceutical University, Shenyang, China, [8] Department of Pharmacy, Shenyang Pharmaceutical University, Shenyang, China

OPEN ACCESS

Edited by:
Shi-Cong Tao,
Shanghai Jiao Tong University, China

Reviewed by:
Salman Khetani,
University of Illinois at Chicago, United States
Andreas Nüssler,
Tübingen University Hospital, Germany

***Correspondence:**
Ken-ichiro Kamei
kamei.kenichiro.7r@kyoto-u.ac.jp;
kkamei@icems.kyoto-u.ac.jp

Specialty section:
This article was submitted to Nanobiotechnology, a section of the journal Frontiers in Bioengineering and Biotechnology

Received: *31 May 2020*
Accepted: *19 August 2020*
Published: *08 September 2020*

Citation:
Yoshimoto K, Minier N, Yang J, Imamura S, Stocking K, Patel J, Terada S, Hirai Y and Kamei K (2020) Recapitulation of Human Embryonic Heartbeat to Promote Differentiation of Hepatic Endoderm to Hepatoblasts. Front. Bioeng. Biotechnol. 8:568092. doi: 10.3389/fbioe.2020.568092

Hepatic development requires multiple sequential physicochemical environmental changes in an embryo, and human pluripotent stem cells (hPSCs) allow for the elucidation of this embryonic developmental process. However, the current *in vitro* methods for hPSC-hepatic differentiation, which employ various biochemical substances, produce hPSC-derived hepatocytes with less functionality than primary hepatocytes, due to a lack of physical stimuli, such as heart beating. Here, we developed a microfluidic platform that recapitulates the beating of a human embryonic heart to improve the functionality of hepatoblasts derived from hepatic endoderm (HE) *in vitro*. This microfluidic platform facilitates the application of multiple mechanical stretching forces, to mimic heart beating, to cultured hepatic endoderm cells to identify the optimal stimuli. Results show that stimulated HE-derived hepatoblasts increased cytochrome P450 3A (CYP3A) metabolic activity, as well as the expression of hepatoblast functional markers (albumin, cytokeratin 19 and CYP3A7), compared to unstimulated hepatoblasts. This approach of hepatic differentiation from hPSCs with the application of mechanical stimuli will facilitate improved methods for studying human embryonic liver development, as well as accurate pharmacological testing with functional liver cells.

Keywords: microfluidic device, human embryonic stem cells (hESC), heart beating, hepatic endoderm, hepatoblast, mechanical stimulation

INTRODUCTION

Hepatocytes are major components of the liver and have essential physiological roles, including protein and glucose synthesis and storage, detoxification, and excretion of exogenous molecules. Meanwhile, disruption of hepatic function can causes fibrosis, cirrhosis and even fatal liver cancers (Marengo et al., 2016; Altamirano-Barrera et al., 2017). Liver transplantation is currently the

only effective curative method for these patients. Thus, new effective drug therapies are needed; however, drug discovery requires the use of primary hepatocytes to evaluate the toxicity of drug candidates prior to clinical trials (Bale et al., 2014). Meanwhile, identification of suitable healthy donors for liver transplantation, or hepatocytes for drug testing, remains challenging, warranting the development of alternative strategies for drug design and development.

One such strategy includes the use of human pluripotent stem cells (hPSCs), such as human embryonic and induced pluripotent stem cells [hESCs (Thomson et al., 1998) and hiPSCs (Takahashi et al., 2007; Yu et al., 2007), respectively], which show high potential due to their capacity for unlimited self-renewal and differentiation to almost any tissue cell type. Although many studies have been performed to obtain hPSC-derived hepatocytes, the resulting cells remain as immature hepatocytes with fewer functional properties. The cause of this limited development stems from the use of various biochemical factors, such as fibroblast growth factor (FGF), and bone morphogenesis protein (BMP) in the current differentiation protocols. These biochemical factors have been intensively investigated, however, the effects of biomechanical forces on the hepatic developmental process remain unknown. As mechanical forces regulate a variety of biological factors, including molecules, cells, tissues, and organs (Sakamoto et al., 2010; Ren et al., 2015), their effects must be considered to provide optimal hepatic differentiation methods from hPSCs.

Physiologically, hepatic endoderm (HE) is formed during the early developmental stages from definitive endoderm (DE), and HE-derived hepatoblasts give rise to hepatocytes or cholangiocytes (Gordillo et al., 2015). Notably, the HE is exposed to oscillating mechanical forces induced by the heart beating. We have hypothesized that such oscillating mechanical forces would influence the hepatic developmental process. However, although biochemical factors have been reported in static culture conditions (Si-Tayeb et al., 2010b; Camp et al., 2017), the effects of mechanical forces on the induction of HE differentiation into hepatoblasts have not yet been investigated due to limited access to human embryos, and the lack of proper *in vitro* models that recapitulate the physiological embryonic developmental process. Therefore, current protocols are incapable of evaluating the effects of mechanical forces induced by embryonic heart beating, and thus, result in immature differentiation of hepatocytes. Hence, more sophisticated platforms are required to address these shortcomings.

Microfluidic technology is a potential platform capable of applying mechanical forces to cells, as it allows for systematic manipulation of the cell-culture conditions (e.g., flow dynamics, cell-cell/matrix interactions, and mechanical stretching) in two- and three-dimensional models, which cannot be achieved using conventional cell-culture models. Recently, organs-on-a-chip platforms based on microfluidic technology have been reported to recapitulate physiological mechanical forces *in vitro* using natural tissues (Ho et al., 2006; Bhatia and Ingber, 2014; Kamei et al., 2017; Ronaldson-Bouchard and Vunjak-Novakovic, 2018). However, most organ-on-a-chip platforms can stimulate cells using only a single mechanical condition (Huh et al., 2010; Pavesi et al., 2015), and thus the optimal mechanical strength for obtaining targeted functional cells cannot be determined.

Here, we report a microfluidic platform for applying multiple mechanical forces to hPSC-derived HE cells to identify the optimal mechanical stress to facilitate differentiation of HE cells to functional hepatoblasts. The microfluidic device is composed of polydimethylsiloxane (PDMS) elastic material with a ballooned thin membrane as the cell-culture substrate, which can be actuated to mimic heart beating in an embryo. The balloons with cells inflate and deflate repeatedly via pressure regulation. We showed that hPSC-derived hepatoblasts differentiated under the optimal stretching condition and expressed enzymes of drug metabolism and proteins specific to hepatoblasts. These findings demonstrate that dynamic mechanical forces are critical for differentiation of HE to hepatoblasts and must, therefore be incorporated into differentiation models for hPSCs.

MATERIALS AND METHODS

Chip Design

The formula for pressure drop, and length in microfluidic channel reported by Shimizu et al. (2011) was adapted. The molds for the pressure chambers and culture chambers were designed with a specific channel height (200 μm), and width (100 μm), and specific branch channel length (1 mm) by computer-aided design. The culture chambers were replaced considering the pressure drops.

Computational Fluid Dynamics (CFD) Simulations

The air flow across the micro channel was simulated by COMSOL Multiphysics (Version 5.5, COMSOL Inc., Burlington, MA, United States) to calculate the pressure drop along the channel and chambers. The simulation was based on the coupling of the Navier-Stokes equation and the continuity equation in the stationary condition (Turgay and Yazıcıoğlu, 2018; Chen et al., 2019). The incompressible laminar flow was used to obtain the solutions. Due to the symmetrical structure, the geometric model of the right-half-side microfluidic channel and chambers were used to conduct the study. A physics-controlled extra fine mesh was used for dividing the domain grids. The flow media was set as the air material from the COMSOL material library. The boundary condition of the wall was set to no slip. The inlet pressure was set as the input pressure (i.e., 18, 32, and 45 kPa) with fully developed flow. The outlet port was assumed to be directly connected to the atmosphere condition and was set as the 0 pressure.

Microfluidic Device Fabrication

A microfluidic device was fabricated using stereolithography 3D-printing techniques and solution cast-molding processes (Kamei et al., 2015). The molds for the top and bottom layer were produced using a 3D printer (Keyence Corporation, Osaka, Japan). After fabrication, the molds were washed with 99.9%

EtOH for 12 h. The molds were dried at 80°C for 30 min. Sylgard 184 PDMS two-part elastomer (10:1 ratio of pre-polymer to curing agent; Dow Corning Corporation, Midland, MI, United States) was mixed, poured into a 3D-printed mold to produce a 5-mm-thick PDMS top layer and a 2-mm-thick PDMS bottom layer, and de-gassed using a vacuum desiccator for 30 min. The PDMS material was then cured in an oven at 80°C for 16 h. After curing, the PDMS form was removed from the mold, trimmed, and cleaned. Sylgard 184 PDMS two-part elastomer (10:1 ratio of pre-polymer to curing agent) was poured onto the silicon wafer, and spin-coated at 500 rpm for 30 s. After baking at 80°C for 10 min, the pressure chamber layer and the PDMS thin membrane on silicon wafer were treated with corona plasma (Kasuga Denki, Inc., Kawasaki, Japan), and subsequently placed at 80°C for 1.5 h for bonding. The bonded PDMS structure was peeled off the silicon wafer. The top layer-thin membrane forms, bottom layer, and glass were corona-plasma-treated and bonded together by placing in an oven at 80°C for 18 h. The devices were used within one day of completion.

Device Control

The PDMS membranes was actuated by air flow from a compressed air resource (regulated at 0–200 kPa), operated with LabVIEW (Version 11.0, National Instrument, Austin, TX, United States) software via solenoid valves (Microfluidic System Works Inc., and THE LEE Company) using a controller board (VC3 8 controller [ALA Scientific Instruments] and NI USB-6501 [National Instruments]).

Measurement of Pressure to Inlet and PDMS Displacement

The pressure was measured close to the inlet with a pressure sensor (ZS-46-5F; SMC, Tokyo, Japan). Vertical displacement of the PDMS thin membrane was measured with a CCD laser displacement sensor (LK-G5000; Keyence).

hPSC Culture

hESCs were used according to the guidelines of the ethics committee of Kyoto University. H9 hESCs (WA09; **RRID:** CVCL_9773) were purchased from WiCell Research Institute (Madison, WI, United States). Prior to culture, hESC-certified Matrigel (Corning, Inc., Corning, NY, United States) was diluted with Dulbecco's modified Eagle medium (DMEM)/F12 (Merck KGaA, Darmstadt, Germany) at a 1:75 (v/v) ratio and coated onto a culture dish. Matrigel was incubated in a dish for 24 h at 4°C. Excess Matrigel was removed, and the coated dish was washed with fresh DMEM/F12.

mTeSR-1-defined medium (Stem Cell Technologies, Vancouver, Canada) supplemented with 1% (v/v) penicillin/streptomycin (Fujifilm Wako, Osaka, Japan) was used for daily culturing of hPSCs. For passaging, the cells were dissociated with TrypLE Express (Thermo Fisher Scientific, Waltham, MA, United States) for 3 min at 37°C and harvested. The cells were centrifuged at 200 × g for 3 min, resuspended in mTeSR-1 medium and counted using Via 1-Cassete™ (ChemoMetec A/S, Gydevang, 43, Denmark) of a NucleoCounter NC-200 (Chemetec, Baton Rouge, LA, United States). mTeSR-1 medium containing 10 μM of the ROCK inhibitor Y-27632 (Fujifilm Wako) was used to prevent apoptosis of dissociated hPSCs on day 1. mTeSR-1 medium without ROCK inhibitor was used on subsequent days, with daily medium changes.

Hepatic Differentiation From hPSCs on Device

Prior to inducing differentiation, the culture chambers of the device were coated with Matrigel at 35°C for 60 min. Matrigel was removed with an aspirator.

To induce endoderm differentiation, cultured hPSCs were washed with D-phosphate-buffered saline (PBS) (no calcium, no magnesium) (Thermo Fisher Scientific) and treated with TrypLE Express at 37°C for 3 min, followed by addition of basal medium, and transfer of the cell suspension into a 15-mL tube. Cells were centrifuged at 200 × g for 3 min, after which the supernatant was removed. The cells were resuspended to 7.00×10^5 cells mL^{-1} in mTeSR-1 medium supplemented with 10 μM Y27632, 100 ng mL^{-1} activin A (human recombinant) (Fujifilm Wako), and 1% (v/v) penicillin/streptomycin. They were then applied in 30 μL $chambers^{-1}$ resuspended solution to a Matrigel-coated culture chambers and cultured in a humidified incubator at 37°C with 5% CO_2 for 24 h. At the end of day 1, the medium was replaced with fresh mTeSR-1 medium supplemented with 10 μM Y27632, 100 ng mL^{-1} activin A and 1% (v/v) penicillin/streptomycin and cultured for an additional 24 h. On day 2, the medium was replaced with mTeSR-1 medium supplemented with 10 μM Y27632, 100 ng mL^{-1} activin A, 10 ng mL^{-1} BMP-4 (human recombinant) (R&D Systems, Minneapolis, MN, United States), 10 μM LY294002 (Cayman Chemical, Arbor, MI, United States), 3 μM CHIR99021(ReproCELL, Kanagawa, Japan), and 1% (v/v) penicillin/streptomycin. The cells were then incubated for 24 h. On day 3, the medium was replaced with mTeSR-1 medium supplemented with 10 μM Y27632, 100 ng mL^{-1} activin A, 10 ng mL^{-1} BMP-4, 10 μM LY294002, and 1% (v/v) penicillin/streptomycin, and the cells were incubated for 24 h. On day 4, the medium was replaced with Roswell Park Memorial Institute 1640 (RPMI) medium, GlutaMax Supplement (Thermo Fisher Scientific), supplemented with 2% (v/v) B-27 supplement (Thermo Fisher Scientific), 1% (v/v) MEM Non-essential Amino Acid Solution without L-glutamine, liquid, sterile-filtered Bioreagent suitable for cell-culture (NEAA) (Merck KGaA), 1% (v/v) penicillin/streptomycin, 10 μM Y27632, 100 ng mL^{-1} activin A, and 100 ng mL^{-1} bFGF (human recombinant) (Fujifilm Wako), and the cells were incubated for 24 h.

To induce HE specification, the cells were treated with RPMI medium GlutaMax Supplement, containing 2% (v/v) B-27 supplement, 1% (v/v) NEAA, 1% (v/v) penicillin/streptomycin, 10 μM Y27632 and 50 ng mL^{-1} activin A, with daily media changes for three days. On day 8, to induce hepatoblast specification, the cells were treated with RPMI medium GlutaMax™ Supplement, containing 2% (v/v) B-27™ supplement, 1% (v/v) NEAA, 1% (v/v) penicillin/streptomycin, 25 mM HEPS (Fujifilm Wako), 10 μM Y27632, 20 ng mL^{-1}

BMP-4, and 10 ng mL^{-1} FGF-10 (human recombinant) (R&D Systems). The cells were then treated with RPMI medium GlutaMax^{TM} Supplement, containing 2% (v/v) B-27^{TM} supplement, 1% (v/v) NEAA, 1% (v/v) penicillin/streptomycin, 25 mM HEPES, 20 ng mL^{-1} BMP-4 and 10 ng mL^{-1} FGF-10, with daily media changes and 0.2 Hz mechanical stimulation for four days.

Definitive Endoderm Differentiation on Dish

Prior to inducing differentiation, a cell-culture dish was coated with 0.1% gelatin from porcine skin, type A (Merck KGaA) in PBS at 25°C room temperature for 30 min. The gelatin solution was then aspirated and DMEM/F12 medium supplemented with 10% (v/v) fetal bovine serum (JRH Biosciences, St, Lenexa, KS, United States), 1% (v/v) L-glutamine, 1% (v/v) penicillin/streptomycin, and 100 μM b-mercaptoethanol (Fujifilm Wako) was introduced onto the culture dish for serum coating at 37°C for 24 h. The coated dish was then rinsed with fresh medium.

To induce endoderm differentiation, cultured hPSCs were washed with PBS and treated with TrypLE Express at 37°C for 3 min, followed by addition of basal medium and transfer of the cell suspension into a 15-mL tube. The cells were centrifuged at 200 × g for 3 min, after which the supernatant was removed. The cells were resuspended in mTeSR-1 medium supplemented with 1% (v/v) penicillin/streptomycin, 10 μM Y27632 and 100 ng mL^{-1} activin A, plated on a serum-coated culture dish, and cultured in a humidified incubator at 37°C with 5% CO_2 for 24 h. After 24 h incubation on day 4, the cells were treated with RPMI medium, GlutaMax^{TM} Supplement, containing 2% (v/v) B-27^{TM} supplement, 1% (v/v) NEAA, 1% (v/v) penicillin/streptomycin, and 50 ng mL^{-1} activin A, with daily media changes for three days. The cells were then treated with RPMI medium, GlutaMax^{TM} Supplement, containing 2% (v/v) B-27^{TM} supplement, 1% (v/v) NEAA, 1% (v/v) penicillin/streptomycin, 20 ng mL^{-1} BMP-4 and 10 ng mL^{-1} FGF-10, with daily media changes for two days. On day 6, the cells were harvested for flow cytometry.

Flow Cytometry

The cells were harvested with TrypLE Express and rinsed with PBS twice prior to cell counting. For antibody staining, the cells were diluted to a final concentration of 1×10^7 cells mL^{-1} in staining buffer (fetal bovine serum) (BD PharMingen, Franklin Lakes, NJ, United States). 2 μL of fluorescence-labeled antibodies (APC mouse anti-human CD184 (CXCR4), clone 12G5; BD PharMingen) were added into 50 μL of cell suspension, and incubated at room temperature for 1 h. As a negative control, specific isotype controls (APC mouse IgG2a k isotype control, clone G155-178; BD PharMingen) were used with the same concentration of the primary antibody. After removing excess antibodies by centrifugation at 300 × g for 5 min, the cells were washed with staining buffer, and cell suspensions were applied to a FACS Canto II (BD Biosciences, Franklin Lakes, NJ, United States) for flow cytometric analysis. Data analysis was performed using FlowJo software (v9; FlowJo, LLC, Ashland, OR, United States).

Cytochrome P450-GloTM Assay With Luciferin

To perform cytochrome P450-GloTM assays with luciferin (Promega, Madison, WI, United States), 20 μL medium was removed. Proluciferin IPA was diluted in RPMI medium, GlutaMax Supplement, containing 2% (v/v) B-27 supplement, 1% (v/v) NEAA, and 1% (v/v) penicillin/streptomycin. (1.5:1000). The air flow, mechanical stimulation was stopped, and 20 μL medium containing proluciferin IPA was applied to the culture chambers. The cells were incubated at 37°C with 5% CO_2 for 1 h. Next, 25 μL × 2 medium containing luciferin IPA was collected from two culture chambers with the same mechanical stimulation and applied to the 96-well plates (White Microwell SI; Thermo Fisher Scientific); 50 μL P450-Glo Reagent was subsequently added, incubated at 28°C for 20 min, and relative light units were measured with a Synergy HTX Microplate Reader (Biotek, Winooski, VT, United States) at 28°C.

Collection of all Proteins in Cells

The cells were rinsed with D-PBS (-) (Fujifilm Wako) three times, harvested with TrypLE Express, and collected into 1.5-mL tubes. Next, 0.5 mL RPMI medium, GlutaMax Supplement, containing 2% (v/v) B-27 supplement, 1% (v/v) NEAA, and 1% (v/v) penicillin/streptomycin was added. The tubes were centrifuged at 3000 × g for 3 min, and the supernatant was removed. The cells were rinsed with cold D-PBS, followed by addition of 100 μL cold 1 × RIPA buffer (Cell Signaling Technology, Danvers, MA, United States) in double distilled water was added. The tubes were then vortexed, incubated on ice for 30 min, sonicated at 4°C (US-1R cleaner; AS ONE, Osaka, Japan), and centrifuged at 4°C, 10,000 × g for 20 min. The supernatant was collected into new 1.5-mL tubes and stored at −20°C.

Protein Quantification

Using a BCA protein kit (TaKaRa, Shiga, Japan), a working solution (BCA reagent A: B = 100:1) and 0.2 mg μL^{-1} BCA standard were mixed with the collected proteins in 100 μL 1 × RIPA buffer in a 96-well plate (Matrix Microplate w/lids 96-well blk/clr, flat bottom, tissue culture, PS; Thermo Fisher Scientific). Proteins were incubated at 37°C for 60 min and measured at a wavelength of 562 nm with a Synergy HTX Microplate Reader.

Immunocytochemistry

The cells were fixed with 4% paraformaldehyde in D-PBS (-) (Fujifilm Wako) for 20 min at 25°C and then permeabilized with 0.1% (v/v) Triton X-100 in D-PBS for 5 min at 25°C. Subsequently, the cells were blocked in D-PBS (5% (v/v) normal goat serum blocking solution (Maravai Life Sciences, San Diego, CA, United States), 5% (v/v) normal donkey serum (Jackson ImmunoResearch, West Grove, PA, United States), 3% (v/v) albumin, essentially globulin-free (Merck KGaA), and 0.1%

Tween-20 (Nacalai Tesque, Kyoto, Japan) at 4°C for 16 h and then incubated at 4°C for 16 h with primary antibodies [anti-human albumin mouse IgG, 1:500; R&D Systems: anti-human cytokeratin 19 (CK19) mouse IgG, 1:500; Thermo Fisher Scientific: anti-human cytochrome P450 3A7 (CYP3A7) rabbit IgG, 1:500; Proteintech, Chicago, IL, United States] in blocking buffer. The cells were then incubated at 37°C for 60 min with a secondary antibody (AlexaFluor 488 Donkey anti-mouse IgG (H + L), 1:1000; Jackson ImmunoResearch: AlexaFluor 594 Donkey anti-rabbit IgG (H + L), 1:1000) in 0.1% Tween-20 prior to a final incubation with 4',6-diamidino-2-phenylindole (DAPI) (Fujifilm Wako) at 25°C for 30 min.

Image Acquisition

The sample containing cells was placed on the stage of a Nikon ECLIPSE Ti inverted fluorescence microscope equipped with a CFI plan fluor 10 × /0.30 N.A. objective lens (Nikon, Tokyo, Japan), CCD camera (ORCA-R2; Hamamatsu Photonics, Hamamatsu City, Japan), mercury lamp (Intensilight; Nikon), XYZ automated stage (Ti-S-ER motorized stage with encoders; Nikon), and filter cubes for fluorescence channels (DAPI, GFP HYQ, TRITC; Nikon). For image acquisition, the exposure times were set to 200 ms for DAPI, 200 ms for GFP HYQ (for ALB), 50 ms for GFP HYQ (for CK19), and 200 ms for TRITC (for CYP3A7).

Image Analysis

Image analysis of immunochemistry was performed with CellProfiler (ver. 3.1.9). The images of each stained protein and DAPI were inputted. In IdentifyPrimaryObejects, DAPI images were selected, and nuclei were identified. Typical diameter of objects, in pixel units was set (Min, Max) = (50, 150). Objects outside the diameter range and touching the border of image were discarded. Parameters were set as follows: Threshold smoothing scale, 6; Threshold correction factor, 0.95; Lower and upper bounds on threshold, 0.0 and 1,0; Size of adaptive window, 50; Method to distinguish clumped objects, shape; Method to draw dividing lines between clumped objects, shape. Size of smoothing filter for declumping, and minimum allowed distance between local maxima were automatically calculated. Handling was sped up by using lower-resolution images to identify local maxima. Holes in identified objects were filled only after declumping. Handling of objects was continued if an excessive number of objects was identified. In IdentifySecondaryObjects, stained protein images were selected, and nuclei, as the input objects, was selected. The parameters were set as follows: Method to identify the secondary objects, Propagation; Threshold strategy, Global; Thresholding method, Minimum cross entropy; Threshold smoothing scale, 0.0; Threshold correction factor, 1.0; Lower and upper bounds on threshold, 0.0 and 1.0; Regularization, 0.05. Holes were filled in identified objects. Objects touching the border of images were not discarded. In IdentifyTertiaryObjects, as the larger identified objects, secondary identified objects were selected, and as the smaller identified objects, primary identified objects were selected. Prior to subtraction, smaller objects were not shrunken. In MeasureObjectIntensity, the intensity of tertiary identified objects, cytoplasm, was measured.

Statistical Analysis

Each sample was labeled alphabetically. The Tukey-Kramer test was carried out with *R* software (ver. 4.0.2).

RESULTS

Fabrication of a Microfluidic Device Mimicking the Beating of an Embryonic Heart

To mimic embryonic heart beating *in vitro* (**Figure 1A**), a microfluidic device with a series of stretchable balloon membranes was fabricated (**Figures 1B–F** and **Supplementary Figure S1**). This microfluidic device consisted of three layers: a top layer for cell-culture wells, middle layer of thin membrane as the stretchable cell-culture substrate, and bottom layer for forming pressure chambers. The top layer was 5 mm thick, and each well in the top layer was 3 mm in diameter. The middle PDMS membrane was 0.14 mm thick. The bottom layer was 2 mm thick with a 0.25-mm channel and chamber height, and 0.2-mm channel width (**Supplementary Figure S2**). The molds for the top and bottom layers were fabricated with a high-resolution 3D printer (Kamei et al., 2015).

The thin ballooned PDMS membrane was actuated with the regulator connected to an air compressor. To test a series of stretching forces within a single device, we used a pressure-drop method (Shimizu et al., 2011) in which air pressure was decreased in an inverse proportion to the length of fluidic flow (**Figure 2A**). Hence, the pressure drop (ΔP) for incompressible fluid flow was determined from the Fanning friction factor (f) using the Fanning formula:

$$\Delta P = 4f\left(\frac{L}{D}\right)\left(\frac{\rho v^2}{2}\right) \quad (1)$$

Where L is the channel length, ρ is the fluid density, and v is the average velocity in a channel. Hydraulic diameter, D (m) was calculated as:

$$D = \frac{2wh}{(w+h)} \quad (2)$$

where w and h represent the channel width and height, respectively.

The amount of air pressure applied to each chamber decreased with increasing channel length. The device was designed to have two sets of 15 culture chambers along a micro channel and negative control chambers in a single device. For the CFD simulation of pressure drop in the device, incompressible flow and laminar flow in microscale channel was considered, and three input pressures (i.e., 18, 32, and 45 kPa), as well as the output pressure (atmosphere) were set. The analytical simulation results showed linear damping characteristic curves of pressures similar to theoretical equation (1) (**Figures 2B,C**). To demonstrate the pressure-drop method over a series of membrane stretching events with the actual device, we applied three input pressures (i.e., 18, 32, and 45 kPa) to the inlet and measured the vertical

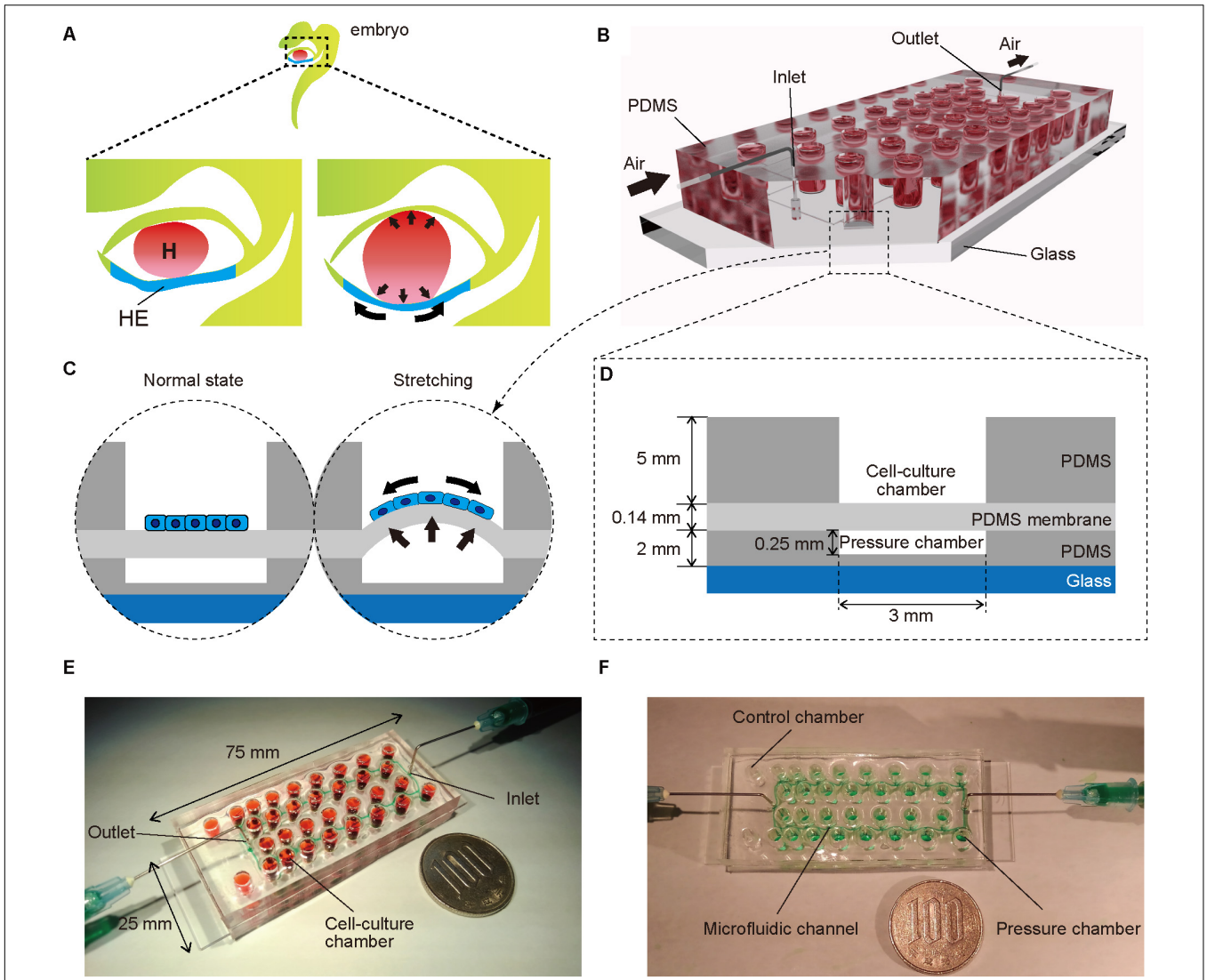

FIGURE 1 | (A) Illustration of an early human embryo. Heart (H: red) beating confers mechanical stimulation to the surrounding cells, and hepatic endoderm (HE: blue), which differentiates to hepatoblasts, is exposed to mechanical forces. **(B,C)** Appearance **(B)** and cross-section **(C)** of a microfluidic device for applying a series of stretching stimulations to hepatic endoderm-like cells (HECs). **(D)** Cross-sectional view of the device, composed of polydimethylsiloxane (PDMS) and consists of a top layer with cell-culture chambers, middle membrane layer, and bottom layer with pressure chambers on a glass slide. **(E)** Photograph of our device fabricated on a glass slide (25 × 75 mm). Culture chambers are filled with red ink. This device has two sets of culture chambers in which cells are cultured under the same intensity of mechanical stimulation. **(F)** Photograph of a microfluidic device. Microfluidic channels and pressure chambers filled with green ink.

displacement from the base of the membrane. As expected, membrane displacement corresponded to pressure decreases for the tested input pressures. When more than 45 kPa pressure was applied to the inlet, the device was unstable due to air leakage. Based on these results, we selected seven significant different displacements and labeled them as the input pressure (kPa), and the distance from the inlet (mm), such as (45, 10.4) (**Figure 2D**, **Supplementary Tables S1, S2**).

Differentiation of hPSCs to Hepatoblasts

Next, hPSCs were differentiated to hepatoblasts in a device (**Figure 3A**; Hannan et al., 2013; Kamei et al., 2019). In our previously reported protocol using a dish, gelatin coating was sufficient for hPSC culture and differentiation, however, was insufficient for PDMS membrane, causing detachment of cells (**Supplementary Figure S3**). Therefore, prior to culturing in a device, the cell-culture chambers were coated with Matrigel, which improved hPSC adhesion and differentiation. The differentiation from hPSCs to hepatoblasts occurred via three stages. Briefly, in the first stage, hPSCs were directed into DE by treatment with 100 ng mL^{-1} activin A, 10 μM ROCK inhibitor, 3 μM CHIR99021, 10 μM LY294002, 10 ng mL^{-1} BMP4, and 100 ng mL^{-1} basic FGF (bFGF). To confirm DE differentiation, expression of C-X-C-motif chemokine receptor 4 (CXCR4), a DE cell-surface marker, as well as SRY-box 17 (SOX17), a DE transcription factor (D'Amour et al., 2005;

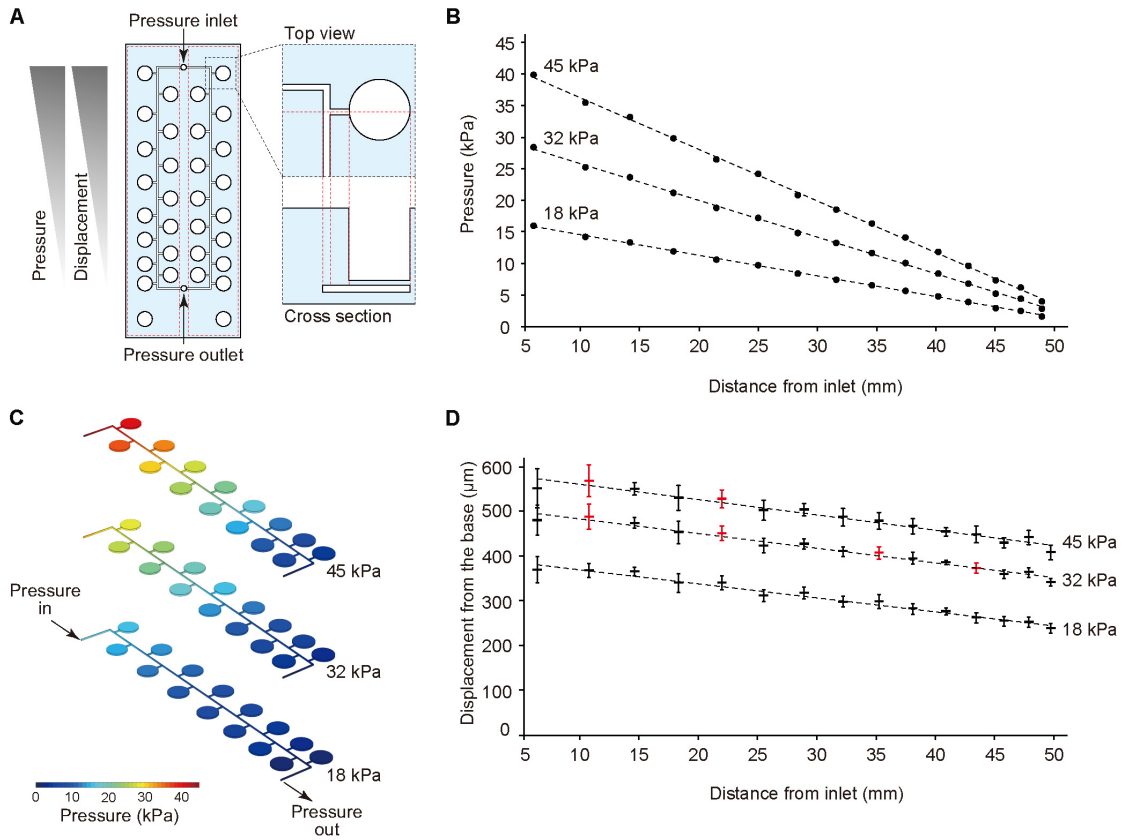

FIGURE 2 | Pressure-drop method to generate a series of PDMS membrane displacements in a single device. **(A)** Membrane displacements are inversely proportional to the distance from the inlet due to a pressure drop along with a microfluidic channel. **(B,C)** The computer simulation for pressure drop was conducted using input pressure (18, 32, and 45 kPa) and output pressure (atmosphere). **(D)** Displacement measurement of the device with CCD laser displacement camera when 18, 32, and 45 kPa were applied at the inlet. The red plots indicated the conditions used for stretching stimulation. ANOVA with Tukey-Kramer test compared with all displacements of the pressure chambers at 18, 32, and 45 kPa. *p*-values were summarized in Supplementary **Tables S1, S2**. Each plot represents the mean ± standard deviation determined from four independent experiments measuring the two chambers in a single device.

Yasunaga et al., 2005), were evaluated by flow cytometry (**Figure 3B**) and immunocytochemistry (**Supplementary Figure S4**) at day 6. More than 99% of the cells were stained for CXCR4, and also showed expression of SOX17, indicating efficient DE differentiation from hPSCs. In the second stage, DE cells were treated with a lower concentration of activin A (50 ng μL^{-1}) to obtain hepatic endoderm-like cells (HECs). In the third stage, HECs were differentiated to hepatoblasts by treatment with 20 ng mL^{-1} BMP4 and 10 ng mL^{-1} FGF10. Frequency of stretching stimulation, set at 0.2 Hz (**Supplementary Video S1**), was applied during the third stage for four days. Cells were observed on the PDMS thin membrane by day 12 (**Supplementary Figure S5** and **Supplementary Video S2**).

Mechanical Forces Enhance Differentiation of hPSCs to Functional Hepatoblasts

To investigate the effect of mechanical forces on the differentiation of HECs to hepatoblasts, the activity of cytochrome P450 3A (CYP3A), which is specifically expressed in hepatic cells (Si-Tayeb et al., 2010b; Danoy et al., 2020), was measured in a bioluminescent CYP3A activity assay at day 12 (**Figure 3C**, **Supplementary Figure S6** and **Supplementary Table S3**). Compared with HECs induced on the device, unstimulated hepatoblasts showed significantly higher activity, as expected. When 32-kPa input pressure was applied to the larger displacements at (32, 21.5) and (32, 10.4), stimulated hepatoblasts showed higher CYP3A activity, whereas activity at (32, 42.7) and (32, 34.6) was not significantly different from that observed for unstimulated haptoblasts. Moreover, at a higher input pressure of 45 kPa, the larger displacements at (45, 21.5) and (45, 10.4) caused significantly higher CYP3A activity in hepatoblasts compared to unstimulated cells, and hepatoblasts at (45, 10.4), which had at least two-fold higher CYP3A activities compared to unstimulated cells. These results suggest that mechanical stimulation, induced by stretching cell-culture substrates, increased hepatoblastic metabolic activities.

To further investigate the effects of stretching stimulation on HEC-hepatoblast differentiation, the expression of albumin (ALB), CYP3A7, and cytokeratin 19 (CK19) proteins, which are specifically expressed in hepatoblasts (Schmelzer et al., 2006;

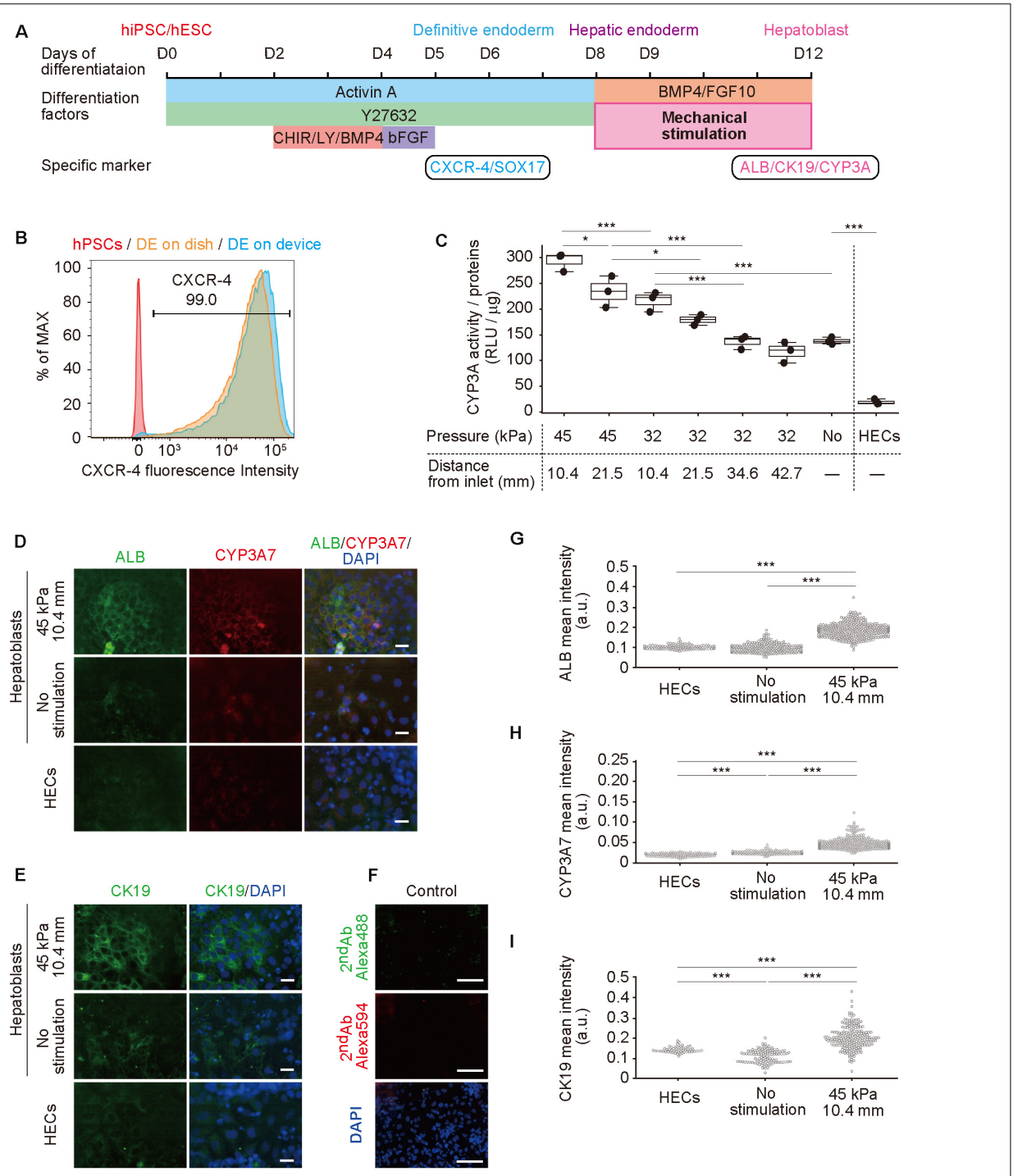

FIGURE 3 | Hepatoblast differentiation from human pluripotent stem cells (hPSCs) promoted by mechanical forces on hepatic endoderm-like cells (HECs). **(A)** Schematic diagram showing hepatic differentiation from hPSCs. ROCK inhibitor (Y27632), WNT inhibitor (CHIR, CHIR99021), PI3K inhibitor (LY, LY294002), bFGF, BMP4, and FGF10 were used for corresponding differentiation stages. **(B)** Flow cytometric analyses showing the proportion of CXCR4 expression in hPSCs, HECs in a dish and HECs in a microfluidic device. **(C)** Bioluminescent CYP3A activity assay for HECs and hepatoblasts. ANOVA with Tukey-Kramer test compared relative light units (RLU) divided by amount of proteins in cell lysates of all samples (**Supplementary Figure S6** and **Supplementary Table S3**). $^{*}P < 0.05$, $^{***}P < 0.001$ ($n = 3$). Max, median, minimum of three independent experiments were shown. **(D,E)** Immunocytochemical analyses showing the expression of ALB, CYP3A7, **(D)** and CK19 **(E)** in HECs and hepatoblasts in the indicated conditions. Nuclei were stained with DAPI. Scale bars represent 50 μm. **(F)** The negative controls of immunochemistry stained with only 2nd antibody labeled with Alexa 488 and Alexa 594 fluorescent dyes shown in **(F)**. Scale bars represent 100 μm. **(G–I)** Quantitative single cell profiling of ALB **(G)**, CYP3A7 **(H)**, and CK19 **(I)** in HECs and hepatoblasts in the device. Fluorescence intensity was obtained from several images per each sample. ANOVA with Tukey-Kramer test compared with mean intensity. $^{***}P < 0.001$.

Yang et al., 2017), were observed by immunocytochemistry (**Figure 3D** for ALB and CYP3A7, **Figure 3E** for CK19, **Figure 3F** for negative controls stained with only 2nd antibodies and **Supplementary Figure S7** for positive control with HepG2 cells). The fluorescence intensity of the single cell was calculated (**Figure 3G** for ALB, **Figure 3H** for CYP3A7, **Figure 3I** for CK19). Hepatoblasts at (45, 10.4) showed higher expression of ALB, CYP3A7, and CK19 proteins than unstimulated hepatoblasts, which agreed with the results observed for CYP3A activities. Notably, HECs did not express any of the examined proteins, and no secreted albumin was detected in the conditioned media (**Supplementary Figure S8**). Generally, these proteins have only been shown to be expressed by hepatoblasts *in vivo,* not *in vitro* (Si-Tayeb et al., 2010b; Danoy et al., 2020). Hence, these results suggest that application of stretching stimulation induces more functionally relevant hPSC-derived hepatoblasts compared to those generated via conventional cell-culture methods.

DISCUSSION

Herein, we recapitulated human embryonic development from hESC-derived HE to hepatoblasts with mechanical stimulation to improve functionality of hepatocytes. Until now, most hepatic differentiation methods for hPSCs are based on treatments with biochemical substances, such as growth factors, cytokines, supplemental chemicals, and extracellular matrices. Although these methods allow for the generation of hPSC-derived hepatocyte-like cells, they do not facilitate the development of fully functional hepatocytes. Hence, methodological developments require a new approach for the differentiation of hPSCs. To this end, we hypothesized that mechanical stimulation, such as the stretching force generated by a heart beating, would influence hepatoblast functionality during hepatic differentiation.

Results from our newly developed model showed that ALB expression of stimulated hepatoblasts at (45, 10.4) was higher than that of unstimulated hepatoblasts. Hence, GATA4, which is reportedly an enhancer of ALB, may be susceptible to mechanical stimulation thorough RhoA (Charron et al., 2001; Si-Tayeb et al., 2010a). Moreover, the expression of CYP3A7 and CK19 was also higher in hepatoblasts at (45, 10.4) compared to unstimulated hepatoblasts. According to Genecards (Zhang et al., 2018), which provides information on genes and their expression mechanisms, the enhancer of CYP3A7 and CK19 is peroxisome proliferator-activated receptor-γ (PPARg), which serves as a co-activator with the transcription factors yes-associated protein (YAP), and transcriptional co-activator with PDZ-binding motif (TAZ), in the Hippo pathway (Piccolo et al., 2014). Recently, it was reported that mechanical stimuli via cell-substrate interactions induces the translocation of YAP/TAZ, and alters the phenotype of epithelial (Acharya et al., 2018), endothelial (Sakamoto et al., 2010; Nakajima et al., 2017), and mesenchymal stem cells (Hong et al., 2005; Dupont et al., 2011; Guo et al., 2018). This process may, therefore, be involved in HEC-hepatoblast differentiation. However, the precise underlying mechanisms associated with this pathway require further investigation to provide specific improvements to the mechanical stimulation of HEC-hepatoblast differentiation in the future.

The use of hPSC-derived hepatocytes has been proposed as an alternative to human primary hepatocytes for drug screening (Bale et al., 2014; Zakikhan et al., 2017); however, no previous studies have described methodology capable of generating cells with the proper functionality, due to insufficient differentiation. Our methodology designed to obtain functional hepatoblasts will allow the generation of more functional hepatocytes that will be directly applicable to Liver-on-a-Chip technologies, for applications in drug screening and toxicological testing (Kamei et al., 2017; Ronaldson-Bouchard and Vunjak-Novakovic, 2018). Furthermore, functional hepatocytes can be used for various *in vitro* disease modeling, including infection (Nie et al., 2018) and non-alcoholic fatty liver disease (Nantasanti et al., 2015; Lauschke et al., 2019). In addition to the *in vitro* applications, since the hepatocytes generated from our device can be harvested, they may also prove applicable for cell transplantation and regenerative medicine (Prior et al., 2019). Therefore, our novel method for the generation of functional hepatoblasts from hPSCs may prove to be a novel platform for both *in vitro* and *in vivo* applications of hPSC-derived hepatocytes.

Certain limitations were noted in this study. For instance, the frequency of stretching stimulation applied in our system was 0.2 Hz, equivalent to 12 beats per minute, which is much slower than that of normal fetal heart rates (110 to 150 beats per minutes) (Pildner von Steinburg et al., 2013). This is largely due to the current experimental setting to actuate the PDMS membrane using the solenoid valve, which is not capable of achieving normal fetal heart rate frequencies. Hence, to truly mimic fetal liver developmental conditions, more rapid stretching stimulation of cells must be applied.

CONCLUSION

In summary, we developed a microfluidic device by applying multiple stretching forces during HEC-hepatoblast differentiation from hPSCs. Using this device, we found that mechanical stimulation improved the functionalities of hepatoblasts. Our device and approach provide not only insights into the hepatic developmental process, but also tools for applications in both drug discovery and regenerative medicine.

DATA AVAILABILITY STATEMENT

The authors acknowledge that the data presented in this study must be deposited and made publicly available in an acceptable repository, prior to publication. Frontiers cannot accept a manuscript that does not adhere to our open data policies.

AUTHOR CONTRIBUTIONS

KY, NM, and KK performed conceptualization, investigation, and methodology. KY, NM, JY, SI, KS, JP, ST, and YH performed data

curation. KY, NM, JY, and YH performed formal analysis. KK performed funding acquisition, project administration, resources, and supervision. YH and KK performed software. KY and KK performed validation and visualization and writing original draft. KY, NM, JY, KS, JP, YH, and KK wrote, reviewed and edited the manuscript. All authors contributed to the article and approved the submitted version.

FUNDING

Funding was generously provided by the Japan Society for the Promotion of Science (JSPS; 16K14660, 17H02083, 18KK0306, and 19H02572), Japan Agency for Medical Research and Development (AMED; 17937667) and LiaoNing Revitalization Talents Program (XLYC1902061). NM was supported by the BME Paris Master program. KS and JP were supported by the Nakatani Foundation for advancement of measuring technologies in biomedical engineering. The WPI-iCeMS is supported by the World Premier International Research Centre Initiative (WPI), MEXT, Japan. This manuscript has been released as a pre-print at *bioRxiv* (Yoshimoto et al.; doi: 10.1101/2020.05.18.103218).

SUPPLEMENTARY MATERIAL

The Supplementary Material for this article can be found online at: https://www.frontiersin.org/articles/10.3389/fbioe.2020.568092/full#supplementary-material

REFERENCES

Acharya, B. R., Nestor-Bergmann, A., Liang, X., Gupta, S., Duszyc, K., Gauquelin, E., et al. (2018). A mechanosensitive RhoA pathway that protects epithelia against acute tensile stress. *Dev. Cell* 47, 439–452.e6. doi: 10.1016/j.devcel.2018.09.016

Altamirano-Barrera, A., Barranco-Fragoso, B., and Méndez-Sánchez, N. (2017). Management strategies for liver fibrosis. *Ann. Hepatol.* 16, 48–56. doi: 10.5604/16652681.1226814

Bale, S. S., Vernetti, L., Senutovitch, N., Jindal, R., Hegde, M., Gough, A., et al. (2014). In vitro platforms for evaluating liver toxicity. *Exp. Biol. Med.* 239, 1180–1191. doi: 10.1177/1535370214531872

Bhatia, S. N., and Ingber, D. E. (2014). Microfluidic organs-on-chips. *Nat. Biotechnol.* 32, 760–772. doi: 10.1038/nbt.2989

Camp, J. G., Sekine, K., Gerber, T., Loeffler-Wirth, H., Binder, H., Gac, M., et al. (2017). Multilineage communication regulates human liver bud development from pluripotency. *Nature* 546, 533–538. doi: 10.1038/nature22796

Charron, F., Tsimiklis, G., Arcand, M., Robitaille, L., Liang, Q., Molkentin, J. D., et al. (2001). Tissue-specific GATA factors are transcriptional effectors of the small GTPase RhoA. *Genes Dev.* 15, 2702–2719. doi: 10.1101/gad.915701

Chen, T., Sun, J., Ma, T., Li, T., Liu, C., Zhu, X., et al. (2019). Design and analysis of particulate matter air-microfluidic grading chip based on MEMS. *Micromachines* 10:497. doi: 10.3390/mi10080497

D'Amour, K. A., Agulnick, A. D., Eliazer, S., Kelly, O. G., Kroon, E., and Baetge, E. E. (2005). Efficient differentiation of human embryonic stem cells to definitive endoderm. *Nat. Biotechnol.* 23, 1534–1541. doi: 10.1038/nbt1163

Danoy, M., Tauran, Y., Poulain, S., Arakawa, H., Mori, D., Araya, K., et al. (2020). Analysis of hiPSCs differentiation toward hepatocyte-like cells upon extended exposition to oncostatin. *Differentiation* 114, 36–48. doi: 10.1016/j.diff.2020.05.006

Dupont, S., Morsut, L., Aragona, M., Enzo, E., Giulitti, S., Cordenonsi, M., et al. (2011). Role of YAP/TAZ in mechanotransduction. *Nature* 474, 179–183. doi: 10.1038/nature10137

Gordillo, M., Evans, T., and Gouon-Evans, V. (2015). Orchestrating liver development. *Development* 142, 2094–2108. doi: 10.1242/dev.114215

Guo, L., Cai, T., Chen, K., Wang, R., Wang, J., Cui, C., et al. (2018). Kindlin-2 regulates mesenchymal stem cell differentiation through control of YAP1/TAZ. *J. Cell Biol.* 217, 1431–1451. doi: 10.1083/jcb.201612177

Hannan, N. R. F., Segeritz, C.-P., Touboul, T., and Vallier, L. (2013). Production of hepatocyte-like cells from human pluripotent stem cells. *Nat. Protoc.* 8, 430–437. doi: 10.1038/nprot.2012.153

Ho, C.-T., Lin, R.-Z., Chang, W.-Y., Chang, H.-Y., and Liu, C.-H. (2006). Rapid heterogeneous liver-cell on-chip patterning via the enhanced field-induced dielectrophoresis trap. *Lab. Chip* 6:724. doi: 10.1039/b602036d

Hong, J.-H., Hwang, E. S., McManus, M. T., Amsterdam, A., Tian, Y., Kalmukova, R., et al. (2005). TAZ, a transcriptional modulator of mesenchymal stem cell differentiation. *Science* 309, 1074–1078. doi: 10.1126/science.1110955

Huh, D., Matthews, B. D., Mammoto, A., Montoya-Zavala, M., Hsin, H. Y., and Ingber, D. E. (2010). Reconstituting organ-level lung functions on a chip. *Science* 328, 1662–1668. doi: 10.1126/science.1188302

Kamei, K., Mashimo, Y., Koyama, Y., Fockenberg, C., Nakashima, M., Nakajima, M., et al. (2015). 3D printing of soft lithography mold for rapid production of polydimethylsiloxane-based microfluidic devices for cell stimulation with concentration gradients. *Biomed. Microdev.* 17:36. doi: 10.1007/s10544-015-9928-y

Kamei, K., Yoshioka, M., Terada, S., Tokunaga, Y., and Chen, Y. (2019). Three-dimensional cultured Liver-on-a-Chip with mature hepatocyte-like cells derived from human pluripotent stem cells. *Biomed. Microdev.* 21:73.

Kamei, K. I., Kato, Y., Hirai, Y., Ito, S., Satoh, J., Oka, A., et al. (2017). Integrated heart/cancer on a chip to reproduce the side effects of anti-cancer drugs: in vitro. *RSC Adv.* 7, 36777–36786. doi: 10.1039/c7ra07716e

Lauschke, V. M., Shafagh, R. Z., Hendriks, D. F. G., and Ingelman-Sundberg, M. (2019). 3D primary hepatocyte culture systems for analyses of liver diseases, drug metabolism, and toxicity: emerging culture paradigms and applications. *Biotechnol. J.* 14, 1–12. doi: 10.1002/biot.201800347

Marengo, A., Rosso, C., and Bugianesi, E. (2016). Liver cancer: connections with obesity, fatty liver, and cirrhosis. *Annu. Rev. Med.* 67, 103–117. doi: 10.1146/annurev-med-090514-013832

Nakajima, H., Yamamoto, K., Agarwala, S., Terai, K., Fukui, H., Fukuhara, S., et al. (2017). Flow-dependent endothelial YAP regulation contributes to vessel maintenance. *Dev. Cell* 40, 523–536.e6. doi: 10.1016/j.devcel.2017.02.019

Nantasanti, S., De Bruin, A., Rothuizen, J., Penning, L. C., and Schotanus, B. A. (2015). Concise review: organoids are a powerful tool for the study of liver disease and personalized treatment design in humans and animals. *Stem Cells Transl. Med.* 5, 325–330. doi: 10.5966/sctm.2013-0118

Nie, Y. Z., Zheng, Y. W., Miyakawa, K., Murata, S., Zhang, R. R., Sekine, K., et al. (2018). Recapitulation of hepatitis B virus-host interactions in liver organoids from human induced pluripotent stem cells. *eBio Med.* 35, 114–123. doi: 10.1016/j.ebiom.2018.08.014

Pavesi, A., Adriani, G., Rasponi, M., Zervantonakis, I. K., Fiore, G. B., and Kamm, R. D. (2015). Controlled electromechanical cell stimulation on-a-chip. *Sci. Rep.* 5, 1–12. doi: 10.1038/srep11800

Piccolo, S., Dupont, S., and Cordenonsi, M. (2014). The biology of YAP/TAZ: hippo signaling and beyond. *Physiol. Rev.* 94, 1287–1312. doi: 10.1152/physrev.00005.2014

Pildner von Steinburg, S., Boulesteix, A.-L., Lederer, C., Grunow, S., Schiermeier, S., Hatzmann, W., et al. (2013). What is the "normal" fetal heart rate? *PeerJ* 1:e82. doi: 10.7717/peerj.82

Prior, N., Inacio, P., and Huch, M. (2019). Liver organoids: from basic research to therapeutic applications. *Gut* 68:gutjnl-2019-319256. doi: 10.1136/gutjnl-2019-319256

Ren, L., Yang, P., Wang, Z., Zhang, J., Ding, C., and Shang, P. (2015). Biomechanical and biophysical environment of bone from the macroscopic to the pericellular and molecular level. *J. Mech. Behav. Biomed. Mater.* 50, 104–122. doi: 10.1016/j.jmbbm.2015.04.021

Ronaldson-Bouchard, K., and Vunjak-Novakovic, G. (2018). Organs-on-a-chip: a fast track for engineered human tissues in drug development. *Cell Stem Cell* 22, 310–324. doi: 10.1016/j.stem.2018.02.011

Sakamoto, N., Saito, N., Han, X., Ohashi, T., and Sato, M. (2010). Effect of spatial gradient in fluid shear stress on morphological changes in endothelial cells in response to flow. *Biochem. Biophys. Res. Commun.* 395, 264–269. doi: 10.1016/j.bbrc.2010.04.002

Schmelzer, E., Wauthier, E., and Reid, L. M. (2006). The phenotypes of pluripotent human hepatic progenitors. *Stem Cells* 24, 1852–1858. doi: 10.1634/stemcells.2006-2036

Shimizu, K., Shunori, A., Morimoto, K., Hashida, M., and Konishi, S. (2011). Development of a biochip with serially connected pneumatic balloons for cell-stretching culture. *Sens. Actuat. B Chem.* 156, 486–493. doi: 10.1016/j.snb.2011.04.048

Si-Tayeb, K., Lemaigre, F. P., and Duncan, S. A. (2010a). Organogenesis and Development of the Liver. *Dev. Cell* 18, 175–189. doi: 10.1016/j.devcel.2010.01.011

Si-Tayeb, K., Noto, F. K., Nagaoka, M., Li, J., Battle, M. A., Duris, C., et al. (2010b). Highly efficient generation of human hepatocyte-like cells from induced pluripotent stem cells. *Hepatology* 51, 297–305. doi: 10.1002/hep.23354

Takahashi, K., Tanabe, K., Ohnuki, M., Narita, M., Ichisaka, T., Tomoda, K., et al. (2007). Induction of pluripotent stem cells from adult human fibroblasts by defined factors. *Cell* 131, 861–872. doi: 10.1016/j.cell.2007.11.019

Thomson, J. A., Itskovitz-Eldor, J., Shapiro, S. S., Waknitz, M. A., Swiergiel, J. J., Marshall, V. S., et al. (1998). Embryonic stem cell lines derived from human blastocysts. *Science* 282, 1145–1147. doi: 10.1126/science.282.5391.1145

Turgay, M. B., and Yazıcıoğlu, A. G. (2018). Numerical simulation of fluid flow and heat transfer in a trapezoidal microchannel with COMSOL multiphysics: a case study. *Numer. Heat Transf. Part A Appl.* 73, 332–346. doi: 10.1080/10407782.2017.1420302

Yang, L., Wang, W., Qiu, W., Guo, Z., Bi, E., and Xu, C. (2017). A single-cell transcriptomic analysis reveals precise pathways and regulatory mechanisms underlying hepatoblast differentiation. *Hepatology* 66, 1387–1401. doi: 10.1002/hep.29353

Yasunaga, M., Tada, S., Torikai-Nishikawa, S., Nakano, Y., Okada, M., Jakt, L. M., et al. (2005). Induction and monitoring of definitive and visceral endoderm differentiation of mouse ES cells. *Nat. Biotechnol.* 23, 1542–1550. doi: 10.1038/nbt1167

Yu, J., Vodyanik, M. A., Smuga-Otto, K., Antosiewicz-Bourget, J., Frane, J. L., Tian, S., et al. (2007). Induced pluripotent stem cell lines derived from human somatic cells. *Science* 318, 1917–1920. doi: 10.1126/science.1151526

Zakikhan, K., Pournasr, B., Vosough, M., and Nassiri-Asl, M. (2017). In vitro generated hepatocyte-like cells: a novel tool in regenerative medicine and drug discovery. *Cell J.* 19, 204–217. doi: 10.22074/cellj.2016.4362

Zhang, W., Bojorquez-Gomez, A., Velez, D. O., Xu, G., Sanchez, K. S., Shen, J. P., et al. (2018). A global transcriptional network connecting noncoding mutations to changes in tumor gene expression. *Nat. Genet.* 50, 613–620. doi: 10.1038/s41588-018-0091-92

Conflict of Interest: The authors declare that the research was conducted in the absence of any commercial or financial relationships that could be construed as a potential conflict of interest.

frontiers in Bioengineering and Biotechnology

ORIGINAL RESEARCH
published: 28 September 2020
doi: 10.3389/fbioe.2020.573775

Design and Validation of a Human Brain Endothelial Microvessel-on-a-Chip Open Microfluidic Model Enabling Advanced Optical Imaging

*Mootaz M. Salman[1,2], Graham Marsh[3], Ilja Kusters[1,2], Matthieu Delincé[1,2], Giuseppe Di Caprio[1,2], Srigokul Upadhyayula[1,2†], Giovanni de Nola[1,2], Ronan Hunt[2], Kazuka G. Ohashi[2], Taylor Gray[3], Fumitaka Shimizu[4], Yasuteru Sano[4], Takashi Kanda[4], Birgit Obermeier[3] and Tom Kirchhausen[1,2,5]**

[1] Department of Cell Biology, Harvard Medical School, Boston, MA, United States, [2] Program in Cellular and Molecular Medicine, Boston Children's Hospital, Boston, MA, United States, [3] Biogen, Cambridge, MA, United States, [4] Yamaguchi University Graduate School of Medicine, Ube, Japan, [5] Department of Pediatrics, Harvard Medical School, Boston, MA, United States

OPEN ACCESS

Edited by:
Shi-Cong Tao,
Shanghai Jiao Tong University, China

Reviewed by:
Khashayar Khoshmanesh,
RMIT University, Australia
Chun-Yuan Chen,
Central South University, China

***Correspondence:**
Tom Kirchhausen
kirchhausen@crystal.harvard.edu

†Present address:
Srigokul Upadhyayula,
Department of Molecular and Cell Biology, University of California, Berkeley, Berkeley, CA, United States

Specialty section:
This article was submitted to Nanobiotechnology, a section of the journal Frontiers in Bioengineering and Biotechnology

Received: 18 June 2020
Accepted: 21 August 2020
Published: 28 September 2020

Citation:
Salman MM, Marsh G, Kusters I, Delincé M, Di Caprio G, Upadhyayula S, de Nola G, Hunt R, Ohashi KG, Gray T, Shimizu F, Sano Y, Kanda T, Obermeier B and Kirchhausen T (2020) Design and Validation of a Human Brain Endothelial Microvessel-on-a-Chip Open Microfluidic Model Enabling Advanced Optical Imaging. Front. Bioeng. Biotechnol. 8:573775. doi: 10.3389/fbioe.2020.573775

We describe here the design and implementation of an *in vitro* microvascular open model system using human brain microvascular endothelial cells. The design has several advantages over other traditional closed microfluidic platforms: (1) it enables controlled unidirectional flow of media at physiological rates to support vascular function, (2) it allows for very small volumes which makes the device ideal for studies involving biotherapeutics, (3) it is amenable for multiple high resolution imaging modalities such as transmission electron microscopy (TEM), 3D live fluorescence imaging using traditional spinning disk confocal microscopy, and advanced lattice light sheet microscopy (LLSM). Importantly, we miniaturized the design, so it can fit within the physical constraints of LLSM, with the objective to study physiology in live cells at subcellular level. We validated barrier function of our brain microvessel-on-a-chip by measuring permeability of fluorescent dextran and a human monoclonal antibody. One potential application is to investigate mechanisms of transcytosis across the brain microvessel-like barrier of fluorescently-tagged biologics, viruses or nanoparticles.

Keywords: blood-brain barrier (BBB), capillary, microvessel, shear stress, microfluidics, live cell imaging

INTRODUCTION

The blood–brain barrier (BBB) is a unique and highly selective vascular interface that separates the peripheral blood circulation from the neural tissue in order to maintain a homeostatic microenvironment within the central nervous system (CNS) that allows the neuronal network to function properly (Abbott et al., 2010; Park et al., 2019).

The BBB is a complex vascular structure with specialized endothelial cells as its core element, surrounded by extracellular matrix (ECM) and supporting cells, such as astrocytes and pericytes (Greene and Campbell, 2016). Brain microvascular endothelial cells (BMVECs) that line the

capillaries of the BBB are of crucial physiological importance since they tightly control the molecular and cellular flux between the blood and the brain, thereby regulating regional changes in nutrients and oxygen levels (Daneman, 2012), maintaining brain energy levels (Bordone et al., 2019) and mediating the local immune response in the CNS (Abbott et al., 2010). BMVECs differ from those found in peripheral vasculature as they have no fenestration and exhibit restricted paracellular passage for water and hydrophilic solutes due to the presence of a unique array of tight junctions and adherens junctions between adjacent endothelial cells (Greene and Campbell, 2016). Moreover, BMVECs have specialized transcellular transport mechanisms ensuring only wanted substances being actively delivered to the brain, and have shown to express a number of broad-spectrum efflux pumps on their luminal surface which severely limit the uptake of lipophilic molecules, including small molecule drugs, from the blood through the endothelium into the CNS. These characteristic anatomical and functional features of the BBB determine its crucial protective role for the CNS (Mahringer et al., 2011; Shawahna et al., 2011).

However, these highly selective barrier properties also extremely limit the therapeutic efficacy of drugs and hinder the treatment of neurological diseases such as Alzheimer's disease, multiple sclerosis, Parkinson's disease, HIV infection and brain tumors (Pardridge, 2006). Beyond therapeutics' insufficient brain exposure, the BBB also plays a major role in the underlying pathophysiology of many of these CNS disorders which are usually associated with vascular hyperpermeability, transporter deficiencies, or an increase in leukocyte adhesion molecules, resulting in an abnormal, uncontrolled movement of cells and neurotoxins across the BBB blood vessel walls (Pardridge, 2006).

For studies of barrier function and dysfunction, *in vivo* models are of highest physiological relevance since the BBB is embedded in its natural microenvironment. These models are, however, limited in their throughput. Furthermore, animal models may not predict BBB penetrance and efficacy of drugs in humans due to interspecies differences in the molecular composition of the BBB microvessels (Uchida et al., 2011; Song et al., 2020). Deciphering the underlying molecular mechanisms and performing translatable real-time quantitative assessments of drug transport across brain microvessels, such as screenings for BBB-penetrant therapeutic antibodies, are therefore greatly limited in an *in vivo* setting. In contrast, *in vitro* brain microvessels and BBB models offer faster, yet simplified approaches for targeted drug screening as well as for fundamental research, and importantly can be humanized to overcome translatability issues.

Human BBB organoids provide a model that enables maintaining endothelial cells in close juxtaposition. A limitation of this system, however, is that they essentially lack flow since microvessel-like structures cannot be formed in organoids, rather endothelium-lined spheres are generated which can negatively impact cellular viability (Urich et al., 2013). Traditional two-dimensional (2D) *in vitro* models such as the Transwell system, in which endothelial cells are cultured on semi-permeable membranes, have extensively been used for cell-based high-throughput screening assays and for studying basic BBB characteristics such as barrier permeability and transepithelial/transendothelial electrical resistance (TEER) (Abbott et al., 1992; Biegel and Pachter, 1994; He et al., 2014). These simplified systems lack simulation of blood flow conditions and have proved to insufficiently recapitulate *in vivo* phenotypes including the expression of key junctional proteins (such as claudin-5) and transporters (such as Glut-1 and insulin receptor) (Campisi et al., 2018). To overcome some of these limitations, several 3D microfluidic and organ-on-a-chip BBB and brain microvessel models have been developed enabling co-culture and fluid flow (Prabhakarpandian et al., 2013; Herland et al., 2016; van Der Helm et al., 2016; Wevers et al., 2018; Oddo et al., 2019; Park et al., 2019). Nevertheless, a number of these models exhibit other limitations such as non-physiological rigid ECM substrates, failure to feature blood vessel-like geometry and the lack of controlled flow that resembles the hemodynamic forces which is known to be crucial for microvascular function (Herland et al., 2016). Hence, there is an essential need for *in vitro* models that better mimic the brain microvessel environment including unidirectional flow, physiological shear stress, absence of artificial membranes, and presence of the cylindrical geometry typical of capillaries to facilitate the complex cell-cell interactions and physical ECM mechanics known to be intrinsic to the *in vivo* BBB and brain microvessels. In order to be capable of providing molecular mechanistic insights, these models need to also be compatible with advanced imaging and live 3D tracking of labeled molecules.

Along these lines, we describe here our efforts to develop and use an *in vitro* human brain microvessel-on-a-chip consisting of a 3D microfluidic model with a hollow channel in which a continuous monolayer of cells can grow at the interphase between the lumen and the underlying ECM. For our studies, we chose the brain microvascular endothelial cell line TY10 which is a well-established BBB model system (Takeshita et al., 2014; Spampinato et al., 2015; Shimizu et al., 2017; Wevers et al., 2018; Shimizu et al., 2019). Moreover, our system may be amenable to any other barrier-forming cell type to mimic vascular beds of different tissues or epithelial barriers. Our system allows controlled unidirectional flow, within the lumen of the artificial microvessel, of media including substrates of interest, for instance drug candidate biologics. An important characteristic of our device is its open design that also allows direct access of reagents from the surrounding space to the underlying ECM. We demonstrate the utility of this open design of organ-on-a-chip model by showing it is amenable for quantitative 3D live fluorescence imaging using spinning disk confocal or lattice light sheet microscopy (LLSM) and for high resolution electron microscopy. This model is set out to provide insights into molecular mechanisms involved in the transcytosis of biologicals at extraordinary detail which will further support the development of antibody-shuttle technologies across the human BBB. Detailed imaging, for example, can be very useful to follow endo-lysosomal trafficking in real-time, informing on fate of antibodies and viruses when entering endothelial cells, thus informing on better designs of biologics and viral vectors that more efficiently penetrate or inhibitors for the transcytosis of pathological viruses.

MATERIALS AND METHODS

Cell Culture

Human brain derived microvascular endothelial cells (TY10 cell line) were isolated from normal brain tissue from a patient with meningioma, and immortalized with retroviral vectors harboring a SV40 large T antigen gene that is engineered to drive proliferation at 33°C (Sano et al., 2010; Maeda et al., 2013; Sano et al., 2013). The TY10 cell line has been used to model the BBB in previous studies (Takeshita et al., 2014; Karassek et al., 2015; Spampinato et al., 2015; Shimizu et al., 2017; Takeshita et al., 2017; Wevers et al., 2018). Cells were cultured at 33°C, 5% CO_2 in T75 flasks BioCoat (Corning, 354485, MA, United States). TY10 cells were used between passage 17–25 and cultured in ScienCell complete endothelial cell medium (ScienCell, 1001, CA, United States). Cell detachment was performed using Accutase® (Corning, 25-058-CI, MA, United States) when cells were ∼80–90% confluent before being seeded into the microfluidic devices. Cells were routinely tested for mycoplasma contamination and found negative.

TY10 Stably Expressing eGFP

A lentiviral vector expressing a plasma membrane targeted eGFP (memGFP) containing a chimera of the N-terminal 41 amino acids of human myristoylated alanine-rich C-kinase substrate (MARCKS) fused to eGFP was made by co-transfection of a plasmid harboring memeGFP and Virapower Packaging Mix (Thermo Fisher, K497500, MA, United States) into 293T cells. Culture media was harvested 72 h later, cellular debris pelleted by low-speed centrifugation, and further clarified by 0.45 μm filtration with Millipore steriflip vacuum filters (EMD, SLHV033RS, MA, United States). The supernatant from the viral preparation was added to a flask of TY10 cells during passaging (4 ml of viral supernatant preparation mixed with 4 ml of cell suspension were added to a T25 Corning BioCoat flask) and allowed to incubate for 24 h at 33°C before switching back to the normal feeding schedule of every other day. The cells were sorted by flow cytometry for eGFP positive cells after 10 days in culture and subsequently expanded and maintained as described above.

hmAb

The recombinant monoclonal human IgG1 antibody (produced by Biogen) was expressed in CHO cells and purified through Protein-A Affinity Chromatography. The purified protein was fluorescently labeled with Alex Fluor™ 568 and 647 protein-labeling kits ((Thermo Fisher Scientific, 10238 and A30009, MA, United States) to produce hmAb-AF568 and hmAb-AF647 following the manufacturer's protocol.

Microvessel-on-a-Chip

Fabrication of Silicon Wafer

Photomasks with the chip design depicted in **Figure 1** were designed with AutoCAD (AutoDesk Corp., CA, United States) and printed by CAD/Art Services, Inc. (OR, United States). Molds of 80 μm depth were produced in a clean room by photolithography using standard protocols and SU-8 2050

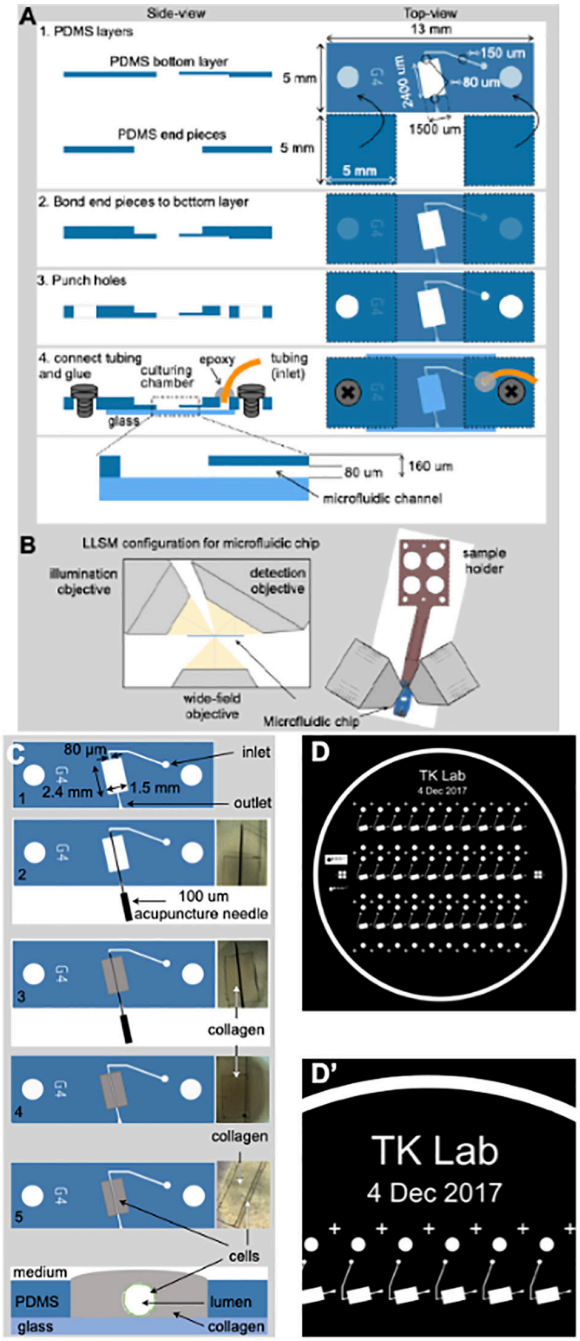

FIGURE 1 | Fabrication of the microvessel-on-a-chip. **(A)** Schematic representation of the sequential steps used to fabricate the microvessel-on-a-chip. The open design permits direct access of aerated medium from the top to the collagen containing embedded cells while at the same time allowing flow of medium along the tubular channel with endothelial cells surrounding the boundary between the lumen of the artificial microvessel and the collagen. See associated **Supplementary Movie 1** for guidance on the fabrication of the microvessel-on-a-chip. **(B)** Arrangement of the microvessel-on-a-chip within the available optical path between the illumination and detection objectives of the lattice light sheet microscope (LLSM). A sample holder is used to place the microvessel-on-a-chip under the LLSM objectives and to facilitate fine adjustments of its position. The chip can

(Continued)

FIGURE 1 | Continued
also be placed on a glass coverslip and placed in an inverted microscope for all modalities of conventional confocal microscope (not shown). **(C)** Steps used to create an artificial microvessel (1–5). An acupuncture needle of 100 μm diameter is placed between the inlet and outlet (2). After the collagen gelled (3), the needle was pulled (4), resulting in a void channel (5) in which endothelial or epithelial cells of choice, here brain endothelial cells, are seeded. The cross section on the bottom shows the final disposition of the brain endothelial cells (green) that line the inner surface of the collagen lumen, representing the artificial brain microvessel. **(D,D')** Images of the mask template used to create the silicon wafer then used to prepare the PDMS mold.

photoresist (Microchem, now Kayaku Advanced Materials, Inc., MA, United States). The 3″ in diameter silicon wafer (University Wafer, 447, MA, United States) was cleaned by sequential solvent treatment in a Headway spin coater at 500 rpm. Each of the following solvents were squirted for 1 min onto the rotating wafer while moving a cotton swab across the surface: isopropyl alcohol, acetone, methanol, pure water. After dehydration on a hotplate at 150°C for 5 min the wafer was activated by oxygen plasma at 130 mTorr and 100 W for 5 min. A walnut sized amount of SU-8 2050 was placed on the wafer fixed in the Headway spin coater and an even film was generated by the following spin conditions: step 1: 500 rpm, 5 s, ramp 100 rpm/s; step 2: 2700 rpm, 30 s, ramp 300 rpm/s; step 3, 0 rpm, 10 s, ramp 300 rpm/s. After 30 min incubation at room temperature (RT), the soft bake was performed at 5 min 65°C and 20 min at 85°C following UV exposure in a MJB3 Mask Aligner (Süss-MicroTec, Munich, Germany) for 10 s at 25 mW/cm^2. The post-exposure baking was the same as for soft baking. The mold was developed for 10 min in 20 ml MicroChem SU-8 developer, rinsed with isopropyl alcohol and blown dry prior silianization by incubating the wafer in a desiccator under reduced pressure in presence of an aluminum cup with 3 drops of (tridecafluoro-1,1,2,2-tetrahydrooctyl) trichlorosilane (Gelest, Morrisville, PA, United States). Hard bake was performed on a hotplate at 150°C for 15 min.

Production of the Microfluidic Device

Microfluidic devices were subsequently produced by soft lithography; Sylgard 184 elastomer Polydimethylsiloxane (PDMS) was mixed with curing agent (Sylgard 184 silicone elastomer kit, Dow Corning, Midlands, United States), at a 5:1 ratio in a mixer including a 2 min de-foaming step before pouring it onto the master silicon wafer designed by our lab and spin-coating at 400 rpm for 40 s. The utilized speed yielded a PDMS film of 160 μm thickness that was degassed in a vacuum desiccator for 10 min and cured in an oven at 65°C for 1 h. The PDMS film was peeled off the master and placed in a plastic petri dish at 65°C overnight to fully cure. To remove non-crosslinked oligomers within the PDMS that can leach out and contaminate the culture medium (Halldorsson et al., 2015), cut PDMS slabs containing the embossed microstructures and 5 × 5 mm end pieces were cleaned by contact with Scotch tape and subjected to organic solvent extraction (Lee et al., 2003). PDMS slabs were incubated in a sealed jar on a rocker for 24 h at RT in each of the following solvents and in this order: triethylamine, toluene, ethyl acetate, and acetone (all ACS grade and from Sigma-Aldrich, MO, United States). To evaporate the acetone, the PDMS slabs were placed on an accordion-shaped aluminum foil rack to reduce contact with any surface and incubation at 100°C for 2 h. Extracted PDMS remains hydrophilic for prolonged times after plasma-activation as it does not contain uncured oligomers (Lee et al., 2003; Kim and Herr, 2013). The PDMS extraction step significantly improves the bonding and microfluidic properties. The PDMS pieces of the chip were placed embossed featured down on a fluorinated ethylene propylene (FEP) sheet and exposed to air plasma at 700 mTorr, 30 W for 1.5 min using the PDC-001 plasma cleaner (Harrick Plasma) to bond the 5 × 5 mm end pieces before punching 1 mm holes for the tubing. PDMS pieces were rinsed with isopropyl alcohol and blow-dried prior plasma-bonding to the #1.5 glass coverslip that was cleaned by incubation in isopropyl alcohol, acetone and 0.5M KOH for 30 min each in a sonication water bath, rinsing five times in pure water and blown dry with filtered nitrogen gas.

To promote bonding, the chips were placed on a hot-plate at 150°C for 15 min. We tested several glues to fix the Tygon microbore tubing, 0.010" × 0.030" OD (Cole-Parmer, EW-06419-00, IL, United States) on the chip and SLOW-CURE™ 30 min epoxy (Bob Smith Industries; BSI206, CA, United States) resulted in the sturdiest connection after overnight incubation and further allowed us to remove air bubbles in the epoxy after mixing through centrifugation for 30 s at 14,000 x g in a tabletop centrifuge. The chip was activated by air plasma treatment as above and further cleaned by injecting sequentially 0.5 ml of each acetonitrile, purified water, 0.5 M KOH and again water.

To functionalize both glass and PDMS surface with primary amine groups, the chips were silanized by pipetting 0.5 ml of a fresh 1% aqueous solution of 3-(Ethoxydimethylsilyl) propylamine (Sigma, 588857, MO, United States) on the chip and incubation for 15 min at RT before rinsing with twice with 1 ml pure water. Subsequently, the surfaces were further functionalized by adding 0.3 ml 2.5% glutaraldehyde (Electron Microscopy Services, 16200, PA, United States) and incubation for 15 min before the devices were rinsed extensively with pure water. The Schiff bases formed on proteins after glutaraldehyde immobilization are stable without further reduction, as has been demonstrated in surface-protein conjugation (Kim and Herr, 2013). To further facilitate adoption of the chip design, a detailed video with step-by-step instructions for chip fabrication has been added (see **Supplementary Movie 1**).

Formation of Lumen and Collagen Matrix

A Pluronic F-127 (Sigma, P2443, MO, United States) passivated 100 μm acupuncture needle was inserted from the outlet toward the inlet of the brain microvessel-on-a-chip to provide the required scaffold for the culturing matrix as indicated in **Figure 1C**. The selected size of the acupuncture needle should prevent the leakage of unpolymerized collagen into the microfluidic channel of a smaller diameter (80 μm). A hydrogel consisting of extracellular matrix (ECM) proteins made of a final concentration of 7.0 mg/ml Type I rat tail collagen (Corning, 354249, MA, United States) was used in all experiments. To make

200 μl of hydrogel solution, 39 μl of Endothelial Cell Medium (ECM basal media with no FBS; 1001b, ScienCell, Carlsbad, CA, United States), 1 μl of a basic solution (1.0 N NaOH, Sigma) and 14 μl of 10X Ham's F-12 (Thermo Fisher, 31765092, MA, United States) were added to 135 μl of the collagen I.

We found that the collagen gel tended to delaminate from the PDMS culturing chamber as soon as we started the flow, and so we enhanced the standard collagen matrix protocol by adding Genipin® (Sigma, G4796, MO, United States). Genipin is a crosslinking agent that covalently attaches to primary amino groups exposed on protein surfaces (Sung et al., 1998). Furthermore, Genipin monomers form covalent intermolecular crosslinks that in the case of a collagen matrix results in bridging adjacent fibers at points of contact (Yoo et al., 2011; Chan et al., 2014). Thus, to achieve a stiff and resilient collagen matrix we mixed collagen with Genipin prior pipetting it into the culturing chamber of the chip. The solution of 135 μl collagen, 39 μl ECM, 14 μl 10X Ham's F-12, 1 μl 1N NaOH and 1 μl 20 mM Genipin was gently mixed and incubated on ice for a period of 5–10 min to get rid of any air bubbles which might generate during the mixing step, before being added to pre-chilled chips kept on ice for at least 15 min. The devices were subsequently incubated at 37°C to allow gel formation of the collagen matrix. Genipin improved the stability of the PDMS-collagen interaction such that delamination was never observed for up to 12 days. After removal of the acupuncture needle, non-reacted Genipin was quenched by covering the top of the collagen brain microvessel-on-a-chip with PBS containing 1 mM Tris pH 8.0 in PBS in addition to flowing the same solution through the cylindrical lumen for 15 min at 1 μl/min. Chips were then washed with 3 ml of PBS alone (added to the top of collagen) and flow of PBS alone for 15 min at 1 μl/min. Prior to cell seeding (see below), a solution containing complete ECM medium was injected to the lumen for 15 min at 1 μl/min.

Cell Seeding

To line the lumen with TY10 cells and generate a perfused microvessel-like structure, two strategies were used to ensure uniform cell seeding. In the first strategy (cell concentrator chip, **Figure 2A**), we designed a gravity-based microfluidic cell concentrator to reach a sufficiently high density of cells for seeding of the collagen lumen using minimal cell concentration. A PDMS chip whose single channel splits up into four microchannels that merge again into a single channel after 5 mm was used as bottom layer with a central 2.5 mm collection chamber. To securely fit a 25 mm long silicon tubing of OD 4 mm/ID 2.5 mm, a second PDMS layer with 4 mm hole was bonded as a lid and the tubing was fixated with epoxy glue. The inlet of the concentrator chip was connected via tubing to a syringe pump and the outlet to the brain microvessel-on-a-chip. TY10 cells were resuspended to 0.1 million cells/ml and transferred into a 1 ml syringe. The cells settled by gravity within 15 min at the collection chamber on the bottom glass surface which was passivated with 0.01 mg/ml Poly-D-Lysine-PEG to prevent the cells from sticking to the glass. A plug comprised of an epoxy filled pipette tip was inserted into the central tubing to prevent upwards flow before initiating the flow. Applying flow through the microfluidic channel resulted in shear force that pushed the cell bolus into the tubing leading to the culturing chamber of the brain microvessel-on-a-chip.

In the second strategy a simplified procedure was implemented in order to enhance the experimental turnover as illustrated in **Figure 2B** and its results section. In brief, TY10 cells were harvested and resuspended to 1 million cells/ml. A total of 900 μl of the cell solution was then mixed with 100 μl solution of collagen IV (Sigma, C5533, MO, United States), fibronectin (Sigma, F2518), and laminin (EMD Millipore, AG56P) at 5:1:1 concentration ratio before transferred into a 1 ml syringe with BD Luer-Lok (BD, 309628, NJ, United States). The syringe was then hanged vertically to allow cell settling by gravity for 10–15 min with no flow. Cell seeding was initiated under flow for about 15–20 min at 1 μl/min. Cell seeding was monitored by visual inspection using a microscope to observe the brain microvessel-on-a-chip placed inside a petri dish kept under sterile conditions.

After either procedure, chips were incubated at 37°C for a minimum of 4 h before being perfused with fresh ECM media via positive pumping to wash out the unattached cells. The chips were maintained under continuous unidirectional flow at a rate of 1 μl/min in a cell culture incubator at 37°C, 5% CO_2. Confluent TY10 monolayers were formed typically after 72 h and the brain microvessel-on-a-chip devices were used for subsequent analyses following 7 days after seeding incubation in all experiments.

Actin Staining in the Microvessel-on-a-Chip

The collagen samples including the lumen were fixed and permeabilized using BD Cytofix/Cytoperm Kit (BD, 554714, CA, United States) according to the manufacturer's protocol. In brief, Cytofix was added to a 1 ml syringe and perfused through the microvessel at a flow rate of 1 μl/min for 30 min before changing to the Cytoperm buffer (diluted 1:10 in PBS) for 1 h at 1 μl/min. The flow was then stopped and the brain microvessel-on-a-chip placed on a well of a six well plate in 2 ml of Cytoperm buffer (diluted 1:10 in PBS) overnight. The microvessel was stained with AlexaFluor488 Phalloidin (Thermo, A12379, at 1:100 dilution) and NucBlue (Thermo, R37606, 1 drop/500 μl) by perfusing the dyes in Cytoperm buffer at 1 μl/min through the microvessel for 1 h, followed by washing with 0.1% BSA in PBS buffer for 4 h at 1 μl/min. Images were collected using Zeiss LSM 710 microscope (10x objective) through the bottom glass slide.

Immunofluorescence

TY10 cells were seeded in a 24-well glass bottom plate (In Vitro Scientific, P24-0-N, CA, United States), coated with rat tail collagen type I (50 μg/ml final concentration in 1% acetic acid) at 1×10^5 cells per well. Cells were allowed to proliferate for 3 days at 33°C, 5% CO_2 before they were switched to 37°C, 5% CO_2 for 3 days to initiate differentiation of TY10 cells. Cells were fixed with 4% PFA (Thermo Fisher Scientific, 50-980-487, MA, United States) for 10 min at 4°C and then blocked with 10% normal goat serum serum (Thermo Fisher Scientific, 16210064, MA, United States) for 30 min at RT. Staining was performed under permeabilized conditions using BD Perm/Wash Buffer

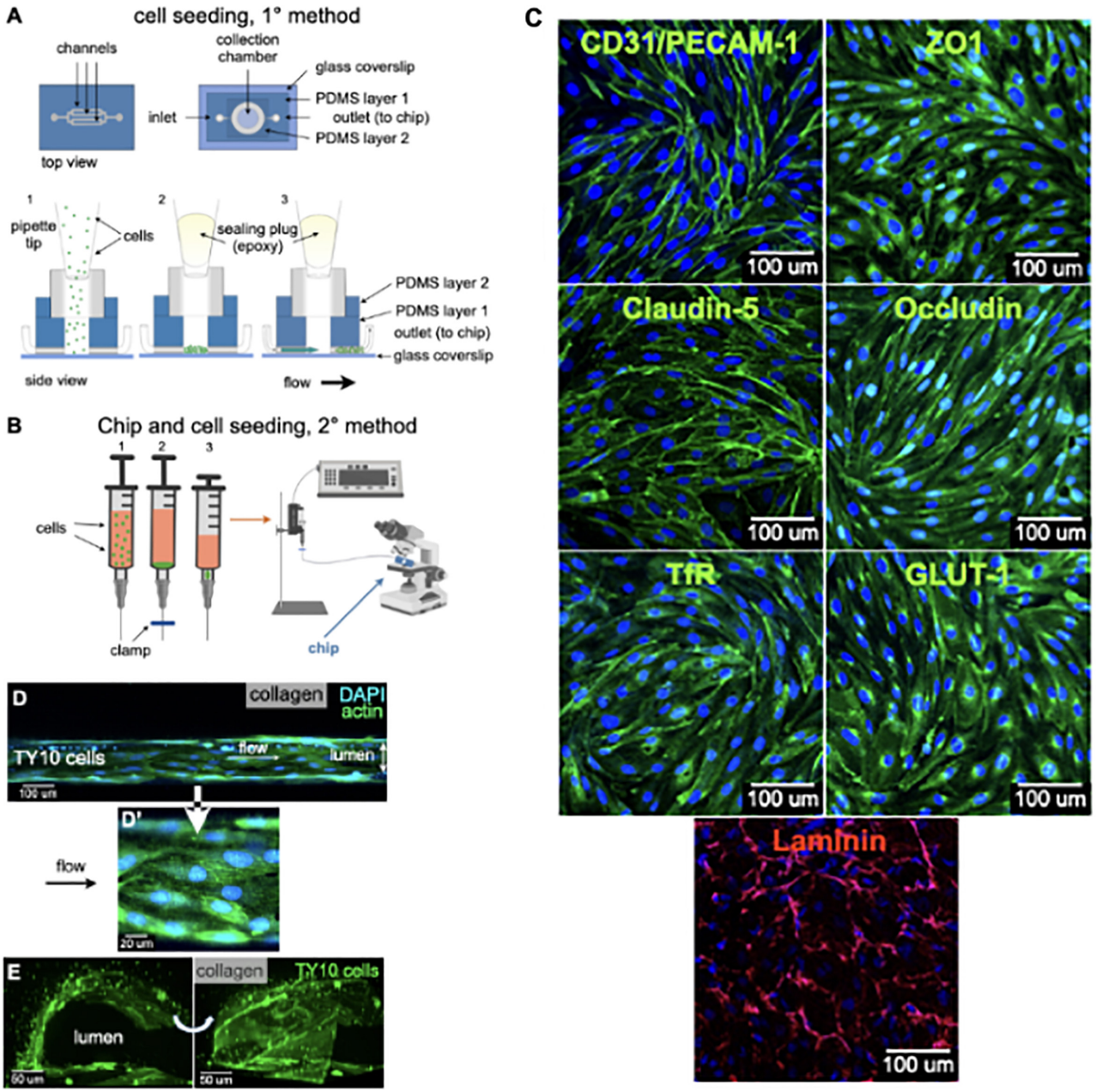

FIGURE 2 | Cell seeding procedures and formation of a human brain microvessel using TY10 cells. **(A)** Cell seeding, 1st method. Representation of the steps used to increase the cell concentration before injection into the chip. Cells are allowed to settle by gravity (left and central panels) in the cell seeder and then injected as a bolus into the hollow lumen. Prior to injection, the chamber is capped with a plugged pipette tip (central panel). **(B)** Cell seeding, 2nd method. Representation of the steps used to inject cells into the chip in a more controlled and uniform manner compared to the 1st method. Cells are allowed to settle at the bottom of a syringe, and are then delivered into the hollow lumen at constant flow controlled by a syringe pump. **(C)** Immunostaining of TY10 monolayers: endothelial cell marker PECAM-1/CD31, transporters Glut-1 and transferrin receptor (TfR), and tight junction proteins ZO-1, Occludin and Claudin-5. Staining for laminin provides evidence that TY10 cells deposit extracellular matrix while in culture. Scale bar, 100 μm. **(D)** Representative image of a chemically fixed sample of TY10 cells after they were grown in the brain microvessel-on-a-chip with medium flowing from left to right at 1 μl/min for 7 days. Volumetric image was obtained using a spinning disk confocal microscope. Maximum z-projection is shown for a sample stained with DAPI (nuclei, blue) and phalloidin (actin, green). Scale bar, 100 μm. **(D')** Representative image of a chemically fixed sample of TY10 cells after they were grown in the microfluidic-on-a-chip with medium flowing from left to right at 1 μl/min for 7 days. Single plane image was obtained using a Zeiss 710 confocal microscope. The image highlights the linear organization of actin stress fibers along the axis of flow. Sample stained with DAPI (nuclei, blue) and phalloidin (actin, green). Scale bar, 20 μm. **(E)** Representative volumetric image of a live sample of TY10-eGFP cells expressing membrane bound eGFP obtained using spinning disk confocal microscopy. The image highlights the organization of the cells as a monolayer at the boundary between the lumen of the artificial microvessel and the collagen scaffold. The cells on the bottom illustrate cells growing between the glass slide and the lumen. Panels are rotated 90-degrees from each other. Scale bar, 50 μm. See associated **Supplementary Movie 2**.

(BD Biosciences, 554723, CA, United States). Primary antibodies were incubated for 3 h at RT. The following primary antibodies were used: anti-CD31 (Thermo Fisher, MA3100, 1:100), anti-ZO1 (Thermo Fisher, 40-2300, 1:60), anti-Occludin (Thermo Fisher, 40-4700, 1:200), anti-Claudin 5 (Thermo Fisher, 35-2500, 1:50), anti-Glut-1 (Thermo Fisher, PA1-1063, 1:100), anti-TfR (Thermo Fisher, A-11130, 1:25) and anti-Laminin (abcam, ab11575, 1:100). The following secondary antibodies were incubated for 45 min at RT: goat anti-mouse AlexaFluor 488 (Thermo Fisher, A11001, 1:1000), goat anti-rabbit AlexaFluor 488 (Thermo Fisher, A11008, 1:1000), and goat anti-rabbit AlexaFluor 568 (Thermo Fisher, A11011, 1:1000), supplemented with Hoechst 33342 (Thermo Fisher, H3570, 1:2000). For imaging, Zeiss LSM 710 Confocal and Leica SP5 Confocal microscopes (40x objective) were used, and image processing was performed in ImageJ (NIH).

Barrier Integrity Assay

Microvessel-on-a-Chip

Chips were washed with ECM culture medium (once with 1 ml added to the top of collagen followed by a flow at 1 μl/min for 15 min) to ensure proper flow profiles during the subsequent barrier integrity assay. Next, all medium was aspirated from the chip and 1 ml of medium without fluorescent compound using Gibco® FluoroBrite™ DMEM (Thermo Fisher, A1896701, MA, United States) was added. Medium containing 25 μg/ml of 10 kDa FITC-dextran (Sigma, FD10S, MO, United States) or hmAb-AF568 was added through the inlet at a flow rate of 1 μl/min for all the experiments. The inlet was connected to microvessels with and without TY10 cells and image acquisition was started. Leakage of the fluorescent substrate (dextran or hmAb) from the lumen of the microvessel into the adjacent collagen matrix was imaged using a spinning disk confocal microscope with 40x water immersion objective. The fluorescence intensity profiles and ratios between the fluorescent signal in the basal and apical region of the microvessel tube were analyzed using MATLAB (MathWorks, MA, United States). Apparent permeability (Papp) was used for quantifying diffusional permeability as described (Yuan et al., 2009). In brief, Papp was calculated by analyzing total fluorescence intensity in the imaged 2D area of the lumen and collagen and then applying $Papp = (1/\Delta I)\,(dI/dt)_0\,(r/2)$, where ΔI is the increase in total fluorescence intensity upon adding labeled dextran or labeled hmAb to the lumen, $(dI/dt)_0$ is the temporal initial rate of linear increase in intensity as the labeled molecules diffuse out of the microvessel into the surrounding collagen matrix, and (r) is the radius of the microvessel (100 μm for our brain microvessel-on-a-chip). All experiments were carried out at n = 4–6; exact numbers are mentioned per experiment in figure captions. Graphs were plotted using GraphPad Prism 6 (GraphPad Software, CA, United States).

Transwell

Transwell inserts (Falcon, 08-771-8, MA, United States) were coated with 50 μg/ml rat tail collagen type I (Corning, Cat# 354236) in 1% acetic acid for 1 h and then washed with PBS prior to cell seeding. Per 12-well transwell insert, 125,000 TY10 cells were seeded in 1 ml ECM (ScienCell, 1001, CA, United States), and 2 ml ECM was added to the bottom chamber (Falcon, 08-771-22, MA, United States). Cells were allowed to proliferate at 33°C, 5% CO_2 for 3 days, then switched to 37°C, 5% CO_2 for another 3 days for differentiation, with media changes every other day. Transwell inserts without cells were used as control. On the day of the permeability assay, media was refreshed in both chambers and 1 mg/ml final concentration of 10 kDa FITC-Dextran (Millipore Sigma, FD10S, MA, United States) was added to the top chamber. The plate was incubated for 1 h at 37°C, 5% CO_2 after which samples of 100 μl were taken from the bottom chamber and transferred to a black/clear bottom 96-well plate. Fluorescence intensity was determined with a plate reader set at excitation 490 nm and emission 535 nm.

Spinning Disk Confocal Imaging

Imaging was done using a Marianas spinning disk confocal microscope (3i, Colorado, United States) with the water immersion objective lens LD C-Apochromat 40x/1.1 (Carl Zeiss, Jena, Germany). The images consisted of 512 x 512 pixels with a pixel size of ∼333 nm. The EMCCD camera settings (gain, speed, intensification, and exposure) and laser power were maintained throughout the imaging experiments. Images were acquired using SlideBook 6 (3i, Colorado, United States) and data analysis carried out using SlideBook 8 and custom-made software using MATLAB 2017A (Natick, MA, United States). For the analysis of heat maps and Papp, ROIs were the entire original field of view.

LLSM Imaging

A microvessel-on-a-chip fabricated on 8*5-mm rectangular #1.5 glass coverslip was picked with forceps, and placed in the sample bath of the 3D LLSM. The sample was imaged in a time series in 3D using a dithered multi-Bessel lattice light-sheet by stepping the sample stage at 200 nm intervals in the s-axis equivalent to ∼104 nm translation in the z-axis. Each 3D stack corresponded to a pre-deskewed volume of ∼80 μm x 120 μm x 47 μm (800 × 1200 × 451 pixels). The sample was excited with a 488-nm laser (∼100 mW operating power with an illumination of ∼77 μW at the back aperture), a 560 nm laser (∼100 mW operating power with an illumination of ∼176 μW at the back aperture) and a 642nm laser (∼100 mW operating power with an illumination of ∼121 μW at the back aperture) to acquire 451 imaging planes, each exposed for ∼44.1 ms and recorded with two Hamamatsu ORCA-flash 4.0-V2 cameras; thus, each 3D image took ∼60 s to acquire. The inner and outer numerical apertures (NAs) of excitation were 0.513 and 0.55, respectively. The overall 3D volume of ∼240 μm × 880 μm × 180 μm was obtained by stitching together 165 (3 × 11 × 5) 3D stacks, with an overlap of 40 and 9 μm in the y-axis and z-axis, respectively.

Transmission Electron Microscopy

The collagen matrix including the lumen was washed 3 times with PBS and then fixed by immersion in 5 ml of fixing solution (2.5% glutaraldehyde, 2% sucrose, 50 mM KCl, 2.5 mM $MgCl_2$, 2.5 mM $CaCl_2$ in 50 mM Cacodylate buffer pH 7.4) (Sigma) and kept at 4°C, overnight in the dark. Fixed collagen samples were washed 3 times with a solution containing 50 mM PIPES pH 7.4 (Sigma, P6757, MO, United States) kept in ice and then they incubated

for 2 h in ice and in the dark in a freshly prepared staining solution (SSI) made of 1% OsO4 (Electron Microscopy Sciences, 19190), 1.25% potassium hexacyanoferrate (II) (Sigma, 455989) and 100 mM PIPES pH 7.4. Samples were rinsed 3 times with ice-cold water and incubated again for a second time for 30 min in ice and in the dark with a freshly prepared staining solution II (SSII). SSII was prepared by 1:100 dilution of SSI in a freshly prepared 1% thiocarbohydrizide (Electron Microscopy Sciences, 21900, PA, United States). Finally, the samples were washed for 3 times with ice-cold H_2O and then incubated overnight in the dark in 1% uranyl acetate (Electron Microscopy Sciences, 22,400, PA, United States) at 4°C.

For the dehydration and embedding step, the fixed and stained samples were first washed 3 times with ice cold water and then subjected to dehydration with a 20-50-70-90-100% ethanol – 100% acetone dehydration series. Samples were then infiltrated overnight, at 4°C with 50-50 acetone-Epon812 epoxy resin (Electron Microscopy Sciences, 14120, PA, United States). Next day, the samples were washed 3 times with 100% Epon812 and then kept in an oven for 36 h at 60°C. Sections of 60–70 nm in thickness were cut transversally to the long axis of the lumen and imaged with a JEOL JEM 1200 EX TEM microscope with a voltage of 80 KV and a nominal magnification of 15,000.

Statistical Analysis

StatsDirect 3 (Liverpool, United Kingdom) was used for one-way ANOVA and student's *t*-test analyses with Bonferroni *post-hoc* correction. Data were presented as mean ± standard error of the mean (SEM) where (***) denotes a statistically significant difference with $p < 0.001$ and (ns) indicates a statistically non-significant difference.

RESULTS AND DISCUSSION

We engineered an open design microfluidic chip to generate a 3D microphysiological model of the human brain endothelial microvessel readily accessible to optical imaging. The unique characteristics of this novel brain microvessel-on-a-chip are the open design of the cell culture chamber and a cylindrical hollow lumen amenable to continuous unidirectional flow within a casted gel of extracellular matrix (ECM) components. The open system allows direct access of the collagen matrix for efficient exchange of gases and medium in addition to readily access to optical imaging while cells growing with continuous unidirectional flow at the interphase between the casted gel and the lumen mimic the environment of a microvessel.

Fabrication of the Microvessel-on-a-Chip

Figure 1A graphically summarizes the sequential steps used to build a microvessel-on-a-chip model. It is based on sequential bonding using soft lithography (Bischel et al., 2013) of thin layers of optically clear PDMS on top on a glass microscope slide. The geometry and dimensions of the microvessel-on-a-chip were optimized for its use with three major complementary forms of live 3D optical imaging, spinning disk confocal, lattice light sheet microscopy (LLSM) and the recently developed variant, LLSM modified with adaptive optics (AO-LLSM) (Gao et al., 2019). We chose to include access to LLSM and AO-LLSM because these imaging modes have revolutionized fluorescence optical microscopy providing volumetric imaging with unprecedented high spatial and temporal precision with minimal bleaching and phototoxicity (Liu et al., 2018).

Spinning disk confocal microscopy is performed through the glass slide at the bottom of the microvessel-on-a-chip, while LLSM or AO-LLSM are carried out from the open top as illustrated in **Figure 1B**. The device is also suited for chemical fixation and the sample preparation required for high-resolution electron microscopy visualization.

The consecutive stages used to generate the cylindrical hollow lumen within the casted gel followed by seeding of endothelial cells on the wall of the lumen are depicted in **Figure 1C** and described in detail in methods. It involved first placing an acupuncture needle between the microfluidic inlet and outlets (**Figures 1C**, **2**) followed by casting a collagen matrix (**Figures 1C**, **3**), gentle removal of the needle after collagen gelation (**Figures 1C**, **4**) and ending with cell seeding under flow (**Figures 1C**, **4**). A Pluronic F-127 passivated 100 μm acupuncture needle was inserted from the outlet toward the inlet to provide the required scaffold for the culturing matrix. Collagen type I (7 mg/ml) has been used to assemble the culturing scaffold. The chosen diameter of the needle enables the device to recreate artificial microvessels where an endothelial monolayer is formed against a collagen matrix and is stably maintained by shear stress and surface tension. See **Supplementary Movie 1** for a brief video with step-by-step instructions to facilitate the construction by other laboratories of the microvessel-on-a-chip.

Cell Seeding and Establishment of an Endothelial Microvessel

Cell seeding was performed with two methods. The first one involved use of a cell-concentrator chip designed and operated as indicated in **Figure 2A**. Cells in suspension were placed on a pipette tip linked to the top of the cell-concentrator, allowed to settle by gravity for 15 min to a cell density of ∼0.1 million/ml, and cells then injected into the hollow lumen with the aid of a syringe pump. Before activation of the syringe pump, we replaced the pipette feeding cells with an epoxy-plugged pipette as a way to prevent backflow. Afterward the bolus with cells reached the hollow lumen, flow was then stopped allowing cells to settle for 24 h so they could attach to the internal walls of the cylindrical lumen of the chip. TY10 cells were grown for 7 days under flow, at which point they established a monolayer and hence were ready for imaging experiments. We used TY10 cells to model the endothelium of the BBB, but any other endothelial or epithelial cell type may be also used to establish a barrier-forming cell model.

The second, and in our hands preferred cell seeding method (**Figure 2B**), involved use of a 1 ml syringe driven by a mechanical syringe pump. A solution containing ∼ 900 μl of 1 million/ml cells in medium mixed with 100 μl of a solution containing laminin, fibronectin and collagen type IV to promote cell attachment, was placed in a vertically oriented syringe and cells

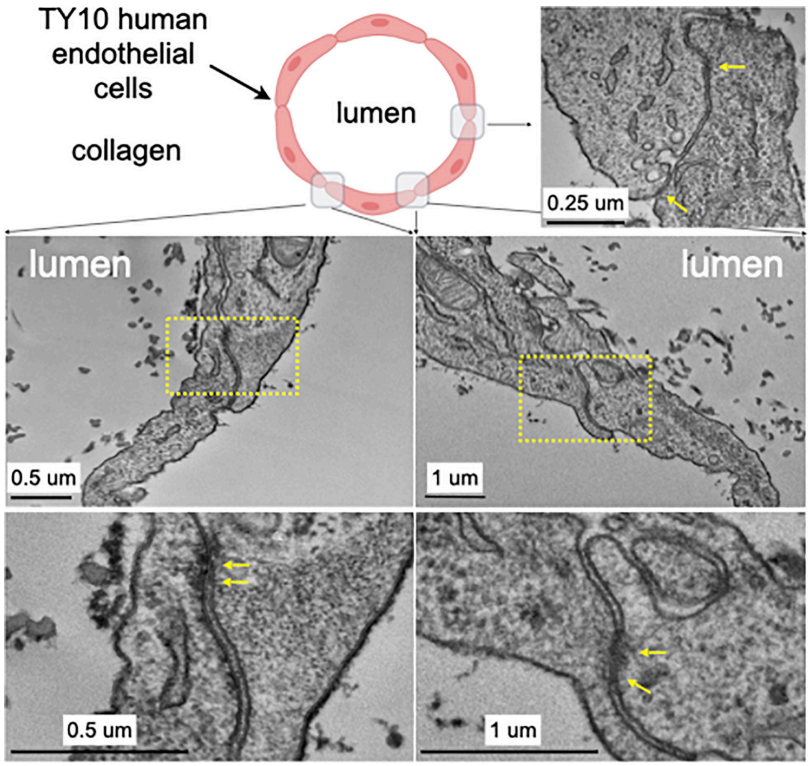

FIGURE 3 | Transmission electron microscopy highlighting the appearance of junctions between TY10 endothelial cells within the brain microvessel-on-a-chip. The upper left panel shows a schematic cross section of the brain microvessel-on-a-chip highlighting the location of the monolayer of TY10 endothelial cells at the interface between the lumen of the microvessel and the collagen. The representative images in the bottom panels derive from junctions between opposite ends of adjacent cells. The yellow arrows highlight electron-density characteristic of tight junctions. Scale bars with corresponding magnifications are indicated.

allowed to settle for ∼10–15 min. Afterward, flow of 1 μl/min was applied for 10–15 min in order to inject the cells into the lumen of the chip; cells were then allowed to settle and attach to the internal walls of the lumen for 4 h at 37°C. As with the first method, cells were then grown for 7 days at a flow rate of 1 μl/min, before their use for imaging. This simpler cell seeding method is particularly advantageous for cases in which the cellular supply might be limited such as when using primary cells or iPSC-derived cells from patients.

Extent of seeding was optically monitored with the aid of an inverted microscope by direct inspection of the device placed inside a closed petri dish to ensure sterility. Cellular viability was determined for both cell seeding methods using exclusion of Trypan Blue. These experiments indicate that the two methods have comparable results (viability of 91% and 96% for methods 1 and 2, respectively). In our hands, method 1 was associated with a 100% success rate ($n = 8$) while method 2 had a lower success of 87% ($n = 29$). Of note, success rate has been defined by a complete cell seeding of the lumen from the first round, resulting in full coverage of the lumen with endothelial cells, without the need for a second round of cell seeding.

To summarize, the two methods are associated with a comparable cell viability. Method 1 has a higher success rate and requires 10x less cells (0.1 million/ml vs. 1 million for method 2) but at the expense of longer incubation time (24 h vs. 4 h required for method 2) and extra time and cost associated with manufacturing of the cell concentrator microfluidic device. For these reasons, we have mainly opted for method 2 in this study, but intended to offer the reader a second option if cell supply is limiting, for instance.

TY10 Cells as a Model for BBB Endothelium

In the brain, the basement membrane surrounding the endothelial cells of the brain vasculature is comprised of fibronectin, laminin (Aumailley et al., 2005) and collagen type IV (Hartmann et al., 2007). Indeed, *in vitro* monolayers of endothelial cells grown on a matrix containing fibronectin, laminin, and collagen type IV exhibit enhanced TEER, suggesting a role for these molecules in promoting the formation of tight junctions (Tilling et al., 1998, 2002; Gautam et al., 2016). To mimic the physiological BBB microenvironment and presumably also to enhance the seeding efficiency in the brain microvessel-on-a-chip, we injected before cell seeding a solution containing fibronectin and laminin for 30 min at 1 μl/min. TY10 cells were allowed to settle for 24 h at 37°C before starting the flow at 1 μl/min.

One of the major challenges of developing physiologically relevant *in vitro* brain microvessel models is the availability of

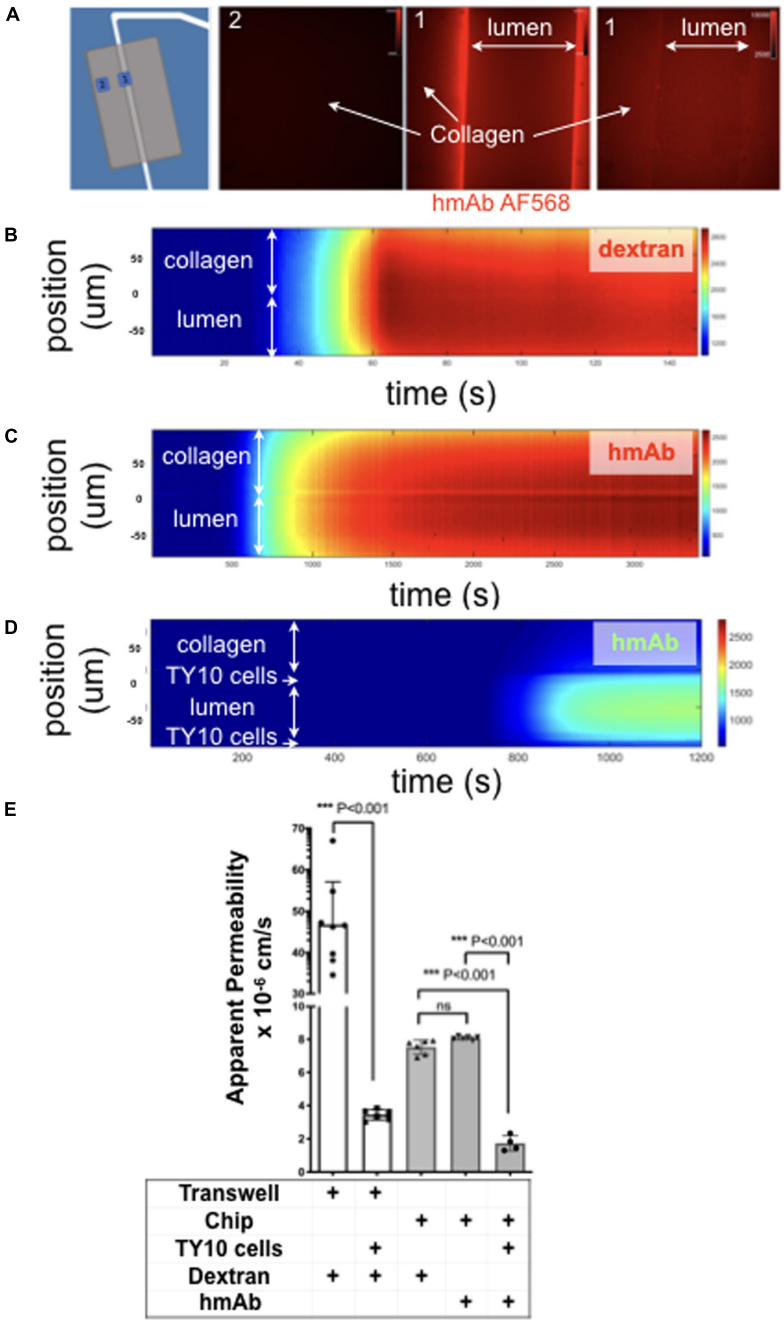

FIGURE 4 | TY10 cells establish a functional barrier in the brain microvessel-on-a-chip. **(A)** The left panel is a schematic representation of the experimental setup used to determine the apparent permeability of fluorescent solutes diffusing between the lumen of the artificial microvessel and the collagen in the absence and presence of TY10 cells. The boxed numbered areas represent typical regions imaged using spinning disk confocal microscopy. The fluorescent images are of hmAb-AF568 (red) applied at constant flow (1 μl/min) for 20 min in the absence (left and central panels) and presence (right panel) of 1 mM TRIS in addition to Genipin (a chemical crosslinker) added to stabilize the collagen matrix (see Methods). Genipin followed by 1 mM TRIS treatment dramatically decreased the non-specific retention of the antibody by the collagen. **(B–D)** Heat map representation of the fluorescence intensity of 10 kDa FITC-Dextran **(B)** or antibody hmAb-AF568 **(C)** diffusing from the lumen through the collagen as a function of time obtained at a flow of 1 μl/min. The significant decrease in the amount of antibody that passes through the endothelial cell layer is highlighted in panel **(D)**, demonstrating that TY10 cells form a functional barrier in the brain microvessel-on-a-chip. See associated **Supplementary Movies 3–5**. **(E)** Apparent permeability data for 10 kDa FITC-Dextran or hmAb-AF588 obtained from experiments carried with a traditional 2D transwell (n = 8 without TY10 cells and n = 6 with cells) and with the brain microvessel-on-a-chip (see **B–D**) without (n = 6) and with (n = 4) cells. The experiments compare the apparent permeability of the soluble molecules in the absence or presence of cells between the two compartments of the transwell, or between the boundary of the lumen and collagen in the brain microvessel-on-a-chip. One-way ANOVA and student's t-test analyses with Bonferroni *post-hoc* correction was used to identify significant differences between samples. Error bars indicate SEM.; ***$p \leq 0.001$, ns: non-significant.

suitable brain-derived cells of endothelial origin and of human origin in particular. Primary human brain endothelial cells or cells differentiated from induced pluripotent stem cells (iPSC) derived from control or diseased patients are preferred for *in vitro* brain microvessels and BBB models. Use of primary cells is restricted to very low passage numbers to prevent down-regulation of the unique features of the BBB (Reichel et al., 2003). More general, the difficulties in collecting and purifying these cells can considerably limit their use and reliability, as well as reproducibility (Bernas et al., 2010). Immortalized brain-derived cell lines can have great advantages such as accessibility and convenience of use especially for optimization purposes despite that some of the available lines might not exhibit all BBB characteristics (Kuhnline Sloan et al., 2012; Eigenmann et al., 2013; Wong et al., 2013). Nonetheless, certain cell lines may still exhibit the required properties for some pathophysiological and medicinal applications in a fit-for-purpose approach.

We therefore chose immortalized human brain derived TY10 microvascular endothelial cells that have been used to model the human BBB in a number of previous studies (Takeshita et al., 2014; Spampinato et al., 2015; Shimizu et al., 2017, 2019; Wevers et al., 2018). TY10 cells are immortalized and proliferate at 33°C, and stop growing and acquire a phenotype of primary brain endothelial cells at 37°C (Maeda et al., 2013). These cells harbor a spindle-shaped morphology, express markers typical for brain endothelial cells, and express P-glycoprotein (P-gp) irrespective of passage number (Sano et al., 2010, 2013). These cells also express the endothelial marker PECAM-1/CD31, transporters Glut-1 and transferrin receptor (TfR), and tight junctions claudin-5, occludin, and zonula occludens (ZO)-1 (**Figure 2C**). TY10 cells have well characterized barrier-forming features and correlation between tight junction expression and barrier function in TY10 cells is well-established in the literature (Spampinato et al., 2015; Shimizu et al., 2017, 2019; Takeshita et al., 2017). We also provide evidence that TY10 cells secret components of the extracellular matrix by staining for laminin (**Figure 2C**).

As depicted in the representative fluorescence microscopy image of a chemically fixed sample stained for actin and DNA shown in **Figure 2D**, TY10 cells grew as a monolayer at the interphase between the cylindrical lumen and the collagen matrix in the microvessel-on-a-chip. Cultured for 7 days with constant flow at 1 μl/min of media, they appeared elongated along the flow axis, in agreement with previous findings (Ohashi and Sato, 2005; Aird, 2007). We have also shown in **Figure 2D** an enlarged region showing elongated actin stress fibers along the axis of flow in the lumen of the microvessel. This confirms the overall elongated organization of the TY10 cells grown in the chip under conditions of unidirectional flow. Importantly, most TY10 cells failed to align when grown in the commercial Mimetas OrganoPlate® platform that subjects the cells to bidirectional instead of unidirectional flow of medium (Figure 1D; Wevers et al., 2018). This is an important characteristic since shear stress is known to play a role in regulating signaling cascades (Conway and Schwartz, 2012), enhancing the expression of key genes associated with transporters and junctional proteins (Cucullo et al., 2011), and plays a pivotal role in BBB regulation (Neuwelt et al., 2008; Neuwelt et al., 2011). Further confirmation for the cell organization was obtained using TY10 cells stably expressing soluble eGFP grown in a similar way and then imaged by live cell fluorescence microscopy 3D imaging (**Figure 2E** and related **Supplementary Movie 2**).

We further characterized, at the ultrastructural level, the TY10 brain microvessel-on-a-chip established under unidirectional flow as a way to detect presence of tight junctions between adjacent TY10 cells grown at the lumen-collagen interphase by using transmission electron microscopy (TEM) (**Figure 3**). The representative images highlight the presence of a narrow gap between adjacent cells and the occurrence of tight junctions. Similar images were observed along most cell-cell contacts between TY10 cells imaged visualized in other regions from this and other TEM sections. The open design provides an ideal tool for advanced imaging strategies since sample preparation in closed microfluidic chips is a real challenge, as one needs to fix the cells *in situ*, and then remove the surrounding polymer and glass to gain access to the cells for further processing. In the study by Lemos et al. (2016), the TEM images presented in the paper were obtained by fixing the cells, freezing the tissue and then cutting the PDMS away while the chip was kept in a container of dry ice. The freeze-thaw cycle negatively impacts the microstructure of the cells as indicated by the loss of the continuity of cell membrane (Figure 6C; Lemos et al., 2016). When trying to extract the hydrogel directly without the freeze-thaw cycle, the lumen was often completely destroyed and no usable data were generated. The clear advantage of the open design chip is that the collagen and cells can be directly embedded for TEM imaging without the risk of damaging the cells with additional manipulations.

TEER is frequently used to evaluate the integrity of the tight junctions and barrier function of *in vitro* models of the BBB. Use of this approach is not practical for our brain microvessel-on-a-chip model because the geometric constrains prevent us from positioning electrodes on opposite sides of the endothelial monolayer between the cylindrical lumen and the collagen matrix. To circumvent this limitation, we capitalized on our ability to use fluorescence optical imaging with our device as a way to determine permeability coefficient across the endothelial monolayer and hence establish the extent of the barrier function of cells grown in the brain microvessel-on-a-chip. Using spinning disk confocal fluorescence microscopy, we determined the rate of transport of fluorescently tagged humanized monoclonal hmAb-AF568 (**Figures 4A,C,D**) or 10 kDa FITC-dextran (**Figure 4B**) across the lumen-matrix interphase in the absence or presence of cells. Unexpectedly, in the absence of cells, we found retention of hmAb-AF568 at the lumen-matrix interface (**Figure 4A**, central fluorescence image). This retention appeared to be due to capture of the antibody by unreacted Genipin (the stabilizing primary amine crosslinker used to stabilize the collagen matrix, see section "Materials and Methods"). Quenching the unreacted reagent (see section "Materials and Methods") fully prevented the hmAb-AF568 capture (**Figure 4A**, right fluorescence image). As shown by the time-dependent heat maps depicted in **Figures 4B,C**, 10 kDa FITC-dextran and hmAb-AF568 freely diffused from the lumen toward the collagen matrix.

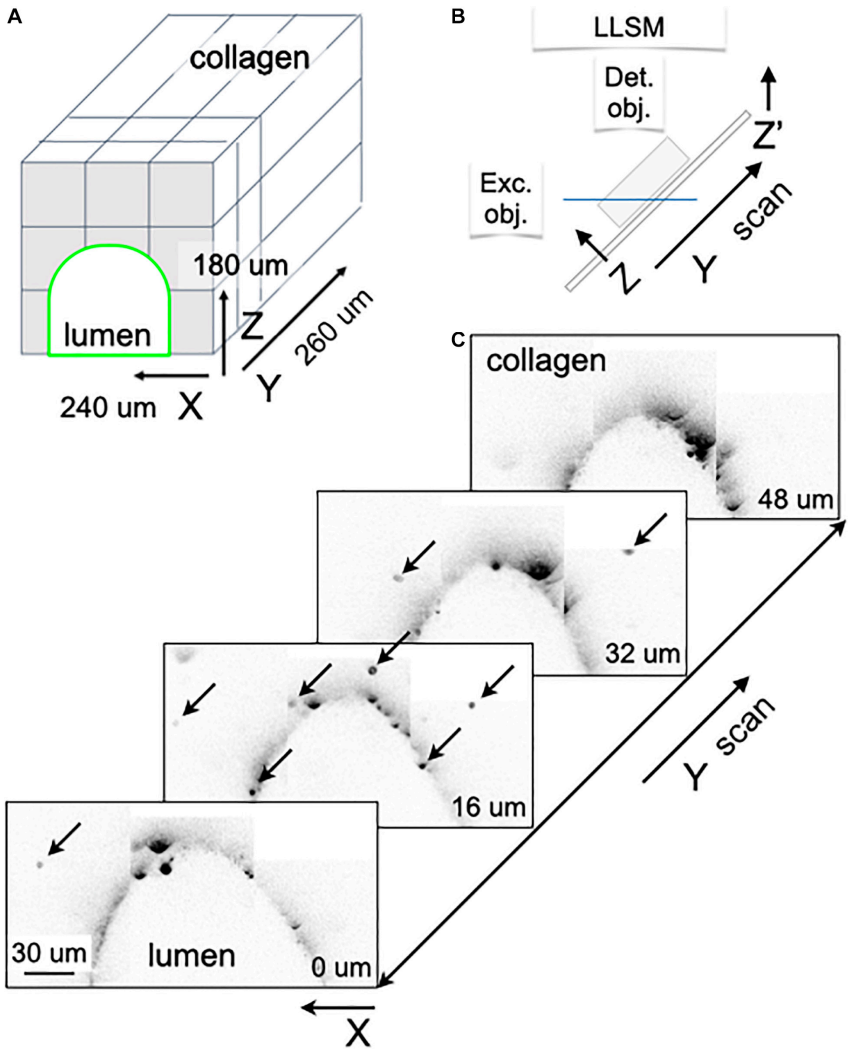

FIGURE 5 | Visualizing IgG antibody diffusion in the microfluidic chip using LLSM. **(A)** Schematic representation of the volumetric imaging strategy used to visualize the lumen of the microvessel and surrounding volume within the chip using LLSM. The cubes represent the adjacent regions imaged by serial scanning of the sample using a distance of 100 nm between planes. **(B)** Schematic representation of the imaging set up used in LLSM. **(C)** Selected planes corresponding to the volumetric imaging obtained using LLSM of a sample containing 3 μm SPHERO^{TM} Goat anti-Human IgG coated polystyrene beads embedded in the collagen matrix. Before imaging, a solution containing hmAb-AF647 was perfused at 1 μl/min for 20 min. The fluorescent spots (marked by arrows in the selected planes located 16 μm apart) highlight beads with captured hmAb-AF647 located within the collagen matrix. The peak fluorescence intensity of the captured hmAb $2.6^{+7} \pm 1.3^{+7}$ (mean ± SEM in arbitrary units) did not show a dependence with distance away from the lumen, consistent with efficient capture of the diffusing antibody. Scale bar, 30 μm.

We designed our system with the goal of enabling the study antibody transcytosis, and thus the 10 kDa FITC-dextran was selected for permeability analysis since it has a similar hydrodynamic radius and appropriate equivalent size-exclusion range as antibodies, hence enabling us to perform a direct comparison.

The apparent permeabilities of hmAb-AF568 and 10 kDa FITC-dextran, determined as the flux through a given unit area under gradient concentration (cm s^{-1}) were also similar (**Figure 4E**) as expected for molecules with comparable radius of gyration (1.86 and 5–6 nm, respectively) (Armstrong et al., 2004; Hawe et al., 2011). In contrast, presence of the TY10 monolayer at the lumen-matrix interphase significantly hindered the transport of hmAb-AF568 (**Figure 4D**), with a significantly lower apparent permeability (**Figure 4E**).

We include as a comparison data from a permeability assay with 10 kDa FITC-dextran carried out in a static transwell model. In these experiments, dextran was added to the top chamber above an endothelial TY10 monolayer, and was then sampled after 1 h from the bottom chamber. In a transwell insert without cells, dextran freely diffused from the top to the bottom chamber, while a significant reduction in dextran flux was observed in the presence of TY10 cells (13.5-fold, $p < 0.0001$), demonstrating that cells formed a functional barrier (**Figure 4E**). TY10 cells appeared

tighter in the microfluidic device compared to the transwell model (average Papp values of 1.73^{-6} vs. 3.44^{-6}, $p = 0.004$) (**Figure 4E**). It is noted that at baseline (no cell controls in transwell and microfluidic chip), the apparent permeability was lower in the collagen microvessel which is likely an effect from pore size, surface area or other parameters attributed to the semipermeable membrane of a transwell insert that do not allow a direct comparison between the two systems. We conclude that TY10 cells, when comparing to its respective no-cell control within each experimental system, established a significant barrier to antibody diffusion, in agreement with similar previous results obtained with these and other cells using different *in vitro* human brain endothelial cell models (Eigenmann et al., 2013; Wevers et al., 2018).

Application of Advanced Lattice Light Sheet Imaging

Our microfluidic device is the only currently available design that can fit within the physical constraints of LLSM objectives (there is only 170 microns left to fit it the entire microfluidic device). In **Figure 5**, we provide a proof-of-concept that our design can fit and be successfully used to image the lumen and the surrounding collagen matrix not readily accessible with conventional microfluidic devices (**Figures 5A,B**).

We show our ability to image beads interspersed in the collagen matrix that have captured fluorescently tagged antibodies diffusing from the lumen of the artificial microvessel (**Figure 5C**). In this case, we placed 3 μm SPHERO^{TM} goat anti-human IgG coated polystyrene beads in the collagen matrix, to then capture hmAb-AF647 labeled antibodies perfused through the lumen of the microvessel within the chip; visualization was done using LLSM (**Figure 5C**, arrows). The peak fluorescence intensity of the captured hmAb $2.6^{+7} \pm 1.3^{+7}$ (mean ± SEM in arbitrary units) did not show dependence with distance away from the lumen, consistent with efficient capture of the diffusing antibody.

In the future, we will capitalize on the recently developed lattice light sheet microscope modified with adaptive optics (AO-LLSM) that has significantly improved optical imaging capabilities to better visualize internal cellular compartments and investigate the transcytosis of antibodies and potentially other biotherapeutics across the endothelial barrier. This system has properties ideal for addressing other biological questions that can benefit from the advantages of LLSM and AO-LLSM because of their high temporal and spatial resolution combined with the very minimal bleaching even when the samples are imaged for prolonged times (Chen et al., 2014; Aguet et al., 2016; Liu et al., 2018).

Compared to traditional closed platforms, our open design facilitates harvesting of cells for gene expression profiling using RNAseq or quantitative PCR, protein expression by Western Blot or Mass Spectrometry, although the number of cells per microvessel may be limiting for some of these applications. Another advantage of the open chip design is the ease for chemical fixation and sample handling of the biological material located within the collagen associated with TEM, with high resolution volumetric imaging using Focused Ion Beam Scanning Electron Microscopy (FIB-SEM) and also with the newly developed modality of expansion microscopy combined with LLSM (Ex-LLSM) (Xu et al., 2017; Gao et al., 2019; Wassie et al., 2019).

Our results provide a supporting evidence showing how the open design of our microfluidic brain microvessel-on-a-chip device can be used to facilitate future studies of brain endothelial physiology at a subcellular level, particularly since cells can be grown under controlled unidirectional flow conditions. A next-generation model of the microvessel-on-a-chip could include addition of supporting cells such as astrocytes and pericytes to generate a more complex and physiologically relevant representation of the *in vivo* BBB. Further, our device is amenable to other barrier-forming cell systems found in vascular beds of peripheral tissues such as kidney or lung, for instance, or systems modeling like the gut epithelium.

The readily imaging accessibility of our open design is particularly suited for investigations of molecular transport mechanisms involved in the transcellular transport of biologicals, viruses or nanoparticles with the potential of providing insights at extraordinary level of detail. Although we exemplified here the implementation with the LLSM system, it is also designed to take advantage of AO-LLSM, which enables capture of high-resolution 3D movies of collective behavior of cells in a multicellular environment (Ji, 2017; Gao et al., 2019).

DATA AVAILABILITY STATEMENT

All datasets used and/or analyzed during the current study are available from the corresponding author TKi upon reasonable request.

AUTHOR CONTRIBUTIONS

MS, MD, GM, and TKi conceived the project. MS and GM were involved in all experiments. MD, MS, GM, SU, and TKi designed the brain microvessel-on-a-chip. RH helped with building the brain microvessel-on-a-chip devices under IK and MS supervision. GM and BO provided advice on all aspects of the cell biology associated with this project. BO performed immunostainings. TG performed dextran permeability assays in transwell. IK and MS performed spinning disk confocal microscopy. KO performed lattice light sheet microscopy under TKi's supervision. GD helped with data analysis. GN performed electron microscopy. FS, YS, and TKa provided the parental TY10 cells and advised on cell culture procedures. TKi supervised the project. MS, BO, and TKi wrote the manuscript with comments from all authors.

FUNDING

This project was funded in part by a Biogen Sponsored Research Agreement to TKi and NNF16OC0022166 Novo Nordisk Foundation/Danish Technical University grant to TKi.

ACKNOWLEDGMENTS

We thank Fang Qian and Benjamin Smith (Biogen) for generating the fluorescent hmAb monoclonal antibody, G. Campbell Kaynor (Biogen) for providing the lentiviral construct expressing memEGFP, Ramiro Massol and Chris Ehrenfels (Cellular Imaging Unit, Biogen), Tegy John Vadakkan (TKi Lab) for assistance with fluorescence microscopy imaging and Robin Kleiman (Biogen) for critical feedback.

SUPPLEMENTARY MATERIAL

The Supplementary Material for this article can be found online at: https://www.frontiersin.org/articles/10.3389/fbioe.2020.573775/full#supplementary-material

MOVIE S1 | Fabrication of the microvessel-on-a-chip. Simplified guide illustrating key steps during the fabrication of the microvessel-on-a-chip. The movie has been uploaded to FigShare® and is available using this link: https://figshare.com/s/bb9ed44327f80a152abb.

MOVIE S2 | Live cell imaging of a brain microvessel-on-a-chip. 3D rendition of a live sample of TY10-eGFP cells expressing membrane bound eGFP grown as a monolayer at the boundary between the lumen of the artificial microvessel and the collagen scaffold within the brain microvessel-on-a-chip. The volumetric image was obtained using spinning disk confocal microscopy.

MOVIE S3 | Absence of a functional barrier between the lumen and the collagen matrix of the brain microvessel-on-a-chip. Time series of the fluorescence intensity presented as a heat map of 10 kDa FITC-Dextran diffusing from the lumen through the collagen as a function of time obtained at a flow of 1 μl/min. Data was obtained in the absence of a cell monolayer at the boundary between the lumen of the artificial microvessel and the collagen scaffold within the brain microvessel-on-a-chip.

MOVIE S4 | TY10 cells establish a functional barrier in the brain microvessel-on-a-chip. Time series of the fluorescence intensity presented as a heat map of antibody hmAb-AF568 diffusing from the lumen through the collagen as a function of time obtained at a flow of 1 μl/min. Data was obtained in the presence of a monolayer of TY10 cells at the boundary between the lumen of the artificial microvessel and the collagen scaffold within the brain microvessel-on-a-chip.

MOVIE S5 | TY10 cells establish a functional barrier in the brain microvessel-on-a-chip. Time series of the fluorescence intensity presented as a heat map of antibody hmAb-AF568 diffusing from the lumen through the collagen as a function of time obtained at a flow of 1 μl/min. Data was obtained in the presence of a monolayer of TY10 cells at the boundary between the lumen of the artificial microvessel and the collagen scaffold within the brain microvessel-on-a-chip.

REFERENCES

Abbott, N. J., Hughes, C., Revest, P. A., and Greenwood, J. (1992). Development and characterisation of a rat brain capillary endothelial culture: towards an in vitro blood-brain barrier. *J. Cell Sci.* 103, 23–37.

Abbott, N. J., Patabendige, A. A., Dolman, D. E., Yusof, S. R., and Begley, D. J. (2010). Structure and function of the blood–brain barrier. *Neurobiol. Dis.* 37, 13–25.

Aguet, F., Upadhyayula, S., Gaudin, R., Chou, Y.-Y., Cocucci, E., He, K., et al. (2016). Membrane dynamics of dividing cells imaged by lattice light-sheet microscopy. *Mol. Biol. Cell* 27, 3418–3435. doi: 10.1091/mbc.e16-03-0164

Aird, W. C. (2007). Phenotypic heterogeneity of the endothelium: I. Structure, function, and mechanisms. *Circ. Res.* 100, 158–173. doi: 10.1161/01.res.0000255691.76142.4a

Armstrong, J. K., Wenby, R. B., Meiselman, H. J., and Fisher, T. C. (2004). The hydrodynamic radii of macromolecules and their effect on red blood cell aggregation. *Biophys. J.* 87, 4259–4270. doi: 10.1529/biophysj.104.047746

Aumailley, M., Bruckner-Tuderman, L., Carter, W., Deutzmann, R., Edgar, D., Ekblom, P., et al. (2005). A simplified nomeclature for laminin. *Matrix Biol.* 24, 326–332. doi: 10.1016/j.matbio.2005.05.006

Bernas, M. J., Cardoso, F. L., Daley, S. K., Weinand, M. E., Campos, A. R., Ferreira, A. J. G., et al. (2010). Establishment of primary cultures of human brain microvascular endothelial cells to provide an in vitro cellular model of the blood-brain barrier. *Nat. Protoc.* 5, 1265–1272. doi: 10.1038/nprot.2010.76

Biegel, D., and Pachter, J. S. (1994). Growth of brain microvessel endothelial cells on collagen gels: applications to the study of blood-brain barrier physiology and CNS inflammation. *In Vitro Cell. Develop. Biol. Anim.* 30, 581–588. doi: 10.1007/bf02631256

Bischel, L. L., Young, E. W., Mader, B. R., and Beebe, D. J. (2013). Tubeless microfluidic angiogenesis assay with three-dimensional endothelial-lined microvessels. *Biomaterials* 34, 1471–1477. doi: 10.1016/j.biomaterials.2012.11.005

Bordone, M. P., Salman, M. M., Titus, H. E., Amini, E., Andersen, J. V., Chakraborti, B., et al. (2019). The energetic brain–A review from students to students. *J. Neurochem.* 151, 139–165.

Campisi, M., Shin, Y., Osaki, T., Hajal, C., Chiono, V., and Kamm, R. D. (2018). 3D self-organized microvascular model of the human blood-brain barrier with endothelial cells, pericytes and astrocytes. *Biomaterials* 180, 117–129. doi: 10.1016/j.biomaterials.2018.07.014

Chan, K. L., Khankhel, A. H., Thompson, R. L., Coisman, B. J., Wong, K. H., Truslow, J. G., et al. (2014). Crosslinking of collagen scaffolds promotes blood and lymphatic vascular stability. *J. Biom. Mater. Res. A* 102, 3186–3195. doi: 10.1002/jbm.a.34990

Chen, B.-C., Legant, W. R., Wang, K., Shao, L., Milkie, D. E., Davidson, M. W., et al. (2014). Lattice light-sheet microscopy: imaging molecules to embryos at high spatiotemporal resolution. *Science* 346, 439–452.

Conway, D., and Schwartz, M. A. (2012). Lessons from the endothelial junctional mechanosensory complex. *F1000 Biol. Rep.* 4:1.

Cucullo, L., Hossain, M., Puvenna, V., Marchi, N., and Janigro, D. (2011). The role of shear stress in Blood-Brain Barrier endothelial physiology. *BMC Neurosci.* 12:40. doi: 10.1186/1471-2202-12-40

Daneman, R. (2012). The blood–brain barrier in health and disease. *Ann. Neurol.* 72, 648–672.

Eigenmann, D. E., Xue, G., Kim, K. S., Moses, A. V., Hamburger, M., and Oufir, M. (2013). Comparative study of four immortalized human brain capillary endothelial cell lines, hCMEC/D3, hBMEC, TY10, and BB19, and optimization of culture conditions, for an in vitro blood–brain barrier model for drug permeability studies. *Fluids Barriers CNS* 10:33. doi: 10.1186/2045-8118-10-33

Gao, R., Asano, S. M., Upadhyayula, S., Pisarev, I., Milkie, D. E., Liu, T.-L., et al. (2019). Cortical column and whole-brain imaging with molecular contrast and nanoscale resolution. *Science* 363:eaau8302. doi: 10.1126/science.aau8302

Gautam, J., Zhang, X., and Yao, Y. (2016). The role of pericytic laminin in blood brain barrier integrity maintenance. *Sci. Rep.* 6, 1–13. doi: 10.1038/s41590-018-0286-9

Greene, C., and Campbell, M. (2016). Tight junction modulation of the blood brain barrier: CNS delivery of small molecules. *Tissue Barriers* 4:e1138017. doi: 10.1080/21688370.2015.1138017

Halldorsson, S., Lucumi, E., Gómez-Sjöberg, R., and Fleming, R. M. (2015). Advantages and challenges of microfluidic cell culture in polydimethylsiloxane devices. *Biosens. Bioelectron.* 63, 218–231. doi: 10.1016/j.bios.2014.07.029

Hartmann, C., Zozulya, A., Wegener, J., and Galla, H.-J. (2007). The impact of glia-derived extracellular matrices on the barrier function of cerebral endothelial cells: an in vitro study. *Exp. Cell Res.* 313, 1318–1325. doi: 10.1016/j.yexcr.2007.01.024

Hawe, A., Hulse, W. L., Jiskoot, W., and Forbes, R. T. (2011). Taylor dispersion analysis compared to dynamic light scattering for the size analysis of therapeutic peptides and proteins and their aggregates. *Pharm. Res.* 28, 2302–2310. doi: 10.1007/s11095-011-0460-3

He, Y., Yao, Y., Tsirka, S. E., and Cao, Y. (2014). Cell-culture models of the blood–brain barrier. *Stroke* 45, 2514–2526. doi: 10.1161/strokeaha.114.005427

Herland, A., van der Meer, A. D., FitzGerald, E. A., Park, T.-E., Sleeboom, J. J., and Ingber, D. E. (2016). Distinct contributions of astrocytes and pericytes to neuroinflammation identified in a 3D human blood-brain barrier on a chip. *PLoS One* 11:e0150360. doi: 10.1371/journal.pone.0150360

Ji, N. (2017). Adaptive optical fluorescence microscopy. *Nat. Methods* 14:374–380. doi: 10.1038/nmeth.4218

Karassek, S., Starost, L., Solbach, J., Greune, L., Sano, Y., Kanda, T., et al. (2015). Pertussis toxin exploits specific host cell signaling pathways for promoting invasion and translocation of *Escherichia coli* K1 RS218 in human brain-derived microvascular endothelial cells. *J. Biol. Chem.* 290, 24835–24843. doi: 10.1074/jbc.m115.650101

Kim, D., and Herr, A. E. (2013). Protein immobilization techniques for microfluidic assays. *Biomicrofluidics* 7:041501. doi: 10.1063/1.4816934

Kuhnline Sloan, C. D., Nandi, P., Linz, T. H., Aldrich, J. V., Audus, K. L., and Lunte, S. M. (2012). Analytical and biological methods for probing the blood-brain barrier. *Annu. Rev. Analyt. Chem.* 5, 505–531. doi: 10.1146/annurev-anchem-062011-143002

Lee, J. N., Park, C., and Whitesides, G. M. (2003). Solvent compatibility of poly (dimethylsiloxane)-based microfluidic devices. *Anal. Chem.* 75, 6544–6554. doi: 10.1021/ac0346712

Lemos, D. R., Marsh, G., Huang, A., Campanholle, G., Aburatani, T., Dang, L., et al. (2016). Maintenance of vascular integrity by pericytes is essential for normal kidney function. *Am. J. Physiol. Renal Physiol.* 311, F1230–F1242.

Liu, T.-L., Upadhyayula, S., Milkie, D. E., Singh, V., Wang, K., Swinburne, I. A., et al. (2018). Observing the cell in its native state: imaging subcellular dynamics in multicellular organisms. *Science* 360:eaaq1392. doi: 10.1126/science.aaq1392

Maeda, T., Sano, Y., Abe, M., Shimizu, F., Kashiwamura, Y., Ohtsuki, S., et al. (2013). Establishment and characterization of spinal cord microvascular endothelial cell lines. *Clin. Exp. Neuroimmunol.* 4, 326–338. doi: 10.1111/cen3.12045

Mahringer, A., Ott, M., Reimold, I., Reichel, V., and Fricker, G. (2011). The ABC of the blood-brain barrier-regulation of drug efflux pumps. *Curr. Pharm. Des.* 17, 2762–2770. doi: 10.2174/138161211797440221

Neuwelt, E., Abbott, N. J., Abrey, L., Banks, W. A., Blakley, B., Davis, T., et al. (2008). Strategies to advance translational research into brain barriers. *Lancet Neurol.* 7, 84–96. doi: 10.1016/s1474-4422(07)70326-5

Neuwelt, E. A., Bauer, B., Fahlke, C., Fricker, G., Iadecola, C., Janigro, D., et al. (2011). Engaging neuroscience to advance translational research in brain barrier biology. *Nat. Rev. Neurosci.* 12, 169–182. doi: 10.1038/nrn2995

Oddo, A., Peng, B., Tong, Z., Wei, Y., Tong, W. Y., Thissen, H., et al. (2019). Advances in microfluidic blood–brain barrier (BBB) models. *Trends Biotechnol.* 37, 1295–1314. doi: 10.1016/j.tibtech.2019.04.006

Ohashi, T., and Sato, M. (2005). Remodeling of vascular endothelial cells exposed to fluid shear stress: experimental and numerical approach. *Fluid Dyn. Res.* 37:40. doi: 10.1016/j.fluiddyn.2004.08.005

Pardridge, W. M. (2006). Molecular Trojan horses for blood–brain barrier drug delivery. *Curr. Opin. Pharmacol.* 6, 494–500. doi: 10.1016/j.coph.2006.06.001

Park, T.-E., Mustafaoglu, N., Herland, A., Hasselkus, R., Mannix, R., FitzGerald, E. A., et al. (2019). Hypoxia-enhanced Blood-Brain Barrier Chip recapitulates human barrier function and shuttling of drugs and antibodies. *Nat. Communicat.* 10, 1–12.

Prabhakarpandian, B., Shen, M.-C., Nichols, J. B., Mills, I. R., Sidoryk-Wegrzynowicz, M., Aschner, M., et al. (2013). SyM-BBB: a microfluidic blood brain barrier model. *Lab Chip* 13, 1093–1101. doi: 10.1039/c2lc41208j

Reichel, A., Begley, D. J., and Abbott, N. J. (2003). An overview of in vitro techniques for blood-brain barrier studies. *Meth. Mol. Med.* 89, 307–324. doi: 10.1385/1-59259-419-0:307

Sano, Y., Kashiwamura, Y., Abe, M., Dieu, L. H., Huwyler, J., Shimizu, F., et al. (2013). Stable human brain microvascular endothelial cell line retaining its barrier-specific nature independent of the passage number. *Clin. Exp. Neuroimmunol.* 4, 92–103. doi: 10.1111/cen3.12001

Sano, Y., Shimizu, F., Abe, M., Maeda, T., Kashiwamura, Y., Ohtsuki, S., et al. (2010). Establishment of a new conditionally immortalized human brain microvascular endothelial cell line retaining an in vivo blood–brain barrier function. *J. Cell. Physiol.* 225, 519–528. doi: 10.1002/jcp.22232

Shawahna, R., Uchida, Y., Decleves, X., Ohtsuki, S., Yousif, S., Dauchy, S., et al. (2011). Transcriptomic and quantitative proteomic analysis of transporters and drug metabolizing enzymes in freshly isolated human brain microvessels. *Mol. Pharmaceut.* 8, 1332–1341. doi: 10.1021/mp200129p

Shimizu, F., Schaller, K. L., Owens, G. P., Cotleur, A. C., Kellner, D., Takeshita, Y., et al. (2017). Glucose-regulated protein 78 autoantibody associates with blood-brain barrier disruption in neuromyelitis optica. *Sci. Translat. Med.* 9:eaai9111. doi: 10.1126/scitranslmed.aai9111

Shimizu, F., Takeshita, Y., Sano, Y., Hamamoto, Y., Shiraishi, H., Sato, T., et al. (2019). GRP78 antibodies damage the blood–brain barrier and relate to cerebellar degeneration in Lambert-Eaton myasthenic syndrome. *Brain* 142, 2253–2264. doi: 10.1093/brain/awz168

Song, H. W., Foreman, K. L., Gastfriend, B. D., Kuo, J. S., Palecek, S. P., and Shusta, E. V. (2020). Transcriptomic comparison of human and mouse brain microvessels. *Sci. Rep.* 10, 1–14.

Spampinato, S. F., Obermeier, B., Cotleur, A., Love, A., Takeshita, Y., Sano, Y., et al. (2015). Sphingosine 1 phosphate at the blood brain barrier: can the modulation of s1p receptor 1 influence the response of endothelial cells and astrocytes to inflammatory stimuli? *PLoS One* 10:e0133392. doi: 10.1371/journal.pone.0133392

Sung, H. W., Huang, R. N., Huang, L. L., Tsai, C. C., and Chiu, C. T. (1998). Feasibility study of a natural crosslinking reagent for biological tissue fixation. *J. Biom. Mat. Res.* 42, 560–567. doi: 10.1002/(sici)1097-4636(19981215)42:4<560::aid-jbm12>3.0.co;2-i

Takeshita, Y., Obermeier, B., Cotleur, A., Sano, Y., Kanda, T., and Ransohoff, R. M. (2014). An in vitro blood–brain barrier model combining shear stress and endothelial cell/astrocyte co-culture. *J. Neurosci. Methods* 232, 165–172. doi: 10.1016/j.jneumeth.2014.05.013

Takeshita, Y., Obermeier, B., Cotleur, A. C., Spampinato, S. F., Shimizu, F., Yamamoto, E., et al. (2017). Effects of neuromyelitis optica–IgG at the blood–brain barrier in vitro. *Neurol. Neuroimmunol. Neuroinflammat.* 4:e311. doi: 10.1212/nxi.0000000000000311

Tilling, T., Engelbertz, C., Decker, S., Korte, D., Hüwel, S., and Galla, H.-J. (2002). Expression and adhesive properties of basement membrane proteins in cerebral capillary endothelial cell cultures. *Cell Tissue Res.* 310, 19–29. doi: 10.1007/s00441-002-0604-1

Tilling, T., Korte, D., Hoheisel, D., and Galla, H. J. (1998). Basement membrane proteins influence brain capillary endothelial barrier function in vitro. *J. Neurochem.* 71, 1151–1157. doi: 10.1046/j.1471-4159.1998.71031151.x

Uchida, Y., Ohtsuki, S., Katsukura, Y., Ikeda, C., Suzuki, T., Kamiie, J., et al. (2011). Quantitative targeted absolute proteomics of human blood–brain barrier transporters and receptors. *J. Neurochem.* 117, 333–345. doi: 10.1111/j.1471-4159.2011.07208.x

Urich, E., Patsch, C., Aigner, S., Graf, M., Iacone, R., and Freskgård, P.-O. (2013). Multicellular self-assembled spheroidal model of the blood brain barrier. *Sci. Rep.* 3:1500.

van Der Helm, M. W., Van Der Meer, A. D., Eijkel, J. C., van den Berg, A., and Segerink, L. I. (2016). Microfluidic organ-on-chip technology for blood-brain barrier research. *Tissue Barriers* 4:e1142493. doi: 10.1080/21688370.2016.1142493

Wassie, A. T., Zhao, Y., and Boyden, E. S. (2019). Expansion microscopy: principles and uses in biological research. *Nat. Methods* 16, 33–41. doi: 10.1038/s41592-018-0219-4

Wevers, N. R., Kasi, D. G., Gray, T., Wilschut, K. J., Smith, B., Van Vught, R., et al. (2018). A perfused human blood–brain barrier on-a-chip for high-throughput assessment of barrier function and antibody transport. *Fluids Barriers CNS* 15:23.

Wong, A., Ye, M., Levy, A., Rothstein, J., Bergles, D., and Searson, P. C. (2013). The blood-brain barrier: an engineering perspective. *Front. Neuroeng.* 6:7. doi: 10.3389/fneng.2013.00007

Xu, C. S., Hayworth, K. J., Lu, Z., Grob, P., Hassan, A. M., Garcia-Cerdan, J. G., et al. (2017). Enhanced FIB-SEM systems for large-volume 3D imaging. *Elife* 6:e25916.

Yoo, J. S., Kim, Y. J., Kim, S. H., and Choi, S. H. (2011). Study on genipin: a new alternative natural crosslinking agent for fixing heterograft tissue. *Korean J. Thorac. Cardiovasc. Surg.* 44, 197–207. doi: 10.5090/kjtcs.2011.44.3.197

Yuan, W., Lv, Y., Zeng, M., and Fu, B. M. (2009). Non-invasive measurement of solute permeability in cerebral microvessels of the rat. *Microvasc. Res.* 77, 166–173. doi: 10.1016/j.mvr.2008.08.004

Conflict of Interest: GM and BO are employees and shareholders of Biogen. TG was employee and shareholder of Biogen at the time the study was performed. TKi is a visiting scientist at Biogen.

The remaining authors declare that the research was conducted in the absence of any commercial or financial relationships that could be construed as a potential conflict of interest.

frontiers in Bioengineering and Biotechnology

ORIGINAL RESEARCH
published: 12 November 2020
doi: 10.3389/fbioe.2020.581163

Modular Microphysiological System for Modeling of Biologic Barrier Function

Matthew Ishahak[1], Jordan Hill[1], Quratulain Amin[1], Laura Wubker[1], Adiel Hernandez[1], Alla Mitrofanova[3], Alexis Sloan[3], Alessia Fornoni[2,3] and Ashutosh Agarwal[1,2]**

[1] Department of Biomedical Engineering, University of Miami, Coral Gables, FL, United States, [2] Department of Biochemistry & Molecular Biology, DJTMF Biomedical Nanotechnology Institute, University of Miami Miller School of Medicine, Miami, FL, United States, [3] Katz Family Division of Nephrology and Hypertension, Department of Medicine, Peggy and Harold Katz Family Drug Discovery Center, University of Miami Miller School of Medicine, Miami, FL, United States

OPEN ACCESS

Edited by:
Nuno M. Neves, University of Minho, Portugal

Reviewed by:
Ken-ichiro Kamei, Kyoto University, Japan
Giuseppe Maruccio, University of Salento, Italy

***Correspondence:**
Alessia Fornoni
AFornoni@med.miami.edu
Ashutosh Agarwal
a.agarwal2@miami.edu

Specialty section:
This article was submitted to Nanobiotechnology, a section of the journal Frontiers in Bioengineering and Biotechnology

Received: *08 July 2020*
Accepted: *21 October 2020*
Published: *12 November 2020*

Citation:
Ishahak M, Hill J, Amin Q, Wubker L, Hernandez A, Mitrofanova A, Sloan A, Fornoni A and Agarwal A (2020) Modular Microphysiological System for Modeling of Biologic Barrier Function. Front. Bioeng. Biotechnol. 8:581163. doi: 10.3389/fbioe.2020.581163

Microphysiological systems, also known as organs-on-chips, are microfluidic devices designed to model human physiology *in vitro*. Polydimethylsiloxane (PDMS) is the most widely used material for organs-on-chips due to established microfabrication methods, and properties that make it suitable for biological applications such as low cytotoxicity, optical transparency, gas permeability. However, absorption of small molecules and leaching of uncrosslinked oligomers might hinder the adoption of PDMS-based organs-on-chips for drug discovery assays. Here, we have engineered a modular, PDMS-free microphysiological system that is capable of recapitulating biologic barrier functions commonly demonstrated in PDMS-based devices. Our microphysiological system is comprised of a microfluidic chip to house cell cultures and pneumatic microfluidic pumps to drive flow with programmable pressure and shear stress. The modular architecture and programmable pumps enabled us to model multiple *in vivo* microenvironments. First, we demonstrate the ability to generate cyclic strain on the culture membrane and establish a model of the alveolar air-liquid interface. Next, we utilized three-dimensional finite element analysis modeling to characterize the fluid dynamics within the device and develop a model of the pressure-driven filtration that occurs at the glomerular filtration barrier. Finally, we demonstrate that our model can be used to recapitulate sphingolipid induced kidney injury. Together, our results demonstrate that a multifunctional and modular microphysiological system can be deployed without the use of PDMS. Further, the bio-inert plastic used in our microfluidic device is amenable to various established, high-throughput manufacturing techniques, such as injection molding. As a result, the development plastic organs-on-chips provides an avenue to meet the increasing demand for organ-on-chip technology.

Keywords: organ-on-chip, lung-on-chip, glomerulus-on-chip, microphysiological system, microfluidic

INTRODUCTION

Microphysiological systems (MPS), commonly referred to as organs-on-chips or tissue chips, have emerged as a novel approach to create *in vitro* models of normal and disease physiology. By incorporating human cells into microfluidic devices that recapitulate physiological tissue architecture and dynamic *in vivo* stimuli, MPS have promised to address the high attrition rate of compounds in drug development by providing a more human-relevant tool to identify therapeutic targets and assess drug toxicity (Bhatia and Ingber, 2014). The rapid development of MPS has been greatly influenced by the widespread use of polydimethylsiloxane (PDMS) as a biocompatible material for microfluidic devices (Duffy et al., 1998; McDonald and Whitesides, 2002; Huh et al., 2013). PDMS demonstrated a number of advantages for early biological applications, including low cytotoxicity, optical transparency, gas permeability, and ease of microfabrication (Sia and Whitesides, 2003). One of the earliest MPS, a lung-on-a-chip, validated PDMS for applications that involve recreating the dynamic flow and mechanical stretching of the *in vivo* alveolar air-liquid interface (ALI) (Huh et al., 2007, 2010). However, the widespread adoption of MPS has been hampered by some of the innate properties of PDMS (Berthier et al., 2012). Of these drawbacks, the absorption of small molecules and leaching of uncrosslinked oligomers have provided the greatest hindrance to the adoption of PDMS-based MPS in the context of drug discover assays (van Meer et al., 2017).

Due to the long history of microfluidic technology, there is extensive literature on the fabrication and use of plastic microfluidic devices, which may serve as an alternative to PDMS for microphysiological systems (Becker and Locascio, 2002; Guckenberger et al., 2015). Poly(methyl methacrylate) (PMMA), a transparent thermoplastic, is not only amenable to a number of microfluidic fabrication techniques, but also highly biocompatible and less absorptive than PDMS. Previously, we have demonstrated the feasibility of a PMMA fluidic platform for biologic applications through the functional assessment and optogenetic control of pancreatic islets (Lenguito et al., 2017). However, designing fluidic channels to recapitulate *in vivo* barriers, such as the alveolar air liquid interface ALI or glomerular filtration barrier (GFB), while maintaining a resealable format is difficult due to the limitations of the subtractive rapid prototyping (SRP) technique employed to fabricate PMMA-based MPS.

Here, we have overcome this limitation and engineered a modular MPS using PMMA to recapitulate the *in vivo* microenvironment of biologic barriers. The two-part microfluidic chip is comprised apical and basal channels separated by a removable porous membrane. We demonstrate that static co-culture models of the lung ALI and GFB can be transferred to the MPS and exposed to physiomimetic dynamic stimuli. This approach aims to simplify cell culture and seeding methods within the microfluidic device and minimize the time to achieve functional constructs within the MPS. Together, these results establish that a robust MPS platform can be developed from commonly used plastics that provide an avenue to meet the increasing demand for organ-on-chip technology.

MATERIALS AND METHODS

Design and Assembly of PDMS-Free Microfluidic Chip

Apical and basal flow channels were incorporated into a two-part, resealable form-factor, based on our previously published platform for interrogation of pancreatic islets. Computer-aided design (CAD) software (SolidWorks, Dassault Systèmes) was used to generate three-dimensional parts and assemblies of the fluidic chip design. SRP of CAD designs was used to fabricate fluidic chips. Briefly, device features were milled from optically-clear, UV-resistant acrylic (0.125″ thick, McMaster-Carr) using a computer numerical control milling machine (MODELA MDX-540, Roland). A 30W CO2 laser machine (Legend Helix, EpilogLaser) was used to laser cut the final form-factor of the chip from the milled workpieces. A fluoropolymer membrane was bonded to the underside of the bottom piece using a silicone adhesive. Custom gaskets were fabricated using a two-part silicone epoxy (Duraseal 1533, Cotronics Corp.). To improve the ease and speed of assembly, the gaskets were bonded to the top piece of the fluidic chip using a 100 μm thick differentially-coated polyester adhesive film (PS-1340, Polymer Science). The fully fabricated fluidic chip is then clamped in a chip holder (Fluidic Connect PRO, Micronit) to create a fluidic seal and introduce tubing connections.

Flow Profile Characterization

The fully fabricated fluidic chip is clamped in a chip holder (Fluidic Connect PRO, Micronit) to create a reversible fluidic seal and introduce tubing connections. Two microfluidic pressure pumps (Flow-EZ, Fluigent) were used to independently provide flow to the apical and basal flow channels. Flow rate was continuously measured at the outlet of the fluidic chip using liquid flow meter microsensor (LG16, Sensirion). The average flow rate was calculated from 60s recordings at pressures ranging from 0 to 150 mbar.

From flow rate measurements, the fluid shear stress τ()n the apical and basal sides of the membrane was calculated using the following equation:

$$\tau = \frac{6\mu Q}{bh^2}$$

ere μ is the fluid viscosity, Q is the volumetric flow rate, b is the channel width at the center of the culture well, and h is the height of the culture well (0.5 mm). In the present design, the width of the culture well for the apical and basal flow channels was 6 and 4.5 mm, respectively, and the height of the channels.

Computational Fluid Dynamics

Computational modeling of fluid dynamics was performed using the FEM software, COMSOL Multiphysics 5.0. Three-dimensional models of the fluidic channels were imported into COMSOL from SolidWorks as a Parasolid file. The Free and

Porous Media Flow physics module was used to solve for velocity and pressure fields of single-phase flow in the channels and the porous membrane separating the channels, simultaneously. Fluid flow was modeled as the incompressible flow of water (density = 1000 kg/m^3 and dynamic viscosity = 0.001 Pa·s) governed by the Navier-Stokes and Brinkman equations. The permeability parameter of the membrane was approximated based on the hydraulic-electrical circuit analogy (Sip et al., 2014; Chung et al., 2018). This approach is based on the similarities of Hagen–Poiseuille's law for fluid flow and Ohm's law for electrical current flow. Assuming each pore of the membrane is a circular pipe, the fluidic resistance of a single pore (R_{pore}) can be calculated:

$$R_{pore} = \frac{8\mu L}{\pi R^4}$$

Where μ is the viscosity of the fluid, L is the thickness of the membrane, and R is the radius of the pore. The fluidic resistance of the whole membrane (R_{memb}) can then be calculated from the area (A) and porosity (ρ_{pore}) of the membrane:

$$R_{memb} = \frac{R_{pore}}{A\rho_{pore}}$$

Using Ohm's law and the above equations, the permeability parameter (k) can then be expressed as a function of the porosity and pore radius:

$$k = \frac{\pi\rho R^4}{8}$$

A stationary solver was implemented to determine the steady state solution of the velocity and pressure fields. Flow rates were derived from the 3D computational models by taking the surface integral of the velocity field across specific regions.

Characterization of Membrane Strain

Bi-axial strain applied to the membrane was calculated based on the membrane deflection due to applied pressure. Membrane deflection was measured using the perfect focus system on a TI-Eclipse microscope (Nikon). First, the pump for basal flow channel was set to 80 mbar to perfuse phosphate buffered saline through the basal channel. Next, the initial focal distance of the center of the membrane was recorded. Then, the pressure for the apical flow channel pump was increased from 0 to 315 mbar in 15 mbar increments. The focal distance at each applied pressure was recorded and membrane deflection was calculated as the change from the initial focal distance. The surface of the area of the membrane could then be calculated by assuming a semi-ellipsoid geometry:

$$SA = 2\pi * \left[\frac{(a*b)^{1.6075}+(a*c)^{1.6075}+(b*c)^{1.6075}}{3}\right]^{\frac{1}{1.6075}} + (\pi * b * c)$$

Were a is the membrane deflection and b and c are the major and minor semi-axes, respectively. Based on the change of surface area, the bi-axial surface expansion (ε_{SA}) can be calculated (Guenat and Berthiaume, 2018):

$$\varepsilon_{SA} = \frac{SA_f - SA_0}{SA_0}$$

Were SA_0s the initial surface area of the membrane when no pressure is applied and SA_fs the surface area of the membrane calculated based on the membrane deflection.

TEER Measurement

Integrity of the cellular layers was assessed by transendothelial/transepithelial electrical resistance (TEER) during static culture on transwells. Resistance measurements were obtained using an epithelial volt/ohm meter (EVOM2, World Precision Instruments) equipped with handheld chopstick electrodes (STX2, World Precision Instruments). To avoid variability in measurements, test samples were brought to room temperature and electrodes were held in place using a universal probe stand. TEER values were obtained using the Ohm's Law Method (Srinivasan et al., 2015). Briefly, the resistance of the cellular layer (R_{cells}) first calculated:

$$R_{\text{cells}} = R_{\text{meas}} - R_{\text{blank}}$$

Were R_{meas} is the resistance measurement of the sample, and R_{blank} is the resistance measurement of a transwell membrane without cells. Then the TEER value was calculated by:

$$TEER = R_{\text{cells}} \times M_{\text{area}}$$

Were M_{area} is 0.336 cm^2, the area of the transwell membrane.

Culture of Alveolar-Capillary Interface

Human alveolar epithelial cells (AECs; ATCC) were propagated according to the manufacturer's instructions in ATCC Modified RPMI1640 (Thermo Fisher). Human lung microvascular endothelial cells (LMECs, Lonza) were cultured in EGM2 with the manufacturer's supplements.

Recapitulation of the alveolar-capillary interface was achieved by generating an air-liquid interface (ALI) co-culture of AECs and LMECs using methods previously described, with minor modifications (Huh et al., 2010, 2013). Briefly, transwell inserts with 0.4 μm pores (Greiner Bio-One), were coated with fibronectin (Sigma), diluted to 5 μg/mL. LMECs and AECs were seeded on inserts as described for GFB co-culture. On day 3 of the co-culture, the media for the AECs was supplemented with 1 μM dexamethasone. Once cells were confluent, after about 7 days, ALI was induced and the media in the lower compartment was changed to a 50/50 mix of EGM2 and ATCC Modified RPMI supplemented with 1 μM dexamethasone.

Glomerular Filtration Barrier Co-culture

Conditionally immortalized human podocytes (CiPodos) were cultured as previously described, with minor modifications (Saleem et al., 2002). Briefly, CiPodos were propagated on collagen-coated flasks in permissive conditions (33°C, 5% CO_2) in RPMI1640 media supplemented with penicillin, streptomycin, insulin, transferrin, selenium, and 10% fetal bovine serum.

Primary human glomerular microvascular endothelial cells (GMECs; Cell Systems) were culture per the manufacturer in complete endothelial cell growth media 2 (PromoCell). Briefly, GMECs were propagated on T75 flasks coated with Attachment Factor (Cell Systems) with media replaced every other day.

Recapitulation of the glomerular filtration barrier (GFB) was achieved by co-culturing CiPodos and GMECs on opposite sides of transwell insert with 3 μm pores (Greiner Bio-One). First, inserts were coated with collagen type I from rat tail (Corning) diluted to 0.1 mg/mL. Then, inserts were inverted and GMECs were seeded on the underside of the insert at a density of 50,000 cells per insert. The inverted inserts were then incubated for approximately 2 h to allow for GMECs to adhere. Finally, the inserts were placed in a 24-well culture plate and CiPodos were seeded in the upper compartment at a density of 50,000 cells per insert. Cells were fed with their respective media every other day.

Immunocytochemistry

Immunoctyochemistry was performed by placing membranes removed from the MPS into a series of 1.5 mL Eppendorf tubes. Cells were first fixed in 4% paraformaldehyde and permeabilized in 0.3% Triton-X. Cells were incubated with primary antibodies, diluted 1:400, for 1 h followed by 3 sequential washes in PBS. Cells were incubated with secondary antibodies, diluted 1:500, for 1 h. Nuclei were stained with either ProLong Diamond Antifade Mountant with DAPI (Invtriogen) or Hoescht (1:2000; Life Technologies). Images were acquired on either a Ti Eclipse widefield microscope (Nikon) or a Zeiss LSM confocal microscope. Image analysis was performed using ImageJ Fiji (Schindelin et al., 2012).

Filtration Assay

For the filtration assay, membranes were cut from their supports after 7 days of culture at 37°C and bonded into a microfluidic device. Two microfluidic pressure pumps (Fluigent, Flow-EZ) were used to drive flow and generate a physiomimetic pressure gradient for 1 h. A pressure of 80 mbar (approximately 60 mmHg) was applied to the basal flow channel and 20 mbar (approximately 15 mmHg) was applied to apical flow channel to perfuse PBS through the system. The basal flow channel was supplemented with 100 μg/mL FITC-conjugated inulin (Sigma-Aldrich, F3272) and/or 2 mg/mL bovine serum albumin (Sigma-Aldrich, A2153). The concentration of albumin was measured in the outflow from each channel based on the absorbance at 280 nm using a NanoDrop UV-Vis Spectrophotometer (Thermo Fisher Scientific). The fluorescence intensity of inulin in the outflow from each channel was measured using a multimode microplate reader (Beckman-Coulter, DTX 880). The amount of albumin or inulin filtered from the basal channel to the apical channel was calculated using the equation for renal clearance (Musah et al., 2017):

$$\boldsymbol{Filtration} = (\,[\boldsymbol{A}] \times \boldsymbol{AV})/[\boldsymbol{B}]$$

Were $[A]$ = concentration in apical outlet, AV = apical volume collected, and $[B]$ = concentration in basal outlet. Filtration of albumin and inulin was normalized to the filtration observed on a blank membrane without cells according to the following equation:

$$\boldsymbol{Normalized\ \ Filtration} = \frac{\boldsymbol{Filtration_{cells}}}{\boldsymbol{Filtration_{blank}}}$$

Sphingolipid Exposure

The ability of podocyte cultures to filter albumin and inulin was assessed after a 1-hour exposure to sphingosine-1-phosphate (S1P), which has previously been shown to cause proteinuria (Schümann et al., 2015). As a control, podocyte cultures not exposed to S1P were also assessed for filtration function. To expose podocytes to S1P, culture media was replaced with RMPI media supplemented with 5 μM S1P 1 h prior to cutting membranes from the supports for bonding into the MPS for filtration assay.

RESULTS

Development of Modular, PDMS-Free MPS

The design of the fluidic chip used in our modular platform, which is analogous to many PDMS-based organs-on-chips, was developed to house an epithelial/endothelial cellular co-culture (**Figure 1A**). Using a three-dimensional (3D) computer-aided design (CAD), a model of the chip was developed to scale to ensure the top and bottom pieces of the chip were compatible and that a porous membrane support would fit in to the culture well (**Figure 1B**). Unlike additive fabrication methods, such as 3D printing and soft lithography, the SRP approach makes fabrication of closed channels in the z-direction difficult. With PDMS-based organs-on-chips, irreversibly bonding two pieces of PDMS is a common solution to create closed fluidic channels. However, this reduces the modularity of the device. SRP, on the other hand allows for fast, low cost fabrication of microfluidic devices from commonly used plastics that can be are resealable. To maintain resealable form-factor of the chip design, the basal flow channel was closed by adhering a fluoropolymer membrane to the underside of the bottom piece. This membrane not only provides a thin, clear window for optical access, but also enables gas permeability in the culture well of the chip.

To recapitulate the dynamic stimuli that occur *in vivo*, the organ-on-chip platform were modular pneumatic microfluidic pumps implemented to drive flow. Using the microfluidic automation tool software, the pumps can generate physiomimetic waveforms that drive independent perfusion of the apical and basal flow channels (**Figure 1C**). To validate the design of the modular organ-on-chip platform, the fluidic chip was tested for leaks. Using a commercially available chip holder, the fluidic chip could be sealed and easily connected to the media reservoirs. Both the apical and basal flow channels were observed to operate without leaks (**Figure 1D**).

Recapitulating the Alveolar ALI Microenvironment

To demonstrate the ability to model *in vivo* microenvironments, we first sought to recapitulate the ALI found at the alveolar-capillary barrier in the lungs. A key feature of the alveolar microenvironment is the cyclic stretching of the alveolar capsule during inspiration (**Figure 2A**). Therefore, we aimed to apply mechanical force to stretch the membrane through the apical

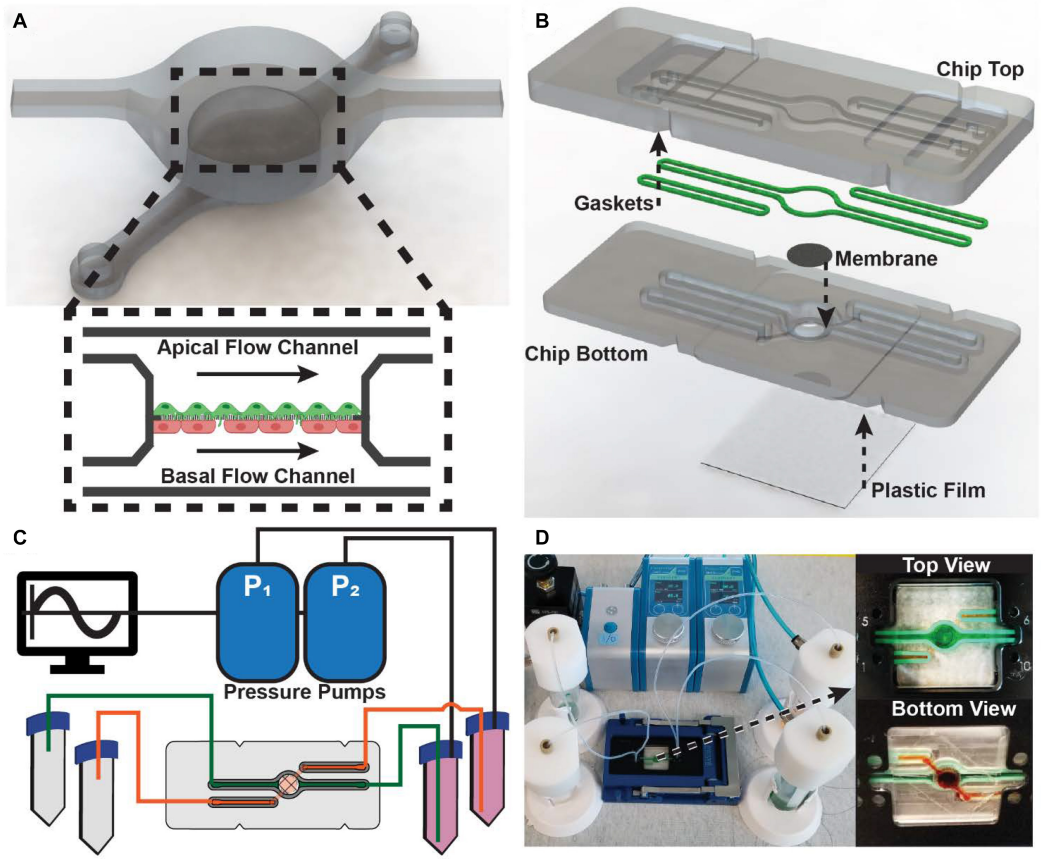

FIGURE 1 | Design and assembly of the modular MPS: **(A)** 3D render of fluidic channel geometry implemented in microfluidic chip **(Inset)** Schematic representation of internal culture well with independent apical and basal channels and a co-culture of endothelial and epithelial cells supported by a porous membrane. **(B)** Exploded view of the microfluidic chip comprised of a top and bottom piece, gaskets, porous support membrane, and an oxygen-permeable plastic film. The arrows indicate how the components are bonded into the chip. **(C)** Schematic representation of the MPS comprised of two pressure pumps controlled by a computer, media reservoirs, and the microfluidic chip. **(D)** Fully assembled and running MPS. (Insets) Top and bottom view showing leak-free perfusion of dyed water through the microfluidic chip.

flow channel of the MPS. By perfusing the basal flow channel with phosphate buffered saline (PBS) and applying air pressure through the apical pneumatic pump, deflection of the porous membrane was observed, and that the degree of deflection was proportional to the pressure applied. From the measured membrane deflection, bi-axial strain could be calculated by assuming a semi-ellipsoid shape of the deformed membrane (**Figure 2B**). The maximum bi-axial strain applied to the membrane without cells was just 4%, slightly lower than 4–12% linear strain thought to occur *in vivo* at the alveolar ALI (Guenat and Berthiaume, 2018). To model the cyclic breathing cycle, a sine wave with an amplitude of 345 mbar and a frequency of 0.33 Hz, corresponding to 20 breaths per minute, was generated in the apical flow channel while the basal flow channel pressure remained constant. The rapid switching of pressure resulted in a pressure profile resembling a human breathing profile more than a sine wave (**Figure 2C**).

Next, an ALI co-culture of lung endothelial and epithelial cells was incorporated in the MPS. Recapitulation of the alveolar-capillary interface was achieved by generating an air-liquid interface (ALI) co-culture of AECs and LMECs using methods previously described, with minor modifications (**Figure 2D**; Huh et al., 2010, 2013). TEER measurements were recorded during the transwell liquid-liquid co-culture (Day 0 to Day 7). Following the addition of dexamethasone on Day 3, a significantly higher TEER value was observed (**Figure 2E**). This is a result of increased mucus production, due to the role of dexamethasone in mucin production (Lu et al., 2005). On Day 10, ALI co-cultures were transferred into the MPS. Physiomimetic culture conditions were generated by the cyclic application of air pressure to the apical channel. Immunocytochemistry revealed that both endothelial cells, indicated by PECAM1, and epithelial cells, indicated by cytokeratin, were maintained within the MPS under physiomimetic culture conditions (**Figure 2F**).

Characterization Flow Profile and Ultrafiltration

An advantage the modular MPS design, is the ability to model multiple without significantly altering the device. As a

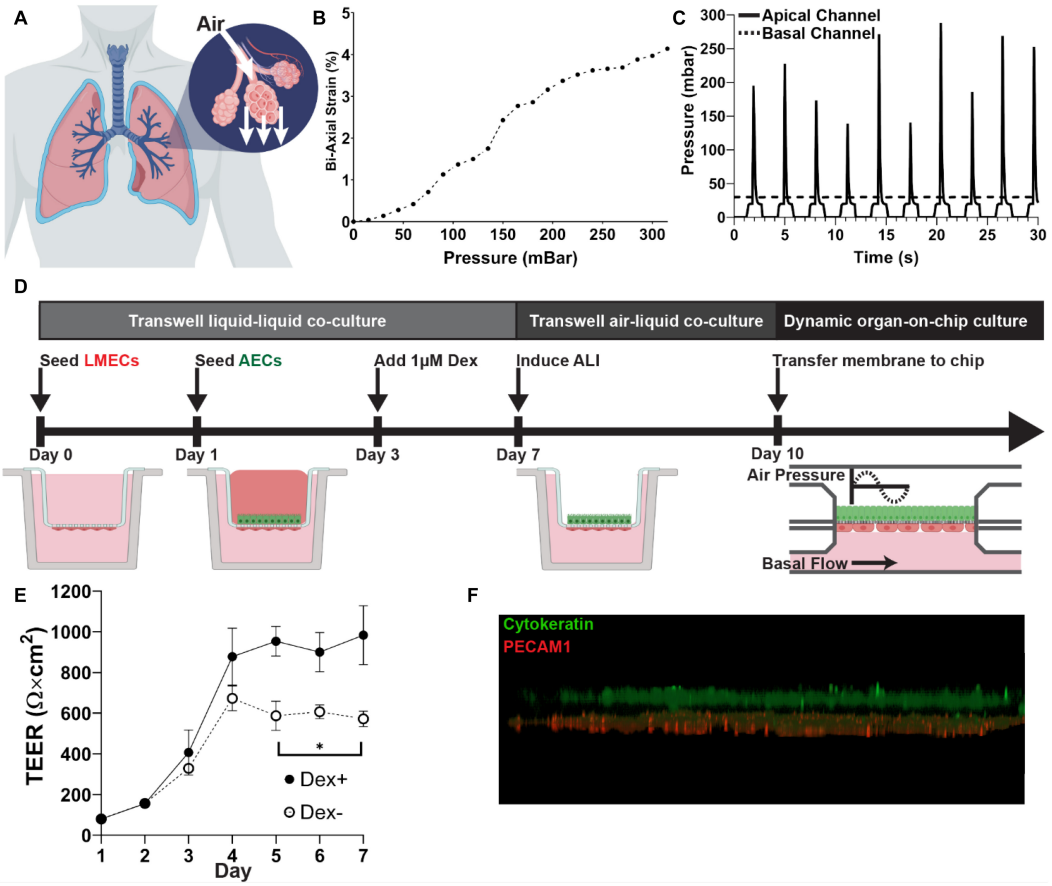

FIGURE 2 | Recapitulating alveolar microenvironment: **(A)** Cartoon of alveolar expansion during inspiration. Created with BioRender.com. **(B)** Calculated bi-axial strain in response to applied pressure in the microfluidic chip. **(C)** Application of a cyclic pressure in the apical channel using a sine wave to mimic breathing at approximately 20 breaths per minute. A constant pressure was applied to the basal channel to drive the flow of PBS. **(D)** Workflow for development of ALI co-culture. Endothelial cells (LMECs) were first seeded on the basal surface of a transwell culture insert, followed alveolar epithelial cells (AECs). Dexamethasone was added to the apical chamber on Day 3 to enhance the epithelial cell barrier. On Day 7, the ALI was induced by removing media from the apical chamber. On Day 10, the membrane was cut from the transwell support and bonded into the microfluidic chip and exposed to dynamic strain. **(E)** TEER measurements during liquid-liquid co-culture in the transwell with (Dex +) and without (Dex-) dexamethasone. Statistical analysis by unpaired *t*-test ($N = 3$). **(F)** 3D visualization of fluorescent *z*-stack after culture for 24 h under cyclic pressure exposure in the MPS. Cytokeratin (green) staining shows the alveolar endothelial cells on the apical side of the membrane, while PECAM1 (red) staining indicates the lung microvascular endothelial cells on the basal side.

result, we sought to also model a liquid-liquid barrier. First, we determined the fluid shear stress at the apical and basal boundaries of the membrane separating the two fluidic channels. This achieved by characterizing the flow rate as a function of the applied pressure. As expected, based on the electronic-hydraulic analogy, a linear relation between flow rate and applied pressure was observed (**Figure 3A**). This can be attributed to the constant fluidic resistance of the channels and the constant applied pressure. *In vivo*, vascular flow is often much faster than interstitial flow. This exposes endothelial cells to high shear stress flow, while epithelial cells experience much less shear stress. Due to the larger channel geometry, the flow rate in the apical channel was slightly higher than the flow rate in the basal channel. However, the fluid velocity and the resulting shear stress at the surface of the membrane, was about an order of magnitude larger in the basal channel than the wall shear stress calculated in the basal channel (**Figure 3B**). Therefore, the MPS design can model the fluid dynamics observed *in vivo*.

Based on these results, it was hypothesized that a pressure gradient would develop across the membrane between the two fluidic channels. A 3D computational model of the velocity and pressure fields within the microfluidic device at 100 μL/min, implemented in COMSOL, confirmed this (**Figure 3C**). The stationary solver calculated the velocity and pressure fields in 129 s using a normal physics-controlled mesh consisting of 262874 elements. The increased hydrostatic pressure in the basal channel suggests that ultrafiltration should occur within the device. By computing the surface integral of the velocity profile at the membrane surface, a flow rate of 2.21 μL/min was observed in the computational model. This result was confirmed experimentally by comparing the volume change in the apical and basal reservoirs after continuous perfusion overnight. In this setup, a peristaltic pump was implemented to recirculate

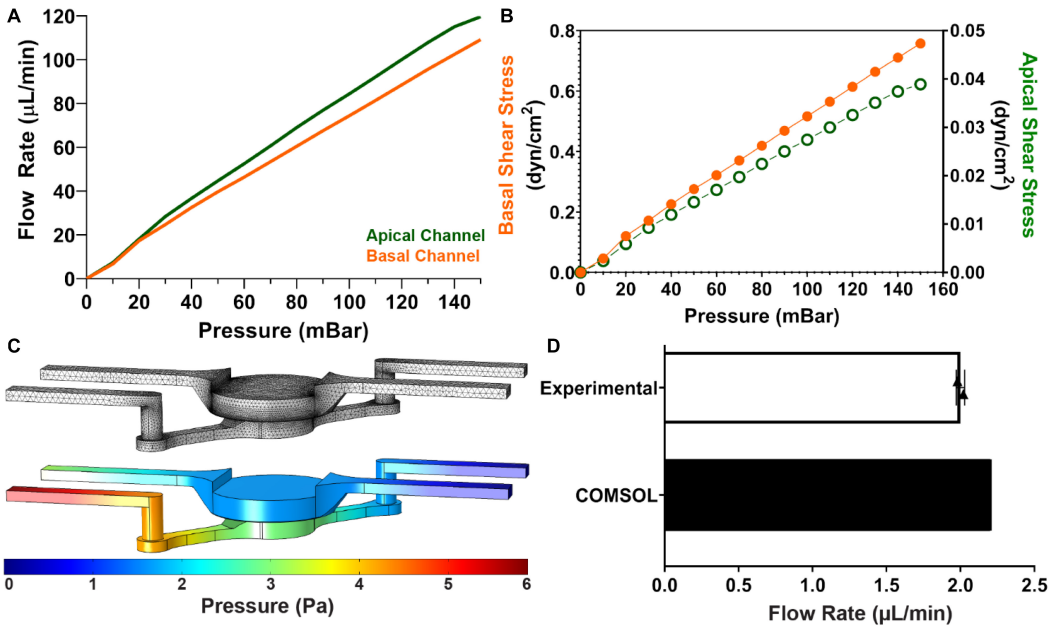

FIGURE 3 | Characterization of Fluid Dynamics in MPS: **(A)** Cartoon of how glomerular anatomy was modeled within the MPS. Created with BioRender.com. **(B)** Calculated wall fluid shear stress at the center of the culture well in apical and basal channels. Here, the differences in geometry results in an order of magnitude difference in shear stress. **(C)** 3D computational fluid dynamics simulation in microfluidic chip. The top image is the mesh implemented for finite element analysis. The bottom image is the 3D volume view of steady state pressure field in MPS at 100 µL/min inlet flow rate in the apical and basal channels. **(D)** Fluid flow rate through the membrane separating the apical and basal flow channels determine experimentally and computationally using COMSOL.

fluid, ensure a constant flow rate, and mimic steady state conditions (**Figure 3D**).

Functional Modeling of the Glomerular Filtration Barrier

To validate that the microfluidic device can recapitulate a functional biologic barrier, a model of the GFB was developed and assessed for albumin filtration. The filtration unit of the kidney, the nephron, begins in the highly selective glomerulus. The GFB is comprised of fenestrated glomerular endothelium and the glomerular epithelial cells, podocytes, separated by the unique glomerular basement membrane (**Figure 4A**). A co-culture of CiPodos and GMECs was established using a permeable membrane cell culture insert (**Figure 4B**). CiPodos were first seeded on the apical side of the membrane and cultured for 48 h under permissive conditions (33°C, 5% CO_2). GMECs were then seeded on the basal side of the membrane and the co-culture were shifted to standard culture conditions (37°C, 5% CO_2).

During the static culture in standard conditions, the integrity of the cellular layers was monitored through TEER measurements. TEER measures the electrical resistance across cellular layers to confirm barrier integrity of prior to evaluation of permeability to specific molecules (Srinivasan et al., 2015). Generally, TEER measurement provides a way to approximate cell coverage of the membrane. Under standard culture conditions, the CiPodos terminally differentiate and stop proliferating. As a result, only a slight increase in TEER is observed when podocytes are cultured alone (**Figure 4C**). On the other hand, GMECs will continue to proliferate when cultured at 37°C, resulting in a more confluent cellular barrier (**Figure 4C**). Therefore, a larger increase in TEER is observed over the course of the culture. As expected, a large increase in TEER was also observed in the co-culture of CiPodos and GMECs. Further, the final TEER measurement of the co-culture was just slightly higher than the TEER measurement of GMECs alone.

To assess the ability of the co-culture model to recapitulate the physiological function of the GFB, an albumin filtration assay was performed. Physiomimetic pressure driven flow was applied to perfusion PBS through the device for 1 h. Based on the results of the flow characterization, we were able to recreate the hydrostatic pressure of the glomerular microenvironment by applying 80 mbar (approximately 60 mmHg) to the basal flow channel and 20 mbar (approximately 15 mmHg) to apical flow channel. The basal flow channel was supplemented with bovine serum albumin (2 mg/mL) to mimic the oncotic pressure gradient. Compared to a blank membrane (i.e., no cells), all three cell models significantly reduced the urinary filtration of albumin (**Figure 4D**). Interestingly, the urinary filtration of albumin was also significantly less in the co-culture model compared to GMECs only, despite similar TEER measurements. These results highlight the importance of the cross-communication between endothelial cells and podocytes, which has been shown to be crucial in the regulation of the GFB (Dimke et al., 2015). Immunocytochemistry revealed that the functional proteins were present in the cells on both the basal and apical sides of the

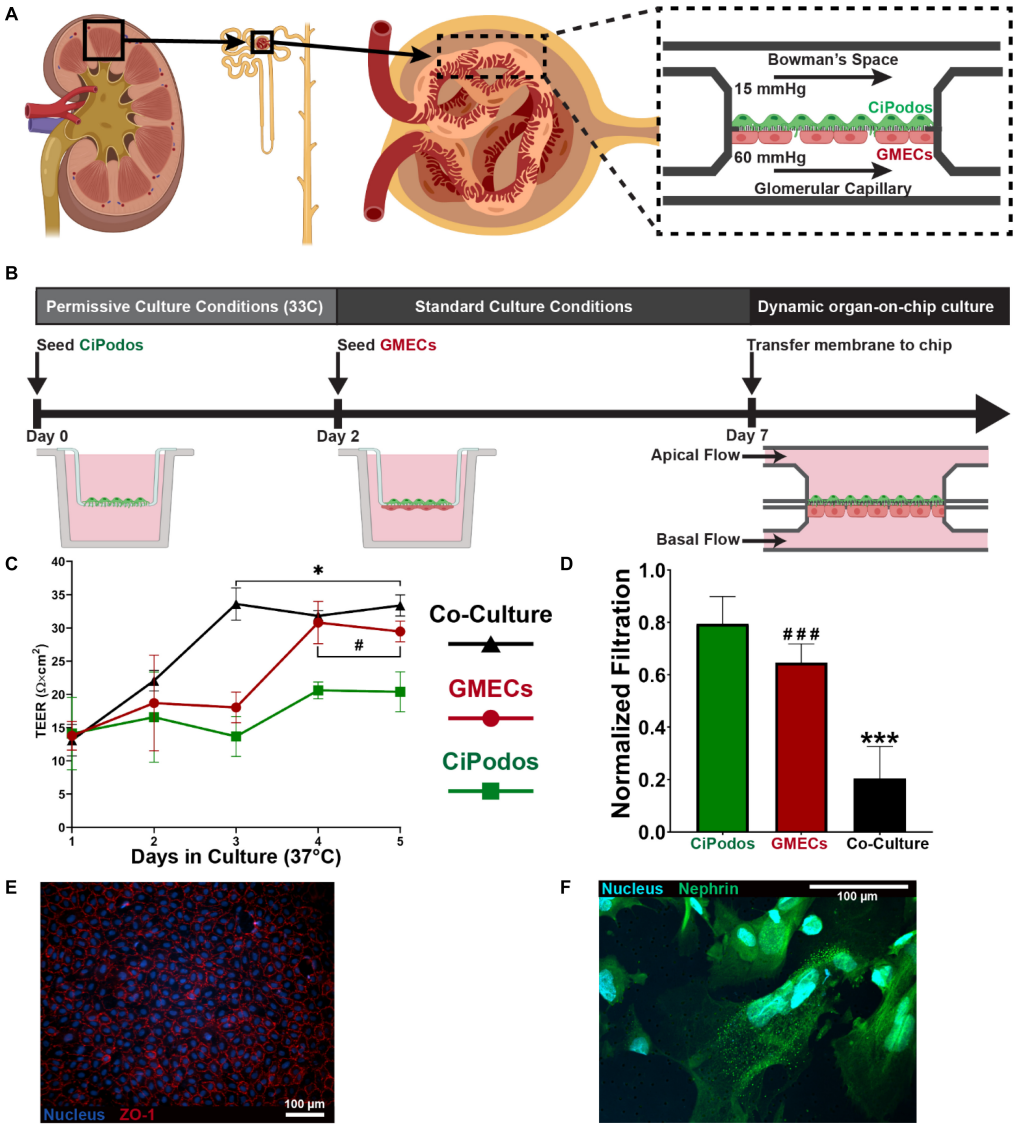

FIGURE 4 | Modeling glomerular filtration barrier; **(A)** Cartoon of how glomerular anatomy was modeled within the MPS **(B)** Schematic representation of the workflow for the development of the co-culture model of the GFB. **(C)** TEER measurements of podocytes only (Green), endothelial cells only (Red), and co-culture (black) during static culture on a transwell insert over the course of 5 days. Data presented as mean ± standard deviation. Statistical analysis by unpaired t-test ($N = 3$; * indicates Co-Culture vs. CiPodos; # indicates GMECs vs. CiPodos). $^{*}p < 0.05$, $^{\#}p < 0.05$. **(D)** Urinary filtration of albumin in 1 h on the microfluidic device. The significant decrease in the urinary filtration of albumin between the co-culture, despite similar TEER values, indicates a functional barrier as opposed to a physical barrier. Statistical analysis by one-way ANOVA with Tukey's multiple comparisons ($N = 5$; * indicates Co-Culture vs. CiPodos; # indicates GMECs vs. CiPodos). $^{***}p < 0.0001$, $^{\#\#\#}p < 0.0001$. **(E)** Tight junctions observed in endothelial cells following culture on the MPS **(F)** Presence of nephrin in CiPodos after culture in the MPS.

membrane. In the endothelial cells, ZO-1 staining indicated the tight junctions (**Figure 4E**). Nephrin, a protein required for proper GFB function, was observed in the CiPodos on the apical side of the membrane (**Figure 4F**).

Sphingolipid Exposure Alters Albumin Filtration

Sphingolipids have been shown to be important second messengers in cellular processes such has growth and apoptosis (Olivera and Spiegel, 1993; Kaipia et al., 1996). S1P, which is generated by phosphorylation of sphingosine, has been indicated to play a role in many diseases, including diabetic kidney disease (Maceyka et al., 2012; Merscher and Fornoni, 2014). Podocytes play a significant role in the filtration of albumin at the GFB (Brinkkoetter et al., 2013). Dysfunction of podocytes can lead to albuminuria, which is a hallmark of kidney disease. In addition, deficiency of sphingosine 1 phosphate lyase in mice (Schümann et al., 2015) and humans (Lovric et al., 2017) has been associated to the development of podocyte injury and albuminuria. To

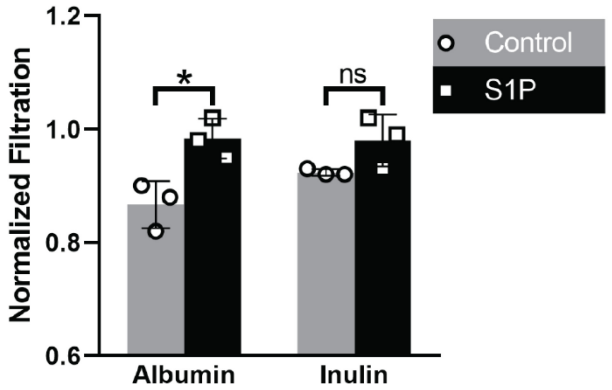

FIGURE 5 | Effect of S1P on Podocyte Filtration: Urinary filtration of albumin was increased as a result of exposure to S1P. Urinary filtration of inulin, which is freely filtered at the GFB, was not significantly altered. Statistical analysis by unpaired *t*-test ($N = 3$, $^*p < 0.05$).

elucidate the effect of S1P podocytes' ability to maintain a functional filtration barrier, cells were exposure to 5 μM S1P for 1 h and then assessed for filtration function. A significant increase the urinary filtration of albumin was observed after just 1 h of exposure to 5 μM S1P (**Figure 5**). Urinary filtration of inulin, which is freely filtered at the GFB, was not significantly altered due to exposure to S1P. The observed change in albumin filtration after exposure to S1P suggests that exposure to this specific active sphingolipid may be sufficient to cause podocyte dysfunction, resulting in albuminuria.

DISCUSSION AND CONCLUSION

For many organs, such as the lung and kidney, the functional unit is a biologic barrier. As a result, modeling of barrier function has been the primary focus of many organ-on-chip devices. The overall design of the microfluidic device is analogous to many biologic barriers and organ-on-chip devices. One the earliest organs-on-chips, a lung-on-chip, was developed using PDMS (Huh et al., 2010). However, PDMS absorption of small molecules is problematic for drug discovery assays (van Meer et al., 2017). Two independent flow channels are separated by a porous membrane that can support the culture of an endothelial and epithelial cell layer. The fabrication of stacked channels is relatively straightforward when using additive manufacturing techniques, such as soft lithography or 3D printing. Through these methods, devices can be assembled in layers either through bonding or material deposition. However, SRP, like all fabrication methods, offers benefits and challenges for the fabrication of microfluidic devices. Since material must be removed, it can be difficult to achieve closed channels at different heights within the device. This challenge has been overcome through the resealable form-factor implemented in the device design and the incorporation of an oxygen-permeable membrane to seal the basal channel. Although, a silicone-based adhesive is utilized in this design, it is not in direct contact with fluid which significantly reduces the potential for absorption or leaching. Further, SRP via micromilling presents advantages in terms of start-up cost, time, and versatility (Guckenberger et al., 2015). Specifically, the acrylic MPS described in this work can be completely fabricated relatively quickly (approximately 6 h) compared to similar PDMS microfluidic chips (approximately 40 h) (Huh et al., 2013). To achieve the same precision and optical using 3D printing would require more expensive and specialized equipment and materials. Here, we demonstrate that these advantages of SRP can be utilized to fabricate a highly functional MPS.

Independent perfusion of the two-channels was achieved using two microfluidic pressure pumps. Pressure-driven flow control provides many advantages over other methods, including stable, pulseless flow, fast response time, and precise flow rate control. Further, the use of pressurized air facilitated the implementation of cyclic air flow to stretch the porous membrane and mimic the human breathing cycle. We demonstrated the ability to create an air-liquid interface co-culture model that can be incorporated into the microfluidic device. Pressure-driven flow also facilitated the generation of hydrostatic pressure gradients, like those that are found at the glomerular filtration barrier. Together, the versatility of the platform enables recapitulation of multiple *in vivo* microenvironments.

The final proof-of-concept experiment for the microfluidic device design was to model the filtration function of the glomerulus. This was achieved by culturing the glomerular endothelial and epithelial cells on a porous membrane which could be transferred into the MPS. We also demonstrated that the ability of podocytes to effectively filter albumin can be directly modulated by exposure to sphingolipids. A significant limitation of traditional static culture systems is the inability to recapitulate organ-level function. The microfluidic device to model biologic barriers enables filtration assays to functionally assess podocytes. Despite the model being limited to just podocytes in the present study, a significant increase was observed in urinary filtration of albumin after exposure to S1P, thus setting the basis for the development of an assay to be utilized for clinically relevant drug discovery in proteinuric kidney diseases. Future studies will focus on recapitulating a more complete GFB by incorporating endothelial cells and a basement membrane. Albumin is one of the most abundant proteins in human blood and the loss of albumin via the urine is a key clinical marker for glomerular diseases. We demonstrate that under physiologically relevant pressures, the co-culture of GMECs and CiPodos can effectively prevent urinary filtration of albumin. In the present model, however, urinary filtration of albumin was not minimized to levels that would be translatable to a clinical setting. This may be attributed to the cell source or the lack of a basement membrane components. The GFB is a complex, highly selective filter and future work will be necessary to improve upon the biologic components.

In conclusion, we report the design and fabrication of a PDMS-free microfluidic device that can recapitulate many of the dynamic stimuli originally described for organs-on-chips. We implemented a resealable form-factor to incorporate a porous

membrane that can support the culture of an endothelial and epithelial cell layer and an oxygen-permeable membrane to seal the basal channel. The versatility of the design was demonstrated by constructing an alveolar air-liquid interface with cyclic stretching to mimic lung breathing and by modeling selective filtration by the kidney at the GFB with a physiomimetic pressure gradient. We establish the utility of the modular MPS design by recapitulating sphingolipid injury to the GFB. Together, our results demonstrate that a multifunctional and modular microphysiological system can be deployed without the use of PDMS. Further, the bio-inert plastic used in our microfluidic device is amenable to various established, high-throughput manufacturing techniques, such as injection molding, to meet the increasing demand for organ-on-chip technology.

DATA AVAILABILITY STATEMENT

The data supporting the findings of this manuscript are available from the corresponding authors upon reasonable request.

AUTHOR CONTRIBUTIONS

MI designed the experiments and wrote the manuscript with the help of AF and AA. MI and JH designed and fabricated the MPS. MI, QA, and LW performed the cell culture. MI and AH performed the membrane strain experiments. AM, AS, and AF provided expertise, cells, and reagents for glomerular filtration experiments. All authors reviewed, edited, and approved the final version of the manuscript.

FUNDING

This work was supported by NIDDK-supported Human Islet Research Network (HIRN, RRID: SCR_014393; https://hirnetwork.org; UC4DK104209 and UG3DK122638 to AA). MI was supported by F31DK118860-01A1. AF was supported by the NIH grants R01DK117599, R01DK104753, R01CA227493, U54KD083912, UM1DK100846, U01DK116101, and UL1TR000460 (Miami Clinical Translational Science Institute).

REFERENCES

Becker, H., and Locascio, L. E. (2002). Polymer microfluidic devices. *Talanta* 56, 267–287. doi: 10.1016/s0039-9140(01)00594-x

Berthier, E., Young, E. W., and Beebe, D. (2012). Engineers are from PDMS-land. *Biologists are from Polystyrenia. Lab Chip* 12, 1224–1237. doi: 10.1039/c2lc20982a

Bhatia, S. N., and Ingber, D. E. (2014). Microfluidic organs-on-chips. *Nat. Biotechnol.* 32, 760–772. doi: 10.1038/nbt.2989

Brinkkoetter, P. T., Ising, C., and Benzing, T. (2013). The role of the podocyte in albumin filtration. *Nat. Rev. Nephrol.* 9, 328–336. doi: 10.1038/nrneph.2013.78

Chung, H. H., Mireles, M., Kwarta, B. J., and Gaborski, T. R. (2018). Use of porous membranes in tissue barrier and co-culture models. *Lab Chip* 18, 1671–1689. doi: 10.1039/C7LC01248A

Dimke, H., Maezawa, Y., and Quaggin, S. E. (2015). Crosstalk in glomerular injury and repair. *Curr. Opin. Nephrol. Hypertens.* 24:231.

Duffy, D. C., McDonald, J. C., Schueller, O. J., and Whitesides, G. M. (1998). Rapid Prototyping of Microfluidic Systems in Poly(dimethylsiloxane). *Anal. Chem.* 70, 4974–4984. doi: 10.1021/ac980656z

Guckenberger, D. J., de Groot, T. E., Wan, A. M., Beebe, D. J., and Young, E. W. (2015). Micromilling: a method for ultra-rapid prototyping of plastic microfluidic devices. *Lab Chip* 15, 2364–2378. doi: 10.1039/c5lc00234f

Guenat, O. T., and Berthiaume, F. (2018). Incorporating mechanical strain in organs-on-a-chip: Lung and skin. *Biomicrofluidics* 12:042207. doi: 10.1063/1.5024895

Huh, D., Fujioka, H., Tung, Y. C., Futai, N., Paine, R. III, Grotberg, J. B., et al. (2007). Acoustically detectable cellular-level lung injury induced by fluid mechanical stresses in microfluidic airway systems. *Proc. Natl. Acad. Sci. U S A.* 104, 18886–18891. doi: 10.1073/pnas.0610868104

Huh, D., Kim, H. J., Fraser, J. P., Shea, D. E., Khan, M., Bahinski, A., et al. (2013). Microfabrication of human organs-on-chips. *Nat. Protoc.* 8, 2135–2157. doi: 10.1038/nprot.2013.137

Huh, D., Matthews, B. D., Mammoto, A., Montoya-Zavala, M., Hsin, H. Y., and Ingber, D. E. (2010). Reconstituting organ-level lung functions on a chip. *Science* 328, 1662–1668. doi: 10.1126/science.1188302

Kaipia, A., Chun, S. Y., Eisenhauer, K., and Hsueh, A. J. (1996). Tumor necrosis factor-alpha and its second messenger, ceramide, stimulate apoptosis in cultured ovarian follicles. *Endocrinology* 137, 4864–4870. doi: 10.1210/endo.137.11.8895358

Lenguito, G., Chaimov, D., Weitz, J. R., Rodriguez-Diaz, R., Rawal, S. A., Tamayo-Garcia, A., et al. (2017). Resealable, optically accessible. PDMS-free fluidic platform for ex vivo interrogation of pancreatic islets. *Lab Chip* 17, 772–781. doi: 10.1039/c6lc01504b

Lovric, S., Goncalves, S., Gee, H. Y., Oskouian, B., Srinivas, H., Choi, W.-I., et al. (2017). Mutations in sphingosine-1-phosphate lyase cause nephrosis with ichthyosis and adrenal insufficiency. *J. Clinic. Investigat.* 127, 912–928.

Lu, W., Lillehoj, E. P., and Kim, K. C. (2005). Effects of dexamethasone on Muc5ac mucin production by primary airway goblet cells. *Am. J. Physiol. Lung Cell. Mol. Physiol.* 288, L52–L60. doi: 10.1152/ajplung.00104.2004

Maceyka, M., Harikumar, K. B., Milstien, S., and Spiegel, S. (2012). Sphingosine-1-phosphate signaling and its role in disease. *Trends Cell Biol.* 22, 50–60. doi: 10.1016/j.tcb.2011.09.003

McDonald, J. C., and Whitesides, G. M. (2002). Poly(dimethylsiloxane) as a material for fabricating microfluidic devices. *Acc. Chem. Res.* 35, 491–499. doi: 10.1021/ar010110q

Merscher, S., and Fornoni, A. (2014). Podocyte pathology and nephropathy - sphingolipids in glomerular diseases. *Front. Endocrinol.* 5:127. doi: 10.3389/fendo.2014.00127

Musah, S., Mammoto, A., Ferrante, T. C., Jeanty, S. S. F., Hirano-Kobayashi, M., Mammoto, T., et al. (2017). Mature induced-pluripotent-stem-cell-derived human podocytes reconstitute kidney glomerular-capillary-wall function on a chip. *Nat. Biomed. Eng.* 1:0069. doi: 10.1038/s41551-017-0069

Olivera, A., and Spiegel, S. (1993). Sphingosine-1-phosphate as second messenger in cell proliferation induced by PDGF and FCS mitogens. *Nature* 365, 557–560. doi: 10.1038/365557a0

Saleem, M. A., O'Hare, M. J., Reiser, J., Coward, R. J., Inward, C. D., Farren, T., et al. (2002). A conditionally immortalized human podocyte cell line demonstrating nephrin and podocin expression. *J. Am. Soc. Nephrol.* 13, 630–638.

Schindelin, J., Arganda-Carreras, I., Frise, E., Kaynig, V., Longair, M., Pietzsch, T., et al. (2012). Fiji: an open-source platform for biological-image analysis. *Nat. Methods* 9, 676–682. doi: 10.1038/nmeth.2019

Schümann, J., Grevot, A., Ledieu, D., Wolf, A., Schubart, A., Piaia, A., et al. (2015). Reduced activity of sphingosine-1-phosphate lyase induces podocyte-related glomerular proteinuria, skin irritation, and platelet activation. *Toxicol. Pathol.* 43, 694–703. doi: 10.1177/0192623314565650

Sia, S. K., and Whitesides, G. M. (2003). Microfluidic devices fabricated in poly(dimethylsiloxane) for biological studies. *Electrophoresis* 24, 3563–3576. doi: 10.1002/elps.200305584

Sip, C. G., Bhattacharjee, N., and Folch, A. (2014). Microfluidic transwell inserts for generation of tissue culture-friendly gradients in well plates. *Lab Chip* 14, 302–314. doi: 10.1039/C3LC51052B

Srinivasan, B., Kolli, A. R., Esch, M. B., Abaci, H. E., Shuler, M. L., and Hickman, J. J. (2015). TEER measurement techniques for in vitro barrier model systems. *J. Lab. Autom.* 20, 107–126. doi: 10.1177/2211068214561025

van Meer, B. J., de Vries, H., Firth, K. S. A., van Weerd, J., Tertoolen, L. G. J., Karperien, H. B. J., et al. (2017). Small molecule absorption by PDMS in the context of drug response bioassays. *Biochem. Biophys. Res. Commun.* 482, 323–328. doi: 10.1016/j.bbrc.2016.11.062

Conflict of Interest: MI and AA are co-founders of Bio-Vitro, which is in the process of licensing the underlying IP for the microfluidic chip described. AF is an investor on pending or issued patents (US 10,183,038 and US 10,052,345) aimed at diagnosing or treating proteinuric kidney diseases. She stands to gain royalties from the future commercialization of these patents. She is Chief Scientific Officer of L&F Health LLC and is a consultant for Variant Pharmaceuticals. Variant Pharmaceuticals has licensed worldwide rights from L&F Research to develop and commercialize hydroxypropyl-beta-cyclodextrin for the treatment of kidney disease.

The remaining authors declare that the research was conducted in the absence of any commercial or financial relationships that could be construed as a potential conflict of interest.

frontiers in Bioengineering and Biotechnology

ORIGINAL RESEARCH
published: 22 December 2020
doi: 10.3389/fbioe.2020.612091

Proteomic Reveals Reasons for Acquired Drug Resistance in Lung Cancer Derived Brain Metastasis Based on a Newly Established Multi-Organ Microfluidic Chip Model

Mingxin Xu[1†], *Yingyan Wang*[2†], *Wenzhe Duan*[1†], *Shengkai Xia*[1†], *Song Wei*[1], *Wenwen Liu*[3*] *and Qi Wang*[1,3*]

[1] Department of Respiratory Medicine, The Second Hospital, Dalian Medical University, Dalian, China, [2] Laboratory Center for Diagnostics, Dalian Medical University, Dalian, China, [3] Cancer Translational Medicine Research Center, The Second Hospital, Dalian Medical University, Dalian, China

OPEN ACCESS

Edited by:
Shang-Chun Guo,
Shanghai Jiao Tong University, China

Reviewed by:
Michele Balsamo,
Kayser, Italy
Fei-Ting Hsu,
China Medical University, Taiwan

***Correspondence:**
Wenwen Liu
liuwenwenphd@163.com
Qi Wang
wqdlmu@163.com

[†] These authors have contributed equally to this work

Specialty section:
This article was submitted to Nanobiotechnology, a section of the journal Frontiers in Bioengineering and Biotechnology

Received: 30 September 2020
Accepted: 25 November 2020
Published: 22 December 2020

Citation:
Xu M, Wang Y, Duan W, Xia S, Wei S, Liu W and Wang Q (2020) Proteomic Reveals Reasons for Acquired Drug Resistance in Lung Cancer Derived Brain Metastasis Based on a Newly Established Multi-Organ Microfluidic Chip Model. Front. Bioeng. Biotechnol. 8:612091. doi: 10.3389/fbioe.2020.612091

Anti-tumor drugs can effectively shrink the lesions of primary lung cancer; however, it has limited therapeutic effect on patients with brain metastasis (BM). A BM preclinical model based on a multi-organ microfluidic chip has been established proficiently in our previous work. In this study, the BM subpopulation (PC9-Br) derived from the parental PC9 cell line was isolated from the chip model and found to develop obvious resistance to antineoplastic drugs including chemotherapeutic agents (cisplatin, carboplatin, pemetrexed) and tyrosine kinase inhibitors (TKIs) which target epidermal growth factor receptor (EGFR); this suggested that the acquisition of drug-resistance by brain metastatic cells was attributable to the intrinsic changes in PC9-Br. Hence, we performed proteomic and revealed a greatly altered spectrum of BM protein expression compared with primary lung cancer cells. We identified the hyperactive glutathione (GSH) metabolism pathway with the overexpression of various GSH metabolism-related enzymes (GPX4, RRM2, GCLC, GPX1, GSTM4, GSTM1). Aldehyde dehydrogenases (ALDH1A1, ALDH3A1) were also found to be upregulated in BM. What's more, loss of EGFR and phosphorylated EGFR in PC9-Br gave reasons for the TKIs resistance. Collectively, our findings indicated potential mechanisms for the acquirement of drug resistance occurred in BM, providing new strategies to overcome therapeutic resistance in lung cancer BM.

Keywords: lung cancer, brain metastasis, microfluidic organ-on-a-chip, drug resistance, proteomic

INTRODUCTION

Lung cancer has been the most common cause of cancer death worldwide with high morbidity and mortality (Siegel et al., 2019). Non-small cell lung cancer (NSCLC), as the most common pathological type of lung cancer with the proportion of 85%, is characterized by a high incidence of distant metastasis within which brain metastasis (BM) accounts for 40% (Steeg et al., 2011; Ali et al., 2013). The prognosis of BM patients is extremely poor with a median survival time of only 4–6 months due to limited treatment alternations (Cheng and Perez-Soler, 2018). Currently available

therapeutic approaches for BM include a combination of surgery, radiotherapy, chemotherapy, molecular targeted therapy, or anti-angiogenesis therapy, as applicable; however, the therapeutic efficacy is particularly poor (Shi et al., 2017).

Drug treatments which mainly based on chemotherapy is an indispensable treatment for BM patients since there are very limited therapeutic indications for surgery and radiation therapy (Yousefi et al., 2017; Achrol et al., 2019), however, the drug response rate in BM populations is extremely low (Sandler et al., 2000; Schiller et al., 2002; Barlesi et al., 2011; Bailon et al., 2012). It is believed that there are two main factors which contribute to the poor efficacy of drug therapy against BM: the presence of blood-brain barrier (BBB) and tumor-intrinsic changes induced by metastasis events. BBB provides a sanctuary site for tumor to escape drug treatment as the barrier can significantly prevent the penetration of anti-tumor drugs into both tumor and brain tissues. However, recent studies have proposed that the disruption of BBB during BM enables the invasion and colonization of tumor cells in brain parenchyma (Li et al., 2012; Liu et al., 2019), suggesting that the barrier which hinder the entry of drugs was impaired during BM. This holds the point that endogenous alteration of metastatic cells may play a vital role in the acquisition of drug resistance. However, it remains unknown to a large extent.

Traditional research models of tumor brain metastasis were established by injecting tumor cells into the left cardiac ventricle of athymic nude mice. Brain metastasis cells (BrMs) derived from parental tumor cells were subsequently isolated from extracted brain metastases (Bos et al., 2009; Liu et al., 2019; Shah et al., 2020). Although BrMs were proved to possess enriched BM properties, the cells did not undergo the whole BM pathological process since the progression of tumor cells *in situ* was skipped. It has to be admitted that intracardiac injection is a better choice to initiate BM efficiently than orthotopic injection. Under the condition of orthotopic injection, animals often die before brain metastasis occurs since they cannot bear the tumor load *in situ*. Hence, there is an urgent need for a reliable and efficient model which can faithfully mimic the entire BM process. Recently, microfluidic organ-on-a-chips have been developed and applied as powerful tools for medical research, enabling the creation of more *in vivo*-like *in vitro* models with high throughput (Ashammakhi et al., 2020; Ding et al., 2020; Moradi et al., 2020; Steinway et al., 2020). In our previous work, a multi-organ microfluidic chip, which consists of two organ chip units–an upstream "lung" and a downstream "brain" unit, was established and proved to be able to effectively reproduce the whole pathological process of lung cancer BM, providing a novel model for BM research (Liu et al., 2019).

In this study, we isolated the brain metastatic cells (PC9-Br) from the metastases on the BM chip and found that PC9-Br developed a significant resistance to multiple anti-tumor drugs compared with its parental PC9 cells. Further proteomic was carried out to reveal possible reasons for the acquirement of drug resistance in the BM, followed by the selection of differentially expressed proteins by western blotting validation. We found the glutathione (GSH) metabolism pathway, which plays an important role in intracellular antioxidant stress response, was remarkably hyperactive in BM, along with the overexpression of a series of GSH metabolism-related enzyme (GPX4, RRM2, GCLC, GPX1, GSTM4, GSTM1). Aldehyde dehydrogenases (ALDH1A1, ALDH3A1), which have been reported to mediate the acquired drug resistance of tumor cells, were also found to be upregulated in BM. What's more, reduced expression of epidermal growth factor receptor (EGFR) and phosphorylated EGFR gave a reasonable explanation for the EGFR targeted drugs resistance of PC9-Br compared with PC-9 parental cells.

MATERIALS AND METHODS

Cell Culture and Drugs

The human lung cancer cell line PC9 was used as the primary lung cancer model and parental cells of BM derivative (PC9-Br) on the chip. To establish the bionic microenvironment for primary lung cancers and secondary BM of lung cancers, human bronchial epithelial cells (16HBE), human pulmonary microvascular endothelial cells (hPMEC), human lung fibroblasts (HFL1), and human mononuclear cells (THP-1) were co-cultured in the upstream "lung" unit while human astrocytes (HA-1800) and human brain microvascular endothelial cells (hBMVEC) were co-cultured dynamically in the downstream "brain" unit as previously reported (Xu et al., 2016; Liu et al., 2019). The purchase sources and culture conditions of all cell lines have also been- described in detail previously (Liu et al., 2019).

Cisplatin (MB1055), Carboplatin (MB1297), Paclitaxel (MB1178), Pemetrexed Disodium (MB1183), Etoposide (MB1102), Gefitinib (MB1112) and AZD3759 (MB4776) were purchased from Meilunbio (China).

Construction and Operation of the Multi-Organ Microfluidic Chip Model to Mimic the Pathological Process From Primary Lung Cancer to Brain Metastasis

It has been described in detail in our previous work (Xu et al., 2016; Liu et al., 2019). In short, after the establishment of upstream bionic "lung" and downstream bionic "brain," human lung cancer cells PC9 which stably express green fluorescent protein (GFP)-luciferase fusion protein, were introduced into the upstream unit to form primary lung cancer model. After the growth, transition and invasion on the upper stream "lung," primary PC9 cells invaded the circulation and were transported to the downstream "brain" along with the dynamic fluid medium. Then metastatic cells attached to and trans-migrate through BBB structure, colonized in brain parenchyma and finally formed brain metastases. The entire BM process on the chip was dynamically monitored with an Olympus IX81 fluorescence microscope (Olympus Corporation, Japan).

Extraction and Isolation of Brain Metastatic Cells of Parental Lung Cancer Cells PC9 (PC9-Br) From Chips

Dovetail clips were used to completely block the connecting passage between upstream and downstream unit. A syringe pump (Pump 11 Elite Series Pumps, USA) was connected to the

injection port of brain parenchymal chamber to drive the flow of 0.25% trypsin-EDTA solution (Gibco, Invitrogen, Inc, USA) at the speed of 0.1 μl/min, while a sterile collection tube was connected to the outlet of brain parenchymal chamber to collect the mixed cell suspensions of brain metastases. After collection, complete medium was added into the tube to stop digestion. A mixed mass of various cells was obtained through centrifuge. Then the BM derivative cells (PC9-Br) of parental PC9 were isolated by GFP fluorescence sorting with a flow cytometer (FACSAriaTMII, BD, USA) and transferred to cell culture dish for routine culture. The sorting efficiency was verified with a fluorescence microscope.

Invasion Assay

Twenty-five thousand cells in 200 μl serum-free medium were seeded into matrigel-coated top chamber of 24-well Transwell inserts (#3422, Corning, USA) while the bottom chambers were filled with 500 μl complete medium. After 24 h the non-invading cells on the upper side were removed with cotton swabs and the invaded cells on the lower surface of the insert were fixed with 4% paraformaldehyde and stained with 0.5% crystal violet (KeyGEN BioTECH Corp., Ltd, China). Images were captured with a microscope (Leica, TCSSP5II). The invaded cells in five random fields of one image were counted and the invasion ability was standardized by making a ratio of PC9-Br invaded cell number to the parental PC9 invaded cell number (100%).

Trans-Endothelial Assay

Twenty thousand were seeded and cultured on the fibronectin-coated 24-well Transwell inserts (#3422, Corning, USA) for 72 h and allowed to form an integrated endothelial mono-layer. Then 25,000 cancer cells in 200 μl serum-free medium were seeded on the insert above the endothelial monolayer while 250 μl complete medium was added to the lower side. After 36 h of culture, the cells on the upper side were removed with cotton swabs and the trans-migrated cells on the lower surface of the insert were fixed with 4% paraformaldehyde and stained with crystal violet (KeyGEN BioTECH Corp., Ltd, China). Images were captured with a microscope (Leica, TCSSP5II). The trans-migrated cells in five random fields of one image were counted and trans-endothelial ability was standardized by making a ratio of PC9-Br trans-migrated cell number to the parental PC9 trans-migrated cell number (100%).

Animal Study

The animal study was reviewed and approved by the Animal Ethics Review Committee of Dalian Medical University (No.00122773). Female BALB-c-nu mice (4–6 weeks) were obtained from the Beijing Vital River Laboratory Animal Technology Co. Ltd., China.

Each mouse was anesthetized with ketamine (100 mg/kg body weight; Sigma, USA) and xylazine (10 mg/kg body weight; Sigma, USA) and then inoculated with 1,000,000 PC9 or PC9-Br cells in 100 μl PBS by intracardiac injection. The BM events in mice were recognized by bioluminescence imaging (BLI) with an IVIS Spectrum Xenogen machine (PerkinElmer, USA) as previously described (Xu et al., 2016; Liu et al., 2019). In brief, after mice were anesthetized and injected retro-orbitally with D-Luciferin (150 mg/kg body weight; Promega, USA), images were obtained and analyzed with Living Image software (version 2.50).

Cell Viability Assay

Cell Counting Kit-8 (CCK8, K1018, ApexBio, USA) was used to assess cell viability according the manufacturer's instructions. Briefly, 5,000 cells were seeded to each well of 96-well plates and allowed to adhere to the wall. Then the culture medium was removed and cells were treated with specific drugs for 72 h. CCK8 solution was added to each well and incubated for 2 h at 37°C in the dark following the instructions. Color change was measured at 450 nm with a microtiter plate reader, and the OD value was observed to be directly proportional to cell viability.

Quantitative Tandem Mass Tag (TMT)-Based Proteomics

This work was supported by the Jingjie PTM BioLab (Hangzhou, China) Co. Ltd. Main experimental procedures of TMT proteomics analysis, including protein extraction, trypsin digestion, TMT labeling, HPLC fractionation, LC-MS/MS analysis, database search and bioinformatics analysis, are presented in the Supplementary methods in detail.

Western Blot

RIPA cell lysis buffer containing a protease inhibitor cocktail (Meilunbio, China) and a phosphatase inhibitor cocktail (Sigma, USA) was used to dissolve proteins extracted from cells. The BCA assay kit (Thermo Fisher Scientific Inc., USA) was used to measure the protein concentration. Protein lysates were then separated by sodium dodecyl sulfate-polyacrylamide gel electrophoresis (SDS-PAGE) and transferred onto nitrocellulose membranes (Millipore, Billerica, USA). The membranes were blocked in 5% skimmed milk solution in 0.05% Tris-buffered saline/Tween-20 (TBST) and then incubated with primary antibodies against GPX4 (1:1,000 dilution; ab125066, Abcam, UK), RRM2 (1:1,000 dilution; ab57653, Abcam, UK), GCLC (1:1,000 dilution; ab190685, Abcam, UK), GPX1 (1:1,000 dilution; ab108427, Abcam, UK), GSTM4 (1:1,000 dilution; ab233281, Abcam, UK), GSTM1 (1:1,000 dilution; ab113432, Abcam, UK), ALDH3A1 (1:1,000 dilution; ab129022, Abcam, UK), ALDH1A1 (1:1,000 dilution; ab52492, Abcam, UK), EGFR (1:1,000 dilution; SB52894, Abcam, UK), p-EGFR (1:1,000 dilution; ab32430, Abcam, UK), phospho-NF-κB p65 (Ser536,1:1000 dilution; #3033, Cell signaling technology, USA) and NF-κB p65 (1:1000 dilution; #8242, Cell signaling technology, USA). After washing with 0.05% TBST, the corresponding secondary antibodies conjugated with horseradish peroxidase (1:5,000; Proteintech, China) were further used. The ECL western blotting substrate (Tanon, China) was used to analyze the chemiluminescence of the blots. Protein expression was quantified by Image J software (National Institutes of Health, USA). The tests were performed with triplicated samples to diminish variability.

Statistical Analysis

Statistical analysis was performed using GraphPad Prism software 5.0 and SPSS 16.0 statistical software package. Quantitative data are presented as mean (± standard deviation) values from at least 3 independent experiments. Differences between two groups were assessed using the *t*-test.

RESULTS AND DISCUSSION

The Brain Metastatic Derivative Isolated From BM Chip Possessed Enriched BM Activities Compared to Parental Cells *in vitro* and *in vivo*

The whole pathological process of BM was simulated on the established multi-organ microfluidic chip by introducing the parental lung cancer cells PC9 into the upstream bionic lung unit as previously reported (Liu et al., 2019), as illustrated in **Figure 1A**. The brain metastases formed in the downstream bionic brain unit were harvest and the brain metastatic populations (PC9-Br) were isolated by GFP fluorescence sorting. The sorting efficiency was assessed with cell co-imaging under the bright field and fluorescence (**Figure 1B**), ensuring that the isolated cells were GFP-expressed tumor cells rather than non-fluorescent mesenchymal cells. Then the BM activities of PC9-Br cells and corresponding parental cells were evaluated *in vitro* and *in vivo*. **Figures 1C,D** showed that PC9-Br cells exhibited stronger invasion and trans-endothelial abilities than PC9 cells. For *in vivo* experiments (**Figure 1E**, **Supplementary Figure 1**), the PC9-Br cells formed BM in 43.8% of mice with a 5–6 weeks tumor formation cycle, while the parental PC9 cells exhibited a BM efficiency of 20.0% with a 6–7 weeks tumor formation cycle. Taken together, the brain metastatic derivative isolated from BM chip possessed enriched BM activities compared to parental cells *in vitro* and *in vivo*. The results also displayed the great potential of organ-on-a-chips in constructing complicated disease models and exploring pathological mechanisms.

The Acquirement of Obvious Resistance to Multiple Anti-tumor Drugs Was Found in PC9-Br Cells

Current drug treatments for patients with lung cancer BM mainly include chemotherapy and targeted drug therapy. Platinum compounds (cisplatin and carboplatin) and pemetrexed, alone or in combination (etoposide, paclitaxel, and radiotherapy) are the most commonly used chemotherapy regimens against BMs from NSCLC (Mehta et al., 2010; Barlesi et al., 2011; Bailon et al., 2012; Shi et al., 2017; Yousefi et al., 2017; Franchino et al., 2018). Since about 33% of patients with non-small cell lung cancer (NSCLC) and EGFR mutations develop BMs, different generations of tyrosine kinase inhibitors (TKIs) were commonly used to target BMs (Burel-Vandenbos et al., 2013; Sekine and Satoh, 2017; Zhuang et al., 2019). Gefitinib is the most typical first-generation TKI and AZD3759 is characterized by its strong ability to effectively penetrate the BBB (Tan et al., 2017; Hochmair, 2018). Historically, the limited use of anti-tumor drugs in cancer patients owing to the presence of the BBB. However, recent studies have proved that the BBB was disrupted in BMs which results in an increased exposure to systemic drugs, suggesting the sensitivity of tumor cells to drugs is the main determinant of therapeutic efficacy. Hence, we explored whether there were differences in drug sensitivity between PC9-Br and PC9 by treating these two groups of cells with the above agents. Results of cell viability assay indicated that PC9-Br developed obvious resistance to platinum compound (both to cisplatin and carboplatin, **Figures 2A,B**), pemetrexed (**Figure 2C**) and TKIs (both to gefitinib and AZD3759, **Figures 2F,G**) compared with the parental PC9 group. However, there was no significant difference in the response to paclitaxel and etoposide (**Figures 2D,E**). Similar changes of drug sensitivity were found in animal model derived BM cells PC9-BrM3 (**Supplementary Figures 2A–E**), a highly brain metastasis cell line by injecting parental tumor cells PC9 into the left-ventricle of immunodeficient mice and isolating the metastatic cells from harvested brain metastases three times repeatedly in our previous work (Liu et al., 2019). Collectively, these results indicated BM cells acquired obvious resistance to multiple anti-tumor drugs. In addition, these findings strongly suggested that endogenous factors of BM cells were the culprit of the poor drug efficacy.

Proteomics Identified the Hyperactive GSH Metabolism Pathway in PC9-Br Cells

Proteomics has become a powerful and promising complementary technology to provide insights into diseases at a more phenomenological level (Altelaar et al., 2013). We employed proteomics to find the potential cellular endogenous factors resulting in the acquired drug resistance of PC9-Br compared to parental PC9 cells. **Figure 3A** showed the good reproducibility of proteomics data. Differential proteins with different ratio folds were identified. To find the potential correlation of protein functions with differential ratio folds, we divided them into 4 parts according to their ratio folds, called Q1 to Q4: Q1 ($0< \text{Ratio} \leq 1/1.3$), Q2 ($1/1.3 < \text{Ratio} \leq 1/1.2$), Q3 ($1.2 < \text{Ratio} \leq 1.3$) and Q4 ($\text{Ratio} > 1.3$). Then we performed KEGG pathway enrichment for each Q group and the results showed a number of pathways were enriched in Q4 protein group with higher ratio folds (**Figure 3C**). Further analysis was carried out on Q4 group while 200 upregulated proteins and 203 downregulated proteins were identified (**Figure 3B**). The specific enrichment results of KEGG pathways in Q4 were visualized by the number of proteins involved respectively and their corresponding p-values (**Figure 3D**). The cell cycle, DNA replication regulation and glutathione (GSH) metabolism pathway were identified to be enriched significantly in PC9-Br cells, giving potential explanations for the enhanced BM abilities, as well as the acquirement of multi-drugs resistance of PC9-Br cells. Hyperactive cell cycle and DNA replication regulations has been well-recognized as one of major malignant behaviors in tumors (Hanahan and Weinberg, 2011), contributing greatly to the proliferation of tumor cells, while GSH metabolism has been demonstrated as the main factor which cause multi-drug resistance, giving a more specific explanation for the drug

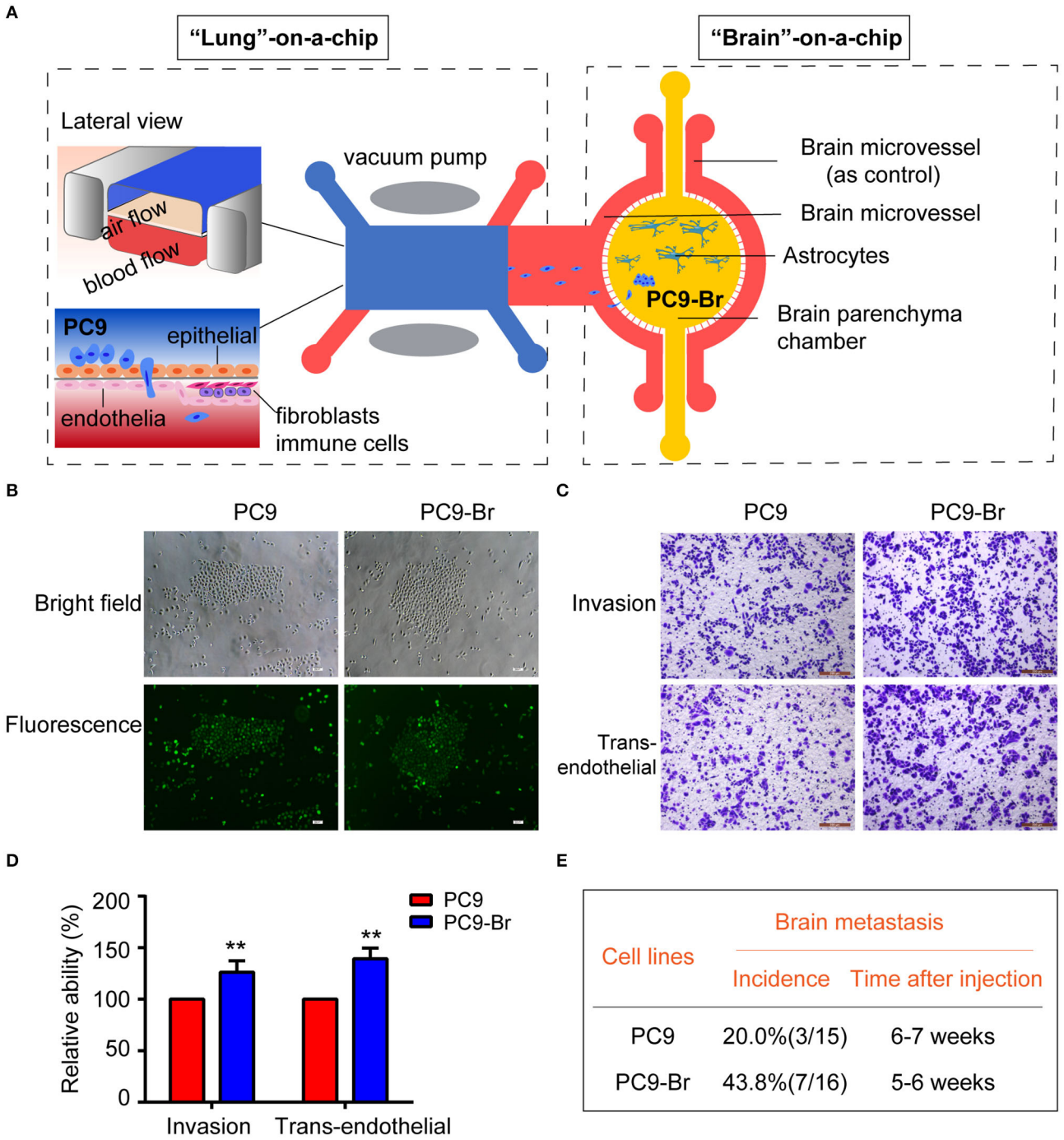

FIGURE 1 | The brain metastatic derivative isolated from BM chip possessed enriched BM activities compared to parental cells *in vitro* and *in vivo*. **(A)** Schematic illustration of the construction and operation of BM process on the multi-organ microfluidic chip as previously described (Liu et al., 2019). **(B)** Representative co-images of PC9 and PC9-Br cells under the bright field and fluorescence. Scar bar, 200 μm. **(C,D)** Representative images showing the invasion and trans-endothelial migration of the PC9 and PC9-Br cells on the Transwell (scale bar, 200 μm). $n = 3$, $^{**}p < 0.01$. **(E)** Frequency and time circle of BM after inoculation of PC9 or PC9-Br cells in nude mice.

resistance occurred in PC9-Br cells. GSH, as the most abundant antioxidant found in living organisms, plays a vital role in maintaining cellular redox homeostasis. Increasing evidence has shown that abnormal GSH metabolism is the main factor causes drug resistance by binding or reacting with drugs, interacting with reactive oxidative species (ROS), preventing

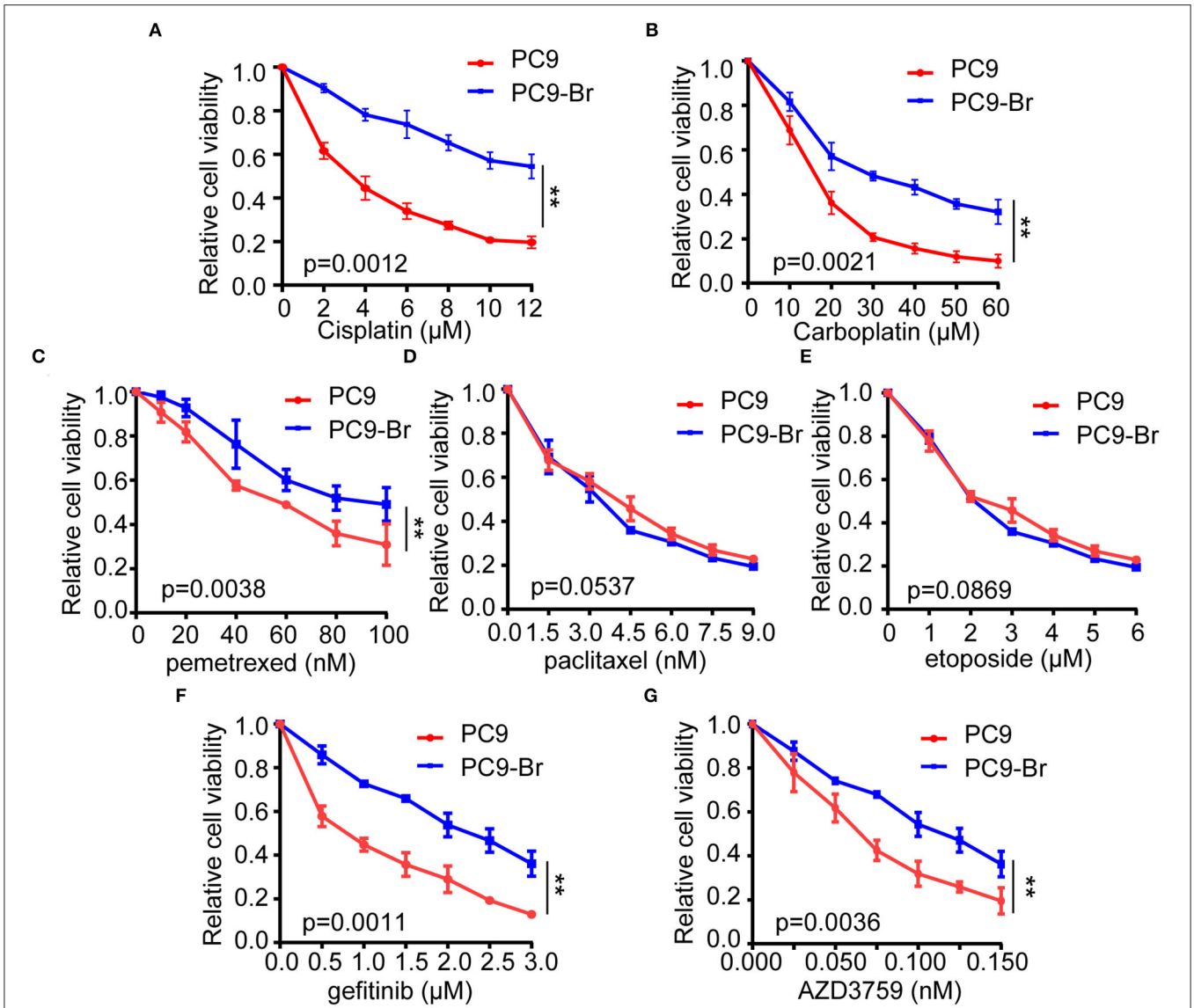

FIGURE 2 | The acquirement of obvious resistance to multiple anti-tumor drugs was found in PC9-Br cells. PC9 and PC9-Br cells were treated with different doses of cisplatin **(A)**, carboplatin **(B)**, pemetrexed **(C)**, paclitaxel **(D)**, etoposide **(E)**, gefitinib **(F)**, and AZD3759 **(G)** for 72 h and CCK-8 assays were performed to determine their viability. $n = 3$, $^{**}p < 0.01$.

protein or DNA damage, or participating in DNA repair process (Traverso et al., 2013; Bansal and Simon, 2018). Hence, we listed the differential proteins involved in GSH metabolism pathway (**Figure 3E**). The results showed that a series of enzymes related to GSH metabolism were significantly overexpressed, indicating that GSH metabolism is hyperactive in PC9-Br cells, which provided reasonable clues for exploring drug resistance developed in BM.

Drug-Resistance Related Proteins Were Confirmed to Be Regulated in BM Cells

Since a string of GSH metabolism related enzymes were found overexpressed in PC9-Br by proteomics, the expression of these enzymes (GPX4, RRM2, GCLC, GPX1, GSTM4, GSTM1) was further verified to be upregulated in PC9-Br by western blotting (**Figures 4A,D**). GSH dependent peroxidases (GPXs) catalyze the conversion of GSH to GSSG under oxidative stress. GPX1 was found to promote the resistance to cisplatin of NSCLC (Chen et al., 2019a), while GXP4 was widely studied as a novel ferroptosis regulator (Dixon et al., 2012; Yang et al., 2014). In addition, increasing evidence suggests that drug-tolerant persister tumor cells are susceptible to GPX4 inhibition (Hangauer et al., 2017). The expression and enzymatic activity of GCLC constitute rate-limiting steps for GSH synthesis (Lu, 2009, 2013), while glutathione transferases (GSTs) have been shown to be involved in the development of multi-drug resistance (MDR)

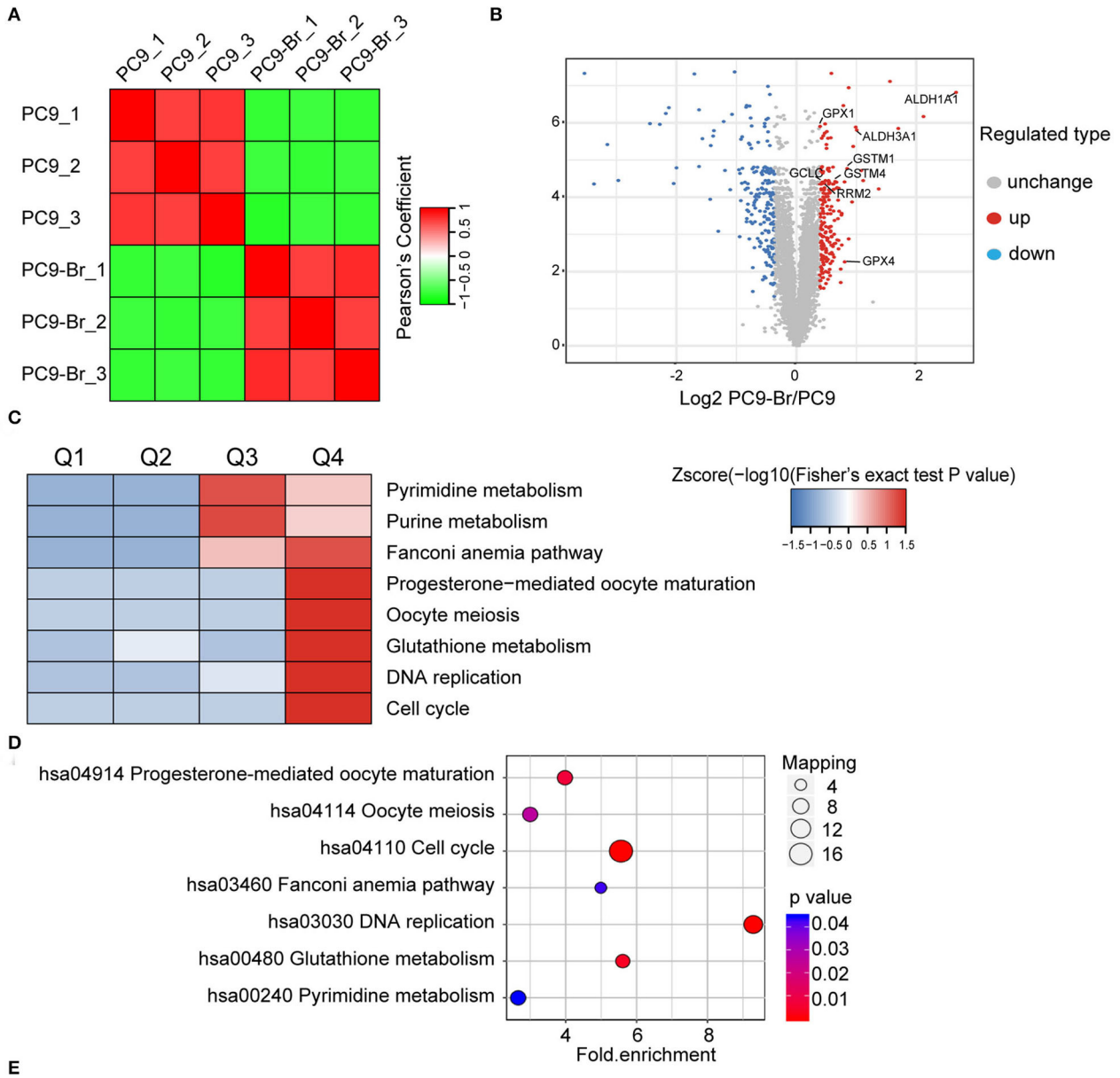

E

KEGG pathway	Protein accession	Gene name	PC9-Br/PC9 Ratio	p value
hsa00480 Glutathione metabolism	P36969	GPX4	1.738	0.006
	P31350	RRM2	1.374	4.29E-05
	P48506	GCLC	1.344	3.95E-05
	P07203	GPX1	1.307	1.25E-06
	Q03013	GSTM4	1.557	3.82E-05
	P09488	GSTM1	1.788	1.71E-05

FIGURE 3 | Proteomics identified the hyperactive GSH metabolism pathway in PC9-Br cells. **(A)** Correlation analysis for reproducibility of proteomics data. **(B)** Volcano plot showed the distribution of differential proteins in Q4 group (ratio fold >1.3). The horizontal axis is Log2 transformed protein expression ratio, and the vertical axis is –Log10 transformed *p*-value. Red dot: up-regulated protein; blue dot: down-regulated protein. **(C)** Functional KEGG enrichment cluster image showing the common enriched pathways in PC9-Br cells. **(D)** Results of KEGG enrichment analysis of differential proteins in groups (PC9-Br/PC9) visualized in bubble diagram (including the number of respective involved proteins and the corresponding *p*-values). **(E)** The specific differential proteins identified in groups (PC9-Br/PC9) involved in GSH metabolism pathway are listed.

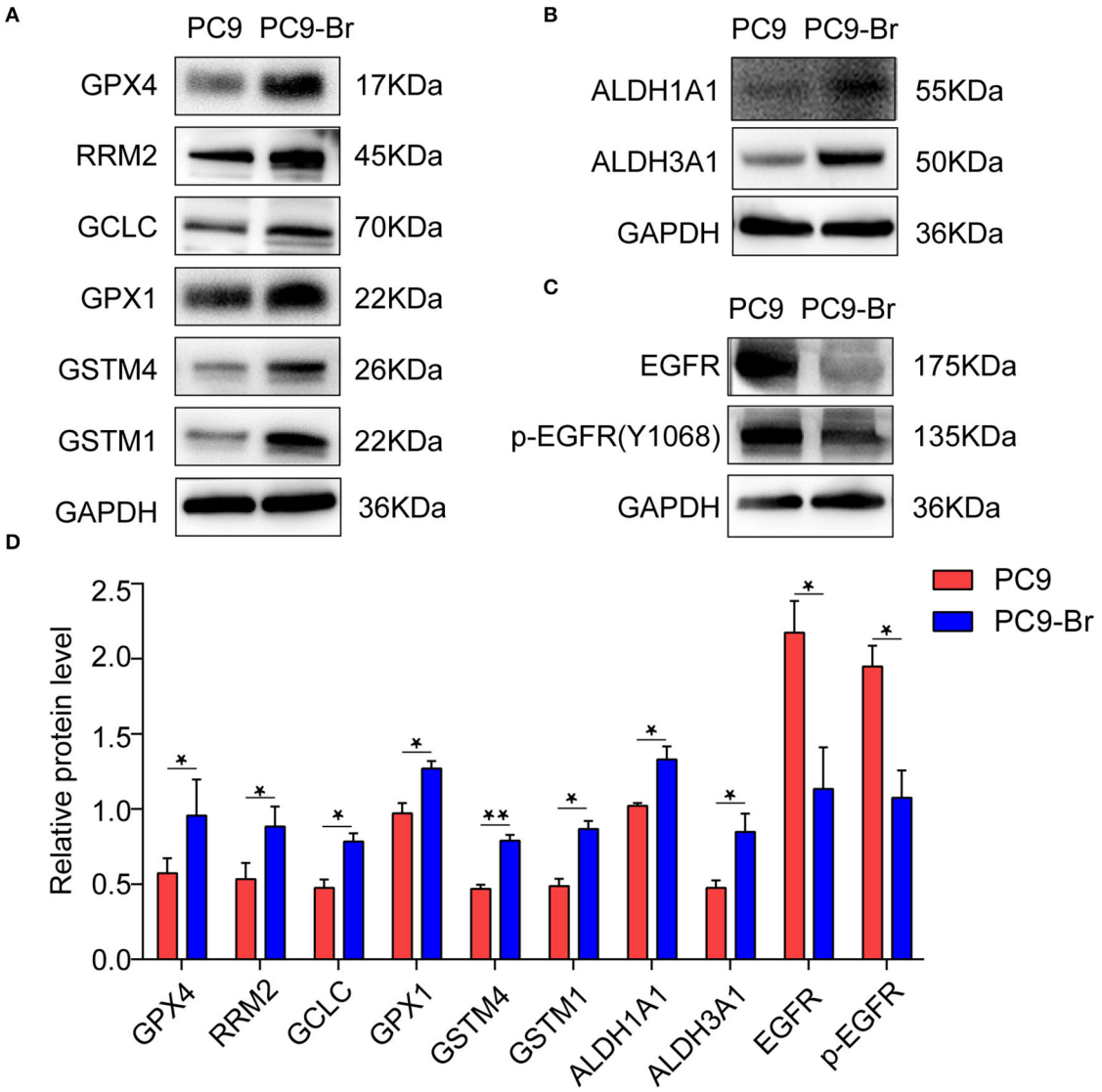

FIGURE 4 | Drug-resistance related proteins were confirmed to be regulated in PC9-Br cells. Representative western blot images showing the expression of GSH metabolism related enzymes **(A)**, ALDH1A1 and ALDH3A1 **(B)**, and EGFR/p-EGFR **(C)** in PC9 and PC9-Br cells. **(D)** Quantitative results of western blotting images for proteins. $n = 3$, $^{*}p < 0.05$, $^{**}p < 0.01$.

toward chemotherapeutic agents (Townsend and Tew, 2003; Chatterjee and Gupta, 2018). RRM2 was also proved to mediate multi-drug resistance in multiple malignant tumors (Shah et al., 2014; Chen et al., 2019b). Furthermore, aldehyde dehydrogenases 1 and 3 (ALDH1A1 and ALDH3A1), which were well recognized to play functional roles in drug resistance of NSCLC (Rebollido-Rios et al., 2020), were also found overexpressed in PC9-Br (**Figures 4B,D**). Consistent with the resistance of PC9-Br to EGFR targeted TKIs, we found the expression of EGFR and p-EGFR were significantly reduced in PC9-Br compared to parental PC-9 (**Figures 4C,D**), which was regarded as an important mechanism of EGFR-TKI resistance in other EGFR-mutant NSCLC cell lines (Tabara et al., 2012; Nozaki et al., 2014; Xu et al., 2018). Similar regulations of these drug resistance related proteins were confirmed in animal derived BM cells PC9-BrM3 (**Supplementary Figures 3A–D**). What's more, NF-κB activation was reported to be responsible for the resistance of tumor cells to EGFR TKIs (Blakely et al., 2015; Lantermann et al., 2015; Li et al., 2020). Similarly, in our study, in addition to the decrease in EGFR/p-EGFR expression, we also found the significant activation of NF-κB pathway in BM cells compared to parental PC9 cells (**Supplementary Figure 4**). Collectively, these findings, on the one hand, revealed potential reasons for drug resistance occurred in both chip model derived PC9-Br and animal model derived PC9-BrM3 cells, which should be further investigated in future studies. One the other hand, consistent results obtained from both models suggested the chip platform is effective to recapitulate the pathologic changes during the course

of *in vivo* metastasis and is an alternative model to further study the pathogenesis of brain metastasis.

CONCLUSIONS

In summary, we established a model of lung cancer brain metastasis based on a newly microfluidic multi-organ chip and isolated the brain metastatic derivative cells (PC9-Br) of parental PC9 from the chip. Drug resistance to most chemotherapeutic agents and EGFR targeted TKIs were found to be developed in PC9-Br compared to parental PC9. Further proteomics revealed the different protein expression profile of PC9-Br and identified the hyperactive GSH metabolism pathway with the general overexpression of various GSH metabolism-related enzymes (GPX4, RRM2, GCLC, GPX1, GSTM4, GSTM1). Increased expression of aldehyde dehydrogenases (ALDH1A1, ALDH3A1), the well-known drug-resistance associated proteins, were also found in BM. What's more, the reduction of EGFR and phosphorylated EGFR expression, together with the significant activation of NF-κB pathway suggested that the PC9-Br cells had lost both the target of EGFR-TKIs and the addiction to EGFR signaling, which might result in the TKIs resistance in PC9-Br. In future studies, multi-omics analysis including genomics, proteomics and metabolomics will be conducted to further investigate novel mechanisms of the intrinsic drug resistance in BM.

DATA AVAILABILITY STATEMENT

The datasets presented in this study can be found in online repositories. The names of the repository/repositories and accession number(s) can be found below: http://www.proteomexchange.org/, PXD021760.

ETHICS STATEMENT

The animal study was reviewed and approved by The Animal Ethics Review Committee of Dalian Medical University.

AUTHOR CONTRIBUTIONS

MX, YW, and WD designed and carried out the study. SX performed the statistical analysis. SW helped the fabrication of chips. WL wrote the first draft of the manuscript. MX and WD wrote sections of the manuscript. QW and WL conceived and supervised the project, designed and analyzed experiments, and revise the manuscript. All authors read and approved the submitted version.

FUNDING

This work was supported by grants from the National Natural Science Foundation (81972916).

ACKNOWLEDGMENTS

The mass spectrometry proteomics data have been deposited to the ProteomeXchange Consortium via the PRIDE partner repository with the dataset identifier PXD021760: (Username: reviewer_pxd021760@ebi.ac.uk; Password: Ug8rZmvj).

SUPPLEMENTARY MATERIAL

The Supplementary Material for this article can be found online at: https://www.frontiersin.org/articles/10.3389/fbioe.2020.612091/full#supplementary-material

REFERENCES

Achrol, A. S., Rennert, R. C., Anders, C., Soffietti, R., Ahluwalia, M. S., Nayak, L., et al. (2019). Brain metastases. *Nat Rev Dis Primers.* 5:5. doi: 10.1038/s41572-018-0055-y

Ali, A., Goffin, J. R., Arnold, A., and Ellis, P. M. (2013). Survival of patients with non-small-cell lung cancer after a diagnosis of brain metastases. *Curr. Oncol.* 20, e300–e306. doi: 10.3747/co.20.1481

Altelaar, A. F., Munoz, J., and Heck, A. J. (2013). Next-generation proteomics: towards an integrative view of proteome dynamics. *Nat. Rev. Genet.* 14, 35–48. doi: 10.1038/nrg3356

Ashammakhi, N., Nasiri, R., Barros, N. R., Tebon, P., Thakor, J., Goudie, M., et al. (2020). Gut-on-a-chip: current progress and future opportunities. *Biomaterials* 255:120196. doi: 10.1016/j.biomaterials.2020.120196

Bailon, O., Chouahnia, K., Augier, A., Bouillet, T., Billot, S., Coman, I., et al. (2012). Upfront association of carboplatin plus pemetrexed in patients with brain metastases of lung adenocarcinoma. *Neuro Oncol.* 14, 491–495. doi: 10.1093/neuonc/nos004

Bansal, A., and Simon, M. C. (2018). Glutathione metabolism in cancer progression and treatment resistance. *J. Cell Biol.* 217, 2291–2298. doi: 10.1083/jcb.201804161

Barlesi, F., Gervais, R., Lena, H., Hureaux, J., Berard, H., Paillotin, D., et al. (2011). Pemetrexed and cisplatin as first-line chemotherapy for advanced non-small-cell lung cancer (NSCLC) with asymptomatic inoperable brain metastases: a multicenter phase II trial (GFPC 07-01). *Ann. Oncol.* 22, 2466–2470. doi: 10.1093/annonc/mdr003

Blakely, C. M., Pazarentzos, E., Olivas, V., Asthana, S., Yan, J. J., Tan, I., et al. (2015). NF-κB-activating complex engaged in response to EGFR oncogene inhibition drives tumor cell survival and residual disease in lung cancer. *Cell Rep.* 11, 98–110. doi: 10.1016/j.celrep.2015.03.012

Bos, P. D., Zhang, X. H., Nadal, C., Shu, W., Gomis, R. R., Nguyen, D. X., et al. (2009). Genes that mediate breast cancer metastasis to the brain. *Nature* 459 :1005–1009. doi: 10.1038/nature08021

Burel-Vandenbos, F., Ambrosetti, D., Coutts, M., and Pedeutour, F. (2013). EGFR mutation status in brain metastases of non-small cell lung carcinoma. *J. Neurooncol.* 111, 1–10. doi: 10.1007/s11060-012-0990-5

Chatterjee, A., and Gupta, S. (2018). The multifaceted role of glutathione S-transferases in cancer. *Cancer Lett.* 433, 33–42. doi: 10.1016/j.canlet.2018.06.028

Chen, B., Shen, Z., Wu, D., Xie, X., Xu, X., Lv, L., et al. (2019a). Glutathione peroxidase 1 promotes NSCLC resistance to cisplatin via ROS-induced activation of PI3K/AKT pathway. *Biomed Res. Int.* 2019:7640547. doi: 10.1155/2019/7640547

Chen, C. W., Li, Y., Hu, S., Zhou, W., Meng, Y., Li, Z., et al. (2019b). DHS (trans-4,4'-dihydroxystilbene) suppresses DNA replication and tumor growth by inhibiting RRM2 (ribonucleotide reductase regulatory subunit M2). *Oncogene* 38, 2364–2379. doi: 10.1038/s41388-018-0584-6

Cheng, H., and Perez-Soler, R. (2018). Leptomeningeal metastases in non-small-cell lung cancer. *Lancet Oncol.* 19, e43–e55. doi: 10.1016/S1470-2045(17)30689-7

Ding, C., Chen, X., Kang, Q., and Yan, X. (2020). Biomedical Application of Functional Materials in Organ-on-a-Chip. *Front. Bioeng. Biotechnol.* 8:823. doi: 10.3389/fbioe.2020.00823

Dixon, S. J., Lemberg, K. M., Lamprecht, M. R., Skouta, R., Zaitsev, E. M., Gleason, C. E., et al. (2012). Ferroptosis: an iron-dependent form of nonapoptotic cell death. *Cell* 149, 1060–1072. doi: 10.1016/j.cell.2012.03.042

Franchino, F., Rudà R., and Soffietti, R. (2018). Mechanisms and therapy for cancer metastasis to the brain. *Front. Oncol.* 8:161. doi: 10.3389/fonc.2018.00161

Hanahan, D., and Weinberg, R. A. (2011). Hallmarks of cancer: the next generation.*Cell* 144, 646–674. doi: 10.1016/j.cell.2011.02.013

Hangauer, M. J., Viswanathan, V. S., Ryan, M. J., Bole, D., Eaton, J. K., Matov, A., et al. (2017). Drug-tolerant persister cancer cells are vulnerable to GPX4 inhibition. *Nature* 551:247–250. doi: 10.1038/nature24297

Hochmair, M. (2018). Medical treatment options for patients with epidermal growth factor receptor mutation-positive non-small cell lung cancer suffering from brain metastases and/or leptomeningeal disease. *Target. Oncol.* 13, 269–285. doi: 10.1007/s11523-018-0566-1

Lantermann, A. B., Chen, D., McCutcheon, K., Hoffman, G., Frias, E., Ruddy, D., et al. (2015). Inhibition of casein kinase 1 alpha prevents acquired drug resistance to erlotinib in EGFR-mutant non-small cell lung cancer. *Cancer Res.* 75, 4937–4948. doi: 10.1158/0008-5472.CAN-15-1113

Li, B., Wang, C., Zhang, Y., Zhao, X. Y., Huang, B., Wu, P. F., et al. (2012). Elevated PLGF contributes to small-cell lung cancer brain metastasis. *Oncogene* 32, 2952–2962. doi: 10.1038/onc.2012.313

Li, L., Wang, T., Hu, M., Zhang, Y., Chen, H., and Xu, L. (2020). Metformin overcomes acquired resistance to EGFR TKIs in EGFR-mutant lung cancer via AMPK/ERK/NF-κB signaling pathway. *Front. Oncol.* 10:1605. doi: 10.3389/fonc.2020.01605

Liu, W., Song, J., Du, X., Zhou, Y., Li, Y., Li, R., et al. (2019). AKR1B10 (Aldo-keto reductase family 1 B10) promotes brain metastasis of lung cancer cells in a multi-organ microfluidic chip model. *Acta Biomater.* 91, 195–208. doi: 10.1016/j.actbio.2019.04.053

Lu, S. C. (2009). Regulation of glutathione synthesis. *Mol. Aspects Med.* 30, 42–59. doi: 10.1016/j.mam.2008.05.005

Lu, S. C. (2013). Glutathione synthesis. *Biochim. Biophys. Acta* 1830, 3143–3153. doi: 10.1016/j.bbagen.2012.09.008

Mehta, M. P., Paleologos, N. A., Mikkelsen, T., Robinson, P. D., Ammirati, M., Andrews, D. W., et al. (2010). The role of chemotherapy in the management of newly diagnosed brain metastases: a systematic review and evidence-based clinical practice guideline. *J. Neurooncol.* 96, 71–83. doi: 10.1007/s11060-009-0062-7

Moradi, E., Jalili-Firoozinezhad, S., and Solati-Hashjin, M. (2020). Microfluidic organ-on-a-chip models of human liver tissue. *Acta Biomater.* 116, 67–83. doi: 10.1016/j.actbio.2020.08.041

Nozaki, K., Kagamu, H., Shoji, S., Igarashi, N., Ohtsubo, A., Okajima, M., et al. (2014). DDX3X induces primary EGFR-TKI resistance based on intratumor heterogeneity in lung cancer cells harboring EGFR-activating mutations. *PLoS ONE* 9:e111019. doi: 10.1371/journal.pone.0111019

Rebollido-Rios, R., Venton, G., Sánchez-Redondo, S., Iglesias I Felip, C., Fournet, G., González, E., et al. (2020). Dual disruption of aldehyde dehydrogenases 1 and 3 promotes functional changes in the glutathione redox system and enhances chemosensitivity in nonsmall cell lung cancer. *Oncogene* 39, 2756–2771. doi: 10.1038/s41388-020-1184-9

Sandler, A. B., Nemunaitis, J., Denham, C., von Pawel, J., Cormier, Y., Gatzemeier, U., et al. (2000). Phase III trial of gemcitabine plus cisplatin versus cisplatin alone in patients with locally advanced or metastatic non-small-cell lung cancer. *J. Clin. Oncol.* 18, 122–130. doi: 10.1200/JCO.2000.18.1.122

Schiller, J. H., Harrington, D., Belani, C. P., Langer, C., Sandler, A., Krook, J., et al. (2002). Comparison of four chemotherapy regimens for advanced non-small-cell lung cancer. *N. Engl. J. Med.* 346, 92–98. doi: 10.1056/NEJMoa011954

Sekine, A., and Satoh, H. (2017). Paradigm shift of therapeutic management of brain metastases in EGFR-mutant non-small cell lung cancer in the era of targeted therapy. *Med. Oncol.* 34, 121. doi: 10.1007/s12032-017-0978-2

Shah, K. N., Mehta, K. R., Peterson, D., Evangelista, M., Livesey, J. C., and Faridi, J. S. (2014). AKT-induced tamoxifen resistance is overturned by RRM2 inhibition. *Mol. Cancer Res.* 12, 394–407. doi: 10.1158/1541-7786.MCR-13-0219

Shah, N., Liu, Z., Tallman, R. M., Mohammad, A., Sprowls, S. A., Saralkar, P. A., et al. (2020). Drug resistance occurred in a newly characterized preclinical model of lung cancer brain metastasis. *BMC Cancer.* 20:292. doi: 10.1186/s12885-020-06808-2

Shi, Y., Sun, Y., Yu, J., Ding, C., Ma, Z., Wang, Z., et al. (2017). China experts consensus on the diagnosis and treatment of brain metastases of lung cancer (2017 version). *Zhongguo Fei Ai Za Zhi.* 20, 1–13. doi: 10.3779/j.issn.1009-3419.2017.01.01

Siegel, R. L., Miller, K. D., and Jemal, A. (2019). Cancer statistics, 2019. *CA Cancer J. Clin.* 69, 7–34. doi: 10.3322/caac.21551

Steeg, P. S., Camphausen, K. A., and Smith, Q. R. (2011). Brain metastases as preventive and therapeutic targets. *Nat. Rev. Cancer.* 11, 352–363. doi: 10.1038/nrc3053

Steinway, S. N., Saleh, J., Koo, B. K., Delacour, D., and Kim, D. H. (2020). Human microphysiological models of intestinal tissue and gut microbiome. *Front. Bioeng. Biotechnol.* 8:725. doi: 10.3389/fbioe.2020.00725

Tabara, K., Kanda, R., Sonoda, K., Kubo, T., Murakami, Y., Kawahara, A., et al. (2012). Loss of activating EGFR mutant gene contributes to acquired resistance to EGFR tyrosine kinase inhibitors in lung cancer cells. *PLoS ONE* 7:e41017. doi: 10.1371/journal.pone.0041017

Tan, C. S., Cho, B. C., and Soo, R. A. (2017). Treatment options for EGFR mutant NSCLC with CNS involvement-can patients BLOOM with the use of next generation EGFR TKIs? *Lung Cancer.* 108, 29–37. doi: 10.1016/j.lungcan.2017.02.012

Townsend, D. M., and Tew, K. D. (2003). The role of glutathione-S-transferase in anti-cancer drug resistance. *Oncogene* 22, 7369–7375. doi: 10.1038/sj.onc.1206940

Traverso, N., Ricciarelli, R., Nitti, M., Marengo, B., Furfaro, A. L., Pronzato, M. A., et al. (2013). Role of glutathione in cancer progression and chemoresistance. *Oxid. Med. Cell. Longev.* 2013:972913. doi: 10.1155/2013/972913

Xu, J., Zhao, X., He, D., Wang, J., Li, W., Liu, Y., et al. (2018). Loss of EGFR confers acquired resistance to AZD9291 in an EGFR-mutant non-small cell lung cancer cell line with an epithelial-mesenchymal transition phenotype. *J. Cancer Res. Clin. Oncol.* 144, 1413–1422. doi: 10.1007/s00432-018-2668-7

Xu, Z., Li, E., Guo, Z., Yu, R., Hao, H., Xu, Y., et al. (2016). Design and construction of a multi-organ microfluidic chip mimicking the *in vivo* microenvironment of lung cancer metastasis. *ACS Appl. Mater. Interfaces.* 8, 25840–25847. doi: 10.1021/acsami.6b08746

Yang, W. S., SriRamaratnam, R., Welsch, M. E., Shimada, K., Skouta, R., Viswanathan, V. S., et al. (2014). Regulation of ferroptotic cancer cell death by GPX4. *Cell* 156, 317–331. doi: 10.1016/j.cell.2013.12.010

Yousefi, M., Bahrami, T., Salmaninejad, A., Nosrati, R., Ghaffari, P., and Ghaffari, S. H. (2017). Lung cancer-associated brain metastasis: molecular mechanisms and therapeutic options. *Cell. Oncol.* 40, 419–441. doi: 10.1007/s13402-017-0345-5

Zhuang, H., Shi, S., and Chang, J. Y. (2019). Treatment modes for EGFR mutations in patients with brain metastases from non-small cell lung cancer: controversy, causes, and solutions. *Transl. Lung Cancer Res.* 8, 524–531. doi: 10.21037/tlcr.2019.07.03

Conflict of Interest: The authors declare that the research was conducted in the absence of any commercial or financial relationships that could be construed as a potential conflict of interest.

frontiers in Bioengineering and Biotechnology

REVIEW
published: 04 February 2021
doi: 10.3389/fbioe.2021.624435

Microfluidic and Organ-on-a-Chip Approaches to Investigate Cellular and Microenvironmental Contributions to Cardiovascular Function and Pathology

Elizabeth L. Doherty[1,2†], *Wen Yih Aw*[2†], *Anthony J. Hickey*[1,2,3] *and William J. Polacheck*[1,4,5*]

[1] Joint Department of Biomedical Engineering, University of Carolina at Chapel Hill and North Carolina State University, Chapel Hill, NC, United States, [2] University of North Carolina Catalyst for Rare Diseases, Eshelman School of Pharmacy, University of North Carolina at Chapel Hill, Chapel Hill, NC, United States, [3] RTI International, Durham, NC, United States, [4] Cell Biology and Physiology, University of North Carolina at Chapel Hill School of Medicine, Chapel Hill, NC, United States, [5] McAllister Heart Institute, School of Medicine, University of North Carolina at Chapel Hill, Chapel Hill, NC, United States

OPEN ACCESS

Edited by:
Shi-Cong Tao,
Shanghai Jiao Tong University, China

Reviewed by:
Wenfu Zheng,
National Center for Nanoscience and Technology (CAS), China
Paola Occhetta,
Politecnico di Milano, Italy
Claudia Fischbach,
Cornell University, United States

***Correspondence:**
William J. Polacheck
polacheck@unc.edu

[†] These authors have contributed equally to this work

Specialty section:
This article was submitted to Nanobiotechnology, a section of the journal Frontiers in Bioengineering and Biotechnology

Received: 31 October 2020
Accepted: 08 January 2021
Published: 04 February 2021

Citation:
Doherty EL, Aw WY, Hickey AJ and Polacheck WJ (2021) Microfluidic and Organ-on-a-Chip Approaches to Investigate Cellular and Microenvironmental Contributions to Cardiovascular Function and Pathology. Front. Bioeng. Biotechnol. 9:624435. doi: 10.3389/fbioe.2021.624435

Over the past decade, advances in microfabrication and biomaterials have facilitated the development of microfluidic tissue and organ models to address challenges with conventional animal and cell culture systems. These systems have largely been developed for human disease modeling and preclinical drug development and have been increasingly used to understand cellular and molecular mechanisms, particularly in the cardiovascular system where the characteristic mechanics and architecture are difficult to recapitulate in traditional systems. Here, we review recent microfluidic approaches to model the cardiovascular system and novel insights provided by these systems. Key features of microfluidic approaches include the ability to pattern cells and extracellular matrix (ECM) at cellular length scales and the ability to use patient-derived cells. We focus the review on approaches that have leveraged these features to explore the relationship between genetic mutations and the microenvironment in cardiovascular disease progression. Additionally, we discuss limitations and benefits of the various approaches, and conclude by considering the role further advances in microfabrication technology and biochemistry techniques play in establishing microfluidic cardiovascular disease models as central tools for understanding biological mechanisms and for developing interventional strategies.

Keywords: microfluidics, endothelial cells, cardiomyocytes, vascular biology, rare disease, microfabrication, biofluid mechanics, organ-on-chip

INTRODUCTION

Cardiovascular disease is the leading cause of death among Americans (Heron and Anderson, 2016), and vascular dysfunction is not only a hallmark but often the underlying cause of morbidity and mortality in many diseases (Rajendran et al., 2013). Current approaches for drug development to treat cardiovascular diseases rely primarily on animal models that lack complete human physiology and do not recapitulate the full disease phenotype. In addition, many inherited diseases are associated with multiple genetic mutations thus requiring multiple animal models for a single

disease. Furthermore, studies of disposition and efficacy of drugs in animals or *ex-vivo* human tissue do not allow a scale of scrutiny that informs our understanding of events in the microenvironment that often characterize genetic disorders or are the foundation for more serious systemic disease. These limitations introduce challenges for inferring therapeutic efficacy in patients based on interventions in animal models, particularly for diseases in which the genetics are not well-characterized, such as rare inherited diseases. An alternative to animal models and organotypic culture are conventional *in-vitro* models, which are commonly used in pharmacokinetic studies and preclinical drug discovery. 2D cell culture models offer simpler, more inexpensive, and higher throughput platforms for discovery and screening. While traditional cell culture systems allow genetic manipulations and offer compatibility with biochemical assays that are not possible in animal models, cells cultured on stiff surfaces do not experience mechanical stimuli and topography of tissue microenvironment and are less reflective of the *in-vivo* conditions.

Microfluidic technology allows fabrication of systems populated by human cells that recapitulate some aspects of organ function (Huh et al., 2010; Bhatia and Ingber, 2014; Low et al., 2020) and can be used to probe key molecular or cellular events, in a physiologically relevant construct, to explore the origins of acute or chronic disease. These microfluidic "organ-on-chip" models have particular relevance in the study of cardiovascular disease where functional outputs such as resistance to mass transport, fluid displacement, and mechanical force can be well-characterized. A key feature of the most recent of such models is the control over microenvironmental parameters such as the content and mechanical properties of extracellular matrix, the inclusion of stromal and supporting cell types, recapitulation of tissue architecture, and physiologic hemodynamics (Nam et al., 2015; Bordeleau et al., 2017; Partyka et al., 2017; Kaneko et al., 2018; Polacheck et al., 2019; Atchison et al., 2020). When combined with modern cellular and molecular techniques, including induced pluripotent stem cell (iPSC) technology, novel methods for isolation and maintenance of primary cells, and gene editing tools, microfluidic cardiovascular models provide a powerful platform for isolating factors associated with cardiovascular disease.

Here, we review microfluidic models that have been developed to study cardiovascular function and pathology from a genetic and microenvironmental perspective. We focus on platforms that have elucidated the role of physical forces in pathophysiology, and we highlight examples of devices that have been used as a testbed for therapeutic intervention. We divide the review into three separate but interrelated sections that elaborate on key parameters of cardiovascular tissue architecture that can be separately controlled and analyzed when using microfluidic approaches as compared to traditional *in-vitro* or animal models (**Figure 1**): (1) Extracellular matrix (ECM)—here we discuss examples of devices developed to recapitulate and pattern native ECM *ex-vivo*, with a focus on models developed to understand the role of ECM in disease progression; (2) Tissue Morphology—we then review devices that leverage the ability to pattern fluid, polymers, and cells to allow modeling of patient-specific pathophysiologic vascular architecture to investigate how tissue structure contributes to disease progression; (3) Cellular Genetics—in the final section, we discuss devices that incorporate primary patient cells and human cells engineered to express disease-specific mutations to characterize the effects of these mutations on tissue function. Combining knowledge and approaches from each of these focus areas is essential to future developments. We conclude with a perspective on how advances in genetic screening and manipulation could further be integrated with next-generation microfluidic models to provide mechanistic insight and screening for interventional strategies for rare cardiovascular diseases for which animal and *ex-vivo* tissue models are unsuitable.

EXTRACELLULAR MATRIX

The cardiovascular system is a closed, pressurized system, which utilizes cyclic pumping to enable convective transport of oxygen and nutrients throughout the body. Thus, the cells and extracellular matrix (ECM) that comprise cardiac and vascular tissue must withstand cyclic pressures and hemodynamic fluid stresses of magnitudes that vary with location within the circulatory system (Secomb, 2016). As a result, the structure and composition of ECM within the cardiovascular system is highly complex and tissue-specific (Potente and Mäkinen, 2017). For example, while vessel ECM is generally composed of fibrillar collagens, elastic fibers, fibronectin, fibrillin, and proteoglycans, the ratio of collagens and elastic fibers vary across vessels. Collagens function to provide tensile strength, and together with elastic fibers ensure vessels elasticity (Wagenseil and Mecham, 2009; Cheng and Wagenseil, 2012), and thus proximal arteries that experience higher wall tension have a higher number of collagens and elastin than distal arteries and veins (Clark and Glagov, 1985). Furthermore, changes in matrix composition and structure are intimately linked with cardiovascular development and disease, and we direct the reader to comprehensive reviews that catalog key ECM constituents in myocardial and vascular ECM (Davis and Senger, 2005; Wagenseil and Mecham, 2009; Rienks et al., 2014). In addition to its structural role, the ECM presents biochemical and biophysical cues to adherent cells that regulate diverse processes from cell fate (Frantz et al., 2010; Cox and Erler, 2011; Daley and Yamada, 2013) to proliferation and apoptosis (Chen et al., 1997). For example, ECM composition modulates developmental angiogenesis through integrin-dependent signaling (Hynes, 2007) and proteoglycan content in the ECM is known to play a critical role in cardiac development and cardiomyocyte differentiation (Chan et al., 2010). Given the central importance of the ECM in cardiovascular development, homeostasis, and disease pathogenesis, the development of cardiovascular disease models requires careful consideration of the composition and architecture of the ECM. Here we review recent progress in the integration of ECM scaffold into microfluidic cardiovascular models and discuss how these methods have been adapted to

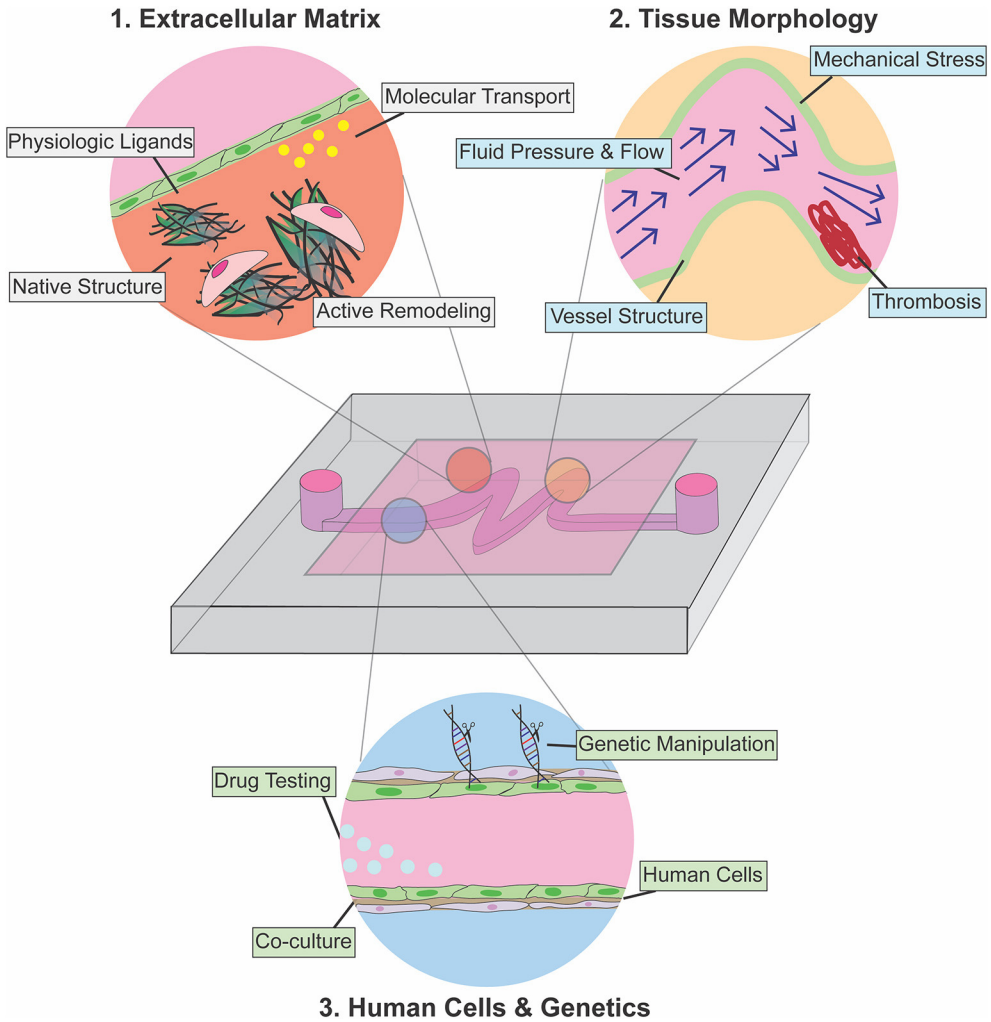

FIGURE 1 | Use of microfluidic devices for modeling cardiovascular disease pathophysiology. Introduction of physiologic ECM enables the investigation of cellular remodeling of ECM in disease conditions (red), and microfluidics also allows patterning and recapitulation of altered tissue morphology and abnormal hemodynamics associated with cardiovascular diseases (yellow). Integration of gene editing with microfluidic technology allows modeling of endothelium-stromal cells interactions within physiological microenvironment in normal development and disease condition (light blue).

effectively model disease processes not captured with traditional cell culture or animal disease models.

Of particular interest in cardiovascular physiology and pathophysiology is the dynamic remodeling of the ECM by resident cells in response to mechanical load, physiological stress, and circulating biochemical signals (Hynes, 2007; Humphrey, 2008). This remodeling is necessary to account for and adapt to changes in cardiac output and vascular resistance associated with aging, chronic disease, and/or wound healing, among other processes (Bonnans et al., 2014). Importantly, dysfunctional remodeling of the ECM is not only correlated with, but often is the underlying cause of various cardiovascular diseases. For example, collagen-rich fibrosis of the myocardium occurs in dilated and hypertrophic cardiomyopathy (Kapelko, 2001; Louzao-Martinez et al., 2016), and the loss of elastic fibers, aberrant collagen and elastin deposition, and increased vascular ECM stiffness are characteristics of hypertension, arterial aging and arterial calcification in response to inflammatory conditions (Arribas et al., 2006; Wagenseil and Mecham, 2012; Sun, 2015). Beyond its role in shaping and maintaining cardiovascular tissue architecture and mechanics, ECM also plays an important role in regulating growth factor transport and signaling, and dysfunctional ECM remodeling can exacerbate pathogenic cell signaling, contributing to the development of aortic aneurysm in rare diseases such as Marfan and Meester-Loeys syndrome (Kolb et al., 2001; Sakai et al., 2016; Meester et al., 2017; Thomson et al., 2019). Therefore, the development of cardiovascular disease models is not only dependent on the environment and mechanics at the time of cell seeding, but also on the ability of cells to remodel the ECM in response to biochemical and mechanical stimuli. This requirement for homeostatic remodeling of the ECM motivates the use of soft 3D substrates within microfluidic

devices, which presents design and fabrication challenges as conventional processes for fabricating microfluidics result in stiff, planar surfaces (Griffith et al., 2020).

Various strategies have emerged for recapitulating native ECM in microfluidic disease models, with varying degrees of experimental difficulty and physiologic relevance. Generally, these approaches can be divided into two broad strategies: (1) surface coatings—reconstituted or synthetic ECM bound to a rigid structural material such as PDMS (Zhou et al., 2010); and (2) 3D hydrogels—highly hydrated 3D scaffolds that are comprised of networks of cross-linked polymer chains (**Figure 2**; Drury and Mooney, 2003). While 3D hydrogels allow for cellular remodeling of ECM composition and structure, inclusion of hydrogels within microfluidics constrains device design and presents experimental and technical challenges associated with applying fluid pressures within and across compliant porous materials (Polacheck et al., 2013; Akbari et al., 2017; Park et al., 2019; Griffith et al., 2020; Low et al., 2020). Therefore, microfluidic devices fabricated with surface coatings are often more sophisticated in terms of device structure and enable application of more physiologically relevant biophysical cues such as cyclic stretch and high fluid pressures and shear stresses, while those fabricated to include 3D hydrogels sacrifice device complexity for more physiologic culture substrates. For further information on hydrogel chemistry for tissue engineering and on microfluidic device design for modeling the vasculature, we refer the reader to relevant comprehensive reviews (Drury and Mooney, 2003; Wong et al., 2012; Huber et al., 2018). Here, we focus on approaches developed specifically for cardiovascular disease modeling and we compare and contrast surface coatings and 3D hydrogels to highlight benefits and drawbacks to each approach. We conclude with a brief discussion on how recent advances in patterning 3D hydrogels might lead to improvements in cardiovascular disease modeling.

ECM Surface Coatings

Various strategies have been developed to coat polydimethylsiloxane (PDMS, the material conventionally used to fabricate microfluidic devices) or glass with ECM-like components from passive adsorption of purified matrix proteins such as collagen (Parenteau-Bareil et al., 2010; Gorgieva and Kokol, 2011) to covalent crosslinking of synthetic ECM presenting specific adhesion ligands (Zhou et al., 2010; Chen et al., 2018). These surface coatings often consist of single or combinations of purified ECM proteins such as collagen, fibronectin, or laminin, which allow for cell adhesion and while these ECM proteins are relevant to cardiovascular ECM composition, they do not completely recapitulate the complexity and tissue-specific combinations of *in vivo* ECM microenvironment. In general, surface coatings impose few restrictions on the device design and fabrication process and thus allow for cell culture in devices with complex geometry. For example, Tsai et al. coated ∼30 μm branching PDMS channels with fibronectin as a substrate for endothelial cells to enable perfusion of human blood to assess the efficacy of vascular occlusion treatment in sickle cell disease and hemolytic uremic syndrome (**Figure 2**; Tsai et al., 2011). An added benefit of surface coating is the ability to culture and image cells in close proximity to a microscope objective to enable high resolution imaging. The authors leveraged this optical advantage to measure occlusion and blood flow velocity within patterned channels to determine whether hydroxyurea, a common treatment for sickle cell disease, impacts blood flow, and occlusion formation. The authors induced hemolytic uremic syndrome-like vascular injury and thrombosis and then tried to recover vessel health through treatment with eptifibatide, a drug that disrupts platelet aggregation. Through examination of clotting within the device, the authors found decreased thrombi formation after treatment, indicating that eptifibatide could be an effective treatment for hemolytic uremic syndrome. Similar approaches have been used extensively to study the role of hemodynamics in platelet activation and thrombosis, as recently reviewed (Zhu et al., 2015; Zhang and Neelamegham, 2017; Herbig et al., 2018).

PDMS affords certain advantages and disadvantages as a culture substrate in cardiovascular disease modeling. While PDMS cannot be remodeled by cells and is generally much stiffer than microvascular ECM (Polacheck and Chen, 2016), its elastic modulus can be tuned to values ranging from 0.1 to 2,700 kPa, which can better mimic physiological stiffness for larger vessels and the myocardium (Brown et al., 2005; Lv et al., 2017). Further, the high toughness and elasticity allow reversible and cyclic strain to be generated in PDMS under driving pressures easily achieved with standard microfluidics. In a highly influential platform technology, Huh et al. coated porous PDMS membranes with either collagen or fibronectin coating as a substrate for endothelial cells and alveolar epithelial cells, which could mimic the cyclic breathing motion of the alveolus (Huh et al., 2010). This system has since been modified to study many cardiovascular diseases including Hutchinson-Guilford progeria syndrome (Ribas et al., 2017) and cardiac fibrosis (Ugolini et al., 2016). For example, Zheng et al. leveraged this device design to simultaneously apply fluid shear stress and cyclic stretch to endothelial cells to recapitulate the mechanical conditions associated with early atherosclerosis (Zheng et al., 2016). They found an increase in reactive oxygen species formation in response to either abnormal fluid shear or cyclic stress, and the effect was more pronounced when cells were subjected to both stresses. They further evaluated endothelial cell response to inflammatory and hyperglycemic conditions and demonstrated increased cell death in endothelial cells cultured in device as compared to 2D cultured cells. Further, treatment of endothelial cells cultured in device under physiological flow and cyclic stress with probucol, a drug pulled from the market due to off target cardiovascular effects, uncovered cardiotoxicity not seen in a traditional cell culture model. They further showed that their device presented similar results to mouse model after treatment with antioxidant functionalized nanoparticles for hyperglycemia. Together these results demonstrate that despite the superphysiological stiffness, lack of cellular remodeling and relevant ECM complexity, microfluidic devices synthesized with ECM-coated PDMS or glass have provided novel insight into cardiovascular disease mechanisms and drug efficacy through their ability to recapitulate mechanical aspects of the microenvironment.

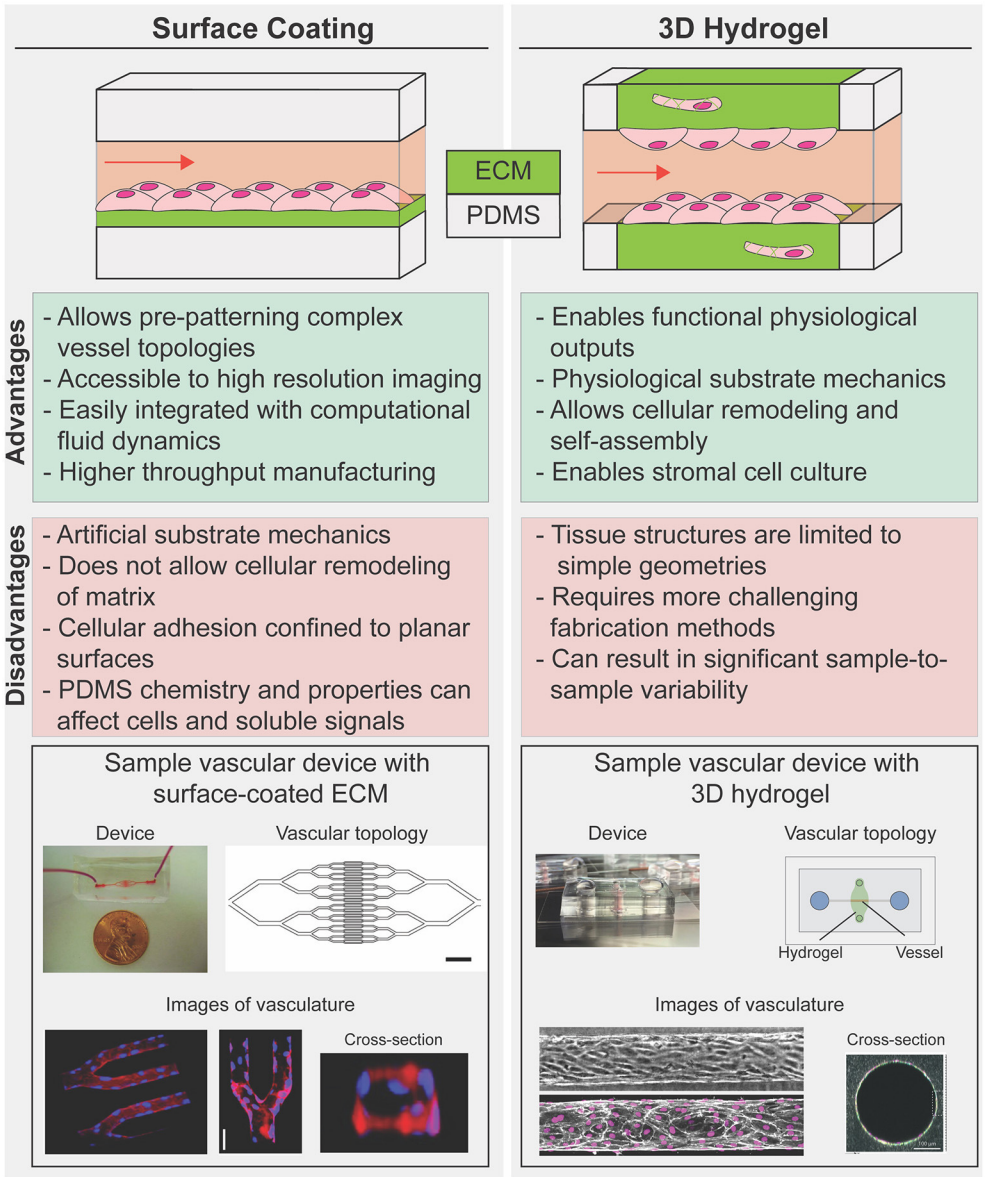

FIGURE 2 | Strategies to reconstruct cells-ECM microenvironments in microfluidic disease models. 2D coated surfaces (left) and 3D hydrogels (right) each provide unique experimental advantages and limitations. Surface coated PDMS membrane is commonly used as substrate in platforms that have been used to investigate the effect of cyclic stress on cellular function or those that require complex geometry (bottom, left). 3D hydrogel systems are often limited to linear geometries but provide an optimal mechanical cellular microenvironment to study how spatial and mechanical cues in 3D influence vascular dynamics in diseases while allowing for cellular co-culture and hydrogel remodeling (bottom, right). [bottom, left: Images republished with permission of American Society for Clinical Investigation from Tsai et al. (2011); permissions conveyed through Copyright Clearance Center Inc. Bottom, right; Top: reproduced from Polacheck et al. (2019); Bottom: Reproduced from Wang et al. (2020) with permission from the Royal Society of Chemistry].

3D Hydrogels

To address the limitations of surface coated PDMS and glass, approaches have been developed to incorporate 3D hydrogels within microfluidic devices. In these systems, the PDMS microfluidic device serves as an initial template and gasket for fluidic access to a dynamic cell-laden hydrogel to mimic cardiac or vascular tissue. There has been considerable interest and effort in patterning hollow channels through the hydrogel to mimic microvascular architecture while enabling perfusion and the establishment of solute and fluid pressure gradients (**Figure 2**; Song and Munn, 2011; Nguyen et al., 2013; Verbridge et al., 2013; Polacheck et al., 2017; Kutys et al., 2020). These systems are particularly useful for studying the effect on disease presentation of changes in surrounding ECM composition and structure. For instance, the use of degradable porous materials as bulk hydrogels in microfluidic

platforms have enabled investigations into the role of substrate stiffness (Bordeleau et al., 2017), chemical gradients (Kim et al., 2013; Nguyen et al., 2013), and fluid flow (Shin et al., 2011; Song and Munn, 2011) in directing endothelial sprouting and angiogenesis—a process that has been associated with atherosclerosis and ischemic heart disease (Khurana et al., 2005). Using a dextran hydrogel, Trappmann et al. investigated the material properties that impact angiogenesis and demonstrated that the degree of ECM degradability influences endothelial cell migration during angiogenesis (Trappmann et al., 2017). Despite the lack of a biologically relevant ECM microenvironment, synthetic hydrogels can be functionalized with integrin binding sequences and cell degradable motifs which allow mimic and study of specific ECM properties such as binding capacity and matrix degradability in development and disease. Specifically, the authors modulated the matrix degradation rate by cross-linking protease sensitive sequences with different protease binding affinities to the hydrogel, and showed that depending on matrix degradability, endothelial cells could migrate as single cells or collectively as a multicellular unit. These results suggest that the angiogenic response to cytokine gradients can vary according to the composition of vascular matrix and local concentration of matrix metalloproteinases. Notably, these observations were enabled by the ability to establish molecular gradients across soft 3D ECM with the integration of high-resolution 3D imaging in microfluidic devices and would not have been captured in traditional 2D cell culture models.

Blood and lymphatic microvessels synthesized in microfluidic devices that incorporate 3D hydrogels have been shown to be effective models for investigating vascular barrier function, as transport between the luminal and surrounding hydrogel compartments can be visualized with high spatiotemporal resolution (Chrobak et al., 2006; Wong et al., 2012; Polacheck et al., 2017). These 3D vascularized models are typically encapsulated in collagen hydrogel, which mimics the multiscale organization of vascular ECM, and allows study of the dynamics of cell-ECM interactions and ECM remodeling in a physiologically relevant setting. Barrier function as measured by vascular permeability is a common indicator of vessel health and is dysregulated in many diseases, including atherosclerosis, cancer, lymphatic malformations, neurological disorders, and chronic inflammation (Bischel et al., 2013; Buchanan et al., 2014; McCurley et al., 2017; Partyka et al., 2017; Polacheck et al., 2019), and tissue-specific 3D vascularized models have been developed to explore the role of vascular permeability in disease progression. For example, Lugo-Cintron et al. developed a microfluidic platform to investigate the role of desmoplasia in modulating lymphatic permeability during breast cancer metastatic progression. The authors demonstrated decreased lymphatic barrier function with increased collagen density, which mimics desmoplasia and associated increased collagen deposition and tissue stiffening. In particular, they found that secretion of pro-inflammatory cytokine, IL-6 increases in a collagen density-dependent manner. They further demonstrated that targeted blocking of IL-6 receptor is sufficient to mitigate vessel leakiness. Similarly, IL-6 was found to mediate blood vascular dysfunction in a model of early breast cancer adapted to include a polarized epithelial duct (Kutys et al., 2020). In a similar bulk hydrogel system, Silvestri et al. developed a tumor organoid-vessel co-culture model to study the process of vascular recruitment and tumor intravasation. The model is designed to be compatible with live cell imaging and allow for real time visualization of tumor-vessel interaction within a physiological relevant ECM microenvironment. Using this platform, they identified multiple cellular mechanisms where tumor cells could interact, displace, and disrupt vascular function (Silvestri et al., 2020). Importantly, these results highlight the utility of the advanced imaging methods that come with using microfluidic platforms for studying cellular processes that are difficult to capture in animal disease models. Overall, these results underscore the importance of incorporating physiological relevant ECM protein into the microenvironment of vascular disease models to provide functional readouts of vasculature in relation to disease progression.

A number of microscale and microfluidic models of functional, contractile cardiac tissue have been made utilizing 3D hydrogels. We direct the reader to recent comprehensive reviews for the development of cardiac-on-chip technology, cardiac microtissues, and microfluidic models and focus our review on platforms that have been used for disease modeling (Ribas et al., 2016; Ronaldson-Bouchard and Vunjak-Novakovic, 2018; Kitsara et al., 2019). Broadly, by encapsulating cardiac cells within 3D hydrogels, these systems allow for the study of cardiac tissue mechanics with (Xiao et al., 2014; Marsano et al., 2016) or without active mechanical stimulation (Legant et al., 2009; Boudou et al., 2012; Aung et al., 2016). These platforms are important tools for cardiac disease modeling as they can be made with iPS-derived cardiac cells (Thavandiran et al., 2013; Hinson et al., 2015; Lu et al., 2017; Ronaldson-Bouchard et al., 2018). While many of these approaches are not traditionally microfluidic in that they do not include enclosed microfabricated channels, they are fabricated with similar approaches and afford many of the benefits for disease modeling discussed in this review.

In general, the models referenced above are created by mixing cardiomyocytes and fibroblasts with a synthetic or natural hydrogel and depositing this mixture into a well with parallel, vertical microposts. Over time, these cells remodel the hydrogel into a dense microtissue that is anchored by the microposts, and micropost deflection can be used to measure the contractile forces generated by the tissue (Polacheck and Chen, 2016). Cardiac microtissues have been used to assess cardiac structure and function in response to patient mutations (Hinson et al., 2015), and increasingly to assess cardiotoxicity as a measure of drug safety. For example Lu et al. generated a 96-well array of cardiac microtissues from iPSC derived cardiomyocytes to assess how eight different drugs with clinically-observed cardiotoxicity affected beating rates and overall viability of the microtissues (Lu et al., 2017). Interestingly, their results showed that many of these drugs did not cause cell death at high doses but did result in lower overall beating rates, a measure of cardiac function. These results demonstrate that the functional measurements enabled by these microtissues provide improved clinical relevance for

safety studies over traditional cardiomyocyte viability assays, highlighting the utility of microscale models for drug screening.

CARDIOVASCULAR TISSUE MORPHOLOGY

The substantial remodeling of blood vessels and vascular networks during tissue growth and morphogenesis during development highlights the intimate and reciprocal relationship between cardiovascular structure and function. While there is some debate as to the relative roles of genetic prespecification vs. adaptation to mechanical load (Jones et al., 2006), results from developmental and animal disease models have made it increasingly clear that consideration of both genetics and morphology are critical in the study of cardiovascular disease, where: (a) genetic mutations can result in dysfunctional structural adaptation that increases morbidity and mortality, for example, in vascular Ehlers-Danlos syndrome where defective collagen production leads to weakened blood vessels, aneurysm formation, and rupture (Bergqvist et al., 2013; Malfait et al., 2020); and (b) tissue morphology can exacerbate disease, for example, curvature and branches in the descending aorta can lead to local hemodynamic recirculation and atherosclerosis (Chiu and Chien, 2011). Through integration of genetic models of disease with approaches for patterning 2D and 3D ECM, as discussed above, microfluidic models have enabled novel insight into the structure-function relationships that underlie cardiovascular disease progression. Due in part to the complex multiscale structure of the vasculature and to the role of hemodynamics in disease progression, much more effort has been devoted to the development of microfluidics for understanding the role of morphology in vascular disease modeling. Thus, we refer the reader to recent reviews on cardiac disease modeling (Mathur et al., 2016; Ribas et al., 2016; Ronaldson-Bouchard and Vunjak-Novakovic, 2018) and focus the subsequent section on models of the vasculature.

Broadly, pathologic vascular morphology manifests at the vessel level, including abnormal vessel length, tortuosity, or diameter, or at the network level, including abnormal vascular density and branching (**Figure 3**; Han, 2012; Xu et al., 2017). The location and dimensions of these abnormalities vary among patients, presenting challenges in the use of animal models to investigate clinical heterogeneity. A key benefit of microfluidics is the ability to develop customized cardiovascular models whose dimensions and complexity can be modulated to recapitulate patient-specific morphologies (Piccinelli et al., 2009; Nam et al., 2015; Costa et al., 2017; Kaneko et al., 2018). Such approaches, developed using micro- and nanoscale patterning and printing, have been effective in elucidating patient specific abnormalities, and the details of model fabrication are reviewed previously by others (McDonald et al., 2000; Ho et al., 2015; Amin et al., 2016; Griffith et al., 2020). Furthermore, the vascular system is subjected to fluid flow and shear stress, variables that can be drastically altered by deviations from normal in vessel morphology (Han, 2012). Using the fabrication methods mentioned above, microfluidics can be used to model severe changes in vessel morphology that correspond to cardiovascular disease and assay the impact of these changes on fluid flow and shear stress profiles. Here, we review implementation of these microfluidic approaches that have been used to understand the mechanisms underlying how focal and global changes in vessel morphology contribute to vascular disease.

Aneurysms are a focal change in vessel structure that increase in prevalence with age and are associated with a variety of disorders such as diabetes, Marfan syndrome, and vascular Ehlers-Danlos syndrome (Muluk et al., 1994; Bergqvist et al., 2013; Raffort et al., 2018). They occur when a blood vessel wall weakens at a specific point and begins to bulge, filling with blood and disturbing blood flow patterns. As fluid builds up in this newly formed bulge, the wall is weakened further, and changes in blood pressure and wall shear stress can eventually lead to rupture (Li and Kleinstreuer, 2005). The progression of aneurysms to dissection has been studied using computational fluid dynamic (CFD) modeling and has shown to be influenced by both aneurysm morphology and hemodynamics (Field, 2003; Xiang et al., 2011). However, using CFD with clinically obtained images alone does not allow for the impact of each of these factors—morphology and blood flow—to be individually analyzed. Reece et al. created a two-dimensional microfluidic model that can be used in tandem with particle image velocimetry to investigate how vessel structure changes due to aneurysm alter fluid flow and wall shear stress to trigger clotting within aneurysms (Reece et al., 2015). Their system allows for the visualization of the flow of beads or cells and thus provides a method for understanding how blood constituents flow differently through the aneurysm and initiate clotting in patients. Platforms created by Mannino et al. and Kaneko et al. built upon this two-dimensional flow model by recapitulating aneurysms using a three-dimensional microfluidic model with hydrogels, the first using more traditional techniques and the latter using patient MRI scans to inform 3D prints to generate their device's structure during fabrication (Mannino et al., 2015; Kaneko et al., 2018). Both groups used their microfluidic models to confirm previous CFD results based on clinical images and show wall shear stress is lower within the aneurysm sac (**Figure 3**). Kaneko et al. further showed that endothelial cells in the aneurysm sac differed in shape from those in the vessel lumen when exposed to fluid flow (Kaneko et al., 2018). By examining cell morphologies at different spots within the vessel, these results give indication of how changes on a cellular level could lead to further weakening and rupture of aneurysms. Collectively, these studies showcase how microfluidic models allow the examination of both the hemodynamics present in the vasculature, such as shear stress and flow profiles, and cellular phenotypes present within aneurysm, a vascular condition with a rather non-uniform morphological presentation.

Stenosis, or abnormal narrowing of blood vessels, is caused by a buildup of plaque in arteries or veins and is the major disease characteristic of atherosclerosis and thrombosis. Over time, these plaques rupture into precipitating thrombi that obstruct blood flow, and can result in stroke or myocardial infarction (Libby et al., 2019). Westein et al. observed that platelets tend to aggregate downstream of a stenosed mouse artery and developed

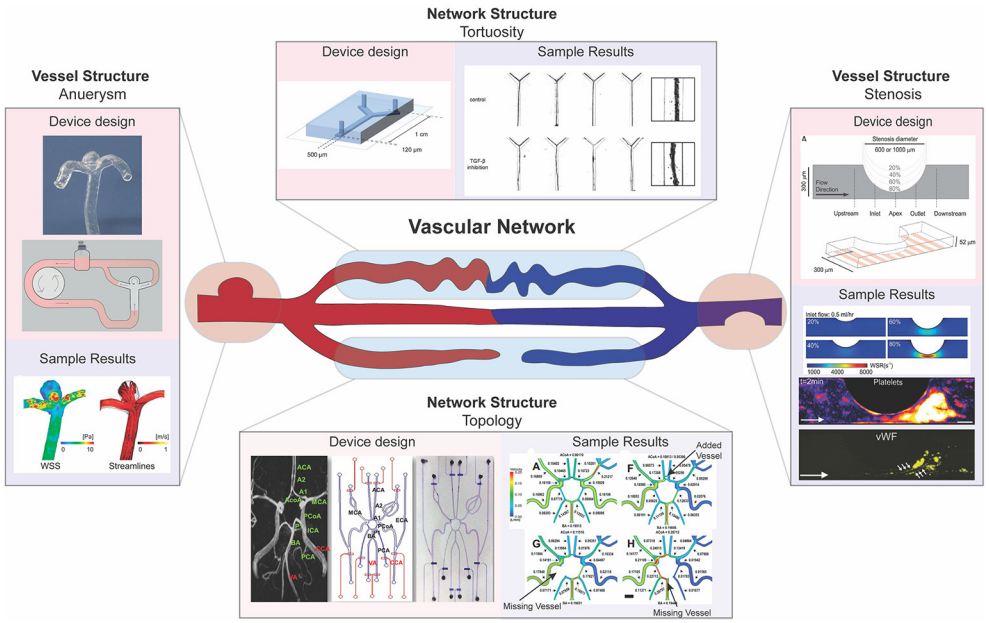

FIGURE 3 | Multi-scale modeling of pathophysiologic vascular morphology associated with vascular diseases. Microfluidic models have been developed to model pathologic alterations in vascular morphology at the vessel and network levels. Examples of investigations into focal vessel pathologies include microfluidics designed to model aneurysm (left) and stenosis (right). Examples of investigations into network pathologies include microfluidics designed to model high vessel tortuosity (top) and developmental pathologies in the circle of Willis (bottom). Functional outputs highlighted include computational fluid dynamic studies using microfluidic system morphology (left, right, bottom), quantitative and qualitative validation of vessel size and shape (top), and biochemical analysis to assess adhesion (right). [left: images reproduced from Kaneko et al. (2018) with permission from BMJ Publishing Group Ltd. Right: images reproduced from Westein et al. (2013). Top: Images republished with permission of Royal Society of Chemistry from van der Meer et al. (2013); permissions conveyed through Copyright Clearance Center Inc. Bottom: images reprinted from Nam et al. (2015), Copyright 2015, with permission from Elsevier].

a microfluidic model to identify hemodynamic changes that could contribute to downstream platelet aggregation. The authors fabricated a microfluidic device that recapitulated the stenosed structure and examined how factors such as wall shear stress, stenosis geometry, and activity of coagulation factors such as von Willebrand factor (vWF) changed along the stenosed structure (**Figure 3**). Their results showed that increased wall shear stresses at the stenosed region correlates with vWF activation and an increased capacity of platelet aggregation downstream to the site of stenosis, highlighting how microfluidic devices can be used to probe different aspects of disease presentation (Westein et al., 2013). Costa et al. took a three-dimensional approach to studying how platelet aggregation is affected by stenosis and used patient CT scans to generate 3D printed, endothelialized, stenosed vessels within a microfluidic chip. The authors fabricated cylindrical vessels with decreased diameter resembling points of stenosis and assessed thrombus formation by visualizing platelet accumulation after perfusion (Costa et al., 2017). Their results showed that changes in blood flow dynamics alone, as assessed by their microfluidic device, could not explain the location of thrombosis, suggesting that there is more to be discovered, and highlighting how the incorporation of patient-informed structure into microfluidic models has the potential to unveil mechanisms unable to be identified using traditional methods.

In addition to local changes in vessel structure, microfluidics have been developed to investigate the role of vascular network structure and remodeling in disease. For example, morphological variation, including absent vessels, within the circle of Willis (a complex network structure in the cerebrum) has been linked to cerebral aneurysm formation due to alteration in blood flow within this network (Nam et al., 2015). To study the relationship between wall shear stress resulting from this altered blood flow, Nam et al. fabricated a microfluidic device that recapitulates normal and disease state circle of Willis structures (**Figure 3**). The authors measured flow rates in the different morphological conditions and used CFD studies to show that higher shear stress correlates with aneurysm formation location in each of these conditions (Nam et al., 2015). Additionally, extreme deviation from straight vessel morphology has been implicated in various cardiovascular diseases, including atherosclerosis and ischemic heart disease (Han, 2012). As such, increased blood vessel tortuosity can be a measure of disease presentation, such as in hereditary hemorrhagic telangiectasia (HHT), a disease associated with disrupted TGF-ß signaling (Sawabe et al., 2001; Jaskolka et al., 2004). To investigate how TGF-ß signaling might impact tortuosity, van der Meer et al. fabricated a microfluidic device that contained endothelial cells and pericytes within a collagen hydrogel (**Figure 3**). By using a collagen hydrogel, these cells are able to remodel the hydrogel to form a self-organized vascular network, which allows probing of signaling

pathways involved in vascular network formation (van der Meer et al., 2013). The authors observed that inhibition of TGF-ß signaling leads to increased vessel tortuosity, which implies that disrupted TGF-ß signaling could exacerbate vessel tortuosity, potentially leading to the development of twisted vascular network structure occurs in HHT. These results highlight the utility of microfluidic models to recapitulate tissue level structure and morphology in investigating disease presentation, which is extremely important in vascular diseases where morphology can impact fluid dynamics, and in turn vascular health.

PATIENT-DERIVED CELLS AND GENETIC MUTATIONS

Due to the small sample sizes and compatibility with primary and patient-derived cells, microfluidic devices also allow the study of genetic disorders under physiologically relevant conditions. These systems are particularly useful for vascular disorders with distinct functional outputs that cannot be recapitulated using traditional *in-vitro* cell culture methods. Furthermore, genetic disorders are commonly caused by a wide diversity of driver gene mutations, which makes modeling the genetic landscape of human disease costly and challenging with animal models. The development of efficient gene editing, stem cell differentiation, and the increasing availability of patient-specific induced pluripotent stem cell (iPSC) lines have enabled the creation of genetically and physiologically relevant organ-on-chip systems for *in-vitro* disease modeling and drug testing. Here, we explore recent progress in genetic cardiovascular disease models, with an emphasis on the integration of patient iPSC derived cardiovascular cells in heart-on-chip and vascular-on-chip platforms for modeling pathologies in genetic disorders, including Barth syndrome, dilated cardiomyopathy, and Hutchinson-Gilford progeria syndrome. For a comprehensive review on the development of microfluidic devices for studying cardiovascular biology and drug development, see Ribas et al. (2016) and Ronaldson-Bouchard and Vunjak-Novakovic (2018).

Traditionally, cardiovascular microfluidic models were limited, as cardiovascular cells are difficult to acquire from patients. The generation of iPSCs and their subsequent differentiation into vascular cells (**Figure 4**) allowed for increasing adoption of cardiovascular microfluidics, as these approaches overcame the previous lack of human vascular cells and allowed for modeling of patient-specific genetic mutations. For example, Wang et al. developed a heart-on-chip platform to model cardiomyopathy in Barth Syndrome using iPSCs (Wang et al., 2014). Barth Syndrome (BTHS) is a rare metabolic disorder caused by recessive loss-of-function mutations in the tafazzin (TAZ) gene that results in dilated cardiomyopathy, skeletal myopathy, neutropenia, and short stature (Barth et al., 1983). TAZ catalyzes acylation of monolysocardiolipin into cardiolipin, a phospholipid that is essential for electron transport chain and ATP synthase function (Chicco and Sparagna, 2007; Houtkooper et al., 2009). In a recent study conducted by Wang et al., iPSCs derived from BTHS patients were differentiated into cardiomyocytes and were shown to have impaired cardiolipin acylation, increased reactive oxygen species production and other metabolic abnormalities associated with BTHS (Wang et al., 2014). The authors further employed a muscular thin film tissue construct (Grosberg et al., 2011) to demonstrate contractile dysfunction in BTHS (**Figure 4**). Cardiomyocytes on thin elastomeric membrane aligned to micropatterned lines and organized into strips of anisotropic muscle tissues. The muscular thin film bends and deflects the membrane during contraction which serves as a functional readout for contractile force. Using this model, they showed that BTHS-derived cardiomyocytes exhibit compromised contractile performance as compared to control cardiomyocytes. They further employed this platform to evaluate potential therapies for BTHS and demonstrated that multiple strategies—reintroducing tafazzin with modified RNA, buffering mitochondrial reactive oxygen species with antioxidant, or providing cells with linoleic acid, an alternative precursor to cardiolipin, can be used to rescue the disease phenotype. The results from this study not only provide novel mechanistic insights into BTHS pathogenesis but also demonstrate the utility of patient-derived iPSC cardiomyocytes and heart-on-chip technology for therapeutic discovery.

Another application for human iPSC-based heart-on-chip platform is the mechanistic investigation of incomplete penetrance in dilated cardiomyopathy caused by titin truncating mutations (Hinson et al., 2015). Titin, the largest known human protein, is known to function structurally as a scaffolding protein for sarcomere assembly and mechanically as a molecular spring that provides elasticity to the muscle (Granzier and Labeit, 2004; LeWinter and Granzier, 2010). The protein is composed of four structural domains: the N-terminal Z-line domain that is anchored to the sarcomeric Z-disk, the distensible I-band region that is responsible for muscle elasticity, the thick filament binding A-band region that functions as a scaffold for filament assembly, and the C-terminal M band region with a kinase domain. In a landmark multi-cohort study of patients with dilated cardiomyopathy, Herman et al. showed that mutations leading to truncations in titin accounts for up to 25 and 18% of familial and sporadic dilated cardiomyopathy cases, respectively (Herman et al., 2012). The truncation variants found in dilated cardiomyopathy cohort clusters around the A-band region. Interestingly, truncating variants located in the I-band region were found in both patient and healthy population, suggesting that truncations located in I-band are better tolerated than truncations in A-band region (Herman et al., 2012; Roberts et al., 2015). Using patient-derived iPSC cardiomyocytes and gene-edited iPSC cardiomyocytes, Hinson et al. investigated the penetrance of titin truncation variants (TTNtv) and missense variants within the A-band and I-band regions (Hinson et al., 2015). The pathophysiology of each variant was evaluated using cardiomyocytes contractility assays, both in 2D single cell and 3D engineered cardiac microtissues (**Figure 4**). While difference in contractile performance was undetectable in individual cardiomyocytes, both A-band and I-band TTNtv lines displayed significantly lower contractile forces compared to control cardiac microtissues. Additionally, contractility defects were less pronounced in I-band TTNtv in comparison with A-band variants, indicating a reduced penetrance of the mutation. Using

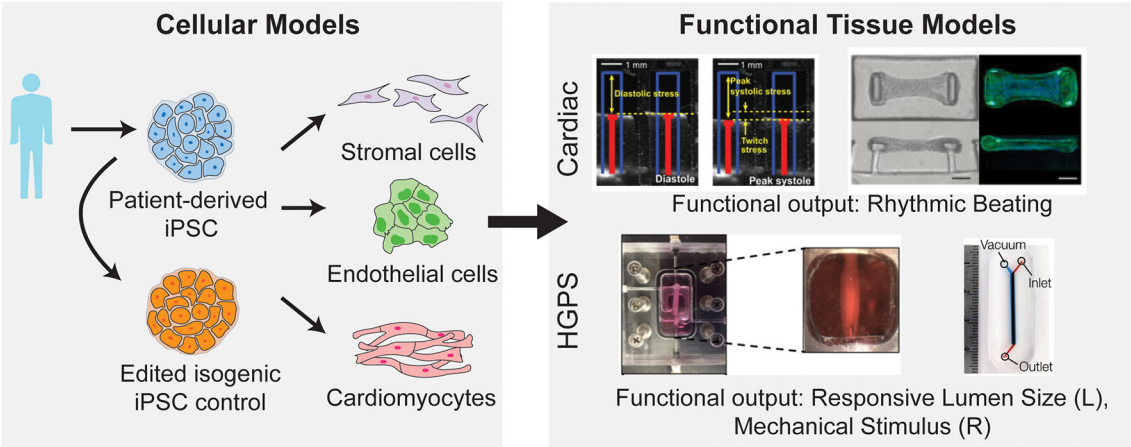

FIGURE 4 | Integration of patient derived iPSC with microfluidic models to study cardiovascular diseases. iPSCs can be generated from patient cells and subsequently differentiated into a variety of vascular cell types. Further these iPSCs can be genetically mutated to create an isogenic control cell line to preserve the genetic background of the patient but erase the mutation of interest (left). After differentiation into vascular cells, these cells can be used in microfluidic disease models of both cardiac and vascular diseases (right). By utilizing microfluidic systems, the disease model can incorporate functional outputs as indicated [top, right; image on the left reprinted by permission from Springer Nature Customer Service Centre GmbH: Springer Nature, Wang et al. (2014), Copyright 2014. Image on the right from Hinson et al. (2015). Reprinted with permission from AAAS. Bottom, right; image on the left reproduced from Atchison et al. (CC by 4.0: http://creativecommons.org/licenses/by/4.0/). Image on the right reprinted with permission from John Wiley and Sons from Ribas et al. (2017), Copyright 2017 WILEY-VCH Verlag GmbH & Co. KGaA, Weinheim].

RNA sequencing, the authors demonstrated that the affected I-band exon can be alternatively spliced and excluded from mature titin transcript. They further suggested alternative exon splicing functions as the predominant mechanism for reduced penetrance of I-band TTNtvs. Collectively, the results of this study demonstrate a successful integration of iPSC, gene editing, transcription profiling with tissue engineering technology and provide a promising platform for studying genotype to phenotype relationships in genetic cardiac condition.

Stem-cell based vessel-on-chip systems have also been developed for modeling vascular dysfunction in rare genetic disorders. Progeria, or Hutchinson-Gilford progeria syndrome is an extremely rare, progressive genetic condition that causes premature aging. The disease is resulted from the buildup of progerin, a mutant nuclear lamin A protein and causes accelerated degenerative aging in multiple systems, including skin, musculoskeletal, and cardiovascular systems (Kudlow et al., 2007). In studies by Atchison et al., 3D arteriole-scale vessel-on-chip were generated with endothelial cells (Atchison et al., 2020) and smooth muscle cells (Atchison et al., 2017, 2020) derived from healthy and Progeria patient iPSCs (**Figure 4**). The tissue-engineered Progeria vessels were shown to have increased inflammatory cytokines and reduced vasoactivity as compared to control vessels. Using these systems, the authors demonstrated that vascular endothelium may play a specific role in initiating inflammatory response and the development of atherosclerosis in Progeria. João Ribas et al. further developed a Progeria-on-chip model to study the impact of pulsatile cyclic strain on pathophysiology of the disease (Ribas et al., 2017). iPSC derived smooth muscle cells were cultured on PDMS membrane and stimulated with continuous pulsatile stretch and relaxation (**Figure 4**). The progeria patient-derived smooth muscle cells showed increased levels of DNA damage, inflammatory markers and senescence markers in response to mechanical strain. Additionally, the authors showed that these phenotypes can be reduced with lovastatin or lonafarnib—a drug that was submitted for the first-ever Progeria treatment. These results point to the utility of patient stem cells in vessel-on-chip platforms to facilitate drug development for rare vascular diseases.

DISCUSSION

Over the past several decades, animal models for cardiovascular disease have enabled great advances in understanding of physiology and disease progression that have led to the development of compounds and therapies that have broadly changed the prognostic landscape for cardiovascular disease. Increasingly, microfluidic devices have contributed to the arsenal of experimental approaches available for understanding cardiovascular biology, and as the efficiency of drug development declines (Scannell et al., 2012), microfluidic approaches hold promise in addressing gaps in current preclinical models (Low et al., 2020). As the technology required for fabrication has been more widely adopted, these devices have moved beyond the proof of concept phase to enable the study of patient derived cells and mutations on disease progression at the tissue scale without sacrificing physiological relevance, thus bridging the gap between human and mouse physiology. Recent developments in 3D printing (Skylar-Scott et al., 2019) and in the development of advanced bioinks (Gladman et al., 2016) are further improving the spatiotemporal resolution with which cells and tissues can be patterned, and advances in organoid technology (Park et al.,

2019) are enabling increasingly complex structures with cellular compositions more closely resembling native tissue. Integration of these technological advances with the ability to apply pressures and flows afforded by microfluidics will enable next-generation studies into the relationship between cardiovascular architecture and disease and open the possibility to develop these *in-vitro* systems into organ replacement or augmentation strategies.

While most recent work has focused on mutations that are conserved in diseased populations, the technology and methods developed to perform these studies will contribute to the development of individualized, patient-specific therapeutic interventions. As the cost and material requirements for gene sequencing continue to reduce, microfluidic cardiovascular disease models will be increasingly useful for understanding the functional consequences of individual and combinations of genetic mutations. Importantly, integration of disease models with information from electronic medical records will also allow study of comorbidities and patient history not well-captured by gene sequencing in cardiovascular disease progression. Such platforms and integrative approaches could also provide individualized preclinical safety and efficacy data to inform how a particular drug will impact a specific patient. Together, these advances will allow microfluidic cardiovascular disease models to study pathophysiological mechanisms and to screen for interventions in individual patients, and recent work supports the viability of this approach (Luna et al., 2020).

Currently, the development of microfluidic systems is intimately dependent on advances in animal models. Advances in understanding cardiovascular physiology inform the development of novel devices, and mechanistic insights into pathophysiology of cardiovascular disease enabled by microfluidics are largely validated with animal models. While this reciprocal relationship between animal models and microfluidics ostensibly ensures physiologic relevance of novel systems and assays, it presents a central obstacle in disease modeling and treatment development for diseases that are lacking translatable animal models. Furthermore, the lack of regulatory oversight on manufacturing standards and guidelines on device performance presents a bottleneck to clinical translation (Reyes-Hernandez et al., 2020). While recent companies have sought to commercialize specific chips, packaging and distribution of 3D hydrogels and cell-laden devices has yet to be achieved at the commercial scale. This requires individual labs to introduce ECM and cells into commercially available devices, which complicates standardization and contributes to a high degree of variability among research groups. As standard operating procedures and biomanufacturing continue to be developed to address these issues, challenges remain in regulatory interactions and strategy. Without standardized processes for determining the relevance and efficacy of microfluidic disease models, validation of new models requires recapitulation of key results in animal studies, which precludes development of microfluidic models for diseases in which animal models do not exist. While initiatives such as the Tissue Chip initiative led by the National Center for Advancing Translational Sciences in coordination with the Food and Drug Administration seek to address these challenges at a higher level, increasing coordination among investigators and laboratories developing the technology will improve adoption.

In summary, the integration of patient derived cells and mutations with microfluidic platforms has enabled novel insights into cardiovascular disease mechanisms that were not possible with standard *in-vitro* or animal disease models. Moving forward, continued advances in biochemistry and fabrication technology will enable these approaches to move beyond academic labs to significantly impact drug development for cardiovascular disease.

AUTHOR CONTRIBUTIONS

ED, WA, and WP drafted the manuscript and figures. WP and AH edited and provided comments on the manuscript and figures. All authors contributed to the article and approved the submitted version.

FUNDING

This work was supported by a research grant from the University of Pennsylvania Orphan Disease Center in partnership with the Lymphangiomatosis & Gorham's Disease Alliance and the Lymphatic Malformation Institute, and by a National Institutes of Health grant T32HL69768 (ED).

ACKNOWLEDGMENTS

The authors would like to thank Julie Blatt, MD for her feedback and commentary on the manuscript.

REFERENCES

Akbari, E., Spychalski, G. B., and Song, J. W. (2017). Microfluidic approaches to the study of angiogenesis and the microcirculation. *Microcirculation* 24:e12363. doi: 10.1111/micc.12363

Amin, R., Knowlton, S., Hart, A., Yenilmez, B., Ghaderinezhad, F., Katebifar, S., et al. (2016). 3D-printed microfluidic devices. *Biofabrication* 8:022001. doi: 10.1088/1758-5090/8/2/022001

Arribas, S. M., Hinek, A., and González, M. C. (2006). Elastic fibres and vascular structure in hypertension. *Pharmacol. Ther.* 111, 771–791. doi: 10.1016/j.pharmthera.2005.12.003

Atchison, L., Abutaleb, N. O., Snyder-Mounts, E., Gete, Y., Ladha, A., Ribar, T., et al. (2020). iPSC-derived endothelial cells affect vascular function in a tissue-engineered blood vessel model of hutchinson-gilford progeria syndrome. *Stem Cell Rep.* 14, 325–337. doi: 10.1016/j.stemcr.2020.01.005

Atchison, L., Zhang, H., Cao, K., and Truskey, G. A. (2017). A tissue engineered blood vessel model of Hutchinson-Gilford progeria syndrome using human iPSC-derived smooth muscle cells. *Sci. Rep.* 7:8168. doi: 10.1038/s41598-017-08632-4

Aung, A., Bhullar, I. S., Theprungsirikul, J., Davey, S. K., Lim, H. L., Chiu, Y. J., et al. (2016). 3D cardiac μtissues within a microfluidic device with real-time contractile stress readout. *Lab Chip* 16, 153–162. doi: 10.1039/C5LC00820D

Barth, P., Scholte, H., Berden, J. J., Van der Klei-Van Moorsel, J. M., Luyt-Houwen, I., Van 't Veer-Korthof, E. T., et al. (1983). An X-linked mitochondrial disease

affecting cardiac muscle skeletal muscle and neutrophil leukocytes. *J. Neurol. Sci.* 62, 327–355. doi: 10.1016/0022-510X(83)90209-5

Bergqvist, D., Björck, M., and Wanhainen, A. (2013). Treatment of vascular Ehlers-Danlos syndrome: a systematic review. *Ann. Surg.* 258, 257–261. doi: 10.1097/SLA.0b013e31829c7a59

Bhatia, S. N., and Ingber, D. E. (2014). Microfluidic organs-on-chips. *Nat. Biotechnol.* 32, 760–772. doi: 10.1038/nbt.2989

Bischel, L. L., Young, E. W., Mader, B. R., and Beebe, D. J. (2013). Tubeless microfluidic angiogenesis assay with three-dimensional endothelial-lined microvessels. *Biomaterials* 34, 1471–1477. doi: 10.1016/j.biomaterials.2012.11.005

Bonnans, C., Chou, J., and Werb, Z. (2014). Remodelling the extracellular matrix in development and disease. *Nat. Rev. Mol. Cell Biol.* 15, 786–801. doi: 10.1038/nrm3904

Bordeleau, F., Mason, B. N., Lollis, E. M., Mazzola, M., Zanotelli, M. R., Somasegar, S., et al. (2017). Matrix stiffening promotes a tumor vasculature phenotype. *Proc. Natl. Acad. Sci. U.S.A.* 114, 492–497. doi: 10.1073/pnas.1613855114

Boudou, T., Legant, W. R., Mu, A., Borochin, M. A., Thavandiran, N., Radisic, M., et al. (2012). A microfabricated platform to measure and manipulate the mechanics of engineered cardiac microtissues. *Tissue Eng. Part A* 18, 910–919. doi: 10.1089/ten.tea.2011.0341

Brown, X. Q., Ookawa, K., and Wong, J. Y. (2005). Evaluation of polydimethylsiloxane scaffolds with physiologically-relevant elastic moduli: interplay of substrate mechanics and surface chemistry effects on vascular smooth muscle cell response. *Biomaterials* 26, 3123–3129. doi: 10.1016/j.biomaterials.2004.08.009

Buchanan, C. F., Verbridge, S. S., Vlachos, P. P., and Rylander, M. N. (2014). Flow shear stress regulates endothelial barrier function and expression of angiogenic factors in a 3D microfluidic tumor vascular model. *Cell Adhesion Migrat.* 8, 517–524. doi: 10.4161/19336918.2014.970001

Chan, C. K., Rolle, M. W., Potter-Perigo, S., Braun, K. R., Van Biber, B. P., Laflamme, M. A., et al. (2010). Differentiation of cardiomyocytes from human embryonic stem cells is accompanied by changes in the extracellular matrix production of versican and hyaluronan. *J. Cell. Biochem.* 111, 585–596. doi: 10.1002/jcb.22744

Chen, C. S., Mrksich, M., Huang, S., Whitesides, G. M., and Ingber, D. E. (1997). Geometric control of cell life and death. *Science* 276, 1425–1428. doi: 10.1126/science.276.5317.1425

Chen, L., Yan, C., and Zheng, Z. (2018). Functional polymer surfaces for controlling cell behaviors. *Mater. Today* 21, 38–59. doi: 10.1016/j.mattod.2017.07.002

Cheng, J. K., and Wagenseil, J. E. (2012). Extracellular matrix and the mechanics of large artery development. *Biomech. Model. Mechanobiol.* 11, 1169–1186. doi: 10.1007/s10237-012-0405-8

Chicco, A. J., and Sparagna, G. C. (2007). Role of cardiolipin alterations in mitochondrial dysfunction and disease. *Am. J. Physiol. Cell Physiol.* 292, C33–C44. doi: 10.1152/ajpcell.00243.2006

Chiu, J.-J., and Chien, S. (2011). Effects of disturbed flow on vascular endothelium: pathophysiological basis and clinical perspectives. *Physiol. Rev.* 91, 327–387. doi: 10.1152/physrev.00047.2009

Chrobak, K. M., Potter, D. R., and Tien, J. (2006). Formation of perfused, functional microvascular tubes *in vitro*. *Microvasc. Res.* 71, 185–196. doi: 10.1016/j.mvr.2006.02.005

Clark, J. M., and Glagov, S. (1985). Transmural organization of the arterial media. The lamellar unit revisited. *Arteriosclerosis* 5, 19–34. doi: 10.1161/01.ATV.5.1.19

Costa, P. F., Albers, H. J., Linssen, J. E. A., Middelkamp, H. H. T, Van Der Hout, L., Passier, R., et al. (2017). Mimicking arterial thrombosis in a 3D-printed microfluidic *in vitro* vascular model based on computed tomography angiography data. *Lab Chip* 17, 2785–2792. doi: 10.1039/C7LC00202E

Cox, T. R., and Erler, J. T. (2011). Remodeling and homeostasis of the extracellular matrix: implications for fibrotic diseases and cancer. *Disease Models Mech.* 4, 165–178. doi: 10.1242/dmm.004077

Daley, W. P., and Yamada, K. M. (2013). ECM-modulated cellular dynamics as a driving force for tissue morphogenesis. *Curr. Opin. Genet. Develop.* 23, 408–414. doi: 10.1016/j.gde.2013.05.005

Davis, G. E., and Senger, D. R. (2005). Endothelial extracellular matrix: biosynthesis, remodeling, and functions during vascular morphogenesis and neovessel stabilization. *Circ. Res.* 97, 1093–1107. doi: 10.1161/01.RES.0000191547.64391.e3

Drury, J. L., and Mooney, D. J. (2003). Hydrogels for tissue engineering: scaffold design variables and applications. *Biomaterials* 24, 4337–4351. doi: 10.1016/S0142-9612(03)00340-5

Field, P. L. (2003). Why do aneurysms burst? *Heart Lung Circ.* 12. S52–S54. doi: 10.1016/S1443-9506(03)90390-8

Frantz, C., Stewart, K. M., and Weaver, V. M. (2010). The extracellular matrix at a glance. *J. Cell Sci.* 123, 4195–4200. doi: 10.1242/jcs.023820

Gladman, A. S., Matsumoto, E. A., Nuzzo, R. G., Mahadevan, L., and Lewis, J. A. (2016). Biomimetic 4D printing. *Nat. Mater.* 15, 413–418. doi: 10.1038/nmat4544

Gorgieva, S., and Kokol, V. (2011). Collagen-vs. gelatine-based biomaterials and their biocompatibility: review and perspectives. *Biomater. Appl. Nanomed.* 2, 17–52. doi: 10.5772/24118

Granzier, H. L., and Labeit, S. (2004). The giant protein titin: a major player in myocardial mechanics, signaling, and disease. *Circ. Res.* 94, 284–295. doi: 10.1161/01.RES.0000117769.88862.F8

Griffith, C. M., Huang, S. A., Cho, C., Khare, T. M., Rich, M., Lee, G. H., et al. (2020). Microfluidics for the study of mechanotransduction. *J. Phys. D Appl. Phys.* 53:224004. doi: 10.1088/1361-6463/ab78d4

Grosberg, A., Alford, P. W., McCain, M. L., and Parker, K. K. (2011). Ensembles of engineered cardiac tissues for physiological and pharmacological study: heart on a chip. *Lab Chip* 11, 4165–4173. doi: 10.1039/c1lc20557a

Han, H.-C. (2012). Twisted blood vessels: symptoms, etiology and biomechanical mechanisms. *J. Vasc. Res.* 49, 185–197. doi: 10.1159/000335123

Herbig, B. A., Yu, X., and Diamond, S. L. (2018). Using microfluidic devices to study thrombosis in pathological blood flows. *Biomicrofluidics* 12:042201. doi: 10.1063/1.5021769

Herman, D. S., Lam, L., Taylor, M. R., Wang, L., Teekakirikul, P., Christodoulou, D., et al. (2012). Truncations of titin causing dilated cardiomyopathy. *N. Engl. J. Med.* 366, 619–628. doi: 10.1056/NEJMoa1110186

Heron, M., and Anderson, R. N. (2016). Changes in the leading cause of death: recent patterns in heart disease and cancer mortality. *NCHS Data Brief* 254, 1–8.

Hinson, J. T., Chopra, A., Nafissi, N., Polacheck, W. J., Benson, C. C., Swist, S., et al. (2015). Titin mutations in iPS cells define sarcomere insufficiency as a cause of dilated cardiomyopathy. *Science* 349, 982–986. doi: 10.1126/science.aaa5458

Ho, C. M. B., Ng, S. H., Li, K. H. H., and Yoon, Y.-J. (2015). 3D printed microfluidics for biological applications. *Lab Chip* 15, 3627–3637. doi: 10.1039/C5LC00685F

Houtkooper, R. H., Turkenburg, M., Poll-The, B. T., Karall, D., Pérez-Cerd,á, C., Morrone, A., et al. (2009). The enigmatic role of tafazzin in cardiolipin metabolism. *Biochim. Biophys. Acta Biomemb.* 1788, 2003–2014. doi: 10.1016/j.bbamem.2009.07.009

Huber, D., Oskooei, A., Casadevall i Solvas, X., Demello, A., and Kaigala, G. V. (2018). Hydrodynamics in cell studies. *Chem. Rev.* 118, 2042–2079. doi: 10.1021/acs.chemrev.7b00317

Huh, D., Matthews, B. D., Mammoto, A., Montoya-Zavala, M., Hsin, H. Y., and Ingber, D. E. (2010). Reconstituting organ-level lung functions on a chip. *Science* 328, 1662–1668. doi: 10.1126/science.1188302

Humphrey, J. (2008). Vascular adaptation and mechanical homeostasis at tissue, cellular, and sub-cellular levels. *Cell Biochem. Biophys.* 50, 53–78. doi: 10.1007/s12013-007-9002-3

Hynes, R. (2007). Cell–matrix adhesion in vascular development. *J. Thromb. Haemost.* 5, 32–40. doi: 10.1111/j.1538-7836.2007.02569.x

Jaskolka, J., Wu, L., Chan, R. P., and Faughnan, M. E. (2004). Imaging of hereditary hemorrhagic telangiectasia. *Am. J. Roentgenol.* 183, 307–314. doi: 10.2214/ajr.183.2.1830307

Jones, E. A., le Noble, F., and Eichmann, A. (2006). What determines blood vessel structure? Genetic prespecification vs. hemodynamics. *Physiology* 21, 388–395. doi: 10.1152/physiol.00020.2006

Kaneko, N., Mashiko, T., Namba, K., Tateshima, S., Watanabe, E., and Kawai, K. (2018). A patient-specific intracranial aneurysm model with endothelial lining: a novel *in vitro* approach to bridge the gap between biology and flow dynamics. *J. Neurointerv. Surg.* 10, 306–309. doi: 10.1136/neurintsurg-2017-013087

Kapelko, V. I. (2001). Extracellular matrix alterations in cardiomyopathy: the possible crucial role in the dilative form. *Exp. Clin. Cardiol* 6, 41–49.

Khurana, R., Simons, M., Martin, J. F., and Zachary, I. C. (2005). Role of angiogenesis in cardiovascular disease: a critical appraisal. *Circulation* 112, 1813–1824. doi: 10.1161/CIRCULATIONAHA.105.535294

Kim, S., Lee, H., Chung, M., and Jeon, N. L. (2013). Engineering of functional, perfusable 3D microvascular networks on a chip. *Lab Chip* 13, 1489–1500. doi: 10.1039/c3lc41320a

Kitsara, M., Kontziampasis, D., Agbulut, O., and Chen, Y. (2019). Heart on a chip: micro-nanofabrication and microfluidics steering the future of cardiac tissue engineering. *Microelectron. Eng.* 203, 44–62. doi: 10.1016/j.mee.2018.11.001

Kolb, M., Margetts, P. J., Sime, P. J., and Gauldie, J. (2001). Proteoglycans decorin and biglycan differentially modulate TGF-β-mediated fibrotic responses in the lung. *Am. J. Physiol. Lung Cell. Mol. Physiol.* 280, L1327–L1334. doi: 10.1152/ajplung.2001.280.6.L1327

Kudlow, B. A., Kennedy, B. K., and Monnat, R. J. (2007). Werner and Hutchinson–Gilford progeria syndromes: mechanistic basis of human progeroid diseases. *Nat. Rev. Mol. Cell Biol.* 8, 394–404. doi: 10.1038/nrm2161

Kutys, M. L., Polacheck, W. J., Welch, M. K., Gagnon, K. A., Koorman, T., Kim, S., et al. (2020). Uncovering mutation-specific morphogenic phenotypes and paracrine-mediated vessel dysfunction in a biomimetic vascularized mammary duct platform. *Nat. Commun.* 11:3377. doi: 10.1038/s41467-020-17102-x

Legant, W. R., Pathak, A., Yang, M. T., Deshpande, V. S., McMeeking, R. M., and Chen, C. S. (2009). Microfabricated tissue gauges to measure and manipulate forces from 3D microtissues. *Proc. Natl. Acad. Sci. U.S.A.* 106, 10097–10102. doi: 10.1073/pnas.0900174106

LeWinter, M. M., and Granzier, H. (2010). Cardiac titin: a multifunctional giant. *Circulation* 121, 2137–2145. doi: 10.1161/CIRCULATIONAHA.109.860171

Li, Z., and Kleinstreuer, C. (2005). Fluid-structure interaction effects on sac-blood pressure and wall stress in a stented aneurysm. *J. Biomech. Eng.* 127, 662–671. doi: 10.1115/1.1934040

Libby, P., Buring, J. E., Badimon, L., Hansson, G. K., Deanfield, J., Bittencourt, M. S., et al. (2019). Atherosclerosis. *Nat. Rev. Disease Prim.* 5:56. doi: 10.1038/s41572-019-0106-z

Louzao-Martinez, L., Vink, A., Harakalova, M., Asselbergs, F. W., Verhaar, M. C., and Cheng, C. (2016). Characteristic adaptations of the extracellular matrix in dilated cardiomyopathy. *Int. J. Cardiol.* 220, 634–646. doi: 10.1016/j.ijcard.2016.06.253

Low, L. A., Mummery, C., Berridge, B. R., Austin, C. P., and Tagle, D. A. (2020). Organs-on-chips: into the next decade. *Nat. Rev. Drug Discov.* 1–17. doi: 10.1038/s41573-020-0079-3. [Epub ahead of print].

Lu, H. F., Leong, M. F., Lim, T. C., Chua, Y. P., Lim, J. K., Du, C., et al. (2017). Engineering a functional three-dimensional human cardiac tissue model for drug toxicity screening. *Biofabrication* 9:025011. doi: 10.1088/1758-5090/aa6c3a

Luna, D. J., Pandian, N. K., Mathur, T., Bui, J., Gadangi, P., Kostousov, V. V., et al. (2020). Tortuosity-powered microfluidic device for assessment of thrombosis and antithrombotic therapy in whole blood. *Sci. Rep.* 10:5742. doi: 10.1038/s41598-020-62768-4

Lv, H., Wang, H., Zhang, Z., Yang, W., Liu, W., Li, Y., et al. (2017). Biomaterial stiffness determines stem cell fate. *Life Sci.* 178, 42–48. doi: 10.1016/j.lfs.2017.04.014

Malfait, F., Castori, M., Francomano, C. A., Giunta, C., Kosho, T., and Byers, P. H. (2020). The Ehlers–Danlos syndromes. *Nat. Rev. Dis. Prim.* 6, 1–25. doi: 10.1038/s41572-020-0194-9

Mannino, R. G., Myers, D. R., Ahn, B., Wang, Y., Rollins, M., Gole, H., et al. (2015). Do-it-yourself *in vitro* vasculature that recapitulates *in vivo* geometries for investigating endothelial-blood cell interactions. *Sci. Rep.* 5:12401. doi: 10.1038/srep12401

Marsano, A., Conficconi, C., Lemme, M., Occhetta, P., Gaudiello, E., Votta, E., et al. (2016). Beating heart on a chip: a novel microfluidic platform to generate functional 3D cardiac microtissues. *Lab Chip* 16, 599–610. doi: 10.1039/C5LC01356A

Mathur, A., Ma, Z., Loskill, P., Jeeawoody, S., and Healy, K. E. (2016). *In vitro* cardiac tissue models: current status and future prospects. *Adv. Drug Deliv. Rev.* 96, 203–213. doi: 10.1016/j.addr.2015.09.011

McCurley, A., Alimperti, S., Campos-Bilderback, S. B., Sandoval, R. M., Calvino, J. E., Reynolds, T. L., et al. (2017). Inhibition of αvβ5 integrin attenuates vascular permeability and protects against renal ischemia-reperfusion injury. *J. Am. Soc. Nephrol.* 28, 1741–1752. doi: 10.1681/ASN.2016020200

McDonald, J. C., Duffy, D. C., Anderson, J. R., Chiu, D. T., Wu, H., Schueller, O. J. A., et al. (2000). Fabrication of microfluidic systems in poly(dimethylsiloxane). *Electrophoresis* 21, 27–40. doi: 10.1002/(SICI)1522-2683(20000101)21:1<27::AID-ELPS27>3.0.CO;2-C

Meester, J. A., Vandeweyer, G., Pintelon, I., Lammens, M., Van Hoorick, L., De Belder, S., et al. (2017). Loss-of-function mutations in the X-linked biglycan gene cause a severe syndromic form of thoracic aortic aneurysms and dissections. *Genet. Med.* 19, 386–395. doi: 10.1038/gim.2016.126

Muluk, S. C., Gertler, J. P., Brewster, D. C., Cambria, R. P., Lamuraglia, G. M., Moncure, A. C., et al. (1994). Presentation and patterns of aortic aneurysms in young patients. *J. Vasc. Surg.* 20, 880–888. doi: 10.1016/0741-5214(94)90224-0

Nam, S.-W., Choi, S., Cheong, Y., Kim, Y. H., and Park, H. K. (2015). Evaluation of aneurysm-associated wall shear stress related to morphological variations of circle of Willis using a microfluidic device. *J. Biomech.* 48, 348–353. doi: 10.1016/j.jbiomech.2014.11.018

Nguyen, D.-H. T., Stapleton, S. C., Yang, M. T., Cha, S. S., Choi, C. K., Galie, P. A., et al. (2013). Biomimetic model to reconstitute angiogenic sprouting morphogenesis *in vitro*. *Proc. Natl. Acad. Sci. U.S.A.* 110, 6712–6717. doi: 10.1073/pnas.1221526110

Parenteau-Bareil, R., Gauvin, R., and Berthod, F. (2010). Collagen-based biomaterials for tissue engineering applications. *Materials* 3, 1863–1887. doi: 10.3390/ma3031863

Park, S. E., Georgescu, A., and Huh, D. (2019). Organoids-on-a-chip. *Science* 364, 960–965. doi: 10.1126/science.aaw7894

Partyka, P. P., Godsey, G. A., Galie, J. R., Kosciuk, M. C., Acharya, N. K., Nagele, R. G., et al. (2017). Mechanical stress regulates transport in a compliant 3D model of the blood-brain barrier. *Biomaterials* 115, 30–39. doi: 10.1016/j.biomaterials.2016.11.012

Piccinelli, M., Veneziani, A., Steinman, D. A., Remuzzi, A., and Antiga, L. (2009). A framework for geometric analysis of vascular structures: application to cerebral aneurysms. *IEEE Trans. Med. Imaging* 28, 1141–1155. doi: 10.1109/TMI.2009.2021652

Polacheck, W. J., and Chen, C. S. (2016). Measuring cell-generated forces: a guide to the available tools. *Nat. Methods* 13, 415–423. doi: 10.1038/nmeth.3834

Polacheck, W. J., Kutys, M. L., Tefft, J. B., and Chen, C. S. (2019). Microfabricated blood vessels for modeling the vascular transport barrier. *Nat. Protoc.* 14, 1425–1454. doi: 10.1038/s41596-019-0144-8

Polacheck, W. J., Kutys, M. L., Yang, J., Eyckmans, J., Wu, Y., Vasavada, H., et al. (2017). A non-canonical Notch complex regulates adherens junctions and vascular barrier function. *Nature* 552, 258–262. doi: 10.1038/nature24998

Polacheck, W. J., Li, R., Uzel, S. G., and Kamm, R. D. (2013). Microfluidic platforms for mechanobiology. *Lab Chip* 13, 2252–2267. doi: 10.1039/c3lc41393d

Potente, M., and Mäkinen, T. (2017). Vascular heterogeneity and specialization in development and disease. *Nat. Rev. Mol. Cell Biol.* 18:477. doi: 10.1038/nrm.2017.36

Raffort, J., Lareyre, F., Clément, M., Hassen-Khodja, R., Chinetti, G., and Mallat, Z. (2018). Diabetes and aortic aneurysm: current state of the art. *Cardiovasc. Res.* 114, 1702–1713. doi: 10.1093/cvr/cvy174

Rajendran, P., Rengarajan, T., Thangavel, J., Nishigaki, Y., Sakthisekaran, D., Sethi, G., et al. (2013). The vascular endothelium and human diseases. *Int. J. Biol. Sci.* 9, 1057–1069. doi: 10.7150/ijbs.7502

Reece, L. M., Khor, J. W., Thakur, R., Amin, A., Wereley, S. T., and Leary, J. F. (2015). "A microfabricated microfluidic bioMEMS device to model human brain aneurisms: the aneurysm-on-a-chip," in *Microfluidics, BioMEMS, and Medical Microsystems XIII, International Society for Optics and Photonics* (San Francisco, CA). doi: 10.1117/12.2076037

Reyes-Hernandez, D. R., van Heeren, H., Guha, S., Herbertson, L., Tzannis, A. P., Ducrée, J., et al. (2020). Accelerating innovation and commercialization through standardization of microfluidic-based medical devices. *Lab Chip*. 21, 9–21. doi: 10.1039/D0LC00963F

Ribas, J., Sadeghi, H., Manbachi, A., Leijten, J., Brinegar, K., Zhang, Y. S., et al. (2016). Cardiovascular organ-on-a-chip platforms for drug discovery and development. *Appl. In Vitro Toxicol.* 2, 82–96. doi: 10.1089/aivt.2016.0002

Ribas, J., Zhang, Y. S., Pitrez, P. R., Leijten, J., Miscuglio, M., Rouwkema, J., et al. (2017). Biomechanical strain exacerbates inflammation on a progeria-on-a-Chip model. *Small* 13:1603737. doi: 10.1002/smll.201603737

Rienks, M., Papageorgiou, A. P., Frangogiannis, N. G., and Heymans, S. (2014). Myocardial extracellular matrix: an ever-changing and diverse entity. *Circ. Res* 114, 872–888. doi: 10.1161/CIRCRESAHA.114.302533

Roberts, A. M., Ware, J. S., Herman, D. S., Schafer, S., Baksi, J., Bick, A. G., et al. (2015). Integrated allelic, transcriptional, and phenomic dissection of the cardiac effects of titin truncations in health and disease. *Sci. Transl. Med.* 7:270ra276. doi: 10.1126/scitranslmed.3010134

Ronaldson-Bouchard, K., Ma, S. P., Yeager, K., Chen, T., Song, L., Sirabella, D., et al. (2018). Advanced maturation of human cardiac tissue grown from pluripotent stem cells. *Nature* 556, 239–243. doi: 10.1038/s41586-018-0016-3

Ronaldson-Bouchard, K., and Vunjak-Novakovic, G. (2018). Organs-on-a-chip: a fast track for engineered human tissues in drug development. *Cell Stem Cell* 22, 310–324. doi: 10.1016/j.stem.2018.02.011

Sakai, L. Y., Keene, D. R., Renard, M., and De Backer, J. (2016). FBN1: The disease-causing gene for Marfan syndrome and other genetic disorders. *Gene* 591, 279–291. doi: 10.1016/j.gene.2016.07.033

Sawabe, M., Arai, T., Esaki, Y., Tsuru, M., Fukazawa, T., and Takubo, K. (2001). Three-dimensional organization of the hepatic microvasculature in hereditary hemorrhagic telangiectasia. *Archiv. Pathol. Lab. Med.* 125, 1219–1223. doi: 10.1043/0003-9985(2001)125<1219:TDOOTH>2.0.CO;2

Scannell, J.W., Blanckley, A., Boldon, H., and Warrington, B. (2012). Diagnosing the decline in pharmaceutical RandD efficiency. *Nat. Rev. Drug Discov.* 11:191. doi: 10.1038/nrd3681

Secomb, T. W. (2016). Hemodynamics. *Compr. Physiol* 6, 975–1003. doi: 10.1002/cphy.c150038

Shin, Y., Jeon, J. S., Han, S., Jung, G. S., Shin, S., Lee, S. H., et al. (2011). *In vitro* 3D collective sprouting angiogenesis under orchestrated ANG-1 and VEGF gradients. *Lab Chip* 11, 2175–2181. doi: 10.1039/c1lc20039a

Silvestri, V. L., Henriet, E., Linville, R. M., Wong, A. D., Searson, P. C., and Ewald, A. J. (2020). A tissue-engineered 3D microvessel model reveals the dynamics of mosaic vessel formation in breast cancer. *Cancer Res.* 80, 4288–4301. doi: 10.1158/0008-5472.CAN-19-1564

Skylar-Scott, M. A., Uzel, S. G. M., Nam, L. L., Ahrens, J. H., Truby, R. L., Damaraju, S., et al. (2019). Biomanufacturing of organ-specific tissues with high cellular density and embedded vascular channels. *Sci. Adv.* 5:eaaw2459. doi: 10.1126/sciadv.aaw2459

Song, J. W., and Munn, L. L. (2011). Fluid forces control endothelial sprouting. *Proc. Natl. Acad. Sci. U.S.A.* 108, 15342–15347. doi: 10.1073/pnas.1105316108

Sun, Z. (2015). Aging, arterial stiffness, and hypertension. *Hypertension* 65, 252–256. doi: 10.1161/HYPERTENSIONAHA.114.03617

Thavandiran, N., Dubois, N., Mikryukov, A., Mass,é, S., Beca, B., Simmons, C. A., et al. (2013). Design and formulation of functional pluripotent stem cell-derived cardiac microtissues. *Proc. Natl. Acad. Sci. U.S.A.* 110, E4698–E4707. doi: 10.1073/pnas.1311120110

Thomson, J., Singh, M., Eckersley, A., Cain, S. A., Sherratt, M. J., and Baldock, C. (2019). Fibrillin microfibrils and elastic fibre proteins: functional interactions and extracellular regulation of growth factors. *Semi. Cell Develop. Biol.* 89, 109–117. doi: 10.1016/j.semcdb.2018.07.016

Trappmann, B., Baker, B. M., Polacheck, W. J., Choi, C. K., Burdick, J. A., and Chen, C. S. (2017). Matrix degradability controls multicellularity of 3D cell migration. *Nat. Commun.* 8:371. doi: 10.1038/s41467-017-00418-6

Tsai, M., Kita, A., Leach, J., Rounsevell, R., Huang, J. N., Moake, J., et al. (2011). *In vitro* modeling of the microvascular occlusion and thrombosis that occur in hematologic diseases using microfluidic technology. *J. Clin. Invest.* 122, 408–418. doi: 10.1172/JCI58753

Ugolini, G. S., Rasponi, M., Pavesi, A., Santoro, R., Kamm, R., Fiore, G. B., et al. (2016). On-chip assessment of human primary cardiac fibroblasts proliferative responses to uniaxial cyclic mechanical strain. *Biotechnol. Bioeng.* 113, 859–869. doi: 10.1002/bit.25847

van der Meer, A. D., Orlova, V. V., ten Dijke, P. A., van den Berg and Mummery, C. L. (2013). Three-dimensional co-cultures of human endothelial cells and embryonic stem cell-derived pericytes inside a microfluidic device. *Lab Chip* 13, 3562–3568. doi: 10.1039/c3lc50435b

Verbridge, S. S., Chakrabarti, A., DelNero, P., Kwee, B., Varner, J. D., Stroock, A. D., et al. (2013). Physicochemical regulation of endothelial sprouting in a 3D microfluidic angiogenesis model. *J. Biomed. Mater. Res. Part A* 101, 2948–2956. doi: 10.1002/jbm.a.34587

Wagenseil, J. E., and Mecham, R. P. (2009). Vascular extracellular matrix and arterial mechanics. *Physiol. Rev.* 89, 957–989. doi: 10.1152/physrev.00041.2008

Wagenseil, J. E., and Mecham, R. P. (2012). Elastin in large artery stiffness and hypertension. *J. Cardiovasc. Transl. Res.* 5, 264–273. doi: 10.1007/s12265-012-9349-8

Wang, G., McCain, M. L., Yang, L., He, A., Pasqualini, F. S., Agarwal, A., et al. (2014). Modeling the mitochondrial cardiomyopathy of Barth syndrome with induced pluripotent stem cell and heart-on-chip technologies. *Nat. Med.* 20, 616–623. doi: 10.1038/nm.3545

Wang, W. Y., Lin, D., Jarman, E. H., Polacheck, W. J., and Baker, B. M. (2020). Functional angiogenesis requires microenvironmental cues balancing endothelial cell migration and proliferation. *Lab Chip* 20, 1153–1166. doi: 10.1039/C9LC01170F

Westein, E. A., van der Meer, D., Kuijpers, M. J., Frimat, J. P., van den Berg, A., and Heemskerk, J. W. (2013). Atherosclerotic geometries exacerbate pathological thrombus formation poststenosis in a von Willebrand factor-dependent manner. *Proc. Natl. Acad. Sci. U.S.A.* 110, 1357–1362. doi: 10.1073/pnas.1209905110

Wong, K. H., Chan, J. M., Kamm, R. D., and Tien, J. (2012). Microfluidic models of vascular functions. *Annu. Rev. Biomed. Eng.* 14, 205–230. doi: 10.1146/annurev-bioeng-071811-150052

Xiang, J., Natarajan, S. K., Tremmel, M., Ma, D., Mocco, J., Hopkins, L. N., et al. (2011). Hemodynamic–morphologic discriminants for intracranial aneurysm rupture. *Stroke* 42, 144–152. doi: 10.1161/STROKEAHA.110.592923

Xiao, Y., Zhang, B., Liu, H., Miklas, J. W., Gagliardi, M., Pahnke, A., et al. (2014). Microfabricated perfusable cardiac biowire: a platform that mimics native cardiac bundle. *Lab Chip* 14, 869–882. doi: 10.1039/C3LC51123E

Xu, X., Wang, B., Ren, C., Hu, J., Greenberg, D. A., Chen, T., et al. (2017). Age-related impairment of vascular structure and functions. *Aging Dis.* 8:590. doi: 10.14336/AD.2017.0430

Zhang, C., and Neelamegham, S. (2017). Application of microfluidic devices in studies of thrombosis and hemostasis. *Platelets* 28, 434–440. doi: 10.1080/09537104.2017.1319047

Zheng, W., Huang, R., Jiang, B., Zhao, Y., Zhang, W., and Jiang, X. (2016). An early-stage atherosclerosis research model based on microfluidics. *Small* 12, 2022–2034. doi: 10.1002/smll.201503241

Zhou, J., Ellis, A. V., and Voelcker, N. H. (2010). Recent developments in PDMS surface modification for microfluidic devices. *Electrophoresis* 31, 2–16. doi: 10.1002/elps.200900475

Zhu, S., Herbig, B. A., Li, R., Colace, T. V., Muthard, R. W., Neeves, K. B., et al. (2015). In microfluidico: recreating *in vivo* hemodynamics using miniaturized devices. *Biorheology* 52, 303–318. doi: 10.3233/BIR-15065

Conflict of Interest: The authors declare that the research was conducted in the absence of any commercial or financial relationships that could be construed as a potential conflict of interest.

frontiers in Bioengineering and Biotechnology

BRIEF RESEARCH REPORT
published: 15 February 2021
doi: 10.3389/fbioe.2020.611802

Microfluidic System to Analyze the Effects of Interleukin 6 on Lymphatic Breast Cancer Metastasis

Hyeon-Yeol Cho[1,2†], *Jin-Ha Choi*[3†], *Kyeong-Jun Kim*[3], *Minkyu Shin*[3] and *Jeong-Woo Choi*[3*]

[1] Department of Bio and Fermentation Convergence Technology, Kookmin University, Seoul, South Korea, [2] Interdisciplinary Program for Bio-Health Convergence, Kookmin University, Seoul, South Korea, [3] Department of Chemical and Biomolecular Engineering, Sogang University, Seoul, South Korea

Metastasis is the primary cause of a large number of cancer-associated deaths. By portraying the precise environment of the metastasis process *in vitro*, the microfluidic system provides useful insights on the mechanisms underlying cancer cell migration, invasion, colonization, and the procurement of supplemental nutrients. However, current *in vitro* metastasis models are biased in studying blood vessel-based metastasis pathways and thus the understanding of lymphatic metastasis is limited which is also closely related to the inflammatory system. To understand the effects of inflammatory cytokines in lymphatic metastasis, we developed a three-channel microfluidic system by mimicking the lymph vessel-tissue-blood vessel (LTB) structure. Based on the LTB chip, we successfully confirmed the inflammatory cytokine, interleukin 6 (IL-6), -mediated intercellular communication in the tumor microenvironment during lymphatic metastasis. The IL-6 exposure to different subtypes of breast cancer cells was induced epithelial-mesenchymal transition (EMT) and improved tissue invasion property (8-fold). And the growth of human vein endothelial cells toward the lymph vessel channel was observed by VEGF secretion from human lymphatic endothelial cells with IL-6 treatment. The proposed LTB chip can be applied to analyze the intercellular communication during the lymphatic metastasis process and be a unique tool to understand the intercellular communication in the cancer microenvironment under various extracellular stimuli such as inflammatory cytokines, stromal reactions, hypoxia, and nutrient deficiency.

Keywords: lymph vessel, cancer metastasis, epithelial-mesenchymal transition, angiogenesis, circulating tumor cells, microfluidics

OPEN ACCESS

Edited by:
Shi-Cong Tao,
Shanghai Jiao Tong University, China

Reviewed by:
Jose M. Ayuso,
University of Wisconsin-Madison, United States
Anca Maria Cimpean,
Victor Babes University of Medicine and Pharmacy, Romania

***Correspondence:**
Jeong-Woo Choi
jwchoi@sogang.ac.kr

†These authors have contributed equally to this work

Specialty section:
This article was submitted to Nanobiotechnology, a section of the journal Frontiers in Bioengineering and Biotechnology

Received: *29 September 2020*
Accepted: *24 December 2020*
Published: *15 February 2021*

Citation:
Cho H-Y, Choi J-H, Kim K-J, Shin M and Choi J-W (2021) Microfluidic System to Analyze the Effects of Interleukin 6 on Lymphatic Breast Cancer Metastasis. Front. Bioeng. Biotechnol. 8:611802. doi: 10.3389/fbioe.2020.611802

INTRODUCTION

Cancer metastasis is a phenomenon involving the spread and proliferation of the primary cancer cells into secondary sites through the circulatory system, including lymph and blood vessels (Gupta and Massague, 2006). Cancer cells are heterogeneous and have different migration properties based on their phenotypes, which are strongly associated with malignancy (Brabletz et al., 2005). However, for the progress of metastasis from a benign cancer cell, epithelial-mesenchymal transition (EMT) and angiogenesis are necessary for the early stages (Kang and Massague, 2004). In the primary cancer microenvironment, EMT can be induced by various extracellular stimuli such

as stromal reactions, hypoxia (Matsuoka et al., 2013), nutrient deficiency (Recouvreux et al., 2020), and inflammatory cytokines (Muller et al., 2001). Epithelial cells undergo a change in their cell polarities, cytoskeletal systems, and cell-cell adhesion properties, and transition to mesenchymal cells with migratory and invasive properties (Yilmaz and Christofori, 2009). Subsequently, these cells present as circulating tumor cells (CTC), circulate the blood vessels and lymph nodes, and metastasize to other organs by the mesenchymal-epithelial transition (MET), which is the opposite of the EMT process (Banyard and Bielenberg, 2015). Subsequently, new blood vessels are generated in the anchored cancer cells by a process called angiogenesis, and the nutrients and oxygen necessary for their maintenance and proliferation are supplied to these cells (Folkman, 2002). This is one of the primary reasons why cancer is a very serious disease and difficult to treat. Therefore, this study is necessary to identify effective cancer therapies involving the prevention and elimination of metastasis.

EMT and angiogenesis are very important steps in the development and progress of cancer metastasis (Panchy et al., 2020). To study these phenomena, several researchers have used diverse model systems, including *in vivo* animals (Pereira et al., 2018) and *in vitro* cell culture models (Webb et al., 2017; Meng et al., 2019). Among these, animal surrogate models have been widely used (Pulaski and Ostrand-Rosenberg, 2000). However, they are extremely complex, and it is difficult to independently and selectively control each contributing factor and analyze the cause and effect. Further, the inherent differences between animal and human species result in inevitable failures in the prediction of pathophysiological progress (Martine et al., 2017). Conversely, *in vitro* models have the advantage of presenting simple and similar analyses owing to the use of human cells (Cho et al., 2018; Bu et al., 2019; Kim et al., 2020). In particular, the microfluidic model can present a system more similar to the human body compared to an animal model, owing to properties like the fluidic flow and shear stress (Sontheimer-Phelps et al., 2019; Mondadori et al., 2020). Moreover, since it is possible to cultivate two or more human cells simultaneously, it can be used to demonstrate intercellular communication, which is a critical point of research in cancer metastasis, including EMT and angiogenesis (Li et al., 2018; Lee et al., 2020). For these reasons, the microfluidic culture system has been used to study EMT and observe metastasis. Moreover, it is relatively easy to develop a microfluidic system for monitoring EMT and mesenchymal-epithelial transition (MET) during metastasis by replicating the capillary blood vessels and EMT-induced circulating tumor cells (CTC).

In this study, we designed a novel three-channel microfluidic chip for lymphatic metastasis by mimicking the lymph vessel-tissue-blood vessel (LTB) structure (**Figure 1**). The LTB chip consisted of a microfluidic chip that illustrated inflammatory cytokine-mediated EMT and angiogenesis in breast cancer, which involves the metastasis of tumor cells through the lymph vessel (**Figure 1A**). The lymphatic endothelial cells, which were critically affected by the CTCs, secreted vascular endothelial growth factor (VEGF), which induced angiogenesis and promoted breast cancer metastasis by promoting tumor invasiveness (Gong et al., 2019). The current *in vitro* microfluidic model of metastasis has focused on blood vessel-mediated metastasis. Recently, several microfluidic chips were developed to monitor the communication between cancer and lymph node, but this system was not showed the interaction with blood vessels (Shim et al., 2019). Also, a microfluidic model for analyzing cooperative effects of vascular angiogenesis and lymphangiogenesis was recently reported but this system was focused on direct interaction between blood and lymph vessel channels, not the effects of inflammatory cytokines (Osaki et al., 2018). Our newly designed LTB chip contained blood and lymph vessel channels to induce angiogenesis as a result of the EMT process of cancer cells (**Figure 1B**). Using this microfluidic chip platform, we reproduced and analyzed metastasis through the interaction between IL-6-treated cells and lymph and blood vessel channels (**Figure 1C**). This is the first study to replicate the metastasis process from EMT to angiogenesis in the lymph and blood vessel channels.

MATERIALS AND METHODS

Materials

The silicone elastomer (polydimethylsiloxane, PDMS) was purchased from Dow Corning (Midland, MI), and the Matrigel matrix was purchased from Corning (Bedford, MA). IL-6 and other chemicals were purchased from Sigma-Aldrich (St. Louis, MO).

Fabrication of the LTB Chip

The microchannel structure of the LTB chip was fabricated using the replica molding technique. First, we designed the device *in silico* using a computer-aided design (CAD) program (Mun et al., 2020). We created a positive relief 100 μm pattern on a silicon wafer by cleaning and dehydrating a 6-inch wafer and coating it uniformly with SU-8, the photoresist, using a spin coater. Subsequently, the coated wafer was pre-baked at 65°C on a level hot plate until the solvent evaporated, and the density of the SU-8 film increased. The coated wafer was then exposed to UV light using a transparent photomask to obtain a positive relief microfluidic channel. The wafer was baked at 95°C on a hot plate for selective cross-linking, and the microfluidic channel was developed using a photoresist developer. Finally, the wafer was briefly rinsed with isopropyl alcohol and dried using nitrogen gas.

A negative replica of the mold was made with PDMS by attaching the disposable chamber to the mold. The PDMS solution was cured in a convection oven at 70°C for 1 h, and the replica was peeled from the mold. Subsequently, the basement (cover glass) was coated with 20 μm thick PDMS and pre-cured for 10 min to establish a stable and strong connection between the replica and the basement. The replica was attached to a PDMS-coated basement and cured for 2 h. To establish a stronger connection between the replica and the basement, air oxygen plasma was treated (5 min for replica and basement) in the attachment step. After, a hole was introduced from the top to the basement, to create an inlet and outlet. The fabricated LTB chip was then autoclaved and sterilized at 120°C for 30 min, washed with deionized water (DW), and stored under dry conditions.

The matrigel was injected into the middle channel of the autoclaved LTB chip to make a hydrogel block in the chip,

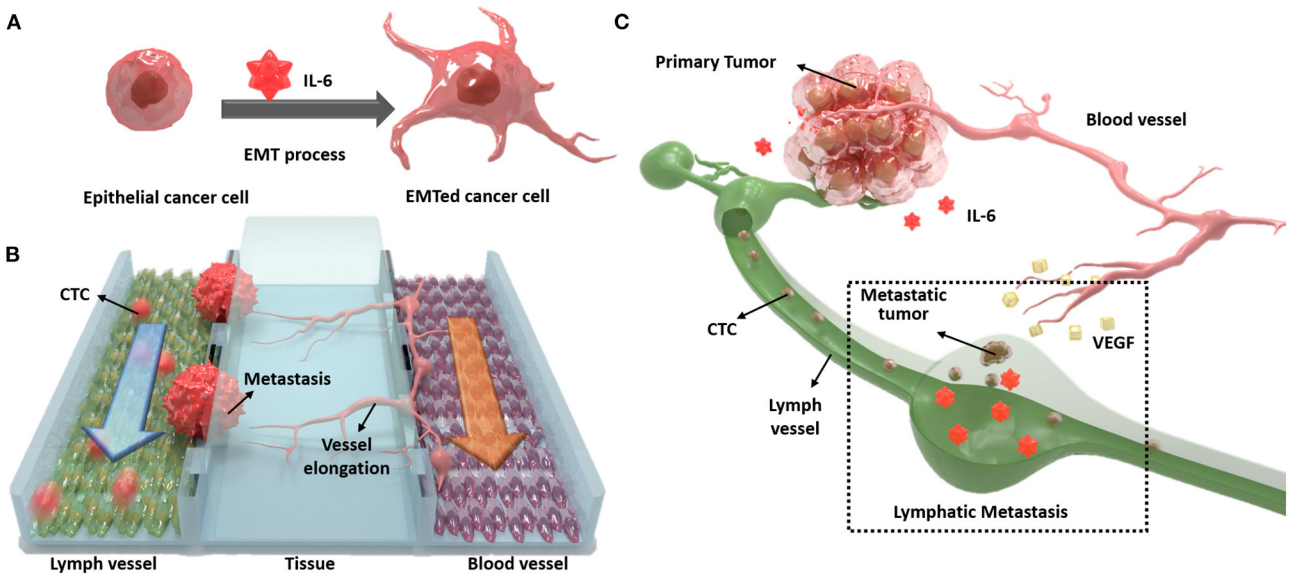

FIGURE 1 | Schematic diagram of the lymph vessel-tissue-blood vessel (LTB) chip. **(A)** Interleukin 6 (IL-6) induces epithelial-mesenchymal transition (EMT) of cancer cells and enhances metastatic properties. **(B)** LTB chip is designed to mimic the metastasis process of circulating tumor cells (CTCs) in the lymph vessel channel including colonization and recruitment of blood vessel cells. **(C)** Illustration of *in vivo* lymphatic metastasis process. The dash-line box indicates where the LTB chip mimics.

and incubated at 37°C for 1 h, under humid conditions, to facilitate gelation.

Cell Culture

Three breast cancer cell lines (MCF-7, MDA-MB-231, and SK-BR-3) were obtained from ATCC (Manassas, VA). All cell culture media and supplements were obtained from Invitrogen (Carlsbad, CA) unless otherwise noted. MDA-MB-231 cancer cell lines were grown in RPMI 1640 media, while MCF-7 and SK-BR-3 cells were grown in Dulbecco's Modified Eagle Medium (DMEM). All media were supplemented with 10% fetal bovine serum (FBS) and 1% Penicillin-Streptomycin. Cells were grown at 37°C and 5% CO_2 in a TC-grade Petri dish (BD Biosciences, San Jose, CA). The stem-like human breast cancer cell (S-HBCC) line and culture media were purchased from Celprogen (36102-29, Torrance, CA). These cells were grown at 37°C and 5% CO_2 in a TC-grade Petri dish (BD Biosciences, San Jose, CA). The media was renewed every 3 days for all three breast cancer cell lines and every 2 days for the S-HBCC. The human umbilical vein endothelial cells (HUVECs, ATCC) and human lymphatic endothelial cells (HLECs) were purchased from ScienCell Research Laboratories and maintained in endothelial cell medium (ECM, Sciencell, San Diego, CA) at 37°C and 5% CO_2. A matrigel coated culture plate was used to maintain HUVECs and HLECs coated with matrigel (1:20) in serum-free media for 1 h, to create a high-affinity surface with endothelial cells.

Cell Culture in the LTB Chip

Prior to the injection of endothelial cells, the inside of the LTB chip was filled with a fresh endothelial cell medium. To form a HUVECs and HLECs layer on the side of the hydrogel block in the LTB chip, each cell solution (300 μL, 1×10^7 cells/ml) was slowly added to the 90° rotated LTB chip and incubated for 12 h to let them attached on the surface of hydrogel block. Following the immobilization of the endothelial cells, fresh endothelial cell medium was added at a constant flow rate of 10 μL/min for 48 h, to form an endothelial cell layer on the side surface of the hydrogel block. Breast cancer cells were injected into the endothelial layer of the LTB chip with a flow rate of 5 μL/min for 6 h, and fresh cancer cell media was added continually. The entire process of cell culture and cell injection was performed in an incubator at 37°C and 5% CO_2. For the tracking purpose, breast cancer cells were labeled with membrane staining dyes (Blue: BioTracker 400 Cytoplasmic Membrane Dye, SCT109, Sigma-Aldrich, Red: DiI, D282, ThremoFisher Scientific).

Image Acquisition

All images were acquired using a confocal laser scanning microscope (Zeiss LSM 710; Carl Zeiss, Oberko, Germany) with a 16-bit monochromatic CCD (Orca R2; Hamamatsu Photonics, Shizuoka, Japan), under the 10x objective lens (LUCPlan FLN, NA: 0.45; Olympus, Tokyo, Japan). Fluorescent images were acquired in three separate channels, sequentially, to minimize potential cross-talk effects. The entire surface of the chip was scanned using a motorized stage to identify CTCs, based on cell morphology and immunofluorescent staining.

Quantification of VEGF Protein Secreted From HLEC

Cellular supernatants were harvested from HLEC and assayed for the amount of vascular endothelial growth factor (VEGF)

secreted using the VEGF Human ELISA Kit (Abcam Cambridge, MA). A total number of 20,000 cells were seeded in 96-well plates and allowed to adhere overnight. Subsequently, the cells were thoroughly rinsed with 1X PBS, and 200 μL of fresh RPMI complete media with IL-6 protein (100 ng/mL) was added to the cells. Cell cultures were incubated for 48 h, and the soluble supernatants were collected and assayed for VEGF protein, by ELISA, following the manufacturer's instructions.

Invasion Assay

The cell invasion ability was determined using a BioCoat Matrigel invasion chamber (BD Biosciences, Bedford, MA). The chamber membrane filter (pore size of 8 μm) was coated with a BD Matrigel Basement Membrane Matrix (BD Biosciences). The upper chamber was loaded with 25,000 cells in 0.5 mL of serum-free medium, and the lower chamber was filled with 0.75 mL of serum-containing medium. Following 22 h of incubation at 37°C and 5% CO_2, the non-invading cells on the upper surface of the membrane were removed using cotton swabs. The invading cells on the lower surface of the membrane were washed in PBS, fixed in paraformaldehyde, and stained with Hoechst 33342. For each membrane filter, the number of invading cells in 10 randomly selected fields were counted under a confocal laser scanning microscope (Zeiss LSM 710; Carl Zeiss, Oberko, Germany).

RNA Extraction and RT-PCR Analysis

Total RNA was isolated using TRIzol (Invitrogen), and cDNA was synthesized from 2 μg of total RNA using the SuperScript III First-Strand Synthesis Kit (Invitrogen). Subsequently, PCR was carried out using the AccuPower PCR-Premix (Bioneer, Daejeon, Korea). The primer sequences and reaction conditions are listed in **Supplementary Table 1**. The relative band intensities were determined using a spectrum imaging system (UVP, Upland, CA, USA). The target mRNA levels were normalized to the control condition after the normalization with a signal obtained for glyceraldehyde-3-phosphate dehydrogenase (GAPDH) mRNA expression.

Statistical Analysis

All experiments were repeated at least five times. Data are shown as means ± standard deviations. Statistical significance was determined by Welch's *t*-test with differences considered statistically significant at a value of $P < 0.05$.

RESULTS

Characterization of IL-6-Treated Breast Cancer Cells

To mimic the cancer metastasis environment, a microfluidic chip was designed *in situ*. The IL-6-treated cancer cells (considered as CTC), colonization, and invasion were monitored using three parallel channels, lymphatic vessel channel, blood vessel channel, and the extracellular matrix between the channels. The middle channel was filled with hydrogel to replicate the three-dimensional extracellular matrix with a tissue. Lymphatic and vascular endothelial cells were immobilized to form a layer on the vertical side of the hydrogel channel in the LTB chip. Prior to the fabrication of the microfluidic chip, EMT was induced to the breast cancer cells by treating various kinds of cytokines and microRNAs that generally exist in the cancer environment and induce the EMT process. These include the transforming growth factor-β1 (TGF-β1) for triggering EMT-associated pathways (Pang et al., 2016), microRNA to regulate pro-metastatic genes (Bullock et al., 2012), and interleukin-6 (IL-6) to downregulate the expression of epithelial markers (Sullivan et al., 2009). After the generation of two endothelial cell layers with the hydrogel, the IL-6-treated breast cancer cells were injected into the lymphatic channel to emulate the cancer metastasis process in the microfluidic system. In this study, we used IL-6 to change the properties of various breast cancer cells from those of epithelial cells to mesenchymal cells.

The exposure of breast cancer cells to IL-6 induced dramatic morphological changes in the cells, from the epithelial to the mesenchymal structure. In **Figure 2A**, HER-2 positive human breast cancer cells (SK-BR-3) were ramblingly stretched and spread out, while the untreated cells presented a round shape. Apart from the morphological changes, the expression of surface markers on the IL-6-treated cancer cells almost reduced to half (**Figure 2B**). This alteration in the expression of surface markers indicates an inherent change in its cellular properties. This was confirmed by measuring the expression levels of three different surface markers, HER2, EGFR, and EpCAM, expressed on breast cancer cells, by immunofluorescence analysis (**Figure 2A**). Interestingly, following IL-6 treatment, only the non-stretched cells showed similar intensity in the expression of specific surface markers.

The morphological changes in SK-BR-3 cells were analyzed by reverse transcription-PCR (RT-PCR) through the measurement of representative epithelial and mesenchymal marker expressions (**Figure 2C**). After 48 h IL-6 exposure, the SK-BR-3 cells showed dramatic downregulation of E-cadherin and upregulation of N-cadherin which is a representative pattern of the EMT process. Moreover, these two proteins are closely related to cell adhesion, motility as well as morphology. Similarly, other subtypes of breast cancer cell lines including MCF-7 (luminal type), and MDA-MB-231 (basal type) also showed a decrease of E-cadherin and an increase of N-cadherin with Vimentin with IL-6 exposure while S-HBCC (cancer stem cell type) was not showed significant change. Consequently, IL-6 induced the EMT process to various subtypes of breast cancer cells except for the stem cell populations.

Additionally, we conducted an invasion assay to confirm the metastatic property of IL-6-treated cells following treatment with IL-6. To determine whether IL-6 exposure functionally enhanced the invasive capacity of breast cancer cells, we used a cell invasion chamber composed of Transwells and embedded with hydrogel. Prior to the seeding of breast cancer cells, HLECs were immobilized on the top side of the hydrogel in the invasion chamber to mimic the actual human lymph vessel. We found that the control and IL-6-treated breast cancer cells exhibited different degrees of invasiveness through the lymphatic, layered-hydrogel in the presence of FBS as a chemoattractant (**Figure 3A**). Every subtype of the IL-6-treated breast cancer cell except the S-HBCC was significantly (*P*-value < 0.01) more

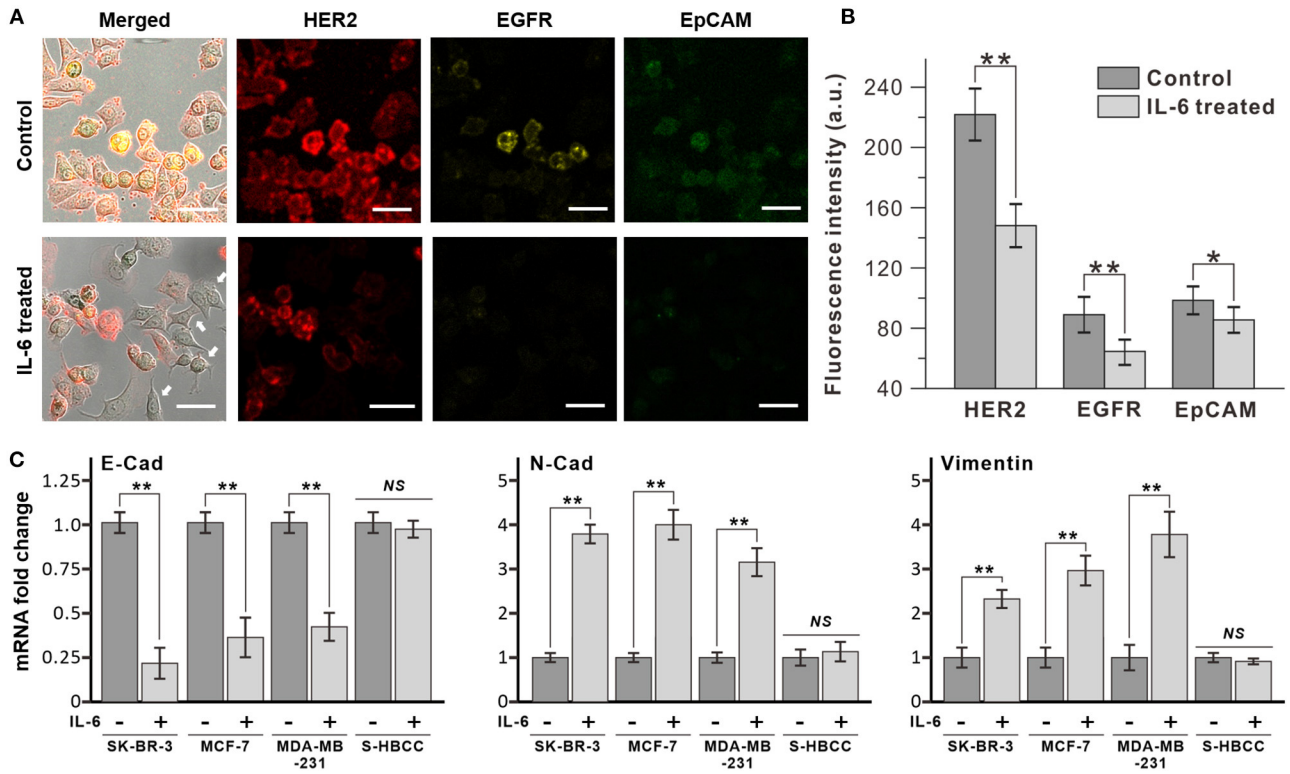

FIGURE 2 | Decrease of epithelial marker expression by interleukin 6 (IL-6). **(A)** Immunofluorescence analysis of breast cancer cell (SK-BR-3) with IL-6 treatment. After 2 days, dramatic morphological changes were shown with decrease surface marker expression (bottom row, IL-6 treated) compared to untreated condition (upper row, control). White arrows indicate cells that have morphology change and lower surface marker expression. **(B)** Comparison of surface marker signal intensity with IL-6 treatment. **(C)** RT-PCR results of EMT-related gene expression on different subtypes of breast cancer cells. The data represent means ± standard deviations (SD) of five different experiments (*$p < 0.05$, **$p < 0.01$). RT-PCR results are normalized with control after the normalization with GAPDH.

invasive and attained over a 5-fold increase compared to the control cells (SK-BR-3: 8-fold; MCF 7: 4.97-fold; and MDA-MB-231: 4.35-fold) (**Figure 3B**). The S-HBCCs showed high invasiveness from both control and IL-6 treated conditions while there were no significant changes, which is concordant with the lack of change in E-cadherin expression at a low level (**Supplementary Figure 1**). Therefore, IL-6 can induce the EMT process on various subtypes of breast cancer cells, except the stem-like subtype, and also enhances the invasiveness of tumor cells.

Inducing VEGF Secretion From HLECs for Cancer Metastasis

According to the *in vivo* research, the interaction between IL-6 and lymphatic endothelial cells in lymphatic metastasis of breast cancer were induced angiogenesis (Lee et al., 2014a,b). To confirm the IL-6-mediated angiogenesis process in a human cell-based LTB chip can mimic a lymph system in the mouse model, 100 ng/mL IL-6 was treated with HLECs in culture media (**Figure 4A**). Among various angiogenic factors, VEGF was selected as a representative marker to follow *in vivo* research (Lee et al., 2014a). The concentration of secreted VEGF was analyzed with the ELISA assay. As expected, secretion of VEGF was stimulated with IL-6 treatment and linearly increased in a time-dependent manner while control condition didn't show VEGF secretion (data not shown). However, the amount of VEGF in media was saturated after 48 h of IL-6 exposure because of the consumption (Gao et al., 2017) or fast degradation (half-life 15.5 h, Kuribayashi, 2018) of IL-6 in batch culture condition.

The VEGF secreted from the lymphatic endothelial cell recruited the blood vessels from pre-existing vessels. To verify the angiogenic effect of cytokines secreted from HLEC with IL-6 treatment on HUVECs, a vascular endothelial cell, the Transwell platform-based density gradient system was utilized (**Figure 4B**). HUVECs were seed on the top side of a hydrogel block in Transwell. The area outside the Transwell was filled with HLEC cultured media with IL-6 for 2 days and HUVEC seeded side was filled with HUVEC culture media to eliminate the nutrient-taxis effects. After 5 days, HUVECs were vertically grown more than 100 μm toward the side containing the HLEC culture media while the control (HLEC cultured media for 2 days without IL-6) didn't show any distinctive change. It indicates that the level of VEGF secreted from HLECs was sufficient to communicate with HUVECs. As similar to the saturation of VEGF secretion in a batch culture condition,

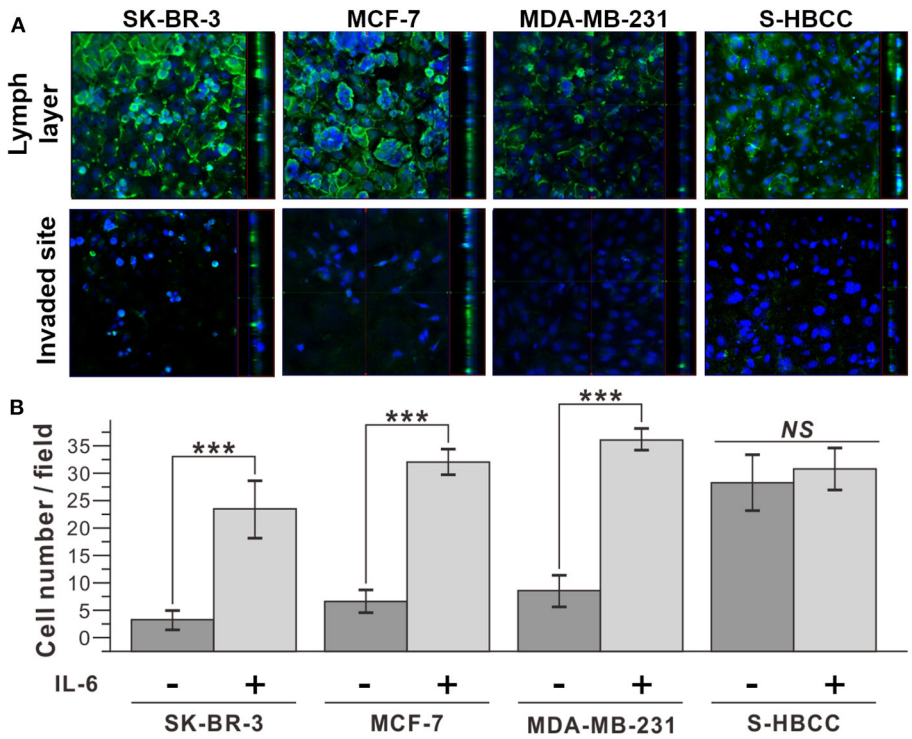

FIGURE 3 | Improved invasiveness of IL-6-treated breast cancer cells with IL-6. **(A)** Confocal microscope images of IL-6 treated breast cancer cells. The upper row shows the top side of the hydrogel block with the HLEC layer and the lower row shows the bottom side of the hydrogel block. (Green: CD31, Blue: Nucleus) **(B)** Cell counting analysis after cell penetration through the hydrogel. IL-6-treated cells were obtained by IL-6 treatment for 2 days. The data represent means ± standard deviations (SD) of five different experiments (***$p < 0.001$).

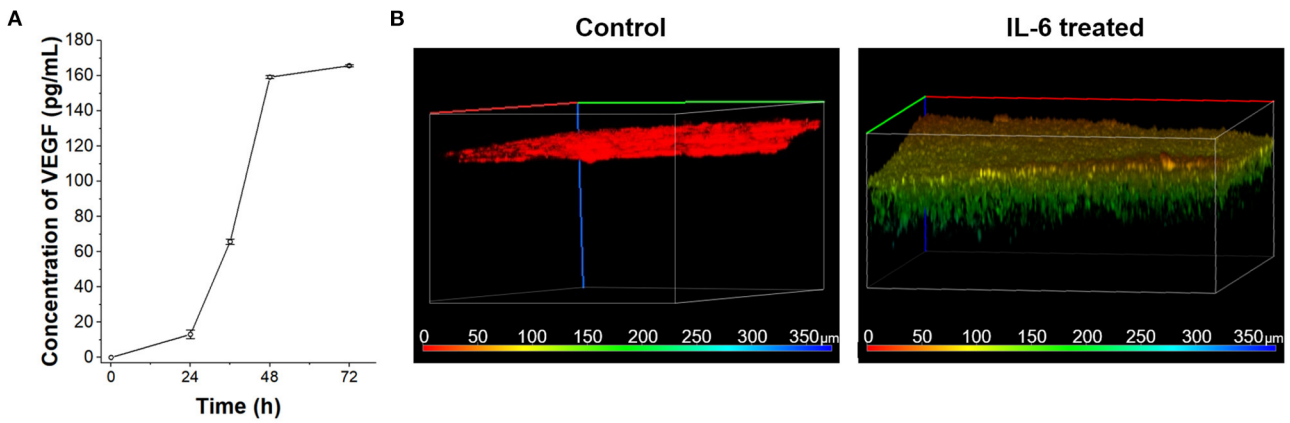

FIGURE 4 | VEGF secretion of HLECs by IL-6 treatment. **(A)** Time-dependent VEGF secretion from HLECs under the IL-6 (100 ng/mL) contained HLEC maintain media. **(B)** Recruitment of blood vessel cells (HUVECs) growth test toward control (HLEC cultured media without IL-6 treatment) and IL-6 treated (HLEC cultured media with IL-6 treatment) conditions. The pseudo color was applied to show the depth profile.

the vertical growth speed of HUVECs was also decreased with the consumption of VEGF (Jeong et al., 2011). Both issues with batch culture conditions can be overcome with the continuous supply of substrates (IL-6) by using the microfluidic chip system.

Monitoring of IL-6-Mediated Cancer Metastasis in the Microfluidic Chip

The LTB chip was fabricated with three-channel structures consisting of a lymph vessel channel, extracellular matrix, and blood vessel channel (**Figure 5A**). Three squared pillars

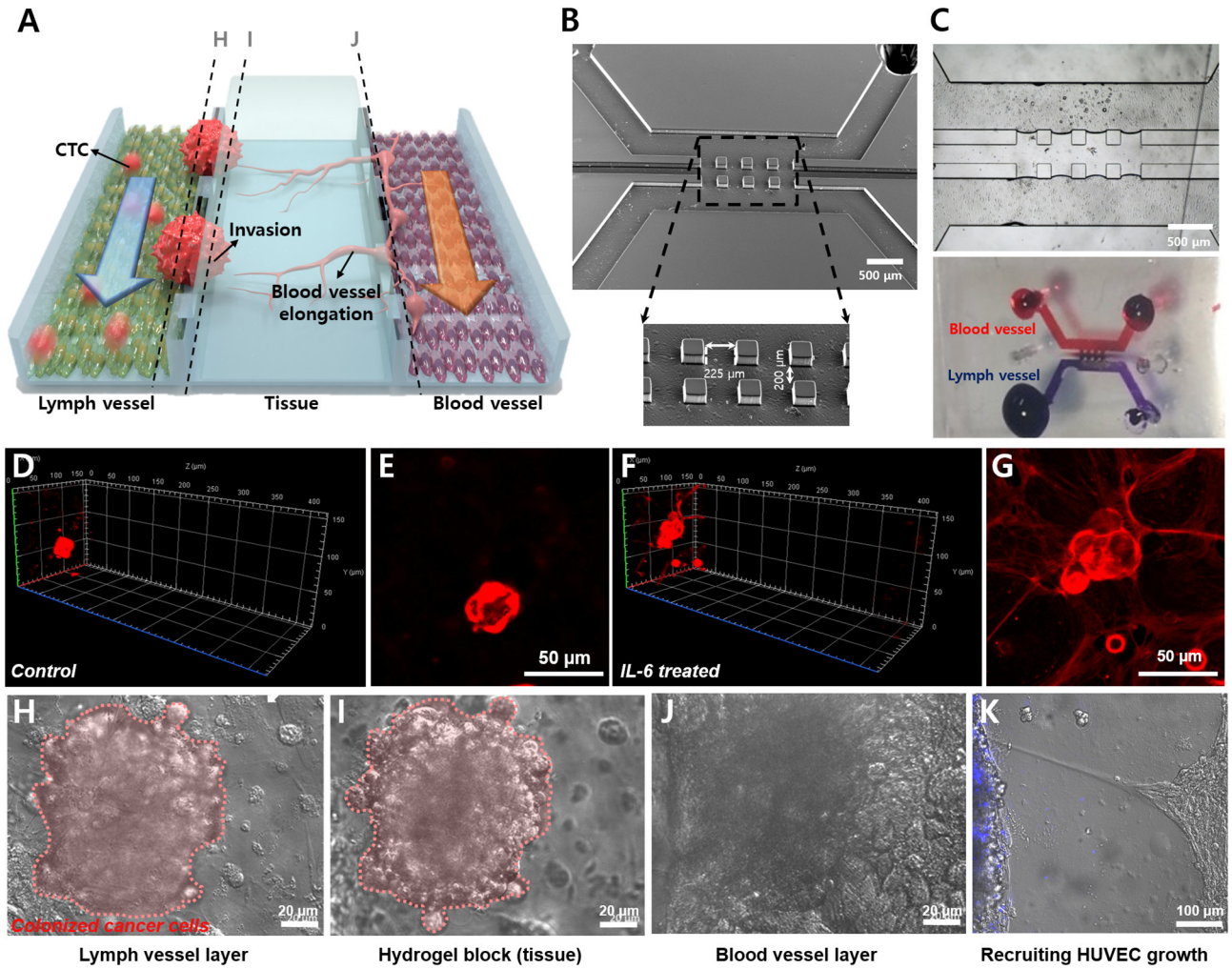

FIGURE 5 | Demonstration of lymphatic metastasis process in LTB chip. **(A)** Schematic diagram of the lymphatic metastasis process in LTB chip. **(B)** SEM image of the three-channel structure of LTB chip. Scale bar: 500 μm. **(C)** Hydrogel block formation in the middle channel. Hydrogel block showed prevention of direct connection between lymph channel and blood channel while small molecules can slowly diffuse to each side. **(D–G)** Colonization of control **(D,E)** and IL-6 treated SK-BR-3 cells **(F,G)** on the endothelial cell seeded hydrogel block. For **(D)** and **(F)**, left side is lymph vessel channel and right side is blood vessel channel. Red: membrane dye (DiI) labeled cancer cells. **(D)** 3D confocal image of IL-6 non-treated SK-BR-3 and **(E)** 2D image on the HLEC layer. **(F)** 3D confocal image of IL-6 treated SK-BR-3 and **(G)** 2D image on the HLEC layer. **(H–J)** Microscopic image of colonized breast cancer cell in LTB chip (vertical section images). **(H)** Colonized breast cancer cell cluster on the surface of HLEC layer (pink color labeled (pseudo color), left side of hydrogel block). **(I)** Tissue penetration of cancer cells. **(J)** The surface of HUVEC layer (right side of the hydrogel block). **(K)** Growth of HUVECs toward lymph channel (left). Blue: membrane dye (BioTracker 400) labeled cancer cells.

separated the three channels and the middle channel was loaded with hydrogel (**Figure 5B**). **Figure 5C** demonstrates the three-dimensional matrix in the middle layer and the flow of fluid in the blood and lymph vessel channels independently, with permeation through the hydrogel. Two different endothelial cells were immobilized separately, HLECs and HUVECs. After the formation of an endothelial layer on the side of the hydrogel block, the breast cancer cells were injected for 6 h with IL-6 containing fresh media, to induce the EMT process on the cancer cells and facilitate VEGF secretion from HLECs. The flow rates of the fluid in the blood and lymph vessel channels were set differently to match *in vivo* conditions (lymph vessel channel: 5 μL/min, blood vessel channel: 15 μL/min). To validate the effects of IL-6 on HLECs and cancer cells in the microfluidic system, we obtained optical images of the cells in each fluidic channel. As expected, the injected breast cancer cells were attached to the sidewall of the lymph channel and colonized as a solid tumor (**Figures 5D–G**). Even though cancer cells were formed clusters in both control and IL-6 treated conditions, but invasion behavior was different. When breast cancer cells were colonized without IL-6, the shape of colonies was similar to spheroids with a plane surface (**Figures 5D,E**). Differently, IL-6 treated breast cancer cell colonies were stretched out to surrounding areas with sharp tip ends (**Figures 5F,G**). However,

after 1 week from the colonization, the size of the colony reached around 100 μm and saturated (**Figures 5H–J**). Subsequently, the HUVECs were grown toward the lymphatic side, forming the shape of a tip (**Figure 5K**). Additionally, we found that when HUVECs were grown toward the lymph vessel channel, the tip end was headed to the cancer cell clustered site (blue labeled). It was known that breast cancer cell-HLEC co-culture induces higher secretion (up to 600%) of VEGF from HLECs with both SK-BR-3 (Tawada et al., 2014) and MDA-MB-231 cells (Lee et al., 2014b). Consequently, we successfully mimicked cancer metastasis, including the EMT process of breast cancer cells and angiogenesis of blood and lymph vessel channels in the microfluidic device.

DISCUSSION

In this study, we fabricated a microfluidic chip replicating the blood and lymph vessel channels in the human body and monitored the effects of inflammatory cytokine, IL-6, on breast cancer metastasis process at the *in vitro* condition. EMT was induced in the breast cancer cells by IL-6 treatment. Every subtype of breast cancer cell showed upregulation of mesenchymal-related gene profile, morphological changes as shown in **Figure 2**. The invasion assay revealed that the IL-6-treated breast cancer cells presented higher transvascular invasiveness compared to the untreated cells as shown in **Figure 3**. To fabricate the LTB chip, a three-channel microfluidic was designed for *in situ* monitoring of cancer cell colonization and invasion. The middle channel was filled with collagen-based hydrogel to replicate the tissues *in vivo*. HLECs and HUVECs were seeded to form a layer on the side of the hydrogel in the LTB chip. Subsequently, the IL-6-treated breast cancer cells were injected along with IL-6-containing media into the LTB chip, and the injected cells were monitored using a confocal microscope. The IL-6-treated breast cancer cells successfully immobilized and colonized on the HLEC layer and began invading into the inner side of the hydrogel layer. Subsequently, the HLECs were stimulated by IL-6 to secrete VEGF, which caused the HUVECs to grow toward the cancer cell clusters near the lymph channel as shown in **Figures 4**, **5**. Even though the LTB chip showed recruitment of blood vessel cells in the chip, morphology of HUVECs in the angiogenesis process has to form the microvascular structure (Ko et al., 2019; Sewell-Loftin et al., 2020). It may happen by forming a small niche between the hydrogel block and bottom substrate during the gelation process. By addressing recent 3D printing-based *in vitro* metastatic model system, the current issue of our LTB chip can be covered and improved to closely mimicked *in vivo* system (Meng et al., 2019).

To this end, effects of IL-6 on lymphatic metastasis of breast cancer cell was mimicked and analyzed with a newly developed LTB chip, therefore, it can be utilized as an analysis platform for understanding the effects of various inflammatory cytokines on metastasis. Moreover, the LTB chip will offer a new platform to understand the interaction between the tumor microenvironment and the lymph system. The improvement of knowledge of subtype-specific tumor behavior in the lymph system will provide crucial information for early diagnosis, prognosis monitoring, and personalized therapy for breast cancer patients.

DATA AVAILABILITY STATEMENT

The original contributions presented in the study are included in the article/**Supplementary Material**, further inquiries can be directed to the corresponding author.

AUTHOR CONTRIBUTIONS

H-YC and J-WC designed the experiment. H-YC and K-JK designed and fabricated the microfluidic device. H-YC, J-HC, MS, and J-WC collected and analyzed the results. All authors collaboratively wrote the manuscript.

FUNDING

This research was supported by the Basic Science Research Program through the National Research Foundation of Korea (NRF) funded by the Ministry of Education (No. NRF−2019R1I1A1A01058888), the National Research Foundation of Korea (NRF) grant funded by the Korea government (MSIT) (No. 2019R1A2C3002300), and the Basic Science Research Program through the National Research Foundation of Korea (NRF) funded by the Ministry of Education (No. 2016R1A6A1A03012845).

SUPPLEMENTARY MATERIAL

The Supplementary Material for this article can be found online at: https://www.frontiersin.org/articles/10.3389/fbioe.2020.611802/full#supplementary-material

REFERENCES

Banyard, J., and Bielenberg, D. R. (2015). The role of EMT and MET in cancer dissemination. *Connect. Tissue Res.* 56, 403–413. doi: 10.3109/03008207.2015.1060970

Brabletz, T., Jung, A., Spaderna, S., Hlubek, F., and Kirchner, T. (2005). Opinion: migrating cancer stem cells–an integrated concept of malignant tumour progression. *Nat. Rev. Cancer* 5, 744–749. doi: 10.1038/nrc1694

Bu, J., Shim, J.-E., Lee, T. H., and Cho, Y.-H. (2019). Multi-modal liquid biopsy platform for cancer screening: screening both cancer-associated rare cells and cancer cell-derived vesicles on the fabric filters for a reliable liquid biopsy analysis. *Nano Converg.* 6, 1–8. doi: 10.1186/s40580-019-0204-3

Bullock, M. D., Sayan, A. E., Packham, G. K., and Mirnezami, A. H. (2012). MicroRNAs: critical regulators of epithelial to mesenchymal (EMT) and mesenchymal to epithelial transition (MET) in cancer progression. *Biol. Cell* 104, 3–12. doi: 10.1111/boc.201100115

Cho, H. Y., Hossain, M. K., Lee, J. H., Han, J., Lee, H. J., Kim, K. J., et al. (2018). Selective isolation and noninvasive analysis of circulating cancer stem cells through Raman imaging. *Biosens. Bioelectron.* 102, 372–382. doi: 10.1016/j.bios.2017.11.049

Folkman, J. (2002). Role of angiogenesis in tumor growth and metastasis. *Semin. Oncol.* 29, 15–18. doi: 10.1016/S0093-7754(02)70065-1

Gao, P., Niu, N., Wei, T., Tozawa, H., Chen, X., Zhang, C., et al. (2017). The roles of signal transducer and activator of transcription factor 3 in tumor angiogenesis. *Oncotarget* 8, 69139–69161. doi: 10.18632/oncotarget.19932

Gong, M. M., Lugo-Cintron, K. M., White, B. R., Kerr, S. C., Harari, P. M., and Beebe, D. J. (2019). Human organotypic lymphatic vessel model elucidates microenvironment-dependent signaling and barrier function. *Biomaterials* 214:119225. doi: 10.1016/j.biomaterials.2019.119225

Gupta, G. P., and Massague, J. (2006). Cancer metastasis: building a framework. *Cell* 127, 679–695. doi: 10.1016/j.cell.2006.11.001

Jeong, G. S., Han, S., Shin, Y., Kwon, G. H., Kamm, R. D., Lee, S. H., et al. (2011). Sprouting angiogenesis under a chemical gradient regulated by interactions with an endothelial monolayer in a microfluidic platform. *Anal. Chem.* 83, 8454–8459. doi: 10.1021/ac202170e

Kang, Y., and Massague, J. (2004). Epithelial-mesenchymal transitions: twist in development and metastasis. *Cell* 118, 277–279. doi: 10.1016/j.cell.2004.07.011

Kim, Y. H., Jung, E., Im, G. B., Kim, Y. J., Kim, S. W., Jeong, G. J., et al. (2020). Regulation of intracellular transition metal ion level with a pH-sensitive inorganic nanocluster to improve therapeutic angiogenesis by enriching conditioned medium retrieved from human adipose derived stem cells. *Nano Converg.* 7:34. doi: 10.1186/s40580-020-00244-5

Ko, J., Ahn, J., Kim, S., Lee, Y., Lee, J., Park, D., et al. (2019). Tumor spheroid-on-a-chip: a standardized microfluidic culture platform for investigating tumor angiogenesis. *Lab Chip* 19, 2822–2833. doi: 10.1039/C9LC00140A

Kuribayashi, T. (2018). Elimination half-lives of interleukin-6 and cytokine-induced neutrophil chemoattractant-1 synthesized in response to inflammatory stimulation in rats. *Lab. Anim. Res.* 34, 80–83. doi: 10.5625/lar.2018.34.2.80

Lee, E., Fertig, E. J., Jin, K., Sukumar, S., Pandey, N. B., and Popel, A. S. (2014a). Breast cancer cells condition lymphatic endothelial cells within pre-metastatic niches to promote metastasis. *Nat. Commun.* 5:4715. doi: 10.1038/ncomms5715

Lee, E., Pandey, N. B., and Popel, A. S. (2014b). Lymphatic endothelial cells support tumor growth in breast cancer. *Sci. Rep.* 4:5853. doi: 10.1038/srep05853

Lee, S., Kim, S., Koo, D. J., Yu, J., Cho, H., Lee, H., et al. (2020). 3D microfluidic platform and tumor vascular mapping for evaluating anti-angiogenic RNAi-based nanomedicine. *ACS Nano Articles* 15, 338-350. doi: 10.1021/acsnano.0c05110

Li, W., Khan, M., Mao, S., Feng, S., and Lin, J. M. (2018). Advances in tumor-endothelial cells co-culture and interaction on microfluidics. *J. Pharm. Anal.* 8, 210–218. doi: 10.1016/j.jpha.2018.07.005

Martine, L. C., Holzapfel, B. M., Mcgovern, J. A., Wagner, F., Quent, V. M., Hesami, P., et al. (2017). Engineering a humanized bone organ model in mice to study bone metastases. *Nat. Protoc.* 12, 639–663. doi: 10.1038/nprot.2017.002

Matsuoka, J., Yashiro, M., Doi, Y., Fuyuhiro, Y., Kato, Y., Shinto, O., et al. (2013). Hypoxia stimulates the EMT of gastric cancer cells through autocrine TGFβ signaling. *PLoS One* 8:e62310. doi: 10.1371/journal.pone.0062310

Meng, F., Meyer, C. M., Joung, D., Vallera, D. A., Mcalpine, M. C., and Panoskaltsis-Mortari, A. (2019). 3D bioprinted *in vitro* metastatic models via reconstruction of tumor microenvironments. *Adv. Mater.* 31:e1806899. doi: 10.1002/adma.201806899

Mondadori, C., Crippa, M., Moretti, M., Candrian, C., Lopa, S., and Arrigoni, C. (2020). Advanced microfluidic models of cancer and immune cell extravasation: a systematic review of the literature. *Front. Bioeng. Biotechnol.* 8:907. doi: 10.3389/fbioe.2020.00907

Muller, A., Homey, B., Soto, H., Ge, N., Catron, D., Buchanan, M. E., et al. (2001). Involvement of chemokine receptors in breast cancer metastasis. *Nature* 410, 50–56. doi: 10.1038/35065016

Mun, S. G., Choi, H. W., Lee, J. M., Lim, J. H., Ha, J. H., Kang, M. J., et al. (2020). rGO nanomaterial-mediated cancer targeting and photothermal therapy in a microfluidic co-culture platform. *Nano Converg.* 7:10. doi: 10.1186/s40580-020-0220-3

Osaki, T., Serrano, J. C., and Kamm, R. D. (2018). Cooperative effects of vascular angiogenesis and lymphangiogenesis. *Regen. Eng. Transl. Med.* 4, 120–132. doi: 10.1007/s40883-018-0054-2

Panchy, N., Azeredo-Tseng, C., Luo, M., Randall, N., and Hong, T. (2020). Integrative transcriptomic analysis reveals a multiphasic epithelial-mesenchymal spectrum in cancer and non-tumorigenic cells. *Front. Oncol.* 9:1479. doi: 10.3389/fonc.2019.01479

Pang, M., Georgoudaki, A., Lambut, L., Johansson, J., Tabor, V., Hagikura, K., et al. (2016). TGF-β1-induced EMT promotes targeted migration of breast cancer cells through the lymphatic system by the activation of CCR7/CCL21-mediated chemotaxis. *Oncogene* 35, 748–760. doi: 10.1038/onc.2015.133

Pereira, E. R., Kedrin, D., Seano, G., Gautier, O., Meijer, E. F., Jones, D., et al. (2018). Lymph node metastases can invade local blood vessels, exit the node, and colonize distant organs in mice. *Science* 359, 1403–1407. doi: 10.1126/science.aal3622

Pulaski, B. A., and Ostrand-Rosenberg, S. (2000). Mouse 4T1 breast tumor model. *Curr. Protoc. Immunol.* 39, 20.2.1–20.2.16. doi: 10.1002/0471142735.im2002s39

Recouvreux, M. V., Moldenhauer, M. R., Galenkamp, K. M. O., Jung, M., James, B., Zhang, Y., et al. (2020). Glutamine depletion regulates Slug to promote EMT and metastasis in pancreatic cancer. *J. Exp. Med.* 217:e20200388. doi: 10.1084/jem.20200388

Sewell-Loftin, M. K., Katz, J. B., George, S. C., and Longmore, G. D. (2020). Micro-strains in the extracellular matrix induce angiogenesis. *Lab Chip* 20, 2776–2787. doi: 10.1039/D0LC00145G

Shim, S., Belanger, M. C., Harris, A. R., Munson, J. M., and Pompano, R. R. (2019). Two-way communication between *ex vivo* tissues on a microfluidic chip: application to tumor–lymph node interaction. *Lab Chip* 19, 1013–1026. doi: 10.1039/C8LC00957K

Sontheimer-Phelps, A., Hassell, B. A., and Ingber, D. E. (2019). Modelling cancer in microfluidic human organs-on-chips. *Nat. Rev. Cancer* 19, 65–81. doi: 10.1038/s41568-018-0104-6

Sullivan, N., Sasser, A., Axel, A. E., Vesuna, F., Raman, V., Ramirez, N., et al. (2009). Interleukin-6 induces an epithelial–mesenchymal transition phenotype in human breast cancer cells. *Oncogene* 28, 2940–2947. doi: 10.1038/onc.2009.180

Tawada, M., Hayashi, S., Ikegame, Y., Nakashima, S., and Yoshida, K. (2014). Possible involvement of tumor-producing VEGF-A in the recruitment of lymphatic endothelial progenitor cells from bone marrow. *Oncol. Rep.* 32, 2359–2364. doi: 10.3892/or.2014.3499

Webb, A. H., Gao, B. T., Goldsmith, Z. K., Irvine, A. S., Saleh, N., Lee, R. P., et al. (2017). Inhibition of MMP-2 and MMP-9 decreases cellular migration, and angiogenesis in *in vitro* models of retinoblastoma. *BMC Cancer* 17:434. doi: 10.1186/s12885-017-3418-y

Yilmaz, M., and Christofori, G. (2009). EMT, the cytoskeleton, and cancer cell invasion. *Cancer Metastasis Rev.* 28, 15–33. doi: 10.1007/s10555-008-9169-0

Conflict of Interest: The authors declare that the research was conducted in the absence of any commercial or financial relationships that could be construed as a potential conflict of interest.

frontiers in Bioengineering and Biotechnology

ORIGINAL RESEARCH
published: 01 March 2021
doi: 10.3389/fbioe.2021.639070

Effects of Shear Stress on Production of FVIII and vWF in a Cell-Based Therapeutic for Hemophilia A

Brady Trevisan[1], Alshaimaa Morsi[1,2†], Julio Aleman[1†], Martin Rodriguez[1], Jordan Shields[3], Diane Meares[4], Andrew M. Farland[4], Christopher B. Doering[3], H. Trent Spencer[3], Anthony Atala[1], Aleks Skardal[1§], Christopher D. Porada[1‡] and Graça Almeida-Porada[1‡]*

[1] Fetal Research and Therapy Program, Wake Forest Institute for Regenerative Medicine, Wake Forest School of Medicine, Winston-Salem, NC, United States, [2] Faculty of Medicine, Zagazig University, Zagazig, Egypt, [3] Aflac Cancer and Blood Disorders Center, Children's Healthcare of Atlanta and Department of Pediatrics, Emory University, Atlanta, GA, United States, [4] Department of Medicine, Section on Hematology and Oncology, Wake Forest School of Medicine, Winston-Salem, NC, United States

Microfluidic technology enables recapitulation of organ-level physiology to answer pertinent questions regarding biological systems that otherwise would remain unanswered. We have previously reported on the development of a novel product consisting of human placental cells (PLC) engineered to overexpress a therapeutic factor VIII (FVIII) transgene, mcoET3 (PLC-mcoET3), to treat Hemophilia A (HA). Here, microfluidic devices were manufactured to model the physiological shear stress in liver sinusoids, where infused PLC-mcoET3 are thought to lodge after administration, to help us predict the therapeutic outcome of this novel biological strategy. In addition to the therapeutic transgene, PLC-mcoET3 also constitutively produce endogenous FVIII and von Willebrand factor (vWF), which plays a critical role in FVIII function, immunogenicity, stability, and clearance. While vWF is known to respond to flow by changing conformation, whether and how shear stress affects the production and secretion of vWF and FVIII has not been explored. We demonstrated that exposure of PLC-mcoET3 to physiological levels of shear stress present within the liver sinusoids significantly reduced mRNA levels and secreted FVIII and vWF when compared to static conditions. In contrast, mRNA for the vector-encoded mcoET3 was unaltered by flow. To determine the mechanism responsible for the observed decrease in FVIII and vWF mRNA, PCR arrays were performed to evaluate expression of genes involved in shear mechanosensing pathways. We found that flow conditions led to a significant increase in KLF2, which induces miRNAs that negatively regulate expression of FVIII and vWF, providing a mechanistic explanation for the reduced expression of these proteins in PLC under conditions of flow. In conclusion, microfluidic technology allowed us to unmask novel pathways by which endogenous FVIII and vWF are affected by shear stress, while demonstrating that expression of the therapeutic mcoET3 gene will be maintained in the gene-modified PLCs upon transplantation, irrespective of whether they engraft within sites that expose them to conditions of shear stress.

Keywords: FVIII, vWF, microfluidics, gene therapy, mRNA, shear stress, miRNA

OPEN ACCESS

Edited by:
Owen Gareth Davies, Loughborough University, United Kingdom

Reviewed by:
Mohammad Ameen Qasaimeh, New York University Abu Dhabi, United Arab Emirates
Ravi Sinha, Maastricht University, Netherlands

***Correspondence:**
Graça Almeida-Porada
galmeida@wakehealth.edu

[†] These authors have contributed equally to this work

[‡] These authors share senior and last authorship

*[§] **Present address:***
Aleks Skardal, Department of Biomedical Engineering, The Ohio State University Comprehensive Cancer Center, Columbus, OH, United States

Specialty section:
This article was submitted to Nanobiotechnology, a section of the journal Frontiers in Bioengineering and Biotechnology

Received: *08 December 2020*
Accepted: *25 January 2021*
Published: *01 March 2021*

Citation:
Trevisan B, Morsi A, Aleman J, Rodriguez M, Shields J, Meares D, Farland AM, Doering CB, Spencer HT, Atala A, Skardal A, Porada CD and Almeida-Porada G (2021) Effects of Shear Stress on Production of FVIII and vWF in a Cell-Based Therapeutic for Hemophilia A. Front. Bioeng. Biotechnol. 9:639070. doi: 10.3389/fbioe.2021.639070

INTRODUCTION

Hemophilia A (HA) is an X-linked genetic disorder caused by mutations in the factor VIII (FVIII) gene, resulting in the lack of functional clotting protein FVIII (Franchini and Mannucci, 2013). In plasma, FVIII circulates tightly bound to von Willebrand factor (vWF), a large multimeric glycoprotein produced in endothelial cells and megakaryocytes (McGrath et al., 2010).

The interaction between vWF and FVIII plays a critical role in the function, stability, and clearance of FVIII protein (Pipe et al., 2016), with changes in vWF concentration affecting overall FVIII levels (Lollar et al., 1988). For instance, the half-life of FVIII in the absence of vWF, as is the case in von Willebrand Disease, is around 3 h, while in the presence of vWF, FVIII half-life is 12 h (Over et al., 1978). The presence of vWF also plays a role in FVIII immunogenicity by shielding the epitopes of FVIII that common inhibitors recognize and preventing the uptake of FVIII by antigen-presenting cells (Dasgupta et al., 2007; Delignat et al., 2012).

We have previously reported that human placental cells (PLC) constitutively produce vWF (Morsi et al., 2018) and FVIII (El-Akabawy et al., 2020), and we developed a potential cell therapy platform by transducing human PLC with a lentiviral vector encoding a myeloid-codon-optimized (mco), bioengineered FVIII transgene that contains high-expression elements from porcine FVIII (ET3) (PLC-mcoET3) (El-Akabawy et al., 2020). Moreover, PLC-mcoET3 secreted FVIII protein with functional procoagulant activity at therapeutic and clinically meaningful levels (El-Akabawy et al., 2020). In addition, after prenatal administration, these cells are thought to lodge in perivascular sites, such as the liver sinusoids (Almeida-Porada et al., 2017), and therefore are subjected to shear stress from fluid flow. vWF has been shown to respond to fluidic shear stress by changing conformation, binding affinity, and protein activity (Vergauwe et al., 2014), but whether and how shear stress affects the amount of vWF secreted has not been explored. Moreover, the role of shear stress from fluid flow on FVIII production and secretion, to our knowledge, has not thus far been described.

These studies used a microfluidic platform designed to generate physiologically relevant levels of shear stress, to investigate how fluidic flow impacted the production and secretion of vWF, FVIII, and mcoET3 in PLC-mco-ET3. The results showed that shear stress did not affect levels of mcoET3, but downregulated the production of both FVIII and vWF in PLC-mco-ET3. In addition, the studies provided new mechanistic insights into how shear stress can decrease the production of both FVIII and vWF by increasing miR-30c and miR-10a *via* Kruppel-like Factor 2 (KLF2) (Wang et al., 2006), through mechanotransduction by integrins *via* the SRC and SHC1 proteins. These findings are of particular importance with respect to using the gene-modified PLCs for therapy, as they show that mcoET3 expression will persist unabated, irrespective of whether the transplanted PLCs engraft within regions that expose them to conditions of shear stress.

MATERIALS AND METHODS

Culture and Transduction of Human Placental Mesenchymal Cells

Human placentas were obtained from full-term deliveries after informed consent, according to the guidelines from the Office of Human Research Protection at Wake Forest Health Sciences. Primary placental mesenchymal cells (PLC) were isolated from the placental chorionic layer after enzymatic digestion and grown in placental cell growth media (PCGM) consisting of α-minimum essential medium (α-MEM) supplemented with 17% AmnioMAX Basal Media, 15% fetal bovine serum (FBS), 2% AmnioMAX Supplement, 1% GlutaMAX, and 2.5 mg/mL gentamicin (ThermoFisher Scientific, Wilmington, DE, United States) (El-Akabawy et al., 2020). PLC were transduced with an HIV-based lentiviral vector encoding a myeloid codon-optimized (mco) B domain-deleted human/porcine hybrid FVIII transgene (ET3), termed mcoET3, at a multiplicity of infection of 10 transducing units/cell (El-Akabawy et al., 2020). Transduced cells (PLC-mcoET3) were passaged at 70–80% confluence using TrypLE (ThermoFisher Scientific, Wilmington, DE, United States) and PLC-mcoET3 were used in these studies after they had been passaged a minimum of three times post-transduction to ensure the absence of any episomal vector. Vector copy number (VCN) was determined using the Lenti-X proviral quantitation kit (Takara Bio, Mountain View, CA, United States) according to the manufacturer's instructions, and established that PLC-mcoET3 had a VCN of 0.93.

Manufacturing of Polydimethylsiloxane Microfluidics Devices

Single-use microfluidic devices were manufactured as previously described (Aleman et al., 2019) using polydimethylsiloxane (PDMS) (10:1 Sylgard 184 silicone elastomer and curing agent, respectively, Dow Corning, Midland, MI, United States). AutoCAD was used to design a 2-dimensional layout of channels that were 0.9 mm wide by 15 mm long. Two layers of double-sided tape (3 M, Maplewood, MN, United States) were then pressed onto a glass slide (VWR, Radnor, PA, United States) to reach the desired channel height of 200 μm. The tape was then laser cut into the designed layout and the outer tape was removed to leave a negative mold of the device channels. The glass slide was then taped around the perimeter to a sheet of aluminum foil that was folded up to create a boat that could hold the PDMS prior to polymerization. PDMS was then dispensed over the mold and allowed to cure to make the device with channels of the specified dimensions. Next, we covered a glass slide with the epoxy-based negative photoresist SU8 (MicroChem, Westborough, MA, United States) and pressed the PDMS device onto the SU8 to fill the channels. SU8 was solidified with UV light to make a permanent mold for production of more PDMS devices. A blunt needle was then used to punch inlet and outlet holes at the ends of the channels in the PDMS device, and the open side of the channels as well as a clean glass slide was then plasma-treated and permanently adhered to create a closed microfluidic device. The device was immediately seeded with cells by resuspending

300,000 PLC-mcoET3 in 200 uL of media, pipetting the cell suspension into a single channel, and incubating overnight to allow the cells to adhere to the channel and form a confluent monolayer to avoid subsequent proliferation. Alternatively, the device was first filled with 200 μL of 0.05% gelatin and allowed to solidify for 15 min, after which the excess gelatin was removed. The gelatin coating was used to provide a softer and more physiological environment for the cells. Tubing was then placed into the inlets and outlets and connected to a reservoir of media.

Manufacturing of Polymethylmethacrylate Devices

Polymethylmethacrylate devices single-use microfluidic devices were manufactured by designing a 2-dimensional layout of the required channel, which was 50 mm long and 3 mm wide, and had a height of 1.5 mm corresponding to the thickness of the PMMA (McMaster-Carr, Elmhurst, IL, United States). This "channel layer" was fabricated by laser cutting the desired channel dimensions into a sheet of PMMA with a layer of double-sided tape adhered to either side. A solid sheet of PMMA (with no channels) served as the base layer, and the inlet layer was created by laser cutting holes in an additional sheet of PMMA to enable attachment of inlet and outlet tubing. These pieces were then sterilized with UV light (365 nm, 7 W cm^{-2}) for at least 20 min. Subsequently, the base and channel layers were attached (with the double-sided tape) to form channels with an open top. The floor of this channel was coated with gelatin by pipetting 300 μL of 0.05% gelatin and allowing it to solidify for 15 min, after which excess gelatin was removed. This quantity of gelatin was necessary to prevent a meniscus effect that caused the center of the channel to remain bare of gelatin. The gelatin-coated device was seeded with 300,000 cells, which were allowed to attach overnight. This cell number was chosen to ensure the cells, upon attachment, formed a confluent monolayer to avoid subsequent proliferation. During this time, tubing was glued to the inlet and outlet holes of the inlet layer with epoxy. On the following day, when the cells had adhered to the floor of the channel, the inlet layer was attached to the top of the channel layer with double-sided tape to form a closed microfluidic device and the tubing connected to a separate well of 1.5 mL of media and hooked up to a peristaltic pump to flow media through the device to generate a set flow rate. Devices were discarded after use, and a new device was created for each experiment.

Induction of Shear Stress on the Microfluidics Devices' Cell Layers

Poiseuille's law $\tau = \frac{6\eta Q}{h^2 w}$ was used to determine the flow rate (Q) required to generate shear stresses (τ) of 0.5 or 0.05 dyne/cm^2, given the height (h) and width (w) of the channel, and the viscosity (η) of 0.96 mPa·s to match previously measured cell culture media with similar levels of FBS. A four-channel precision micro peristaltic pump (Elemental Scientific, Omaha, NE, United States) was used to circulate cell culture media (1.5 mL) from the reservoir, through the device using 1.14 mm inner diameter tubing connected to the peristaltic pump, set at 10 and 100 rpm as determined to be required to generate the desired flow rate. The device was left in flow for 24 h before the cells and supernatant were collected for analysis.

Computational Fluid Dynamics Analysis

The devices were created in Autodesk Fusion 360 (Autodesk, San Rafael, CA, United States) with a single solid piece to model each device, with a second separate piece created to model the media inside of the channel and in the inlet and outlet. The material of the device was set to acrylic and the material of the fluid was set to water to approximate the actual material of our devices and the properties of our media. A boundary condition of the flow rate applied by the peristaltic pump was set to the inlet and default settings were used to generate the mesh before the model was solved for the shear stress and visualized.

Protein Quantification

Cell culture supernatant was collected at the 24-h time point, immediately centrifuged to remove cell debris, aliquoted, and frozen at −80°C. After supernatant collection, PLC-mcoET3 were harvested, counted as described below, and the cell number for each sample recorded. FVIII activity in the supernatant was quantified using aPTT assays, which were performed by the Wake Forest Baptist Medical Center Special Hematology Laboratory in accordance with standard clinical procedures, using a Top 300 CTS clinical coagulometer (Instrumentation Laboratories, Bedford, MA, United States). Quantification of vWF protein in the supernatants was determined by using a vWF-specific ELISA (ThermoFisher Scientific, Wilmington, DE, United States), as detailed in the **Supplementary Material**. The presence of interferon-γ in the supernatant was also measured using a high-sensitivity human ELISA Kit (assay range: 0.16−10.0 pg/mL) (ThermoFisher Life Technologies, Carlsbad, CA, United States), as detailed in the **Supplementary Material**.

Cell Staining

Immediately after supernatant removal, cells were washed 3X with PBS (ThermoFisher Scientific, Wilmington, DE, United States) before fixing for 1 h in 4% paraformaldehyde (Electron Microscopy Sciences, Hatfield, PA, United States). To decrease background fluorescence, cells were treated with 0.1% sodium borohydride (Sigma-Aldrich, St. Louis, MO, United States) in PBS for 10 min, washed, and then blocked with blocking buffer [10% normal goat serum (NGS) in PBS], and finally washed with 2% NGS in PBS (working buffer). Mouse anti-human FVIII (Bio-Rad Laboratories, Hercules, CA, United States) at a dilution of 1:1,000 and rabbit anti-human vWF (Abcam, Cambridge, United Kingdom) at a dilution of 1:100 in working buffer were added, and the devices were placed on a shaker for 20 min before then being placed at 4°C overnight. The devices were washed with working buffer, and donkey anti-mouse Alexa Fluor 594 and mouse anti-rabbit Alexa Fluor 488 secondary antibodies (Invitrogen, Carlsbad, CA, United States) diluted 1:400 in working buffer were added to the devices and incubated for 30 min on a shaker. After washing with PBS, DAPI at a dilution of 1:1,000 was added for 5 min, followed by an additional wash before being coverslipped and imaged. The cells

were then imaged in representative areas of each device using an Olympus BX30 microscope with a 10X objective.

Image Analysis

DAPI images were imported into ImageJ and a threshold was run to remove the background fluorescence fully and leave only the cell nuclei. A particle analysis in ImageJ was performed to precisely quantify the number of cells that were present in the image. Three representative images for each sample were analyzed to achieve an average cell count within one frame, and this value was multiplied by a scaling factor to estimate the total number of cells present in each device. This total cell number was then used to normalize our protein production and secretion results to the number of cells present.

Flow Cytometric Analysis of Cell Surface Integrins

Flow cytometric evaluation of PLC-mcoET3 was performed by staining 10^5 cells per tube in 50 μL of BD Horizon Brilliant Stain Buffer with 10 μL of directly conjugated antibodies against CD61/Alexa Fluor 488, CD49a/PE, CD49e/BB700, and Integrin αvβ5/Alexa Fluor 647 (Becton Dickinson Biosciences, San Jose, CA, United States). Cells were washed with PBS with 0.1% Na Azide (Sigma-Aldrich, St. Louis, MO, United States) and centrifuged for 5 min at 1,500 rpm. The cells were resuspended in 500 μl of 1% paraformaldehyde (Electron Microscopy Sciences, Hatfield, PA, United States) in PBS. Background fluorescence was set using non-specific isotype-matched antibodies with respective fluorochromes. Cells were analyzed using a BD Accuri-C6 and data assessed using the FlowJo software using CD49a (Integrin α1) as selection criteria for PLC since 100% of the cells expressed this marker (Becton Dickinson Immunocytometry Systems, San Jose, CA, United States).

RNA Extraction

RNA was extracted from devices immediately after the flow was stopped and the media removed, by adding RNAprotect (QIAGEN, Valencia, CA, United States) directly to the cells and scraping the gelatin layer with a pipette tip to ensure that all the cells were detached. The RNAprotect containing the cells was then collected and the RNeasy Mini Kit (QIAGEN, Valencia, CA, United States) was used as detailed in the **Supplementary Material**. Since sample contamination with gelatin present in the wells clogged the spin columns provided in the RNeasy kit, alternatively, samples were collected by adding TRIzol Reagent (ThermoFisher Scientific, Wilmington, DE, United States) directly to the cells, and RNA was isolated as detailed in the **Supplementary Material**. The use of TRIzol allowed high-quality RNA to be extracted at high yield (Alves et al., 2016). RNA integrity and purity were then verified using the Agilent RNA 6000 Nano Kit, as described in the **Supplementary Material** (Agilent Technologies, Santa Clara, CA, United States).

Quantitative Reverse Transcription PCR

Quantitative reverse transcription PCR (RT-qPCR) was performed by generating cDNA from the collected RNA using the Omniscript RT kit (QIAGEN, Valencia, CA, United States), as described in the **Supplementary Material**. RNA was quantified using a NanoDrop 2000 (ThermoFisher Scientific, Inc., Wilmington, DE, United States), and RNA integrity was assessed using the Bioanalyzer RNA 6000 Nano assay and 2100 Bioanalyzer (Agilent, Santa Clara, CA, United States). RNA samples were then normalized to have a concentration of 20 ng/μl. 10 ng of DNA-free RNA was converted into cDNA using an Omniscript RT kit (Qiagen, Valencia, CA, United States). SYBR Green-based qPCR was conducted using PrimeTime qPCR Primer Assays (Integrated DNA Technologies, Inc., Coralville, IA, United States) using primers specific to: (1) the 3′ untranslated region (UTR) of FVIII (3′ UTR); (2) the modified FVIII transgene (mco-ET3); and (3) vWF. Human GAPDH served as an internal reference/housekeeping gene and was amplified using commercially available primers (Cat. Number PPH00150E, Qiagen, Valencia, CA, United States). The qPCR master mix was loaded into MicroAmp™ Optical 96-well reaction plates and processed in the 7300 QuantStudio 3 RealTime-PCR system (Applied Biosystems, Foster City, CA, United States).

FAM-based qPCR using commercially available primers for KLF2, miR10a, miR30c, and GAPDH (ThermoFisher Scientific, Inc., Wilmington, DE, United States) was performed using TaqMan. TaqMan Fast Advanced master mix was loaded into MicroAmp™ optical 96-well reaction plates and processed on a 7300 QuantStudio 3 RealTime-PCR system on the 96-well fast setting (Applied Biosystems, Foster City, CA, United States).

Fold-change of mRNA for a specific gene was calculated by the ΔΔCT method. First, the average CT of the housekeeping gene (GAPDH) for each sample was subtracted from the average CT of the gene of interest to obtain ΔCT. The average of the static ΔCT was calculated and subtracted from each individual static and flow ΔCT to obtain the individual ΔΔCT values. The fold-change was then calculated using $2^{-\Delta\Delta CT}$. RT^2 Profiler™ Human Focal Adhesion PCR Array (QIAGEN, Valencia, CA, United States) was performed as described in the **Supplementary Material** to investigate the impact of shear stress on cell-extracellular matrix (ECM) adhesion.

Statistical Analysis

Experimental results are presented as the mean plus/minus the standard error of the mean (SEM). All statistical analysis was performed using the R coding language in RStudio (RStudio, PBC, Boston, MA, United States). One-way ANOVA was employed for multiple comparisons. A p value <0.05 was considered statistically significant. Statistical analysis of the RT^2 Profiler™ PCR Array was performed using the RT^2 Profiler RNA QC PCR Array Data Analysis Spreadsheet 1808 (Qiagen, Valencia, CA, United States).

RESULTS

Manufacturing and Evaluation of Microfluidic Devices

To determine the effect of fluidic laminar shear stress on PLC transduced with a lentiviral vector encoding a mco bioengineered

FVIII containing high expression elements from porcine FVIII (PLC-mcoET3), we manufactured several microfluidic devices designed to induce shear stresses similar to those generated in sites where PLC-mcoET3 lodge after prenatal transplantation (Almeida-Porada et al., 2017), such as the liver sinusoids. Specifically, we wanted to investigate whether shear stresses affected constitutive production and secretion of FVIII and vWF and/or expression of the mcoET3 transgene by PLC-mcoET3. The first microfluidics devices were fabricated using PDMS, as described in detail in the Materials and Methods and shown in **Figures 1A,B**. The devices were connected to a peristaltic pump (**Figure 1C**) to produce the necessary flow rates to reproduce the level of shear stress present within the liver sinusoids *in vivo*, assuming a flow velocity of 500 μm/s and a vessel inner diameter of 5 − 10 μm (Lalor and Adams, 1999). Poiseuille's law was used to calculate the necessary flow rate in the devices to reach the desired level of shear stress, as described in the Materials and Methods. A static control device was manufactured to hold 1.5 mL of media, the same amount of media as the "in-flow" devices plus reservoir. After the media circulated within the device for 24 h, the supernatant was collected and the PLC-mcoET3 were stained and counted as described in the Material and Methods. Computational fluid dynamics was used to determine the levels of shear stress experienced by PLC. Analysis showed that PLC was experiencing either 0.05 or 0.5 dyne/cm^2 throughout the channel, with a slight increase in the very center of the channel (**Figures 1D,E**).

Although these devices were effective in generating fluid flow at the desired rates, they often leaked from either the glass-PDMS interface or the tubing inlet and outlet. In addition, PDMS and glass have been reported to be able to initiate the activation of the intrinsic coagulation cascade, which could potentially lead to activation of FVIII in the supernatant of the cultured PLC-mcoET3, thereby skewing the measured FVIII activity (van Oeveren et al., 2002). Moreover, since placental tissues produce IFNγ upon stress (Banerjee et al., 2005) and IFNγ has been shown to have an effect on the production of tissue factor, which plays an important role in initiation of the coagulation cascade (van der Poll et al., 2001), we also used a high-sensitivity ELISA to test the culture supernatants of PLC-mcoET3 cultured in the devices to account for FVIII activation related to induced cell stress. **Figure 1F** shows that culturing PLC-mcoET3 on PDMS-on-glass led to an increase in IFNγ secretion (n = 3).

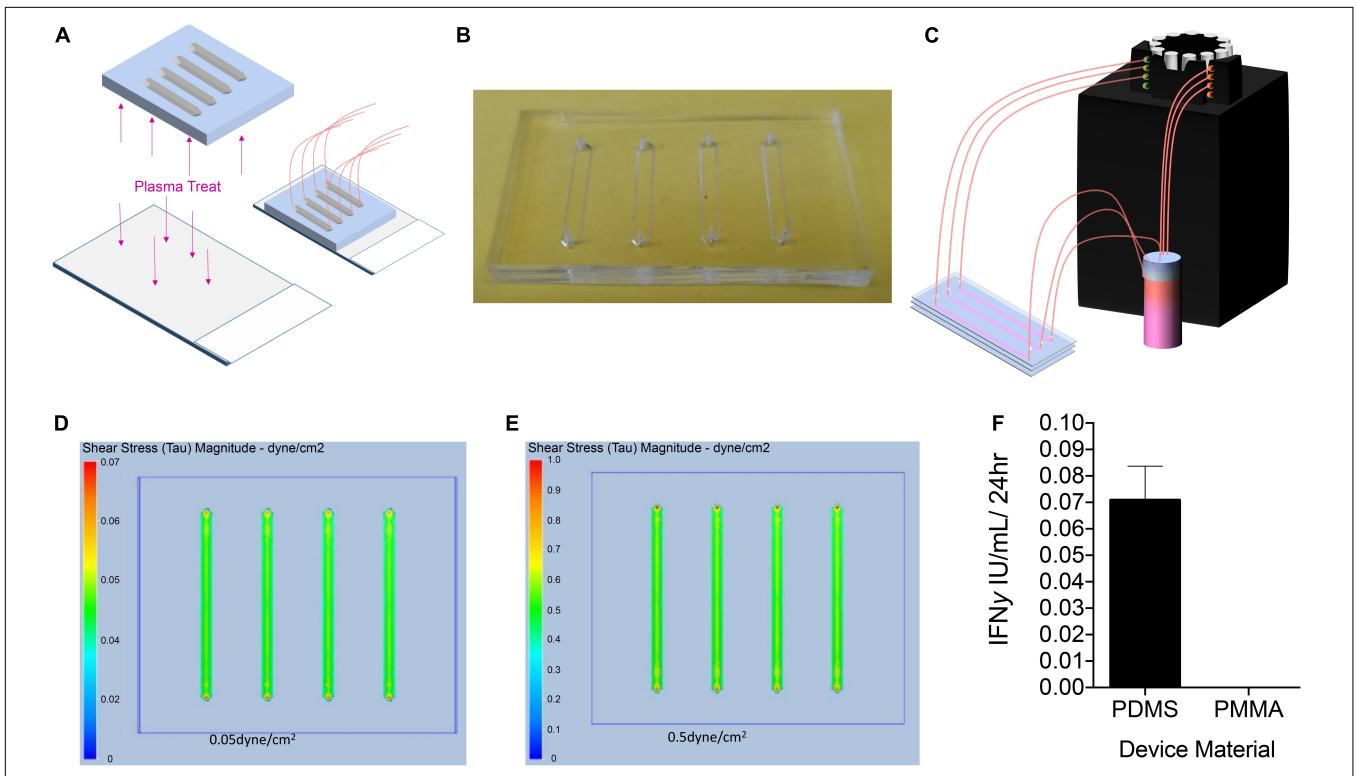

FIGURE 1 | Design, Manufacturing, and Analysis of Microfluidic PDMS Devices. **(A)** To determine the effect of fluidic laminar shear stress on PLC transduced with a lentiviral vector encoding a myeloid codon-optimized bioengineered FVIII containing high expression elements from porcine FVIII (PLC-mcoET3), we designed and manufactured PDMS devices with the soft lithography method and adhered them to plasma-treated glass to form a closed channel. **(B)** Representative image of single-use PDMS device. **(C)** Upon completion, devices were connected to a reservoir of media and to a peristaltic pump to flow media through the devices to generate shear stresses of 0.05 or 0.5 dyne/cm^2. **(D,E)** Computational fluid dynamics analysis showing shear stress maps at the base of the channels, demonstrating that PLC were experiencing either **(D)** 0.05 dyne/cm^2 or **(E)** 0.5 dyne/cm^2 throughout the channel, with a slight increase in the very center of the channel. **(F)** IFNγ secretion by PLC on microfluidic devices. PLC cultured on plasma-treated glass slides produced IFNγ while cells cultured on a PMMA device did not (n = 3).

In order to overcome the limitations described above, we next coated the inside of the devices with gelatin. This resulted in uneven channel surfaces, irregular flow rates, and clogging. It also proved difficult to harvest cells or extract RNA from cells within devices, which was needed to analyze the effects of shear stress on the cells. These challenges led us to develop another device that would overcome the current issues.

Polymethylmethacrylate devices has successfully been used in microfluidic devices to assess whole blood coagulation (Maji et al., 2018). Therefore, we next laser cut polymethyl methacrylate (PMMA) into several layers: a solid base layer, a layer with channels cut out, and a layer with holes at either side of the channel to use as inlets and outlets as is displayed in **Figure 2A**. These three layers of PMMA were held together using double-sided tape as described in the Materials and Methods. The need to easily collect cells, and RNA from the cells, within our devices led to the design of larger channels that would hold larger numbers of cells and could be opened to use like a well. The channels within these devices were 1.5 mm tall and 3 mm wide with a length of 50 mm and were coated with gelatin and seeded with 300,000 cells per channel (**Figure 2B**). The devices were hooked to the peristaltic pump (**Figure 2B**) to generate a flow rate able to produce the calculated shear stress of 0.05 and 0.5 dyne/cm^2. Static control devices were also manufactured by adhering multiple 3 mm thick channel layers of PMMA on top of a single base layer to generate a well large enough to hold 1.5 mL of media (**Figure 2C**), the same amount of media used in the "in flow" devices. Evaluation of culture supernatants for the presence of IFNγ demonstrated that PLC-mcoET3 cultured in the PMMA devices did not secrete this cytokine (n = 3) (**Figure 1F**). Bright field images of the cells within the devices were taken after 24 h in either static or flow conditions. Static devices show a random distribution of PLC within the devices (**Figure 2D**, left). After PLC experienced shear stress of 0.05 dyne/cm^2 for 24 h, they exhibited flow-induced changes in shape (**Figure 2D**, center). Further changes in morphology were seen in PLC that experienced the higher shear stress of 0.5 dyne/cm^2 (**Figure 2D**, right).

Computational fluid dynamics analysis was used to determine the levels of shear stress that PLC was experiencing in the devices. Analysis of the PMMA devices under conditions that were used to generate about 0.05 dyne/cm^2 was shown to create shear levels ranging from 0.05 dyne/cm^2 at the edges to a slightly elevated shear stress of 0.06 dyne/cm^2 in the center of the channel (**Figure 2E**). In PMMA devices under conditions set to generate 0.5 dyne/cm^2, the variation was larger. Analysis showed that the shear stresses at the edges of the channel were 0.5 dyne/cm^2, but this gradually increased to 0.7 dyne/cm^2 in the center of the channel (**Figure 2F**). Of note is that all of the channels had increased shear stress in the area around the inlet and outlet of the devices, but this effect was not seen throughout the majority of the device.

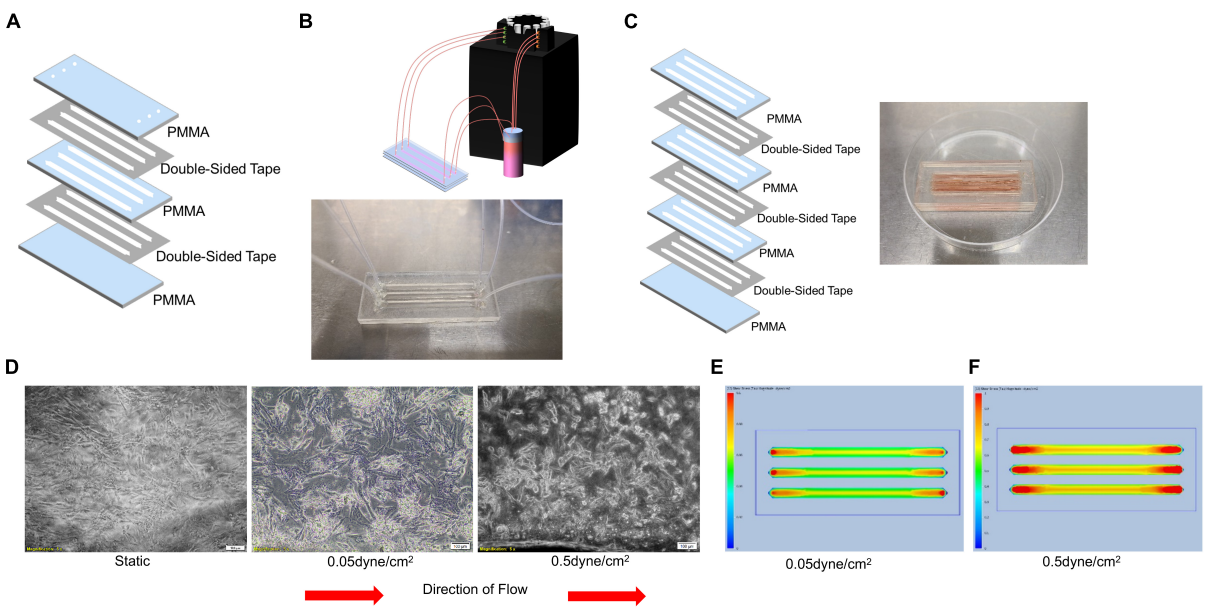

FIGURE 2 | Design, Manufacturing, and Analysis of Microfluidic PMMA Devices. **(A)** PMMA devices were manufactured by adhering three laser-cut layers of PMMA and double-sided tape. **(B)** Representative image of single-use PMMA devices. These were connected to a reservoir of media and to a peristaltic pump to flow media through the devices to generate shear stresses of 0.05 or 0.5 dyne/cm^2. **(C)** Static control devices were made by including multiple thicker channel layers to form a deep well to hold the same amount of media. Representative image of single-use static control PMMA devices. **(D)** Bright field images (5X magnification) of PLC in either static (left) or flow conditions (center and right). After PLC experienced shear stress of 0.05 dyne/cm^2 for 24 h, they exhibited flow-induced changes in shape (center) with further changes in morphology seen after PLC experienced the higher shear stress of 0.5 dyne/cm^2 for 24 h (right). **(E)** Computational fluid dynamics analysis showing shear stress maps at the base of the of channels, demonstrating that shear levels ranged from 0.05 dyne/cm^2 at the edges to a slightly elevated shear stress of 0.06 dyne/cm^2 in the center of the channel. **(F)** Computational fluid dynamics analysis showing shear stress maps at the base of the channels, demonstrating that the shear stress at the edges of the channel was 0.5 dyne/cm^2, with a gradual increase to 0.7 dyne/cm^2 in the center of the channel.

Evaluation of FVIII and vWF Secretion From PLC-mcoET3 Under Static and Shear Stress Conditions

After PLC-mcoET3 was stably seeded in the channels of the devices, the media was changed and media was circulated through the devices at the shear stresses described above. After 24 h, the media was collected, briefly spun down, and frozen, to determine the FVIII activity as well as vWF content at a later time point. The inlet layer of the devices was then removed, and the cells stained with DAPI and imaged as shown in **Figure 3A**. These images were then analyzed in ImageJ (**Figure 3B**) as described in detail in the Materials and Methods to determine the total number of cells in each channel. The total number of cells in each channel was then used to normalize the quantification of proteins within the supernatant to 10^6 cells. Quantification of fVIII/mco-ET3 activity in the supernatants was performed as previously described (El-Akabawy et al., 2020) using an activated prothrombin time (aPTT). PLC-mcoET3 under static conditions produced 3.69 ± 0.4 IU/10^6 cells/24 h of fVIII/mco-ET3 (n = 15), but under the shear stresses of 0.05 and 0.5 dyne/cm^2 fVIII/mco-ET3 secretion significantly reduced to 2.03 ± 0.2 IU/10^6 cells/24 h (n = 11) and 1.99 ± 0.2 IU/10^6 cells/24 h (n = 10), respectively (**Figure 3C**) ($p < 0.05$). However, no significant difference in fVIII/mco-ET3 was found in supernatants of cells subjected to 0.05 and 0.5 dyne/cm^2 (**Figure 3C**). A human vWF-specific ELISA was used to determine vWF concentration in the supernatants of PLC-mcoET3 under static and fluidic flow conditions. In static settings, PLC-mcoET3 produced 339.9 ± 25 ng/10^6 cells/24 h (n = 15) of vWF, but this concentration decreased significantly ($p < 0.05$) to 216.89 ± 32 ng/10^6 cells/24 h in conditions of low shear stress (n = 9), and at a higher shear stress, vWF in supernatants was further reduced to 123 ± 20 ng/10^6 cells/24 h (n = 9) ($p < 0.05$) (**Figure 3D**).

Evaluation of FVIII, mcoET3, and vWF mRNA Under Static and Shear Stress Conditions

Quantitative reverse transcription PCR with primers specific to vWF, the FVIII 3′ UTR (to measure constitutive levels of

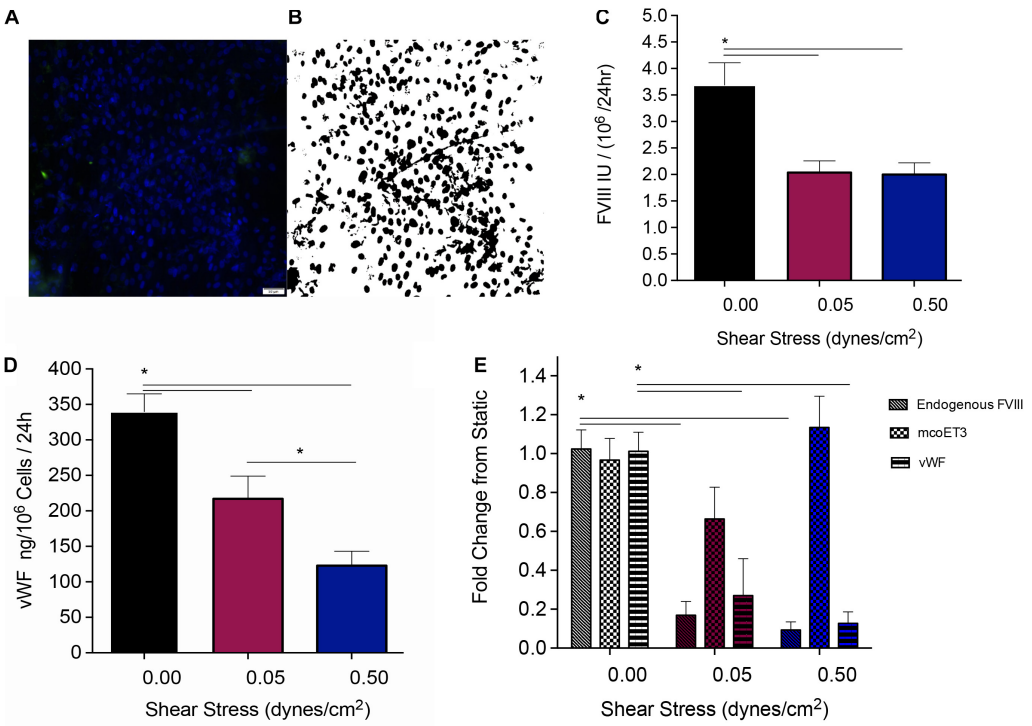

FIGURE 3 | Quantification of the protein production and secretion from PLC-mcoET3 under conditions of shear stress. **(A)** Representative image of cell quantification: In order to quantify the number of cells in the devices, they were first stained with DAPI, and then **(B)** a black and white threshold was applied before a particle analysis was performed in ImageJ to count cells in representative areas. This count was scaled to the full area of the device channel and used to normalize our data to cell count. **(C)** fVIII/mcoET3 activity in PLC-mcoET3 supernatants was significantly reduced in conditions under flow when compared to static conditions (static conditions n = 15; 0.05 dyne/cm^2 n = 11; and 0.5 dyne/cm^2 n = 10) ($p < 0.05$). No difference in fVIII/mco-ET3 activity was found between shear stress conditions of 0.05 dyne/cm^2 and 0.5 dyne/cm^2. **(D)** ELISA was used to measure the vWF protein concentration in the supernatant (static conditions n = 15; 0.05 dyne/cm^2 n = 9; 0.5 dyne/cm^2 n = 8). vWF concentration in supernatants from PLC-mcoET3 under shear rates of 0.05 dyne/cm^2 were significantly decreased when compared to those of under static conditions ($p < 0.05$). At the higher shear rate of 0.5 dyne/cm^2, vWF concentration was significantly decreased when compared to both 0.05 dyne/cm^2 ($p < 0.05$) and to static conditions ($p < 0.05$). **(E)** RNA expression of these proteins was examined with RT-qPCR performed in triplicate (endogenous FVIII n = 6; mcoET3 n = 5; and vWF n = 3). Endogenous/constitutive expression of both FVIII and vWF mRNA was decreased significantly at both shear rates ($p < 0.05$). However, mcoET3 mRNA expression was not affected by conditions of flow. *$p < 0.05$.

endogenous FVIII mRNA), and to the mco-ET3 transgene was performed to determine whether the decrease in FVIII and vWF protein by conditions of flow was due to a decrease in mRNA. **Figure 2E** depicts fold-change in levels of vWF, FVIII, and mcoET3 mRNA when compared to static conditions. Endogenous FVIII mRNA decreased by 10-fold and 11.3-fold when cells were placed at a shear stress of 0.05 dyne/cm^2 and 0.5 dyne/cm^2, respectively, when compared to static conditions. In similarity, vWF mRNA decreased fivefold at the lower shear stress and 8.4-fold when cells were subjected to the higher shear stress. However, mcoET3 mRNA was not significantly affected by any conditions of flow (**Figure 3E**).

Determining the Impact of Fluidic Shear Stress on PLC-mcoET3 Integrin Expression

Cells sense mechanical stimuli, such as fluidic shear stress, through several mechanosensitive molecules including integrins (Martino et al., 2018). We, therefore, next investigated if and how conditions of shear stress impacted integrins expressed by PLC-mcoET3. We used flow cytometry to characterize the expression of integrins α1 (n = 4), α5 (n = 4), β3 (n = 4), and αvβ5 (n = 4), which have previously been reported to be affected by shear stress. Shear stress at 0.05 dyne/cm^2 and 0.5 dyne/cm^2 did not affect the percentage of cells positive for integrins α1, α5, β3, or αvβ5 (**Figure 4A**). To investigate if the levels of integrin expression were altered under flow, mean fluorescent intensity (MFI) was also calculated (**Figure 4B**), and no statistically significant difference in cell surface integrin expression was found between cells in static conditions and the cells under fluidic shear stress.

Investigating Molecular Pathways Involved in Mechanotransduction in PLC-mcoET3

Although differences in integrin protein expression were not found to be statistically significant between static and the different fluidic shear conditions, the data showed that shear stress-sensitive integrins are present on PLC-mcoET3, suggesting that signaling through the expressed integrins could be responsible, at least in part, for the alterations observed in PLC-mcoET3 in conditions of flow. Therefore, we next performed PCR array-based pathway-focused gene expression analysis on RNA isolated from the PLC-mcoET3 cultured under static conditions and conditions of shear stress (0.5 dyne/cm^2) to elucidate the molecular pathways responsible for the observed flow-induced alterations in expression of FVIII and vWF. Because integrity of RNA molecules is crucial to be able to replicate the gene expression signature at the precise moment of

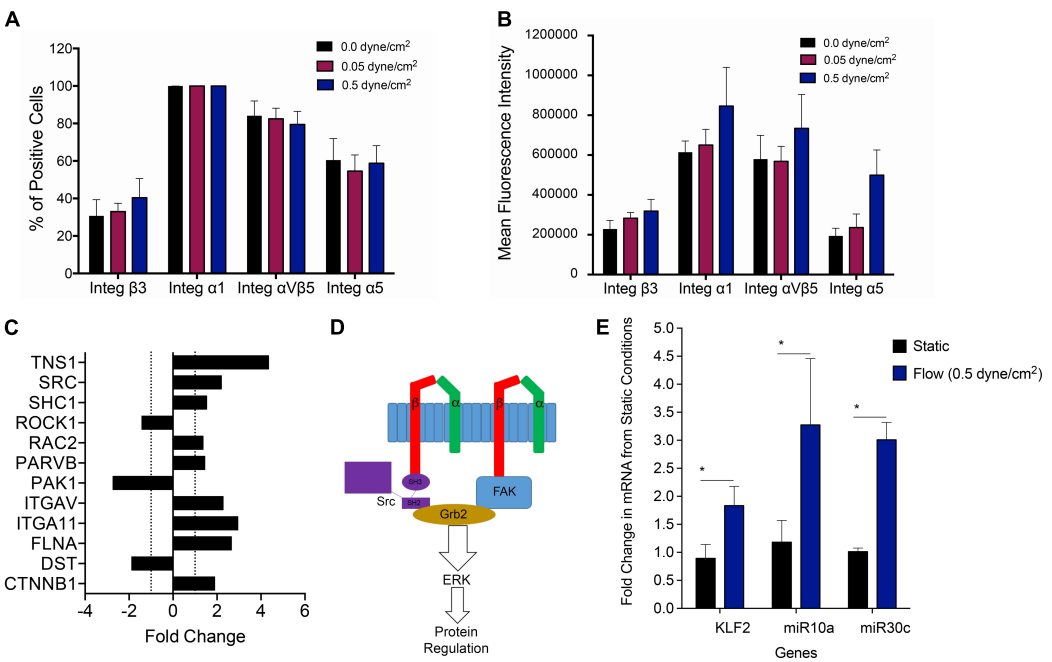

FIGURE 4 | Investigating molecular pathways involved in mechanotransduction in PLC-mcoET3. **(A)** Flow cytometric analysis of integrins which have previously been reported to be affected by shear stress (n = 4 for each integrin). Shear stress did not affect the percentage of cells positive for any of the integrins studied. **(B)** Mean fluorescent intensity (MFI) obtained by dividing each integrin MFI by the respective isotype's MFI (n = 4) was also used to investigate differences in cell surface integrin expression. No statistically significant differences were found between cells in static conditions and the cells under fluidic shear stress. **(C)** PCR array-based pathway-focused gene expression analysis on RNA isolated from the PLC-mcoET3 cultured under static conditions (n = 3) and conditions of shear stress (0.5 dyne/cm^2) to examine possible shear-responsive pathways affected by shear stress (n = 3) demonstrating upregulation (+fold change) or downregulation (- fold change) of several genes related to shear-sensing pathways. **(D)** Mechanotransduction of the SRC pathway and FAK through beta integrins initiates the ERK pathway as a possible mechanism for the flow regulation of PLC-mcoET3. **(E)** RT-qPCR to quantify KLF2 (n = 6), miR10a (n = 4), and miR30c (n = 3) under static and flow conditions demonstrated that KFL2, miR10a, and miR30c are significantly increased under flow ($p < 0.05$). *corresponds to $p < 0.05$.

RNA extraction (Schroeder et al., 2006), the quality of all isolated RNA samples was tested on an Agilent 2100 Bioanalyzer, and only samples with an RNA integrity number (RIN) higher than eight were used.

The full results of this array analysis can be found in **Supplementary Figure 1**. Of interest was that, in addition to the upregulation/downregulation of several beta integrins, analysis of our focused array data also showed a 2.2-fold and a 1.5-fold increase in SRC and SHC1 gene expression, respectively (**Figure 4C**). These proteins are known to be involved in the process of shear mechanotransduction through their association with specific integrins in a pathway that uses shear mechanotransduction to initiate the ERK pathway through GRB2, as portrayed in **Figure 4D**. Importantly, this SRC/SHC1-driven activation of the ERK pathway has been shown to mediate the shear-dependent increase in levels of the zinc finger transcription factor lung Krüppel-like factor (KLF2) (Wang et al., 2006), which can regulate the transcription of vWF (Dekker et al., 2006). We therefore next performed RT-qPCR-based studies to investigate whether KLF2 was playing a role in the downregulation of endogenous expression of FVIII and vWF in PLCs and identify the responsible downstream effectors. As can be seen in **Figure 4E**, culture of PLCs in conditions of flow/shear stress (0.5 dyne/cm^2) led to a statistically significant ($p < 0.05$) ∼2-fold increase in KLF2 mRNA levels compared to PLCs cultured in static conditions.

Shear stress has also been shown to induce the expression, nuclear accumulation, and association of retinoid acid receptor-α (RARα) and retinoid X receptor-α (RXRα). RARα and RXRα then serve as a "director" and an "enhancer," respectively, to augment RARα binding to RA-responsive element (RARE) and thereby enhance miR-10a expression, in a KLF2-dependent fashion. Since GATA6 contains a target site for miR-10a (Lee et al., 2017) and GATA6 is known to bind to the promoter of vWF to activate its transcription (Wang et al., 2004), we next performed RT-qPCR to quantitate levels of miR-10a in PLCs cultured in static vs. flow conditions. These analyses **Figure 4E** showed a marked 3.3-fold upregulation of miR-10a ($p < 0.05$).

Next, we performed studies to investigate why exposure of PLC-mcoET3 to conditions of flow/shear stress markedly reduced the levels of mRNA for endogenous FVIII while having no effect on expression of the lentiviral vector-driven expression of mcoET3. Human FVIII and mcoET3 share greater than 90% identity at the nucleotide level, thus we reasoned that the differential response of these two FVIII molecules by flow must arise as a result of differences in their regulatory elements. A key difference between the endogenous/native FVIII transcript and that produced from the lentiviral vector is the absence of the 3′ untranslated region (UTR) in the vector-encoded mcoET3, which is derived from cDNA. Since in addition to miR10a, KLF2 upregulates various micro RNAs such as miR30c, and overexpression of miR-30c has been shown to decrease FVIII expression, we next examined the levels of miR30c in PLC-mcoET3 in static vs. flow conditions. These studies demonstrated that exposure to flow resulted in a nearly threefold induction of miR-30c message in PLC-mcoET3 ($p < 0.05$) (**Figure 4E**), providing a mechanistic explanation for the differential response of the endogenous/native FVIII and the mcoET3 transgene to conditions of flow.

DISCUSSION

Amid the rapid recent progress in HA therapies (DiMichele, 2018), FVIII transgene-modified cell platforms have arisen as a new class of promising biologicals (Shi et al., 2006; Porada et al., 2010; Doering et al., 2018). To fulfill their therapeutic promise, however, several challenging criteria must be met, including an optimized transgene that enables production and secretion of a functional FVIII molecule at therapeutic levels without inducing cellular stress responses (Zolotukhin et al., 2016). In addition, the gene-modified cells must possess the ability to efficiently produce and secrete FVIII, they should lodge/engraft and persist long-term within a broad range of tissues upon infusion, and they need to evade the recipient's immune system, despite expressing a therapeutic protein that is perceived as foreign. We recently reported the development of a platform, based upon human PLC engineered with a lentiviral vector to express a mco human/porcine hybrid FVIII (ET3) molecule, PLC-mcoET3, that fulfills all of these criteria (El-Akabawy et al., 2020).

To restore hemostasis upon transplantation, the PLC-mcoET3 must lodge in perivascular sites to provide the secreted mcoET3 ready access to the circulation. As such, these cells will be placed in conditions of flow-induced shear stress, the biological effects of which have never before been explored in the context of FVIII transgene-modified cell platforms. PLC endogenously express low levels of FVIII. Moreover, they also express low levels of the FVIII carrier protein vWF, the conformation of which is known to be impacted by shear stress. Specifically, hydrodynamic forces have been shown to be responsible for extensive conformational transitions in the vWF multimers that change their globular form, a stretched structure, to a linear conformation, with flow acceleration favoring extension and thickening of vWF strands (Zheng et al., 2015). However, to our knowledge, the effect of flow on the expression of FVIII and vWF has not yet been explored. PLC-mcoET3 thus provide a unique paradigm in which to define the effects of flow-induced shear stress on the expression of both the transgene-encoded mcoET3 and the native FVIII locus, as well as the FVIII carrier vWF, and to delineate the molecular mechanism(s) driving any observed effects. For such studies to be possible, however, it is first necessary to culture PLC-mcoET3 in conditions of flow-induced shear stress that recapitulate those present within the anatomic sites of engraftment within the body.

As the liver sinusoids are the site where PLC-mcoET3 are thought to lodge after administration (Almeida-Porada et al., 2017), in the present studies, we designed, manufactured, and validated a cell culture device based on microfluidic technology to simulate the unique physiology of these structures. Specifically, we designed this device to accurately recapitulate the flow-induced shear stress to which resident cells are exposed in these minimal functional units of the liver. We then used this new device to obtain some of the first data to-date on the effects that these relatively low levels of shear stress exert on the levels of expression of FVIII and vWF in a novel cell

therapy product (PLC-mcoET3) we have developed to treat HA. Previous studies have examined the effect of flow-induced shear stress on endothelial cells, however, it is important to note, that this prior work was designed to model the high shear present in the microcirculation (arterioles and capillaries), where the values of forces are typically $>20-30$ dyne/cm^2. At these high shear stresses, vWF undergoes micro- and macro-conformational changes from a globular state to a stretched chain conformation, where especially the A1 domain undergoes structural changes relevant to its functionality (Schneider et al., 2007). Another study using similarly high shear stresses provided evidence that the expression of vWF may also be affected (Hough et al., 2008). The conditions within the liver sinusoids are markedly different, as flow rates and intravascular pressures within the venous circulation are much lower, and the resultant shear stress is on the order of 0.05−0.5 dyne/cm^2. We, therefore, designed our microfluidic device to model these low shear stresses to enable us to gain insight into how the production and secretion of FVIII and vWF are affected by the physiological conditions that the cells synthesizing these coagulation proteins experience *in vivo*.

The molecular (RT-qPCR) and functional (aPTT) assays we performed herein demonstrated that the production and secretion of endogenous FVIII and vWF are both decreased under levels of shear stress present in the liver sinusoids, but the production of FVIII from our engineered mcoET3 transgene was unaffected by flow. The levels of vWF in the supernatant were further decreased when the shear stress rate was increased from 0.05 to 0.5 dyne/cm^2 (still within the physiological range for the liver sinusoids), but the levels of FVIII were not further reduced beyond those seen at 0.05 dyne/cm^2.

To elucidate the mechanism for this flow-induced downregulation of FVIII and vWF, we first used a pathway-focused PCR array to determine what shear responsive pathways are being activated in PLC-mcoET3. This analysis showed that both the SHC and SRC genes, which have both previously been shown to be a part of the β integrin-dependent cellular shear stress response (Arias-Salgado et al., 2003; Liu et al., 2008), are upregulated in PLC-mcoET3 exposed to flow conditions. Following its activation by flow-sensing β integrins, c-Src then binds to the SH2 domain of the Shc1 protein, triggering tyrosine phosphorylation of Shc1, and allowing it to bind growth factor receptor bound protein 2 (Grb2). This then leads to the activation of the extracellular signal-regulated kinase 2 (ERK2), Ras/mitogen activated protein (MAP) kinase, and ERK5 pathways (Jalali et al., 1998). Importantly, this Src/Shc1-driven activation of the ERK pathway has been shown to mediate the shear-dependent increase in levels of the zinc finger transcription factor KLF2 (Kumar et al., 2018) which in recent years, has emerged as a prime and pivotal candidate for directly relaying biomechanical shear forces into a gene transcription profile that might determine endothelial phenotype in response to flow (Dekker et al., 2002; van Thienen et al., 2006; Wang et al., 2006). This shear stress-induced upregulation of KLF2 expression is abrogated by blocking various β integrins or disrupting F-actin, supporting the notion that signaling/crosstalk between β integrins (expressed on human PLCs) and the actin cytoskeleton regulate KLF2 expression (Chu et al., 2019). Of particular note, other studies have provided evidence that KLF2 can regulate the transcription of several of the best-known endothelial signature genes, including vWF (Dekker et al., 2006). In agreement with these prior reports in endothelial cells, the present studies demonstrated that culture of PLC-mcoET3 in conditions of flow/shear stress present in liver sinusoids (0.5 dyne/cm^2) led to a ∼2-fold increase in KLF2 mRNA levels compared to PLC-mcoET3 cultured in static conditions, supporting the conclusion that KLF2 was playing a role in the observed downregulation of endogenous expression of FVIII and vWF in PLCs. Moreover, these enhanced levels of KLF2 led to upregulation in expression of miR-10a, which is known to target GATA6, precluding it from binding to the vWF promoter to activate its transcription, ultimately leading to downregulation of vWF (Wang et al., 2004; Lee et al., 2017).

Other heavily up- or down-regulated genes could also be important to note. For example, in shear conditions, we found that TNS1 the gene encoding tensin 1, a key protein in cell adhesion, is markedly upregulated. Tensin 1 has been shown to be essential in the creation of ECM and has been shown to positively regulate cell migration (Bernau et al., 2017). As such, tensin could play a role in repair in damaged areas where shear stress is increased. The most down-regulated gene seen in our analysis was ITGA6, an alpha integrin. High expression of this integrin has been shown to enhance tumor cell invasion (Brooks et al., 2016), while its downregulation with miR-143-3p has been shown to suppress tumor growth (Jin et al., 2018). This could be further studied to determine if this miRNA is upregulated in shear stress and if this pathway could be harnessed to create a cell therapy or other treatment to prevent tumor growth. Another gene that was heavily downregulated is PAK1, which has previously been shown to be downregulated in shear stress by KLF2 through the ERK5 pathway, to inhibit endothelial migration (Komaravolu et al., 2015). Further studies of the focal adhesion genes that are influenced by shear stress can be performed to understand the mechanism and possible ways to harness these genes and interactions. Cells engrafted within the body, such as in the liver sinusoids, exist in a complex environment and are affected by many mechanical signals in addition to shear stress. These cues and signals, such as tissue stiffness, which could differ in physiological conditions compared to our devices, or cell orientation, which develops in physiological conditions, could alter the way that the cells experience shear stress or behave in response to it. The relevance of other mechanical signals and properties should be further studied to gain a complete understanding of the way that these forces, alongside shear stress, can regulate gene expression.

Having delineated a plausible pathway by which flow was decreasing vWF expression in the PLC-mcoET3, we next undertook studies to explain the seemingly paradoxical observation that exposure of PLC-mcoET3 to conditions of flow/shear stress markedly reduced the levels of mRNA for endogenous FVIII while having no effect on expression of the lentiviral vector-driven expression of mcoET3. Since mcoET3 shares greater than 90% identity with human FVIII at the nucleotide level, we reasoned that the differential response of these two FVIII molecules by flow must arise as a result of

differences in their regulatory elements. A key difference between the endogenous/native FVIII transcript and that produced from the lentiviral vector is the absence of the 3′ untranslated region (UTR) in the vector-encoded mcoET3, which is derived from cDNA. A recent report of HA in human patients who lack F8 mutations, showed that overexpression of miR-30c decreased FVIII expression, while a miR-30c inhibitor partially restored FVIII expression in two cell lines that constitutively express FVIII (Jankowska et al., 2020a). These findings led the authors to hypothesize that expression of miRNAs targeting the 3'-UTR of FVIII mRNA can modulate FVIII levels and may be responsible for a FVIII-deficiency phenotype that clinically manifests as HA (Jankowska et al., 2020b). Because KLF2 overexpression has been shown to induce upregulation of the miR-30 family members miR 30b and 30c (Doebele et al., 2018), we next examined the levels of miR30c in PLC-mcoET3 in static vs. flow conditions and demonstrated that exposure to flow led to a nearly threefold induction of miR-30c in PLC-mcoET3, providing a mechanistic explanation for the differential response of the endogenous/native FVIII and the mcoET3 transgene to conditions of flow. These findings are of particular note with respect to using the gene-modified PLCs for therapy, as they suggest that mcoET3 expression will persist, even following engraftment of the transplanted PLC-mcoET3 within regions that expose them to conditions of shear stress. Collectively, the results of our focused array and RT-qPCR studies provide mechanistic insight into how shear stress can decrease the production of both FVIII and vWF through increasing miR-30c and miR-10a *via* KLF2 through mechanotransduction by integrins through the c-Src and Shc1 proteins.

In conclusion, we have developed a novel physiologically relevant microfluidic-based device that models the shear stress present within the liver sinusoids and have used this device to show, for the first time, that the low levels of shear stress present in this unique vascular bed down-regulate the production of both FVIII and vWF through a signaling cascade involving beta-integrins, c-Src, KLF2, and miRs. These newly defined shear stress-induced pathways could facilitate the identification of new targets that can regulate the production of both FVIII and vWF and thereby provide novel ways of treating HA and von Willebrand disease. Given the importance of underlying mechanical forces in the normal physiological response to maintain hemostasis (Spronk et al., 2003), there is no doubt that, in the coming years, the increasing use of microfluidics will allow for new and important findings in the fields of endothelial cell behavior, mechanotransduction pathways, coagulation protein production and behavior, and the testing of novel therapeutics *in vitro* (Trevisan et al., 2020).

DATA AVAILABILITY STATEMENT

The original contributions presented in the study are included in the article/**Supplementary Material**, further inquiries can be directed to the corresponding author/s.

AUTHOR CONTRIBUTIONS

BT, AM, JA, and MR performed experiments, data analysis, and interpretation. JA, DM, AF, and AS provided expertise. CD, HS, and AA provided reagents. BT drafted the manuscript. GA-P and CP approved final version of the manuscript. BT, GA-P, and CP conception and experimental design. GA-P and CP supervised experiments and secured funding. All authors contributed to the article and approved the submitted version.

FUNDING

This work was supported by NHLBI, HL130856, HL135853, and HL148681. BT is supported by NIBIB 2T32EB014836-06A1.

ACKNOWLEDGMENTS

We would like to thank Wake Forest Baptist Health Special Hematology Laboratory for their excellent technical support and the performance of FVIII testing, and the Wake Forest Institute for Regenerative Medicine Clinical Center for providing the PLC.

SUPPLEMENTARY MATERIAL

The Supplementary Material for this article can be found online at: https://www.frontiersin.org/articles/10.3389/fbioe.2021.639070/full#supplementary-material

REFERENCES

Aleman, J., George, S. K., Herberg, S., Devarasetty, M., Porada, C. D., Skardal, A., et al. (2019). Deconstructed microfluidic bone marrow on-a-chip to study normal and malignant hemopoietic cell-niche interactions. *Small* 15:e1902971.

Almeida-Porada, G., George, S., Morsi, A., El-Akabawy, N., Figueiroa, J., Shields, J., et al. (2017). Prenatal transplantation of placental cells engineered to express FVIII leads to corrective plasma levels of FVIII after birth. *Blood* 130:361.

Alves, M. G., Perez-Sayans, M., Padin-Iruegas, M. E., Reboiras-Lopez, M. D., Suarez-Penaranda, J. M., Lopez-Lopez, R., et al. (2016). Comparison of RNA extraction methods for molecular analysis of oral cytology. *Acta Stomatol. Croat.* 50, 108–115. doi: 10.15644/asc50/2/2

Arias-Salgado, E. G., Lizano, S., Sarkar, S., Brugge, J. S., Ginsberg, M. H., and Shattil, S. J. (2003). Src kinase activation by direct interaction with the integrin β cytoplasmic domain. *Proc. Natl. Acad. Sci.* 100, 13298–13302. doi: 10.1073/pnas.2336149100

Banerjee, S., Smallwood, A., Moorhead, J., Chambers, A. E., Papageorghiou, A., Campbell, S., et al. (2005). Placental expression of interferon-gamma (IFN-gamma) and its receptor IFN-gamma R2 fail to switch from early hypoxic to late normotensive development in preeclampsia. *J. Clin. Endocrinol. Metab.* 90, 944–952. doi: 10.1210/jc.2004-1113

Bernau, K., Torr, E. E., Evans, M. D., Aoki, J. K., Ngam, C. R., and Sandbo, N. (2017). Tensin 1 is essential for myofibroblast differentiation and extracellular

matrix formation. *Am. J. Respir. Cell Mol. Biol.* 56, 465–476. doi: 10.1165/rcmb.2016-0104oc

Brooks, D. L., Schwab, L. P., Krutilina, R., Parke, D. N., Sethuraman, A., Hoogewijs, D., et al. (2016). ITGA6 is directly regulated by hypoxia-inducible factors and enriches for cancer stem cell activity and invasion in metastatic breast cancer models. *Mol. Cancer* 15:26.

Chu, H. R., Sun, Y. C., Gao, Y., Guan, X. M., Yan, H., Cui, X. D., et al. (2019). Function of Kruppellike factor 2 in the shear stressinduced cell differentiation of endothelial progenitor cells to endothelial cells. *Mol. Med. Rep.* 19, 1739–1746.

Dasgupta, S., Repesse, Y., Bayry, J., Navarrete, A. M., Wootla, B., Delignat, S., et al. (2007). VWF protects FVIII from endocytosis by dendritic cells and subsequent presentation to immune effectors. *Blood* 109, 610–612. doi: 10.1182/blood-2006-05-022756

Dekker, R. J., Boon, R. A., Rondaij, M. G., Kragt, A., Volger, O. L., Elderkamp, Y. W., et al. (2006). KLF2 provokes a gene expression pattern that establishes functional quiescent differentiation of the endothelium. *Blood* 107, 4354–4363. doi: 10.1182/blood-2005-08-3465

Dekker, R. J., van Soest, S., Fontijn, R. D., Salamanca, S., de Groot, P. G., VanBavel, E., et al. (2002). Prolonged fluid shear stress induces a distinct set of endothelial cell genes, most specifically lung Kruppel-like factor (KLF2). *Blood* 100, 1689–1698. doi: 10.1182/blood-2002-01-0046

Delignat, S., Repesse, Y., Navarrete, A. M., Meslier, Y., Gupta, N., Christophe, O. D., et al. (2012). Immunoprotective effect of von Willebrand factor towards therapeutic factor VIII in experimental haemophilia A. *Haemophilia* 18, 248–254. doi: 10.1111/j.1365-2516.2011.02679.x

DiMichele, D. M. (2018). Navigating speed bumps on the innovation highway in hemophilia therapeutics. *Hemasphere* 2:e144. doi: 10.1097/hs9.0000000000000144

Doebele, C., Hergenreider, E., Boon, R., Reinfeld, N., Zeiher, A. M., and Dimmeler, S. (2018). The miR-30 family is regulated by shear stress and affects the expression of inflammatory cell-cell adhesion molecules. *Circulation* 2011:A15893.

Doering, C. B., Denning, G., Shields, J. E., Fine, E. J., Parker, E. T., Srivastava, A., et al. (2018). Preclinical development of a hematopoietic stem and progenitor cell bioengineered factor VIII lentiviral vector gene therapy for hemophilia A. *Hum. Genet. Ther.* 29, 1183–1201. doi: 10.1089/hum.2018.137

El-Akabawy, N., Rodriguez, M., Ramamurthy, R., Rabah, A., Trevisan, B., Morsi, A., et al. (2020). Defining the optimal FVIII transgene for placental cell-based gene therapy to treat hemophilia A. *Mol. Ther. Methods Clin. Dev.* 17, 465–477. doi: 10.1016/j.omtm.2020.03.001

Franchini, M., and Mannucci, P. M. (2013). Hemophilia A in the third millennium. *Blood Rev.* 27, 179–184. doi: 10.1016/j.blre.2013.06.002

Hough, C., Cameron, C. L., Notley, C. R., Brown, C., O'Brien, L., Keightley, A. M., et al. (2008). Influence of a GT repeat element on shear stress responsiveness of the VWF gene promoter. *J. Thromb. Haemost.* 6, 1183–1190. doi: 10.1111/j.1538-7836.2008.03011.x

Jalali, S., Li, Y.-S., Sotoudeh, M., Yuan, S., Li, S., Chien, S., et al. (1998). Shear stress activates p60src-Ras-MAPK signaling pathways in vascular endothelial cells. *Arterioscler. Thromb. Vasc. Biol.* 18, 227–234. doi: 10.1161/01.atv.18.2.227

Jankowska, K. I., McGill, J., Pezeshkpoor, B., Oldenburg, J., Atreya, C. D., and Sauna, Z. E. (2020a). Clinical manifestation of hemophilia A in the absence of mutations in the F8 gene that encodes FVIII: role of microRNAs. *Transfusion* 60, 401–413. doi: 10.1111/trf.15605

Jankowska, K. I., McGill, J., Pezeshkpoor, B., Oldenburg, J., Sauna, Z. E., and Atreya, C. D. (2020b). Further evidence that MicroRNAs can play a role in hemophilia A disease manifestation: F8 gene downregulation by miR-19b-3p and miR-186-5p. *Front. Cell Dev. Biol.* 8:669. doi: 10.3389/fcell.2020.00669

Jin, Y. P., Hu, Y. P., Wu, X. S., Wu, Y. S., Ye, Y. Y., Li, H. F., et al. (2018). miR-143-3p targeting of ITGA6 suppresses tumour growth and angiogenesis by downregulating PLGF expression via the PI3K/AKT pathway in gallbladder carcinoma. *Cell Death Dis.* 9: 182.

Komaravolu, R. K., Adam, C., Moonen, J. R., Harmsen, M. C., Goebeler, M., and Schmidt, M. (2015). Erk5 inhibits endothelial migration via KLF2-dependent down-regulation of PAK1. *Cardiovasc. Res.* 105, 86–95. doi: 10.1093/cvr/cvu236

Kumar, P., Gao, K., Wang, C., Pivetti, C., Lankford, L., Farmer, D., et al. (2018). In utero transplantation of placenta-derived mesenchymal stromal cells for potential fetal treatment of hemophilia A. *Cell Transplant.* 27, 130–139. doi: 10.1177/0963689717728937

Lalor, P. F., and Adams, D. H. (1999). Adhesion of lymphocytes to hepatic endothelium. *Mol. Pathol.* 52, 214–219. doi: 10.1136/mp.52.4.214

Lee, D. Y., Lin, T. E., Lee, C. I., Zhou, J., Huang, Y. H., Lee, P. L., et al. (2017). MicroRNA-10a is crucial for endothelial response to different flow patterns via interaction of retinoid acid receptors and histone deacetylases. *Proc. Natl. Acad. Sci. U.S.A.* 114, 2072–2077. doi: 10.1073/pnas.1621425114

Liu, Y., Sweet, D. T., Irani-Tehrani, M., Maeda, N., and Tzima, E. (2008). Shc coordinates signals from intercellular junctions and integrins to regulate flow-induced inflammation. *J. Cell Biol.* 182, 185–196. doi: 10.1083/jcb.200709176

Lollar, P., Hill-Eubanks, D. C., and Parker, C. G. (1988). Association of the factor VIII light chain with von Willebrand factor. *J. Biol. Chem.* 263, 10451–10455. doi: 10.1016/s0021-9258(19)81537-5

Maji, D., De La Fuente, M., Kucukal, E., Sekhon, U. D. S., Schmaier, A. H., Sen Gupta, A., et al. (2018). Assessment of whole blood coagulation with a microfluidic dielectric sensor. *J. Thromb. Haemost.* 16, 2050–2056. doi: 10.1111/jth.14244

Martino, F., Perestrelo, A. R., Vinarsky, V., Pagliari, S., and Forte, G. (2018). Cellular mechanotransduction: from tension to function. *Front. Physiol.* 9:824. doi: 10.3389/fphys.2018.00824

McGrath, R. T., McRae, E., Smith, O. P., and O'Donnell, J. S. (2010). Platelet von Willebrand factor – structure, function and biological importance. *Br. J. Haematol.* 148, 834–843. doi: 10.1111/j.1365-2141.2009.08052.x

Morsi, A., El-Akabawy, N., George, S., Shields, J., Meares, D., Farland, A., et al. (2018). Overexpression of FVIII production in placental cells (PLCs) increases endogenous vWF. *Mol. Ther.* 26:79.

Over, J., Sixma, J. J., Bruine, M. H., Trieschnigg, M. C., Vlooswijk, R. A., Beeser-Visser, N. H., et al. (1978). Survival of 125iodine-labeled Factor VIII in normals and patients with classic hemophilia. Observations on the heterogeneity of human Factor VIII. *J. Clin. Invest.* 62, 223–234. doi: 10.1172/jci109120

Pipe, S. W., Montgomery, R. R., Pratt, K. P., Lenting, P. J., and Lillicrap, D. (2016). Life in the shadow of a dominant partner: the FVIII-VWF association and its clinical implications for hemophilia A. *Blood* 128, 2007–2016. doi: 10.1182/blood-2016-04-713289

Porada, C. D., Sanada, C., Kuo, E., Colletti, E. J., Moot, R., Doering, C., et al. (2010). Phenotypic correction of hemophilia A by postnatal intraperitoneal transplantation of FVIII-expressing MSC. *Blood* 116:249. doi: 10.1182/blood.v116.21.249.249

Schneider, S. W., Nuschele, S., Wixforth, A., Gorzelanny, C., Alexander-Katz, A., Netz, R. R., et al. (2007). Shear-induced unfolding triggers adhesion of von Willebrand factor fibers. *Proc. Natl. Acad. Sci.* 104, 7899–7903. doi: 10.1073/pnas.0608422104

Schroeder, A., Mueller, O., Stocker, S., Salowsky, R., Leiber, M., Gassmann, M., et al. (2006). The RIN: an RNA integrity number for assigning integrity values to RNA measurements. *BMC Mol. Biol.* 7:3. doi: 10.1186/1471-2199-7-3

Shi, Q., Wilcox, D. A., Fahs, S. A., Weiler, H., Wells, C. W., Cooley, B. C., et al. (2006). Factor VIII ectopically targeted to platelets is therapeutic in hemophilia A with high-titer inhibitory antibodies. *J. Clin. Invest.* 116, 1974–1982. doi: 10.1172/jci28416

Spronk, H. M. H., Govers-Riemslag, J. W. P., and ten Cate, H. (2003). The blood coagulation system as a molecular machine. *BioEssays* 25, 1220–1228. doi: 10.1002/bies.10360

Trevisan, B. M., Porada, C. D., Atala, A., and Almeida-Porada, G. (2020). Microfluidic devices for studying coagulation biology. *Semin. Cell Dev. Biol.* (in press). doi: 10.1016/j.semcdb.2020.06.002

van der Poll, T., de Jonge, E., and Levi, M. (2001). Regulatory role of cytokines in disseminated intravascular coagulation. *Semin. Thromb. Hemost.* 27, 639–652. doi: 10.1055/s-2001-18868

van Oeveren, W., Haan, J., Lagerman, P., and Schoen, P. (2002). Comparison of coagulation activity tests in vitro for selected biomaterials. *Artif. Organs.* 26, 506–511. doi: 10.1046/j.1525-1594.2002.06872.x

van Thienen, J. V., Fledderus, J. O., Dekker, R. J., Rohlena, J., van Ijzendoorn, G. A., Kootstra, N. A., et al. (2006). Shear stress sustains atheroprotective endothelial KLF2 expression more potently than statins through mRNA stabilization. *Cardiovasc. Res.* 72, 231–240. doi: 10.1016/j.cardiores.2006.07.008

Vergauwe, R. M. A., Uji-i, H., Ceunynck, K. De, Vermant, J., Vanhoorelbeke, K., and Hofkens, J. (2014). Shear-stress-induced conformational changes

of von willebrand factor in a water–glycerol mixture observed with single molecule microscopy. *J. Phys. Chem. B* 118, 5660–5669. doi: 10.1021/jp5022664

Wang, N., Miao, H., Li, Y.-S., Zhang, P., Haga, J. H., Hu, Y., et al. (2006). Shear stress regulation of Krüppel-like factor 2 expression is flow pattern-specific. *Biochem. Biophys. Res. Commun.* 341, 1244–1251. doi: 10.1016/j.bbrc.2006.01.089

Wang, X., Peng, Y., Ma, Y., and Jahroudi, N. (2004). Histone H1–like protein participates in endothelial cell–specific activation of the von Willebrand factor promoter. *Blood* 104, 1725–1732. doi: 10.1182/blood-2004-01-0082

Zheng, Y., Chen, J., and Lopez, J. A. (2015). Flow-driven assembly of VWF fibres and webs in in vitro microvessels. *Nat. Commun.* 6:7858.

Zolotukhin, I., Markusic, D. M., Palaschak, B., Hoffman, B. E., Srikanthan, M. A., and Herzog, R. W. (2016). Potential for cellular stress response to hepatic factor VIII expression from AAV vector. *Mol. Ther. Methods Clin. Dev.* 3:16063. doi: 10.1038/mtm.2016.63

Conflict of Interest: The authors declare that the research was conducted in the absence of any commercial or financial relationships that could be construed as a potential conflict of interest.

frontiers in Bioengineering and Biotechnology

ORIGINAL RESEARCH
published: 18 March 2021
doi: 10.3389/fbioe.2021.627877

Engineering a Human Pluripotent Stem Cell-Based *in vitro* Microphysiological System for Studying the Metformin Response in Aortic Smooth Muscle Cells

Nan Chen[1,2†], Mieradilijiang Abudupataer[1,2†], Sisi Feng[3†], Shichao Zhu[1,2], Wenrui Ma[1,2], Jun Li[1,2], Hao Lai[1,2], Kai Zhu[1,2] and Chunsheng Wang[1,2]**

[1] Department of Cardiac Surgery, Zhongshan Hospital, Fudan University, Shanghai, China, [2] Shanghai Institute of Cardiovascular Diseases, Shanghai, China, [3] State Key Laboratory of Cell Biology, CAS Center for Excellence in Molecular Cell Science, Institute of Biochemistry and Cell Biology, University of Chinese Academy of Sciences, Chinese Academy of Sciences, Shanghai, China

OPEN ACCESS

Edited by:
Nuno M. Neves,
University of Minho, Portugal

Reviewed by:
Nicolas Christoforou,
Pfizer, United States
Leo R. Quinlan,
National University of Ireland Galway, Ireland

***Correspondence:**
Kai Zhu
zhu.kai1@zs-hospital.sh.cn
Chunsheng Wang
wangchunsheng@fudan.edu.cn

† These authors have contributed equally to this work

Specialty section:
This article was submitted to Nanobiotechnology, a section of the journal Frontiers in Bioengineering and Biotechnology

Received: 10 November 2020
Accepted: 22 February 2021
Published: 18 March 2021

Citation:
Chen N, Abudupataer M, Feng S, Zhu S, Ma W, Li J, Lai H, Zhu K and Wang C (2021) Engineering a Human Pluripotent Stem Cell-Based in vitro Microphysiological System for Studying the Metformin Response in Aortic Smooth Muscle Cells. Front. Bioeng. Biotechnol. 9:627877. doi: 10.3389/fbioe.2021.627877

Aortic aneurysm is a common cardiovascular disease characterised by continuous dilation of the aorta, and this disease places a heavy burden on healthcare worldwide. Few drugs have been suggested to be effective in controlling the progression of aortic aneurysms. Preclinical drug responses from traditional cell culture and animals are usually controversial. An effective *in vitro* model is of great demand for successful drug screening. In this study, we induced an *in vitro* microphysiological system to test metformin, which is a potential drug for the treatment of aortic aneurysms. Human pluripotent stem cell-derived aortic smooth muscle cells (hPSC-HASMCs) were cultured on an *in vitro* microphysiological system, which could replicate the cyclic stretch of the human native aortic wall. By using this system, we found that HASMCs were more likely to present a physiologically contractile phenotype compared to static cell cultures. Moreover, we used hPSC-HASMCs in our microphysiological system to perform metformin drug screening. The results showed that hPSC-HASMCs presented a more contractile phenotype via NOTCH 1 signalling while being treated with metformin. This result indicated that metformin could be utilised to rescue hPSC-HASMCs from phenotype switching during aortic aneurysm progression. This study helps to elucidate potential drug targets for the treatment of aortic aneurysms.

Keywords: aortic aneurysm, metformin, drug screening, human pluripotent stem cells, microphysiological system

INTRODUCTION

Aortic aneurysm, which is defined as a pathological dilation of the aorta, presents as a life-threatening disease due to the potential to develop dissection or rupture (Goldfinger et al., 2014). Recent studies suggest an average annual death rate increasing by 12% to 2.8/100000 in the last two decades due to aortic aneurysm (Sampson et al., 2014). However, clinical management that has been proven to be curative of aortic aneurysms is limited to surgical replacement or endovascular repair.

Thus, great interest in discovering drug therapies that may be positive for reducing continuous dilatation of aortic aneurysms has been shown in many studies (Sweeting et al., 2012). Few efficiencies in reducing aortic aneurysm growth or rupture were associated with these prescribed drugs, including angiotensin-converting enzyme inhibitors, β-blockers, calcium channel blockers and antiplatelet agents (Golledge, 2019). Recently, some clinical studies focusing on the reduction of aortic aneurysm growth in patients receiving metformin prescription were reported (Fujimura et al., 2016; Golledge et al., 2017; Hinchliffe, 2017; Yu et al., 2019). In contrast, an epidemiological study reported that a non-significantly reduced risk of aortic aneurysm rupture was associated with metformin prescription (Kristensen et al., 2017). To address whether the prolonged progress of aortic aneurysm is associated with metformin prescription, a number of randomised, controlled trials (RCTs) are being developed to date.

Some emerging biotechnologies associated with drug screening *in vitro* have been developed. Benefitting from the development of microfluidics, the combination of these techniques can mimic the biological environment of an organ or multiple organs in an *in vitro* microphysiological system, which can be utilised in understanding disease mechanisms and drug effects *in vivo* (Sackmann et al., 2014). Different from traditional *in vitro* models, microphysiological systems can replicate the biomechanical parameters of the human body, which cannot be achieved in 2D cell culture (Horvath et al., 2016; Fang and Eglen, 2017; Xiao et al., 2017). Moreover, microphysiological systems are more cost-effective than *in vivo* experiments, including animal models and preclinical trials in humans. Thus, these emerging techniques can significantly improve the testing efficacy compared to traditional biotechniques. To date, several reports have established different kinds of microphysiological *in vitro* models and related disease models (Huh et al., 2010; Yoon No et al., 2015; Jastrzebska et al., 2016; Musah et al., 2017; Bein et al., 2018). For instance, a vascular micro-physiological system was applied in the construction of models simulating vascular biology, including a biological pulse, cyclic stretching and even shear stress, achieving relevant biophysical conditions for cardiovascular study with cheaper, smaller sample volumes and more precise control compared with animal models and preclinical trails (Beebe et al., 2002; Plouffe et al., 2009).

Based on this evidence, we attempted to detect the drug effect of metformin prescription on the progression of aortic aneurysms using a microphysiological system. In this study, we established a microphysiological *in vitro* model associated with the microfluidic technique. The simulation of the *in vivo* pulse and cyclic stretch function of this *in vitro* model was evaluated with human aortic smooth muscle cells (HASMCs). Furthermore, we used human pluripotent stem cells (hPSCs) to generate HASMCs according to a published protocol to detect the drug effect of metformin in the established system. As a result, the hPSC-HASMCs were switched to a contractile phenotype associated with cyclic stretching and metformin prescription. Moreover, we found that the phenotypic switch may be related to the presence of NOTCH 1 signalling, showing the potential to serve as a therapeutic target in preventing the progression of aortic aneurysm. The schematic of our study is shown in **Figure 1**.

MATERIALS AND METHODS

Design and Fabrication of the HASMC Microphysiological System

The framework of the microphysiological system (100 × 40 × 8 mm) was polydimethylsiloxane (PDMS) carved from polymethyl methacrylate (PMMA) moulds. The PMMA moulds were engraved utilising a computer numerical control (CNC) machine (Jingyan Technology). Then, the PDMS was cast at a ratio of 10:1 (w/w) monomer to curing agent in PMMA moulds and crosslinked at 70°C for 2 h. There were two layers of PDMS in the microdevice, with the top layer containing a medium channel (70 × 2 × 2 mm) and the bottom layer containing a gas channel (70 × 2 × 2 mm). After the construction of the two layers, the bottom layer was attached to the commercialised PDMS membrane using oxygen plasma (Harrick Plasma). Then, the top layer was attached to the bottom membrane layer with oxygen plasma. Finally, the medium channel and the gas channel were connected to different pumps, providing a medium flow and cyclic negative pressure.

Cell Culture of HASMCs

The HASMC cell line (CRL1999) was purchased from the American Type Culture Collection (ATCC). Smooth muscle cell medium (SMCM, ScienCell) supplemented with 10% (FBS) was used to maintain cell proliferation. The medium channel was coated with collagen (80 μg/mL) and subsequently incubated for 1 h. Then, the microdevice was dried at 70°C for 2 h, and the medium channel was washed with phosphate-buffered saline (PBS). HASMCs were seeded at a density of 2×10^6 per mL in the medium channel. After seeding, the microdevice was incubated at 37°C and 5% CO_2 for 24 h. Finally, the microdevice system was ready for mechanical stimulation experiments.

Human PSC Maintenance and hPSC-HASMC Differentiation

The human embryonic stem cell line H9 was provided by the Core Facility for Stem Cell Research (Shanghai Institute of Biochemistry and Cell Biology, China) and selected for differentiation. hPSCs were cultured in mTeSR1 media (StemCell Technologies), passaged with Accutase (StemCell Technologies) and seeded at a density of 3,7000 cells per square centimetre. For differentiation, hPSCs were dissociated with Accutase and plated on Matrigel (BD Biosciences)-coated plates at a density of 3,7000 cells per square centimetre in mTeSR1 media supplied with Y-27632 (10 mM, Selleck). The next day, the medium was refreshed with Mesoderm Specification Medium, which was a mixture of DMEM/F12 and neurobasal media (1:1) supplemented with 2 mM Glutamax, 1× N2 (Life Technologies), 1× B27 (Life Technologies), CHIR99021 (8 mM, Selleck) and BMP4 (25 ng/ml, R&D Systems). After 3 days, the Mesoderm Specification Medium was changed to Vessel Smooth Muscle Cells (VSMCs) Induction Medium, which was a mixture of DMEM/F12 and neurobasal media (1:1) with 1× N2 (Life

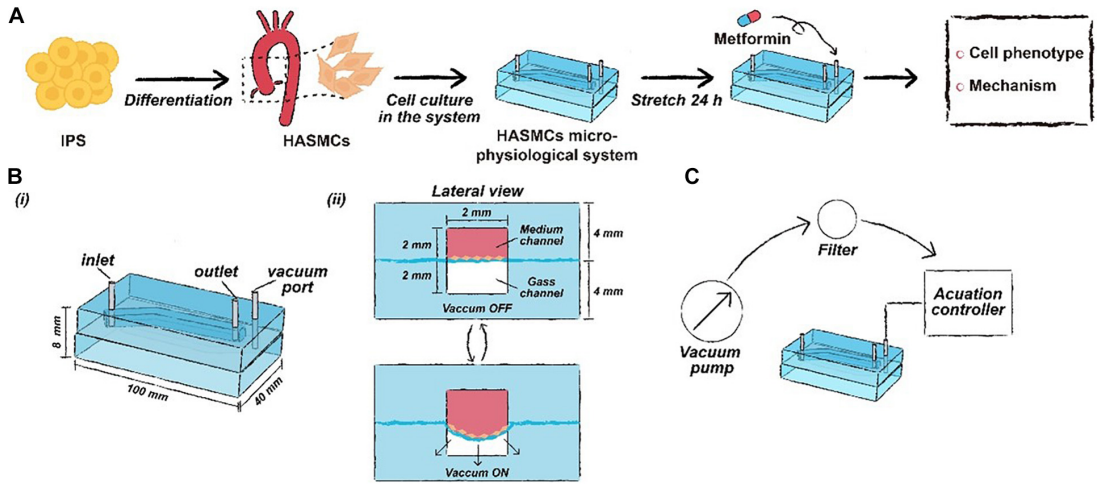

FIGURE 1 | The schematic workflow of this study. **(A)** Drug functional testing of metformin performed in the hPSC-HASMC microphysiological system. **(B)** The parameters of the microphysiological system. **(C)** The schematic of the microfluidic based microphysiological system.

Technologies), 1× B27 (Life Technologies), PDGF-BB (10 ng/ml, Pepro Tech) and Activin A (2 ng/ml, Pepro Tech). The medium was refreshed every other day. Until day 6, cultures were passaged with Accutase and reseeded at 35,000 cells per square centimetre on gelatine-coated 6-well plates in Vessel Smooth Muscle Cells (VSMCs) Induction Medium reduced Activin A (2 ng/ml, Pepro Tech) to obtain synthetic hPSC-HASMCs. After the hPSC-HASMCs were obtained, the seeding and culturing of the cells in the microdevice system was the same as that of the HASMCs cell line.

Simulation of Vessel-Like Cyclic Stretching

The simulation of cyclic stretching of the cells was achieved by applying cyclic strain derived from the negative pressure in the gas channel using a microfluidic pump. The pump was connected to the computer-controlled solenoid system, which can provide cyclic stretching with various frequencies (0.5, 1 and 2 Hz). We used a pressure regulator to adjust the negative pressure. Static conditions (0% strain, i.e., 0 kPa, meaning *in vitro* experiments) and cyclic stretch conditions (15% strain, i.e., approximately 6.75 KPa, meaning *in vivo* experiments) were used throughout this study. The normal deformation of the native aorta was reported to range from 9 to 16% in previous studies (Stefanadis et al., 1995; Williams, 1998). We measured the deformation of the PDMS membrane on the cross section of the microphysiological system and the corresponding negative pressure. Then, the relationship between them was characterised. We found that when the deformation of the PDMS membrane was 15%, the corresponding vacuum pressure was 6.75 kPa (**Supplementary Figure S1**). Thus, we set 6.75 kPa, which can be treated as a theoretically normal strain, as the negative pressure in the stretching group. After 24 h of cyclic stretching, samples were collected for immunofluorescence, RT-qPCR and western blotting analyses.

Knockdown of NOTCH 1 in hPSC-HASMCs

NOTCH 1-targeted short hairpin RNAs (shRNA, hU6-MCS-Ubiquitin-EGFP-IRES-puromycin) were designed and composed by GeneChem (Shanghai, China). hPSC-HASMCs were seeded into 6-well plates (6×10^5 cells per well) and incubated in a cell incubator. Cells were divided into 3 groups, including the control group, shRNA control (scrambled) group and NOTCH 1 knockdown group (NOTCH 1-KD), when they reached 30% confluency. The shRNA control and NOTCH 1-KD groups were infected with LV-non-specific shRNA and LV-shRNA-NOTCH-1 at an MOI of 10 according to the product manual. After an infection time of 12 h, virus particles were removed from the respective wells, and then, the wells were replenished with fresh SMCM. Cells were further cultured for 72 h in cell culture incubation. Then, the cells were treated with 2.0 μg/mL puromycin, and GFP-positive cells were selected. After the GFP-positive cells reached approximately 80% confluency, they were harvested. The efficiency of NOTCH 1 knockdown was verified by RT-qPCR and western blotting analyses.

Drug Screening

Metformin (Selleck) was dissolved in deionised water to an initial concentration of 50 mM and stored at −20°C after allocation. We determined the optimal concentration of metformin through RT-qPCR. Among the concentrations, 2 mM increased the expression of SM22 and CNN1 maximally (**Supplementary Figure S2**). A 2 mM final concentration of metformin was made with fresh medium before use. When the attachment of cells to the PDMS membrane after seeding was achieved (almost 24 h), the medium was exchanged with fresh medium containing metformin at a final concentration (2 mM). Then, cyclic stretching was initiated and lasted for 24 h. The samples were collected for relative analysis after the completion of stretching.

Cell Viability

After seeding the cells into the microdevice, the viability was analysed at day 1, day 2 and day 3 by a LIVE/DEAD kit (Thermo Fisher Scientific). In brief, the medium channel was gently washed three times with PBS. Second, the microdevice was incubated in the dark for 30 min with the working solution soaking the medium channel. Then, the medium channel was washed three times with PBS to remove the remaining reagents. Finally, the microdevice was disassembled for better observation of the viability in the microdevice using a fluorescence microscope (Leica, DMi8). ImageJ software was utilised to analyse the results.

Immunofluorescence Analysis

Immunofluorescence analysis was performed directly with a microdevice. The medium was removed, and the medium channel was washed with PBS. The cells were fixed with 4% paraformaldehyde (Sigma-Aldrich) for 30 min at 37°C. Then, the cells were treated with Triton X-100 (1%, Sigma-Aldrich) for 15 min. Bovine serum albumin (5%, Sigma-Aldrich) was selected as the blocking solution and used to treat the cells for 30 min at room temperature. Incubation overnight at 4°C with primary antibodies was performed following blocking. The microdevices were washed three times with PBS and treated with secondary antibodies (1:300) (Alexa 488 anti-rabbit, Thermo Fisher Scientific) for 1 h at room temperature. Nuclei were dyed with 4,6-diamidino-2-phenyllindole (DAPI, Thermo Fisher Scientific) for 15 min. Rhodamine phalloidin (F-actin, Thermo Fisher Scientific) staining was performed to identify the cytoskeletons of the analysed cells. The microdevice was disassembled when the staining was completed. The disassembled microdevice can be more easily observed with a fluorescence microscope (Leica DMi8). ImageJ software was utilised to analyse the obtained images.

RT-qPCR

RNA was collected from the microdevice by TRIzol (Invitrogen) after 24 h of cyclic stretching. Complementary DNA (cDNA) was synthesised with a PrimeScript RT reagent kit (Takara) according to the product manual. Real-time PCR was performed with TB Green Premix Ex Taq. RT-PCR assays were repeated for triplicate samples of each target gene. Gene expression was normalised using housekeeping glyceraldehyde 3-phosphate dehydrogenase (GAPDH). All primer sequences for the analysed genes are listed in **Supplementary Table S1**.

Western Blot Analyses

Cells were lysed by ultrasonication on ice with RIPA (Beyotime, Shanghai, China) lysis buffer supplemented with phenylmethylsulfonyl fluoride (PMSF) protease inhibitor. To obtain an appropriate concentration of protein for western blotting, we lysed cells from 3 microdevices together. A follow-up incubation for 30 min on ice was performed for complete lysis of the cells. The extracts were harvested at a speed of 14,000 rpm at 4°C for 20 min, and the supernatants were collected. Then, the supernatants were treated with a BCA Protein Assay kit (Thermo Fisher Scientific) to quantify the protein concentrations using a spectrophotometric plate reader. The obtained proteins were diluted with loading buffer and heated for 5 min at 95°C. Then, 10 μg of each protein sample was separated by 10% SDS-PAGE and subsequently transferred to 0.2-μm polyvinylidene fluoride (PVDF) membranes (Millipore, Sigma-Aldrich). The PVDF membranes were blocked with non-fat dry milk (5%) for 1 h at room temperature and then incubated with different primary antibodies (**Supplementary Table S2**) overnight at 4°C. Then, the membranes were incubated with horseradish peroxidase-conjugated goat anti-rabbit (1:6000) and goat anti-mouse IgG secondary antibodies (Cell Signaling Technology) for 1 h at room temperature. The membranes were treated with Super Signal chemiluminescence reagent substrate (Millipore). The protein concentration was normalised using housekeeping β-actin protein. Quantitative evaluation of the intensity of the signals was performed with ImageJ software.

Statistical Analyses

The results were shown as the mean ± SD. All the experiments in our study were repeated twice, and at least three biological replicates were used in each experiment. Statistical analyses were performed with GraphPad Prism 8 software. Two-tailed Student's *t* tests were used to evaluate the difference between two groups, and one-way ANOVA followed by Tukey's *post hoc* tests was used to evaluate the difference between more than two groups.

RESULTS

Construction of HASMCs Microphysiological System

It is known that the aorta undergoes periodic contraction and relaxation at the same frequency as the cardiac cycle. As the main component in the middle layer of the aorta, HASMCs are also stimulated by cyclic stretching *in vivo*, which cannot be simulated under traditional 2D cell culture. Therefore, we used flexible PDMS to fabricate a two-layer structure of the framework in a microphysiological system to mimic cyclic beating conditions (**Figure 2A**). There was an elastic PDMS membrane in the middle of the top and bottom layers, dividing the inside chamber into medium and gas channels. The gas channel was controlled with a computer-controlled solenoid system. A change in pressure in the gas channel led to the deformation of the elastic PDMS membrane, which could mimic contraction and relaxation of the aorta *in vivo*. The parameters of the microdevice design are shown in **Figure 1B**, and the fabrication of the microphysiological system is described in detail in **Figure 2A**. For the medium channel, we used a peristaltic pump to control the flow. We first used HASMCs (CRL1999) to evaluate the system. Cells showed high viability (≥90%) in the microdevice system at days 1, 2 and 3 (**Figure 2B**). Furthermore, we stained the HASMCs with F-actin and DAPI, showing the good morphology of the seeded HASMCs (**Figure 2C**).

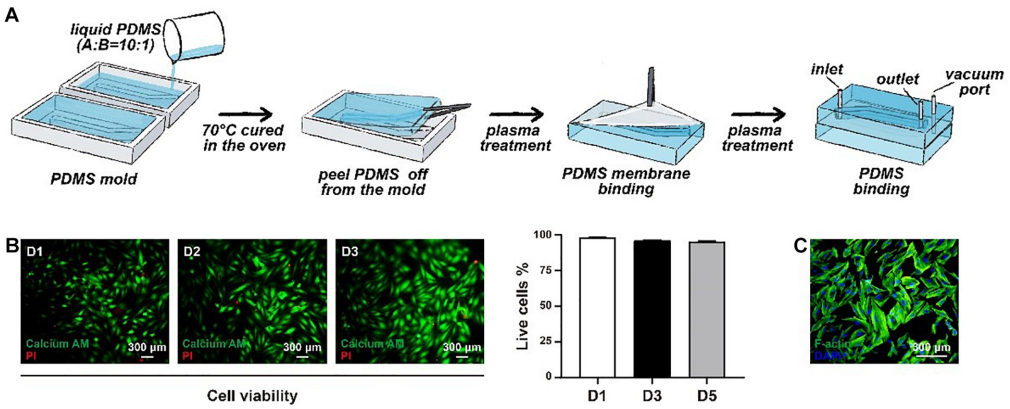

FIGURE 2 | The construction of the microphysiological system. **(A)** The framework of the system was fabricated using elastic PDMS. **(B)** The viability of HASMCs was detected after seeding on days 1, 2 and 3. **(C)** F-actin and DAPI staining of HASMCs in the microphysiological system on day 3.

Effect of Cyclic Strain on HASMCs

There are two phenotypes, contractile and synthetic, interact with different environmental simulations in HASMCs. The transition between these two states is called a phenotypic switch, which is essential for HASMCs to perform normal biofunctions *in vivo*. To evaluate the effect of cyclic strain on HASMCs, we first detected the influence of stretching treatment with a fixed frequency at 1 Hz on the cells (**Figure 3A**). HASMCs were divided into two groups: the static group and the stretching group. The phenotypic switch was evidenced by immunofluorescence staining and the expression of SM22 and CNN1 (contraction markers in HASMCs). As a result, the number of SM22- and CNN1-positive cells in the stretching group (stretching for 24 h) increased significantly compared to that in the static group (**Figure 3B** and **Supplementary Figures S4A,B**). The expression levels of SM22 and CNN1 presented a remarkable increase in the stretching group, which is consistent with the results of immunofluorescence staining (**Figure 3C**). Moreover, we tested the influence of different stretching frequencies (0.5, 1 and 2 Hz) with a fixed stretch (15%, stretching for 24 h) on the cells. The results of immunofluorescence staining showed that there were more SM22-positive HASMCs in the 1 Hz and 2 Hz groups than in the 0.5 Hz groups, while no significant difference was found between these groups (**Figure 3D** and **Supplementary Figure S4C**). In terms of the expression of SM22, the results of RT-qPCR showed a similar trend (**Figure 3E**). In addition, the results of immunofluorescence staining showed that there were more CNN1-positive HASMCs in the 1 Hz and 2 Hz groups than in the 0.5 Hz groups, while no significant difference was found between these groups (**Figure 3D** and **Supplementary Figure S4D**). In terms of the expression of CNN1, the results of RT-qPCR showed that higher expression was accompanied with higher stretching frequencies, while no significant difference was found (**Figure 3E**). To determine an appropriate frequency of cyclic stretching in our study, we subsequently explored the expression of IL-1β, IL-6, MMP-2 and MMP-9 in different groups. As the stretching frequency increased, the expression of IL-6 (an inflammatory marker) increased significantly (**Figure 3E**). Furthermore, the expression of the extracellular matrix (ECM)-related proteins MMP-2 and MMP-9 showed a remarkable increase with a higher frequency of cyclic stretching (**Figure 3E**).

Efficient Differentiation of hPSCs Into HASMCs

To differentiate different hPSCs, a 2D differentiation system was developed to generate mesoderm and LM-HASMCs (**Supplementary Figure S2A**). First, hPSCs were plated as single cells at a density of 3,7000 cells per square centimetre. Then, cells were differentiated into mesoderm under CHIR and BMP4 treatment. Finally, after PDGF-BB and Activin A induction, mesoderm cells gradually turned into hPSC-HASMCs (**Supplementary Figure S2B**). During differentiation, mesoderm specification was characterised by dramatic upregulation of the mesodermal marker NK2.5 at day 3, and vascular smooth muscle formation was identified by the upregulation of VSMCs-associated genes, such as SM22, ACAT2 and CNN1 (**Supplementary Figure S2C**). Immunostaining of hPSC-HASMCs on day 5 showed high levels of calponin, Nestin and SM22 expression (**Supplementary Figure S2D**). Furthermore, flow cytometry analyses revealed that approximately 99% of cells were positive for a-SMA, which is a marker of vascular smooth muscle (**Supplementary Figure S3E**). Thus, we were able to generate hPSC-HASMCs from hPSCs with high purity.

Metformin Switched hPSC-HASMCs to a Contractile Phenotype via NOTCH 1

The main objective of this study was to detect whether metformin prescription could retard the progression of aortic aneurysm and discover the associated mechanism. We seeded the obtained hPSC-HASMCs into the assembled microdevice and connected it to a microfluidic system. Three groups (static group, stretch group and stretch + Met group) were established to evaluate the protective effect of metformin on hPSC-HASMCs. The static group was treated with nothing. The stretch group was treated with cyclic stretching. The stretch + Met group

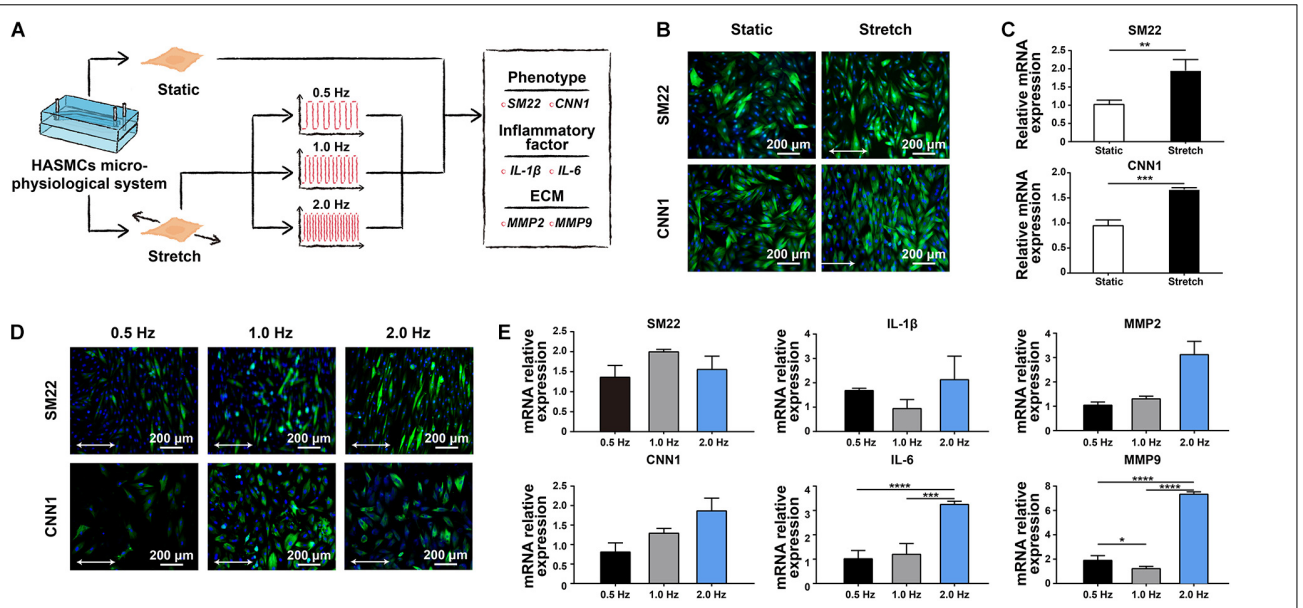

FIGURE 3 | The effect of cyclic stretching on the biology of HASMCs. **(A)** Schematic workflow showing the detection of the effect of cyclic stretching on HASMCs. **(B)** Immunofluorescence staining of SM22 and CNN1 in both the static and stretching culture groups. **(C)** The mRNA expression of SM22 and CNN1 analysed by RT-qPCR. **(D)** Immunofluorescence staining of SM22 and CNN1 in groups treated with different stretching frequencies. **(E)** The mRNA expression of SM22, CNN1, IL-1b, IL-6, MMP-2 and MMP-9 analysed by RT-qPCR. $^{*}P < 0.05$, $^{**}P < 0.01$, $^{***}P < 0.001$ and $^{****}P < 0.0001$.

was treated with cyclic stretching and additional metformin. The stretching frequency was set at 1 Hz, and the period of stretching was 24 h. The results of immunofluorescence staining (**Figure 4A**) and subsequent western blots (**Figure 4B**) showed that the number of SM22- and CNN1-positive cells increased accordingly with stretching and metformin treatment. This result indicated that cyclic stretching and additional metformin treatment could switch more hPSC-HASMCs to a contractile phenotype. To detect the underlying mechanism, we performed a NOTCH 1 knockdown assay in hPSC-HASMCs (NOTCH 1-KD-hPSC-HASMCs). The same treatments were performed in NOTCH 1-KD-hPSC-HASMCs, as mentioned above. The results of immunofluorescence staining showed that the additional metformin treatment could not induce the phenotypic switch of the hPSC-HASMCs with the knockdown of NOTCH 1 (**Figure 4A**). Furthermore, the western blot analysis also presented no relevant level-up of the contractile proteins SM22 and CNN1 in NOTCH 1-KD-hPSC-HASMCs with additional metformin treatment (**Figure 4B**). Based on this evidence, we deduced that metformin may protect hPSC-HASMCs by switching them to a contractile phenotype via NOTCH 1 to delay the progression of aortic aneurysm.

DISCUSSION

HASMCs in native aortae usually present with a contractile phenotype that allows the vessel wall to withstand cyclic strain from blood pressure (Owens et al., 2004). It has been reported that HASMCs would switch to a synthetic phenotype under pathological conditions. The phenotypic switch from contractile to synthetic will subsequently initiate aneurysms in the aorta under pathological conditions (Petsophonsakul et al., 2019). The results of our study showed that stretching treatment could switch more HASMCs into a contractile phenotype, which is closer to native conditions than those achieved in traditional 2D cell culture. Moreover, the stretching frequency also affects the biological behaviour of HASMCs. Under physiological condition, the normal heart rate varied from 60-100 beats per minute. Our research suggested that different stretching frequencies (with the same stretching amplitude) have no significant influence in phenotype switching of HASMCs. While the expression of IL-6 and MMP-9 increased significantly with 2 Hz stretching frequency (that is 120 beats per minute). It indicated that excessive stretching frequency could increase the expression of inflammation which might do harm to the cell biology of HASMCs. Similarly, it has been reported that arrhythmia, such as atrial fibrillation, was accompanied with a higher risk of aortic aneurism (Ramchand et al., 2021). The underlying mechanism maybe the increased inflammation of VSMCs.

Several population screening studies have revealed that diabetes is associated with a reduced incidence of aortic aneurysms and reduced growth of aortic aneurysms. However, some studies have suggested that the reduction in the prevalence and growth of aortic aneurysms in diabetes might result from the treatment rather than the presence of the disease (Golledge, 2019). To the best of our knowledge, among the drug therapies for diabetes, metformin prescription seems to be the most promising candidate associated with limiting the progression of aortic aneurysm. Due to the lack of RCTs with a high level of evidence, there is still a debate on whether metformin prescription could limit the progression of aortic aneurysm. Thus, many studies

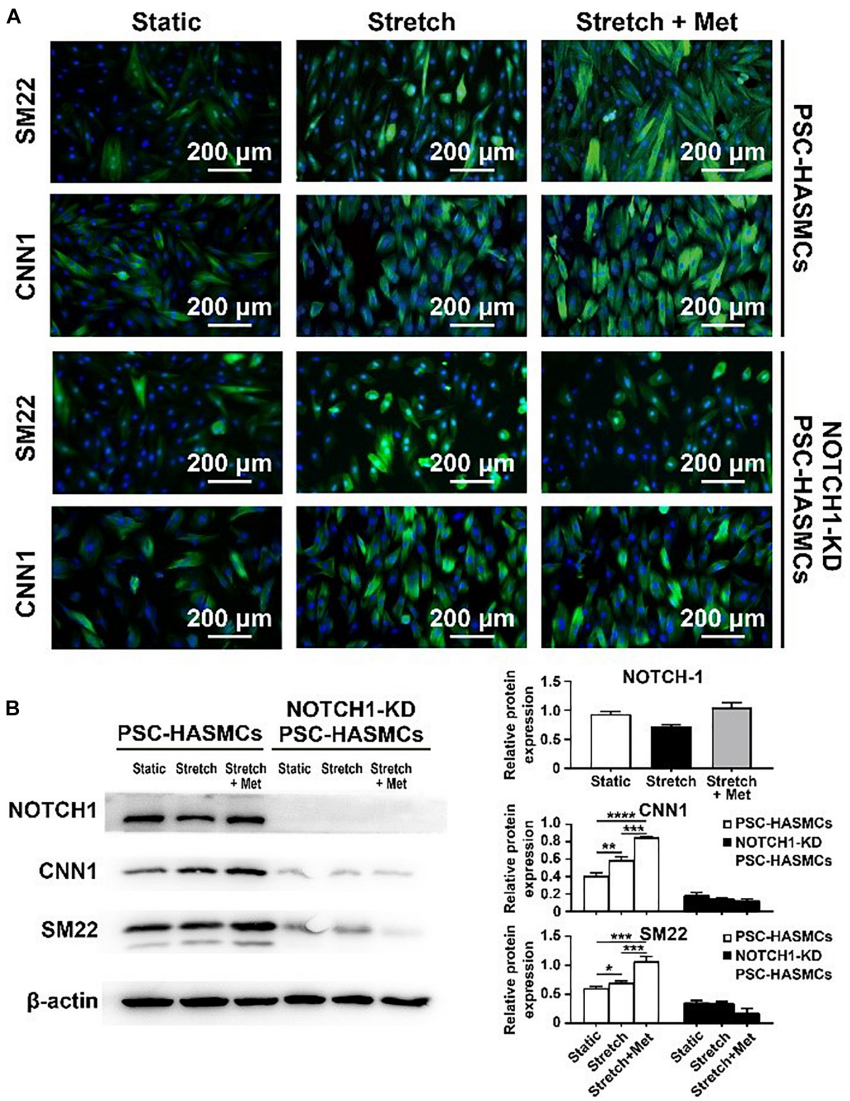

FIGURE 4 | Drug functional testing of metformin in the hPSC-HASMC microphysiological system. **(A)** Immunofluorescence staining of SM22 and CNN1 in hPSC-HASMCs or NOTCH 1-KD hPSC-HASMCs under static, stretching or stretching with metformin treatment. **(B)** The western blot results and statistical analyses of western blots of NOTCH 1, SM22 and CNN1 in different groups. $^{*}P < 0.05$, $^{**}P < 0.01$, $^{***}P < 0.001$ and $^{****}P < 0.0001$.

focusing on drug functional testing of metformin prescriptions are being explored to address this issue. In our study, we decided to perform functional drug testing of metformin with some emerging biotechnologies. Recently, the utilisation of hPSC-HASMCs extracted from patients with Hutchinson-Gilford progeria syndrome (HGPS) was reported to construct a HASMCs based microphysiological system (Ribas et al., 2017). The HGPS microphysiological system was used to explore the influence on vascular pathophysiology induced by gene mutations in HGPS and to detect the effect of cyclic stretching on HASMCs in HGPS. Disease model-based microfluidic chips combined with hPSCs have unique advantages. They can bridge the gap of species differences between mice and humans and overcome the shortcomings of traditional 2D cell culture. On the basis of this evidence, we established an hPCS-HASMC microphysiological system to detect the effects of metformin on the biology of hPSC-HASMCs.

CNN1 and SM22 we used in this study are biomarkers of contractile function in VSMCs and are related to the pathophysiological of blood vessels. In pathological conditions, including hereditary cardiovascular diseases, hypertension, atherosclerosis and other acquired vascular diseases, the expression of contractile proteins (CNN1, SM22, α-SMA, etc.) will decrease, while the expression of synthetic proteins (OPN, MMP-2, MMP-9, etc.) will increase due to genetic defects, abnormal biomechanical environment or inflammation. As a result, VSMCs will subsequently switch to a synthetic phenotype. Thus, the phenotype switch has been used to evaluate the function and pathophysiological of VSMCs according to many studies (Rensen et al., 2007;

Anwar et al., 2012; Granata et al., 2017). In our study, we performed immunofluorescence and western blot to detect the expression of CNN1 and SM22 to directly show the contractile function of VSMCs. Moreover, we detected the expression of MMP-2 and MMP-9, which are commonly used as biomarkers of synthetic phenotype of VSMCs, to show the synthetic function of VSMCs as contrary. The results of metformin testing showed that more hPSC-HASMCs switched to a contractile phenotype with additional metformin treatment than with stretching alone. It indicated that metformin prescription might delay the progress of aneurysms by switching more VSMCs to a contractile phenotype.

NOTCH 1 is a transmembrane receptor protein that participates in cell signalling and the control of cell fate. Loss of the NOTCH 1 gene will induce abnormal differentiation of VSMCs, leading to relevant aortic diseases (Alexander and Owens, 2012; van Varik et al., 2012; Koenig et al., 2017). Previous studies have reported a strong pathophysiological association between NOTCH 1 and the biomechanical forces in cells, especially in blood vessels (Tzemos et al., 2008; Harrison et al., 2019). VSMCs are subjected to continuous mechanical force derived from blood flow *in vivo*. Cyclic stretching and shear stress can be induced by endothelial cells and the ECM to VSMCs. It has been established that NOTCH 1 acts as a biomechanical sensor located in the cell membrane. The presence of NOTCH 1 is necessary for initiating biological responses of VSMCs to haemodynamic forces in arteries (Mack et al., 2017). Meanwhile, it has been reported that NOTCH 1 signalling plays a vital role in the regulation of VSMC differentiation and the expression of contractile proteins. Noseda et al. (2006) found that NOTCH 1 activation is needed for expression of the contractile phenotype protein α-SMA in VSMCs via the NOTCH/CSL axis. High et al. (2007) reported that the loss of NOTCH 1 leads to immature differentiation of the induced pluripotent stem cells into SMCs and the decreased expression of α-SMA, SM22 and CNN1. Moreover, several reports found that metformin can affect the proliferation and differentiation of cells through NOTCH signalling. For instance, Chen et al. found that metformin can alter macrophages toward different phenotypes and inhibit the proliferation and migration of HepG2 cells through Notch signalling (Chen et al., 2015). Rana et al. (2020) reported that metformin can activate AMP-Kinase function via Notch signalling to improve angiogenesis in neonatal pulmonary hypertension. On the basis of these evidence, we hypothesised that metformin prescription might delay the progress of aneurysms through upregulating contractile phenotype in VSMCs via NOTCH 1 signalling. In order to verify this hypothesis, we blocked the NOTCH 1 signalling using lentivirus shRNA targeting NOTCH 1 in hPSC-HASMCs to conform whether the effect of metformin would be inhibited. Our results showed that metformin treatment can up-regulate the expression of contractile phenotype in hPSC-HASMCs. While the up-regulation disappeared with the knockdown of NOTCH 1 in hPSC-HASMCs. Thus, we suggested that metformin might delay the progress of aneurysms through enhancing the phenotype switch in VSMCs via NOTCH 1 signalling.

There are still some limitations in our study. Additional detection is needed to investigate a more specific underlying mechanism between metformin treatment and NOTCH 1 signalling. In addition, the phenotypic switch of VSMCs and the relationship between metformin and NOTCH 1 have been observed in our *in vitro* models, and animal models for performing metformin testing are still needed to confirm the therapeutic effects in parallel. Recently, several studies have reported that the response to metformin varies by age in not only mammals but also invertebrates. Elderly individuals are more likely to suffer from aortic aneurysms compared to youths. Detection of the response to metformin in patients with aortic aneurysms at different ages may also make sense in the future.

CONCLUSION

We established a hPSC-HASMCs based microphysiological system to perform drug functional testing of metformin in this study. We found that a contractile phenotype of HASMCs was induced by cyclic stretching in our system, which was closer to the native biology of HASMCs than those from traditional 2D cell culture. Moreover, more phenotypic switching into contractile was found in hPSC-HASMCs treated with additional metformin than in hPSC-HASMCs treated with stretching treatment alone. The response of hPSC-HASMCs to metformin was subsequently verified to be related to NOTCH 1 signalling. Thus, as the evidence in our study showed, we inferred that metformin prescription may be able to limit the progress of aortic aneurysm via NOTCH 1 signalling. More importantly, our study provides strong evidence for the development of preclinical biotechnologies, especially for drug screening and pathophysiological research.

DATA AVAILABILITY STATEMENT

The original contributions presented in the study are included in the article/**Supplementary Material**, further inquiries can be directed to the corresponding author/s.

AUTHOR CONTRIBUTIONS

NC, MA and SF were involved in the completion of the experiments, data analysis and the manuscript preparation. SZ performed the cell culture experiments. WM helped with the data processing. HL and JL helped with the revision of the manuscript. CW and KZ designed the study and contributed to the data analysis and writing of the manuscript. All authors contributed to the article and approved the submitted version.

FUNDING

The authors would like to acknowledge the grants from the National Natural Science Foundation of China (81771971), Science and Technology Commission of Shanghai Municipality (20ZR1411700 and 18ZR1407000) and Shanghai Sailing Program (20YF1406900).

SUPPLEMENTARY MATERIAL

The Supplementary Material for this article can be found online at: https://www.frontiersin.org/articles/10.3389/fbioe.2021.627877/full#supplementary-material

Supplementary Figure 1 | Characterisation of stretching parameters of the microphysiological system.

Supplementary Figure 2 | The mRNA expression of SM22 and CNN1 in different concentrations of metformin.

Supplementary Figure 3 | The differentiation and characterisation of hPSC-HASMCs.

Supplementary Figure 4 | The fluorescence intensity of the images of SM22 and CNN1 in **Figure 3**.

Supplementary Table 1 | Primers used for RT-qPCR.

Supplementary Table 2 | Primary antibodies used for western blotting and immunohistochemistry.

Supplementary Video 1 | The stretching movement of the microphysiological system.

REFERENCES

Alexander, M. R., and Owens, G. K. (2012). Epigenetic control of smooth muscle cell differentiation and phenotypic switching in vascular development and disease. *Annu. Rev. Physiol.* 74, 13–40. doi: 10.1146/annurev-physiol-012110-142315

Anwar, M. A., Shalhoub, J., Lim, C. S., Gohel, M. S., and Davies, A. H. (2012). The effect of pressure-induced mechanical stretch on vascular wall differential gene expression. *J. Vasc. Res.* 49, 463–478. doi: 10.1159/000339151

Beebe, D. J., Mensing, G. A., and Walker, G. M. (2002). Physics and applications of microfluidics in biology. *Annu. Rev. Biomed. Eng.* 4, 261–286. doi: 10.1146/annurev.bioeng.4.112601.125916

Bein, A., Shin, W., Jalili-Firoozinezhad, S., Park, M. H., Sontheimer-Phelps, A., Tovaglieri, A., et al. (2018). Microfluidic organ-on-a-chip models of human intestine. *Cell. Mol. Gastroenterol. Hepatol.* 5, 659–668. doi: 10.1016/j.jcmgh.2017.12.010

Chen, M., Zhang, J., Hu, F., Liu, S., and Zhou, Z. (2015). Metformin affects the features of a human hepatocellular cell line (HepG2) by regulating macrophage polarization in a co-culture microenviroment. *Diabetes Metab. Res. Rev.* 31, 781–789. doi: 10.1002/dmrr.2761

Fang, Y., and Eglen, R. M. (2017). Three-dimensional cell cultures in drug discovery and development. *Slas Discov. Adv. Sci. Drug Discov.* 22, 456–472. doi: 10.1177/1087057117696795

Fujimura, N., Xiong, J., Kettler, E. B., Xuan, H., Glover, K. J., Mell, M. W., et al. (2016). Metformin treatment status and abdominal aortic aneurysm disease progression. *J. Vascular Surg.* 64, 46.e8–54.e8. doi: 10.1016/j.jvs.2016.02.020

Goldfinger, J. Z., Halperin, J. L., Marin, M. L., Stewart, A. S., Eagle, K. A., and Fuster, V. (2014). Thoracic aortic aneurysm and dissection. *J. Am. Coll. Cardiol.* 64, 1725–1739. doi: 10.1016/j.jacc.2014.08.025

Golledge, J. (2019). Abdominal aortic aneurysm: update on pathogenesis and medical treatments. *Nat. Rev. Cardiol.* 16, 225–242. doi: 10.1038/s41569-018-0114-9

Golledge, J., Moxon, J., Pinchbeck, J., Anderson, G., Rowbotham, S., Jenkins, J., et al. (2017). Association between metformin prescription and growth rates of abdominal aortic aneurysms. *Br. J. Surg.* 104, 1486–1493. doi: 10.1002/bjs.10587

Granata, A., Serrano, F., Bernard, W. G., McNamara, M., Low, L., Sastry, P., et al. (2017). An iPSC-derived vascular model of Marfan syndrome identifies key mediators of smooth muscle cell death. *Nat. Genet.* 49, 97–109. doi: 10.1038/ng.3723

Harrison, O. J., Visan, A. C., Moorjani, N., Modi, A., Salhiyyah, K., Torrens, C., et al. (2019). Defective NOTCH signaling drives increased vascular smooth muscle cell apoptosis and contractile differentiation in bicuspid aortic valve aortopathy: a review of the evidence and future directions. *Trends Cardiovasc. Med.* 29, 61–68. doi: 10.1016/j.tcm.2018.06.008

High, F. A., Zhang, M., Proweller, A., Tu, L., Parmacek, M. S., Pear, W. S., et al. (2007). An essential role for Notch in neural crest during cardiovascular development and smooth muscle differentiation. *J. Clin. Invest.* 117, 353–363. doi: 10.1172/JCI30070

Hinchliffe, R. J. (2017). Metformin and abdominal aortic aneurysm. *Eur. J. Vasc. Endovasc. Surg.* 54, 679–680. doi: 10.1016/j.ejvs.2017.08.016

Horvath, P., Aulner, N., Bickle, M., Davies, A. M., Nery, E. D., Ebner, D., et al. (2016). Screening out irrelevant cell-based models of disease. *Nat. Rev. Drug Discov.* 15, 751–769. doi: 10.1038/nrd.2016.175

Huh, D., Matthews, B. D., Mammoto, A., Montoya-Zavala, M., Hsin, H. Y., and Ingber, D. E. (2010). Reconstituting organ-level lung functions on a chip. *Science* 328, 1662–1668. doi: 10.1126/science.1188302

Jastrzebska, E., Tomecka, E., and Jesion, I. (2016). Heart-on-a-chip based on stem cell biology. *Biosens Bioelectron* 75, 67–81. doi: 10.1016/j.bios.2015.08.012

Koenig, S. N., LaHaye, S., Feller, J. D., Rowland, P., Hor, K. N., Trask, A. J., et al. (2017). Notch1 haploinsufficiency causes ascending aortic aneurysms in mice. *JCI Insight* 2:e91353. doi: 10.1172/jci.insight.91353

Kristensen, K. L., Pottegard, A., Hallas, J., Rasmussen, L. M., and Lindholt, J. S. (2017). Metformin treatment does not affect the risk of ruptured abdominal aortic aneurysms. *J. Vasc. Surg.* 66, 768e.2–774e.2. doi: 10.1016/j.jvs.2017.01.070

Mack, J. J., Mosqueiro, T. S., Archer, B. J., Jones, W. M., Sunshine, H., Faas, G. C., et al. (2017). NOTCH1 is a mechanosensor in adult arteries. *Nat. Commun.* 8:1620. doi: 10.1038/s41467-017-01741-8

Musah, S., Mammoto, A., Ferrante, T. C., Jeanty, S. S. F., Hirano-Kobayashi, M., Mammoto, T., et al. (2017). Mature induced-pluripotent-stem-cell-derived human podocytes reconstitute kidney glomerular-capillary-wall function on a chip. *Nat. Biomed. Eng.* 1:0069. doi: 10.1038/s41551-017-0069

Noseda, M., Fu, Y., Niessen, K., Wong, F., Chang, L., McLean, G., et al. (2006). Smooth muscle α-Actin is a direct target of Notch/CSL. *Circ. Res.* 98, 1468–1470. doi: 10.1161/01.Res.0000229683.81357.26

Owens, G. K., Kumar, M. S., and Wamhoff, B. R. (2004). Molecular regulation of vascular smooth muscle cell differentiation in development and disease. *Physiol. Rev.* 84, 767–801.

Petsophonsakul, P., Furmanik, M., Forsythe, R., Dweck, M., Schurink, G. W., Natour, E., et al. (2019). Role of vascular smooth muscle cell phenotypic switching and calcification in aortic aneurysm formation. *Arterioscler Thromb Vasc. Biol.* 39, 1351–1368. doi: 10.1161/atvbaha.119.312787

Plouffe, B. D., Kniazeva, T., Mayer, J. E., Murthy, S. K., and Sales, V. L. (2009). Development of microfluidics as endothelial progenitor cell capture technology for cardiovascular tissue engineering and diagnostic medicine. *FASEB J.* 23, 3309–3314. doi: 10.1096/fj.09-130260

Ramchand, J., Bansal, A., Saeedan, M. B., Wang, T. K. M., Agarwal, R., Kanj, M., et al. (2021). Incidental thoracic aortic dilation on chest computed tomography in patients with atrial fibrillation. *Am. J. Cardiol.* 140, 78–82. doi: 10.1016/j.amjcard.2020.10.059

Rana, U., Callan, E., Entringer, B., Michalkiewicz, T., Joshi, A., Parchur, A. K., et al. (2020). AMP-kinase dysfunction alters notch ligands to impair angiogenesis in neonatal pulmonary hypertension. *Am. J. Respir. Cell Mol. Biol.* 62, 719–731. doi: 10.1165/rcmb.2019-0275OC

Rensen, S. S., Doevendans, P. A., and van Eys, G. J. (2007). Regulation and characteristics of vascular smooth muscle cell phenotypic diversity. *Neth. Heart. J.* 15, 100–108. doi: 10.1007/BF03085963

Ribas, J., Zhang, Y. S., Pitrez, P. R., Leijten, J., Miscuglio, M., Rouwkema, J., et al. (2017). Biomechanical strain exacerbates inflammation on a Progeria-on-a-Chip model. *Small* 13:1603737. doi: 10.1002/smll.201603737

Sackmann, E. K., Fulton, A. L., and Beebe, D. J. (2014). The present and future role of microfluidics in biomedical research. *Nature* 507, 181–189. doi: 10.1038/nature13118

Sampson, U. K., Norman, P. E., Fowkes, F. G., Aboyans, V., Yanna, S., Harrell, F. E. Jr., et al. (2014). Global and regional burden of aortic dissection and aneurysms: mortality trends in 21 world regions, 1990 to 2010. *Glob. Heart* 9, 171e10–180.e10. doi: 10.1016/j.gheart.2013.12.010

Stefanadis, C., Stratos, C., Vlachopoulos, C., Marakas, S., Boudoulas, H., Kallikazaros, I., et al. (1995). Pressure-diameter relation of the human aorta. A new method of determination by the application of a special ultrasonic dimension catheter. *Circulation* 92, 2210–2219. doi: 10.1161/01.cir.92.8.2210

Sweeting, M. J., Thompson, S. G., Brown, L. C., and Powell, J. T. (2012). Meta-analysis of individual patient data to examine factors affecting growth and rupture of small abdominal aortic aneurysms. *Br. J. Surg.* 99, 655–665. doi: 10.1002/bjs.8707

Tzemos, N., Therrien, J., Yip, J., Thanassoulis, G., Tremblay, S., Jamorski, M. T., et al. (2008). Outcomes in adults with bicuspid aortic valves. *JAMA* 300, 1317–1325. doi: 10.1001/jama.300.11.1317

van Varik, B. J., Rennenberg, R. J., Reutelingsperger, C. P., Kroon, A. A., de Leeuw, P. W., and Schurgers, L. J. (2012). Mechanisms of arterial remodeling: lessons from genetic diseases. *Front. Genet.* 3:290. doi: 10.3389/fgene.2012.00290

Williams, B. (1998). Mechanical influences on vascular smooth muscle cell function. *J. Hypertens.* 16(Pt 2), 1921–1929. doi: 10.1097/00004872-199816121-00011

Xiao, S., Coppeta, J. R., Rogers, H. B., Isenberg, B. C., Zhu, J., Olalekan, S. A., et al. (2017). A microfluidic culture model of the human reproductive tract and 28-day menstrual cycle. *Nat. Commun.* 8:14584. doi: 10.1038/ncomms14584

Yoon No, D., Lee, K. H., Lee, J., and Lee, S. H. (2015). 3D liver models on a microplatform: well-defined culture, engineering of liver tissue and liver-on-a-chip. *Lab. Chip* 15, 3822–3837. doi: 10.1039/c5lc00611b

Yu, X., Jiang, D., Wang, J., Wang, R., Chen, T., Wang, K., et al. (2019). Metformin prescription and aortic aneurysm: systematic review and meta-analysis. *Heart* 105, 1351–1357. doi: 10.1136/heartjnl-2018-314639

Conflict of Interest: The authors declare that the research was conducted in the absence of any commercial or financial relationships that could be construed as a potential conflict of interest.

frontiers in Molecular Biosciences

REVIEW
published: 26 March 2021
doi: 10.3389/fmolb.2021.627454

Oncoimmunology Meets Organs-on-Chip

Fabrizio Mattei[1], Sara Andreone[1], Arianna Mencattini[2,3], Adele De Ninno[4], Luca Businaro[4], Eugenio Martinelli[2,3] and Giovanna Schiavoni[1]**

[1] Department of Oncology and Molecular Medicine, Istituto Superiore di Sanità, Rome, Italy, [2] Department of Electronic Engineering, University of Rome Tor Vergata, Rome, Italy, [3] Interdisciplinary Center for Advanced Studies on Lab-on-Chip and Organ-on-Chip Applications (ICLOC), University of Rome Tor Vergata, Rome, Italy, [4] Institute for Photonics and Nanotechnologies, Italian National Research Council, Rome, Italy

OPEN ACCESS

Edited by:
Shi-Cong Tao,
Shanghai Jiao Tong University, China

Reviewed by:
Julio Aleman,
University of Pittsburgh, United States
Wenfu Zheng,
National Center for Nanoscience and Technology (CAS), China
Alessandro Polini,
Institute of Nanotechnology, Italian National Research Council, Italy

***Correspondence:**
Fabrizio Mattei
fabrizio.mattei@iss.it
Giovanna Schiavoni
giovanna.schiavoni@iss.it

Specialty section:
This article was submitted to Nanobiotechnology, a section of the journal Frontiers in Molecular Biosciences

Received: *09 November 2020*
Accepted: *04 March 2021*
Published: *26 March 2021*

Citation:
Mattei F, Andreone S, Mencattini A, De Ninno A, Businaro L, Martinelli E and Schiavoni G (2021) Oncoimmunology Meets Organs-on-Chip. Front. Mol. Biosci. 8:627454. doi: 10.3389/fmolb.2021.627454

Oncoimmunology represents a biomedical research discipline coined to study the roles of immune system in cancer progression with the aim of discovering novel strategies to arm it against the malignancy. Infiltration of immune cells within the tumor microenvironment is an early event that results in the establishment of a dynamic cross-talk. Here, immune cells sense antigenic cues to mount a specific anti-tumor response while cancer cells emanate inhibitory signals to dampen it. Animals models have led to giant steps in this research context, and several tools to investigate the effect of immune infiltration in the tumor microenvironment are currently available. However, the use of animals represents a challenge due to ethical issues and long duration of experiments. Organs-on-chip are innovative tools not only to study how cells derived from different organs interact with each other, but also to investigate on the crosstalk between immune cells and different types of cancer cells. In this review, we describe the state-of-the-art of microfluidics and the impact of OOC in the field of oncoimmunology underlining the importance of this system in the advancements on the complexity of tumor microenvironment.

Keywords: cancer immunology, microfluidic device, Cell on Chip, Organ on Chip, tumor microenvironment, personalized medicine, Oncoimmuno chip, human on chip

INTRODUCTION

Microfluidic platforms represent an emergent and promising technology for life science research aiming to reproduce specific biological environments that recapitulate the *in vivo* scenario with higher fidelity with respect to conventional *in vitro* techniques (Jiménez-Díaz et al., 2019; Wang L. et al., 2019). They are generically composed of a device coupled to pump circuits or wells for liquid circuits and a microscope to make real time acquisitions during the experiment. These systems represent useful tools for multiple purposes, spacing in all the areas of life sciences, and imply the involvement of multidisciplinary sciences. Indeed, while biologists and physicians pose the scientific problem, physicists conceive the devices and, finally, statisticians or mathematicians extrapolate results by processing the large array of data obtained by microfluidic-based studies.

An emerging field of application of microfluidic chips comprise the study of complex cell microenvironments, such as the tumor microenvironment (TME) and how immune cells and tumor cells interact within it. The TME is a complex environment composed by multiple cell types, including blood vessels, immune cells, stromal cells, fibroblasts, and by soluble factors, which closely and constantly interact with tumor cells, thereby determining the fate of tumor progression (Schiavoni et al., 2013; Anderson and Simon, 2020). The advancements of molecular and cellular profiling technologies has gained key information on how distinct immune cell populations interact with the tumor and the other TME components (Liu et al., 2019; Davidov et al., 2020). However, these methodologies do not allow to investigate complex interactions, processes and mechanisms behind the full TME functioning. The detailed knowledge of the tissue microenvironment and the associated dynamics led to the development of Tissue-On-Chip (TOC) platforms. These systems aim at recapitulating the specific functions of tissues on microfluidic devices, i.e., blood, bone marrow, lung, liver, just to cite some examples. However, they are often defined as Organs-On-Chip (OOC) to indicate the organ they aim to recapitulate (Li et al., 2019b). The OOC definition is optimal for the majority of advanced multicellular living systems and can be extended to particularly heterogeneous organs such as tumors. The use of TOC definition is particularly recommended to mimic cell-cell interactions on-chip in several tissues with undefined compartmentalization or boundaries, such as blood, bone-marrow and specific hematopoietic niches (Aleman et al., 2019). TOCs can also be employed for the generation of microfluidic systems supplemented by spheroids (Duarte Campos et al., 2020). Spheroids are indeed entities similar to organs but not completely resembling them. This concept can also be extended to tumor spheroids when the cells forming the spheroid are of malignant nature.

Over time, the definition OOC has been mostly preferred to TOC since OOC comprise all tissue types. The advent of OOC has boosted the research on cell-cell interactions in basilar and advanced cell systems. This platform proved to be fundamental for the study of cell-cell interaction and migratory behaviors upon specific perturbations (Kim and Haynes, 2013; Menon et al., 2014). Moreover, OOC can be considered as a "simplified organ" potentially useful to bypass diverse problems intrinsic for *in vitro* and *in vivo* experiments. In addition, OOCs better recapitulate multicellular systems (e.g., an organ) and are ideal tools to study dynamically complex organs, including the TME. In other words, the use of OOCs aim to achieve an appropriate degree of simplification by reconstituting an *in vivo* system to an *in vivo*-like model of study. In these settings, it is possible to follow the system's components without altering their original function. Thus, OOC systems can be classified as advanced *in vitro* smart platforms evolved from *in vitro* and *in vivo* scientific knowledge (Boussommier-Calleja et al., 2016).

In this review, we describe the state-of-the-art of microfluidic devices and explain how and why the advent of microfluidic platforms markedly impacted the study of multicellular systems with emphasis on their employment for oncoimmunology studies.

FROM PIONEERS OF MICROFLUIDICS TO ADVANCED OOC SYSTEMS

The term microfluidics defines all the systems, simple or advanced, where a fabrication process that generates micrometers-sized scale channels is the key component of that system. More than 50 years ago, researchers perceived that microfluidic systems can dramatically impact the study of chemical compounds and cells. Of note, the advances in materials technology has certainly facilitated the expansion of microfluidic systems. These pioneer research studies evidence how the distinction between the terms Lab-on-a-Chip (LC) and Cell-on-a-Chip (CC) is generally represented by the nature of the elements investigated within the device. In general, LC covers all studies in which microdevices are used alongside with chemicals or proteins or other substances such as lipids. CC systems are employed for live cell investigations and OOC platforms are usually employed to follow simple or complex multicellular environments. All the three terms, LC CC and OOC, can sometimes overlap, due to lack of standardization of these three definitions. This adds further grade of complexity to the problem of searching univocal definitions for the microfluidic chip-based systems. A history of the birth of the first microfluidic systems and how they became advanced platforms such as OOC is delineated, with emphasis on the use of OOC in an oncoimmunology context.

First Approaches to Microfluidics Systems: LC

The first literature data on microfluidic approaches is a paper by Lew and Fung (1969). They were the first to outline the concept of simulation theory in the attempt to mimic the fluidic dynamics of the blood flow circulation and bronchioles air flow simulations within lung tissue. They asserted that the flow generated by the uniform axial velocity is relevant for blood flow in branching blood vessels and for the motion of plasma in the capillary blood vessels. This theoretic microtube system, with a diameter equal or less to 100 μm, is generated by complex algorithms governing the fluid dynamics. These Authors were the first to introduce the notion of inlet/outlet in the liquid flow simulations for live systems such as blood circulation and lung bronchioles. This fluidic model has been repurposed by an independent laboratory 20 years later (Xue and Fung, 1989). The importance of this first simulation study lies on the notion that the main role of microfluidic devices is to recapitulate the multicellular living systems in their multifaceted aspects, including biochemical cues behind the cell-cell communication. This key milestone could not be reached without the LC systems. LCs proved decisive for a better knowledge of cell-cell signaling, mimicking specific inner events including those relative to immune cells.

The first use of a LC for investigative purposes on living (eukaryotic) cells was made by Esch et al. (2001a,b) for the detection of *Cryptosporidium Parvum*, a waterborne pathogen. They used a method relying on the ability of these bacteria to release some typical and exclusive DNA sequences that are

PCR-amplified within *ad hoc* fabricated microfluidic chips. These studies demonstrated that microdevices can be used to investigate the effects of chemicals and proteins released from bacteria and cells. For these reasons, the majority of scientists coined the term LC to evidence how these devices can be conceived as actual miniaturized laboratories. Such mini-labs are focused at investigating specific substances such as chemicals or proteins, but are not suitable for living cells.

In 2012, Farmer and co-Workers generated a LC microfluidic system to recapitulate a red blood cell. They were the first to mimic a cell model, even though not a living cell, with microfluidic approaches (Farmer et al., 1988). This first study in a microfluidic cartridge has certain been facilitated by the non-living nature of the system. This work can be considered as one of the first attempts to obtain a primitive cell-mimicking system. The first microfluidic system to immobilize particular types of proteins came on the 1990s, with a study from Johnsson et al. (1991). This research describes how microfluidic systems can be applied in the field of sensors engineering. On the other hand, it represents one of the first studies reporting a complete microfluidic chip fabrication process as an important part of device design.

A relevant giant step on the creation of LCs as sensors useful for cancer prevention comes from an elegant paper of Bahavarnia and co-Workers. Here a paper-based immunosensor has been generated, coupled to a fluidic chamber to propagate the fluid toward the sensor area in which the CA125 protein will be detected by an ELISA-based assay (Bahavarnia et al., 2019). Similar approaches based on the immunosensors have been described in literature, useful to study apoptotic activity (Dang et al., 2019) or soluble immune checkpoint inhibitors (Reza et al., 2019) in biological fluids or clinical samples. These studies represent interesting examples of LCs to be applied for oncoimmunology applications.

Lab-on-Chip are generally appropriate to study specific mechanical activities or fluidic phenomena, often to be addressed to specific living cell mimicry events. With the development of more advanced microfluidic fabrication techniques and with the advent of sophisticated biotechnology tools, LC platforms have evolved into complex systems to investigate on some features of single cells. For instance, an LC platform was developed with the aim to identify the disparate antigen specific antibodies secreted by single B-lymphocytes during the development of innate immune responses (Gérard et al., 2020). Fabrication technologies have also allowed implementation of LC into efficient and affordable biosensors. LC biosensors have been recently developed and optimized to be applied in oncoimmunology. A clear example is represented by LC biosensors to detect cancer biomarkers, where the main LC biomaterial is represented by paper and nano-inks (Bahavarnia et al., 2019). Despite the discovery of disparate materials well suited for biological studies, the use of Polydimethylsiloxane (PDMS)-based techniques still remains the elected methodology to fabricate all microfluidic devices, including LC biosensors. Next generation chips will be represented by microfluidic platforms where the use of the PDMS may be supplemented, rather than superseded, by the use of other biomaterials needed for chip optimization.

Beyond the LC Platforms: The CC Systems

While *in vitro* Two dimensional (2D) and Three dimensional (3D) culture systems are useful to study specific cell features, the advent of LC equipped investigators with versatile tools to monitor cell behaviors in real time. This began the initiation of the CC era.

In 1997 Li and co-Workers carried out a glass microfluidic CC system suitable to monitor the mobilization of red blood cells, yeast cells as well as *Escherichia Coli* bacteria in a device composed by several interconnected channels. This chip constituted one of the first approaches to study living cells by means of a device composed by multiple substructural units (Li and Harrison, 1997). A first study analyzing cell docking and alignment was produced by Yang and co-Workers on 2002 with human hematological HL-60 tumor cell lines (Yang et al., 2002). Another report where cells were monitored in a CC system employed a feochromocytoma derived PC12 cell line (Huang et al., 2004) in the attempt to follow their mobilization features. The development of CC research with tumor cells has been facilitated by the fact that these cells do not require stringent factors for their growth, compared to primary cells (Zielinski et al., 2017). For this reason, tumor cells can be easily studied on chip, in particular for long-term time points. In 2005, primary cells were successfully studied on a CC system in an interesting work focused at recapitulating the cardiac myocyte contraction (Li and Li, 2005). This and other studies (Ho et al., 2006; Kokkinos et al., 2008; Zhao et al., 2012) constitute some representative examples of the first primitive studies carried out in CC systems. All of them utilized a single cell type with simple analyses and evaluations, such as mobilization within microscale-sized spatial units and brief time intervals.

The first attempt to study a specific immune cell population on chip was reported in 2006 by Matsumura and co-Workers, who investigated the ability of macrophages to start and sustain zymosan-induced phagocytosis in fibronectin-coated CC by time-lapse microscopy. This represented a first study in which a functional immune event has been reproduced on chip (Matsumura et al., 2006). Another interesting CC system has been generated by Kang and co-Workers. Their structure is represented by a chamber where bead-labeled blood cells flow upon a micromagnetic field. This field has a key role in capturing rare circulating tumor cells or metastatic cells (Kang et al., 2012). The particularity of this microfluidic chip is the possibility to culture a single cell type by flushing away the other undesired cells, such as circulating leukocytes.

An important phenomenon to be investigated in the field of oncoimmunology is the migratory behavior of immune cells toward the primary tumor site. Thus, it is not surprising that researchers pay particular attention on the study of immune cell migration on chip. A first example of such studies was provided by Molino and co-Workers. They described a CC system properly designed to follow leukemic cell migration toward an oil droplet

(Molino et al., 2016). For some aspects, these droplets resemble immune cell moving in the CC microchannel. This work is a clear example of how CC studies inspired experimental implementations to design the more complex OOC systems, in order to study the interaction between immune cells and cancer within *ad hoc* fabricated microfluidic devices.

Putting Different Cell Types on a Chip: The OOC Platforms

The term OOC underlines the attempt to load different cell types residing organs or multicellular complexes inside a microfluidic device, often coupled to sophisticated microscopy systems. In general, such a definition fits also for chips loaded with at minimum two different cell populations, even if these are not able to develop in complex multicellular systems (Sackmann et al., 2014; Reardon, 2015; Chen P. et al., 2020). The simpler the OOC is the easier cells are monitored within it.

A first approach to study immune system on chip has been developed by Whitesides and co-Workers. They created a simple OOC platform to co-culture two different types of macrophage-like cells (Wong et al., 2008). In this report, BAC1.2F5 and LADMAC macrophage cell lines were loaded in separated chambers of the microdevice. Then, the production of the colony stimulating factor-1 (CSF-1), released by LADMAC and required by BAC.2F5 cells for survival, was monitored over time. This simple OOC prototype can also be used to study the mutual crosstalk between immune and cancer cells.

The first attempt to design a microfluidic platform employing different cell types on chip was reported by Shuler and co-Workers on 2009. They adapted a microfluidic chip for simultaneous co-culture of tumor cells (colon cancer cells HCT-116 or Hepatoma cells HepG2, embedded in hydrogels) with liver and bone marrow cells (Sung and Shuler, 2009). This system allowed to elegantly test the cytotoxicity of a specific anticancer agent on tissues when directly delivered on chip. Despite allowing the simultaneous loading of different cells, this OOC system does not allow to study the crosstalk between loaded cells, such as migration of bone-marrow cells toward the tumor in response to the drugs. In a study investigating the crosstalk between immune cells and cancer cells, Businaro and co-Workers successfully attempted to investigate on the mutual behavior of melanoma and immune cells (Businaro et al., 2013). This approach was inspired by the difficulty to study the events behind the immune cell infiltration inside the TME, and represents a new dawn for the oncoimmunology on chip. Previous work *in vivo* showed that accelerated B16.F10 melanoma progression in non-immunocompetent mice was the result of altered cytokine/chemokine production and impaired infiltration of different murine immune cell subsets in the TME (Mattei et al., 2012). Based on these observations, microfluidic devices were employed as a simple OOC system to evaluate gradient-dependent interactions between B16.F10 melanoma cells and spleen-derived immune cells from naïve immunocompetent vs non-immunocompetent mice. In detail, a PDMS microdevice constituted by a 1,000 μm-sized central chamber connected to two side chambers by two arrays of 12 μm-sized microchannels has been used. The two side chambers were loaded with spleen cells (from immunocompetent or IRF-8 deficient mice) and B16.F10 melanoma cells. Time-lapse video recording was carried out over a 48 h-period in a region comprising the B16 side chambers and the adjacent microchannels. The results evidenced a mutual crosstalk between B16 cells and spleen cells. Specifically, in OOC loaded with splenocytes from immunocompetent mice, these cells displayed a high migratory ability toward the B16 chamber coupled to a slow B16 invasion extent. Conversely, IRF-8 deficient splenocytes displayed poor migratory extent toward the tumor, which reflected a high invasion ability of melanoma cells. This report constitutes the first evidence of mutual interaction between two different cell types in a microfluidic chip. Further analysis on time-lapse videos demonstrated that the migration of immune cells can be quantitatively and qualitatively evaluated by extrapolating single cell tracking profiles of each cell migrating toward melanoma cells (Agliari et al., 2014). From an oncoimmunology view, these tracking profiles represent relevant functional data expressing the overall behavior of immunocompetent *vs* non-immunocompetent cells faced to melanoma cells into this OOC system.

On the other hand, time-lapse microscopy is useful to evaluate the tumor cell membrane elasticity as a function of cell viability during their permanence in the OOC system. Fully functional tumor cells show high variations in the membrane fluctuation over each image frame (**Figure 1**). On the contrary, the membrane fluctuations are less evident in dying or stressed tumor cells. This perturbation factor has been quantified by Agliari and co-Workers by targeting time-lapse on single tumor cells inside the OOC. It can be used as a function of the stress status of a cancer cell after migration in the chip and reflects the ability of immune cells to limit cancer cell growth on chip as a consequence of tumor-immune cell interactions (Agliari et al., 2014). This "migrate-to-interact" concept can be adapted for every OOC platform designed to study how cancer cells respond to the presence of immune cells (**Figure 1**).

Further advancements in OOC development in oncoimmunology have been made by using human hepatitis B virus (HBV)-derived cancer cells and T cells that can be loaded and monitored on chip. Here, a customizable OOC was used to load engineered T cells expressing HBV-specific antibodies in liquid media with tumor cells derived from the same cancer patient. Tumor cells were loaded in a central chamber resuspended in a collagen matrix, thus recapitulating the TME on chip. In this setting, it was possible to follow and quantitate the tumor cell killing activity of T cells with accuracy (Pavesi et al., 2017). Moreover, this study allowed a better knowledge of the suitability of extracellular matrices for OOC systems, such as Matrigel, hydrogels or collagen complexes to better recapitulate the TME. Indeed, extracellular matrices represent a mix of extracellular proteins markedly improving the capability of cells to survive inside the microfluidic devices. In this situation, the cells engage chemical bonds with the components of these matrices then activating intracellular survival signals. Thus, the use of these matrices is particularly relevant for the activation and survival of some primary cell types, such as dendritic cells and hepatocytes (Mehta et al.,

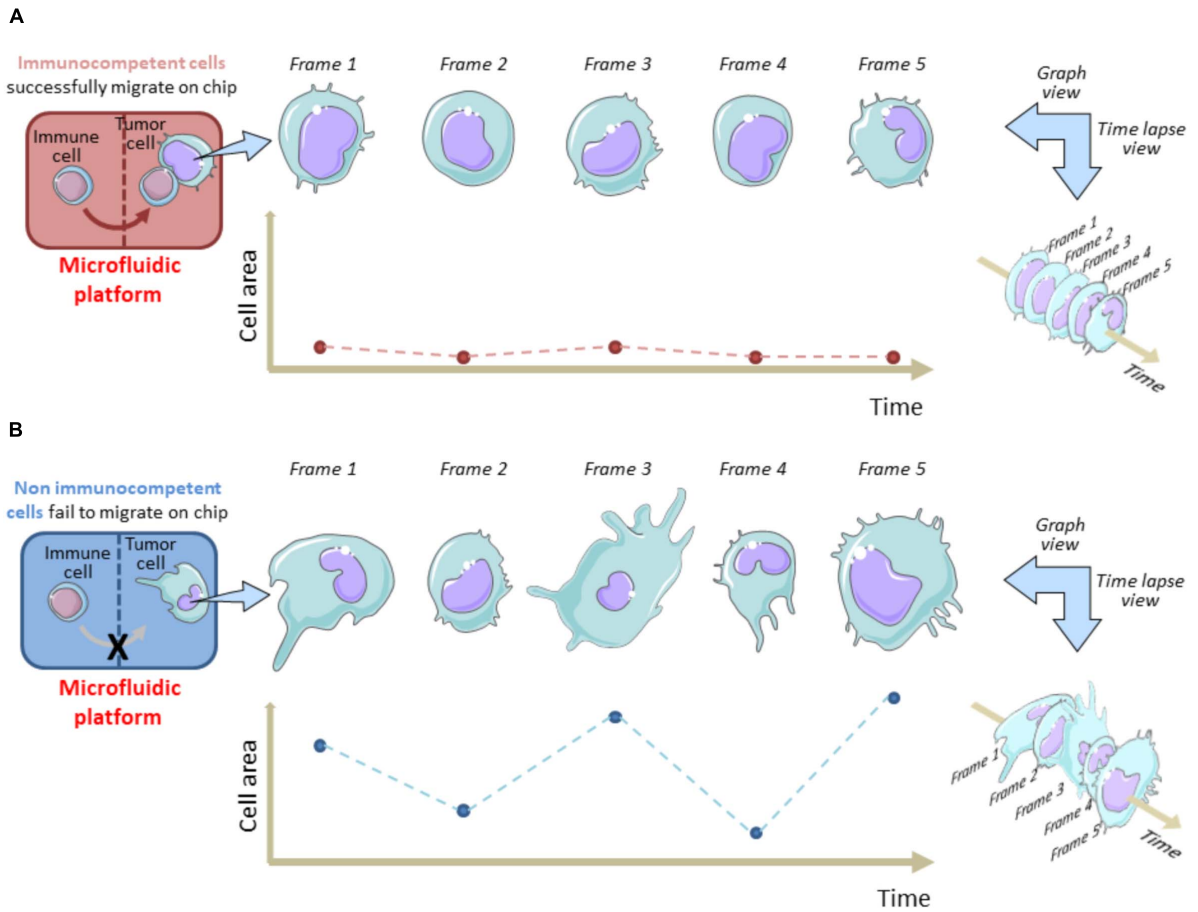

FIGURE 1 | Tracking cell perturbation changes on chip during melanoma cell-immune cell interactions and after immune cell migration. A single cell area variation analysis is shown in immunocompetent **(A)** versus non-immunocompetent cells **(B)**. The area of a cancer cell is analyzed at fixed time intervals (e.g., 1 min) from an acquired time-lapse video, after the immune cell enters the cancer cell compartment and interacts **(A)** or fails to interact **(B)** with the malignant cell. Migrated immune cells do interact for longer time with cancer cells and this reflects in a minor frame-by-frame variation of the cell area. Hypothetically, this status is indicative of a dying/apoptotic cancer cell. This model underlines the migrate-to-interact strategy of an immune cell. The vertical brown/blue dotted lines within rectangles symbolically represent the complexity of the chip architecture and delimit the immune cell compartment from cancer cell compartment. The brown/blue dotted lines and points within graphs depict the area values for each frame referred to each time interval.

2010; Mölzer et al., 2019; Serna-Márquez et al., 2020). On the other hand, it is becoming increasingly evident that the use of gel matrices represents an important step to an optimal development of OOC platforms in oncoimmunology, as evidenced by the key role of the disparate types of matrices employed to reproduce the TME (Narkhede et al., 2017; Hassell et al., 2018; Sontheimer-Phelps et al., 2019).

In a recent study, Fang and co-Workers reported the realization of an OOC system with human tumor spheroids or murine organoids (Fang et al., 2019). They loaded the device with fibroblasts and MCF7 or 4T1.2 breast tumor cells to allow the on-chip generation of tumor organoids, with the fibroblasts spontaneously infiltrating the tumor mass. In this case they used the agarose as main biomaterial of the OOC. In addition, a microfluidic prototype has been developed by Borenstein and co-Workers to study the immune checkpoint inhibitors in human cancer (Beckwith et al., 2019). Specifically, this OOC system allows the trapping of a lung tumor biopsy and a real-time monitoring of the programmed cell death protein-1 (PD-1) expression. The originality of this study is represented by the development of an OOC platform optimized to monitor PD-1 on fresh biopsies in 24 h.

All these studies facilitated the *ad hoc* development of OOC systems and led to a new generation of more complex OOCs. Another representative example in using diverse cell populations in OOC research is the development of multi-organ units on chip, outlined by a recent work depicting a platform aimed at generating and connecting liver and gut on chip (Sung, 2020). The **Supplementary Table 1** illustrates the technical and analytic details of several OOC systems and their potential use for oncoimmunology studies. This list suggests that OOC can be designed by lithographic techniques and 3D bioprinting methods, with or without gel matrices. As expected, the structural

composition of the microdevices largely changes in function of their specific functional and analytic requirements.

ANALYTIC TOOLS TO STUDY THE INTERACTIONS BETWEEN IMMUNE CELLS AND CANCER CELLS IN MICROFLUIDIC PLATFORMS

Organs-On-Chip allow to study TME *in vitro* avoiding the use of expensive animal models in complex *in vivo* experiments. When planning an OOC experimental design, animal models should be used uniquely for initial validation of the specific OOC setting. Besides, OOC platforms are very useful for the extrapolation of hidden entities directly or indirectly associated to the migratory ability of immune cells and their capacity to reach and interact with cancer cells. These parameters are strictly dependent on the behavior of the two cell types within the OOC and, seemingly, in the TME. In this section we describe these hidden entities and their quantitation cues.

OncoImmuno Chip: A Specific OOC System to Study Interactions Between Cancer Cells and Immune System

An *OncoImmuno chip* defines a microdevice in which the TME's main components are isolated, reconstituted on-chip and coupled to time-lapse and image analysis systems to monitor immune and tumor cells overtime, for a maximum of 72 h (Biselli et al., 2017; Mencattini et al., 2020a; Torres-Simón et al., 2020; **Figure 2**).

There are several important advantages to track immune cell migratory behavior toward cancer cells. For example, in an experiment where immune and drug pre-treated cancer cells are loaded into two separate compartments, it will be possible to acquire, frame-by-frame (FBF), a set of single cell tracks throughout the entire duration of the time-lapse (**Figure 3**). This FBF acquisition of immune cells yields an array of cell tracks, namely the *immune cell tracking profile*, whose behavior is strictly dependent on the anti-tumor effects of an administered drug (**Figure 3**). When each immune cell reaches the compartment containing drug-treated cancer cells, it interacts with them for a variable time. The computation of the duration of such an interaction is then fundamental for the quantification of therapeutic efficacy. Such a post-migration interaction represents a functional parameter indicative of the ability of the immune cell to "sense" cancer cells inside the device upon drug exposure (**Figure 3**).

There are some typical classes of trajectories relative to immune cell motion that are highly indicative of the response to attractant or repellent substances emanated from tumor cells (Biselli et al., 2017; Comes et al., 2020b). These distinct track patterns have functional effect on cancer cell fate (**Figure 4**) and can be represented by several kinematic and non-kinematic factors. The first, *directionality ratio* (Gorelik and Gautreau, 2014), expresses the ability of an immune cell to reach its target cancer cell by taking the shortest route possible.

The *mean step length* of a track is another kinematic entity intrinsically associated to the track of an immune cell (**Figure 4**). It expresses the mean walking displacement of the immune cells between two consecutive points of the time-lapse (**Figures 3**, **4**). Assuming that a single step length, *s,* is yielded by the formula A delineated in **Figure 5** (Caplan, 1972; Simmons et al., 2010). Here, Δx and Δy represent the projections of the cell step length s on the X and Y axes in a Cartesian XY domain (**Figure 5**). By denoting as (x_1, y_1) and (x_2, y_2) the starting and the ending points of a generic displacement, i.e., $\triangle x = x_2 - x_1$ and $\triangle y = y_2 - y_1$, then the single step length of an immune cell can be also obtained by the formula B in **Figure 5**. The mean step length is calculated as the average s value among all the steps of the immune cell along its track and directly depends on the speed of that cell (Perner and Perner, 2009; Dewan et al., 2011; Biselli et al., 2017).

Immune cell speed returns the step length s from a starting (x_1, y_1) point to an ending point (x_2, y_2) divided by the time required to move from the two points (**Figures 4**, **5**).

The track angle represents another important quantity of the immune cell migration path strictly associated to the directionality of the track. It is expressed by the angle α (in degrees) the current step vector s forms with the X reference axis (**Figure 5**). The *angular deviation* can be yielded by the difference between the two α values of the immune cell at two consecutive points.

Assuming that the step length is an s vector composed by its projection on X and Y axes, as mentioned in **Figure 5**, the angular deviation a constitutes the angle between the s vector and its projection on X axis. Such an angular deviation α of the immune cell can then be expressed with a generalized formula C in **Figure 5**, derived from the Pythagorean theorem, and is also a function of the attractive forces exerted by the adjacent cancer cell. As delineated by the two formula D and E in **Figure 5**, Δy and Δx represent the projections of the step lengths on Y and X axes, respectively. The two catheti Δy, Δx and the hypotenuse s constitute a right-angled triangle (**Figure 5**), where the angular variation α a is easily computable by the inverse tangent formula C in **Figure 5** (Dummer et al., 2016; Lin, 2019; Cankaya et al., 2020; Zhang et al., 2020). Of note, each step length s of the immune cell track is indissolubly linked to its relative α value conventionally referred to the X axis, as evidenced in **Figure 5**.

Not less relevant, one of the most important parameter used to describe the type of motion for an immune cell is the *mean square displacement* (MSD)(Gorelik and Gautreau, 2014). Early studies that attempted to mathematically model cell migration in isotropic medium assumed that a cell moves like a Brownian particle (Dunn, 1983). Namely, an immune cell was assumed to undertake a persistent random walk, in which it moves directionally at short time intervals, but it loses its persistence at longer time intervals. The time to cross from the persistent regime to the random one is the directional persistence time, whose estimation requires a fitting of the MSD curve (Gorelik and Gautreau, 2014). The MSD is a crucial factor since it embeds global as well as local kinematic characteristics of the immune cell track at different time lag, thus evidencing cell behavior at shorter time but also the overall trend at larger time. In

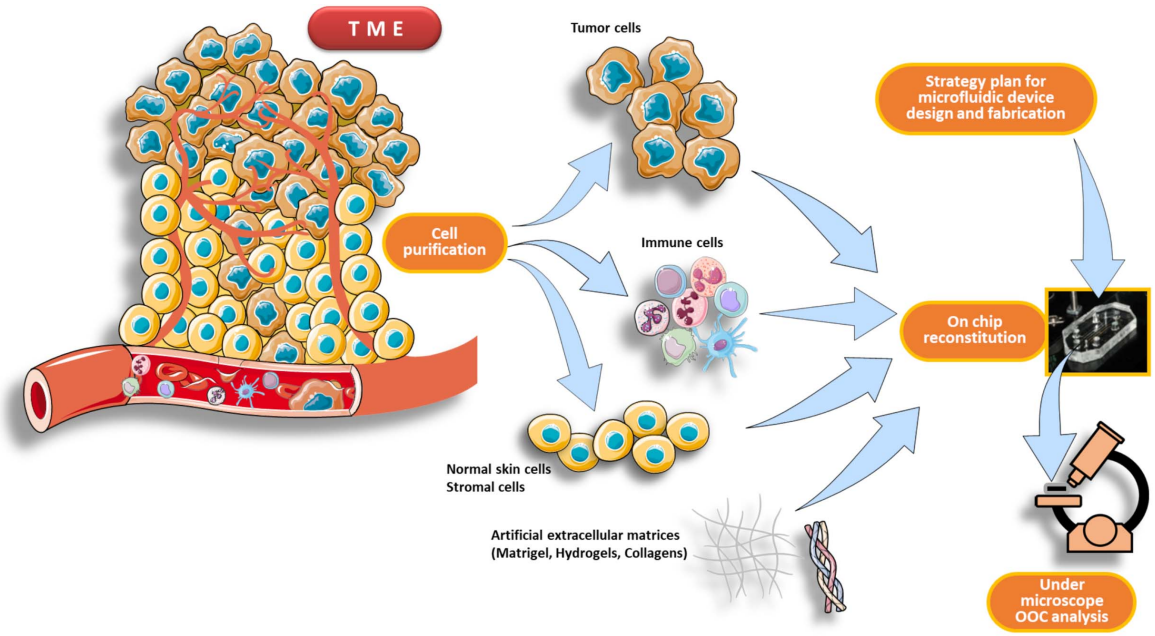

FIGURE 2 | Schematic pipeline for TME reconstitution on an OncoImmuno chip. The first part of the workflow consists in a purification process of the main components of the TME, such as immune cells, tumor cells and normal skin cells plus stromal cells (if needed). When the design strategy of the microfluidic device is completed, the cells are then reconstituted inside the chip loading units. This reconstituted chip, resembling to an OOC, is then analyzed by a microscope platform. The TME can be derived from patients' primary tumor or from an *in vivo* experimental tumor.

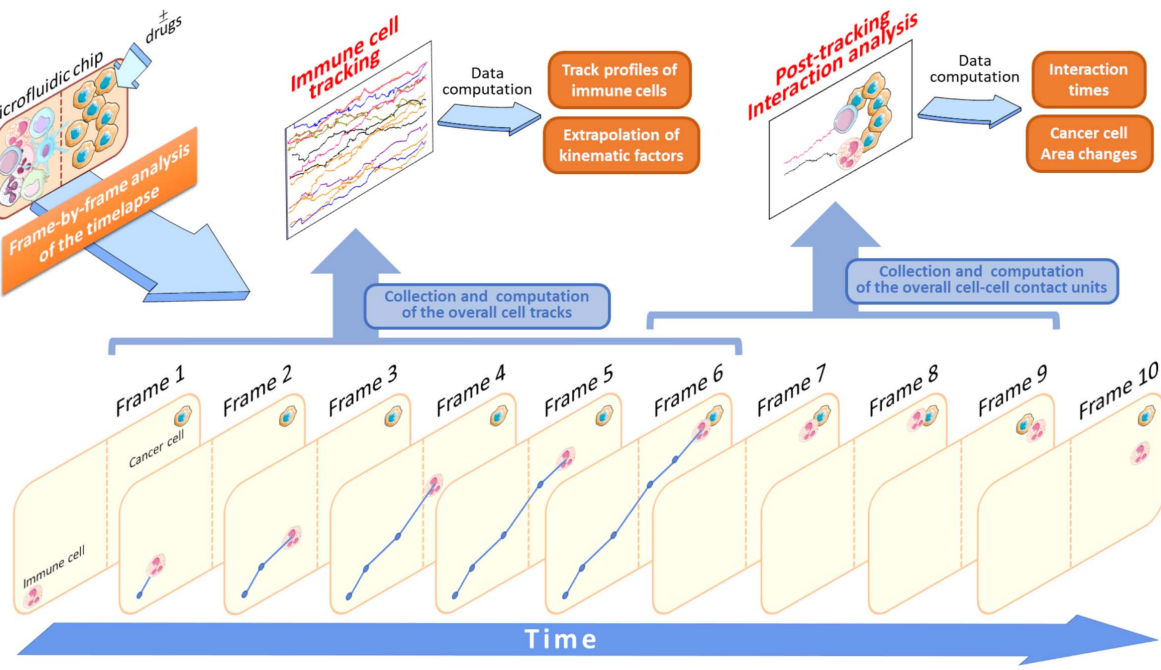

FIGURE 3 | Application of the FBF tracking analysis to study immune cells versus cancer cells crosstalk. In this schematic model, the starting time-lapse recorded during the experiment execution is processed and all the variables associated to tracking analysis are extrapolated (Data computation). Specifically, when an immune cell is identified it will be tracked in each frame (Frame 1–6) to yield its associated trajectory (blue lines and points). This is done for each cell identified in the initial frame (Frame 1) of the video sequence. At the end of its walking, if the immune cell interacts with an adjacent cancer cell the duration of this interaction is computed and stored as a single interaction time value. In this example, this value is provided by the interval time difference between Frame 6 and Frame 9. The brown-dotted lines inside the microfluidic chip symbolize the compartment structures and ideally delimit the two immune and cancer cell compartments.

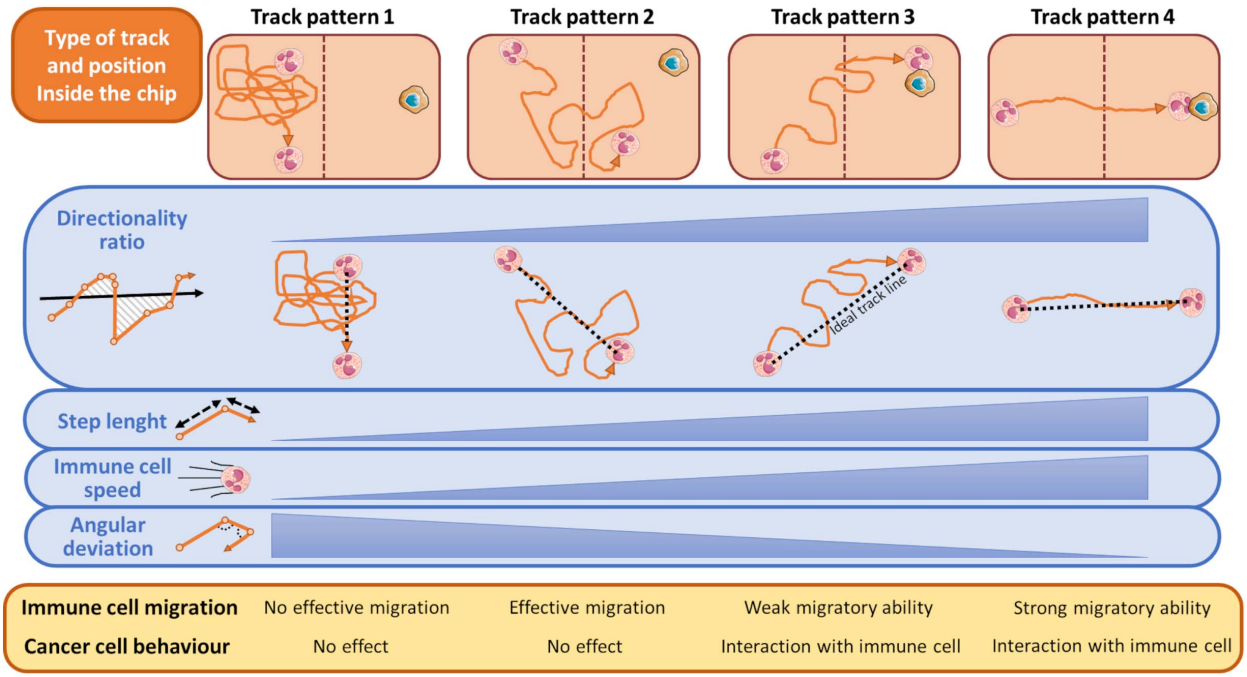

FIGURE 4 | Schematic representation of most typical tracks of immune cells in relation to the presence of cancer cells during a time-lapse from an OOC experiment. During its walking toward the cancer cell, an immune cell can assume one of the indicated pattern motions. When the cancer cell exerts no influence on immune cells these can assume a track described by Pattern 1, namely a casual motion with no specific direction. This scenario is indicated by a very low directionality ratio compared to an ideal linear track (black dashed line), short mean step lengths, low speed, and high angular deviation of the immune cells. Conversely, if an immune cell moves forward by adopting the Track Pattern 4, it does successfully reach the opposite chip compartment and interacts with the neighboring cancer cell. This track is featured by an high directionality ratio (high linearity), step length and immune cells speed, and low angular deviation. In Track Pattern 2, immune cells pass through the opposite compartment but are unable to interact with the cancer cell. In Track Pattern 3 the scenario is similar to that described by Pattern 4, except for a low directionality ratio and then a weak migratory ability toward the cancer cell. Track Pattern 3 usually ends with a successful interaction between cancer and immune cell. The brown-dotted lines inside the microfluidic chip symbolize the compartment structures and ideally delimit the two immune and cancer cell compartments.

an oncoimmunology context, the MSD is strictly dependent on how cancer cell drug treatment can affect the immune cell trajectory on chip.

In conclusion, cell tracking analysis returns several hidden kinematic and non-kinematic values, that are an intrinsic feature of the FBF analysis in a time-lapse video. This can be easily extrapolated in an OncoImmuno chip, by analyzing the time-lapse video and single image frames with a specific image analysis software. In this regard, the open source software ImageJ is equipped with a number of plug-ins (i.e., Manual Tracking or Automated Tracking plug-ins) that allow to automatically process all the aforementioned entities, then facilitating the extrapolation of all kinematic factors associated to each single tracked immune cell. The use of ImageJ with the integrated Automated Tracking plug-in is a clear example of image-assisted analysis of cell migration tracking. A list of the most commonly used cell migration tracking software are depicted in **Supplementary Table 2** (Emami et al., 2021).

Overall, the use of tracking analysis in OncoImmuno chips can recapitulate the interactions between cancer and immune cells in TME in the steady-state or following a defined therapy by exploiting hidden data acquired exclusively through these platforms and not accessible by *in vivo* TME methodologies.

Generative Adversarial Networks to Evaluate the Interactions Between Immune Cells and Cancer Cells on Chip

The massive advent of sophisticated biotechnologies has been accompanied by a parallel evolution of instruments in which these technologies were computationally implemented. These analytical methods are recently exploiting the beginning of the Artificial Intelligence framework that is revolutionizing the field of biomedicine with its diverse applicative approaches (Ramesh et al., 2004; Buch et al., 2018; Balkanyi and Cornet, 2019; Holzinger et al., 2019; Mintz and Brodie, 2019; Kaul et al., 2020). In the area of machine learning (Rajkomar et al., 2019; Sidey-Gibbons and Sidey-Gibbons, 2019; Alsuliman et al., 2020), a novel kind of algorithm-based methodologies have recently gained a profound interest. These advanced methods belong to a sub-branch of machine learning, the deep-learning (Cao et al., 2018; Wainberg et al., 2018; Bock et al., 2021), and, in particular, often refer to the so called Generative Adversarial Networks (GAN). GANs can have disparate practices, covering social sciences, image analysis and biological problem solving. To this purpose, GANs have been applied for prediction of human actions (Liu et al., 2017), image processing applications

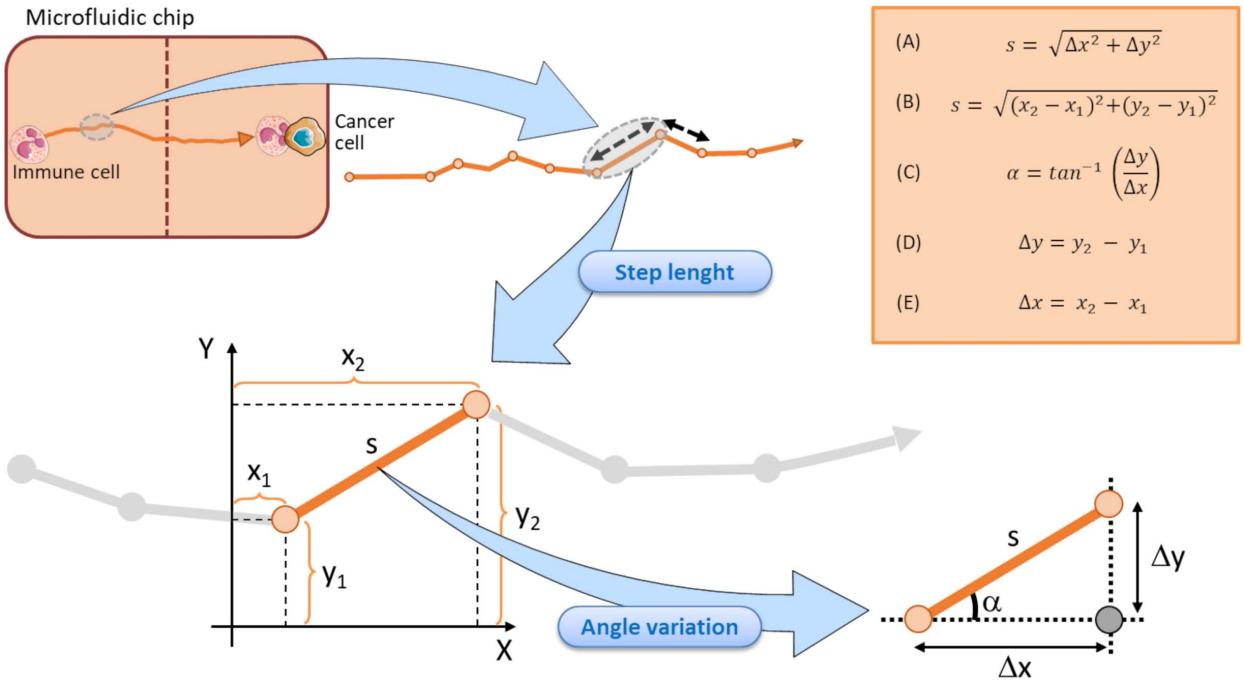

FIGURE 5 | Schematic representation of the step length components in a tracking immune cell moving toward a cancer cell within a microfluidic chip. Each step length is calculated by returning the doublet of coordinates in starting (x_1, y_1) and finish (x_2, y_2) points. A single step length is depicted by the vector *s*, that can in turn be decomposed in the Δy and Δx units (representing the projection of the *s* vector to *Y* and *X* axes, respectively). Each step is associated to its relative angle deviation α conventionally referred to the *X* axis. Vertical dotted brown line symbolizes the structural components of the microfluidic device and ideally delimits the two immune and cancer compartments. Top right orange box displays the key formula associated to the step length and angle variation computations.

(Nie et al., 2018; Li et al., 2019c; Xue et al., 2020; Yang et al., 2020), and computational analysis of natural environments (Saleemi et al., 2009; Negin and Brémond, 2019; Comes et al., 2020a,b). GAN are based on a game scenario where the generator network must compete with an adversary, the discriminator network. The two network models are trained together until the discriminator network is fooled about half the time from the image created by the generative network, meaning that it is generating plausible examples (Sahoo and Narayanan, 2019; Xu et al., 2020).

The gradually increased use of time-lapse microscopy together with the use of microfluidic platforms provided oncoimmunologists with potent tools to perform long-term live cell imaging and high-throughput analysis of on chip platforms (Comes et al., 2019, 2020a; Mencattini et al., 2020b). In this context, GANs constitute potent machine learning tools to predict how a cell migratory path will evolve starting from the real cell tracking captured by a time-lapse video. Specifically, an updated version of the GAN, social GAN (Comes et al., 2020b), can be useful to predict the post-migratory behavior of an immune cell when it is in proximity of a cancer cell in a microfluidic device (**Figure 6**). To this purpose, all the single immune cells are identified and tracked starting from the original time-lapse video sequence. To do so, GAN algorithm need to be "trained" by inputting a number of initial immune cell positions, namely the Input Tracks in **Figure 6**. After the training procedure, GAN is able to return high-fidelity immune cell trajectories by extrapolating them from GAN-dependent hidden entities (Fernando et al., 2019; Comes et al., 2020b). This approach is particularly useful to predict the behavior of poorly identifiable immune cells, or simply to accelerate the uptake of the experiment and to avoid phototoxic effects on the cells (**Figure 6**). GAN can provide a meaningful estimation of the probability for each immune cell to physically interact with the cancer cell in the vicinity (**Figure 6**).

In conclusion, a GAN learning system can be helpful for the envision of the so called *in silico* OOC experiments (Swayden et al., 2019). The main goal of such a system is the evaluation of a real OOC experiment without performing until the end reducing time and experimental costs. Moreover, this process can also generate an *in silico* OOC simulation potentially useful to plan new optimized OOC experiments.

OOC SYSTEMS FOR DRUG INVESTIGATIONS IN ONCOIMMUNOLOGY

One of the most active research fields in oncoimmunology is the dissection of drug properties for cancer therapy. OCC platforms represent a valid alternative in this context. Indeed, in the last years OOC systems have shown potential for discovering indirect or direct drug properties on tumor cells. Simple OOC systems have been developed in which only target cells and drugs are loaded to assess direct effects of the drug (Kwak et al., 2014;

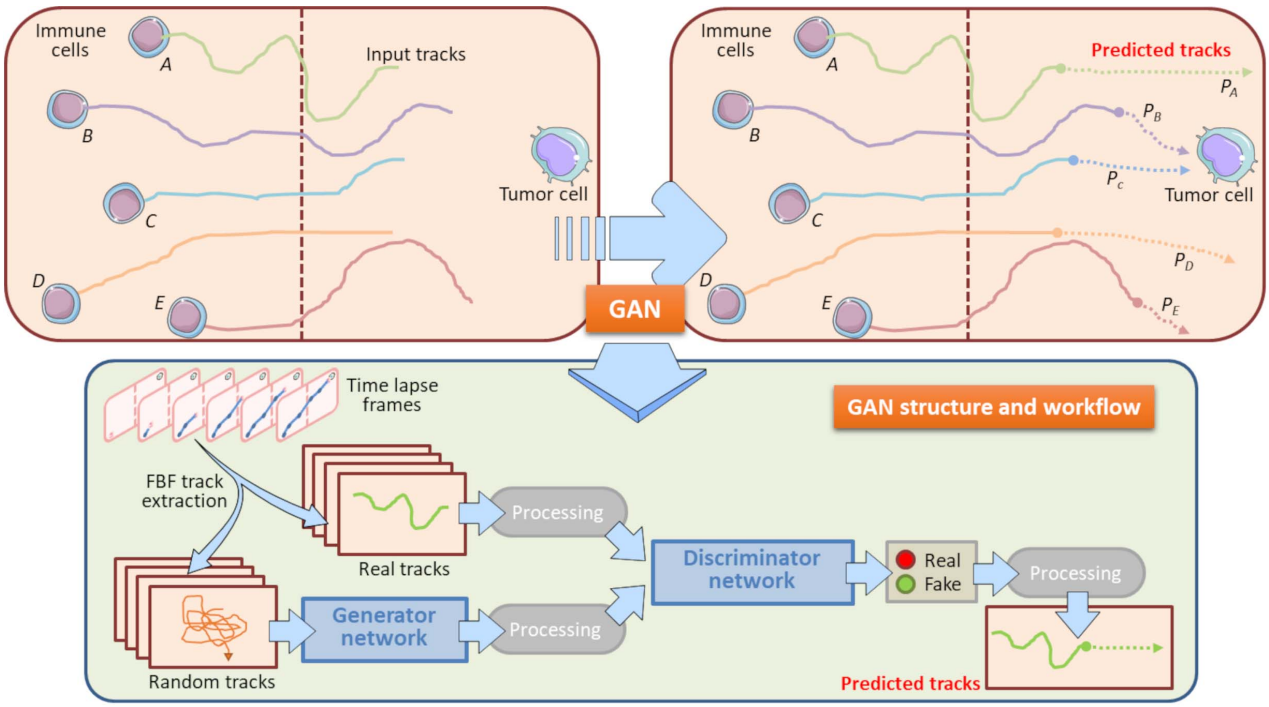

FIGURE 6 | Role of GAN in immune cell trajectory prediction. Machine learning by GAN represents a practical manner to predict the whole track of a migrating immune cell. In this model, GAN predicts the migratory trajectory of immune cells (A, B, C, D, and E) and is helpful to foresee the behavior of immune cells when these encounter a tumor cell during their walking. GAN uses a Generator Network and a Discriminator Network to develop the predicted tracks from Real and Random tracks, extrapolated from each frame of the time-lapse. The Real tracks will then be processed into the Discriminator Network, whereas the Random tracks will constitute the input variables for the Generator Network, where they will be further processed and entered in the Discriminator Network. This Network exploits specific sigmoidal functions (Real, Fake) to distinguish the true predicted trajectories from fictitious tracks. The final result is constituted by all the predicted tracks associated to their input tracks originally entered. In this model, the computation of the predicted tracks P_B and P_C does allow to assert that the immune cells B and C will interact with the neighboring tumor cell with meaningful probability. Conversely, the predicted tracks P_A, P_D, and P_E indicate that Immune cells A, B and E will interact with the same cancer cell with a very low probability. These information are relevant to check potential immune cells to be selected for post-migration Interaction time computations. Brown-dotted vertical lines symbolize the structural components of the chip and ideally delimit the immune and cancer compartments.

Shin et al., 2016). In this section we will review the impact of microfluidic devices in boosting research on oncoimmunology in the context of anti-cancer therapy, providing an innovative tool to evaluate how drugs can affect the interactions between cancer cells and immune system.

OOC Systems for the Evaluation of Anti-Tumor Therapies

One of the first studies aimed to assess the effects of pharmacological treatments for cancer therapy by using an on chip approach is represented by a study addressing the role of formyl peptide receptor 1 (FPR1)/annexin a1 (Anxa1) axis in anti-tumor response to anthracycline-based chemotherapy (Vacchelli et al., 2015). In this report, OOC experiments in humans and mouse settings were crucial to demonstrate the importance of the integrity of the FPR1/Anxa1 axis to allow immune cell migration and interaction with cancer cells undergoing chemotherapy-induced immunogenic cell death. Indeed, cancer cells treated with anthracyclines (i.e., Doxorubicin or Mitoxantrone) release Anxa1, which acts as a danger signal for immune cells. Single cell tracking profiles extrapolated by OOC system displayed that FPR1 expressed by immune cells, particularly dendritic cells (DCs), is required to "sense" Anxa1 emanated from dying tumor cells and to migrate toward them engaging in stable interactions. Interestingly, in the OOC setting only DC with an intact FPR1 successfully migrate toward anthracycline-killed tumor cells and capture apoptotic bodies released from these dying cells. Post-analysis of time-lapse video recordings in this OOC system allowed the extrapolation of high numbers of single cell tracks associated to high interaction times between immune cells (including DCs) and cancer cells, showing that immune cells with intact FPR1 perform biased random walks toward anthracycline-treated cancer cells, while those with mutated FPR1 show uncorrelated random walks (Biselli et al., 2017). Thus, numerical descriptors and statistical physics applied to OOC systems provide an additional tool for a quantitative description of the immune response to cancer during chemotherapy.

Organs-On-Chip systems can undergo further step-by-step implementations in their structural complexity which do not compromise their state-of-simplicity. In this regard, Nguyen and co-Workers have successfully visualized and quantified the effects

of the anticancer drug Trastuzumab in a TME reconstituted on chip, composed by cancer-associated fibroblasts (CAF), an $HER2^{+}$ breast cancer cell line (bearing a HER2-receptor gene amplification), and immune cells (Nguyen et al., 2018). This study demonstrates that an OOC system hold potential for further implementation by adding other TME key cell components, such as cancer associated fibroblasts (CAFs). Addition of CAFs in this system still contributes to maintain a simplified and smart OOC platform. Here, the OOC system has been utilized to dissect the role of Trastuzumab, a reference anti-cancer for HER2+ breast cancer patients, on such a tumor-on-chip complemented with CAFs plus hydrogels to reproduce a central endothelium compartment. The microdevice is constituted by two side chambers, containing the immune cells (embedded in a collagen matrix), cancer cells and CAFs, and a central compartment with endothelial cells. These chips where monitored with or without the presence of Trastuzumab. The extrapolation of interaction times, cancer cell speed and tracking profiles by time-lapse demonstrated that Trastuzumab inhibited breast cancer cell growth with a concomitant induction of cell death. In addition, CAFs hindered the interactions between cancer and immune cells. Overall, these on-chip observations suggests that this tumor-on-chip effectively recapitulates the *in vivo* scenario referred to the effects of Trastuzumab in human breast cancer. A similar concept was applied in a study illustrating the crosstalk between lung cancer cells and epithelial cells in an OOC system mimicking the lung alveoli. Here, H1975 non-small-cell lung cancer (NSCLC) cells were loaded in a microfluidic device to evaluate the effects of Erlotinib and Rociletinib, two representative third generation Tyrosine Kinase inhibitors. The authors designed a chip composed by two side compressible chambers for air flow, mimicking respiratory processes, and a central compartment further subdivided in two separated chambers, containing cancer cells and endothelial cells. This design had the purpose to recapitulate the alveoli of lungs, under normal or cancer settings. These studies not only showed the feasibility of this lung-on-chip system to study the anti-tumoral effects of Tyrosine Kinase inhibitors, but also revealed an unexpected role of breathing in contrasting cancer growth (Hassell et al., 2018).

Organs-On-Chip systems have also been exploited to investigate the role of epithelial-mesenchymal transition (EMT). For instance, an interesting OOC model has been generated to study these phenomena. Here, EMT has been recreated on chip with human lung tumor cell spheroids (NCI-H460 or HCC827 cells) resuspended in Matrigel and human umbilical vein endothelial cells (HUVECs). The microdevice is composed of a nylon mesh matrix which recapitulates the separation system between cancer cells and HUVECs. In this microdevice tumor cells and HUVECs are separated by the mesh membrane. When recombinant TGF-β was added in this OOC system tumor spheroids displayed an activated expression of the EMT factors Snail, and Akt, paralleled by decreased levels of E-cadherin. In addition, tumor cells acquired the ability to migrate toward HUVECs. This OOC system may represent an optimal model to study the effects of anti-cancer drugs in terms of control of processes involved in EMT (Li et al., 2019a). Another representative example of on chip anticancer agent evaluation is the development of a metastasis-on-chip model of study (Wang et al., 2020). This OOC is assembled with methyl methacrylate for structural and spatial components, whereas PDMS is used to allow gas and liquid exchange between cells. The PDMS is used to create sheets to which a 10 μm sized resin membrane is sliced. This PDMS plus resin system is then inserted inside the OOC and used for cell loading. Such device was employed for the evaluation of anti-tumor activity of 5-Fluorouracyl (5-FU) on Caki-1 kidney cancer cells loaded with immortalized HepLL hepatocytes. Of note, this OOC system was integrated with a programmable electronic pump to feed cells with nutrients in the chip. This study can inspire the generation of implemented metastasis-on-chip platforms suitable for other metastatic tumors.

The described OOC platforms represent a starting point for implemented systems specially designed to evaluate the efficacy of emerging immunotherapy strategies in the presence of immune cells. Recently, OOC devices were successfully employed to culture murine- and patient-derived organotypic tumor spheroids preserving the immune compartment of the TME and to evaluate the sensitivity and resistance to PD-1 blockade (Jenkins et al., 2018). This system accurately recapitulated the *in vivo* scenario, was compatible for long-term culture (up to 1 month) and allowed to evaluate multiple parameters of response, such as cell death and growth of tumor organoids from mice or patient-derived organoids loaded inside the microdevice. The microdevice consists in two side chambers utilized to load the conditioned medium (i.e., the anti-PD-1 antibodies) and a central compartment employed to load human tumor spheroids or tumor cells from mouse colon cancer lesions which develop organoids several days after loading (Aref et al., 2018). This platform can be adapted to evaluate other immune checkpoints (i.e., CTLA-4) expressed on cancer cells. OOCs have also revealed as useful systems to study the effect of folic acid in ovarian cancer. Folic acid is the elected anti-tumoral drug to cure this and other solid malignancies. Here, Wimalachandra and co-Workers have proposed an OOC in which the main chamber was rounded by HUVEC cells and filled with OVCAR-3 tumor cells. This microfluidic device has been used to evaluate the migration of DCs and T cells, in presence or absence of folic acid-loaded nanoparticles (Wimalachandra et al., 2019). These encouraging studies suggest not only that nanoparticles are a useful to assess anti-cancer drugs on chip, but can also inspire the use of OOC platforms for the study of tumor cell functions by nanoparticle-encapsulating drugs.

OOC Applications for the Evaluation of Anticancer Drug Combinations

Single agent-based strategies are often insufficient for a successful and complete tumor eradication in cancer patients. Current strategies aim at combining therapies with a second (or even third) drug to amplify anti-tumor responses and/or to broaden the spectrum of responding patients (Bao et al., 2020; Crunkhorn, 2020; GajdÁcs et al., 2020; Iratni and Ayoub, 2020; Jonnalagadda et al., 2020; Karimi et al., 2020; Kawachi et al., 2020; Kim et al., 2020; Mollica et al., 2020; Qian et al., 2020; Song et al.,

2020; Yamashita et al., 2020; Zhu et al., 2020). The development of microfluidic devices for oncoimmunology applications based on the use of drug combinations is only beginning to emerge. One of the major challenges to deal with is the precise architectural optimization of the chip devoted to these purposes. Indeed, the evaluation of multiple factors on a single chip implies an adjunctive difficult level, not only in the chip fabrication, but also in choosing the bio-architectural components of the chip. For instance, if one plans to construct a complex 3D chip this should not compromise the control easiness of the cells within it. In this regard, an example comes from an elegant report where Caco-2 colorectal adenocarcinoma cell lines were co-cultured on an OOC platform with hepatic HepG2 cells acting as an artificial liver producing metabolites. This microfluidic system has been successfully employed to evaluate and quantitate the effects of Irinotecan and Temozolomide, alone or in combination (Jie et al., 2017). Noticeably, a superior ability of the double condition to induce apoptotic cell death of tumor cells has been showed. This encouraging study suggests that a chip-based system, when properly designed and loaded with the right cell subsets can be effectively exploited to follow unexpected drug combination effects. Other similar findings come from a simple CC system optimized for use of two anticancer agents at different drug concentrations. Here, PC3 tumor cells have been loaded with Doxorubicin or Mitoxantrone with TRAIL (Kim et al., 2012; Desyatnik et al., 2019).

A significant step forward is the optimization of OOC for evaluating drug combinations by taking into account the role of immune cells to provide a more complete and faithful scenario. OOC platforms have been developed employing immune cells *in toto* and cancer cells resuspended in Matrigel adapted for the exposure to two different drugs acting alone or in synergy. This OOC design has allowed to demonstrate the superior anticancer activity of the DNA demethylating agent Decitabine (DAC) when administered with Interferon-α (IFN-α) against melanoma in a competitive assay (Lucarini et al., 2017). In detail, this device is composed by a central chamber used to load immune cells (PBMC from healthy donors) and two side channels for loading Matrigel-resuspended human A375 metastatic melanoma cells with or without DAC and IFN-α, alone or in combination. Fluorescence microscopy evaluation and time-lapse experiments have shown that immune cells preferentially migrate toward the A375 cells containing both drugs rather than each single agent (DAC or IFN-α), or no drugs. This approached mirrored *in vivo* studies performed in melanoma-bearing mice, where combined DAC and IFN treatment promoted immune cell infiltration, limiting tumor progression (Lucarini et al., 2017). The same OOC device was employed to evaluate the behavior of specific immune cell subsets, i.e., dendritic cells (DC) toward tumor cells undergoing combined therapy. Here, IFN-α-conditioned DC (IFN-DC) were monitored within 3D tumor spaces for their ability to infiltrate and engulf collagen-embedded SW620 colorectal cancer cells treated with a combination of drugs (Romidepsin and IFN-α) with respect to untreated (Parlato et al., 2017). We hypothesize an OOC scenario in which DAC induces cancer cells to undergo apoptosis, with a concomitant release of apoptosis-dependent chemokines or *via* the activation of pathways strictly related to cell death such as the FPR1/Anxa1 axis (Vacchelli et al., 2015). In parallel, IFN activates immune cells as they infiltrate the matrigel microenvironment. This, in turn, favors immune cells to interact with A375 cells and to complete their tumor cell killing activity, leading to further release of apoptotic factors. On the other hand, in the opposite side chamber containing the single drug or saline, immune cells fail to infiltrate the melanoma microenvironment. Overall, this system can be regarded as an OOC provided with two functional TMEs, each responding to local environmental stimuli represented by direct effects of the drugs and by subsequent infiltration of immune cells (**Figure 7**). Of note, this dual competitive condition chip can is an useful tool to evaluate how these differently shaping TMEs will evolve in function of the immune cells behavior. Indeed, the preferential migration of the immune cells toward one of the two conditions is the peculiar effect noted in this particular device, and is strictly dependent on type of drugs cancer cells are exposed to. To this extent, tumor cells can be elegantly monitored by using this specific dual condition chip to study the cellular dynamics of some drugs endowed with cell death-induction activity, compared to an internal control (**Figure 7**).

MICROFLUIDIC DEVICES FOR STUDYING THE EFFECTS OF RADIATIONS IN IMMUNE CELLS AND CANCER CELLS

Radiation therapy (RT) is employed to cure localized cancers and is known to act both by killing malignant cells and by activating anti-tumor immune responses (Atwell et al., 2019, 2020; Bellia et al., 2019; Fellin et al., 2019; Chen Y. et al., 2020; Gupta and Chatterjee, 2020; Koukourakis and Giatromanolaki, 2020). Despite the wide use of RT to overcome the main problem of cancer resistance, the mechanisms by which radiations activate immune system to kill cancer cells are still under intense debate. Tumor mouse models constitute an invaluable tool to carry out research on how immune system interacts with cancer cells in the TME under RT regimens (Frey et al., 2012; Thiemann et al., 2012; Du et al., 2016; Dobiasch et al., 2017; Keisari, 2017; Bellia et al., 2019; Domankevich et al., 2020; Hader et al., 2020; Qin et al., 2020). The exploitation of animal models in this context has played a relevant role for the determination of radiation doses to be used to adequately activate immune cells, or certain type of immune cells, to efficiently eradicate cancer. These premises clearly evidence that RT represent an important strategy to fight cancer and hence is of key relevance for oncoimmunology research. Considering the evident limitations in animal handling imposed by European community legislation (Bassi et al., 2020; Mocho, 2020; Tian et al., 2020; Vinken, 2020), the generation of innovative tools to investigate how radiations can affect the immune system in fighting cancer represent an urgent need.

Recently, microfluidic systems have been adapted to investigate the anti-cancer effects of RT. An example of this

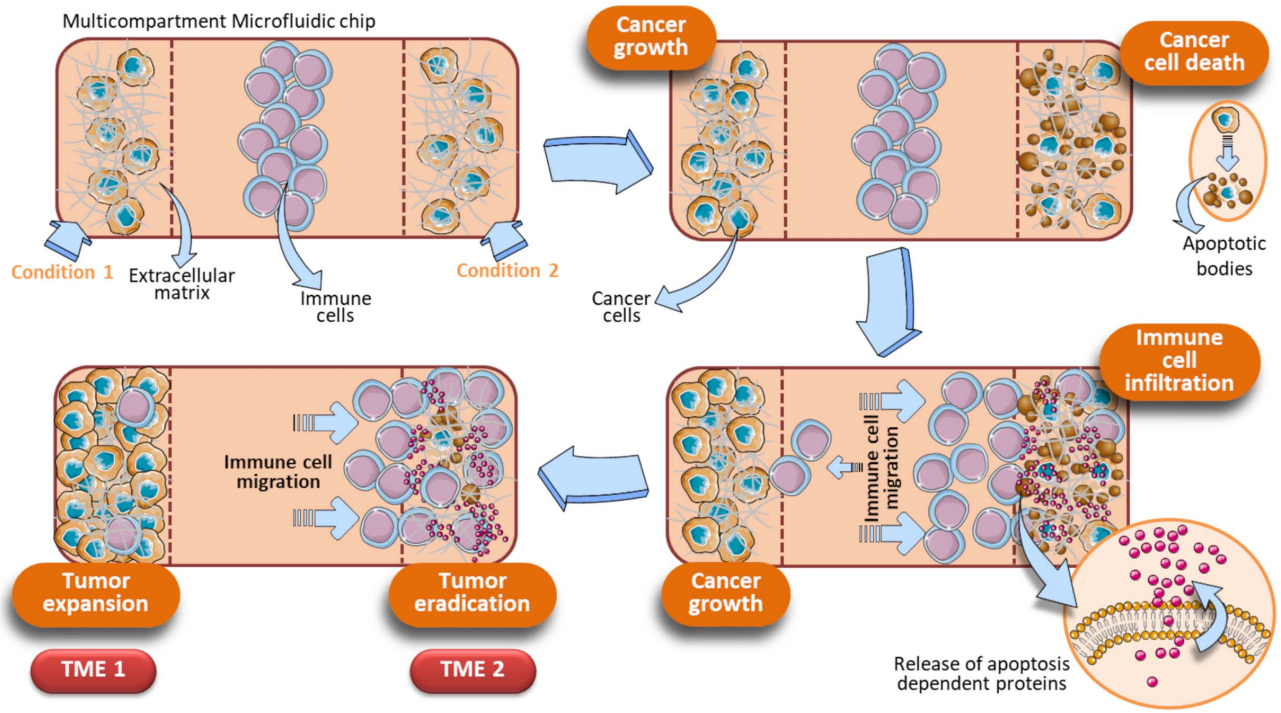

FIGURE 7 | Schematic representation of a dual condition chip to study the dynamics of apoptosis-induced anticancer drugs. Immune cells are loaded in the central chamber of the device. In parallel, cancer cells were loaded in presence of an extracellular matrix (e.g., Hydrogels, Collagen, or Matrigel) and specific drugs to be evaluated (Condition 1, Condition 2). Assuming that the Condition 1 is represented by untreated cancer cells and Condition 2 by tumor cells exposed to a cell death inducer (or a drug combo whose final action is cell death), these different on chip parallel treatment trigger a gradually divergent behavior of the cancer cells, reflecting in the final generation of two different TMEs (TME 1 and TME 2). TME 1 generates when the Condition 1 is a pro-tumoral drug or no treatment. In these cases, cancer cells will proliferate and a growing tumor will develop (TME 1). Concomitantly, an opposite effect due to tumor cells treated with anticancer agents occurs in the opposite microfluidic chamber (TME 2). The TME 2 is shaped by immune cells, that migrate under the effect of apoptotic factors released by cancer cells upon treatment with anticancer drugs. How immune cells shape the TME development is strictly dependent on how cancer cells are treated in the two side compartments. The initial key event of the TME 2 is the generation of apoptotic bodies as a consequence of tumor cell killing operated by immune cells. When cancer cells are exposed to a drug combination (Condition 2), the associated Condition 1 at the opposite side chamber can be a single drug of that combination or no exposure. Vertical dotted brown lines symbolically represent the structural units of the device.

type of approach has been carried out for an on-chip study of RT in head and neck squamous cell carcinoma (HNSCC) (Cheah et al., 2017). A very simple PDMS-based OOC system has been designed to investigate how single dose irradiation (5, 10, 15, and 20 Gy) could affect the growth of HNSCC primary tumor cells derived from patient biopsies. This OOC is composed by a central chamber connected to an inlet and an outlet well. The wells are connected to the chamber by a single microchannel. The chamber has been used to insert a little fragment of patient's biopsy, and the inlet well serves to let media to flow-through in the OOC system. Irradiation of HNSCC tissue in the microfluidic device was carried out inside a custom-made Perspex Block (Butson et al., 1996), adequately applied to the microfluidic device. The irradiation doses of the tumor tissue were chosen as appropriate as to avoid the degradation of the microdevice biomaterials. This device allowed to follow the effects of RT on HNSCC tissues derived from primary tumors or metastatic lymph nodes. This study represents an interesting attempt to validate the concept of personalized medicine by using an OOC platform coupled to RT systems.

Lately, a new CC has been developed to study effects of radiations on soft tissue sarcoma (STS) (Patra et al., 2019). This device has been employed to follow the effect of combined RT and chemotherapy (CT) on STS spheroids grown inside the chip. Three different radiation doses were used (0.5, 2, and 8 Gy), combined with Doxorubicin at two different concentrations (2 and 20 μM). The device has been designed to favor the isolation of growing spheroids after the tests. This allowed to further analyze the spheres by flow cytometry (to evaluate apoptosis) and clonogenic assays (to evaluate survival). Spheroids were also monitored for changes in the size as a function of tumor progression. Two different tumor cell lines, STS93 and STS117 were used. The STS117 cells, bearing a mutated p53 protein, appeared to be more resistant to the combined action of Doxorubicin plus RT, compared to the STS93 tumor cells (bearing the WT p53). The device is constituted of a 5 × 3 array chamber, each containing 24 microchambers for STS spheroid trapping and culture. This chip was used to appropriately apply two independent RT and CT gradients around the growing spheroids. The irradiation apparatus is constituted by a clinical linear accelerator system that does not affect the microdevice

biomaterial quality (PDMS). This representative study proposes a simple method to generate RT and CT combination gradients on chip to apply different radiation doses. In a similar work based on the use of ovarian cancer cell lines OV1946, a microfluidic cell culture platform equipped with a spheroid culture chamber array was designed. Although this study is not directly employed to test cancer drugs, the authors propose it to be used in combination with drugs and RT because of the peculiar configuration of the PDMS chip. The chip is composed by a 4 × 4 array of main chambers, separated by magnetic-actionable sensors (700 μm metal bar, in opened/closed states) which redirect the liquid flows through the chambers. Each chamber contains a 5 × 5 matrix of spheroid-trapping microwells (300 μm diameter), to yield a maximum of 25 replicates per chamber. In this system, OV1946 cells were left to generate spheroids in microwells and then RT (8 Gy) is given to appropriate chamber by a GammaCell3000 system. The presence of the actionable sensors allows to combine RT with a drug flowing into the desired wells. This system allows tumor spheroids to be monitored overtime upon RT and CT, with different radiation doses and drug concentrations (Brunet et al., 2017).

To date, no studies have been performed yet to investigate how radiation can impact on the crosstalk between immune cells and cancer cells on chip. Considering that RT often exerts immunogenic effect on cancer cells, a dual tumor-immune OOC may represent a valid alternative to study the behavior of immune cells in presence of RT-treated tumor cells (**Figure 7**).

USE OF OOC PLATFORMS TO STUDY PATIENT-DERIVED XENOGRAFTS

The use of laboratory animals has been widely exploited in studies involving microfluidic chips, due to the availability of immune cells from representative organs composing the immune system (i.e., bone marrow, spleen, and lymph nodes)(Mattei et al., 2010; Hickey and Chow, 2017; Elmore, 2018). On the other hand, the demand of immune cells still represents a great obstacle when planning microfluidic experiments with human cells. In fact, blood circulating immune cells can be easily available but cells residing in bone marrow, spleen and other lymphoid organs are unreachable. Based on these premises, there is an urgent need to overcome these difficulties to allow microfluidic experiments to be carried out in translational and clinical research contexts.

Recently, innovative humanized models have been developed for cancer immunotherapy research (Sanmamed et al., 2016). Among these, patient-derived xenografts (PDX) mice are immunodeficient animals adapted to receive a fragment of a fresh tumor excised from a cancer patient (Cho, 2020; Powley et al., 2020). A major advantage of PDX models, compared to simple cell line transplants, organoid xenografts or traditional tumor mouse models is represented by the retention of the TME architecture and genetic complexity of patient's tumor. In this manner, the human tumor can be faithfully recapitulated in PDX mice.

In perspective, PDX models may represent an invaluable tool for oncoimmunology studies of human tissues by microfluidic systems. Indeed, one can collect blood samples and tumor lesions from cancer patients in order to generate a biobank of patients' specimens. Little fragments of the tumor lesion excised from each patient can be transplanted in PDX mice (**Figure 8**). The resulting growing tumor in PDX mice is characterized for genomic profiling and histological analysis to confirm the TME morphology and TME architecture fidelity (**Figure 8**). At this point, *in vivo* drug testing can be performed in the PDX animals. This will allow to determine the therapeutic efficacy of anticancer agents or combination of drugs. The limitation of this approach, however, is the impossibility to evaluate immune responses, due to the fact that the PDX mice display an immunocompromised compartment. In this respect, OOC platforms may be used as an extension of PDX models. Indeed, autologous immune cells from patient's blood sample can be loaded onto the chip together with a fragment of the tumor lesion from the same patient. The use of devices with different compartmentalization levels (e.g., Microfluidic OncoImmuno Chip 1 and Microfluidic OncoImmuno Chip 2, **Figure 8**) allows more reliable cell tracking results and may constitute a doubly mutual control. In addition, multi-compartment chip systems open new alternatives in the evaluation of a single drug or drug combos. Interestingly, these PDX-based OOC systems may represent a smart and reliable approach to study the crosstalk between cancer cells and immune cells all derived from a specific cancer patient (**Figure 8**). Noticeably, the development of PDX-based OOC platforms is a valid alternative to the expensive *in vivo* drug evaluation and permit to obtain the results in quick time, compared to the *in vivo* drug testing, requiring 14–20 days for results (**Figure 8**). In summary, PDX-based OOC systems can be viewed as an added value to *in vivo* humanized models and a potential tool for personalized anti-cancer therapies.

THE HUMAN-ON-CHIP: A NEW FRONTIER IN ONCOIMMUNOLOGY?

Organs-On-Chip platforms currently used to investigate the disparate open questions on oncoimmunology are gradually evolving in complex systems formed by multiple interconnected OOC units. The main purpose of such an intricate OOC network will be to study specific immune organ's physiology in different types of cancer. This innovative approach certainly constitutes a future useful application for oncoimmunologists. In addition, it can represent the best platform ever developed, recapitulating the *in vivo* scenarios with superior affordability. However, the lack of definitive standardization criteria and the persistence of poor ethical policies for applications of advanced OOC systems in clinical research represent a strong limitation to this evolution.

Whether or not the development of a Human-on-Chip (HOC) will symbolize a groundbreaking frontier in oncoimmunology is still an unsolved question. The generation of HOC platforms is a common ambitious objective of several ongoing multidisciplinary projects. Besides, microfluidic platforms are beginning to be designed having in mind the requirement of multiple cell types and multi-compartmentalization approaches (Zhang et al., 2009; Berry et al., 2020; Langerak et al., 2020;

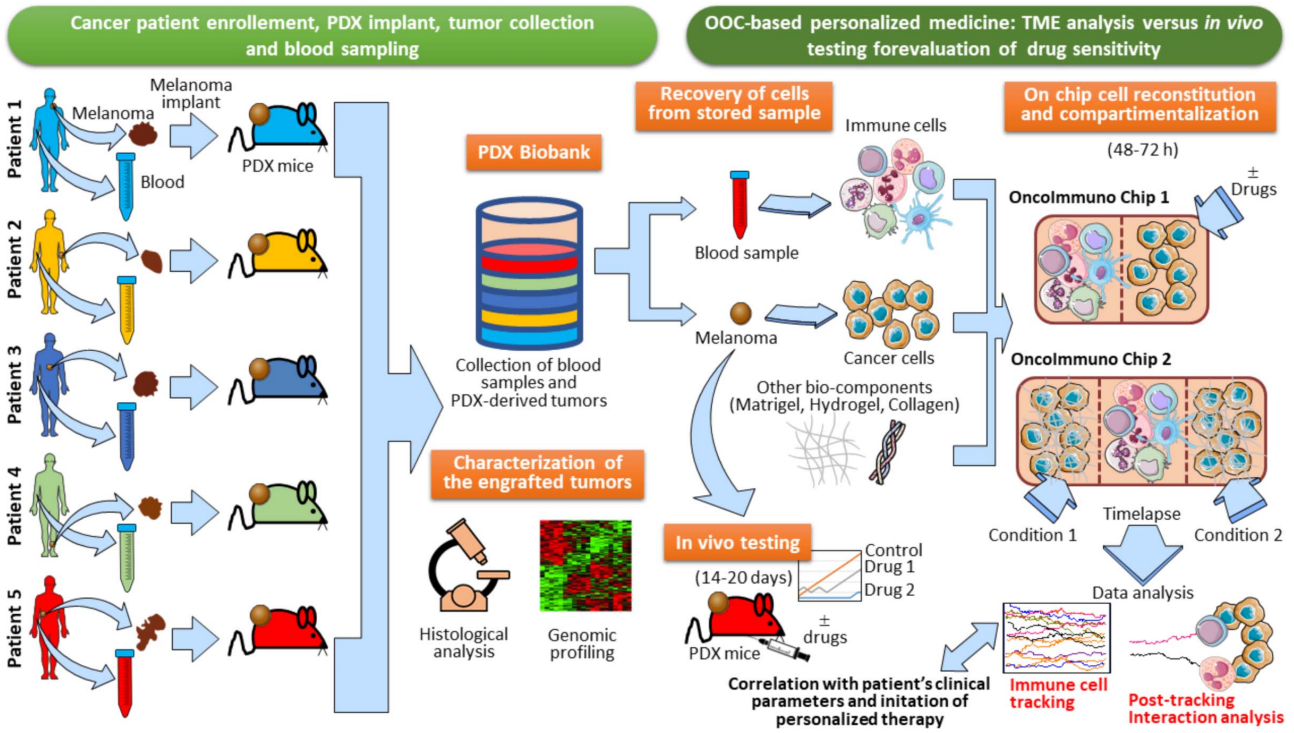

FIGURE 8 | Establishment of PDX-based OncoImmuno chip platform for melanoma patient's personalized therapy. Melanoma lesions and blood samples are collected from enrolled patients. and tumors are then implanted in PDX mice. When the tumors reach an adequate size, they are excised and stored in a Biobank with the associated blood samples. In parallel, samples are assayed for immunohistochemistry, Hematoxylin/Eosin staining and Gene expression profiling. When a patient is recruited to initiate a therapy, there are two alternatives to assay the sensitivity of anticancer drugs: *in vivo* testing with re-engraftment of the stored melanoma lesion (requiring 14–20 days), and OOC-based analysis (requiring 48–72 h). Immune and cancer cells are obtained from the patient's blood and tumor tissue, previously stored in the Biobank. Cells are then loaded in several types of customized microfluidic chips, with simple (OncoImmuno chip 1) or complex compartmentalization levels (OncoImmuno chip 2). Complex compartmentalization may require the use of other bio-components mimicking the TME matrix and the stroma (Matrigel, Hydrogel and collagen). In OncoImmuno chip 1, immune cells are left untreated whereas cancer cells are exposed on chip to a drug or left untreated (control condition). In OncoImmuno chip 2, Immune cells can be left untreated or treated with a single drug (Condition 1), whereas cancer cells on the opposite side chamber are exposed to a drug combo (Condition 2). Time-lapse is then started and the resulting video sequence is used for automated single cell tracking. Drug sensitivity is assayed by the extent of migration of immune cells (Immune cell tracking). To assess the vitality of melanoma cells, FBF area variation of these cells is evaluated and interaction times between cancer and immune cells are assessed (Post-tracking interaction analysis). For OncoImmuno chip 2 preferential migration of immune cells toward Condition 1 or Condition 2 is determined. Tracking profiles, interaction times and the associated kinematic variables will be compared to patient's clinical parameters and exploited to start the cancer patient's personalized therapy. Vertical brown dotted lines symbolically depict microfluidic device structural units and ideally delimit the immune and cancer compartments.

Sung, 2020). However, the road to obtain a fully functional HOC platform is still far to be reached and certainly fraught with obstacles. The final purpose of the HOC platform development must necessarily include the connection of at minimum two multicellular chips to recapitulate the *in vivo* function of at minimum two equivalent organs (Vunjak-Novakovic et al., 2013; Skardal et al., 2016; Sontheimer-Phelps et al., 2019). This implies that a HOC platform will be effectively finalized when at least a set of key human organs will be successfully connected in a complex OOC network, accompanied by AI (Artificial Intelligence) analysis algorithms, i.e., GAN (Comes et al., 2020a; Mencattini et al., 2020b), and advanced system biology tools (Jurisic, 2020). Such an intricated HOC can be conceived as a modular network where every single node is represented by a matrix of properly interconnected multicellular chip modules. Each Multicellular chip module recapitulates a physiologically functional human cell compartment on a microfluidic device (**Figure 9**). There are disparate obstacles to the composition of this modular HOC. One of the most relevant difficulty comes from the identification of the precise way each multicellular chip module must be interconnected with the units in close vicinity. Another problem can be to establish how these OOC should communicate with distant modules. Hence, a solution to overcome these issues may be the development of a complex module-based microfluidic network representing modular structures composed of interconnected units (**Figure 9**). In this scenario, a fully modular HOC model can be theoretically hypothesized, formed by Multicellular modules, OOC networks and Multi-organ modules, accurately interconnected to compose a functional HOC network recapitulating human physiology (**Figure 9**). Of note, each module unit is always constituted by inlet and outlet connections, denoted by the two points of each connection line between units. This will theoretically sustain fluidic circulation in the system.

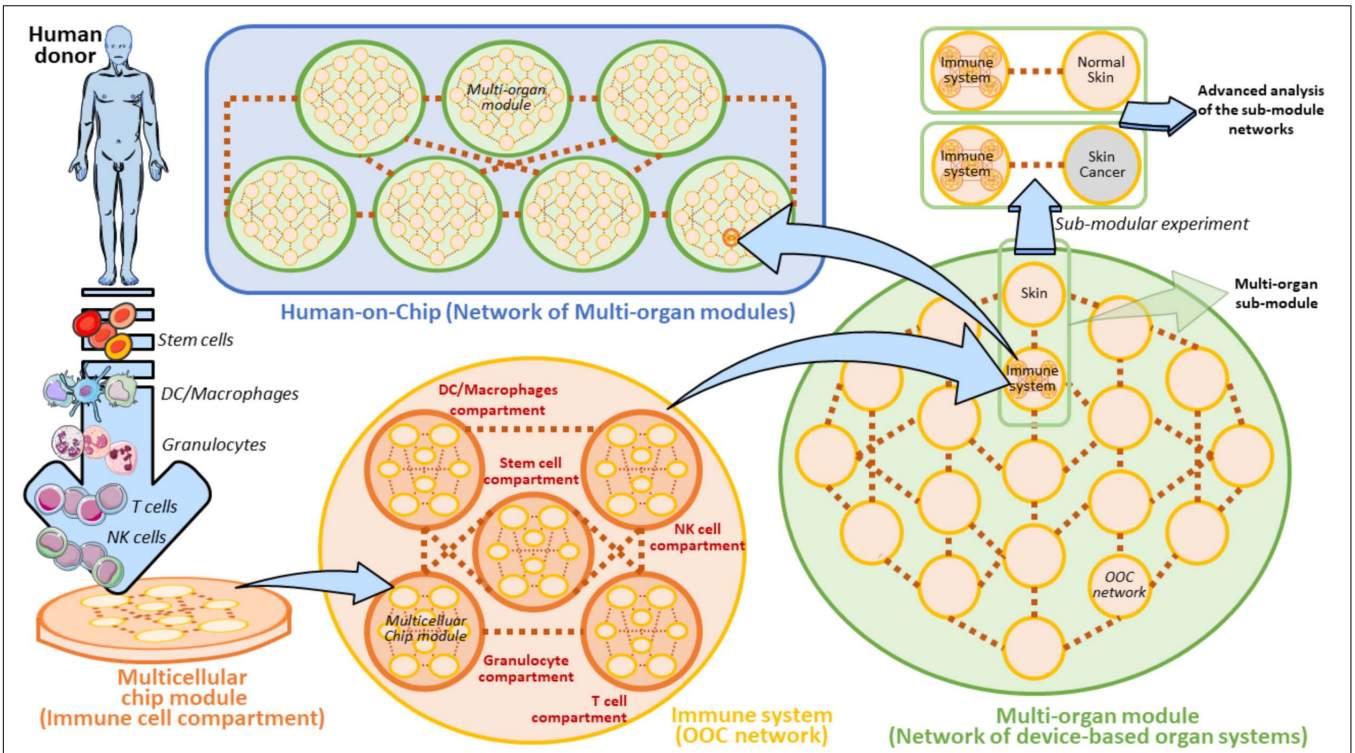

FIGURE 9 | Modular view of a Human-on-Chip with emphasis on a hypothetical on chip immune system model. A Multicellular chip module is a unit containing all the key cellular components and extracellular factors derived from a specific human donor's immune cells. In the Immune system these organs can be represented by five main cell populations (Stem cells, DC/Macrophages, Granulocytes, T cells, and NK cells). These cell subsets are properly loaded to form the five equivalent Multicellular chip modules (Immune cell compartments). Several Multicellular chip modules can generate an OOC Network. In this modular view, Immune system can be defined as an OOC Network composed by five Multicellular chip modules. Several OOC Networks compose a superior network of device-based organ systems, namely the Multi-organ module. The Human-on-Chip is composed of several serially connected Multi-organ modules. A Multi-organ module can also contain several subunits (Multi-organ sub-modules) to be employed for some isolated and targeted experiments (Sub-modular experiment) in which the sub-module is separated by its own Multi-organ module. In the case of the Immune system on chip, a Sub-modular experiment may be planned by a comparison of two connected OOC networks derived from two Multi-organ sub-modules (Immune system versus Normal skin or Skin cancer, respectively). Such an experiment can be aimed at comparing the immunosurveillance network activity to normal skin versus skin cancer. These experiments can be carried out with the help of AI algorithms and system biology approaches. Brown dots ideally represent the interconnections between the depicted units. The light-blue arrows evidence the passage to gradually superior levels of module complexity.

It is widely reported that bone-marrow, lymph nodes and spleen represent key immune organs maintaining immune cell homeostasis and immune surveillance (Le Bouteiller and Asherson, 1982; Olszewski, 2003; Mattei et al., 2010; Snell et al., 2012; Ruddle, 2016). In our modular HOC model, the immune system is defined as an OOC network of several main immune cell compartments derived from a human donor (**Figure 9**). These compartments are defined as heterogeneous containers of a certain cell subtype. For example, DC/Macrophages compartment is represented by all the common types of dendritic cells existing in the immune system (i.e., Conventional DCs, Plasmacytoid DCs, etc.) (Austyn, 2016; Tucci et al., 2019). When another OOC network (e.g., a skin OOC network) is directly connected to the OOC immune system we obtain a Multi-organ sub-module defined by two unique OOC networks. Interestingly, this sub-module can be easily re-developed as an isolated entity to perform specific sub-modular experiments (**Figure 9**). These targeted experimental layouts are oriented at extrapolating the complex crosstalk between the immune system and skin on chip, and represent an important starting point to the development of a module-based HOC platform (Henderson et al., 2020). Specifically, normal skin could be substituted by skin cancer cells (e.g., KRT14 primary skin cells and A375 melanoma cells) being expressed by circulating tumor cells and metastases (Lima et al., 2017; Hanley et al., 2020; Ibrahim et al., 2020), in order to carry out comparative sub-modular strategies between two different sub-module units. These units uniquely differ for the presence of normal skin cells or melanoma cells. In these settings, it is possible to compare how the immune system does respond to the presence of normal skin cells or melanoma in confined sub-modular microfluidic experiments (**Figure 9**). This theoretic modular model can be a good starting point to plan the development of distinct on chip organ systems defining a specific function (or set of functions) in the human body.

Recently, several bodies of evidence have been published proposing complex and functional HOC, which have been developed by exploiting the modular concept and submodular experiments illustrated in **Figure 9**

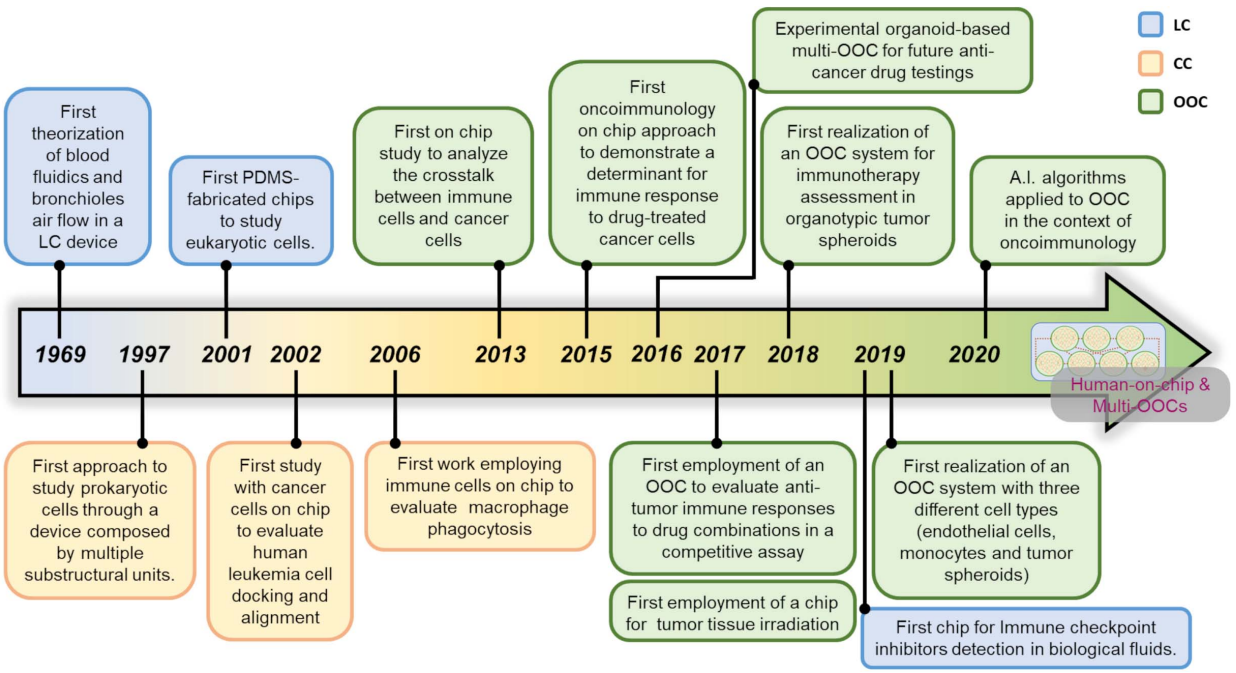

FIGURE 10 | From the dawn of microfluidic devices to the future Human-on-chip for oncoimmunology. Time-line of microfluidic chip evolution from simple Lab-on-Chip (LC) and CC (Cell-on-Chip) devices to Organ-on-Chip (OOC) platforms integrated by AI algorithms for on chip oncoimmunology applications, toward the development of complex multi-organs on chip for in-depth investigations.

(Vunjak-Novakovic et al., 2013; Skardal et al., 2016; Sontheimer-Phelps et al., 2019). Vunjak and co-Workers finalized a first validated Heart-Liver-Vascular HOC prototype, experimentally suitable for drug testing (Vunjak-Novakovic et al., 2013). These studies inspired the creation of a HOC platform based on modular organoid-containing microdevices. Here, the authors proposed the setting up of a complete circuitry to recapitulate a modular microfluidic system where each organoid-based OOC is adequately connected to form a HOC system composed by three modular liver, cardiac, and vascular organoid-containing microdevices. This platform is well suitable to study the effects of drugs in hepatic tumors, i.e., by evaluating the organoid sizes, immune cell infiltration or drug toxicity in each microdevice. This device was recently employed to quantitatively evaluate the effects of Propranolol and Epinephrine on this multiorgan platform (Skardal et al., 2016). These recent efforts represent an encouraging promise to an affordable and safe engagement of HOC for oncoimmunology purposes.

DISCUSSION AND CONCLUSION

The advent of microfluidic technology is gradually impacting the field of biophysics and biomedicine. Microfluidic devices are smart systems potentially useful in disparate and divergent types of scientific problems covering medicine, including research in tumor immunology.

Organs-On-Chip platforms for oncoimmunology (OncoImmuno chips) can be considered as flexible boxes capable of containing the diverse types of immune cells, cancer cells and extracellular matrices, coupled to optimized technologies to monitor the distinct cell behaviors throughout the time (e.g., time lapse microscopy). OncoImmuno chips can be fabricated in a customized manner, depending on the specific type of biological event dealing with or to be investigated. This is a great advantage for using microfluidic devices to study relationships between cancer and immunity.

The major boost to the development of OOCs, starting from simple LC and CC systems to sophisticated OOC has been the main big goal to design a functional HOC platform. When this will occur, clinical research, cancer research and patient's personalized medicine and all the research converging to oncoimmunology will certainly benefit of these scientific milestones. The era in which anticancer drug testing to evaluate immune response will be performed in a HOC patient's personalized avatar (resembling to a human *ad hoc* bio-avatar) can certainly be reached in the long-term future. The application of the deep learning algorithms to the development of these bio-avatars is crucial and can revolutionize the conceptual view and development of such advanced HOC models, particularly in the prediction of anticancer drug effects in immune response to tumors. In conclusion, research to implement advanced OOC platforms, including the OncoImmuno chip is indissolubly linked to the parallel research in neural network systems. The recent encouraging bodies of literature have demonstrated that OncoImmuno chips can be experimentally implemented in an HOC platform with integrated modular microdevices recapitulating a vascular system (Vunjak-Novakovic et al., 2013).

Figure 10 delineates the major breakthroughs that led to advanced OOC systems and that can boost the realization of complex HOC integrated by AI algorithms and advanced smart OncoImmuno chips. In this regard, a HOC recapitulating the systemic metastatic spread has been proposed, which exploits the OOC modular concept. In this hypothetical model, there are multiple OOC modules (Blood-Brain barrier on-chip, Bone chip, Lung cancer chip and Liver chip) which have been previously successfully tested as working submodules (**Figure 9**). These chips can, in the mid-term future, be connected to generate a working metastasis HOC (Sontheimer-Phelps et al., 2019). This represents an encouraging example on the efforts to recreate an immune-oncology HOC by modular addiction of working OOCs *via* separate submodular experiments.

In oncoimmunology, the affordability and accuracy of drug testing methods constitute urgent needs (Rebelo et al., 2016; Dehne et al., 2017). A module-based HOC may represent an optimal way to obtain advanced OOC networks, including immune system, in a fully modular bionetwork. Once finalized, this intricated bionetwork can certainly represent a powerful tool to develop novel anticancer drugs or therapies. The road developing a multi-organ connection is still extremely tangled and far to reach a real HOC system. However, the advent of new encouraging technologies, such as 3D bioprinting (Mota et al., 2020), mathematical models of networks (Cao et al., 2018; Wang Y. et al., 2019) and systems biology (Li et al., 2020), will represent relevant resources to reach this revolutionary scope.

An important issue to deal with is linked by the use of Matrigel for the assembly of microfluidic devices. This gel matrix was initially used in large scale for the recreation of the TME on chip. However, it holds several limitations, such as variability during manufacturing and complexity in composition. In fact, Matrigel is very difficult to handle, often subjected to batch-to-batch concentration variation and there are also some ethical issues related to its use (Aisenbrey and Murphy, 2020). For this reason, the assembly of microfluidic chips is gradually moving toward the use of other biocompatible gels, such as A PEG–maleimide hydrogel scaffold or a fibronectin-derived three-amino-acid peptide Arg-Gly-Asp, which binds to both αvβ3 and αvβ5 integrins, more affordable and ease to assembly. The constant research of new gel matrices suitable for the recapitulation of the TME on chip is of paramount relevance for boosting OOCs and HOCs platform optimization for unsolved oncoimmunology questions.

A final consideration should be outlined on the relationship between the evolution of on chip models and clinical research. If one is oriented to the development of an OncoImmuno chip platform aimed at solving a very specific biological problem, such as the response of immune cells to a tumor, this can require the design of a very simple chip. This will not be a time-consuming process and will not be expensive. On the contrary, if the main purpose is to solve advanced scientific problems, including sophisticated organ simulations, the development of a chip that will satisfy this condition will be time-consuming and very expensive. The developed OncoImmuno chip platform will be useful for basic research purposes rather than to solve a specific clinical problem. The **Supplementary Table 3** defines all the major pros and cons to be considered for the use of microfluidic devices in oncoimmunology applications.

AUTHOR CONTRIBUTIONS

FM and GS planned, supervised and wrote the manuscript. FM and SA realized the illustrations. SA, AM, AD, LB, and EM reviewed the current literature and contributed to the writing of the manuscript. All authors contributed to the article and approved the submitted version.

FUNDING

This work was funded by the Italian Association for Cancer Research (AIRC IG 21366 to GS).

SUPPLEMENTARY MATERIAL

The Supplementary Material for this article can be found online at: https://www.frontiersin.org/articles/10.3389/fmolb.2021.627454/full#supplementary-material

REFERENCES

Agliari, E., Biselli, E., De Ninno, A., Schiavoni, G., Gabriele, L., Gerardino, A., et al. (2014). Cancer-driven dynamics of immune cells in a microfluidic environment. *Sci. Rep.* 4:6639. doi: 10.1038/srep06639

Aisenbrey, E. A., and Murphy, W. L. (2020). Synthetic alternatives to Matrigel. *Nat. Rev. Mater.* 5, 539–551. doi: 10.1038/s41578-020-0199-8

Aleman, J., George, S. K., Herberg, S., Devarasetty, M., Porada, C. D., Skardal, A., et al. (2019). Deconstructed microfluidic bone marrow on-a-chip to study normal and malignant hemopoietic cell-niche interactions. *Small* 15:e1902971. doi: 10.1002/smll.201902971

Alsuliman, T., Humaidan, D., and Sliman, L. (2020). Machine learning and artificial intelligence in the service of medicine: necessity or potentiality? *Curr. Res. Transl. Med.* 68:1016. doi: 10.1016/j.retram.2020.01.002

Anderson, N. M., and Simon, M. C. (2020). The tumor microenvironment. *Curr. Biol.* 30, R921–R925. doi: 10.1016/j.cub.2020.06.081

Aref, A. R., Campisi, M., Ivanova, E., Portell, A., Larios, D., Piel, B. P., et al. (2018). 3D microfluidic ex vivo culture of organotypic tumor spheroids to model immune checkpoint blockade. *Lab. Chip.* 18, 3129–3143. doi: 10.1039/c8lc00322j

Atwell, D. B., Booth, C., Vignarajah, D. D., Knesl, M., Buddle, N., Hoozer, M., et al. (2019). Radiation oncology quality assessment tool: a proposal for a new audit tool in modern radiation oncology. *J. Med. Imaging Radiat. Oncol.* 63, 691–697. doi: 10.1111/1754-9485.12928

Atwell, D., Elks, J., Cahill, K., Hearn, N., Vignarajah, D., Lagopoulos, J., et al. (2020). A review of modern radiation therapy dose escalation in locally advanced head and neck cancer. *Clin. Oncol. (R. Coll. Radiol.)* 32, 330–341. doi: 10.1016/j.clon.2019.12.004

Austyn, J. M. (2016). Dendritic cells in the immune system-history, lineages, tissues, tolerance, and immunity. *Microbiol. Spectr.* 4:1128. doi: 10.1128/microbiolspec.MCHD-0046-2016

Bahavarnia, F., Saadati, A., Hassanpour, S., Hasanzadeh, M., Shadjou, N., and Hassanzadeh, A. (2019). Paper based immunosensing of ovarian cancer tumor protein CA 125 using novel nano-ink: a new platform for efficient diagnosis of cancer and biomedical analysis using microfluidic paper-based analytical devices (μPAD). *Int. J. Biol. Macromol.* 138, 744–754. doi: 10.1016/j.ijbiomac.2019.07.109

Balkanyi, L., and Cornet, R. (2019). The interplay of knowledge representation with various fields of artificial intelligence in medicine. *Yearb. Med. Inform.* 28, 27–34. doi: 10.1055/s-0039-1677899

Bao, H., Zheng, N., Li, Z., and Zhi, Y. (2020). Synergistic effect of tangeretin and atorvastatin for colon cancer combination therapy: targeted delivery of these dual drugs using RGD Peptide decorated nanocarriers. *Drug. Des. Devel. Ther.* 14, 3057–3068. doi: 10.2147/DDDT.S256636

Bassi, A. M., Ahluwalia, A., Penco, S., Chiono, V., Fiore, G. B., and Visai, L. (2020). 2nd centro3r annual meeting: 3Rs in Italian universities. *ALTEX* 37, 493–495. doi: 10.14573/altex.2001171

Beckwith, A. L., Velásquez-García, L. F., and Borenstein, J. T. (2019). Microfluidic model for evaluation of immune checkpoint inhibitors in human tumors. *Adv. Healthc. Mater.* 8:e1900289. doi: 10.1002/adhm.201900289

Bellia, S. R., Feliciani, G., Duca, M. D., Monti, M., Turri, V., Sarnelli, A., et al. (2019). Clinical evidence of abscopal effect in cutaneous squamous cell carcinoma treated with diffusing alpha emitters radiation therapy: a case report. *J. Contemp. Brachyther.* 11, 449–457. doi: 10.5114/jcb.2019.88138

Berry, S. B., Gower, M. S., Su, X., Seshadri, C., and Theberge, A. B. (2020). A modular microscale granuloma model for immune-microenvironment signaling studies in vitro. *Front. Bioeng. Biotechnol.* 8:931.

Biselli, E., Agliari, E., Barra, A., Bertani, F. R., Gerardino, A., De Ninno, A., et al. (2017). Organs on chip approach: a tool to evaluate cancer -immune cells interactions. *Sci. Rep.* 7:12737. doi: 10.1038/s41598-017-13070-3

Bock, C., Moor, M., Jutzeler, C. R., and Borgwardt, K. (2021). Machine learning for biomedical time series classification: from shapelets to deep learning. *Methods Mol. Biol.* 2190, 33–71. doi: 10.1007/978-1-0716-0826-5_2

Boussommier-Calleja, A., Li, R., Chen, M. B., Wong, S. C., and Kamm, R. D. (2016). Microfluidics: a new tool for modeling cancer-immune interactions. *Trends Cancer* 2, 6–19. doi: 10.1016/j.trecan.2015.12.003

Brunet, A. R., Labelle, F., Wong, P., and Gervais, T. (2017). Reconfigurable microfluidic magnetic valve arrays: towards a radiotherapy-compatible spheroid culture platform for the combinatorial screening of cancer therapies. *Sensors (Basel)* 17:2271. doi: 10.3390/s17102271

Buch, V. H., Ahmed, I., and Maruthappu, M. (2018). Artificial intelligence in medicine: current trends and future possibilities. *Br. J. Gen. Pract.* 68, 143–144. doi: 10.3399/bjgp18X695213

Businaro, L., De Ninno, A., Schiavoni, G., Lucarini, V., Ciasca, G., Gerardino, A., et al. (2013). Cross talk between cancer and immune cells: exploring complex dynamics in a microfluidic environment. *Lab. Chip.* 13, 229–239. doi: 10.1039/c2lc40887b

Butson, M. J., Mathur, J. N., and Metcalfe, P. E. (1996). Effect of block trays on skin dose in radiotherapy. *Austr. Phys. Eng. Sci. Med.* 19, 248–251.

Cankaya, C., Ozsoy, E., Demirel, E. E., Polat, N., and Gunduz, A. (2020). Estimation of angle kappa and pupil barycentre configuration in myopic tilted disc syndrome. *Clin. Exp. Optom.* 103, 192–196. doi: 10.1111/cxo.12897

Cao, C., Liu, F., Tan, H., Song, D., Shu, W., Li, W., et al. (2018). Deep learning and its applications in biomedicine. *Genom. Proteom. Bioinform.* 16, 17–32. doi: 10.1016/j.gpb.2017.07.003

Caplan, R. M. (1972). Pythagorean theorem revisited. *J. Iowa. Med. Soc.* 62:275.

Cheah, R., Srivastava, R., Stafford, N. D., Beavis, A. W., Green, V., and Greenman, J. (2017). Measuring the response of human head and neck squamous cell carcinoma to irradiation in a microfluidic model allowing customized therapy. *Int. J. Oncol.* 51, 1227–1238. doi: 10.3892/ijo.2017.4118

Chen, P., Li, S., Guo, Y., Zeng, X., and Liu, B. F. (2020). A review on microfluidics manipulation of the extracellular chemical microenvironment and its emerging application to cell analysis. *Anal. Chim. Acta* 1125, 94–113. doi: 10.1016/j.aca.2020.05.065

Chen, Y., Pan, W., Gao, P., Shi, M., Wu, T., Li, N., et al. (2020). Boosting the abscopal effect of radiotherapy: a smart antigen-capturing radiosensitizer to eradicate metastatic breast tumors. *Chem. Commun. (Camb.)* 56, 10353–10356. doi: 10.1039/d0cc01080d

Cho, S. Y. (2020). Patient-derived xenografts as compatible models for precision oncology. *Lab. Anim. Res.* 36:14. doi: 10.1186/s42826-020-00045-1

Comes, M. C., Casti, P., Mencattini, A., Di Giuseppe, D., Mermet-Meillon, F., De Ninno, A., et al. (2019). The influence of spatial and temporal resolutions on the analysis of cell-cell interaction: a systematic study for time-lapse microscopy applications. *Sci. Rep.* 9:6789. doi: 10.1038/s41598-019-42475-5

Comes, M. C., Filippi, J., Mencattini, A., Casti, P., Cerrato, G., Sauvat, A., et al. (2020a). Multi-scale generative adversarial network for improved evaluation of cell–cell interactions observed in organ-on-chip experiments. *Neur. Comput. Appl.* doi: 10.1007/s00521-020-05226-6

Comes, M. C., Filippi, J., Mencattini, A., Corsi, F., Casti, P., De Ninno, A., et al. (2020b). Accelerating the experimental responses on cell behaviors: a long-term prediction of cell trajectories using social generative adversarial network. *Sci. Rep.* 10:15635. doi: 10.1038/s41598-020-72605-3

Crunkhorn, S. (2020). Combination therapy combats aggressive breast cancer. *Nat. Rev. Drug. Discov.* 19:310. doi: 10.1038/d41573-020-00065-5

Dang, B. V., Hassanzadeh-Barforoushi, A., Syed, M. S., Yang, D., Kim, S. J., Taylor, R. A., et al. (2019). Microfluidic actuation via 3D-printed molds toward multiplex biosensing of cell apoptosis. *ACS Sens.* 4, 2181–2189. doi: 10.1021/acssensors.9b01057

Davidov, V., Jensen, G., Mai, S., Chen, S. H., and Pan, P. Y. (2020). Analyzing one cell at a TIME: Analysis of myeloid cell contributions in the tumor immune microenvironment. *Front. Immunol.* 11:1842. doi: 10.3389/fimmu.2020.01842

Dehne, E. M., Hasenberg, T., and Marx, U. (2017). The ascendance of microphysiological systems to solve the drug testing dilemma. *Future Sci. OA* 3:FSO185. doi: 10.4155/fsoa-2017-0002

Desyatnik, I., Krasner, M., Frolov, L., Ronen, M., Guy, O., Wasserman, D., et al. (2019). An integrated microfluidics approach for personalized cancer drug sensitivity and resistance assay. *Adv. Biosyst.* 3:e1900001. doi: 10.1002/adbi.201900001

Dewan, M. A., Ahmad, M. O., and Swamy, M. N. (2011). Tracking biological cells in time-lapse microscopy: an adaptive technique combining motion and topological features. *IEEE Trans. Biomed. Eng.* 58, 1637–1647. doi: 10.1109/TBME.2011.2109001

Dobiasch, S., Kampfer, S., Burkhardt, R., Schilling, D., Schmid, T. E., Wilkens, J. J., et al. (2017). BioXmark for high-precision radiotherapy in an orthotopic pancreatic tumor mouse model : experiences with a liquid fiducial marker. *Strahlenther. Onkol.* 193, 1039–1047. doi: 10.1007/s00066-017-1193-y

Domankevich, V., Efrati, M., Schmidt, M., Glikson, E., Mansour, F., Shai, A., et al. (2020). RIG-1-like receptor activation synergizes with intratumoral alpha radiation to induce pancreatic tumor rejection, triple-negative breast metastases clearance, and antitumor immune memory in mice. *Front. Oncol.* 10:990. doi: 10.3389/fonc.2020.00990

Du, S., Lockamy, V., Zhou, L., Xue, C., LeBlanc, J., Glenn, S., et al. (2016). Stereotactic body radiation Therapy delivery in a genetically engineered mouse model of lung cancer. *Int. J. Radiat. Oncol. Biol. Phys.* 96, 529–537. doi: 10.1016/j.ijrobp.2016.07.008

Duarte Campos, D. F., Lindsay, C. D., Roth, J. G., LeSavage, B. L., Seymour, A. J., Krajina, B. A., et al. (2020). Bioprinting cell- and spheroid-laden protein-engineered hydrogels as tissue-on-chip platforms. *Front. Bioeng. Biotechnol.* 8:374. doi: 10.3389/fbioe.2020.00374

Dummer, A., Poelma, C., DeRuiter, M. C., Goumans, M. J., and Hierck, B. P. (2016). Measuring the primary cilium length: improved method for unbiased high-throughput analysis. *Cilia* 5:7. doi: 10.1186/s13630-016-0028-2

Dunn, G. A. (1983). Characterising a kinesis response: time averaged measures of cell speed and directional persistence. *Agents Actions Suppl.* 12, 14–33. doi: 10.1007/978-3-0348-9352-7_1

Elmore, S. A. (2018). Enhanced histopathology evaluation of lymphoid organs. *Methods Mol. Biol.* 1803, 147–168. doi: 10.1007/978-1-4939-8549-4_10

Emami, N., Sedaei, Z., and Ferdousi, R. (2021). Computerized cell tracking: current methods, tools and challenges. *Vis. Inform.* 5, 1–13. doi: 10.1016/j.visinf.2020.11.003

Esch, M. B., Baeumner, A. J., and Durst, R. A. (2001a). Detection of *Cryptosporidium parvum* using oligonucleotide-tagged liposomes in a competitive assay format. *Anal. Chem.* 73, 3162–3167. doi: 10.1021/ac010012i

Esch, M. B., Locascio, L. E., Tarlov, M. J., and Durst, R. A. (2001b). Detection of viable *Cryptosporidium parvum* using DNA-modified liposomes in a microfluidic chip. *Anal. Chem.* 73, 2952–2958. doi: 10.1021/ac001508n

Fang, G., Lu, H., Law, A., Gallego-Ortega, D., Jin, D., and Lin, G. (2019). Gradient-sized control of tumor spheroids on a single chip. *Lab. Chip.* 19, 4093–4103. doi: 10.1039/c9lc00872a

Farmer, M. C., Johnson, S. A., Beissinger, R. L., Gossage, J. L., Lynn, A. B., and Carter, K. A. (1988). Liposome-encapsulated hemoglobin: a synthetic red cell. *Adv. Exp. Med. Biol.* 238, 161–170. doi: 10.1007/978-1-4684-7908-9_13

Fellin, F., Iacco, M., D'Avino, V., Tommasino, F., Farace, P., Palma, G., et al. (2019). Potential skin morbidity reduction with intensity-modulated proton therapy for breast cancer with nodal involvement. *Acta Oncol.* 58, 934–942. doi: 10.1080/0284186X.2019.1591638

Fernando, T., Denman, S., Sridharan, S., and Fookes, C. (2019). "GD-GAN: generative adversarial networks for trajectory prediction and group detection in crowds," in *Computer Vision – ACCV 2018. ACCV 2018. Lecture Notes in Computer Science*, eds L. H. Jawahar, C. G. Mori, and K. Schindler (Cham: Springer).

Frey, B., Rubner, Y., Wunderlich, R., Weiss, E. M., Pockley, A. G., Fietkau, R., et al. (2012). Induction of abscopal anti-tumor immunity and immunogenic tumor cell death by ionizing irradiation - implications for cancer therapies. *Curr. Med. Chem.* 19, 1751–1764. doi: 10.2174/092986712800099811

GajdÁcs, M., NovÉ, M., Csonka, Á, Varga, B., SanmartÍn, C., DomÍnguez-Álvarez, E., et al. (2020). Phenothiazines and selenocompounds: a potential novel combination therapy of multidrug resistant cancer. *Anticancer Res.* 40, 4921–4928. doi: 10.21873/anticanres.14495

Gérard, A., Woolfe, A., Mottet, G., Reichen, M., Castrillon, C., Menrath, V., et al. (2020). High-throughput single-cell activity-based screening and sequencing of antibodies using droplet microfluidics. *Nat. Biotechnol.* 38, 715–721. doi: 10.1038/s41587-020-0466-7

Gorelik, R., and Gautreau, A. (2014). Quantitative and unbiased analysis of directional persistence in cell migration. *Nat. Protoc.* 9, 1931–1943. doi: 10.1038/nprot.2014.131

Gupta, T., and Chatterjee, A. (2020). Modern radiation therapy for pituitary adenoma: review of techniques and outcomes. *Neurol. India* 68(Suppl.), S113–S122. doi: 10.4103/0028-3886.287678

Hader, M., Savcigil, D. P., Rosin, A., Ponfick, P., Gekle, S., Wadepohl, M., et al. (2020). Differences of the immune phenotype of breast cancer cells after ex vivo hyperthermia by warm-water or microwave radiation in a closed-loop system alone or in combination with radiotherapy. *Cancers (Basel)* 12:1082. doi: 10.3390/cancers12051082

Hanley, C. J., Henriet, E., Sirka, O. K., Thomas, G. J., and Ewald, A. J. (2020). Tumor resident stromal cells promote breast cancer invasion through regulation of the basal phenotype. *Mol. Cancer Res.* 18, 1615–1622. doi: 10.1158/1541-7786.MCR-20-0334

Hassell, B. A., Goyal, G., Lee, E., Sontheimer-Phelps, A., Levy, O., Chen, C. S., et al. (2018). Human organ chip models recapitulate orthotopic lung cancer growth, therapeutic responses, and tumor dormancy in vitro. *Cell Rep.* 23:3698. doi: 10.1016/j.celrep.2018.06.028

Henderson, A. R., Choi, H., and Lee, E. (2020). Blood and lymphatic vasculatures on-chip platforms and their applications for organ-specific in vitro modeling. *Micromachines (Basel)* 11:147. doi: 10.3390/mi11020147

Hickey, M. J., and Chow, Z. (2017). Viewing immune regulation as it happens: in vivo imaging for investigation of regulatory T-cell function. *Immunol. Cell Biol.* 95, 514–519. doi: 10.1038/icb.2017.33

Ho, C. T., Lin, R. Z., Chang, W. Y., Chang, H. Y., and Liu, C. H. (2006). Rapid heterogeneous liver-cell on-chip patterning via the enhanced field-induced dielectrophoresis trap. *Lab. Chip.* 6, 724–734. doi: 10.1039/b602036d

Holzinger, A., Langs, G., Denk, H., Zatloukal, K., and Müller, H. (2019). Causability and explainability of artificial intelligence in medicine. *Wiley Interdiscip. Rev. Data Min. Knowl. Discov.* 9:e1312. doi: 10.1002/widm.1312

Huang, W. H., Cheng, W., Zhang, Z., Pang, D. W., Wang, Z. L., Cheng, J. K., et al. (2004). Transport, location, and quantal release monitoring of single cells on a microfluidic device. *Anal. Chem.* 76, 483–488. doi: 10.1021/ac035026y

Ibrahim, M. R., Medhat, W., El-Fakahany, H., Abdel-Raouf, H., and Snyder, E. Y. (2020). Deriving keratinocyte progenitor cells and keratinocytes from human-induced pluripotent stem cells. *Curr. Protoc. Stem. Cell Biol.* 54:e119. doi: 10.1002/cpsc.119

Iratni, R., and Ayoub, M. A. (2020). Sildenafil in combination therapy against cancer: a literature review. *Curr. Med. Chem.* doi: 10.2174/0929867327666200730165338

Jenkins, R. W., Aref, A. R., Lizotte, P. H., Ivanova, E., Stinson, S., Zhou, C. W., et al. (2018). Profiling of PD-1 blockade using organotypic tumor spheroids. *Cancer Discov.* 8, 196–215. doi: 10.1158/2159-8290.CD-17-0833

Jie, M., Mao, S., Liu, H., He, Z., Li, H. F., and Lin, J. M. (2017). Evaluation of drug combination for glioblastoma based on an intestine-liver metabolic model on microchip. *Analyst* 142, 3629–3638. doi: 10.1039/c7an00453b

Jiménez-Díaz, E., Cano-Jorge, M., Zamarrón-Hernández, D., Cabriales, L., Páez-Larios, F., Cruz-Ramírez, A., et al. (2019). Micro-macro: selective integration of microfeatures inside low-cost macromolds for PDMS microfluidics fabrication. *Micromachines (Basel)* 10:576. doi: 10.3390/mi10090576

Johnsson, B., Löfås, S., and Lindquist, G. (1991). Immobilization of proteins to a carboxymethyldextran-modified gold surface for biospecific interaction analysis in surface plasmon resonance sensors. *Anal. Biochem.* 198, 268–277. doi: 10.1016/0003-2697(91)90424-r

Jonnalagadda, B., Arockiasamy, S., and Krishnamoorthy, S. (2020). Cellular growth factors as prospective therapeutic targets for combination therapy in androgen independent prostate cancer (AIPC). *Life Sci.* 259:118208. doi: 10.1016/j.lfs.2020.118208

Jurisic, V. (2020). Multiomic analysis of cytokines in immuno-oncology. *Exp. Rev. Proteom.* 17, 663–674. doi: 10.1080/14789450.2020.1845654

Kang, J. H., Krause, S., Tobin, H., Mammoto, A., Kanapathipillai, M., and Ingber, D. E. (2012). A combined micromagnetic-microfluidic device for rapid capture and culture of rare circulating tumor cells. *Lab. Chip.* 12, 2175–2181. doi: 10.1039/c2lc40072c

Karimi, H., Soleimanjahi, H., Abdoli, A., and Banijamali, R. S. (2020). Combination therapy using human papillomavirus L1/E6/E7 genes and archaeosome: a nanovaccine confer immuneadjuvanting effects to fight cervical cancer. *Sci. Rep.* 10:5787. doi: 10.1038/s41598-020-62448-3

Kaul, V., Enslin, S., and Gross, S. A. (2020). History of artificial intelligence in medicine. *Gastrointest. Endosc.* 92:807. doi: 10.1016/j.gie.2020.06.040

Kawachi, A., Yamashita, S., Okochi-Takada, E., Hirakawa, A., Tsuda, H., Shimomura, A., et al. (2020). BRCA1 promoter methylation in breast cancer patients is associated with response to olaparib/eribulin combination therapy. *Breast Cancer Res. Treat.* 181, 323–329. doi: 10.1007/s10549-020-05647-w

Keisari, Y. (2017). Tumor abolition and antitumor immunostimulation by physico-chemical tumor ablation. *Front. Biosci. (Landmark Ed.)* 22, 310–347. doi: 10.2741/4487

Kim, D., and Haynes, C. L. (2013). On-chip evaluation of neutrophil activation and neutrophil-endothelial cell interaction during neutrophil chemotaxis. *Anal. Chem.* 85, 10787–10796. doi: 10.1021/ac4020098

Kim, H., Lee, S. J., Lee, I. K., Min, S. C., Sung, H. H., Jeong, B. C., et al. (2020). Synergistic effects of combination therapy with AKT and mTOR inhibitors on bladder cancer cells. *Int. J. Mol. Sci.* 21:2825. doi: 10.3390/ijms21082825

Kim, J., Taylor, D., Agrawal, N., Wang, H., Kim, H., Han, A., et al. (2012). A programmable microfluidic cell array for combinatorial drug screening. *Lab. Chip.* 12, 1813–1822. doi: 10.1039/c2lc21202a

Kokkinos, C., Economou, A., Raptis, I., and Speliotis, T. (2008). Disposable mercury-free cell-on-a-chip devices with integrated microfabricated electrodes for the determination of trace nickel(II) by adsorptive stripping voltammetry. *Anal. Chim. Acta* 622, 111–118. doi: 10.1016/j.aca.2008.05.051

Koukourakis, M. I., and Giatromanolaki, A. (2020). Tumor microenvironment, immune response and post-radiotherapy tumor clearance. *Clin. Transl. Oncol.* 22, 2196–2205. doi: 10.1007/s12094-020-02378-8

Kwak, B., Ozcelikkale, A., Shin, C. S., Park, K., and Han, B. (2014). Simulation of complex transport of nanoparticles around a tumor using tumor-microenvironment-on-chip. *J. Control Release* 194, 157–167. doi: 10.1016/j.jconrel.2014.08.027

Langerak, N., Ahmed, H. M. M., Li, Y., Middel, I. R., Amirabadi, H. E., Malda, J., et al. (2020). A theoretical and experimental study to optimize cell differentiation in a novel intestinal chip. *Front. Bioeng. Biotechnol.* 8:763. doi: 10.3389/fbioe.2020.00763

Le Bouteiller, P. P., and Asherson, G. L. (1982). Regulation of B cell development in mouse bone marrow. *Adv. Exp. Med. Biol.* 149, 31–38. doi: 10.1007/978-1-4684-9066-4_5

Lew, H. S., and Fung, Y. C. (1969). On the low-Reynolds-number entry flow into a circular cylindrical tube. *J. Biomech.* 2, 105–119. doi: 10.1016/0021-9290(69)90046-3

Li, K., Yang, X., and Gao, X. (2019a). Probing tumor microtissue formation and epithelial-mesenchymal transition on a well-mesh microchip. *Biomicrofluidics* 13:014102. doi: 10.1063/1.5064838

Li, K., Yang, X., Xue, C., Zhao, L., Zhang, Y., and Gao, X. (2019b). Biomimetic human lung-on-a-chip for modeling disease investigation. *Biomicrofluidics* 13:031501. doi: 10.1063/1.5100070

Li, P. C., and Harrison, D. J. (1997). Transport, manipulation, and reaction of biological cells on-chip using electrokinetic effects. *Anal. Chem.* 69, 1564–1568. doi: 10.1021/ac9606564

Li, X., and Li, P. C. (2005). Microfluidic selection and retention of a single cardiac myocyte, on-chip dye loading, cell contraction by chemical stimulation, and quantitative fluorescent analysis of intracellular calcium. *Anal. Chem.* 77, 4315–4322. doi: 10.1021/ac048240a

Li, Y., McGrail, D. J., Latysheva, N., Yi, S., Babu, M. M., and Sahni, N. (2020). Pathway perturbations in signaling networks: linking genotype to phenotype. *Semin. Cell Dev. Biol.* 99, 3–11. doi: 10.1016/j.semcdb.2018.05.001

Li, Z., Wu, M., Zheng, J., and Yu, H. (2019c). Perceptual adversarial networks with a feature pyramid for image translation. *IEEE Comput. Graph. Appl.* 39, 68–77. doi: 10.1109/MCG.2019.2914426

Lima, L., Neves, M., Oliveira, M. I., Dieguez, L., Freitas, R., Azevedo, R., et al. (2017). Sialyl-Tn identifies muscle-invasive bladder cancer basal and luminal subtypes facing decreased survival, being expressed by circulating tumor cells and metastases. *Urol. Oncol.* 35, 675.e1–675.e8. doi: 10.1016/j.urolonc.2017.08.012

Lin, P. D. (2019). First-order derivative matrix of a ray: a simple and flexible alternative computation method. *Opt. Exp.* 27, 35402–35417. doi: 10.1364/OE.27.035402

Liu, C. C., Steen, C. B., and Newman, A. M. (2019). Computational approaches for characterizing the tumor immune microenvironment. *Immunology* 158, 70–84. doi: 10.1111/imm.13101

Liu, Z., Yeh, R., Tang, X., Liu, Y., and Agarwala, A. (2017). "Video frame synthesis using deep voxel flow," in *Proceedings of the 2017 IEEE International Conference on Computer Vision*, Venice.

Lucarini, V., Buccione, C., Zicchedda, G., Peschiaroli, F., Sestili, P., Puglisi, R., et al. (2017). Combining type I interferons and 5-Aza-2′-deoxycitidine to improve anti-tumor response against melanoma. *J. Invest. Dermatol.* 137, 159–169. doi: 10.1016/j.jid.2016.08.024

Matsumura, K., Orita, K., Wakamoto, Y., and Yasuda, K. (2006). Phagocytic response to fully controlled plural stimulation of antigens on macrophage using on-chip microcultivation system. *J. Nanobiotechnol.* 4:7. doi: 10.1186/1477-3155-4-7

Mattei, F., Schiavoni, G., and Tough, D. F. (2010). Regulation of immune cell homeostasis by type I interferons. *Cytokine Growth Factor. Rev.* 21, 227–236. doi: 10.1016/j.cytogfr.2010.05.002

Mattei, F., Schiavoni, G., Sestili, P., Spadaro, F., Fragale, A., Sistigu, A., et al. (2012). IRF-8 controls melanoma progression by regulating the cross talk between cancer and immune cells within the tumor microenvironment. *Neoplasia* 14, 1223–1235. doi: 10.1593/neo.121444

Mehta, G., Williams, C. M., Alvarez, L., Lesniewski, M., Kamm, R. D., and Griffith, L. G. (2010). Synergistic effects of tethered growth factors and adhesion ligands on DNA synthesis and function of primary hepatocytes cultured on soft synthetic hydrogels. *Biomaterials* 31, 4657–4671. doi: 10.1016/j.biomaterials.2010.01.138

Mencattini, A., De Ninno, A., Mancini, J., Businaro, L., Martinelli, E., Schiavoni, G., et al. (2020a). High-throughput analysis of cell-cell crosstalk in ad hoc designed microfluidic chips for oncoimmunology applications. *Methods Enzymol.* 632, 479–502. doi: 10.1016/bs.mie.2019.06.012

Mencattini, A., Di Giuseppe, D., Comes, M. C., Casti, P., Corsi, F., Bertani, F. R., et al. (2020b). Discovering the hidden messages within cell trajectories using a deep learning approach for in vitro evaluation of cancer drug treatments. *Sci. Rep.* 10:7653. doi: 10.1038/s41598-020-64246-3

Menon, N. V., Chuah, Y. J., Cao, B., Lim, M., and Kang, Y. (2014). A microfluidic co-culture system to monitor tumor-stromal interactions on a chip. *Biomicrofluidics* 8:064118. doi: 10.1063/1.4903762

Mintz, Y., and Brodie, R. (2019). Introduction to artificial intelligence in medicine. *Minim. Invasive Ther. All. Technol.* 28, 73–81. doi: 10.1080/13645706.2019.1575882

Mocho, J. P. (2020). 3Rs – reduce reuse recycle. *Lab. Anim.* 54:194. doi: 10.1177/0023677220909272

Molino, D., Quignard, S., Gruget, C., Pincet, F., Chen, Y., Piel, M., et al. (2016). On-chip quantitative measurement of mechanical stresses during cell migration with emulsion droplets. *Sci. Rep.* 6:29113. doi: 10.1038/srep29113

Mollica, V., Maggio, I., Lopez-Beltran, A., Montironi, R., Cimadamore, A., Cheng, L., et al. (2020). Combination therapy in advanced urothelial cancer: the role of PARP, HER-2 and mTOR inhibitors. *Exp. Rev. Anticancer Ther.* 20, 755–763. doi: 10.1080/14737140.2020.1807334

Mölzer, C., Shankar, S. P., Griffith, M., Islam, M. M., Forrester, J. V., and Kuffová, L. (2019). Activation of dendritic cells by crosslinked collagen hydrogels (artificial corneas) varies with their composition. *J. Tissue Eng. Regen. Med.* 13, 1528–1543. doi: 10.1002/term.2903

Mota, F., Braga, L., Rocha, L., and Cabral, B. (2020). 3D and 4D bioprinted human model patenting and the future of drug development. *Nat. Biotechnol.* 38, 689–694. doi: 10.1038/s41587-020-0540-1

Narkhede, A. A., Shevde, L. A., and Rao, S. S. (2017). Biomimetic strategies to recapitulate organ specific microenvironments for studying breast cancer metastasis. *Int. J. Cancer* 141, 1091–1109. doi: 10.1002/ijc.30748

Negin, F., and Brémond, F. (2019). An unsupervised framework for online spatiotemporal detection of activities of daily living by hierarchical activity models. *Sensors (Basel)* 19, 1–27. doi: 10.3390/s19194237

Nguyen, M., De Ninno, A., Mencattini, A., Mermet-Meillon, F., Fornabaio, G., Evans, S. S., et al. (2018). Dissecting effects of anti-cancer drugs and cancer-associated fibroblasts by on-chip reconstitution of immunocompetent tumor microenvironments. *Cell Rep.* 25, 3884–3893.e3. doi: 10.1016/j.celrep.2018.12.015

Nie, D., Trullo, R., Lian, J., Wang, L., Petitjean, C., Ruan, S., et al. (2018). Medical image synthesis with deep convolutional adversarial networks. *IEEE Trans. Biomed. Eng.* 65, 2720–2730. doi: 10.1109/TBME.2018.2814538

Olszewski, W. L. (2003). The lymphatic system in body homeostasis: physiological conditions. *Lymphat. Res. Biol.* 1, 11–21; discussion 21–4. doi: 10.1089/15396850360495655

Parlato, S., De Ninno, A., Molfetta, R., Toschi, E., Salerno, D., Mencattini, A., et al. (2017). 3D Microfluidic model for evaluating immunotherapy efficacy by tracking dendritic cell behaviour toward tumor cells. *Sci. Rep.* 7:1093. doi: 10.1038/s41598-017-01013-x

Patra, B., Lafontaine, J., Bavoux, M., Zerouali, K., Glory, A., Ahanj, M., et al. (2019). On-chip combined radiotherapy and chemotherapy testing on soft-tissue sarcoma spheroids to study cell death using flow cytometry and clonogenic assay. *Sci. Rep.* 9:2214. doi: 10.1038/s41598-019-38666-9

Pavesi, A., Tan, A. T., Koh, S., Chia, A., Colombo, M., Antonecchia, E., et al. (2017). A 3D microfluidic model for preclinical evaluation of TCR-engineered T cells against solid tumors. *JCI Insight* 2:89762. doi: 10.1172/jci.insight.89762

Perner, H., and Perner, P. (2009). Similarity-based motion tracking of cells in microscopic images. *Stud. Health Technol. Inform.* 150, 851–855.

Powley, I. R., Patel, M., Miles, G., Pringle, H., Howells, L., Thomas, A., et al. (2020). Patient-derived explants (PDEs) as a powerful preclinical platform for anti-cancer drug and biomarker discovery. *Br. J. Cancer* 122, 735–744. doi: 10.1038/s41416-019-0672-6

Qian, K., Yan, B., and Xiong, Y. (2020). The application of chemometrics for efficiency enhancement and toxicity reduction in cancer treatment with combined therapy. *Curr. Drug Deliv.* doi: 10.2174/1567201817999200817152235

Qin, H., Zhang, V., Bok, R. A., Santos, R. D., Cunha, J. A., Hsu, C., et al. (2020). Simultaneous metabolic and perfusion imaging using hyperpolarized. *Int. J. Radiat. Oncol. Biol. Phys.* 107, 887–896. doi: 10.1016/j.ijrobp.2020.04.022

Rajkomar, A., Dean, J., and Kohane, I. (2019). Machine learning in medicine. *N. Engl. J. Med.* 380, 1347–1358. doi: 10.1056/NEJMra1814259

Ramesh, A. N., Kambhampati, C., Monson, J. R., and Drew, P. J. (2004). Artificial intelligence in medicine. *Ann. R. Col. Surg. Engl.* 86, 334–338. doi: 10.1308/147870804290

Reardon, S. (2015). 'Organs-on-chips' go mainstream. *Nature* 523:266. doi: 10.1038/523266a

Rebelo, S. P., Dehne, E. M., Brito, C., Horland, R., Alves, P. M., and Marx, U. (2016). Validation of Bioreactor and human-on-a-chip devices for chemical safety assessment. *Adv. Exp. Med. Biol.* 856, 299–316. doi: 10.1007/978-3-319-33826-2_12

Reza, K. K., Sina, A. A., Wuethrich, A., Grewal, Y. S., Howard, C. B., Korbie, D., et al. (2019). A SERS microfluidic platform for targeting multiple soluble immune checkpoints. *Biosens. Bioelectron.* 126, 178–186. doi: 10.1016/j.bios.2018.10.044

Ruddle, N. H. (2016). High endothelial venules and lymphatic vessels in tertiary lymphoid organs: characteristics, functions, and regulation. *Front. Immunol.* 7:491. doi: 10.3389/fimmu.2016.00491

Sackmann, E. K., Fulton, A. L., and Beebe, D. J. (2014). The present and future role of microfluidics in biomedical research. *Nature* 507, 181–189. doi: 10.1038/nature13118

Sahoo, A., and Narayanan, V. (2019). Optimization of sampling intervals for tracking control of nonlinear systems: a game theoretic approach. *Neural. Netw.* 114, 78–90. doi: 10.1016/j.neunet.2019.02.008

Saleemi, I., Shafique, K., and Shah, M. (2009). Probabilistic modeling of scene dynamics for applications in visual surveillance. *IEEE Trans. Pattern. Anal. Mach. Intell.* 31, 1472–1485. doi: 10.1109/TPAMI.2008.175

Sanmamed, M. F., Chester, C., Melero, I., and Kohrt, H. (2016). Defining the optimal murine models to investigate immune checkpoint blockers and their combination with other immunotherapies. *Ann. Oncol.* 27, 1190–1198. doi: 10.1093/annonc/mdw041

Schiavoni, G., Gabriele, L., and Mattei, F. (2013). The tumor microenvironment: a pitch for multiple players. *Front. Oncol.* 3:90. doi: 10.3389/fonc.2013.00090

Serna-Márquez, N., Rodríguez-Hernández, A., Ayala-Reyes, M., Martínez-Hernández, L. O., Peña-Rico, M., Carretero-Ortega, J., et al. (2020). Fibrillar collagen type i participates in the survival and aggregation of primary hepatocytes cultured on soft hydrogels. *Biomimetics (Basel)* 5:30. doi: 10.3390/biomimetics5020030

Shin, K., Klosterhoff, B. S., and Han, B. (2016). Characterization of cell-type-specific drug transport and resistance of breast cancers using tumor-microenvironment-on-chip. *Mol. Pharm.* 13, 2214–2223. doi: 10.1021/acs.molpharmaceut.6b00131

Sidey-Gibbons, J. A. M., and Sidey-Gibbons, C. J. (2019). Machine learning in medicine: a practical introduction. *BMC Med. Res. Methodol.* 19:64. doi: 10.1186/s12874-019-0681-4

Simmons, M. N., Ching, C. B., Samplaski, M. K., Park, C. H., and Gill, I. S. (2010). Kidney tumor location measurement using the C index method. *J. Urol.* 183, 1708–1713. doi: 10.1016/j.juro.2010.01.005

Skardal, A., Shupe, T., and Atala, A. (2016). Organoid-on-a-chip and body-on-a-chip systems for drug screening and disease modeling. *Drug Discov. Today* 21, 1399–1411. doi: 10.1016/j.drudis.2016.07.003

Snell, L. M., Lin, G. H., and Watts, T. H. (2012). IL-15-dependent upregulation of GITR on CD8 memory phenotype T cells in the bone marrow relative to spleen and lymph node suggests the bone marrow as a site of superior bioavailability of IL-15. *J. Immunol.* 188, 5915–5923. doi: 10.4049/jimmunol.1103270

Song, X., Qi, W., Guo, J., Sun, L., Ding, A., Zhao, G., et al. (2020). Immune checkpoint inhibitor combination therapy for gastric cancer: research progress. *Oncol. Lett.* 20:46. doi: 10.3892/ol.2020.11905

Sontheimer-Phelps, A., Hassell, B. A., and Ingber, D. E. (2019). Modelling cancer in microfluidic human organs-on-chips. *Nat. Rev. Cancer* 19, 65–81. doi: 10.1038/s41568-018-0104-6

Sung, J. H. (2020). A body-on-a-chip (BOC) system for studying gut-liver interaction. *Methods Cell Biol.* 158, 1–10. doi: 10.1016/bs.mcb.2020.01.003

Sung, J. H., and Shuler, M. L. (2009). A micro cell culture analog (microCCA) with 3-D hydrogel culture of multiple cell lines to assess metabolism-dependent cytotoxicity of anti-cancer drugs. *Lab. Chip.* 9, 1385–1394. doi: 10.1039/b901377f

Swayden, M., Soubeyran, P., and Iovanna, J. (2019). Upcoming revolutionary paths in preclinical modeling of pancreatic adenocarcinoma. *Front. Oncol.* 9:1443. doi: 10.3389/fonc.2019.01443

Thiemann, M., Oertel, S., Ehemann, V., Weichert, W., Stenzinger, A., Bischof, M., et al. (2012). In vivo efficacy of the histone deacetylase inhibitor suberoylanilide hydroxamic acid in combination with radiotherapy in a malignant rhabdoid tumor mouse model. *Radiat. Oncol.* 7:52. doi: 10.1186/1748-717X-7-52

Tian, S., Cyr, A., Zeise, K., Bryce, S. M., Hall, N., Bemis, J. C., et al. (2020). 3Rs-friendly approach to exogenous metabolic activation that supports high-throughput genetic toxicology testing. *Environ. Mol. Mutagen.* 61, 408–432. doi: 10.1002/em.22361

Torres-Simón, A., Marino, M. H., Gómez-Cruz, C., Cañadas, M., Marco, M., Ripoll, J., et al. (2020). Development of an inverted epifluorescence microscope for long-term monitoring of bacteria in multiplexed microfluidic devices. *Sensors (Basel)* 20:140. doi: 10.3390/s20154140

Tucci, M., Passarelli, A., Mannavola, F., Felici, C., Stucci, L. S., Cives, M., et al. (2019). Immune System evasion as hallmark of melanoma progression: the role of dendritic cells. *Front. Oncol.* 9:1148. doi: 10.3389/fonc.2019.01148

Vacchelli, E., Ma, Y., Baracco, E. E., Sistigu, A., Enot, D. P., Pietrocola, F., et al. (2015). Chemotherapy-induced antitumor immunity requires formyl peptide receptor 1. *Science* 350, 972–978. doi: 10.1126/science.aad0779

Vinken, M. (2020). 3Rs toxicity testing and disease modeling projects in the European Horizon 2020 research and innovation program. *EXCLI J.* 19, 775–784. doi: 10.17179/excli2020-1463

Vunjak-Novakovic, G., Bhatia, S., Chen, C., and Hirschi, K. (2013). HeLiVa platform: integrated heart-liver-vascular systems for drug testing in human health and disease. *Stem. Cell Res. Ther.* 4(Suppl. 1):S8. doi: 10.1186/scrt369

Wainberg, M., Merico, D., Delong, A., and Frey, B. J. (2018). Deep learning in biomedicine. *Nat. Biotechnol.* 36, 829–838. doi: 10.1038/nbt.4233

Wang, L., Li, Z., Xu, C., and Qin, J. (2019). Bioinspired engineering of organ-on-chip devices. *Adv. Exp. Med. Biol.* 1174, 401–440. doi: 10.1007/978-981-13-9791-2_13

Wang, Y., Fang, H., Yang, D., Zhao, H., and Deng, M. (2019). Network clustering analysis using mixture exponential-family random graph models and its application in genetic interaction data. *IEEE/ACM Trans. Comput. Biol. Bioinform.* 16, 1743–1752. doi: 10.1109/TCBB.2017.2743711

Wang, Y., Wu, D., Wu, G., Wu, J., Lu, S., Lo, J., et al. (2020). Metastasis-on-a-chip mimicking the progression of kidney cancer in the liver for predicting treatment efficacy. *Theranostics* 10, 300–311. doi: 10.7150/thno.38736

Wimalachandra, D. C., Li, Y., Liu, J., Shikha, S., Zhang, J., Lim, Y. C., et al. (2019). Microfluidic-based immunomodulation of immune cells using upconversion nanoparticles in simulated blood vessel-tumor system. *ACS Appl. Mater. Interfaces* 11, 37513–37523. doi: 10.1021/acsami.9b15178

Wong, A. P., Perez-Castillejos, R., Christopher Love, J., and Whitesides, G. M. (2008). Partitioning microfluidic channels with hydrogel to construct tunable 3-D cellular microenvironments. *Biomaterials* 29, 1853–1861. doi: 10.1016/j.biomaterials.2007.12.044

Xu, Y., Jiang, B., and Yang, H. (2020). Two-level game-based distributed optimal fault-tolerant control for nonlinear interconnected systems. *Ieee Trans. Neural. Netw. Learn. Syst.* 31, 4892–4906. doi: 10.1109/TNNLS.2019.2958948

Xue, H., and Fung, Y. C. (1989). Persistence of asymmetry in nonaxisymmetric entry flow in a circular cylindrical tube and its relevance to arterial pulse wave diagnosis. *J. Biomech. Eng.* 111, 37–41. doi: 10.1115/1.3168337

Xue, J., Wang, B., Ming, Y., Liu, X., Jiang, Z., Wang, C., et al. (2020). Deep learning-based detection and segmentation-assisted management of brain metastases. *Neuro. Oncol.* 22, 505–514. doi: 10.1093/neuonc/noz234

Yamashita, T., Kawaguchi, H., Masuda, N., Kitada, M., Narui, K., Hattori, M., et al. (2020). Efficacy of the eribulin, pertuzumab, and trastuzumab combination therapy for human epidermal growth factor receptor 2-positive advanced or metastatic breast cancer: a multicenter, single arm, phase II study (JBCRG-M03 study). *Invest. New Drugs* 39, 217–225. doi: 10.1007/s10637-020-00991-6

Yang, M., Li, C. W., and Yang, J. (2002). Cell docking and on-chip monitoring of cellular reactions with a controlled concentration gradient on a microfluidic device. *Anal. Chem.* 74, 3991–4001. doi: 10.1021/ac025536c

Yang, Q., Li, N., Zhao, Z., Fan, X., Chang, E. I., and Xu, Y. (2020). MRI cross-modality image-to-image translation. *Sci. Rep.* 10:3753. doi: 10.1038/s41598-020-60520-6

Zhang, C., Zhao, Z., Abdul Rahim, N. A., van Noort, D., and Yu, H. (2009). Towards a human-on-chip: culturing multiple cell types on a chip with compartmentalized microenvironments. *Lab. Chip.* 9, 3185–3192. doi: 10.1039/b915147h

Zhang, W., Zeng, J., Huang, Q., Liu, Z., and Li, J. (2020). The feasibility analysis of calculating proptosis by simple Pythagorean theorem. *Eur. J. Ophthalmol.* 20:1120672120901704. doi: 10.1177/1120672120901704

Zhao, Q., Wang, S., Xie, Y., Zheng, W., Wang, Z., Xiao, L., et al. (2012). A rapid screening method for wound dressing by cell-on-a-chip device. *Adv. Healthc. Mater.* 1, 560–566. doi: 10.1002/adhm.201200008

Zhu, G., Wang, K., Qin, H., Zhao, X., Chen, W., Xu, L., et al. (2020). Internal cross-linked polymeric nanoparticles with dual sensitivity for combination therapy of muscle-invasive bladder cancer. *J. Nanobiotechnol.* 18:124. doi: 10.1186/s12951-020-00686-3

Zielinski, D. C., Jamshidi, N., Corbett, A. J., Bordbar, A., Thomas, A., and Palsson, B. O. (2017). Systems biology analysis of drivers underlying hallmarks of cancer cell metabolism. *Sci. Rep.* 7:41241. doi: 10.1038/srep41241

Conflict of Interest: The authors declare that the research was conducted in the absence of any commercial or financial relationships that could be construed as a potential conflict of interest.

frontiers in Bioengineering and Biotechnology

ORIGINAL RESEARCH
published: 26 May 2021
doi: 10.3389/fbioe.2021.624553

A Multitubular Kidney-on-Chip to Decipher Pathophysiological Mechanisms in Renal Cystic Diseases

Sarah Myram[1], Bastien Venzac[1†], Brice Lapin[1†], Aude Battistella[1], Fanny Cayrac[1], Bertrand Cinquin[2], Charles Cavaniol[1,3], Giacomo Gropplero[1], Isabelle Bonnet[1], Sophie Demolombe[4], Stéphanie Descroix[1†] and Sylvie Coscoy[1*†]*

[1] Institut Curie, Université PSL (Paris Sciences & Lettres), Sorbonne Université, CNRS UMR 168, Laboratoire Physico Chimie Curie, Paris, France, [2] Institut Pierre-Gilles de Gennes, IPGG Technology Platform, UMS 3750 CNRS, Paris, France, [3] Fluigent SA, France, [4] Université Côte d'Azur, Centre National de la Recherche Scientifique, Institut National de la Santé et de la Recherche Médicale, Institut de Pharmacologie Moléculaire et Cellulaire, Labex ICST, Valbonne, France

OPEN ACCESS

Edited by:
Shi-Cong Tao,
Shanghai Jiao Tong University, China

Reviewed by:
Hayne Park,
Kangnam Sacred Heart Hospital, South Korea
Gopi Rangan,
Westmead Institute for Medical Research, Australia

***Correspondence:**
Stéphanie Descroix
Stephanie.Descroix@curie.fr
Sylvie Coscoy
Sylvie.Coscoy@curie.fr

[†] These authors have contributed equally to this work

Specialty section:
This article was submitted to Nanobiotechnology, a section of the journal Frontiers in Bioengineering and Biotechnology

Received: 31 October 2020
Accepted: 22 March 2021
Published: 26 May 2021

Citation:
Myram S, Venzac B, Lapin B, Battistella A, Cayrac F, Cinquin B, Cavaniol C, Gropplero G, Bonnet I, Demolombe S, Descroix S and Coscoy S (2021) A Multitubular Kidney-on-Chip to Decipher Pathophysiological Mechanisms in Renal Cystic Diseases. Front. Bioeng. Biotechnol. 9:624553. doi: 10.3389/fbioe.2021.624553

Autosomal Dominant Polycystic Kidney Disease (ADPKD) is a major renal pathology provoked by the deletion of *PKD1* or *PKD2* genes leading to local renal tubule dilation followed by the formation of numerous cysts, ending up with renal failure in adulthood. *In vivo*, renal tubules are tightly packed, so that dilating tubules and expanding cysts may have mechanical influence on adjacent tubules. To decipher the role of this coupling between adjacent tubules, we developed a kidney-on-chip reproducing parallel networks of tightly packed tubes. This original microdevice is composed of cylindrical hollow tubes of physiological dimensions, parallel and closely packed with 100–200 μm spacing, embedded in a collagen I matrix. These multitubular systems were properly colonized by different types of renal cells with long-term survival, up to 2 months. While no significant tube dilation over time was observed with Madin-Darby Canine Kidney (MDCK) cells, wild-type mouse proximal tubule (PCT) cells, or with PCT *Pkd1*$^{+/-}$ cells (with only one functional *Pkd1* allele), we observed a typical 1.5-fold increase in tube diameter with isogenic PCT *Pkd1*$^{-/-}$ cells, an ADPKD cellular model. This tube dilation was associated with an increased cell proliferation, as well as a decrease in F-actin stress fibers density along the tube axis. With this kidney-on-chip model, we also observed that for larger tube spacing, PCT *Pkd1*$^{-/-}$ tube deformations were not spatially correlated with adjacent tubes whereas for shorter spacing, tube deformations were increased between adjacent tubes. Our device reveals the interplay between tightly packed renal tubes, constituting a pioneering tool well-adapted to further study kidney pathophysiology.

Keywords: ADPKD, microfabrication, tube deformation, hydrogel, kidney-on-chip

INTRODUCTION

Autosomal Dominant Polycystic Kidney Disease (ADPKD) is the most common genetic renal disease (incidence 1/1,000), and the fourth most common cause of end-stage renal failure worldwide, without curative therapies except dialysis or transplantation (Ghata and Cowley, 2017; Li, 2017). It is due to mutations in *PKD1* (85% of cases) or *PKD2* (15% of cases) genes that code for

transmembrane proteins, polycystins 1 and 2 (PC1 and PC2), whose expression level is fundamental to maintain the renal epithelium architecture (Lu et al., 1997; Rossetti et al., 2009). Polycystins are involved in many signaling pathways coupled to proliferation, apoptosis, cell cycle, planar polarity and the regulation of cell adhesion and cytoskeleton organization (Chapin and Caplan, 2010; Castelli et al., 2013; Mochizuki et al., 2013; Cornec-Le Gall et al., 2019; Douguet et al., 2019).

ADPKD is characterized by enlarged kidneys in which progressive numerous and bilateral fluid-filled cysts extend from renal tubular epithelial cells (Grantham et al., 1987; Fick et al., 1993; Chapin and Caplan, 2010; Cornec-Le Gall et al., 2019). Fundamental mechanisms involved in cystogenesis are based on increased proliferation of epithelial tubular cells (Terzi et al., 1996; Yamaguchi et al., 2003; Cowley et al., 2006; Grimm et al., 2006; Lee, 2016) coupled with de-regulated apoptosis (Boca et al., 2006; Foy et al., 2012; Kurbegovic and Trudel, 2020), loss of planar polarity and misorientation during mitosis (Fischer et al., 2006; Castelli et al., 2013), and remodeling of extracellular matrix (ECM) (Wilson et al., 1992; Schafer et al., 1994; Ramasubbu et al., 1998; Joly et al., 2003; Subramanian et al., 2012). Relying on those mechanisms, human cysts reaching up to 3 mm in diameter detach from the parent tubule and migrate away while continuing expanding (Ghata and Cowley, 2017). Expanding cysts constrain the functional renal parenchyma, and participate to its progressive failure during ADPKD evolution.

Many studies focused on genetic and molecular factors involved in cystogenesis process during ADPKD (Chapin and Caplan, 2010; Cornec-Le Gall et al., 2014). However, the prominent influence of geometrical and mechanical factors has not yet been investigated. Recent studies on ADPKD patients and specific mice models suggest that primary cysts are randomly formed along the renal tubules, but that secondary cyst formation tends to be spatially clustered. An exponential increase in the probability of secondary cyst formation over time was even reported (Leonhard et al., 2015), in relation with the exponential growth in total kidney volume observed for patients (Grantham et al., 2006, 2008). These cascading events led to the snowball effect theory, relating that primary cyst growth would trigger secondary cyst formation in adjacent tubes and favor abnormal signaling pathways activation within renal epithelial cells. Indeed, neighboring non-cystic tubules were reported to have increased proliferation and apoptosis in the presence of cysts (Nadasdy et al., 1995; Woo, 1995; Grantham et al., 2011).

This snowball effect may be due to chemical coupling between adjacent tubes (El-Achkar and Dagher, 2015), combined or not to local mechanical alterations. Expanding cysts or dilating tubules may exert a mechanical influence on adjacent tubules, either by direct cell compression, or by flow disturbance due to the locally altered shape of tubules (Grantham et al., 2011). It is noteworthy that polycystins are key molecular actors in the control of mechanotransduction in renal tubules (Qian et al., 2005; Patel and Honoré, 2010). Polycystins are present in primary cilia, where their role as direct flow sensors through PC2 channel activity is still debated (Nauli et al., 2003; Delling et al., 2016), as well as in cell-cell and cell-matrix contacts (Huan and van Adelsberg, 1999; Wilson, 2001; Markoff et al., 2007; Lee et al., 2014). They have been centrally involved in mechanosensitive control of cytoskeletal organization and actomyosin contractility (Sharif-Naeini et al., 2009; Bhoonderowa et al., 2016; Nigro et al., 2019). The RhoA-YAP-c-Myc axis has been identified as a key mediator in ADPKD cystogenesis (Happe et al., 2011b; Cai et al., 2018), with YAP mechanosensing (Hippo pathway) playing a central role in the control of the size and shape of tissues and organs.

The geometrical organization of the kidney with densely packed tubules may have a key influence for mechanical or biochemical cross-talks between them. Hence, to decipher the geometrical factors involved in the propagation of deformations between adjacent tubes, we propose here to reproduce those physical properties by developing an array of renal tubules in advanced *in vitro* models called kidney-on-chips. Several microphysiological kidney-on-chips have already been developed to mimic different features of renal tubules, most of them reproducing the proximal tubule-like phenotype and metabolism. The first devices designed were composed of one or two channels in close contact (120–550 μm width) with renal epithelial cells, and were dedicated to the study of renal reabsorption (Jang et al., 2013; Vedula et al., 2017; Lin et al., 2019). More recent works intended to recreate the cylindrical geometry of tubules. Indeed, renal tubules are circular tubes of small diameters (50 μm in the proximal part), and in this range important confinement and curvature effects have been reported for the control of the collective organization of renal cells (Vedula et al., 2012; Yevick et al., 2015). 3D printing techniques were also used to generate circular tubes reproducing the proximal tubule (Homan et al., 2016; Lin et al., 2019), however typically with diameters larger than physiological ones. A versatile technology to generate cylindrical tubes is based on the principle of wire molding (Dolega et al., 2014). It was used to recapitulate the fundamental biochemistry of renal tubular epithelium displaying intracellular enzymatic functions with the vitamin D metabolism (Weber et al., 2016). It was also used to study renal collective dynamics in function of tube diameters (Xi et al., 2017), or to reproduce a change in diameter characteristic for transitions between the different parts of renal tubes (Venzac et al., 2018). While these different approaches have been focused on the study of renal transport function, morphology or collective cell organization, exploring cystic diseases with kidney-on-chips has been scarcely addressed. Recently, microlithography-based approaches were used to generate parallelepiped structures in a collagen-Matrigel matrix, with tube to cyst transition upon cAMP stimulation (Subramanian et al., 2018).

Nevertheless, a kidney-on-chip reproducing the geometry of tightly and cylindrical packed tubules to explore a renal disorder is still missing. In this paper, we report on a microfabrication approach to recapitulate renal tubes of physiological geometries, positioned in parallel with 100 or 200 μm spacing, in a biocompatible and deformable hydrogel. Using this unique device, we studied tube behavior upon seeding with several epithelial renal cell lines, and focused on tube deformation with an ADPKD cellular model.

MATERIALS AND METHODS

Cell Culture

MDCK cells (CCL-34 ATCC, NBL-2), stably expressing Lifeact-GFP, were maintained in DMEM supplemented with 10% FCS and 0.4 mg/ml geneticin at 37°C and 5% CO_2. Mouse PCT-wild type cells, kindly given by Amanda Patel and Eric Honoré (Peyronnet et al., 2012), were maintained in DMEM/HamF12 (Thermo Fisher Scientific) supplemented with 1% SVF, 15 mM $NaHCO_3$, 20 mM HEPES adjusted at pH 7.4 (Thermo Fisher Scientific), 2 mM glutamine, 5 μg/ml insulin (Sigma), 50 nM dexamethasone (Sigma), 1 μg/l EGF (Sigma), 5 mg/l transferrin (Sigma), 30 nM Na selenite (Sigma), 10 nM triiodo-L-thyronine (Sigma) and 125 μg/ml G418 (Sigma), at 37°C, 5% CO_2. Maintained in a T75 flask, both cell types were split twice a week, when they reached around 70–80% of confluence. All cells were rinsed twice with DPBS (Sigma) and trypsinized with 2 ml of 0.05% Trypsin- ethylenediamine tetraacetic acid (EDTA) (Sigma) at 37°C. All the cell lines were used at a low passage in the different experiments: mostly between passage 6 and 20.

Mouse PCT *Pkd1*$^{+/-}$ and *Pkd1*$^{-/-}$ cells (respectively, PH2 and PN24 clones) were a kind gift of S. Somlo (Joly et al., 2006; Shibazaki et al., 2008; Wei et al., 2008). These cells, containing the Immortomouse transgene for the interferon-inducible expression of a thermolabile large tumor antigen, were amplified in proliferation conditions (33°C, with γ-interferon) and differentiated in differentiation conditions (37°C, without γ-interferon). Proliferation conditions were 33°C, 5% CO_2, in DMEM/HamF12 supplemented with 3% SVF, 7.5 nM Na selenite, 1.9 nM triiodo-L-thyronine, 5 mg insulin, 5 mg transferrin, 100 UI/ml penicillin/streptomycin, 5 mg/ml nystatin (all from Sigma), and 10 UI/ml γ-interferon (Millipore). Cells were differentiated in the same media without γ-interferon, and with 1% SVF instead of 3% SVF, at 37°C, 5% CO_2. For 2D immunofluorescence and qRT-PCR experiments, cells were cultured in this medium 7 days before using them in the experiments, at 37°C with 5% CO_2, to favor cell epithelialization. According to S. Somlo's group's specifications, we confirmed by PCR on genomic DNA the presence of a null *Pkd1* allele on exon 1, the insertion of *lox* sites flanking exons 2–4 in one allele of *Pkd1*$^{+/-}$ cells, and the deletion of this floxed *Pkd1* part in *Pkd1*$^{-/-}$ cells.

qRT-PCR Experiments

2D data correspond to PCT cells differentiated for more than 1 week in differentiation media. Primer sequences, designed with: https://www.ncbi.nlm.nih.gov/tools/primer-blast, were as follow. Primer efficiency was measured on 4 serial dilutions from 1× to 1,000× cDNA. The efficiency E was calculated according to $E = 10^{1/slope}$. Efficiencies calculated were between 93 and 111%. mATP1A1 primers were found on Origene (atp1a1-mouse-qpcr-primer-pair-nm_144900). See SI for the sequences of primers.

Total RNA was extracted from differentiated cells using NucleoSpin RNA (Macherey-Nagel). Reverse transcription reactions were performed on 2 μg of total RNA with the high-capacity cDNA reverse transcription kit (Thermo Fisher Scientific) with random hexamers, and mixed with the Applied Biosystems™ PowerUp™ SYBR™ Green Master Mix (Thermo Fisher Scientific) and 5 pmol of both forward and reverse primers (see below). cDNA was diluted 50×. Real-time PCR was carried out using a SteponePlus PCR system (Thermo Fisher Scientific) with the following cycles: 95°C for 10 min (95°C for 15 sec, 60°C for 1 min) × 40 times and read plate. Melting curves from 55 to 95°C (read every 1°C and hold 1 s) were generated. Reactions were run in technical triplicates. Expression data were normalized to the GAPDH housekeeping gene. Analyze used DeltaCt between target and normalizator, then $2^{-DeltaCt}$. Statistical *t*-tests were performed on DeltaCt values. *Pkd1*$^{-/-}$ vs. *Pkd1*$^{+/-}$ fold values are represented.

Microfabrication and Device Design

The design of the chip was first drawn with Catya (Dassault Systems, France) and milled on a 50 × 50 × 3 mm brass bloc with a micromilling machine (Minitech, Georgia, United States). The patterns were then transferred via hot embossing (130°C, 7 bars, 10 min) on a 2-mm thick Cyclic Olefin Copolymer (COC, TOPAS 8007-04) plate, a thermoplastic displaying an optimal optical index for the tubes visualization under a microscope (Mottet et al., 2014). On the COC plate, the patterns comprised a rectangular reservoir (1 mm wide, 5 mm long and 300 μm deep) in which the tubes were molded in collagen I, five 1 mm long, 90 μm wide and 90 μm deep grooves on each side of the reservoir, separated by 100 or 200 μm and in which the wires to mold the tubes were positioned (see **Figure 1**). Two connectors with a semi cylindrical bottom at the side of the COC plate were placed at both extremities of those grooves, with a continuous transition. Liquids and cells were injected through those two connectors.

In order to obtain an adequate covalent adhesion of collagen I, the COC reservoir surface was first treated with an oxygen plasma (Cute, Femto Science, South Korea) at 50 W, 50 kHz, 0.7 mbar during 1 min, and then silanized with 2% of (3-Aminopropyl) triethoxysilane (Sigma) in Phosphate Buffer Saline (Sigma) followed by 0.5% of glutaraldehyde in PBS, each incubation lasting 30 min at room temperature. Between both incubations, the chip was washed three times in deionized water before immersing it in water, and incubating it at 4°C overnight. Two short silicone tubings were bonded in the connectors with epoxy glue (Sader). Then, five tungsten wires of 80 μm diameter (Goodfellow, United Kingdom) were first incubated during 30 min at room temperature in a 1% bovine serum albumin (BSA) solution in PBS, then gathered through the two silicone tubings before being positioned in the grooves of this COC base. Afterward, the COC plate was covered with a pressure sensitive PCR tape (ThermalSeal RTS™, Excel Scientific, Sigma) except for the reservoir which stayed open (Serra et al., 2017). Finally, the central reservoir and the connectors were then incubated in degassed and filtered PBS for 1 h, at 37°C to absorbed bubbles forming at the grooves. Collagen I mix was prepared on ice by mixing collagen I from rat tail (Corning), PBS 10X, NaOH 1N and distilled water to obtain a final collagen concentration of 6 mg/ml at pH 7. As the collagen I mix is highly sensitive to temperature changes, the collagen I mix was continuously kept on ice at 4°C, and was gently blended with an appropriate

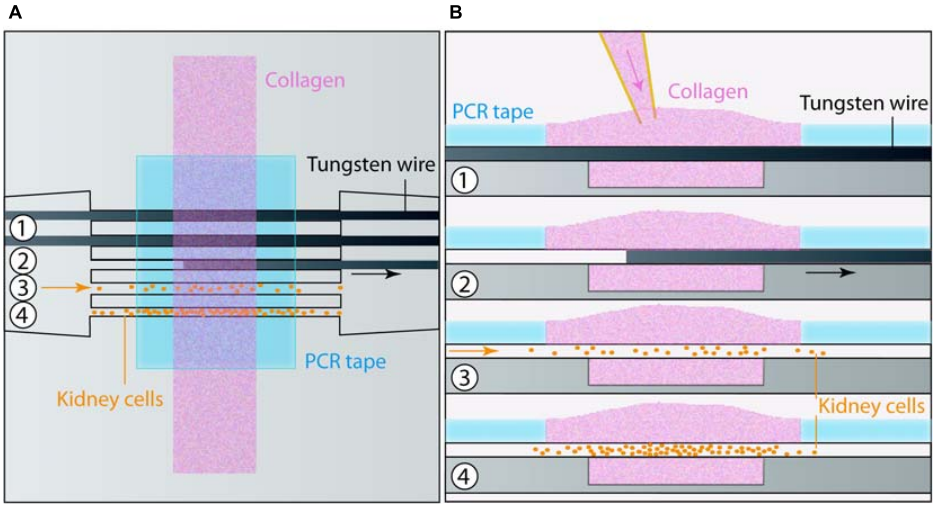

FIGURE 1 | Chip microfabrication and cell seeding. **(A)** Top and **(B)** side views of the sequential steps for microfabrication and cell seeding: (1) Collagen was poured on top of the tungsten wires placed in a micromold and maintained by PCR tape. (2) Wires were removed. At this stage an additional coating could be applied. (3) Cells were seeded in tubes, and (4) colonized it in a few days.

spatula before being centrifuged less than 30 s to prevent air bubbles trapping and to pull them up, respectively. Afterward, the degassed PBS was removed from the COC plate beforehand put at 4°C during 15 min, and replaced with 80 µl of collagen I mix, gently poured above the open reservoir. The whole set-up was incubated at 37°C, 5% CO_2 and under humidified atmosphere for 2 h, before placing a PBS droplet above the collagen I mix to keep it wet. This last step was crucial to shape empty tubes: the polymerized collagen I never stayed dry. Eventually, after collagen I polymerization, wires were gently removed through the connectors in order to get five empty cylindrical microchannels. From this step, the chip remained immersed in PBS or cell culture medium after the seeding.

Coating and Cell Culture On-Chip

Once empty tubes in collagen I were shaped, they were covered with a thin layer of different proteins composing the ECM for 1 h, at 37°C, before cell seeding. Several proteins were individually investigated: collagen IV (Sigma), laminin (Sigma), and Matrigel (Corning; derived from the basal lamina secreted by a murine tumor, composed of many different proteins). To this end, laminin (Sigma) coupled or not with a fluorescent dye, rhodamin (Laminin-Rhodamin, Tebu-bio), was diluted in culture medium (0.02 mg/ml), as well as Matrigel (50:50). Collagen IV was mixed with water and NaOH 1N to reach a final concentration of 0.5 mg/ml. An acid acetic solution was used to adjust its pH to 7.4 (neutral pH). Afterward, 50 µl of those different coating proteins were slowly and gently manually injected with a P10 pipette in the collagen I tubes from a connector. The chip was then immersed in PBS, and incubated at 37°C, under humidified atmosphere, with 5% CO_2 for 1 h. The channels were finally washed twice with PBS, and seeded.

Cells were concentrated at 5.10^6 cells/ml in the appropriate culture medium. The MDCK cells were directly and carefully injected by pipetting within the tubes. However, they quickly passed through the tubes, decreasing the cell adhesion probability on the channel walls. Consequently, *Pkd1* cells that were smaller after the trypsinization step, were concentrated at 5.10^6 cells/ml in differentiation medium mixed with 4% Dextran (70 kDa, Sigma). As for the coating proteins, cells were slowly and gently injected manually in the tubes, with a P10 pipette, to prevent air bubbles entry as much as possible with a liquid-liquid interface between the connector and the pipette tip. It was usually realized on both sides of the chip, through the two connectors. After the cell seeding, the chip was immersed in 8 ml of cell culture medium, in a Petri dish placed in the incubator, at 37°C, 5% CO_2 atmosphere. Half of the medium was changed every 2 or 3 days and cells were followed during several weeks (generally more than 3 weeks).

3D Cell Labelling and Imaging

For live cells experiments lining the tubes, bright light images were acquired every 2–5 days with a cell culture microscope (Leica). For immunostaining experiments, chips were washed three times with PBS containing $CaCl_2$ and $MgCl_2$ (Sigma), then fixed with 4% paraformaldehyde for 15 min at room temperature: 3 ml of each solution were successively deposited on collagen I. During all the immunostaining protocol, the collagen I scaffold remained immersed in liquid to prevent it from drying. Carefully detached from the COC surface with thin tweezers, the collagen I scaffold was then immersed in a permeabilization buffer composed of 0.1% Triton X-100 (LifeTechnologies) and 2% BSA (Sigma) diluted in PBS for 5 min. The collagen I scaffold was then washed again three times with PBS to remove Triton X-100, and blocked in a solution of PBS with 4% BSA-0.1% Tween 20 for 2 h at room temperature, and under humidified atmosphere. For F-actin labeling, the tubular scaffold was labeled with phalloidin-TRITC (Sigma) and nuclei were

counterstained with Hoechst (Sigma), in a humidified chamber and at room temperature for 45 min. Rinsed three times with the blocking buffer for 30 min each, the collagen I scaffold was then mounted with the VectaShield mounting medium (Vector Laboratories) in a homemade PDMS chamber, and imaged under a confocal microscope (Zeiss, PICT-IBiSA Imaging platform from Institut Curie).

Image Representation and Analysis

Images acquired were analyzed on ImageJ software (NIH). For visual representation in figures, color balance was individually adjusted for each image. For some images in **Figure 3**, a denoising was performed with Safir ImageJ plugin (Kervrann and Boulanger, 2006).

For analysis of 3D confocal stacks at high resolution, *Pkd1*$^{+/-}$ and *Pkd1*$^{-/-}$ tube diameters in a horizontal section were manually measured at the center part of the field. Quantification of cell density was performed by manually counting nuclei on 100 × 50 μm^2 area, randomly chosen for each image at the middle of the inferior half of the tube. Four images (over 28) with *Pkd1*$^{+/-}$ tubes of aberrant sizes (superior to 125 μm), very likely corresponding to initial aberrant tubes, were removed from analysis. A home-written ImageJ macro was also developed in order to analyze confocal high-resolution images, and was used here to check shape modifications induced by *Pkd1*$^{-/-}$ culture. Sequential steps were (1) enhancing of the local contrast of each image with the CLAHE plugin, (2) reducing the background noise, (3) fitting the external contour of the F-actin labeled tubes with an ellipse, producing an envelope of the tube and its transversal section over its length.

For F-actin orientation analysis in tubes, the ImageJ OrientationJ plugin was used (written by Daniel Sage at the Biomedical Image Group (BIG), EPFL, Switzerland)[1] (Rezakhaniha et al., 2012). Briefly, for each pixel-centered window, the orientation is analyzed based on a structure tensor, and both an angle value (local predominant orientation) and a coherency value were obtained. Coherency is a measurement of the "strength" of the local orientation (coherency close to 1 for a strong local orientation, and to 0 for no preferential local orientation), and is defined as the ratio between the difference and the sum of the maximum and minimum tensor eigenvalues.

Images acquired with confocal at high resolution (40× objective) were rotated to yield horizontal tubes, and a maximum *z* projection of the inferior half of the tube (with the highest signal) was performed. The analysis was done on a rectangle corresponding to the center half of the projection (white rectangles in **Figures 4A,D**). This rectangle was drawn in the middle of the projection, where the effects of the curvature of the cylinder are minimal: we thus neglected this curvature in our analysis. "Distribution of orientation" menu was selected, giving a weighted histogram, with weight being the coherency. Histogram values presented were normalized by the surface area of the window (in pixels^2). Following parameters were used: min-coherency = 0, local window σ corresponding to 2 μm (between 5 and 12 pixels depending on image zoom), gradient: cubic spline.

[1]http://bigwww.epfl.ch/demo/orientation/

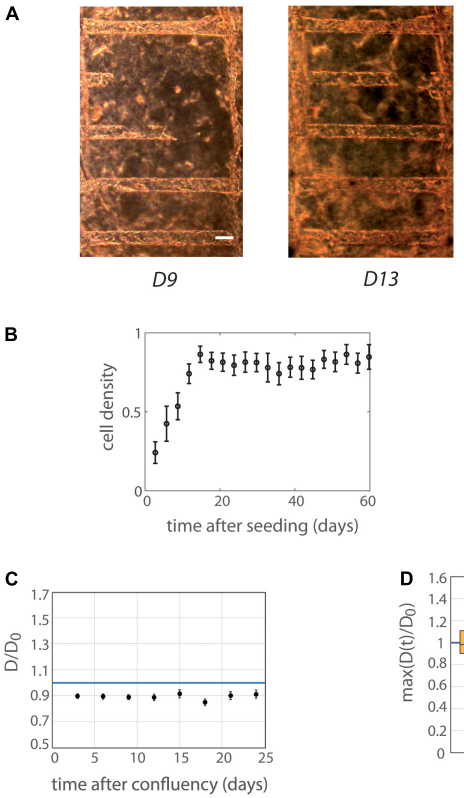

FIGURE 2 | Behavior of MDCK cells in tubes. **(A)** MDCK-Lifeact-GFP cells were seeded within tubes molded in collagen I at 6 mg/ml, and observed under an optical microscope over time. The temporal evolution at days 9 and 13 after seeding is represented (before and at confluency) is represented. Scale bar: 100 μm. **(B)** Mean cell density over time (n = 12 MDCK chips). The temporal scale refers to time after cell seeding for colonization curves. Tubes with or without laminin coating were pooled, because of similar behaviors in these two conditions (see **Supplementary Figure 8** for separated behavior). The mean curve remains below cell density 1 (corresponding to full colonization) reflecting the fact that some tubes were never fully colonized with cells. Error bars: S.E.M. **(C)** Kinetic evolution of mean tubes diameter normalized by diameters at seeding as function of the time after tube confluency. The temporal scale refers to time after confluency for curves of tube deformation. A blue horizontal line at D/D_0 = 1, corresponding to no change in diameter, is indicated. Chips with or without laminin coating were pooled. Each time point corresponds to 19–30 tubes. Error bars: S.E.M. **(D)** Maximum (over time) of the mean normalized diameter. Tubes with or without laminin coating were pooled. Points correspond to individual tube values. Central bar, median; cross, mean; box, values between Q1 and Q3 quartiles; error bars, extreme values [between Q1 - 1.5*(Q3 - Q1) and Q3 + 1.5*(Q3 - Q1)]. **(C,D)** were computed only for tubes having reached full confluency during the observation period.

A parallel analysis was performed with local windows of 8 μm with close results.

For the analysis of tubes along time: after acquisition of time movies of live cells experiments lining the tubes (Δt = 2–5 days, typical images in **Supplementary Figure 2A**), masks of cylindrical channel contours (**Supplementary Figure 2B**, left, day1 corresponding to **Supplementary Figure 2A**) and masks of regions filled with cells (example in **Supplementary Figure 2B**, right) were drawn using a drawing tablet (Cintiq, Wacom,

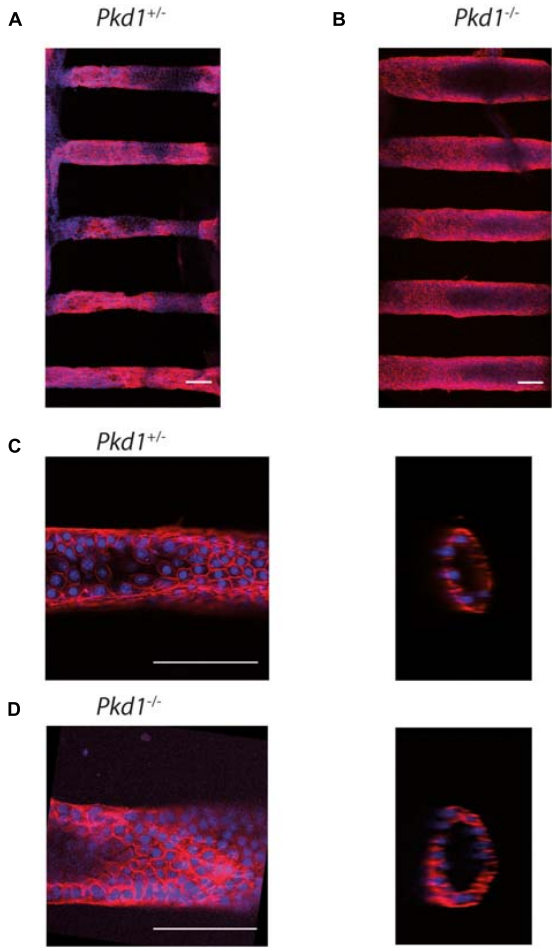

FIGURE 3 | PCT *Pkd1*$^{+/-}$ and *Pkd1*$^{-/-}$ organization in tubes. Cells were labeled for F-actin and nuclei, and imaged at confocal both at low and high resolution to study the global cell organization and F-actin organization. Confocal images of tubes labeled with phalloidin-TRITC (red) and Hoechst (blue). **(A,B)** global organization of *Pkd1*$^{+/-}$ **(A)** and *Pkd1*$^{-/-}$ **(B)** tubes imaged at a low resolution (10× objective). Maximal *z* projections. Mean tube diameters of tubes in the chips shown, as assessed by *z* projection, were, respectively, ∼85 and 135 μm for the chips shown in **(A,B)**, in agreement with *Pkd1*$^{-/-}$ tube deformation. **(C,D)** *Pkd1*$^{+/-}$ **(C)** and *Pkd1*$^{-/-}$ **(D)** tubes imaged at a high resolution (40× objective) in steps corresponding to the first early steps of tube dilation for Pkd1$^{-/-}$ cells. Confocal section (left) and orthogonal projection (right). A median filter (3 pixels) was applied on orthogonal projection images. Scale bar, 100 μm. Mean diameters measured for tubes imaged at high resolution were 85 ± 10 μm for the *Pkd1*$^{+/-}$ condition and 95 ± 5 μm for the *Pkd1*$^{-/-}$ condition for high resolution images (S.D. are indicated). Here 24 images of *Pkd1*$^{+/-}$ tubes and 10 images of *Pkd1*$^{-/-}$ tubes were done (performed, respectively, on 8 and 7 chips).

Japan) and a home-written ImageJ macro. Superimposed images of mask-tubes (green) and mask cells (red) are shown in **Supplementary Figure 2C**: the yellow parts correspond to cells present in channels, the green parts to empty channel regions, the red parts above or under channel to cell "invasion" (protrusions or cells extending in collagen matrix). The analysis shown here is focused on the part of tubes that is common to all channels and all times (**Supplementary Figure 2D**, right): indeed, some chips encountered defects at left or right moieties of the chip along time, mainly due to cell growth from the groove region, that prevented the analysis of the corresponding part of the tube for these time-points. However, total individual channel data (**Supplementary Figure 2D**, left) were also collected, giving only marginal differences in the results.

In more details: first, for a given stack, horizontal contours were extracted from tube masks for diameter analysis (**Supplementary Figure 2E**), with the approximation that tubes were revolution surfaces and that the projection visible on images corresponded to local cylinder diameter. For cell density (**Supplementary Figure 2F**) and invasion (**Supplementary Figure 2H**) analysis, we determined the intersection between cell masks and tube masks (cell areas inside tubes), and cell masks with the exclusion of this intersection (cell invasion); global areas were calculated, as well as local cell densities (in function of *x*, principal direction of the tubes), defined as the sum of contributions of the different cell masks.

Data generated by the analysis of individual stacks were afterward aggregated for global statistics. Tubes with important deformations at initial times were excluded for the analysis (for the whole analysis, it concerned 25 out of 48 × 5 = 240 tubes, i.e., ∼10% of the tubes).

Binned cell densities as a function of time after seeding correspond to following sequential operations: 1. Mean of each tube local diameters along *x*; 2. For each time, mean on the selected tubes in each individual chip; 3. For each time bin (]0 3[days, [3 6[days), mean of the different values if the considered chip has several time points in the considered bin, 4. Mean and S.E.M. (Standard Error of the Mean) of the different chips were calculated (and represented at the upper limit of the binning interval). Correlations reported are the mean between tubes of the correlation coefficients (Matlab corcoeff) at each time, between adjacent external contours of two different tubes (tube correlation), or between the local diameter of one tube and the local spacing of the adjacent intertube. The kinetics of tube deformation were computed as a function of time after confluency, determined independently for each tube. For the study of maximal tube deformation over time, only tubes monitored for at least 6 days after confluency were selected, and we also checked that the results and the difference between conditions were similar considering a similar duration of observation after confluency.

Means and plots were performed on Kaleidagraph, Matlab and and Excel. Error bars refer to S.E.M. unless otherwise specified. *F*- and *t*-tests for statistical analysis were performed on Excel, assuming a normal distribution of the data.

RESULTS

Reproducing Kidney Architecture on Chip

In order to investigate the formation of renal cysts and the likely associated snowball effect, the development of new *in vitro* models recapitulating the tightly packed organization of nephrons in the kidney is necessary. Here we focused on

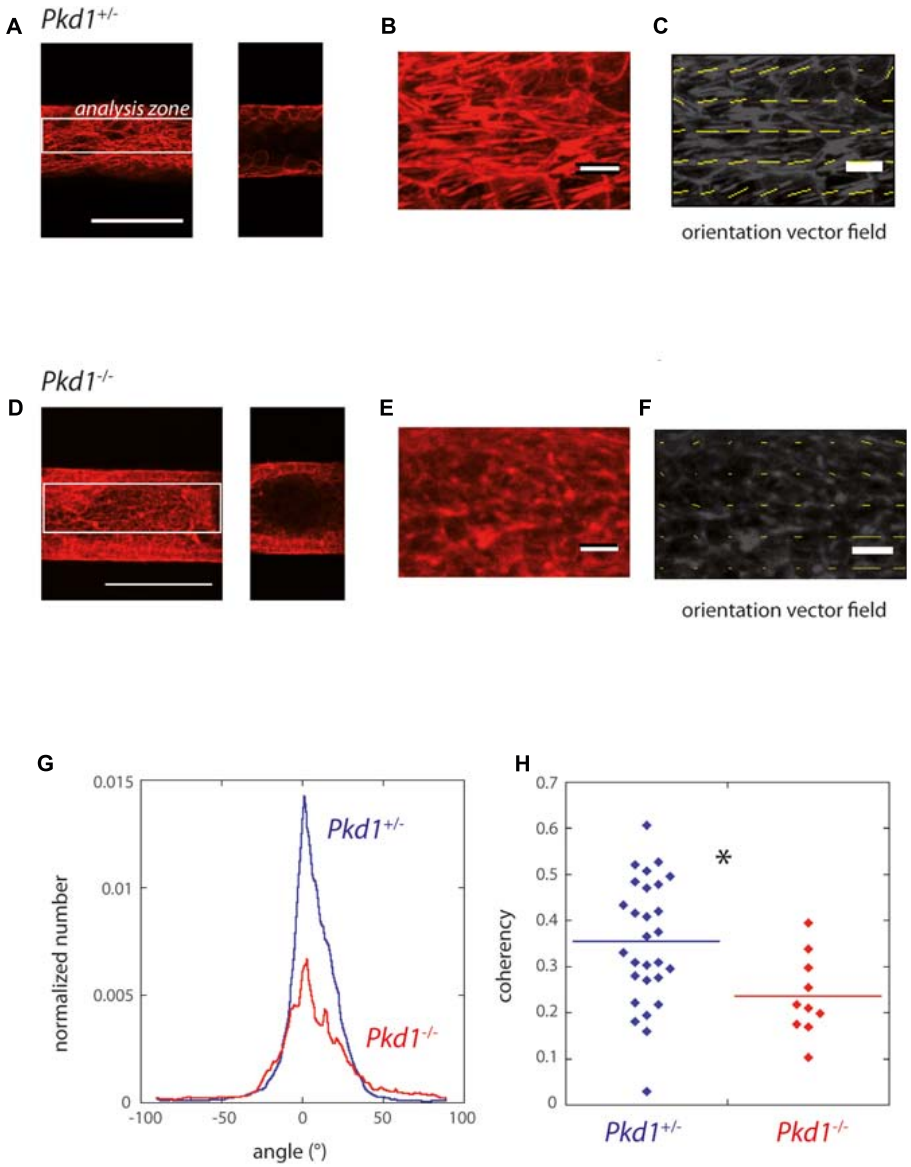

FIGURE 4 | F-actin orientation of PCT *Pkd1*$^{+/-}$ and *Pkd1*$^{-/-}$ cells in tubes. **(A–F)** F-actin labeling in *Pkd1*$^{+/-}$ **(A–C)** and *Pkd1*$^{-/-}$ **(D–F)** tubes. **(A,D)** Left: *z* projection of the inferior half of the tube is shown, scale bar 100 μm. Right, confocal section at the middle of the tube. OrientationJ analysis was performed in a central rectangle corresponding to half of the tube (white rectangle in **A,D**), in order to get rid of border effects. **(B,E)** Zoomed part, **(C,F)** Orientation vector fields (yellow arrows). Magnitude normalized by the strength of orientation (coherency) is represented. Coherency is low in the *Pkd1*$^{-/-}$ condition, so that arrows are barely visible in **(F)**. **(G)** Distribution of F-actin local orientation as assessed by OrientationJ software for PCT *Pkd1*$^{+/-}$ (blue) and *Pkd1*$^{-/-}$ (red) cells. The analysis was done at a subcellular scale, with a 2 μm local analysis window. Histograms given by OrientationJ are pondered by coherency, meaning that the angle determined for a given window has a more important contribution if there is a clear-cut local orientation. Each histogram is normalized by the size of the analyzed area (in pixels^2) before averaging. The analysis was performed on pooled coating conditions (laminin, ECM and collagen), with the majority of tubes corresponding to laminin coating in *Pkd1*$^{-/-}$ and *Pkd*$^{+/-}$ conditions. **(H)** Mean coherency (per pixel) for PCT *Pkd1*$^{+/-}$ (blue) and *Pkd1*$^{-/-}$ (red) cells. *Statistically significant difference with $p < 0.05$. Each point corresponds to one image.

mimicking the geometrical and mechanical characteristics of parallel proximal tubules (the first segment of the nephron). We chose to develop a biomimetic scaffold with aligned, parallel and regularly spaced circular channels in a biocompatible and deformable hydrogel, in order to allow both mechanical and chemical coupling between tubes. Tube diameter should be as close as possible as *in vivo*, in the range of 50 μm for the lumen diameter (Knepper et al., 1977; Xi et al., 2017; Venzac et al., 2018). For that purpose, a microfabrication technique based on wire molding (Dolega et al., 2014; Weber et al., 2016; Venzac et al., 2018) was developed, in which collagen hydrogel was gelled around pre-positioned 80 μm diameter tungsten wires, followed by the removal of the wires to create parallel circular hollow channels in the hydrogel.

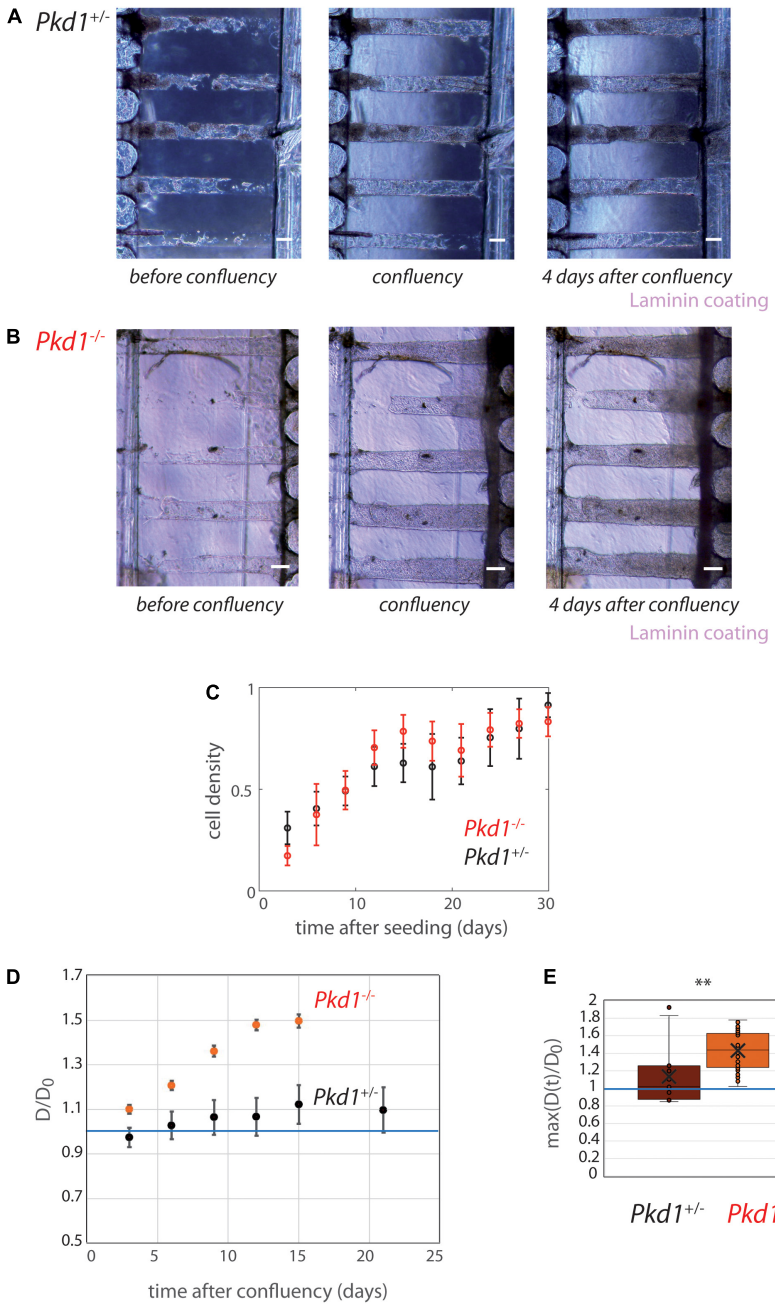

FIGURE 5 | PCT *Pkd1*$^{+/-}$ and *Pkd1*$^{-/-}$ tube deformation in chips with 200 μm spacing. **(A,B)** Examples of temporal evolution of tubes with laminin coating, for *Pkd1*$^{+/-}$ cells **(A)** and *Pkd1*$^{-/-}$ cells **(B)**. Scale bar:100 μm. Days after seeding: **(A)** 11, 16 (confluency), 20, **(B)** 9, 10 (confluency), 14. **(C–E)** Quantitative analysis, n = 12 *Pkd1*$^{+/-}$ chips (black) and n = 14 *Pkd1*$^{-/-}$ chips (red), all coatings pooled (see **Supplementary Figure 8** for separated behavior). **(C)** Mean cell density over time. Error bars: S.E.M. **(D)** Kinetic evolution of mean tubes diameter normalized by diameters at seeding, in function of the time after tube confluency. A blue horizontal line at D/D_0 = 1, corresponding to no change in diameter, is indicated. Each time point corresponds to 8–35 tubes for *Pkd1*$^{-/-}$, 9–20 tubes for *Pkd1*$^{+/-}$. Error bars: S.E.M. **(E)** Maximum (over time) of the mean normalized diameter. Points correspond to individual tube values. Central bar, median; cross, mean; box, values between Q1 and Q3 quartiles; error bars, extreme values [between Q1 - 1.5*(Q3 - Q1) and Q3 + 1.5*(Q3 - Q1)]. **(D,E)** were computed only for tubes having reached full confluency during the observation period. ** indicates statistically significant difference with p = 0.0002.

In practice, an open microfluidic chip was embossed on a cyclic olefin copolymer (COC) plate using a micro-milled brass mold. The structures consisted of an open rectangular reservoir to contain collagen I, with channels on each side containing five grooves each, sealed with a pressure sensitive PCR tape (Serra et al., 2017), in order to control the wire positions. We used horizontal connectors to silicone tubings to seed cells after collagen polymerization and wire removal (**Figure 1**). The

production of a long-lasting mold with 3D features (including slopes and half cylindrical connectors) was only possible through micro-milling. Embossed COC allowed the reusability of the rigid microfluidic chip, and a good imaging due to its transparency, controlled thickness and low autofluorescence (Van Midwoud et al., 2012; Roy et al., 2013).

For hydrogel injection in the central chamber, we used collagen I, the main ECM component, at different concentrations: 2.5, 4, and 6 mg/ml. For 2.5 and 4 mg/ml, the circular channels were not stable and uniform, and some of them collapsed. Proper molding of five parallel channels was obtained with 6 mg/ml collagen, as previously reported (Weber et al., 2016), with a success rate of 90%. Diameters after demolding, and immediately after cell seeding (D_0), were compared to the initial diameter of the 80 μm tungsten wire: we observed an increase of diameter, as assessed by its horizontal projection, of about 20% of the expected diameter after the different microfabrication steps, principally due to the demolding step (**Supplementary Figure 1A**). The first experiments were performed with a distance of 200 μm between the cylinders, which was afterward reduced to 100 μm to obtain more tightly packed tubes.

These cylindrical channels were then coated or not with different proteins constituting the basal membrane, which is mainly composed of laminin and collagen IV (Rahilly et al., 1991; Miner, 1999; Ogawa et al., 1999): both laminin and Matrigel were used, with efficient coating assessed with fluorescent laminin-Rhodamin (**Supplementary Figure 1B**). To evaluate the potential of this device to reproduce nephron structures, different renal cell lines were used to create kidney tubes: MDCK cells, and cells derived from mouse proximal tubule and models for ADPKD (**Supplementary Figure 5**, *Pkd1*$^{-/-}$ and *Pkd1*$^{+/-}$). Cells were seeded from the horizontal inlet with a density of 5.10^6 cells/ml. The initial density after cell adhesion in tubes was difficult to control, so that in order to limit any related bias, the kinetics of each tube deformation was analyzed taking tube confluency at the starting point. The cells were then kept in culture during up to 2 months, cell colonization and tube deformation were monitored and analyzed over time.

Control MDCK Cells Colonize Tubes and Do Not Lead to Tube Dilation

MDCK cells were first used as a classical model of renal cells (de Beco et al., 2009; Delous et al., 2009; Reffay et al., 2014; Bhoonderowa et al., 2016) for initial tests on cell viability, colonization and mechanical deformations of collagen-based tubes. MDCK cells were able to colonize nicely tubes, and to survive 1–2 months in tubes (**Figure 2**). Cells in tubes were organized in monolayer, and reached confluency with cohesive intercellular junctions, as assessed by ZO1 (Zonula occludens-1) labeling of tight junctions (**Supplementary Figures 3A,B**). Tubes exhibited no or minimal dilation over time, up to two months. We did not observe any significant influence of the coating on the colonization time or tube diameters (**Supplementary Figure 3C**). Mean data binned with 3-days interval are presented in **Figures 2B,C**. Confluency was achieved in ∼2 weeks after cell seeding (**Figure 2B**). A mild decrease of mean tube diameters (normalized with diameter at seeding, **Figure 2C**) occurred at early time points even before confluency, with an amplitude of ∼10% of the initial diameter. The tube diameter remained thereafter constant after confluency, for about 1 month (**Figure 2C**). **Figure 2D** depicts the maximum over time of the mean diameter of all different individual tubes. It was very close to 1 (1.03 ± 0.04, $n = 31$), further illustrating the absence of tube dilation after seeding with cells.

Altogether, these results show that MDCK cells colonized efficiently tubes, without dilating the tubes along time.

Organization of PCT *Pkd1*$^{-/-}$ and *Pkd1*$^{+/-}$ Cells in Tubes

In order to assess the specific mechanical behaviors of cells model for ADPKD in this biomimetic multitubular device, PCT *Pkd1*$^{-/-}$ and *Pkd1*$^{+/-}$ cells were seeded in tubes. These isogenic cell lines were derived from proximal tubule cells of a transgenic *Pkd1*$^{flox/-}$ mice; the resulting cell line was transfected or not with Cre recombinase to yield *Pkd1*$^{-/-}$ cells and *Pkd1*$^{flox/-}$ cells that function effectively as *Pkd1*$^{+/-}$ cell lines (Shibazaki et al., 2008). The PCT *Pkd1*$^{-/-}$ cells were previously characterized as an ADPKD model, forming cysts when cultured in a 3D collagen/Matrigel matrix, while the control *Pkd1*$^{+/-}$ cells self-organized in tubules instead (Wei et al., 2008). Concerning the choice of a proximal cell line, it is important to note that ADPKD cysts have been observed in all parts of the nephron (proximal and distal) (Baert, 1978; Torres and Harris, 2006; Vujic et al., 2010). In human models, a contribution of proximal cysts was observed from aquaporin immunolabeling and early microdissection studies (Huseman et al., 1980; Bachinsky et al., 1995; Hayashi et al., 1997), while in the different animal models the situation appears heterogeneous, with studies suggesting cysts originate from the collecting tubes before extending to the different segments (Hopp et al., 2012; Saito et al., 2018), but with possible underestimation of the proximal contribution due to differentiation issues (Hopp et al., 2012), and high sensitivity to initial conditions (Leonhard et al., 2016). In our experiments, while heterozygous *Pkd1*$^{+/-}$ cells mostly behaved like WT PCT cells in 2D or 3D (not shown), homozygous PCT *Pkd1*$^{-/-}$ cells, lacking the functional *Pkd1* gene on both chromosomes, exhibited hallmarks characteristic for ADPKD, including an increased proliferation rate (∼1.8-fold, **Supplementary Figure 4**) (Wei et al., 2008) and an increased extrusion in confluent cultures (not shown). Basic properties of adhesion and apico-basal polarity were assessed by RT-qPCR on cells cultured in 2D. We observed no significant change in the expression of actin or cell-matrix adhesion genes, but a significant decreased expression for apico-basal polarity markers ezrin and Na/K-ATPase, and for intercellular adhesion E-cadherin and N-cadherin genes, in PCT *Pkd1*$^{-/-}$ compared to *Pkd1*$^{+/-}$ cells (**Supplementary Figure 5**).

To promote efficient tube colonization, cells were seeded in tubes in proliferative state, and differentiation was initiated right after seeding. All PCT cell lines colonized the tubes and could be kept in culture up to 1 month. The prominent feature was that *Pkd1*$^{-/-}$ cells dilated tubes over time, whereas control *Pkd1*$^{+/-}$ cells did not. Before describing how renal cells could affect tube structure, we first present their global organization in the

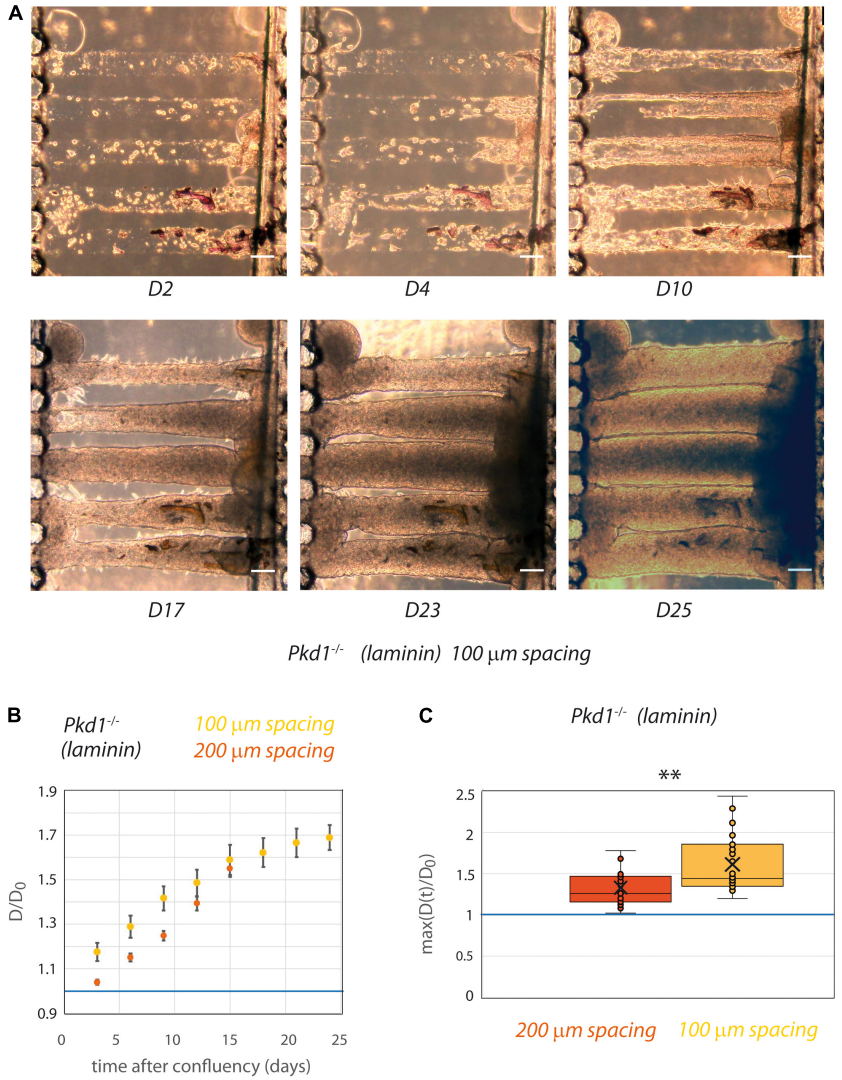

FIGURE 6 | PCT *Pkd1*$^{-/-}$ tube deformation in chips with 100 µm spacing. **(A)** Example of temporal evolution of tubes seeded with *Pkd1*$^{-/-}$ cells at days 2, 4, 10, 17, 23, and 25 after seeding. Scale bar:100 µm. **(B,C)** The behavior in 100 µm spacing tubes (yellow) was assessed with laminin coating and compared to the behavior in 200 µm spacing laminin-coated tubes (red). **(B)** Kinetic evolution of mean tube diameter normalized by diameter at seeding, in function of the time after tube confluency. A blue horizontal line at $D/D_0 = 1$, corresponding to no change in diameter, is indicated. Each time point corresponds to 9–26 tubes for 100 µm spacing, 4–19 tubes for 200 µm spacing. Error bars: S.E.M. **(C)** Maximum (over time) of the mean normalized diameter. Points correspond to individual tube values. Central bar, median; cross, mean; box, values between Q1 and Q3 quartiles; error bars, extreme values [between Q1 - 1.5*(Q3 - Q1) and Q3 + 1.5*(Q3 - Q1)]. **(B,C)** were computed only for tubes having reached full confluency during the observation period. ** indicates statistically significant difference with $p = 0.001$.

3D collagen scaffold (**Figure 3**). Cell monolayers with lumen formation were observed a few days after confluency for both cell lines. At this early stage, *Pkd1*$^{-/-}$ tubes already appeared more dilated and circular than *Pkd1*$^{+/-}$ tubes (**Figures 3C,D**). We also observed an increased cell density in *Pkd1*$^{-/-}$ tubes compared to *Pkd1*$^{+/-}$, respectively, 94 ± 7 cells/10 000 µm^2 ($n = 10$), vs. 53 ± 3 cells/10 000 µm^2 ($n = 22$; $p < 10^{-5}$), in line with the increased proliferation for the ADPKD model already reported in 2D.

ADPKD is associated with disorders in cellular orientation, in particular misaligned divisions and loss of planar polarity (Fischer et al., 2006; Happe et al., 2011a; Nigro et al., 2015). The orientation of the F-actin fibers, reflecting cytoskeleton organization and cell orientation, was specifically assessed in our system. We observed in most cases numerous stress fibers, mostly aligned along the *Pkd1*$^{+/-}$ tube axis, while *Pkd1*$^{-/-}$ tubes exhibited either a similar pattern or more disorganized fibers. A quantification was performed by OrientationJ analysis of the *z* projection of the lower half of tubes, a global measurement which included primarily stress fibers in the basal plane, but also the contour of cells in the middle plane (**Figures 4A–F**). Both *Pkd1*$^{+/-}$ tubes and *Pkd1*$^{-/-}$ tubes exhibited a clear F-actin alignment along the tube axis (**Figure 4G**), with about half of angles ranging between −10° and 10° for both cell lines (55% for *Pkd1*$^{+/-}$ tubes and 42% for *Pkd1*$^{-/-}$). An important difference between the two

conditions is that the density of oriented fibers appeared higher in the *Pkd1*$^{+/-}$ condition (**Figures 4A–F**). This was quantified by a coherency measurement (Rezakhaniha et al., 2012; Clemons et al., 2018), where coherency is a measurement of the strength of orientation, close to 1 for a strong local orientation, and to 0 for no preferential local orientation. **Figure 4H** shows a statistically significant difference between the coherency in *Pkd1*$^{+/-}$ and *Pkd1*$^{-/-}$ tubes ($p < 0.05$, **Figure 4C**, respective coherency values 0.35 ± 0.03, $n = 28$, and 0.23 ± 0.03, $n = 10$). This illustrates a denser organization of parallel F-actin fibers oriented along the tube axis for *Pkd1*$^{+/-}$ cells. This denser array of F-actin may be linked to two phenomena: the orientation of the cell division axis (not quantified), and the mechanical stabilization of the soft tube. This observation is in agreement with a model where dividing *Pkd1*$^{+/-}$ cells would tend to push cells in the direction of tube elongation, and not to dilate tubes, contrary to dividing *Pkd1*$^{-/-}$ cells.

In conclusion, shortly after confluence, cells were organized in monolayers in the 3D circular collagen scaffold in the different coating conditions. *Pkd1*$^{-/-}$ tubes, slightly dilated even for short culture time and exhibited an increased cell density, and a decreased density of F-actin fibers oriented along the tube axis.

PCT *Pkd1*$^{-/-}$ Cells Lead to Strong Tube Dilation, Contrary to Their Isogenic Control

The behavior of PCT *Pkd1*$^{-/-}$ and *Pkd1*$^{+/-}$ cells lining collagen tubes after confluency was further investigated as a function of time (**Figure 5** and **Supplementary Figures 7–9**). Both cell types colonized efficiently the tubes in 10–15 days, with a colonization rate that seemed quicker for *Pkd1*$^{-/-}$ cells (**Figure 5C**). As already observed right after confluency and as expected for non-ADPKD conditions, no significant dilation of the tubes was observed for *Pkd1*$^{+/-}$ tubes, regardless of the coating (**Figure 5A** and **Supplementary Figures 7**, **8**). In particular, D/D_0 remained close to 1 over time (**Figure 5D**), as well as the maximum over time of the normalized diameters (1.13 ± 0.09, $n = 15$, **Figure 5E**). Short cytoplasmic extensions into the collagen were rarely observed for both cell types (**Supplementary Figures 7A**, 10). At last, first results on PCT WT cells suggested that they behaved similarly to PCT *Pkd1*$^{+/-}$ cells, with no mean tubular dilation (**Supplementary Figure 6**).

On contrary, tube dilation was consistently observed in *Pkd1*$^{-/-}$ tubes independently of coating conditions (**Figure 5B** and **Supplementary Figures 7**, **8**). The kinetic evolution illustrates a mean *Pkd1*$^{-/-}$ dilation of ∼60% compared to the initial value (**Figure 5D**). The maximum deformation (over time) was 1.43 ± 0.03 ($n_{tubes} = 28$) reflecting a large tube dilation (**Figure 5E**). Tubes remained globally homogeneous in diameter when dilated (**Supplementary Figure 9A**). Altogether, these experiments showed that *Pkd1*$^{-/-}$ lining collagen tubes induce a significant tube dilation.

Once demonstrated that *Pkd1*$^{-/-}$ cells induced a significant tube dilation, we investigated whether the five tubes present in collagen were mechanically coupled. To do so, we performed several quantifications. The intertube spacing was measured and showed a decrease from 190 μm to ∼160 μm 25 days after seeding (**Supplementary Figure 9B**). This intertube spacing was compared to the local tube deformation: a clear anticorrelation was observed (**Supplementary Figure 9C**), in agreement with the idea that the tube deformation led to a short-scale remodeling of the intertube matrix. This suggested that each dilation event was independent. At last, correlation coefficients were calculated between adjacent contour lines in adjacent tubes (**Supplementary Figure 9D**), in order to evaluate if local deformations of one tube spatially corresponded to local deformations of the neighbor tube. These data showed that, in these conditions (tube spacing of 200 μm), tube dilations were not significantly coupled.

Pkd1$^{-/-}$ Tubes Come in Contact After Dilation in 100 μm Spaced Chips

Although the matrix stiffness allowed the tubes to be mechanically deformed in an ADPKD model, a spacing of 200 μm seems to be too important for the propagation of a mechanical coupling. The spacing between tubes was thus reduced to 100 μm after optimization of the micro-milling technique (**Figure 6**). Similar experiments with laminin coating only were conducted with tube spacing of 100 μm. As a control, we verified that even in this close proximity *Pkd1*$^{+/-}$ cells still did not deform collagen tubes (not shown). Strikingly, with this reduced spacing between tubes, some *Pkd1*$^{-/-}$ tubes could be in close proximity after dilation, with the creation of a plane interface between tubes (**Figure 6A**). We observed that both the rate of deformation and the maximal deformation induced by *Pkd1*$^{-/-}$ cells were increased in the 100 μm spaced tubes compared to the 200 μm spaced condition (**Figures 6B,C**). The maximum over time of the normalized diameters in 100 μm spacing chips was significantly larger than in the corresponding laminin-coated 200 μm spacing chips (respectively, 1.6 ± 0.07, $n = 26$, vs. 1.33 ± 0.06 for laminin-coated conditions, $n = 15$, $p = 0.001$, **Figure 6C**). These data strongly suggest that tube proximity modulates the geometry and the rate between neighbor tube deformation in an ADPKD model.

DISCUSSION

In this paper, we describe the development of a new generation of kidney-on-chip with parallel aligned circular tubes, of 80 μm diameter and 100 or 200 μm spacing, in a biocompatible and deformable collagen I. This chip was designed in order to reproduce geometrical, mechanical and biological characteristics of an array of renal proximal tubules with the aim to study physiopathological mechanisms of ADPKD. We first observed that our tubes were nicely colonized by different renal cells, with a long-term survival, in agreement with literature (Weber et al., 2016). No mean tubule dilation was observed with MDCK tubes. It is noteworthy to mention that MDCK tube dilation might have been triggered with some drug treatments, like cAMP agonists, as reported for renal cells in a bioengineered guided kidney tubule array system, where forskolin treatment of mIMCD3 cells induced a transformation from tubules to progressively dilating cystic structures (Subramanian et al., 2018). However, the scope

of our study was to study the behavior of specific ADPKD models. Then we showed that contrary to *Pkd1*$^{+/-}$ cells, *Pkd1*$^{-/-}$ cells, as an ADPKD model, were able to induce an important tube deformation. These observations are in agreement with tubular dilation expected for this disease demonstrating the physiological relevance of our model. Furthermore, our multitube chip design with spacing between tubes reduced to 100 μm allowed for the first time to reveal possible mechanical coupling between tubes, which could play a central role in ADPKD cyst propagation.

The behavior of proximal tubular cells has recently been described in single tubes in collagen I (120 μm diameter) with collagen IV coating (Weber et al., 2016). The authors showed that in this system, proximal tubular cells were able to recapitulate most of their physiological functions. In our study, we extended the potential of such approach by recapitulating for the first time the close proximity observed between parallel adjacent nephrons on chip, and we specifically focused on an ADPKD cellular model.

In vivo, the spacing between nephrotic tubes is heterogeneous, and no mean value between nearest neighbors could be extracted from the literature. However, *in vivo*, tubes are mostly in closer contacts (tens of μm). The initial choice of 200 μm spacing was mainly imposed by ease of microfabrication. However, to further investigate the possible coupling between tubes we also push the microfabrication limits to reduce the spacing to 100 μm. Importantly, the latter spacing was small enough so that ADPKD tubes could be in direct contact after dilation, thus opening the way to a study of mechanical coupling between tubes.

Regarding the implementation of kidney features on chip, the collagen scaffold stiffness (around 1 kPa; Verhulsel et al., 2016) was in the same order of magnitude, albeit a little lower, as the kidney stiffness measured by elastography techniques (4–10 kPa, or higher in some pathologies; Derieppe et al., 2012; Moon et al., 2015; Samir et al., 2015; Hassan et al., 2016; Liu et al., 2017). However, these elastography-derived values are global values for kidney, and not local values.

Moreover, the application of a physiological flow within the tube will be central in future implementations of our chips, as tubular cells mediate flow information by mechanotransduction pathways (including primary cilia) for the organization of architecture. Technological challenges result here from the common input between tubes due to their very close proximity, and resulting in inhomogeneities in flow values because of different diameters or obstructions. Flow might also be useful to prevent possible cell aggregation in tubes that might occur in late stages, although our data suggest that at least initial tube deformation occurred for cells monolayers. Indeed, 3D organization in the whole time course of deformation remains to be studied, and may include transient events of multilayering or fillling that will be addressed in further studies. Concerning ECM composition, the basal ECM *in vivo* consists mainly in laminin and collagen IV isoforms (Miner, 1999). These coatings were reproduced on chip, but we did not observed any significant difference of the global behaviors with laminin coating compared to the situation of collagen I without coating (Zhang et al., 2009); a slight increase in *Pkd1*$^{-/-}$ tube dilation was observed in uncoated conditions, but would need further confirmation. In addition, the coating may have an influence on subtler cellular behaviors within tubes, that were not analyzed here in details. A weak influence of the coating on the parameters assessed may be due to a degradation by cells, or to the secretion of their own extracellular matrix, possibly coupled to a lack of stability of the coating before full colonization (which could last 1–2 weeks).

Finally, our chip allowed to reproduce tube dilation observed for ADPKD tubes. In our configuration where we seeded a homogeneous *Pkd1*$^{-/-}$ population, we expect a rather homogeneous tube dilation, which was indeed observed here. In the disease, primary cyst formation results from a local tube dilation, which is believed to be due to a somatic second-hit mutation (Cornec-Le Gall et al., 2014) generating heterogeneous cell populations in one tube; this more complex configuration was not studied here. Several causes, including proliferation and altered planar polarity, are known to be involved in ADPKD cyst formation (Nadasdy et al., 1995; Fischer et al., 2006; Castelli et al., 2013). Both factors were seen in our *in vitro* tubes, and in particular F-actin orientation could be assessed in a geometrically and mechanically relevant controlled environment. We observed that both *Pkd1*$^{+/-}$ and *Pkd1*$^{-/-}$ cells were able to sense tube curvature and to generate F-actin stress fibers aligned with tube direction. However, the density of oriented F-actin fibers was significantly higher for *Pkd1*$^{+/-}$ cells. First, the orientation of division axis may be related to F-actin dynamic organization imposed by the geometry of the substrate, as described in other systems (Théry et al., 2005, 2007; Fink et al., 2011). In that case, dividing *Pkd1*$^{+/-}$ cells would tend to push cells in the direction of tube elongation, and not to dilate tubes. Second, a dense array of parallel F-actin fibers may provide a mechanical consolidation for the shape of the tube, still helping to prevent its deformation.

The strong tube dilation observed with *Pkd1*$^{-/-}$ cells led to tubes coming in very close contact after dilation, in the chips with 100 μm spaced tubes. When in close contact through a thin deformable substrate, tubes were mechanically coupled as expected, as also revealed by the linear shape of the created interface. But even before the complete contact was reached, tubes deformed more, and at a higher rate, than tubes separated with 200 μm, highly suggesting that an interaction at distance already occurred at this stage. This behavior could be due to mechanical or chemical effects, or a combination or both. Although the determination of the mechanisms involved in cooperative tube dilation is beyond the scope of this paper, some possible mechanisms are discussed here. First, chemical communication, which can occur at small distances inferior to 200 μm (Gerecht et al., 2010), could be involved in communication between renal tubes (El-Achkar and Dagher, 2015), with possible release of signaling molecules promoting proliferation or cyst growth (Kenter et al., 2019), including cytokines that may be released by epithelial cells upon mechanical stimulation (Kishikawa et al., 2002; Yamamoto et al., 2002; Wu et al., 2017). Second, mechanical mechanisms could include both cell reactions to mechanical stimuli by mechanotransduction pathways, and physical effects linked to the thinning of the ECM layer between adjacent tubes. Mechanotransduction events triggered by mechanical stimuli may include the YAP pathway, and it will be important to study how the impaired mechanotransduction by polycystins, including the RhoA-YAP-c-Myc axis (Happe et al., 2011b; Cai et al., 2018), is related to the

tube deformation observed. Additive physical mechanisms may be related to ECM characteristics, with on one side possible easier ECM thinning for very thin layers between two tubes (Shull and Creton, 2004); on the other side a possible weakening of the ECM due to cell protrusions, in line with a possible metalloproteinase involvement in ADPKD (Obermüller et al., 2001; Tan and Liu, 2012).

CONCLUSION

In conclusion, the strengths of our approach are the recapitulation of arrays of tightly packed deformable proximal tubes, and its application to an ADPKD model, with tube dilations and cooperative deformations. In the future, our study may also advantageously be extended to the study of human ADPKD models. While the reconstitution of the complete interactions involved in tubular cell behavior is beyond the scope of this study, the current limitations of our system include the absence of surrounding structures, like the peritubular capillary network. They also include the absence of a continuous physiological flow, and possible events of multilayering at middle or late stages of tube dilation.

Future studies will aim to distinguish mechanical and chemical contributions by applying pure mechanical stimulations on tubes, and to analyze matrix digestions or other possible mechanical modifications. Altogether, the cross-talk between renal tubes in our multitube chip is in good agreement with the cooperative behavior of snowball effect involved in cyst propagation in ADPKD. In line with these results, our device may also be of interest to screen for drugs that would inhibit this cross-talk behavior favoring renal cyst propagation.

DATA AVAILABILITY STATEMENT

The original contributions presented in the study are included in the article/**Supplementary Material**, further inquiries can be directed to the corresponding author/s.

AUTHOR CONTRIBUTIONS

SC, SDs, and SDm conceived the study. SM, BV, and BL performed the majority of the experiments. GG participated to the microfabrication and microfluidic experiments. FC and AB were involved in the cell culture and cell characterization. BC, CC, and IB participated in the image analysis. SC wrote the manuscript with input from all authors. SC and SDs supervised the project. All authors contributed to the article and approved the submitted version.

FUNDING

This work was received the support of "Institut Pierre-Gilles de Gennes" laboratoire d'excellence, "Investissements d'avenir" program ANR-10-IDEX-0001-02 PSL and ANR-10-LABX-31. SM was the recipient of an IPGG grant. This work received support from the Grants ANR-11-LABX-0038, ANR-10-IDEX-0001-02 [LabEx CelTisPhyBio—Cell(n)Scale]. This work was funded by CNRS (Centre National de la Recherche Scientifique), Institut Curie, and Sorbonne Université.

ACKNOWLEDGMENTS

We acknowledge all the members of the PBME group (Pascal Silberzan, Axel Buguin), in particular Pierre Ucla, and of the MMBM group (SDs), Physico-Chimie Curie, for their precious support in the process development and in microfabrication. We are very grateful to BMBC platform for their technical assistance in cell culture. We thank Ludovic Leconte, Olivier Leroy, the IPGG platform (ANR-10-EQPX-34) and the Curie imaging platform (PICT-IBiSA) for discussions and support in image processing. We are grateful to Marco Pontoglio, Fabiola Terzi, Frank Bienaimé, Sophie Saunier, Stefan Somlo, Eric Honoreì, and Amanda Patel for insightful discussions about renal diseases, and Philippe Marcq, François Amblard, Jean-Louis Viovy, Jean-François Joanny, and Jacques Prost for important discussions about the physical aspects. We thank George M. O'Brien Kidney Center at Yale (NIH P30 DK079310) and Stefan Somlo for the kind gift of PCT Pkd1 cell lines, and Amanda Patel and Eric Honoré for the kind gift of WT PCT cells. We thank the Cell and Tissue Imaging core facility (PICT IBiSA), Institut Curie, member of the French National Research Infrastructure France-BioImaging (ANR10-INBS-04).

SUPPLEMENTARY MATERIAL

The Supplementary Material for this article can be found online at: https://www.frontiersin.org/articles/10.3389/fbioe.2021.624553/full#supplementary-material

REFERENCES

Bachinsky, D. R., Sabolic, I., Emmanouel, D. S., Jefferson, D. M., Carone, F. A., Brown, D., et al. (1995). Water channel expression in human ADPKD kidneys. *Am. J. Physiol.* 268(3 Pt 2):F398. doi: 10.1152/ajprenal.1995.268.3.f398

Baert, L. (1978). Hereditary polycystic kidney disease (adult form): a microdissection study of two cases at an early stage of the disease. *Kidney Int.* 13, 519–525. doi: 10.1038/ki.1978.75

Bhoonderowa, L., Hameurlaine, F., Arbabian, A., Faqir, F., Amblard, F., and Coscoy, S. (2016). Polycystins and intercellular mechanotransduction: a precise dosage of polycystin 2 is necessary for alpha-actinin reinforcement of junctions upon mechanical stimulation. *Exp. Cell Res.* 348, 23–35. doi: 10.1016/j.yexcr.2016.08.021

Boca, M., Distefano, G., Qian, F., Bhunia, A. K., Germino, G. G., and Boletta, A. (2006). Polycystin-1 induces resistance to apoptosis through the phosphatidylinositol 3-kinase/Akt signaling pathway. *J. Am. Soc. Nephrol.* 17, 637–647.

Cai, J., Song, X., Wang, W., Watnick, T., Pei, Y., Qian, F., et al. (2018). A RhoA–YAP–c-Myc signaling axis promotes the development of polycystic kidney disease. *Genes Dev.* 32, 781–793. doi: 10.1101/gad.315127.118

Castelli, M., Boca, M., Chiaravalli, M., Ramalingam, H., Rowe, I., Distefano, G., et al. (2013). Polycystin-1 binds Par3/aPKC and controls convergent extension during renal tubular morphogenesis. *Nat. Commun.* 4:2658.

Chapin, H. C., and Caplan, M. J. (2010). The cell biology of polycystic kidney disease. *J. Cell Biol.* 191, 701–710. doi: 10.1083/jcb.201006173

Clemons, T. D., Bradshaw, M., Toshniwal, P., Chaudhari, N., Stevenson, A. W., Lynch, J., et al. (2018). Coherency image analysis to quantify collagen architecture: implications in scar assessment. *RSC Adv.* 8, 9661–9669. doi: 10.1039/c7ra12693j

Cornec-Le Gall, E., Alam, A., and Perrone, R. D. (2019). Autosomal dominant polycystic kidney disease. *Lancet* 393, 919–935. doi: 10.1016/S0140-6736(18)32782-X

Cornec-Le Gall, E., Audrézet, M.-P., Le Meur, Y., Chen, J.-M., and Férec, C. (2014). Genetics and pathogenesis of autosomal dominant polycystic kidney disease: 20 years on. *Hum. Mutat.* 35, 1393–1406. doi: 10.1002/humu.22708

Cowley, B. D., Smardo, F. L., Grantham, J. J., and Calvet, J. P. (2006). Elevated c-myc protooncogene expression in autosomal recessive polycystic kidney disease. *Proc. Natl. Acad. Sci. U S A.* 84, 8394–8398. doi: 10.1073/pnas.84.23.8394

de Beco, S., Gueudry, C., Amblard, F., and Coscoy, S. (2009). Endocytosis is required for E-cadherin redistribution at mature adherens junctions. *Proc. Natl. Acad. Sci. U S A.* 106, 7010–7015.

Delling, M., Indzhykulian, A. A., Liu, X., Li, Y., Xie, T., Corey, D. P., et al. (2016). Primary cilia are not calcium-responsive mechanosensors. *Nature* 531, 656–660.

Delous, M., Hellman, N. E., Gaude, H. M., Silbermann, F., Le Bivic, A., Salomon, R., et al. (2009). Nephrocystin-1 and nephrocystin-4 are required for epithelial morphogenesis and associate with PALS1/PATJ and Par6. *Hum. Mol. Genet.* 18, 4711–4723.

Derieppe, M., Delmas, Y., Gennisson, J. L., Deminière, C., Placier, S., Tanter, M., et al. (2012). Detection of intrarenal microstructural changes with supersonic shear wave elastography in rats. *Eur. Radiol.* 22, 243–250. doi: 10.1007/s00330-011-2229-2229

Dolega, M. E., Wagh, J., Gerbaud, S., Kermarrec, F., Alcaraz, J. P., Martin, D. K., et al. (2014). Facile bench-top fabrication of enclosed circular microchannels provides 3D confined structure for growth of prostate epithelial cells. *PLoS One* 9:e99416. doi: 10.1371/journal.pone.0099416

Douguet, D., Patel, A., and Honoré, E. (2019). Structure and function of polycystins: insights into polycystic kidney disease. *Nat. Rev. Nephrol.* 15, 412–422. doi: 10.1038/s41581-019-0143-146

El-Achkar, T. M., and Dagher, P. C. (2015). Tubular cross talk in acute kidney injury: a story of sense and sensibility. *Am. J. Physiol. - Ren. Physiol.* 308, F1317–F1323. doi: 10.1152/ajprenal.00030.2015

Fick, G. M., Johnson, A. M., Strain, J. D., Kimberling, W. J., Kumar, S., Manco-Johnson, M. L., et al. (1993). Characteristics of very early onset autosomal dominant polycystic kidney disease. *J. Am. Soc. Nephrol.* 3, 1863–1870.

Fink, J., Carpi, N., Betz, T., Betard, A., Chebah, M., Azioune, A., et al. (2011). External forces control mitotic spindle positioning. *Nat. Cell Biol.* 13, 771–778.

Fischer, E., Legue, E., Doyen, A., Nato, F., Nicolas, J. F., Torres, V., et al. (2006). Defective planar cell polarity in polycystic kidney disease. *Nat. Genet.* 38, 21–23.

Foy, R. L., Chitalia, V. C., Panchenko, M. V., Zeng, L., Lopez, D., Lee, J. W., et al. (2012). Polycystin-1 regulates the stability and ubiquitination of transcription factor Jade-1. *Hum. Mol. Genet.* 21, 5456–5471.

Gerecht, S., Ferreira, L. S., and Langer, R. (2010). Vascular differentiation of human embryonic stem cells in bioactive hydrogel-based scaffolds. *Methods Mol. Biol.* 584, 333–354. doi: 10.1007/978-1-60761-369-5_18

Ghata, J., and Cowley, B. D. (2017). Polycystic kidney disease. *Compr. Physiol.* 7, 945–975. doi: 10.1002/cphy.c160018

Grantham, J. J., Cook, L. T., Torres, V. E., Bost, J. E., Chapman, A. B., Harris, P. C., et al. (2008). Determinants of renal volume in autosomal-dominant polycystic kidney disease. *Kidney Int.* 73, 108–116. doi: 10.1038/sj.ki.5002624

Grantham, J. J., Geiser, J. L., and Evan, A. P. (1987). Cyst formation and growth in autosomal dominant polycystic kidney disease. *Kidney Int.* 31, 1145–1152. doi: 10.1038/ki.1987.121

Grantham, J. J., Mulamalla, S., and Swenson-Fields, K. I. (2011). Why kidneys fail in autosomal dominant polycystic kidney disease. *Nat. Rev. Nephrol.* 7, 556–566.

Grantham, J. J., Torres, V. E., Chapman, A. B., Guay-Woodford, L. M., Bae, K. T., King, B. F. Jr., et al. (2006). Volume progression in polycystic kidney disease. *N. Engl. J. Med.* 354, 2122–2130.

Grimm, D. H., Karihaloo, A., Cai, Y., Somlo, S., Cantley, L. G., and Caplan, M. J. (2006). Polycystin-2 regulates proliferation and branching morphogenesis in kidney epithelial cells. *J. Biol. Chem.* 281, 137–144. doi: 10.1074/jbc.M507845200

Happe, H., de Heer, E., and Peters, D. J. (2011a). Polycystic kidney disease: the complexity of planar cell polarity and signaling during tissue regeneration and cyst formation. *Biochim. Biophys. Acta* 1812, 1249–1255.

Happe, H., van der Wal, A. M., Leonhard, W. N., Kunnen, S. J., Breuning, M. H., de Heer, E., et al. (2011b). Altered Hippo signalling in polycystic kidney disease. *J. Pathol.* 224, 133–142. doi: 10.1002/path.2856

Hassan, K., Loberant, N., Abbas, N., Fadi, H., Shadia, H., and Khazim, K. (2016). Shear wave elastography imaging for assessing the chronic pathologic changes in advanced diabetic kidney disease. *Ther. Clin. Risk Manag.* 12, 1615–1622. doi: 10.2147/TCRM.S118465

Hayashi, M., Yamaji, Y., Monkawa, T., Yoshida, T., Tsuganezawa, H., Sasamura, H., et al. (1997). Expression and localization of the water channels in human autosomal dominant polycystic kidney disease. *Nephron* 75, 321–326. doi: 10.1159/000189556

Homan, K. A., Kolesky, D. B., Skylar-Scott, M. A., Herrmann, J., Obuobi, H., Moisan, A., et al. (2016). Bioprinting of 3D convoluted renal proximal tubules on perfusable chips. *Sci. Rep.* 6:34845. doi: 10.1038/srep34845

Hopp, K., Ward, C. J., Hommerding, C. J., Nasr, S. H., Tuan, H. F., Gainullin, V. G., et al. (2012). Functional polycystin-1 dosage governs autosomal dominant polycystic kidney disease severity. *J. Clin. Invest.* 122, 4257–4273.

Huan, Y., and van Adelsberg, J. (1999). Polycystin-1, the PKD1 gene product, is in a complex containing E-cadherin and the catenins. *J. Clin. Invest.* 104, 1459–1468. doi: 10.1172/JCI5111

Huseman, R., Grady, A., Welling, D., and Grantham, J. (1980). Macropuncture study of polycystic disease in adult human kidneys. *Kidney Int.* 18, 375–385. doi: 10.1038/ki.1980.148

Jang, K. J., Mehr, A. P., Hamilton, G. A., McPartlin, L. A., Chung, S., Suh, K. Y., et al. (2013). Human kidney proximal tubule-on-a-chip for drug transport and nephrotoxicity assessment. *Integr. Biol.* 5, 1119–1129.

Joly, D., Ishibe, S., Nickel, C., Yu, Z., Somlo, S., and Cantley, L. G. (2006). The polycystin 1-C-terminal fragment stimulates ERK-dependent spreading of renal epithelial cells. *J. Biol. Chem.* 281, 26329–26339.

Joly, D., Morel, V., Hummel, A., Ruello, A., Nusbaum, P., Patey, N., et al. (2003). Beta4 integrin and laminin 5 are aberrantly expressed in polycystic kidney disease: role in increased cell adhesion and migration. *Am. J. Pathol.* 163, 1791–1800.

Kenter, A. T., Van Rossum-Fikkert, S. E., Salih, M., Verhagen, P. C. M. S., Van Leenders, G. J. L. H., Demmers, J. A. A., et al. (2019). Identifying cystogenic paracrine signaling molecules in cyst fluid of patients with polycystic kidney disease. *Am. J. Physiol. - Ren. Physiol.* 316, F204–F213. doi: 10.1152/ajprenal.00470.2018

Kervrann, C., and Boulanger, J. (2006). Optimal spatial adaptation for patch-based image denoising. *IEEE Trans. Image Process.* 15, 2866–2878.

Kishikawa, H., Miura, S., Yoshida, H., Hirokawa, M., Nakamizo, H., Higuchi, H., et al. (2002). Transmural pressure induces IL-6 secretion by intestinal epithelial cells. *Clin. Exp. Immunol.* 129, 86–91. doi: 10.1046/j.1365-2249.2002.01895.x

Knepper, M. A., Danielson, R. A., Saidel, G. M., and Post, R. S. (1977). Quantitative analysis of renal medullary anatomy in rats and rabbits. *Kidney Int.* 12, 313–323.

Kurbegovic, A., and Trudel, M. (2020). The master regulators Myc and p53 cellular signaling and functions in polycystic kidney disease. *Cell. Signal.* 71:109594. doi: 10.1016/j.cellsig.2020.109594

Lee, E. J. (2016). Cell proliferation and apoptosis in ADPKD. *Adv. Exp. Med. Biol.* 933, 25–34. doi: 10.1007/978-981-10-2041-4_3

Lee, K., Boctor, S., Barisoni, L. M., and Gusella, G. L. (2014). Inactivation of integrin-beta1 prevents the development of polycystic kidney disease after the loss of Polycystin-1. *J. Am. Soc. Nephrol.* 26, 888–895.

Leonhard, W. N., Happe, H., and Peters, D. J. M. (2016). Variable cyst development in autosomal dominant polycystic kidney disease: the biologic context. *J. Am. Soc. Nephrol.* 27, 3530–3538. doi: 10.1681/ASN.2016040425

Leonhard, W. N., Zandbergen, M., Veraar, K., van den Berg, S., van der Weerd, L., Breuning, M., et al. (2015). Scattered deletion of PKD1 in kidneys causes a cystic snowball effect and recapitulates polycystic kidney disease. *J. Am. Soc. Nephrol.* 26, 1322–1333.

Li, A. (2017). Diagnosis and treatment status and progress of autosomal dominant polycystic kidney disease. *Int. J. Nephrol. Ther.* 3, 40–45.

Lin, N. Y. C., Homan, K. A., Robinson, S. S., Kolesky, D. B., Duarte, N., Moisan, A., et al. (2019). Renal reabsorption in 3D vascularized proximal tubule models. *Proc. Natl. Acad. Sci. U S A.* 116, 5399–5404. doi: 10.1073/pnas.1815208116

Liu, X., Li, N., Xu, T., Sun, F., Li, R., Gao, Q., et al. (2017). Effect of renal perfusion and structural heterogeneity on shear wave elastography of the kidney: an in vivo and ex vivo study. *BMC Nephrol.* 18:265. doi: 10.1186/s12882-017-0679-672

Lu, W., Peissel, B., Babakhanlou, H., Pavlova, A., Geng, L., Fan, X., et al. (1997). Perinatal lethality with kidney and pancreas defects in mice with a targetted pkd1 mutation. *Nat. Genet.* 17, 179–181. doi: 10.1038/ng1097-179

Markoff, A., Bogdanova, N., Knop, M., Ruffer, C., Kenis, H., Lux, P., et al. (2007). Annexin A5 interacts with polycystin-1 and interferes with the polycystin-1 stimulated recruitment of E-cadherin into adherens junctions. *J. Mol. Biol.* 369, 954–966.

Miner, J. H. (1999). Renal basement membrane components. *Kidney Int.* 56, 2016–2024.

Mochizuki, T., Tsuchiya, K., and Nitta, K. (2013). Autosomal dominant polycystic kidney disease: recent advances in pathogenesis and potential therapies. *Clin. Exp. Nephrol.* 17, 317–326. doi: 10.1007/s10157-012-0741-740

Moon, S. K., Kim, S. Y., Cho, J. Y., and Kim, S. H. (2015). Quantification of kidney fibrosis using ultrasonic shear wave elastography: experimental study with a rabbit model. *J. Ultrasound Med.* 34, 869–877. doi: 10.7863/ultra.34.5.869

Mottet, G., Perez-Toralla, K., Tulukcuoglu, E., Bidard, F. C., Pierga, J. Y., Draskovic, I., et al. (2014). A three dimensional thermoplastic microfluidic chip for robust cell capture and high resolution imaging. *Biomicrofluidics* 8:024109. doi: 10.1063/1.4871035

Nadasdy, T., Laszik, Z., Lajoie, G., Blick, K. E., Wheeler, D. E., and Silva, F. G. (1995). Proliferative activity of cyst epithelium in human renal cystic diseases. *J. Am. Soc. Nephrol.* 5, 1462–1468.

Nauli, S. M., Alenghat, F. J., Luo, Y., Williams, E., Vassilev, P., Li, X., et al. (2003). Polycystins 1 and 2 mediate mechanosensation in the primary cilium of kidney cells. *Nat. Genet.* 33, 129–137.

Nigro, E. A., Castelli, M., and Boletta, A. (2015). Role of the polycystins in cell migration, polarity, and tissue morphogenesis. *Cells* 4, 687–705.

Nigro, E. A., Distefano, G., Chiaravalli, M., Matafora, V., Castelli, M., Pesenti Gritti, A., et al. (2019). Polycystin-1 regulates actomyosin contraction and the cellular response to extracellular stiffness. *Sci. Rep.* 9:16640. doi: 10.1038/s41598-019-53061-53060

Obermüller, N., Morente, N., Kränzlin, B., Gretz, N., and Witzgall, R. (2001). A possible role for metalloproteinases in renal cyst development. *Am. J. Physiol. Ren. Physiol.* 280, F540–F550. doi: 10.1152/ajprenal.2001.280.3.f540

Ogawa, S., Ota, Z., Shikata, K., Hironaka, K., Hayashi, Y., Ota, K., et al. (1999). High-resolution ultrastructural comparison of renal glomerular and tubular basement membranes. *Am. J. Nephrol.* 19, 686–693. doi: 10.1159/000013543

Patel, A., and Honoré, E. (2010). Polycystins and renovascular mechanosensory transduction. *Nat. Rev. Nephrol.* 6, 530–538.

Peyronnet, R., Sharif-Naeini, R., Folgering, J. H., Arhatte, M., Jodar, M., El Boustany, C., et al. (2012). Mechanoprotection by polycystins against apoptosis is mediated through the opening of stretch-activated K(2P) channels. *Cell Rep.* 1, 241–250.

Qian, F., Wei, W., Germino, G., and Oberhauser, A. (2005). The nanomechanics of polycystin-1 extracellular region. *J. Biol. Chem.* 280, 40723–40730.

Rahilly, M. A., Salter, D. M., and Fleming, S. (1991). Composition and organization of cell–substratum contacts in normal and neoplastic renal epithelium. *J. Pathol.* 165, 163–171. doi: 10.1002/path.1711650212

Ramasubbu, K., Gretz, N., and Bachmann, S. (1998). Increased epithelial cell proliferation and abnormal extracellular matrix in rat polycystic kidney disease. *J. Am. Soc. Nephrol.* 9, 937–945.

Reffay, M., Parrini, M. C., Cochet-Escartin, O., Ladoux, B., Buguin, A., Coscoy, S., et al. (2014). Interplay of RhoA and mechanical forces in collective cell migration driven by leader cells. *Nat. Cell Biol.* 16, 217–223. doi: 10.1038/ncb2917

Rezakhaniha, R., Agianniotis, A., Schrauwen, J. T., Griffa, A., Sage, D., Bouten, C. V., et al. (2012). Experimental investigation of collagen waviness and orientation in the arterial adventitia using confocal laser scanning microscopy. *Biomech. Model. Mechanobiol.* 11, 461–473. doi: 10.1007/s10237-011-0325-z

Rossetti, S., Kubly, V. J., Consugar, M. B., Hopp, K., Roy, S., Horsley, S. W., et al. (2009). Incompletely penetrant PKD1 alleles suggest a role for gene dosage in cyst initiation in polycystic kidney disease. *Kidney Int.* 75, 848–855. doi: 10.1038/ki.2008.686

Roy, S., Yue, C. Y., Venkatraman, S. S., and Ma, L. L. (2013). Fabrication of smart COC chips: advantages of N-vinylpyrrolidone (NVP) monomer over other hydrophilic monomers. *Sens. Actuators B Chem.* 178, 86–95. doi: 10.1016/j.snb.2012.12.058

Saito, T., Tanaka, Y., Morishita, Y., and Ishibashi, K. (2018). Proteomic analysis of AQP11-null kidney: proximal tubular type polycystic kidney disease. *Biochem. Biophys. Reports* 13, 17–21. doi: 10.1016/j.bbrep.2017.11.003

Samir, A. E., Allegretti, A. S., Zhu, Q., Dhyani, M., Anvari, A., Sullivan, D. A., et al. (2015). Shear wave elastography in chronic kidney disease: a pilot experience in native kidneys. *BMC Nephrol.* 16:119. doi: 10.1186/s12882-015-0120-127

Schafer, K., Bader, M., Gretz, N., Oberbaumer, I., and Bachmann, S. (1994). Focal overexpression of collagen IV characterizes the initiation of epithelial changes in polycystic kidney disease. *Exp. Nephrol.* 2, 190–195.

Serra, M., Pereiro, I., Yamada, A., Viovy, J. L., Descroix, S., and Ferraro, D. (2017). A simple and low-cost chip bonding solution for high pressure, high temperature and biological applications. *Lab Chip.* 17, 629–634. doi: 10.1039/c6lc01319h

Sharif-Naeini, R., Folgering, J. H., Bichet, D., Duprat, F., Lauritzen, I., Arhatte, M., et al. (2009). Polycystin-1 and -2 dosage regulates pressure sensing. *Cell* 139, 587–596.

Shibazaki, S., Yu, Z., Nishio, S., Tian, X., Thomson, R. B., Mitobe, M., et al. (2008). Cyst formation and activation of the extracellular regulated kinase pathway after kidney specific inactivation of Pkd1. *Hum. Mol. Genet.* 17, 1505–1516.

Shull, K. R., and Creton, C. (2004). Deformation behavior of thin, compliant layers under tensile loading conditions. *J. Polym. Sci. Part B Polym. Phys.* 42, 4023–4043. doi: 10.1002/polb.20258

Subramanian, B., Kaya, O., Pollak, M. R., Yao, G., and Zhou, J. (2018). Guided tissue organization and disease modeling in a kidney tubule array. *Biomaterials* 183, 295–305. doi: 10.1016/j.biomaterials.2018.07.059

Subramanian, B., Ko, W. C., Yadav, V., DesRochers, T. M., Perrone, R. D., Zhou, J., et al. (2012). The regulation of cystogenesis in a tissue engineered kidney disease system by abnormal matrix interactions. *Biomaterials* 33, 8383–8394. doi: 10.1016/j.biomaterials.2012.08.020

Tan, R. J., and Liu, Y. (2012). Matrix metalloproteinases in kidney homeostasis and diseases. *Am. J. Physiol. - Ren. Physiol.* 302, F1351–F1361. doi: 10.1152/ajprenal.00037.2012

Terzi, F., Cheval, L., Barlet-Bas, C., Younes-Ibrahim, M., Buffin-Meyer, B., Burtin, M., et al. (1996). Na-K-ATPase along rat nephron after subtotal nephrectomy: effect of enalapril. *Am. J. Physiol.* 270, F997–F1003.

Théry, M., Jiménez-Dalmaroni, A., Racine, V., Bornens, M., and Jülicher, F. (2007). Experimental and theoretical study of mitotic spindle orientation. *Nature* 447, 493–496. doi: 10.1038/nature05786

Théry, M., Racine, V., Pépin, A., Piel, M., Chen, Y., Sibarita, J. B., et al. (2005). The extracellular matrix guides the orientation of the cell division axis. *Nat. Cell Biol.* 7, 947–953. doi: 10.1038/ncb1307

Torres, V. E., and Harris, P. C. (2006). Mechanisms of disease: autosomal dominant and recessive polycystic kidney diseases. *Nat. Clin. Pract. Nephrol.* 2, 40–55;quiz55. doi: 10.1038/ncpneph0070

Van Midwoud, P. M., Janse, A., Merema, M. T., Groothuis, G. M. M., and Verpoorte, E. (2012). Comparison of biocompatibility and adsorption properties of different plastics for advanced microfluidic cell and tissue culture models. *Anal. Chem.* 84, 3938–3944. doi: 10.1021/ac300771z

Vedula, E. M., Alonso, J. L., Arnaout, M. A., and Charest, J. L. (2017). A microfluidic renal proximal tubule with active reabsorptive function. *PLoS One* 12:e0184330. doi: 10.1371/journal.pone.0184330

Vedula, S. R., Leong, M. C., Lai, T. L., Hersen, P., Kabla, A. J., Lim, C. T., et al. (2012). Emerging modes of collective cell migration induced by geometrical constraints. *Proc. Natl. Acad. Sci. U S A.* 109, 12974–12979.

Venzac, B., Madoun, R., Benarab, T., Monnier, S., Cayrac, F., Myram, S., et al. (2018). Engineering small tubes with changes in diameter for the study of kidney cell organization. *Biomicrofluidics* 12:024114. doi: 10.1063/1.5025027

Verhulsel, M., Shivokhin, M. E., Simon, A., Descroix, S., Frétigny, C., and Talini, L. (2016). High bandwidth noninvasive measurements of the linear viscoelasticity of collagen gels. *J. Rheol.* 60:1269. doi: 10.1122/1.4965039

Vujic, M., Heyer, C. M., Ars, E., Hopp, K., Markoff, A., Örndal, C., et al. (2010). Incompletely penetrant PKD1 alleles mimic the renal manifestations of ARPKD. *J. Am. Soc. Nephrol.* 21, 1097–1102. doi: 10.1681/ASN.2009101070

Weber, E. J., Chapron, A., Chapron, B. D., Voellinger, J. L., Lidberg, K. A., Yeung, C. K., et al. (2016). Development of a microphysiological model of human kidney proximal tubule function. *Kidney Int.* 90, 627–637. doi: 10.1016/j.kint.2016.06.011

Wei, F., Karihaloo, A., Yu, Z., Marlier, A., Seth, P., Shibazaki, S., et al. (2008). Neutrophil gelatinase-associated lipocalin suppresses cyst growth by Pkd1 null cells in vitro and in vivo. *Kidney Int.* 74, 1310–1318.

Wilson, P. D. (2001). Polycystin: new aspects of structure, function, and regulation. *J. Am. Soc. Nephrol.* 12, 834–845.

Wilson, P. D., Hreniuk, D., and Gabow, P. A. (1992). Abnormal extracellular matrix and excessive growth of human adult polycystic kidney disease epithelia. *J. Cell. Physiol.* 150, 360–369. doi: 10.1002/jcp.1041500220

Woo, D. (1995). Apoptosis and loss of renal tissue in polycystic kidney diseases. *N. Engl. J. Med.* 333, 18–25. doi: 10.1056/NEJM199507063330104

Wu, S., Lu, Q., Wang, N., Zhang, J., Liu, Q., Gao, M., et al. (2017). Cyclic stretch induced-retinal pigment epithelial cell apoptosis and cytokine changes. *BMC Ophthalmol.* 17:208. doi: 10.1186/s12886-017-0606-600

Xi, W., Sonam, S., Beng Saw, T., Ladoux, B., and Teck Lim, C. (2017). Emergent patterns of collective cell migration under tubular confinement. *Nat. Commun.* 8:1517. doi: 10.1038/s41467-017-01390-x

Yamaguchi, T., Nagao, S., Wallace, D. P., Belibi, F. A., Cowley, B. D., Pelling, J. C., et al. (2003). Cyclic AMP activates B-Raf and ERK in cyst epithelial cells from autosomal-dominant polycystic kidneys. *Kidney Int.* 63, 1983–1994. doi: 10.1046/j.1523-1755.2003.00023.x

Yamamoto, H., Teramoto, H., Uetani, K., Igawa, K., and Shimizu, E. (2002). Cyclic stretch upregulates interleukin-8 and transforming growth factor-β1 production through a protein kinase C-dependent pathway in alveolar epithelial cells. *Respirology* 7, 103–109. doi: 10.1046/j.1440-1843.2002.00377.x

Yevick, H. G., Duclos, G., Bonnet, I., and Silberzan, P. (2015). Architecture and migration of an epithelium on a cylindrical wire. *Proc. Natl. Acad. Sci. U S A.* 112, 5944–5949.

Zhang, H., Tasnim, F., Ying, J. Y., and Zink, D. (2009). The impact of extracellular matrix coatings on the performance of human renal cells applied in bioartificial kidneys. *Biomaterials* 30, 2899–2911. doi: 10.1016/j.biomaterials.2009.01.046

Conflict of Interest: The authors declare that the research was conducted in the absence of any commercial or financial relationships that could be construed as a potential conflict of interest.

frontiers in Bioengineering and Biotechnology

ORIGINAL RESEARCH
published: 27 August 2021
doi: 10.3389/fbioe.2021.622175

Chlorpyrifos Disrupts Acetylcholine Metabolism Across Model Blood-Brain Barrier

*Dusty R. Miller[1], Ethan S. McClain[1], James N. Dodds[1,2,3,4,5], Andrzej Balinski[1,2,3,4,5], Jody C. May[1,2,3,4,5], John A. McLean[1,2,3,4,5] and David E. Cliffel[1,3,5]**

[1]Department of Chemistry, Vanderbilt University, Nashville, TN, United States, [2]Center for Innovative Technology, Vanderbilt University, Nashville, TN, United States, [3]Vanderbilt Institute of Chemical Biology, Vanderbilt University, Nashville, TN, United States, [4]Vanderbilt-Ingram Cancer Center, Vanderbilt University, Nashville, TN, United States, [5]Vanderbilt Institute for Integrative Biosystems Research and Education, Vanderbilt University, Nashville, TN, United States

Despite the significant progress in both scientific understanding and regulations, the safety of agricultural pesticides continues to be called into question. The need for complementary analytics to identify dysregulation events associated with chemical exposure and leverage this information to predict biological responses remains. Here, we present a platform that combines a model organ-on-chip neurovascular unit (NVU) with targeted mass spectrometry (MS) and electrochemical analysis to assess the impact of organophosphate (OP) exposure on blood-brain barrier (BBB) function. Using the NVU to simulate exposure, an escalating dose of the organophosphate chlorpyrifos (CPF) was administered. With up to 10 μM, neither CPF nor its metabolites were detected across the BBB (limit of quantitation 0.1 μM). At 30 μM CPF and above, targeted MS detected the main urinary metabolite, trichloropyridinol (TCP), across the BBB (0.025 μM) and no other metabolites. In the vascular chamber where CPF was directly applied, two primary metabolites of CPF, TCP and diethylthiophosphate (DETP), were both detected (0.1–5.7 μM). In a second experiment, a constant dose of 10 μM CPF was administered to the NVU, and though neither CPF nor its metabolites were detected across the BBB after 24 h, electrochemical analysis detected increases in acetylcholine levels on both sides of the BBB (up to 24.8 ± 3.4 μM) and these levels remained high over the course of treatment. In the vascular chamber where CPF was directly applied, only TCP was detected (ranging from 0.06 μM at 2 h to 0.19 μM at 24 h). These results provide chemical evidence of the substantial disruption induced by this widely used commercial pesticide. This work reinforces previously observed OP metabolism and mechanisms of impact, validates the use of the NVU for OP toxicology testing, and provides a model platform for analyzing these organotypic systems.

Keywords: organophosphate, mass spectrometry, organ-on-a-chip, electrochemistry, pesticide

OPEN ACCESS

Edited by:
Wei Seong Toh,
National University of Singapore, Singapore

Reviewed by:
Jie Liu,
South China Agricultural University, China
Oksana Lockridge,
University of Nebraska Medical Center, United States
Jordan Smith,
Pacific Northwest National Laboratory, United States

****Correspondence:***
David E. Cliffel
d.cliffel@vanderbilt.edu

Specialty section:
This article was submitted to Nanobiotechnology, a section of the journal Frontiers in Bioengineering and Biotechnology

Received: *27 October 2020*
Accepted: *16 July 2021*
Published: *27 August 2021*

Citation:
Miller DR, McClain ES, Dodds JN, Balinski A, May JC, McLean JA and Cliffel DE (2021) Chlorpyrifos Disrupts Acetylcholine Metabolism Across Model Blood-Brain Barrier. Front. Bioeng. Biotechnol. 9:622175. doi: 10.3389/fbioe.2021.622175

INTRODUCTION

Organophosphates (OPs) are a class of compounds commonly used in commercial pesticides (e.g., parathion, chlorpyrifos, and diazinon) but also include nerve gas chemical warfare agents such as sarin, VX, and Novichok agents. While OPs are widely used throughout the world for insect control, concerns about their toxicity to humans and animals led to restrictions in the United States for residential use in 2001. In 2018, a United States federal appeals court ordered the United States

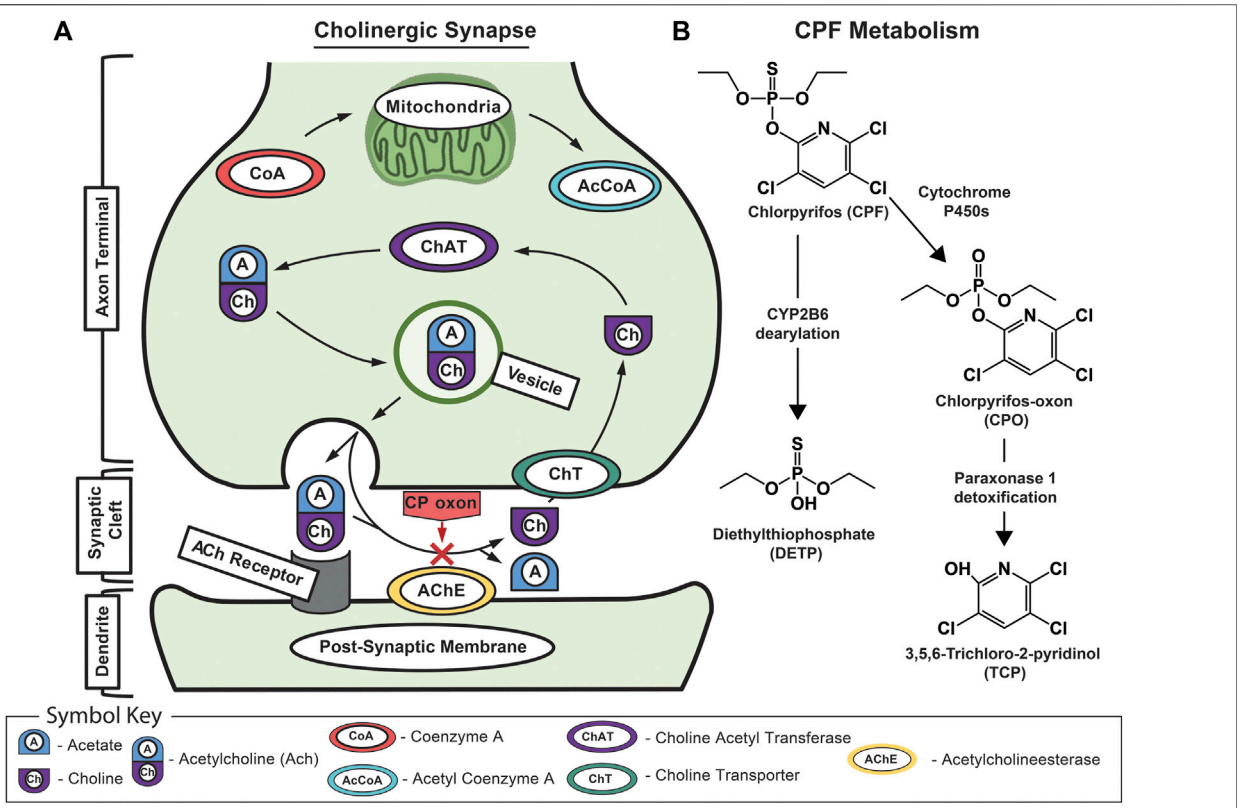

FIGURE 1 | Schematic of acetylcholine and chlorpyrifos biochemistry. **(A)** Schematic of the mechanism of CPF toxicology at the cholinergic synapse showing normal signaling where acetylcholine is recognized by the acetylcholine receptor on the dendrite's postsynaptic membrane before being rapidly broken down by acetylcholinesterase into acetic acid and choline. Normally, the free choline is taken back up into the presynaptic neuron where choline acetyltransferase turns it back into acetylcholine before it is packaged into vesicles for subsequent release. The red "X" indicates CPO-induced inhibition of acetylcholinesterase that leads to a buildup of acetylcholine in the synaptic cleft and, eventually, excitotoxicity, neuropathy, and death. **(B)** The major metabolic pathway for CPF bioactivation, dearylation, and biodegradation showing associated primary metabolites including CPF; chlorpyrifos oxon (CPO); diethylthiophosphate (DETP); and 3,5,6-trichloro-2-pyridinol (TCP).

Environmental Protection Agency to completely ban the use of the broad-spectrum organophosphate pesticide chlorpyrifos (CPF) based in part on epidemiological studies linking prenatal CPF exposure to neurobehavioral deficits in children (Rauh et al., 2011; Rauh et al., 2012). To gain additional insights into CPF-induced chemical and morphological perturbations, *in vitro* organotypic models offer medium-throughput systems that complement traditional cell culture techniques and may replace or reduce animal testing (Pridgeon et al., 2018; Low et al., 2021). These organotypic models aim to replicate human physiology and provide the experimental flexibility necessary to address the effects of OPs on human health (Nolan et al., 1984; Marín-Padilla, 2012; Shamir and Ewald, 2014; Bruner-Tran et al., 2017; Vernetti et al., 2017; Theobald et al., 2018).

The primary mechanism of CPF neurotoxicity is through the inhibition of acetylcholinesterase, yet its full metabolic response remains unclear. At a cellular level, cholinergic signal transmission is accomplished by acetylcholine release into the neuronal synapse before it is broken down by acetylcholinesterase and taken back up by presynaptic neurons (**Figure 1**; Taylor et al., 1999). OPs inhibit acetylcholinesterase by binding to serine in the active site, preventing acetylcholine from interacting with the enzyme (Mileson et al., 1998; Prendergast et al., 1998; Karanth et al., 2006). Before binding, CPF is metabolically converted by cytochrome P450s into the bioactive chlorpyrifos oxon (CPO) form. When acetylcholinesterase is inhibited, acetylcholine can accumulate in motor neuron synapses causing excitotoxicity, seizures, and brain damage (Prendergast et al., 1998; Yang et al., 2001; Timchalk et al., 2005; Slotkin, 2011). OP neurotoxicity can also extend to necrosis, apoptosis, and oxidative stress-mediated pathways (Carlson et al., 2000; Kashyap et al., 2010; Moore et al., 2010; Kashyap et al., 2011; Kashyap et al., 2013; Park et al., 2015a). Mice and rats are considered standard models for controlled toxicological studies although historical studies include human volunteers (Levin et al., 2001). In mice, CPF has been shown to cause alterations to the integrity of the BBB upon exposure, enabling CPF and other toxicants to enter the brain (Levin et al., 2001; Li and Ehrich, 2013). These risks associated with CPF exposure combined with its continued use in the United States demand further investigation and refinement of our ability to identify dysregulation events associated with chemical exposure and leverage this information to predict biological responses (Rauh et al., 2012; Smith et al., 2014).

In developing models for studying BBB toxicity, organs-on-chips offer several advantages (Cucullo et al., 2011; Griep et al.,

2013; Prabhakarpandian et al., 2013; Adriani et al., 2017; Phan et al., 2017; Wang et al., 2017; Maoz et al., 2018). Built upon the knowledge gained from early experiments with cocultures and Transwells, the development of organ-on-chip technologies aims to combine the versatility of *in vitro* experimentation with cutting-edge engineering and analytics to refine the questions that can be addressed (Parran et al., 2005; Balbuena et al., 2010; Daneman and Prat, 2015; Hopkins et al., 2015; Helms et al., 2016; Voorhees et al., 2017; Zhang et al., 2017; Grebenyuk and Ranga, 2019). Organs-on-chips vary in construction but all contain three-dimensional supports that spatially orient cultures to develop organ-like qualities (Dingle et al., 2015; Adriani et al., 2017; Soscia et al., 2017). Recent advances include modifying the physical dimensions and mechanical properties by incorporating gels or matrices, encouraging the production of an extracellular matrix (ECM), and investigating novel materials (Tang-Schomer et al., 2014; Jeong et al., 2015; Lozano et al., 2015; Hutson et al., 2016; Zhuang et al., 2018; Zhuang et al., 2018; Grebenyuk and Ranga, 2019). Within these structures, perfusion of media enables the exchange of nutrients and metabolites and provides the shear stress needed to stimulate cell proliferation and differentiation. Perfusion has been driven by gravity, pneumatic, piezoelectric, or mechanical systems (Takayama et al., 1999; Araci and Quake, 2012; Brown et al., 2015; Park et al., 2015b; Fernandes et al., 2016; Koo et al., 2018; Wang et al., 2018; Balaji et al., 2018). The miniaturization of these features reduces the quantity of reagents used, thereby decreasing cost and supporting the incorporation of cells that are either difficult to culture or difficult to isolate (Herculano-Houzel, 2009; Volpatti and Yetisen, 2014; Mohammed et al., 2015; DiMasi et al., 2016; Bang et al., 2017; Campisi et al., 2018). Additionally, efforts to instrument these chips can provide real-time, nondestructive measurements of these systems (Booth and Kim, 2012; Griep et al., 2013; Kilic et al., 2016). For example, neuron excitability can be studied by integrating organ-on-chip technology with electrodes to both stimulate and report the burst-firing frequency rate and power (Hasan and Berdichevsky, 2016; Soscia et al., 2017). Perhaps the most important role for organotypic cultures resides in their application in toxicology, supplementing preclinical cell culture methods, and reducing animal testing (Nolan et al., 1984; Low et al., 2021). There are now a wide range of platforms available with a high degree of specialization allowing researchers to ask detailed questions about BBB health and disease (Lancaster et al., 2013; Banerjee et al., 2016; Kilic et al., 2016; Adriani et al., 2017).

Recently, Wikswo and colleagues developed a neurovascular unit (NVU), an organotypic model that approximates the human BBB, by creating a paracellular barrier comprised of endothelial cells, astrocytes, and pericytes and seeding it with neurons (Brown et al., 2015). This NVU has been shown to be a useful model to assess both acute (seconds to minutes) and chronic (days to weeks) toxic exposure (Brown et al., 2015; Brown et al., 2016). The dual-chamber NVU design—a neuronal (2.9 μL) and a vascular (17.5 μL) section—is equipped with independent microfluidic perfusion control so that environmental exposure can be simulated by administration of toxicants to the vascular side while analyzing the neuronal side for metabolic changes and for the infiltration of toxicants that breach the engineered BBB. Furthermore, these two chambers can be seeded with as little as twenty thousand cells, making the NVU feasible for culturing rare or difficult to isolate cells. Taken together, these features make the NVU well suited for transbarrier analysis of OP exposure and, with careful consideration, as a regulatory tool for toxicology (Fennema et al., 2013; Andersen, 2014; Schadt et al., 2014; Koo et al., 2018; Wang et al., 2018; Pimentel et al., 2020; Raimondi et al., 2020).

This work presents a platform for simulating and analyzing toxicological events that supports the prediction of biological responses through morphological and metabolic analysis. NVUs seeded with the four cell types necessary for proper BBB function were cultured and the vascular side of these NVUs was then dosed with the organophosphate CPF, simulating environmental exposure. Eluate from the vascular and neuronal sides was assessed using liquid chromatography coupled to tandem mass spectrometry (LC-MS/MS) for targeted toxicant profiling and electrochemical analysis for targeted metabolite profiling. These data validate the predictive power of the NVU, the high analytical utility of combined MS, and electrochemical measurements and provide insight into the substantial disruption induced by this widely used commercial pesticide. Applying this unique platform with expanded analytics is an important advance in studying OP toxicity.

MATERIALS AND METHODS

NVU Bioreactor Fabrication. The NVU bioreactor was designed for independent perfusion of the two chambers and is described in detail elsewhere (Brown et al., 2015), with some minor modifications. The NVU is a two-chamber device made with three layers of polydimethylsiloxane (PDMS) separated by a 0.4 μM pore polyethylene terephthalate (PET) membrane (Fisher Scientific, Hampton, NH). First, the neuronal layer and the vascular layer were created by pouring 2.5 and 16g, respectively, of PDMS precursors (10:1 wt:wt ratio of base: curing agent, Sylgard 184, Dow Corning) into encapsulated wafers, cured (65°C, 4 h), and demolded. To fabricate the middle layer, 30 g of PDMS precursors was poured into the middle layer mold with spacers and placed in a dish. The dish was covered and placed under vacuum until bubbles formed and repressurized and the process was repeated. The dish was then removed from vacuum and bubbles were blown off. To control for layer thickness, the top mold of the middle layer was then placed on the spacers with weights (≤70g) on top and allowed to cure at room temperature for 48 h. After drying, excess PDMS was trimmed off and the middle layer was removed and cured at 65°C for 2 h.

With all three layers cured and trimmed to size, the NVU could be assembled. First, the vascular layer and a glass plate (50 mm × 75 mm) were both plasma-activated (40 s, high power setting, air metered into vacuum, Harrick Plasma Cleaner, Ithaca, NY) and brought together to bond with the chamber facing upwards. Meanwhile, the neuronal layer was punched with inlet and outlet ports (Miltex 1.5 mm OD, Integra York, Inc., York PA) to accommodate microfluidic perfusion. Both the middle and

neuronal layers were plasma-activated and bonded together with the neuronal layer channels facing the middle layer, and the assembly was placed in a 65°C oven for 10 min to complete the bonding process. After bonding, both the middle-neuronal and the vascular-plate layer assemblies were annealed at 200°C for 4 h. PET membranes were plasma-activated and immersed in an 80°C solution of 0.2% bis-amino (Sigma Aldrich, St. Louis, MO) and 0.1% deionized water in IPA. After drying, these membranes were placed in 70% ethanol (30 min, room temperature) and blown dry with filtered N_2. The membranes were then brought together with the vascular layer to bond, and the neuronal-middle layer was added by facing the middle layer to the membrane so that the reliefs in the PDMS-created chambers overlapped completely with one another except for the inlet and outlet ports. The assembled device was placed in the oven (60°C) overnight to finish curing. Completed NVU vascular and neuronal chambers (2.9 and 17.5 μL, respectively) each incorporated an entrance and exit port to facilitate independent perfusion. A noteworthy change from previous versions of this device fabrication is the incorporation of 0.4 μM pore PET membrane that is more transparent and enhances imaging (previous iterations of this device used a polycarbonate membrane). The transition to PET membranes was done because of the manufacturer's change in membrane properties that made them unsuitable for the NVU and also to increase visibility for enhanced microscopy. All NVU devices were packaged and gamma sterilized overnight (Mark 1 Cesium Irradiator, Glendale, CA) before use. Schematics of the NVU were made to scale in CAD with the help of the Vanderbilt Institute for Integrative Biosystems Research and Education.

PDMS Absorption of CPF. To determine the extent to which CPF is absorbed into PDMS, a floating disk experiment was conducted as before with some modifications (Auner et al., 2019). First, 3 mm thick medical grade PDMS (same as that used in the NVU fabrication) was cut with a biopsy punch (diameter = 6 mm) to form disks. Using a 20 mM stock solution of CPF made in DMSO, 25, 50 75, and 100 μM CPF solutions were made in 10 mM SDS (to aid solubility). Then, each disk (3) was submerged in 2 ml of 100 μM CPF solution inside of a 4 ml glass vial and the absorption of this solution as well as that of calibrants (25, 50, 75, and 100 μM CPF) was measured every hour at 290 nm. From these data, the concentration of CPF still in solution was calculated.

Harvesting Primary Rat Neurons. Primary rat neurons were harvested as previously described with some modifications (McKenzie et al., 2012). Briefly, pure neuronal cultures were obtained from embryonic day 18 Sprague-Dawley rats. To obtain primary rat neurons, brains from anesthetized rats were dissected, and cortices were trypsinized (Sigma, United States) before being transferred to 10 ml of neurobasal media (Sigma). This solution was then strained (40 μm), counted, and centrifuged (1,000 RCF, 5 min). The resulting pellet was resuspended [neurobasal media, 10% DMSO (Sigma), at either 7.5×10^5 or 5×10^8 cells/ml] and frozen down until needed for either plating in well plates or NVU seeding, respectively.

Staining Primary Rat Neurons. Neurons were stained to confirm the presence of cholinergic neurons in culture. Neurons stored at −80°C at 750,000 cells/ml were plated 2 ml/6 well Transwell plates coated with polyornithine and maintained in plating media [Dulbecco's modified Eagle's medium (DMEM) media (Gibco) with 8% F12, 8% fetal bovine serum (FBS), 80 μM L-glutamate, and 1% penicillin/streptomycin (Fisher)] for days *in vitro* (DIV) 0–13. During this time, the cells were maintained with half media changes every 2–3 days. Two weeks after harvest, the neurons had a half media change to D2C media (94% DMEM, L-glutamine, 2% FBS, 0.025 M HEPES, 0.0125 mM L-glutamine, 24 U/mL penicillin, and 24 μg/ml streptomycin), and two drops of AraC were added through a plugged pasture pipette for a final concentration of 1–2 M/well. From then on, cells were maintained with D2C media until use. Neurochemical staining for choline acetyltransferase (ChAT), Neuron Specific Tubulin (NST), and 4′,6-diamidino-2-phenylindole (DAPi) to stain all cells merged to show overlap as done before with some modifications (Lizama et al., 2018).

Neuronal Response to CPF. Neurons were either treated with a media change control or 100 μM CPF for 18 h and imaged as before (Lizama et al., 2018). Experiments were conducted at 37°C and 5% CO_2.

Cell Culture. Endothelial cells, astrocytes, and pericytes were cultured as before with some modifications (Brown et al., 2016). Primary human brain microvascular endothelial cells (hBMVECS, Applied Cell Biology, Kirkland WA, United States) were maintained in endothelial basal media 2 (EBM2, Lonza, Basa, Switzerland) containing 5% FBS, growth bullet kit (hEGF, hydrocortisone, GA-1000 [gentamicin and amphotericin-B], VEGF, hFGF-B, R3-IGF-1, ascorbic acid, and heparin), and 1% penicillin/streptomycin (complete EBM-2). Human astrocytes from brain tissue of a first trimester fetus and SV40 transformed (SVG p12, ATCC, Manassas, VA, United States) and pericytes isolated from human brain tissue (Cat # 1200, ScienCell, Carlsbad, CA, United States) were maintained in a 1:1 DMEM and F-12 with 10% FBS (Allt and Lawrenson, 2001). Endothelial cells, astrocytes, and pericytes were maintained in T-25 flasks (Fisher) under standard culture procedures until collected (passage three) for seeding into the NVU.

NVU Seeding and Culturing. The NVU supported the growth of all four cell types necessary for proper BBB function and is described in detail previously with some modifications (Brown et al., 2015). Prior to cell seeding, NVU devices were first coated with poly-D-lysine (10 μg/ml) in carbonate buffer (0.2 M, pH 9.6, 37°C, 4 h, Fisher) followed by coating with fibronectin and collagen IV (both 400 μg/ml, overnight, 37°C, Sigma). After washing the devices with warm complete EBM-2 media to remove any unbound fibronectin or collagen, endothelial cells were loaded into the vascular chamber ($5–10 \times 10^6$ cells/ml). The NVU was then placed vascular side up and incubated overnight (37°C, 5% CO_2). The next day, the vascular chamber was connected to a syringe pump (Harvard Apparatus) and perfused under low flow conditions (2 μL/min) with complete EBM-2 media for 9 days. After this time, the neuronal chamber was loaded with astrocytes (6×10^6 cells/ml) and pericytes (1×10^6 cells/ml) and the device was placed neuronal chamber side up (37°C, 5% CO_2) to allow the cells to settle and adhere for 2 h before flow was restarted. After culturing these three cell types

together for 2 days under low flow conditions, primary rat neurons were loaded into the neuronal chamber (10×10^6 cells/ml) and allowed to attach for 2 h before flow was again restarted. Within each NVU, all four cell types were cultured for 3 days before these devices were ready for leakage and toxicological testing. During the course of these experiments, sister cultures of the cells loaded into the NVU devices were plated and no contamination was detected.

To ensure proper barrier formation, leakage across the engineered BBB was tested using 10 kDa fluorescein isothiocyanate-dextran (FITC-dextran, Sigma) as previously described (Brown et al., 2016). Briefly, FITC-dextran was prepared (100 nM, cell culture media) and administered to the vascular compartment of the NVU (23 h, 2 μL/min), allowing the FITC-dextran to diffuse across the BBB and into the neuronal chamber, reflecting barrier permeability. The effectiveness of the BBB was evaluated by measuring the fluorescent intensity in the neuronal side eluate using a plate reader (TECAN M1000). The permeability, P, was calculated from the FITC concentration using **Eq. 1** where V_r is the volume in the receiving chamber, t is the time of the experiment, A is the area of the membrane (0.29 cm^2), C_i is the initial concentration, and C_f is the measured concentration.

$$P = \frac{V_r \times C_f}{C_i \times A \times t} \quad (1)$$

The permeability of the NVU device with no cells was also measured for comparison. This device was irradiated and soaked in water but otherwise bare. The control device was treated with DMSO as described below in *NVU Treatment With Chlorpyrifos*.

NVU Treatment With Chlorpyrifos. In normal operation, both the vascular and neuronal side chambers of each NVU were perfused with media under low flow (2 μL/min) to maintain the viability of the cell layers that comprise the engineered BBB. To investigate the effects of OPs on the engineered BBB, either CPF (Sigma) or vehicle (dimethyl sulfoxide, DMSO, Sigma) was introduced to the vascular chamber and eluate exiting both vascular and neuronal chambers was collected to be analyzed for biochemical changes. Two experimental setups were executed with this approach: an escalating dose experiment and a time course experiment.

The dose escalation experiment was conducted with varying concentrations of CPF (0, 1, 3, 10, 30, and 100 μM) and six NVU devices (two control devices and four test devices). First, CPF was dissolved in DMSO to 200 mM, filter-sterilized (0.22 μm membrane, Sigma), and stored at −80°C until use. Then, 1 μM CPF was added to complete EBM-2 media and perfused on the vascular side of each test device for 2 h. After collecting that effluent, the syringe containing the 1 μM CPF was exchanged for one containing 3 μM CPF and the process was repeated in this way for all of the CPF concentrations tested. The control NVU was treated with vehicle alone. Eluate samples (240 μL) were collected from both the vascular and neuronal chamber of all NVUs immediately prior to administering each dose and stored at −80°C prior to analysis.

After the escalating dose experiment was conducted, a 10 μM dose of CPF was chosen to investigate the effects of exposure time. A total of five NVU devices (three treated and two control) were prepared and used for the exposure experiments described herein. Additionally, the NVU devices were first perfused with serum-free EBM-2 media before CPF exposure (although the other supplements and growth factors that contribute to the complete media formulation, e.g., hFGF-B, VEGF, R3-IGF, hEGF, GA-1000, ascorbic acid, and hydrocortisone, were added to the media). To add statistical power while reducing the number of NVUs used in the experiment, effluent was collected from the three test devices prior to treatment to serve as a baseline. Two control NVUs were treated with vehicle alone. However, one control device was compromised during the course of the experiment and was subsequently excluded. Therefore, the results between the time-dependent control and the baseline controls were compared for time differences, and after verifying their similarity, the data from both of these controls were pooled for analysis. For the test devices, 10 μM CPF was added to this serum-free media and perfused on the vascular side of each test device. Eluate samples (~240 μL) from all devices were collected from both the vascular and neuronal chamber of all NVUs at 0, 2, 4, 8, and 24 h and stored at −80°C prior to analysis.

NVU Microscopy. After treatment with CPF or vehicle, NVUs were imaged for morphological analysis. First, live/dead stain was applied to the NVU devices as per manufacturer recommendation (Thermo Fisher) and incubated for 15 min. Fluorescent images of cells stained within the NVU were then collected using an EVOS (Thermo Fisher) automated microscope.

MS Analysis of NVU Eluate. A minimal-handling sample preparation strategy was used, which limited metabolic turnover and degradation while maximizing metabolite recovery. In this strategy, metabolites were extracted from media using a volume of 800 μL of cold (−20°C) methanol added to a 100 μL aliquot of NVU media eluate, vortexed for 30 s, and incubated at −80°C overnight to precipitate proteins. After incubation, samples were cleared by centrifugation (21130 RCF,15 min), and the resulting supernatant was removed and evaporated to dryness in a vacuum concentrator. Dried extracts were reconstituted in 60 μL reconstitution solvent [98:2 (v:v) water:acetonitrile with 0.1% formic acid] for reverse phase LC-MS analysis. The reconstituted samples were then centrifuged (15,000 rpm, 5 min) to remove insoluble debris. Quality control samples were prepared by combining equal volumes (10 μL) of each sample type.

Ultra-high-performance liquid chromatography-mass spectrometry (UHPLC-MS) and multiple reaction monitoring (MRM) were performed on a triple quadrupole mass spectrometer (6,470, Agilent Technologies, Santa Clara, CA, United States) equipped with an Infinity II UHPLC system (1,290, Agilent). Chlorpyrifos and its metabolites were separated on a reverse phase Hypersil Gold RPLC column (1.9 μm, 2.1 mm × 50 mm, Thermo Fisher, Waltham, MA) at ambient temperature. Chromatography was performed at 300 μL/min using solvent A (0.05% formic acid in water) and solvent B (0.05% formic acid in acetonitrile) with the following gradient profile—60% B for 0.5 min, 60–95% B over 3.5 min, and

95–60% B over 0.1 min—and reequilibrated at 60% B over 2 min (gradient length 4.1 min). The injection volume used was 1 μL, with an autosampler temperature of 4°C. The exogenous small molecule, 2,6-di-*tert*-butylpyridine (DtBP), was used as an internal standard. Serial dilutions of DtBP at 10 concentrations were used to determine instrument limits of detection (LOD), quantitation (LOQ), and the calibration curve necessary to convert instrument response to analyte concentrations.

Data acquisition was carried out in fast polarity switching MRM mode using a thermally assisted ESI source (Jet Stream, Agilent) operated with the following conditions: a capillary voltage of 4 kV (positive ion mode) and 2.5 kV (negative ion mode), a nebulizer gas temperature of 300°C with the flow of 8 L/min, and a sheath gas temperature of 300°C with the flow of 11 L/min. Data were acquired using MassHunter Workstation Data Acquisition software (Agilent) and analyzed using MassHunter Quantitative Analysis software (Agilent). A list of metabolites, mass transitions, retention times, and ion polarities used for targeted MS analysis can be found in supplemental materials (**Supplementary Table S1**). Data represent between four and eight replicate measurements (two–four NVU devices and two technical replicates per sample).

Acetylcholine Sensor Fabrication and Calibration. A screen-printed electrode (SPE) array was enzymatically modified to be selective to acetylcholine (acetylcholine chloride, Sigma) and incorporated into the microclinical analyzer (μCA) microfluidic flow system for automated calibration and analysis as before with some modifications (McKenzie et al., 2015). The μCA consisted of a MicroFormulator and an electrochemical detection cell. The MicroFormulator was designed by and purchased from the Vanderbilt Institute for Integrative Biosystems Research and Education (VIIBRE)/Vanderbilt Microfabrication Core (VMFC) and consisted of a rotary planar peristaltic micropump (US patents 9,874,285 and 9,725,687 and applications claiming priority from US patent application 13/877,925) for delivering flow and a normally closed rotary planar valve (US patent 9,618,129) to select solutions. Microcontrollers and computer software for the MicroFormulator were also purchased from VMFC. The electrochemical detection cell, designed and fabricated by VIIBRE/VMFC, was composed of an electrode array and a microfluidic housing. The electrode array, designed in-house and commissioned for fabrication (Pine Research, Durham, NC), (McKenzie et al., 2015), was composed of five different electrodes: three platinum disk electrodes and two band electrodes. The disk electrodes ($A = 1.8\,mm^2$) were used for enzymatic detection of acetylcholine. The largest band electrode ($A = 19\,mm^2$) was silver plated and used as an Ag/AgCl quasireference.

To make the electrodes selective to acetylcholine, a two-enzyme solution of acetylcholinesterase (Sigma) from *Electrophorus electricus* and choline oxidase (Sigma) from *Alcaligenes* was prepared and deposited on the working electrodes. First, each enzyme was dissolved separately to 10 mg/ml in phosphate buffer (2 mM PBS, pH 7, Fisher) containing 800 mg/ml of bovine serum albumin (Sigma) and stored (−18°C) until use. These enzyme solutions were retrieved as required, combined equally by volume, mixed with glutaraldehyde (0.5% wt/v, Sigma), and vortexed (~5 s). Immediately following vortexing, 1 μL of the mixed enzyme solution was drop-cast onto each working electrode, allowed to air dry for 1 h, and either used immediately or stored (low light, 4°C, 2 mM PBS, 120 mM KCl, pH 7).

The LOD, LOQ, and linearity for the acetylcholine sensor were determined as performed previously (McKenzie et al., 2015; Miller et al., 2018). To incorporate the sensor into the μCA, the SPE was sealed within a polymethylmethacrylate closed-cell housing. The housing was plumbed with Tygon tubing (Cole Parmer, Vernon Hills, IL) to a debubbler (Molecular Devices Inc., Sunnyvale, CA) and attached to a MicroFormulator to facilitate automated calibration and analysis. Calibrations were performed by monitoring the current generated by 21 calibrant solutions (5 μM–5 mM acetylcholine) in buffer (2 mM PBS; 120 mM KCl, pH 7). Calibrants were sampled through a MicroFormulator at a flow rate of 100 μL/min and monitored by a CHI 1,440 potentiostat (CH Instruments, Austin, TX) held at 0.6 V vs. Ag/AgCl with buffer in between to provide a baseline (2 min each). The detection and quantitation limits, along with the sensitivity and linear range of the sensor, were determined by performing a linear regression on the calibration data. The maximum limit of linearity was determined by visual analysis of the calibration curve. The LOD was calculated by dividing three times (10X for LOQ) the error of the blank (y values) by the slope of the determined linear range. Dividing the slope by the area of the disk electrode (1.8 mm^2) resulted in the sensitivity of the electrode.

Electrochemical Analysis of Acetylcholine in NVU Eluate. The μCA electrochemical detection platform (Miller et al., 2018) was used to determine the acetylcholine levels in NVU samples both with and without CPF treatment. The acetylcholine SPE containing three enzymatically modified acetylcholine sensors was loaded into the μCA housing and the current was monitored by all three to provide technical replicates. Using the MicroFormulator, calibrants were sampled at a flow rate of 100 μL/min (as above, but with six calibrants from 0 to 114 μM). After calibration, NVU eluate was sampled with buffer (2 min, 2 mM PBS, 120 mM KCl, pH 7.0) in between each sample run to establish a baseline. The sensor was recalibrated before and after each NVU sample set to check for sensor degradation/inhibition. The acetylcholine concentration in the sample was determined using the current generated by the sample and the slope and intercept of the calibration curve that was generated by performing a linear regression on the calibration data. *p*-values between sample sets were determined using *t*-test with unequal variance.

RESULTS AND DISCUSSION

This study was designed to assess the utility of the NVU and an electrochemical/MS analytical platform to address three critical aspects of CPF toxicity: 1) How does CPF degrade and what CPF metabolites persist? 2) Does CPF or its metabolites cross the BBB?

3) What effects does CPF exposure have on cellular metabolism at and across the BBB? To this end, environmental exposure to CPF was simulated within the NVU and morphological and metabolic analysis was performed.

To answer these critical questions, it was important to model CPF exposure resulting in significant metabolic disruption without inducing cell death. A few benchmarks for CPF exposure include the United States federally allowed dose of up to 0.03 mg/L of CPF in drinking water (0.085 μM CPF). Detailed murine studies for sublethal doses, report 0.5–5 mg/kg IV doses to result in 10–100 μM CPF in blood (Smith et al., 2012). These dosing levels have been carefully compared to oral administration and historical human studies (Nolan et al., 1984; Smith et al., 2012; Smith et al., 2014). Because CPF binds quickly upon administration, the *in vivo* range of 0–100 μM CPF and a slightly higher dose (300 μM) were chosen for investigation (Lowe et al., 2009).

Using this range of CPF concentrations, we first explored the response of the barrier-forming cells—the endothelial cells—outside of the NVU. Endothelial cells were grown on well plates, exposed to 0, 10, 30, 100, and 300 μM CPF, and visually inspected for morphological changes at 24 h. The treatments resulted in a range of perturbations. The lowest concentration exposure (10 μM) showed slight changes in morphology. At 30μM CPF, treatment was nonlethal but resulted in morphological changes to more circular-shaped cells. The highest exposure tested (300 μM) resulted in the majority of the cells displaying punctate cell morphology and clumping of cells indicating cell death (**Supplementary Figure S1**). These initial endothelial cell experiments demonstrated varied effects across the range of CPF concentrations. CPF concentrations that were not expected to induce significant cell death in the NVU were tested further (0–100 μM CPF).

Primary neuronal cultures were chosen to ensure that their state of differentiation is representative of mammalian neurons. Specifically, cholinergic neurons were desired to accurately represent susceptibility to OPs. The primary cultures used in this work were 90% neurons and 10% microglia and determined to be 10% positive for choline acetyltransferase, indicating active cholinergic signaling (**Supplementary Figure S2**). When these neurons were tested for their response to CPF (100 μM), the cells showed a "halo" effect indicating cell death (**Supplementary Figure S3**). However, if the membrane stays intact, CPF may never reach the neuronal chamber. Historically, research on cholinergic neuronal cultures has been conducted on primary cells, although recently a cholinergic neuronal line was introduced (Ortiz-Virumbrales et al., 2017; Moreno et al., 2018). We are currently working to bring this cholinergic technology into our lab to integrate with the NVU.

The NVU incorporates all four cell types necessary to model BBB function within a three-dimensional, dual-chambered device (Brown et al., 2015; Brown et al., 2016). First, the NVU's vascular chamber (17.5 μL) was seeded with a human endothelial cell line and grown to confluency. Next, the neuronal chamber (2.9 μL) was seeded with three different cell types: human astrocytic and pericytic cell lines and primary rat neurons (Hamilton, 2010). The neurons were harvested from the forebrain of the rat and the addition of these neurons created a chimeric model fusing a majority of human-derived cells with primary rat neurons. With all four cell types within the device, both chambers were equipped with microfluidic perfusion control in preparation for simulating acute environmental exposure to CPF (device schematic shown in **Supplementary Figure S4**).

To assess the full-range response of the model BBB to CPF exposure, the NVU was treated with an escalating dose of CPF. A total of five NVU devices were used to serve as biological model replicates. Under perfusion, the vascular sides of each NVU device were exposed to varying concentrations of CPF (0, 1, 3, 10, 30, and 100 μM) in an escalating dose format (successive exposures) over the course of 24 h. Media were collected from both chambers of each NVU prior to each exposure point. Barrier permeability was tested by spiking the vascular side media with 10 kDa fluorescein isothiocyanate-dextran (FITC) and monitoring fluorescence across the barrier (Helms and Brodin, 2014). When an empty device was tested (no cells), the permeability was $(2.0 \pm 0.4) \times 10^{-6}$ cm/s (**Supplementary Figure S5**). Compared to the permeability of the empty device (no cells), when the four cell types were added (but before CPF exposure), permeability decreased [0 μM CPF: $(0.27 \pm 0.05) \times 10^{-6}$ cm/s, control treated with DMSO: $(0.28 \pm 0.05) \times 10^{-6}$ cm/s]. After exposing the NVUs to 1 μM CPF, the permeability increased [$(0.67 \pm 0.27) \times 10^{-6}$ cm/s] and continued to increase upon adding 3 μM CPF [$(1.15 \pm 0.24) \times 10^{-6}$ cm/s] at which point it stabilized [$(1.01 \pm 0.46) \times 10^{-6}$ cm/s, 100 μM CPF]. To definitively report the concentration-dependent effects of exposure on permeability without accumulation effects, individual experiments at each concentration are needed. However, this increased permeability indicates that CPF may be able to cross the engineered BBB and enter the neuronal chamber.

To directly investigate the potential crossover of CPF, MS analysis of the media samples was used to track CPF and its primary metabolites at and across the BBB. The canonical pathway for CPF detoxification illustrates that CPF can proceed through the toxic intermediate, CPO, or can be metabolized directly to inactive compounds (**Figure 1**; Sultatos, 1994). A targeted MS assay, was used to monitor CPF and its metabolites in the escalating dose experiment. MS analysis did not detect CPF nor CPO in either vascular or neuronal eluate samples (**Supplementary Figure S6**, and numerically in **Supplementary Table S2**). However, in all conditions in which CPF was administered, TCP—the primary urinary metabolite of CPF—was detected in the vascular effluent, indicating CPF detoxification. At 30 μM CPF and above, TCP was detected across the BBB in the neuronal effluent. At the highest dose of CPF (100 μM), diethylthiophosphate (DETP), another CPF metabolite, was also detected in the vascular effluent. These CPF metabolites are a result of CPF detoxification, which is limited by the enzymatic rate of chlorpyrifos dearylation and/or CPO detoxification (Tang et al., 2006). However, components in the serum used in this experiment such as acetylcholinesterase may have scavenged the CPF and contributed to its lack of detection (Lowe et al., 2009). Still, the observation that neither CPF nor any of the primary metabolites were detected across the

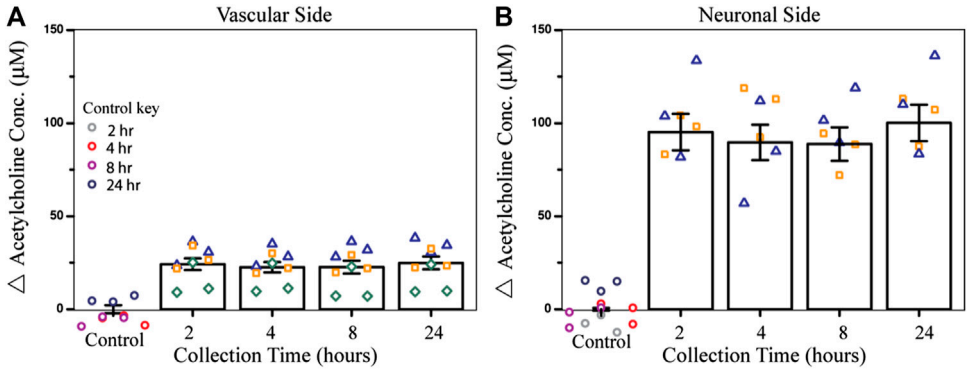

FIGURE 2 | Effect of CPF on acetylcholine metabolism within the NVU as determined from the electrochemical assay. **(A)** Bar graph indicating the change in acetylcholine concentration from control (DMSO) in vascular side eluate over time (2, 4, 8, or 24 h treatment), showing elevated acetylcholine levels (24 ± 3 μM) after 2 h of CPF treatment (10 μM CPF, *p*-value < 0.003). **(B)** Bar graph indicating a change in acetylcholine concentration in neuronal side eluate over time showing elevated acetylcholine (95 ± 10 μM) 2 h after CPF was administered to the vascular side, a significant increase from the control (*p*-value < 0.04). Data are represented as the means and standard errors, symbols represent technical replicates, *n* = 6–9 for samples, and *n* = 9–12 for controls. Control samples were collected over 24 h and their respective collection time is indicated in the control key.

BBB with up to 10 μM CPF suggests that barrier integrity was maintained under these conditions. Ultimately, the 10 μM dose—a dose that was thought to have measurable effects in our system without degrading the membrane—was chosen for further investigation.

Before the second NVU experiment was conducted, an electrochemical sensor previously developed by Cliffel and coworkers for the detection of acetylcholine was evaluated for possible interference in this system. The sensor was shown to be sensitive, selective, and stable in the absence of serum (**Supplementary Table S4**; McClain et al., 2019). Therefore, the second NVU experiment was conducted without serum being added to the media during CPF treatment (although the other components of the Lonza growth bullet kit were added) so that metabolic disruption in specific pathways—such as cholinergic signaling and/or metabolism—could be sensitively and selectively monitored using electrochemical microphysiometry.

To test the effect of an acute dose of CPF on metabolism within the NVU over time, the vascular sides of the NVUs were dosed with 10 μM CPF and the effluent was electrochemically analyzed. In this study, four NVU devices were used in parallel. When exposed to 10 μM CPF, the vascular eluate exhibited a significant increase in acetylcholine (24 ± 3 μM, *p*-value < 0.003, **Figure 2A**) after just 2 h and remained elevated for at least 24 h (24 ± 3 μM) compared to control. This acetylcholine buildup is a hallmark of organophosphate poisoning and can interfere with the muscarinic, nicotinic, and central nervous systems causing essential autonomic processes to fail such as respiration and circulation. This acetylcholine buildup may be a result of CPF bioactivation to the ultimate toxicant CPO. Bioactivation is thought to take place primarily in the liver by a cytochrome P450 enzyme (CYP). Within the NVU, a similar CYP produced by the endothelial cells may be responsible for the bioactivation of CPF (Dauchy et al., 2008; Ghosh et al., 2010). Future models of CPF toxicity could include a kidney or liver chip in tandem with the NVU to investigate CYP-dependent effects (Vernetti et al., 2017).

In this same experiment, acetylcholine metabolism was also significantly dysregulated on the neuronal side of the NVU, despite not being treated directly with CPF. Across the BBB, acetylcholine levels increased after 2 h (95 ± 10 μM, *p*-value < 0.04, **Figure 2B**) and stayed elevated for 24 h (100 ± 10 μM) compared to control. The cholinergic neurons on the neuronal side of the NVU are thought to be primarily responsible for acetylcholine production, perhaps accounting for the even greater change in acetylcholine levels compared to the vascular side. This increase also suggests that either CPF, its toxic metabolites, or other soluble factors were able to cross the BBB and interact directly with the neurons. In future experiments, recently published protocols describing cholinergic neuron differentiation from human-induced pluripotent stem cells (hiPSCs) can be implemented and integrated with this platform so that these results can be compared with those of human cholinergic neurons (McCracken et al., 2014; Paşca et al., 2015; Amin et al., 2016; Moreno et al., 2018; Pas, 2018; Liu et al., 2020).

To investigate how BBB morphology changed over time in response to a long-term CPF exposure at 10 μM, microscopic images were collected after CPF treatment. Treated NVUs displayed some punctate cell morphology (contracted cells) indicative of cellular stress and a compromised BBB, whereas the control NVUs exhibited evenly dispersed cells characteristic of a healthy BBB (**Figure 3**; **Supplementary Figure S7**). At moderate levels (1–20 μM), other studies have also found CPF to be tolerated by cells in culture, causing cellular stress but not being directly cytotoxic (chlorpyrifos; Saulsbury et al., 2009; Middlemore-Risher et al., 2011).

To directly investigate the potential crossover and metabolism of 10 μM CPF over time, MS was used again to track CPF and its primary metabolites at and across the BBB. Similar to the escalating dose experiment, targeted MS did not detect CPF

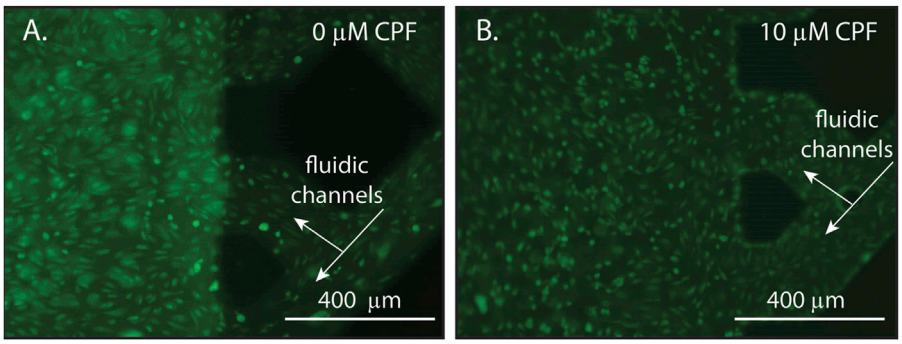

FIGURE 3 | Representative microscopy images of endothelial cells within an NVU following 24 h of continuous exposure with either **(A)** DMSO (vehicle control, *panel A*) or **(B)** CPF (10 μM, *panel B*). The lattice seen at the right of each image is the microfluidic channels of the vascular side of the NVU. **(A)** A control NVU showing evenly dispersed cells with typical morphology, indicating a healthy BBB. **(B)** A CPF-treated NVU showing punctate cell morphology (contracted cells), indicating cellular stress in response to the CPF treatment. For these experiments, the NVUs were perfused with neurobasal media on the neuronal side and EBM2 media on the vascular side either with or without CPF. All cultures were maintained at 37°C and 5% CO_2.

nor CPO in either vascular or neuronal eluate samples (**Figure 4** and displayed numerically in **Supplementary Table S2**). Only one metabolite, TCP, was detected above the limit of quantitation (~0.01 μM) and only on the vascular side. TCP was detected at ~0.05 μM after 2 h of treatment and increased in concentration to ~0.19 μM after 24 h (**Figure 4**, *top plots*). When targeted MS was applied to the neuronal side eluate, none of the CPF primary metabolites were observed in any of the neuronal samples (**Figure 4**, *bottom plots*). Because CPF treatment also corresponded to serum removal from the media, these changes cannot be exclusively attributed to the effects of CPF and more experiments are required to parse the effects of serum versus CPF on barrier integrity. These data along with other studies show TCP to be the primary urinary metabolite of CPF in both humans and rodents (Timchalk et al., 2005; Atabila et al., 2019).

Although the CPF degradation observed in this work agrees with what is seen in humans, the fact that the metabolite concentration decreased tenfold compared to the administered concentration raises questions as to the fate of CPF. One hypothesis is that CPF is removed from the effluent by the PDMS used to fabricate the NVUs. To test PDMS absorption of CPF (Auner et al., 2019), a floating disk experiment was conducted that demonstrated that, after 2 h, 14 ± 1% of the CPF was lost, whereas after 24 h, as much as 67 ± 1.6% of CPF was lost to PDMS (**Supplementary Figure S8**). These results indicate that the absorption/adsorption of CPF is substantial for PDMS, which has important implications in the design and interpretation of PDMS-based microfluidic experiments. Despite this loss to PDMS, the experiments conducted in this work were run under a continuous flow of 2 μL/min. Under this flow, the CPF-dosed media took less than 9 min to flow through the PDMS-based device. Therefore, uptake of CPF by PDMS only accounts for a small portion of the total CPF removal observed.

If CPF is metabolized within the NVU, where is it going and how can it be tracked? Other *in vitro* BBB studies that have set out to utilize MS to monitor CPF were unable to detect CPF or its metabolites, leading researchers to rely on acetylcholinesterase inhibition instead (Balbuena et al., 2010). Although the CPF metabolites detected in this current work give promise to MS as a tool for tracking organophosphate toxicity, the analysis may need to be expanded beyond the NVU eluate. The increased acetylcholine levels measured on the neuronal side indicate that perhaps CPF, CPO, or other soluble factors were able to cross the BBB but attached to the cells or matrix in the neuronal chamber, allowing them to remain undetected by targeted MS methods. The results encourage additional targeted MS developments to assay the cellular/matrix components for retained CPF.

Alternatively, the low detection of CPF may be due to it being bound to other soluble molecules in the media. CPF plasma protein binding has been measured using varying concentrations of rat and human albumin in buffer (0.04–20 mg/ml) and CPF (0.009 and 0.29 μM). At both of these CPF concentrations, it was reported that when albumin concentrations were high, 99% of the CPF was bound (Lowe et al., 2009). All the experiments presented in this work have either serum or growth factors added to the media that may be binding the CPF and/or CPO in solution. Because CPF is highly bound to proteins *in vivo*, removing the supplement proteins in addition to the serum would lead to higher unbound CPF and greater ability to cross the membrane, but the biological relevance would be compromised (Smith et al., 2012; Smith et al., 2017). Indeed, it has been reported that under physiological conditions CPF membrane transport increases, whereas CPF membrane permeability increases when physiological conditions are removed. In these reports, serum protein concentration was the most substantial factor affecting this transition (Smith et al., 2012). Acid hydrolysis has also been used to recover CPF lost to conjugation, doubling CPF recovery in some cases (Nolan et al., 1984). CPF recovery has also been increased by treating with glucuronidase, liberating TCP glucuronide conjugates (Nolan et al., 1984). These insights into tracking CPF in eluate encourage future studies that include additional processing steps to increase CPF recovery or MS studies which implement broad, untargeted MS assays to assess wide-scale unanticipated metabolic changes (Balbuena et al., 2010; May et al., 2015; May et al., 2016; Sherrod and McLean, 2016; Huang et al., 2019).

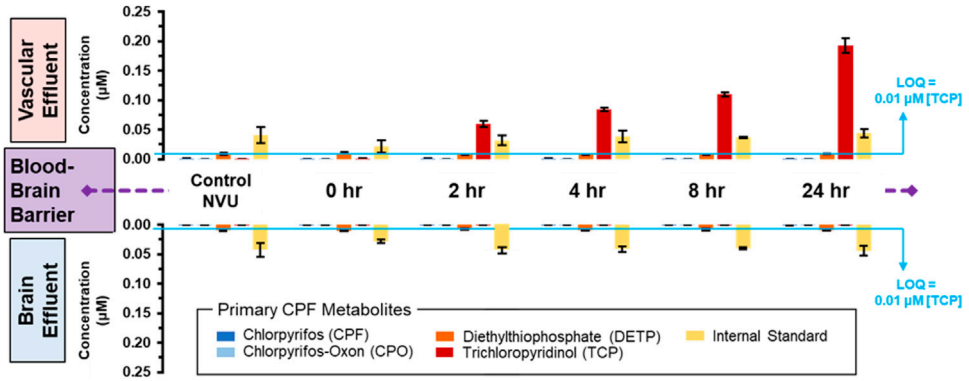

FIGURE 4 | Distribution of CPF and its three primary metabolites at and across the BBB with lengthening exposure times. Using targeted MS, CPF and its metabolites were quantified in both the vascular (**upper plots**) and neuronal (**lower plots**) eluate media samples. These samples were obtained at lengthening durations of exposure to 10 μM CPF within the NVU. The limit of quantitation (LOQ) was determined from serial dilutions of a TCP standard. An internal standard, DtBP, was used to calibrate instrument response during each sample injection.

CONCLUSION

This study demonstrates the potential of the NVU and the power of electrochemistry and MS as a predictive platform for organophosphate toxicology. CPF's role in society at the intersection of food security and environmental policy in addition to its potential hazard to human health makes understanding its effects critical. When environmental exposure was simulated by challenging the vascular side of the NVU with CPF, neither the pesticide nor any of its metabolites were observed to cross the engineered BBB until the CPF concentration rose to 30 μM. Interestingly, neither CPF nor its active oxon form, CPO, was detected in any of the samples, whereas the inactive metabolites, TCP and DETP, were detected. Although CPF metabolism was observed, a majority of CPF was unaccounted for, suggesting that the analysis may need to be expanded past the NVU eluate. Regardless of the fate of CPF, the treatments were found to cause significant disruption of acetylcholine metabolism at and across the BBB, providing chemical evidence of the substantial disruption induced by this widely used commercial pesticide. These results support previous studies showing that organotypic cultures and their respective analytical platforms enable the identification of primary and secondary mechanisms of action across the BBB. These data validate the predictive power of the NVU and the utility of electrochemistry and MS in identifying chemical exposure events while providing chemical evidence of the substantial disruption in acetylcholine metabolism induced by this widely used commercial pesticide.

DATA AVAILABILITY STATEMENT

The original contributions presented in the study are included in the article/**Supplementary Material**; further inquiries can be directed to the corresponding author.

AUTHOR CONTRIBUTIONS

DM contributed to the experimental design, executed experiments, analyzed data, and wrote the manuscript. JCM and EM analyzed data, prepared figures, and wrote the manuscript. AB prepared figures and executed experiments. JAB and JD executed experiments. JAM and DC contributed to the experimental design and wrote the manuscript.

FUNDING

This work was supported in part by IARPA grant number 2017-17081500003 and used the resources of the Vanderbilt Microfabrication Core operated by the Vanderbilt Institute for Integrative Biosystems Research and Education (VIIBRE) as well as resources of the Center for Innovative Technology (CIT) at Vanderbilt University.

ACKNOWLEDGMENTS

The authors thank John P. Wikswo, Jacquelyn A. Brown, and David Schaffer for their expertise, microscopic images, and NVU schematics, BethAnn McLaughlin and Amy Palubinksy for providing the primary neurons and investigating their acetylcholinesterase expression and response to CPF, Simona G. Codreanu for preparing media samples for MS analysis, and Stacy D. Sherrod for reviewing experimental results.

SUPPLEMENTARY MATERIAL

The Supplementary Material for this article can be found online at: https://www.frontiersin.org/articles/10.3389/fbioe.2021.622175/full#supplementary-material

REFERENCES

Adriani, G., Ma, D., Pavesi, A., Kamm, R. D., and Goh, E. L. K. (2017). A 3D Neurovascular Microfluidic Model Consisting of Neurons, Astrocytes and Cerebral Endothelial Cells As a Blood-Brain Barrier. *Lab. Chip* 17 (3), 448–459. doi:10.1039/c6lc00638h

Allt, G., and Lawrenson, J. G. (2001). Pericytes: Cell Biology and Pathology. *Cells Tissues Organs* 169, 1–11. doi:10.1159/000047855

Amin, H., Maccione, A., Marinaro, F., Zordan, S., Nieus, T., and Berdondini, L. (2016). Electrical Responses and Spontaneous Activity of Human IPS-Derived Neuronal Networks Characterized for 3-Month Culture with 4096-Electrode Arrays. *Front. Neurosci.* 10, 121. doi:10.3389/fnins.2016.00121

Andersen, M. E. (2014). Developing Microphysiological Systems for Use as Regulatory Tools - Challenges and Opportunities. *ALTEX* 31 (3), 364–367. doi:10.14573/altex.1405151

Araci, I. E., and Quake, S. R. (2012). Microfluidic Very Large Scale Integration (MVLSI) with Integrated Micromechanical Valves. *Lab. Chip* 12 (16), 2803–2806. doi:10.1039/c2lc40258k

Atabila, A., Phung, D. T., Sadler, R., Connell, D., and Chu, C. (2019). Comparative Evaluation of Chlorpyrifos Exposure Estimates from Whole-Body Dermal Dosimetry and Urinary Trichloro-2-Pyridinol (TCP) Methods. *Ecotoxicology Environ. Saf.* 172, 439–443. doi:10.1016/J.ECOENV.2019.01.077

Auner, A. W., Tasneem, K. M., Markov, D. A., McCawley, L. J., and Hutson, M. S. (2019). Chemical-PDMS Binding Kinetics and Implications for Bioavailability in Microfluidic Devices. *Lab. Chip* 19 (5), 864–874. doi:10.1039/c8lc00796a

Balaji, V., Castro, K., and Folch, A. (2018). A Laser-Engraving Technique for Portable Micropneumatic Oscillators. *Micromachines* 9 (9), 426. doi:10.3390/mi9090426

Balbuena, P., Li, W., Magnin-Bissel, G., Meldrum, J. B., and Ehrich, M. (2010). Comparison of Two Blood-Brain Barrier *In Vitro* Systems: Cytotoxicity and Transfer Assessments of Malathion/Oxon and Lead Acetate. *Toxicol. Sci.* 114 (2), 260–271. doi:10.1093/toxsci/kfq001

Banerjee, J., Shi, Y., and Azevedo, H. S. (2016). *In Vitro* blood-brain Barrier Models for Drug Research: State-Of-The-Art and New Perspectives on Reconstituting These Models on Artificial Basement Membrane Platforms. *Drug Discov. Today* 21, 1367–1386. Elsevier Ltd September 1. doi:10.1016/j.drudis.2016.05.020

Bang, S., Lee, S.-R., Ko, J., Son, K., Tahk, D., Ahn, J., et al. (2017). A Low Permeability Microfluidic Blood-Brain Barrier Platform with Direct Contact between Perfusable Vascular Network and Astrocytes. *Sci. Rep.* 7 (1), 1–10. doi:10.1038/s41598-017-07416-0

Booth, R., and Kim, H. (2012). Characterization of a Microfluidic *In Vitro* Model of the Blood-Brain Barrier (μBBB). *Lab. Chip* 12 (10), 1784–1792. doi:10.1039/c2lc40094d

Brown, J. A., Codreanu, S. G., Shi, M., Sherrod, S. D., Markov, D. A., Neely, M. D., et al. (2016). Metabolic Consequences of Inflammatory Disruption of the Blood-Brain Barrier in an Organ-On-Chip Model of the Human Neurovascular Unit. *J. Neuroinflammation* 13 (1), 306. doi:10.1186/s12974-016-0760-y

Brown, J. A., Pensabene, V., Markov, D. A., Allwardt, V., Neely, M. D., Shi, M., et al. (2015). Recreating Blood-Brain Barrier Physiology and Structure on Chip: A Novel Neurovascular Microfluidic Bioreactor. *Biomicrofluidics* 9 (5), 054124. doi:10.1063/1.4934713

Bruner-Tran, K. L., Gnecco, J., Ding, T., Glore, D. R., Pensabene, V., and Osteen, K. G. (2017). Exposure to the Environmental Endocrine Disruptor TCDD and Human Reproductive Dysfunction: Translating Lessons from Murine Models. *Reprod. Toxicol.* 68, 59–71. doi:10.1016/j.reprotox.2016.07.007

Campisi, M., Shin, Y., Osaki, T., Hajal, C., Chiono, V., and Kamm, R. D. (2018). 3D Self-Organized Microvascular Model of the Human Blood-Brain Barrier with Endothelial Cells, Pericytes and Astrocytes. *Biomaterials* 180, 117–129. doi:10.1016/j.biomaterials.2018.07.014

Carlson, K., Jortner, B. S., and Ehrich, M. (2000). Organophosphorus Compound-Induced Apoptosis in SH-Sy5y Human Neuroblastoma Cells. *Toxicol. Appl. Pharmacol.* 168 (2), 102–113. doi:10.1006/taap.2000.8997

National Pesticide Information Center (2019). Chlorpyrifos Technical Fact Sheet. Available at: http://npic.orst.edu/factsheets/archive/chlorptech.html (Accessed Dec 18, 2019).

Cucullo, L., Marchi, N., Hossain, M., and Janigro, D. (2011). A Dynamic *In Vitro* BBB Model for the Study of Immune Cell Trafficking into the Central Nervous System. *J. Cereb. Blood Flow Metab.* 31 (2), 767–777. doi:10.1038/jcbfm.2010.162

Daneman, R., and Prat, A. (2015). The Blood-Brain Barrier. *Cold Spring Harb. Perspect. Biol.* 7 (1), a020412. doi:10.1101/cshperspect.a020412

Dauchy, S., Dutheil, F., Weaver, R. J., Chassoux, F., Daumas-Duport, C., Couraud, P.-O., et al. (2008). ABC Transporters, Cytochromes P450 and Their Main Transcription Factors: Expression at the Human Blood-Brain Barrier. *J. Neurochem.* 107 (6), 1518–1528. doi:10.1111/j.1471-4159.2008.05720.x

DiMasi, J. A., Grabowski, H. G., and Hansen, R. W. (2016). Innovation in the Pharmaceutical Industry: New Estimates of R&D Costs. *J. Health Econ.* 47, 20–33. doi:10.1016/j.jhealeco.2016.01.012

Dingle, Y.-T. L., Boutin, M. E., Chirila, A. M., Livi, L. L., Labriola, N. R., Jakubek, L. M., et al. (2015). Three-Dimensional Neural Spheroid Culture: AnIn VitroModel for Cortical Studies. *Tissue Eng. C: Methods* 21 (12), 1274–1283. doi:10.1089/ten.tec.2015.0135

Fennema, E., Rivron, N., Rouwkema, J., Van Blitterswijk, C., and De Boer, J. (2013). Spheroid Culture as a Tool for Creating 3D Complex Tissues. *Trends Biotechnol.* 31, 108–115. doi:10.1016/j.tibtech.2012.12.003

Fernandes, J. T. S., Chutna, O., Chu, V., Conde, J. P., and Outeiro, T. F. (2016). A Novel Microfluidic Cell Co-culture Platform for the Study of the Molecular Mechanisms of Parkinson's Disease and Other Synucleinopathies. *Front. Neurosci.* 10, 511. doi:10.3389/fnins.2016.00511

Ghosh, C., Gonzalez-Martinez, J., Hossain, M., Cucullo, L., Fazio, V., Janigro, D., et al. (2010). Pattern of P450 Expression at the Human Blood-Brain Barrier: Roles of Epileptic Condition and Laminar Flow. *Epilepsia* 51 (8), 1408–1417. doi:10.1111/j.1528-1167.2009.02428.x

Grebenyuk, S., and Ranga, A. (2019). Engineering Organoid Vascularization. *Front. Bioeng. Biotechnol.* 7, 39. doi:10.3389/fbioe.2019.00039

Griep, L. M., Wolbers, F., de Wagenaar, B., ter Braak, P. M., Weksler, B. B., Romero, I. A., et al. (2013). BBB on CHIP: Microfluidic Platform to Mechanically and Biochemically Modulate Blood-Brain Barrier Function. *Biomed. Microdevices* 15 (1), 145–150. doi:10.1007/s10544-012-9699-7

Hamilton, N. B. (2010). Pericyte-Mediated Regulation of Capillary Diameter: A Component of Neurovascular Coupling in Health and Disease. *Front. Neuroenerg.* 2, 5. doi:10.3389/fnene.2010.00005

Hasan, M., and Berdichevsky, Y. (2016). Neural Circuits on a Chip. *Micromachines* 7, 157. doi:10.3390/mi7090157

Helms, H. C., Abbott, N. J., Burek, M., Cecchelli, R., Couraud, P.-O., Deli, M. A., et al. (2016). *In Vitro* models of the Blood-Brain Barrier: An Overview of Commonly Used Brain Endothelial Cell Culture Models and Guidelines for Their Use. *J. Cereb. Blood Flow Metab.* 36 (5), 862–890. doi:10.1177/0271678X16630991

Helms, H. C., and Brodin, B. (2014). Generation of Primary Cultures of Bovine Brain Endothelial Cells and Setup of Cocultures with Rat Astrocytes. *Methods Mol. Biol.* 1135, 365–382. doi:10.1007/978-1-4939-0320-7_30

Herculano-Houzel, S. (2009). The Human Brain in Numbers: A Linearly Scaled-Up Primate Brain. *Front. Hum. Neurosci.* 3, 31. doi:10.3389/neuro.09.031.2009

Hopkins, A. M., DeSimone, E., Chwalek, K., and Kaplan, D. L. (2015). 3D *In Vitro* Modeling of the Central Nervous System. *Prog. Neurobiol.* 125, 1–25. Elsevier Ltd February 1. doi:10.1016/j.pneurobio.2014.11.003

Huang, R., Grishagin, I., Wang, Y., Zhao, T., Greene, J., Obenauer, J. C., et al. (2019). The NCATS BioPlanet - an Integrated Platform for Exploring the Universe of Cellular Signaling Pathways for Toxicology, Systems Biology, and Chemical Genomics. *Front. Pharmacol.* 10, 445. doi:10.3389/fphar.2019.00445

Hutson, M. S., Alexander, P. G., Allwardt, V., Aronoff, D. M., Bruner-Tran, K. L., Cliffel, D. E., et al. (2016). Organs-on-Chips as Bridges for Predictive Toxicology. *Appl. Vitro Toxicol.* 2 (2), 97–102. doi:10.1089/aivt.2016.0003

Jeong, G. S., Chang, J. Y., Park, J. S., Lee, S.-A., Park, D., Woo, J., et al. (2015). Networked Neural Spheroid by Neuro-Bundle Mimicking Nervous System Created by Topology Effect. *Mol. Brain* 8, 17. doi:10.1186/s13041-015-0109-y

Karanth, S., Liu, J., Mirajkar, N., and Pope, C. (2006). Effects of Acute Chlorpyrifos Exposure on *In Vivo* Acetylcholine Accumulation in Rat Striatum. *Toxicol. Appl. Pharmacol.* 216 (1), 150–156. doi:10.1016/J.TAAP.2006.04.006

Kashyap, M. P., Singh, A. K., Kumar, V., Tripathi, V. K., Srivastava, R. K., Agrawal, M., et al. (2011). Monocrotophos Induced Apoptosis in PC12 Cells: Role of Xenobiotic Metabolizing Cytochrome P450S. *PLoS One* 6 (3), e17757. doi:10.1371/journal.pone.0017757

Kashyap, M. P., Singh, A. K., Kumar, V., Yadav, D. K., Khan, F., Jahan, S., et al. (2013). Pkb/Akt1 Mediates Wnt/GSK3β/β-Catenin Signaling-Induced Apoptosis in Human Cord Blood Stem Cells Exposed to Organophosphate Pesticide Monocrotophos. *Stem Cell Develop.* 22 (2), 224–238. doi:10.1089/scd.2012.0220

Kashyap, M. P., Singh, A. K., Siddiqui, M. A., Kumar, V., Tripathi, V. K., Khanna, V. K., et al. (2010). Caspase Cascade Regulated Mitochondria Mediated Apoptosis in Monocrotophos Exposed PC12 Cells. *Chem. Res. Toxicol.* 23 (11), 1663–1672. doi:10.1021/tx100234m

Kilic, O., Pamies, D., Lavell, E., Schiapparelli, P., Feng, Y., Hartung, T., et al. (2016). Brain-on-a-Chip Model Enables Analysis of Human Neuronal Differentiation and Chemotaxis. *Lab. Chip* 16 (21), 4152–4162. doi:10.1039/c6lc00946h

Koo, Y., Hawkins, B. T., and Yun, Y. (2018). Three-Dimensional (3D) Tetra-Culture Brain on Chip Platform for Organophosphate Toxicity Screening. *Sci. Rep.* 8 (1), 1–7. doi:10.1038/s41598-018-20876-2

Lancaster, M. A., Renner, M., Martin, C.-A., Wenzel, D., Bicknell, L. S., Hurles, M. E., et al. (2013). Cerebral Organoids Model Human Brain Development and Microcephaly. *Nature* 501 (7467), 373–379. doi:10.1038/nature12517

Levin, E. D., Addy, N., Nakajima, A., Christopher, N. C., Seidler, F. J., and Slotkin, T. A. (2001). Persistent Behavioral Consequences of Neonatal Chlorpyrifos Exposure in Rats. *Develop. Brain Res.* 130 (1), 83–89. doi:10.1016/S0165-3806(01)00215-2

Li, W., and Ehrich, M. (2013). Transient Alterations of the Blood-Brain Barrier Tight Junction and Receptor Potential Channel Gene Expression by Chlorpyrifos. *J. Appl. Toxicol.* 33 (10), 1187–1191. doi:10.1002/jat.2762

Liu, L., Koo, Y., Russell, T., Gay, E., Li, Y., and Yun, Y. (2020). Three-dimensional Brain-On-Chip Model Using Human iPSC-Derived GABAergic Neurons and Astrocytes: Butyrylcholinesterase post-treatment for Acute Malathion Exposure. *PLoS One* 15 (3), e0230335. doi:10.1371/journal.pone.0230335

Lizama, B. N., Palubinsky, A. M., Raveendran, V. A., Moore, A. M., Federspiel, J. D., Codreanu, S. G., et al. (2018). Neuronal Preconditioning Requires the Mitophagic Activity of C-Terminus of HSC70-Interacting Protein. *J. Neurosci.* 38 (31), 6825–6840. doi:10.1523/JNEUROSCI.0699-18.2018

Low, L. A., Mummery, C., Berridge, B. R., Austin, C. P., and Tagle, D. A. (2021). Organs-on-Chips: Into the Next Decade. *Nat. Rev. Drug Discovnature Res. May* 20, 345–361. doi:10.1038/s41573-020-0079-3

Lowe, E. R., Poet, T. S., Rick, D. L., Marty, M. S., Mattsson, J. L., Timchalk, C., et al. (2009). The Effect of Plasma Lipids on the Pharmacokinetics of Chlorpyrifos and the Impact on Interpretation of Blood Biomonitoring Data. *Toxicol. Sci.* 108 (2), 258–272. doi:10.1093/toxsci/kfp034

Lozano, R., Stevens, L., Thompson, B. C., Gilmore, K. J., Gorkin, R., Stewart, E. M., et al. (2015). 3D Printing of Layered Brain-like Structures Using Peptide Modified Gellan Gum Substrates. *Biomaterials* 67, 264–273. doi:10.1016/j.biomaterials.2015.07.022; in

Maoz, B. M., Herland, A., FitzGerald, E. A., Grevesse, T., Vidoudez, C., Pacheco, A. R., et al. (2018). A Linked Organ-On-Chip Model of the Human Neurovascular Unit Reveals the Metabolic Coupling of Endothelial and Neuronal Cells. *Nat. Biotechnol.* 36 (9), 865–874. doi:10.1038/nbt.4226

Marín-Padilla, M. (2012). The Human Brain Intracerebral Microvascular System: Development and Structure. *Front. Neuroanat.* 6, 1–14. doi:10.3389/fnana.2012.00038

May, J. C., Gant-Branum, R. L., and McLean, J. A. (2016). Targeting the Untargeted in Molecular Phenomics with Structurally-Selective Ion Mobility-Mass Spectrometry. *Curr. Opin. Biotechnol.* 39, 192–197. doi:10.1016/j.copbio.2016.04.013

May, J. C., Goodwin, C. R., and McLean, J. A. (2015). Ion Mobility-Mass Spectrometry Strategies for Untargeted Systems, Synthetic, and Chemical Biology. *Curr. Opin. Biotechnol.* 31, 117–121. doi:10.1016/j.copbio.2014.10.012

McClain, E. S., Miller, D. R., and Cliffel, D. E. (2019). Communication—Microfluidic Electrochemical Acetylcholine Detection in the Presence of Chlorpyrifos. *J. Electrochem. Soc.* 166 (16), 178–181. doi:10.1149/2.0711916jes

McCracken, K. W., Catá, E. M., Crawford, C. M., Sinagoga, K. L., Schumacher, M., Rockich, B. E., et al. (2014). Modelling Human Development and Disease in Pluripotent Stem-Cell-Derived Gastric Organoids. *Nature* 516 (7531), 400–404. doi:10.1038/nature13863

McKenzie, J. R., Cognata, A. C., Davis, A. N., Wikswo, J. P., and Cliffel, D. E. (2015). Real-Time Monitoring of Cellular Bioenergetics with a Multianalyte Screen-Printed Electrode. *Anal. Chem.* 87 (15), 7857–7864. doi:10.1021/acs.analchem.5b01533

McKenzie, J. R., Palubinsky, A. M., Brown, J. E., McLaughlin, B., and Cliffel, D. E. (2012). Metabolic Multianalyte Microphysiometry Reveals Extracellular Acidosis Is an Essential Mediator of Neuronal Preconditioning. *ACS Chem. Neurosci.* 3 (7), 510–518. doi:10.1021/cn300003r

Middlemore-Risher, M.-L., Adam, B.-L., Lambert, N. A., and Terry, A. V. (2011). Effects of Chlorpyrifos and Chlorpyrifos-Oxon on the Dynamics and Movement of Mitochondria in Rat Cortical Neurons. *J. Pharmacol. Exp. Ther.* 339 (2), 341–349. doi:10.1124/jpet.111.184762

Mileson, B. E., Chambers, J. E., Chen, W. L., Dettbarn, W., Ehrich, M., Eldefrawi, A. T., et al. (1998). Common Mechanism of Toxicity: A Case Study of Organophosphorus Pesticides. *Toxicol. Sci.* 41 (1), 8–20. doi:10.1006/toxs.1997.243110.1093/toxsci/41.1.8

Miller, D. R., McClain, E. S., and Cliffel, D. E. (2018). Electrochemical Microphysiometry Detects Cellular Glutamate Uptake. *J. Electrochem. Soc.* 165 (12), G3120–G3124. doi:10.1149/2.0201812jes

Mohammed, M. I., Haswell, S., and Gibson, I. (2015). Lab-On-A-Chip or Chip-In-A-Lab: Challenges of Commercialization Lost in Translation. *Proced. Technol.* 20, 54–59. doi:10.1016/J.PROTCY.2015.07.010

Moore, P. D., Yedjou, C. G., and Tchounwou, P. B. (2010). Malathion-Induced Oxidative Stress, Cytotoxicity, and Genotoxicity in Human Liver Carcinoma (HepG2) Cells. *Environ. Toxicol.* 25 (3), 221–226. doi:10.1002/tox.20492

Moreno, C. L., Della Guardia, L., Shnyder, V., Ortiz-Virumbrales, M., Kruglikov, I., Zhang, B., et al. (2018). iPSC-derived Familial Alzheimer's PSEN2 N141I Cholinergic Neurons Exhibit Mutation-dependent Molecular Pathology Corrected by Insulin Signaling. *Mol. Neurodegeneration* 13 (1), 33. doi:10.1186/s13024-018-0265-5

Nolan, R. J., Rick, D. L., Freshour, N. L., and Saunders, J. H. (1984). Chlorpyrifos: Pharmacokinetics in Human Volunteers. *Toxicol. Appl. Pharmacol.* 73 (1), 8–15. doi:10.1016/0041-008X(84)90046-2

Ortiz-Virumbrales, M., Moreno, C. L., Kruglikov, I., Marazuela, P., Sproul, A., Jacob, S., et al. (2017). CRISPR/Cas9-Correctable Mutation-Related Molecular and Physiological Phenotypes in iPSC-Derived Alzheimer's PSEN2 N141I Neurons. *Acta Neuropathol. Commun.* 5 (1). doi:10.1186/s40478-017-0475-z

Park, J. H., Ko, J., Hwang, J., and Koh, H. C. (2015a). Dynamin-Related Protein 1 Mediates Mitochondria-Dependent Apoptosis in Chlorpyrifos-Treated SH-Sy5y Cells. *Neurotoxicology* 51, 145–157. doi:10.1016/j.neuro.2015.10.008

Park, J., Lee, B. K., Jeong, G. S., Hyun, J. K., Lee, C. J., and Lee, S.-H. (2015b). Three-dimensional Brain-On-A-Chip with an Interstitial Level of Flow and its Application as an *In Vitro* Model of Alzheimer's Disease. *Lab. Chip* 15 (1), 141–150. doi:10.1039/c4lc00962b

Parran, D. K., Magnin, G., Li, W., Jortner, B. S., and Ehrich, M. (2005). Chlorpyrifos Alters Functional Integrity and Structure of an *In Vitro* BBB Model: Co-Cultures of Bovine Endothelial Cells and Neonatal Rat Astrocytes. *Neurotoxicology* 26 (1), 77–88. doi:10.1016/j.neuro.2004.07.003

Pas, S. P. (2018). The Rise of Three-Dimensional Human Brain Cultures. *Nature* 24, 437–445. doi:10.1038/nature25032

Paşca, A. M., Sloan, S. A., Clarke, L. E., Tian, Y., Makinson, C. D., Huber, N., et al. (2015). Functional Cortical Neurons and Astrocytes from Human Pluripotent Stem Cells in 3D Culture. *Nat. Methods* 12 (7), 671–678. doi:10.1038/nmeth.3415

Phan, D. T., Bender, R. H. F., Andrejecsk, J. W., Sobrino, A., Hachey, S. J., George, S. C., et al. (2017). Blood-brain Barrier-On-A-Chip: Microphysiological Systems that Capture the Complexity of the Blood-central Nervous System Interface. *Exp. Biol. Med. (Maywood)* 242 (17), 1669–1678. doi:10.1177/1535370217694100

Pimentel, E., Sivalingam, K., Doke, M., and Samikkannu, T. (2020). Effects of Drugs of Abuse on the Blood-Brain Barrier: A Brief Overview. *Front. Neurosci.* 14, 513. doi:10.3389/fnins.2020.00513

Prabhakarpandian, B., Shen, M.-C., Nichols, J. B., Mills, I. R., Sidoryk-Wegrzynowicz, M., Aschner, M., et al. (2013). SyM-BBB: A Microfluidic Blood Brain Barrier Model. *Lab. Chip* 13 (6), 1093. doi:10.1039/c2lc41208j

Prendergast, M. A., Terry, A. V., and Buccafusco, J. J. (1998). Effects of Chronic, Low-Level Organophosphate Exposure on Delayed Recall, Discrimination, and Spatial Learning in Monkeys and Rats. *Neurotoxicology and Teratology* 20 (2), 115–122. doi:10.1016/S0892-0362(97)00098-6

Pridgeon, C. S., Schlott, C., Wong, M. W., Heringa, M. B., Heckel, T., Leedale, J., et al. (2018). Innovative Organotypic *In Vitro* Models for Safety Assessment: Aligning with Regulatory Requirements and Understanding Models of the Heart, Skin, and Liver as Paradigms. *Arch. Toxicol.* 92, 557–569. doi:10.1007/s00204-018-2152-9

Raimondi, I., Izzo, L., Tunesi, M., Comar, M., Albani, D., and Giordano, C. (2020). Organ-On-A-Chip *In Vitro* Models of the Brain and the Blood-Brain Barrier and Their Value to Study the Microbiota-Gut-Brain Axis in Neurodegeneration. *Front. Bioeng. Biotechnol.* 7, 435. doi:10.3389/fbioe.2019.00435

Rauh, V. A., Perera, F. P., Horton, M. K., Whyatt, R. M., Bansal, R., Hao, X., et al. (2012). Brain Anomalies in Children Exposed Prenatally to a Common Organophosphate Pesticide. *Proc. Natl. Acad. Sci.* 109 (20), 7871–7876. doi:10.1073/pnas.1203396109

Rauh, V., Arunajadai, S., Horton, M., Perera, F., Hoepner, L., Barr, D. B., et al. (2011). Seven-Year Neurodevelopmental Scores and Prenatal Exposure to Chlorpyrifos, a Common Agricultural Pesticide. *Environ. Health Perspect.* 119 (8), 1196–1201. doi:10.1289/ehp.1003160

Saulsbury, M. D., Heyliger, S. O., Wang, K., and Johnson, D. J. (2009). Chlorpyrifos Induces Oxidative Stress in Oligodendrocyte Progenitor Cells. *Toxicology* 259 (1–2), 1–9. doi:10.1016/J.TOX.2008.12.026

Schadt, E. E., Buchanan, S., Brennand, K. J., and Merchant, K. M. (2014). Evolving toward a Human-Cell Based and Multiscale Approach to Drug Discovery for CNS Disorders. *Front. Pharmacol.* 5, 252. doi:10.3389/fphar.2014.00252

Shamir, E. R., and Ewald, A. J. (2014). Three-Dimensional Organotypic Culture: Experimental Models of Mammalian Biology and Disease. *Nat. Rev. Mol. Cel Biol* 15, 647–664. Nature Publishing Group January. doi:10.1038/nrm3873

Sherrod, S. D., and McLean, J. A. (2016). Systems-Wide High-Dimensional Data Acquisition and Informatics Using Structural Mass Spectrometry Strategies. *Clin. Chem.* 62 (1), 77–83. doi:10.1373/clinchem.2015.238261

Slotkin, T. A. (2011). Does Early-Life Exposure to Organophosphate Insecticides Lead to Prediabetes and Obesity? *Reprod. Toxicol.* 31 (3), 297–301. doi:10.1016/j.reprotox.2010.07.012

Smith, J. N., Carver, Z. A., Weber, T. J., and Timchalk, C. (2017). Predicting Transport of 3,5,6-Trichloro-2-Pyridinol into Saliva Using a Combination Experimental and Computational Approach. *Toxicol. Sci.* 157 (2), 438–450. doi:10.1093/toxsci/kfx055

Smith, J. N., Hinderliter, P. M., Timchalk, C., Bartels, M. J., and Poet, T. S. (2014). A Human Life-Stage Physiologically Based Pharmacokinetic and Pharmacodynamic Model for Chlorpyrifos: Development and Validation. *Regul. Toxicol. Pharmacol.* 69 (3), 580–597. doi:10.1016/j.yrtph.2013.10.005

Smith, J. N., Wang, J., Lin, Y., Klohe, E. M., and Timchalk, C. (2012). Pharmacokinetics and Pharmacodynamics of Chlorpyrifos and 3,5,6-Trichloro-2-Pyridinol in Rat Saliva after Chlorpyrifos Administration. *Toxicol. Sci.* 130 (2), 245–256. doi:10.1093/toxsci/kfs251

Soscia, D., Belle, A., Fischer, N., Enright, H., Sales, A., Osburn, J., et al. (2017). Controlled Placement of Multiple CNS Cell Populations to Create Complex Neuronal Cultures. *PLoS One* 12 (11), e0188146. doi:10.1371/journal.pone.0188146

Sultatos, L. G. (1994). Mammalian Toxicology of Organophosphorus Pesticides. *J. Toxicol. Environ. Health* 43 (3), 271–289. doi:10.1080/15287399409531921

Takayama, S., McDonald, J. C., Ostuni, E., Liang, M. N., Kenis, P. J. A., Ismagilov, R. F., et al. (1999). Patterning Cells and Their Environments Using Multiple Laminar Fluid Flows in Capillary Networks. *Proc. Natl. Acad. Sci.* 96 (10), 5545–5548. doi:10.1073/pnas.96.10.5545

Tang, J., Rose, R. L., and Chambers, J. E. (2006). "Metabolism of Organophosphorus and Carbamate Pesticides," in *Toxicology of Organophosphate & Carbamate Compounds* (Redmond, Washington: Elsevier), 127–143. doi:10.1016/B978-012088523-7/50011-9

Tang-Schomer, M. D., White, J. D., Tien, L. W., Schmitt, L. I., Valentin, T. M., Graziano, D. J., et al. (2014). Bioengineered Functional Brain-like Cortical Tissue. *Proc. Natl. Acad. Sci.* 111 (38), 13811–13816. doi:10.1073/pnas.1324214111

Taylor, P., and Brown, J. (1999). *Basic Neurochemistry: Synthesis, Storage and Release of Acetylcholine*, 6th ed. Editor-in-Chief G J. Siegel, B. W. Agranoff, R. W. Albers, S. K. Fisher, and M. D. Uhler. Philidelphia, PA: Lippincott-Raven.

Theobald, J., Ghanem, A., Wallisch, P., Banaeiyan, A. A., Andrade-Navarro, M. A., Taškova, K., et al. (2018). Liver-Kidney-on-Chip to Study Toxicity of Drug Metabolites. *ACS Biomater. Sci. Eng.* 4 (1), 78–89. doi:10.1021/acsbiomaterials.7b00417

Timchalk, C., Poet, T. S., Hinman, M. N., Busby, A. L., and Kousba, A. A. (2005). Pharmacokinetic and Pharmacodynamic Interaction for a Binary Mixture of Chlorpyrifos and Diazinon in the Rat. *Toxicol. Appl. Pharmacol.* 205 (1), 31–42. doi:10.1016/J.TAAP.2004.09.004

Vernetti, L., Gough, A., Baetz, N., Blutt, S., Broughman, J. R., Brown, J. A., et al. (2017). Functional Coupling of Human Microphysiology Systems: Intestine, Liver, Kidney Proximal Tubule, Blood-Brain Barrier and Skeletal Muscle. *Sci. Rep.* 7, 42296. doi:10.1038/srep42296

Volpatti, L. R., and Yetisen, A. K. (2014). Commercialization of Microfluidic Devices. *Trends Biotechnol.* 32 (7), 347–350. doi:10.1016/J.TIBTECH.2014.04.010

Voorhees, J. R., Rohlman, D. S., Lein, P. J., and Pieper, A. A. (2017). Neurotoxicity in Preclinical Models of Occupational Exposure to Organophosphorus Compounds. *Front. Neurosci.* 10, 590. doi:10.3389/fnins.2016.00590

Wang, Y. I., Abaci, H. E., and Shuler, M. L. (2017). Microfluidic Blood-Brain Barrier Model Provides In Vivo-like Barrier Properties for Drug Permeability Screening. *Biotechnol. Bioeng.* 114 (1), 184–194. doi:10.1002/bit.26045

Wang, Y., Wang, L., Zhu, Y., and Qin, J. (2018). Human Brain Organoid-On-A-Chip to Model Prenatal Nicotine Exposure. *Lab. Chip* 18 (6), 851–860. doi:10.1039/c7lc01084b

Yang, J., Mutkus, L. A., Sumner, D., Stevens, J. T., Eldridge, J. C., Strandhoy, J. W., et al. (2001). Transendothelial Permeability of Chlorpyrifos in RBE4 Monolayers Is Modulated by Astrocyte-Conditioned Medium. *Mol. Brain Res.* 97 (1), 43–50. doi:10.1016/S0169-328X(01)00296-0

Zhang, Y. S., Aleman, J., Shin, S. R., Kilic, T., Kim, D., Mousavi Shaegh, S. A., et al. (2017). Multisensor-Integrated Organs-On-Chips Platform for Automated and Continual *In Situ* Monitoring of Organoid Behaviors. *Proc. Natl. Acad. Sci. USA* 114 (12), E2293–E2302. doi:10.1073/pnas.1612906114

Zhuang, P., Sun, A. X., An, J., Chua, C. K., and Chew, S. Y. (2018). 3D Neural Tissue Models: From Spheroids to Bioprinting. *Biomaterials* 154, 113–133. doi:10.1016/j.biomaterials.2017.10.002

Author Disclaimer: The views expressed in this document are solely those of the authors and do not necessarily reflect those of IARPA or the United States Government.

Conflict of Interest: The authors declare that the research was conducted in the absence of any commercial or financial relationships that could be construed as a potential conflict of interest.

Publisher's Note: All claims expressed in this article are solely those of the authors and do not necessarily represent those of their affiliated organizations, or those of the publisher, the editors and the reviewers. Any product that may be evaluated in this article, or claim that may be made by its manufacturer, is not guaranteed or endorsed by the publisher.

Advantages of publishing in Frontiers

OPEN ACCESS
Articles are free to read for greatest visibility and readership

FAST PUBLICATION
Around 90 days from submission to decision

HIGH QUALITY PEER-REVIEW
Rigorous, collaborative, and constructive peer-review

TRANSPARENT PEER-REVIEW
Editors and reviewers acknowledged by name on published articles

Frontiers
Avenue du Tribunal-Fédéral 34
1005 Lausanne | Switzerland

Visit us: www.frontiersin.org
Contact us: frontiersin.org/about/contact

REPRODUCIBILITY OF RESEARCH
Support open data and methods to enhance research reproducibility

DIGITAL PUBLISHING
Articles designed for optimal readership across devices

FOLLOW US
@frontiersin

IMPACT METRICS
Advanced article metrics track visibility across digital media

EXTENSIVE PROMOTION
Marketing and promotion of impactful research

LOOP RESEARCH NETWORK
Our network increases your article's readership